A COMBINED EXPERIMENTAL AND COMPUTATIONAL APPROACH TO STUDY THE BIOLOGIC EFFECT OF HEMODYNAMICS IN END-TO-SIDE VASCULAR BYPASS GRAFTS

by

Stephanie Michelle Kute

B.S.E., Tulane University, 1995

M.S.E., Tulane University, 1996

Submitted to the Graduate Faculty of

The School of Engineering in partial fulfillment

of the requirements for the degree of

Doctor of Philosophy

University of Pittsburgh

2002

UNIVERSITY OF PITTSBURGH SCHOOL OF ENGINEERING

This dissertation was presented by

Stephanie Michelle Kute

It was defended on

July 17, 2002

and approved by

David A. Vorp, Ph.D.

Harvey S. Borovetz, Ph.D.

Satish Muluk, M.D.

Anne Robertson, Ph.D.

William Wagner, Ph.D.

ABSTRACT

A COMBINED EXPERIMENTAL AND COMPUTATIONAL APPROACH TO STUDY THE BIOLOGIC EFFECT OF HEMODYNAMICS IN END-TO-SIDE VASCULAR BYPASS GRAFTS

Stephanie Michelle Kute, Ph.D.

University of Pittsburgh, 2002

A diseased artery often becomes blocked, compromising blood flow to downstream tissues and organs. One common surgical intervention is to bypass this blocked region with a vascular graft. However, these grafts can fail due to an overhealing response, known as intimal hyperplasia (IH), which occurs at the graft/artery junction (i.e., anastomosis). The goal of this research was to determine if a quantitative correlation exists between the hemodynamic phenomena at the distal anastomosis of a vascular bypass graft and carefully selected, acute biological precursors of intimal hyperplasia.

To accomplish this task, we perfused porcine, artery-artery, end-to-side and end-to-end anastomoses *ex vivo* and developed computational fluid dynamics (CFD) models incorporating the reconstructed geometry and perfusion conditions present in each experimental anastomosis. The perfusion experiments allowed us to assess the levels of immediate early gene (IEG) proteins and vascular cell apoptosis at various regions along the anastomoses. Since the pressure and flow rate in the *ex vivo* perfusion model were precisely

known, the CFD models utilized this information along with the 3D reconstructed anastomotic geometries to accurately estimate wall shear stress (WSS) and WSS gradient (WSSG) in the same regions of interest. This process allowed for a distinct and unique coupling between the perfusion experiments and the computational simulations that has not been achieved previously. Through linear and nonlinear regression analyses on this directly-coupled data, we found that low levels of WSS and WSSG cause upregulation of IEG proteins. Because increased levels of IEG expression lead to IH formation, our results suggest that low levels of WSS and WSSG correlate with increased IH formation.

Our coupled experimental and computational approach has allowed us to evaluate IEG protein expression by vascular cells in response to the hemodynamics present in vascular anastomoses. Based on the correlations we found between low levels of WSS and WSSG and the subsequent increase in IEG protein expression, treatments such as graft geometry optimization or targeted gene therapy may improve the clinical success rate of vascular bypass grafts. However, some issues need to be addressed before the results of this study can be applied clinically.

DESCRIPTORS

Shear Stress	C-fos
Computational Fluid Dynamics	C-jun
3D Reconstruction	Egr-1
Correlation	Apoptosis
Endothelial Cells	Smooth Muscle Cells

ACKNOWLEDGMENTS

I have independently pursued this research and sacrificed life and limb (almost) to complete this project. However, it would not have been possible without the assistance of many talented people around me. I greatly appreciate everyone who has helped me, on both a professional and personal level, and eagerly acknowledge some of them here.

First, I would like to thank my advisor, David Vorp, for his support throughout this process. He has helped me problem solve along the way and, more recently, has read countless pages and suggested key revisions that have made me proud to distribute this dissertation.

Sincere thanks to Harvey Borovetz, William Wagner, Satish Muluk and Anne Robertson for volunteering to be members of my committee. I appreciate their willingness to be part of this process and for their suggestions. Special thanks to Dr. Borovetz who not only helped me get involved with the Artificial Heart Program but also allowed me to be a Teaching Assistant for his Artificial Organs class. I still have nightmares.

There are many people that helped with the perfusion experiments. Thanks to the staff of Green Valley Packing Company - there are few people I know that could actually make getting out of bed at 4:30 in the morning and driving 45 miles to a slaughterhouse, agreeable. I appreciate the enthusiasm and energy of Wolff Kirsch who not only taught me how to use the vascular clips but invented them in the first place. Thanks to Rachelle Prantil and Ben Novak for all their help in setting up, running and breaking down the systems. We were a well-oiled machine last summer. I also acknowledge the help of Don Severyn who still knows more about the lab than anyone.

Determining the staining techniques was quite an involved process. Many thanks to Sue Gleixner who spent hours teaching an engineer (me) proper biologic techniques: from autoclaving and pipetting to the tissue factor functional assay. I appreciate the assistance of Deb Williams and Melina Kibbe from the Billiar lab and the staff at the Center for Biologic Imaging for helping me finally get a staining protocol that worked. Special thanks to Erin Pekarcik and Kelly Bratic for the countless hours they spent in the cold, dark "bat cave" doing microscopy. Also, in honor of the time they spent staring at a computer and counting cells, I am changing their middle names to "Bioquant".

For the computational aspect of this project, I acknowledge those from Tulane University who gave me a strong basis in computational modeling. Don Gaver not only taught me how to "code" but pushed me to achieve beyond my own expectations. Melissa Krueger is a UNIX (and all-around) guru and her technical instruction and friendship have helped me tremendously. I also thank Peter Moore who was the first person to put the idea of getting a Ph.D. into my head.

On a more personal level, I want to thank my friends and family that have supported me during this time. Kristie Henchir was always there to tell me a funny story and make me laugh. Thanks to the lunch crew that gave me a much needed break during the days of writing. Special thanks to my family - Mom, Dad, Jenny and Casey - who always knew I could do it: I am a Kute, afterall! The daily emails, knock knock jokes and interest in the details of my day-to-day life kept me going.

Most of all, I wish to thank Samir Ghadiali, my husband. Words could never express my deep gratitude. You not only cooked me dinner but double checked my shear stress derivations. You are the smartest man I know and the most loving. Thank you for everything. You are the love of my life.

Finally, I acknowledge the sources of funding that allowed me to pursue and complete my Ph.D. The National Science Foundation, American Heart Association and American Association of University Women, University of Pittsburgh Medical Center, University of Pittsburgh Department of Bioengineering and the Provost Development Fund all believed in my research enough to provide financial resources.

TABLE OF CONTENTS

LIST OF TABLES

LIST OF FIGURES

1 .0 INTRODUCTION

1.1 Vascular Grafts

A diseased artery often becomes blocked, compromising blood flow to downstream tissues and organs. One common surgical intervention is to bypass this blocked region with a vascular graft. These blockages are usually caused by the build-up of atherosclerotic plaque, which can occur anywhere in the arterial tree. The most frequently bypassed regions occur in the coronary and peripheral arterial networks. Coronary heart disease is the leading cause of death in the United States, accounting for more than 40% of all deaths [1]. Over 570,000 coronary artery bypass grafting (CABG) procedures (see Figure 1.1) were performed in 1999 and the total direct and indirect costs of coronary heart disease was estimated to be over $111 billion [1]. Peripheral arterial disease, usually involving the lower extremity, is less prevalent than coronary heart disease but still affects a large number of patients [2]. Approximately 12% of the adult population in the U.S., 8 to 10 million people, are affected by peripheral arterial disease and need bypass grafts to restore blood flow to

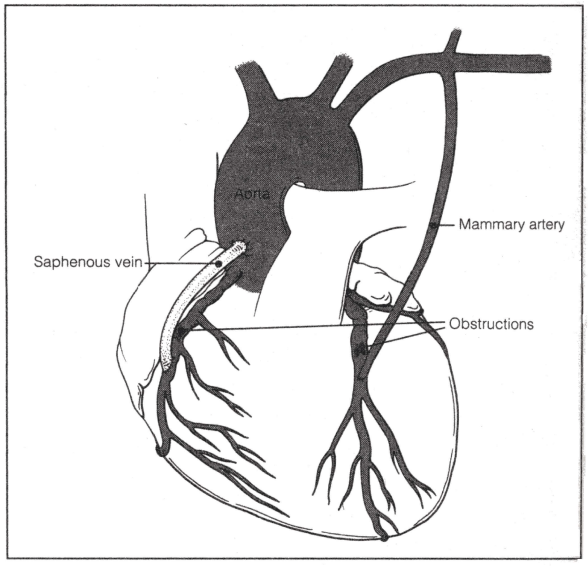

Figure 1.1 Coronary artery bypass grafts (CABG). On the left, the vessel blockage is bypassed using a saphenous vein and another blockage on the right is bypassed using the internal mammary artery. Image from [3].

their extremities in order to avoid amputation [4]. Therefore, vascular bypass grafting is a frequent and important surgical procedure.

For small arteries such as the coronary or peripheral arteries, autologous vascular segments are normally the grafts of choice, if a suitable artery or vein can be extracted from the patient. Arteries, such as the internal mammary, are the most successful bypass conduits but there is a severely limited supply of available autologous arteries for grafting procedures [5]. The autologous vessel most frequently used, for both coronary and peripheral bypass grafts, is the saphenous vein obtained from the leg. Although this is the gold-standard, there are a number of problems with using the saphenous vein including a limited length, the possibility of disease and the detrimental biological changes that occur when a vein is placed into the high pressure, pulsatile environment of the arterial system [5-8]. Also, the caliber of the patient's saphenous vein may not be suitable for the vessel that needs to by bypassed [9]. When the autologous vessels can not be utilized, prosthetic tubes made from Dacron or Polytetrafluoroethylene (PTFE) may be used as bypass conduits. However, these non-biologic grafts are more likely to thrombose (i.e., clot) and do not have the biomechanical characteristics of the native artery, including arterial compliance and vasoreactivity (i.e., the ability of the vessel to change diameter in response to a mechanical and chemical stimulus) [2]. Therefore, there are a number of challenges to be overcome in the field of vascular grafts.

1.2 Anastomosis Construction

1.2.1 Suturing and Vascular Clips

The junction between the graft and the host artery is called the anastomosis. The upstream junction is known as the proximal anastomosis and the downstream junction is the distal anastomosis. The anastomosis can be secured using either surgical suture or vascular clips. The use of surgical suture to connect the anastomosis involves sewing the vessels together to form an intact conduit. First, the vessels are brought close to one another and a needle with suture is passed through the vessel walls [10]. Two to four individual sutures are placed around the circumference of the anastomosis to initially attach the vessels. Then the

anastomosis is completed by one of a number of conventional sewing techniques including interrupted (separate, individual sutures) or continuous suturing. These techniques are designed to provide a blood-tight connection as well as to provide adequate tensile strength without constricting or tearing the vessels [10].

Another technique for creating vascular anastomoses is the VCS™ vascular clip system [11]. It was originally designed for use in microvascular reconstructions and has shown promising results for creating all size vascular reconstructions. These arcuate-legged, titanium clips do not puncture the vessel walls and therefore have the potential of causing less trauma to the vessels. Also, anastomoses can be created in significantly less time than using conventional suturing techniques [12]. A drawing of an end-to-end anastomosis being created with the VCS™ system is shown in Figure 1.2 [13]. For the VCS™ clip procedure, the graft and native vessel are approximated and the ends of the vessels are everted so that the intimal, or inner, surface of the vessels touch. Special everting forceps, shown in the top of Figure 1.2, are used to facilitate this process. One mattress suture is placed at the 12 and 6 o'clock positions in order to stabilize the vessels and the nonpenetrating clips are squeezed into place using the clip applier seen in the bottom of the Figure 1.2. There are four sizes of VCS™ clips (0.9, 1.4, 2.0 and 3.0 mm) and the chosen size depends on the caliber of the vessels being anastomosed. An example of a completed anastomosis created with VCS™ clips is shown in Figure 1.3 [13].

1.2.2 End-to-End and End-to-Side Anastomoses

Two anastomosis configurations used for vascular reconstruction are end-to-end (ETE) and end-to-side (ETS). For the ETE anastomosis, the end of the graft is connected to the end of the native vessel, as seen in Figures 1.2 and 1.3. In this case, the blocked region of the native vessel is physically removed and the graft is sewn in its place. For the ETS anastomosis, the blockage in the native vessel is bypassed instead of removed. The end of the graft is connected to the side of the native vessel, making this is a more technically-involved procedure. A schematic of a distal ETS anastomosis is shown in Figure 1.4, and depicts the regions known as the heel, toe and floor. For the ETS anastomosis, a slit is cut in the side of the native vessel in a region of healthy tissue downstream from the blockage. The distal section of the graft is then cut at a

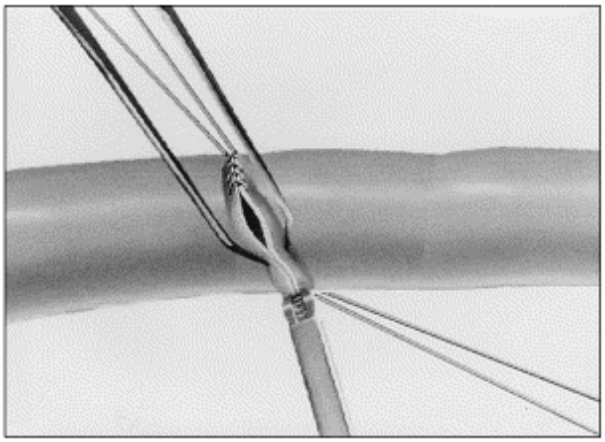

Figure 1.2 Pictorial representation of and end-to-end anastomosis being created with the VCS™ system. Image from [13].

Figure 1.3 Actual end-to-end anastomosis created with VCS™ system. Image from [13].

specified angle, depending on the size of the graft, size of the native vessel and the desired angle of graft insertion (see Figure 1.5 A-E). For the conventional suturing technique, the first needle puncture typically occurs near the heel (12 o'clock position) of the anastomosis and the suturing continues around the circumference of the anastomosis to the toe (6 o'clock position) and meets at the 9 o'clock position as shown in Figure 1.5 F-H. For the VCS™ vascular clip technique, the graft and native vessel tissue is everted and single mattress sutures are placed at the heel and toe of the anastomosis to stabilize the vessels. The clips are placed from the heel to the toe on one side and then this process is repeated on the other side to complete the anastomosis.

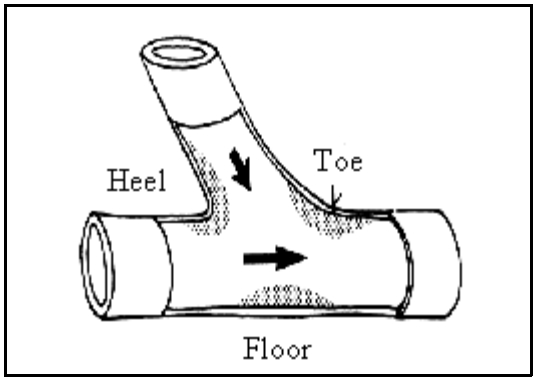

Figure 1.4 Distal end-to-side anastomosis depicting the characteristic heel, toe and floor regions. Image from [14].

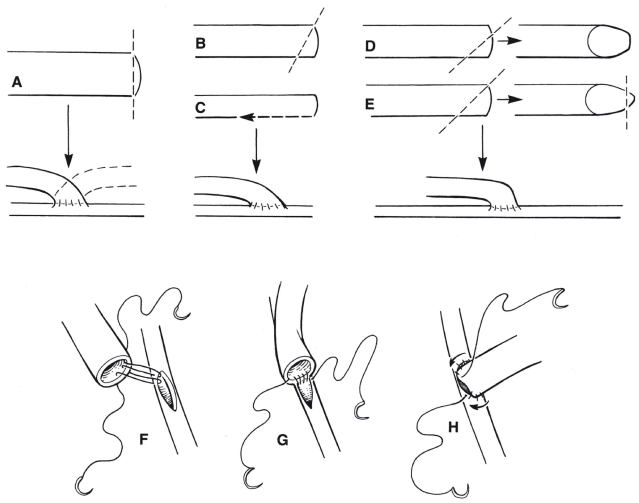

Figure 1.5 Construction of the end-to-side anastomosis A-E) Illustrations of the different techniques of preparing the graft for insertion F-H) Illustrations of the conventional suturing procedure. Image from [15].

1.3 Graft Failure Mechanisms and Costs

Although most bypass grafting procedures are at least initially successful, a large number of bypass grafts fail. Angina, or chest pain, occurs in up to 20% of patients undergoing CABG within the first year after surgery [16]. Repeat grafting procedures are required for 4% of patients within 5 years of their initial surgery, 19% of patients within 10 years and 31% of patients within 12 years [16]. According to the American Heart Association, 216,000 repeat CABG procedures were performed in 1999 at an estimated cost of $42 billion [1]. Lower extremity peripheral bypass grafts have similar failure rates, up to 20-30% at 5 years post-operation [17]. Because of the high percentage of graft failures and the high cost of subsequent repeat grafting procedures, it is important to find a way to increase the success rate of vascular bypass grafts.

Advances in the field will require an understanding of the mechanisms that cause graft failure. Within one month of bypass graft surgery, the principal cause of graft failure is thrombosis, which is the formation of a blood clot that compromises flow in the graft. For autologous grafts, early thrombosis is associated with the disruption of the antithrombotic inner lining of the blood vessel, the endothelium. The endothelium can be destroyed or damaged during the extraction of the vessel, handling of the tissue and surgical insertion of

the graft. In addition, for veins used in the arterial system, the graft is suddenly exposed to a high pressure and pulsatile environment that can damage the venous endothelium [7]. For prosthetic grafts, thrombotic occlusion occurs in response to blood contacting the artificial surface. Additionally, thrombosis for any graft can occur for technical reasons including low blood flow through the graft, anastomotic constriction and/or poor graft placement. Therefore, a number of factors promote thrombosis and can lead to graft failure [15].

Intimal hyperplasia (IH), or overgrowth of the innermost layer of the graft, is usually responsible for graft failures occurring one month to one year after surgery. A blood vessel is composed of three layers; intima, media and adventitia as seen in Figure 1.6. The intima is the blood-contacting layer of the vessel and is lined by a single layer of endothelial cells (EC). The media is the middle region of the vessel and is comprised mostly of smooth muscle cells (SMC), which give the vessel its tone. The adventitia is the outermost layer and is composed mostly of loose, connective tissue. In intimal hyperplasia, the SMC proliferate and migrate from the media to the intima and increase extracellular matrix production [6, 18]. This causes an increase in intimal thickness that decreases the cross-sectional (luminal) area available for blood flow. This blockage of blood flow leads to graft failure [15].

Late graft failure, occurring anytime after the first year post-surgery, is caused by accelerated atherosclerosis. This atherosclerotic formation is similar to the disease process that was initially present in

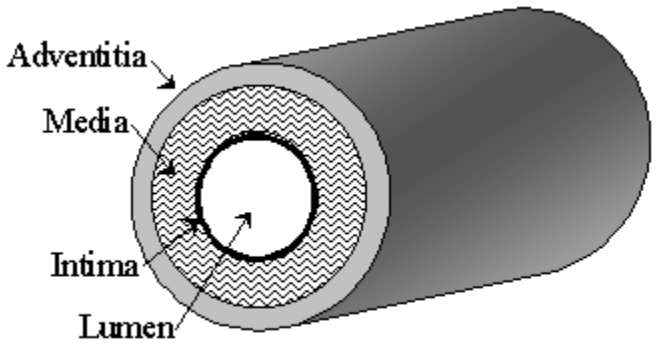

Figure 1.6 Schematic diagram of a blood vessel showing the intima, media and adventitia.

the native vessel requiring bypass, but this atherosclerotic formation occurs on a much faster timescale. The initial disease process may have taken many decades before presenting clinically whereas vascular graft atherosclerosis can occur within a few years. Vascular graft atherosclerosis is an extension of the formation of intimal hyperplasia whereby mononuclear leukocytes accumulate in the hyperplastic intimal layer. These leukocytes accumulate lipids and become foam cells that form the fatty streak which is the first grossly recognizable stage of atherosclerosis [17]. This fatty streak formation further decreases the cross-sectional area available for blood flow so that grafts that previously did not have a critical blockage due to intimal hyperplasia become symptomatic. The final stage of atherosclerosis is the formation of a plaque. Unstable plaques can rupture, initiating the coagulation cascade and causing acute thrombosis of the graft. This may completely block blood flow and therefore cause graft failure [15].

1.4 Etiology of Intimal Hyperplasia

The failure mechanism that this dissertation has addressed is intimal hyperplasia. It is generally accepted that IH is initiated as a "response to injury" of the endothelial cells [19-21]. Because endothelial cells (EC) are in direct contact with the blood, they are affected by changes in hemodynamics (e.g., shear stress) and can respond by modulating their expression of a number of vasoreactive substances including growth factors, vasorelaxation and vasoconstriction molecules, coagulation products and chemotactic agents. These vasoreactive substances not only affect neighboring EC but also the SMC in the media of the vessel as well as circulating cells such as leukocytes [19-22]. In this manner, EC are able to initiate a global reaction to a changing hemodynamic environment.

As stated, IH is characterized by the proliferation and migration of SMC and by the accumulation of extracellular matrix within the intima. This intimal thickening is not solely dependent on the proliferation of SMC; it is a net result of the *balance* between proliferation and regulated cell death (apoptosis). That is, IH occurs when the normal balance between cell proliferation and apoptosis is altered [23]. An increase in SMC proliferation and migration, by definition, favors IH formation. The role of apoptosis, however, is less

clear. Increased apoptosis results in voids in the tissue structure that can promote SMC proliferation and migration as well as ECM production. Conversely, decreased apoptosis inherently results in a larger quantity of cells in the tissue since they are not being removed via this regulated process of cell death. Therefore, it may simply be an alteration in the normal apoptosis process, as well as the proliferation rate, that leads to IH formation.

The proliferation and apoptosis cycles are not independent processes; a single stimulus can regulate both processes [24-26]. In particular, certain immediate early genes (IEG) are involved in the signaling pathways for both regulatory mechanisms [25, 27-29]. When IEG are expressed due to extracellular stimulation, their protein products translocate to the nucleus. These proteins form transcription factors that are responsible for regulating the expression of a number of different genes. Which genes they upregulate and downregulate, to what degree and during what timespan, eventually cause the cell to either become proliferative or apoptotic. Because IEG are involved in both proliferation and apoptosis and the overall balance of these processes leads to IH, IEG are pivotal in the failure of vascular bypass grafts.

The individual processes of cell proliferation and apoptosis as well as the specific roles of certain IEG in these processes are further described in the subsections below.

1.4.1 Cell Proliferation

Cell proliferation is the process of reproduction in which offspring cells with similar phenotypes are produced via mitosis. This is a highly regulated process and only occurs when cells need to be replaced to maintain homeostasis. However, this regulatory mechanism can become dysfunctional causing an excessive amount of proliferation and subsequent disease formation such as intimal hyperplasia [30].

There are a number of external stimuli that can cause a cell to proliferate including biochemical agents (i.e. growth factors), microbiological factors (i.e. viruses) and biomechanical forces (i.e. shear stress). These external stimuli must be transduced to the nucleus of the cell in order to initiate proliferation. This is accomplished through a complex cell signaling process. An external stimulus is sensed by receptors on the cell surface that have intracellular kinase domains and this initiates a cascade of kinase phosphorylations.

The activated end products of these cascades in turn activate genes whose protein products translocate to the nucleus. Once in the nucleus, these proteins either act independently or dimerize to form transcription factors. These transcription factors then regulate the expression of late-response genes such as growth factors and adhesion molecules that modulate proliferation. This signaling cascade allows the cell to respond quickly to external stimuli and is an evolutionary mechanism that allows the cell to adapt to its environment in order to survive [30].

Vascular cell proliferation is an integral part of the formation of IH in vascular bypass grafts. Galea *et al.* measured SMC proliferation in human saphenous veins used for coronary artery bypass [31]. Pressure distended veins and non-distended control vessels were kept in organ culture for 24 hours to determine cell proliferation via tritiated thymidine. There was a significant decrease in thymidine incorporation in the distended vein versus the non-distended control. However, there was no difference in proliferation rates when assessed with immunohistochemical staining for proliferating cell nuclear antigen (PCNA) [31]. Hayakawa *et al.* determined the SMC proliferation in radial arteries of patients undergoing repeat AV shunt surgery for hemodialysis [32]. They determined SMC proliferation using immunohistochemical staining for PCNA and found a positive correlation between SMC proliferation and the percent stenosis of the vessel [32]. Kockx *et al.* obtained significantly (70% or greater) occluded human aortocoronary grafts from patients undergoing repeat coronary bypass operation [33]. They found that a significant fraction of the cells in the neointima were positive for PCNA and Ki-67, another immunohistochemical marker of proliferation. Similarly, Wang *et al.* studied occluded human aortocoronary grafts and found an increase in PCNA positive cells in the thickened but non-atherosclerotic regions of the intima and media [34].

These studies demonstrate that the proliferation of vascular cells is altered when human vessels are used as vascular bypass grafts.

1.4.2 Apoptosis

Apoptosis is the natural counterpart to cell proliferation. It is regulated cell death, distinct from necrosis, and occurs naturally to maintain tissue homeostasis while necrosis (i.e. accidental cell death) results

when the cell is unable to maintain homeostasis. Apoptosis affects a single cell at a time and is initiated from inside the cell as opposed to necrosis, which usually involves entire areas of tissue at a time and is caused by external disruption of the cellular membranes. Apoptosis is characterized morphologically by cell membrane shrinkage, condensation of nuclear chromatin, DNA segmentation, cellular fragmentation into apoptotic bodies and phagocytosis by neighboring cells [35]. In general, this process of cell death does not elicit an inflammatory response [24].

Analogous to cell proliferation, the process of apoptosis involves complex signaling pathways to translate an extracellular stimulus to intracellular death mechanisms. In fact, many of the same signaling pathways that lead to proliferation can alternatively result in apoptosis [36]. Therefore, it is likely that an interaction between a large number of pathway substrates and the timing of the production of these molecular products determines if a cell will ultimately respond in a proliferative or apoptotic manner [37, 38].

Apoptosis has been implicated in the formation of IH in vascular bypass grafts. Galea *et al.* measured SMC apoptosis in pressure distended human saphenous veins and non-distended control vessels kept in organ culture for 24 hours [31]. There was a significant increase in the number of apoptotic cells in the distended vein versus the non-distended control. Hayakawa *et al.* determined the SMC apoptosis in radial arteries of patients undergoing repeat AV shunt surgery for hemodialysis [32]. They found a positive correlation between SMC apoptosis (in the intima and media) and the percent stenosis of the vessel. In the same study of occluded human, aortocoronary grafts by Kockx *et al.* mentioned in the previous section, a large fraction of apoptotic SMC were found in the thickened intima along with the proliferating cells [33]. Similarly, in the study of occluded bypass grafts by Wang *et al.* mentioned in the previous section, the numbers of apoptotic cells in the non-atherosclerotic but thickened regions of the intima and media correlated with the number of proliferating cells.

These studies demonstrate that increased SMC apoptosis occurs in human vessels used for vascular bypass grafts. This apoptosis leads to an imbalance in the usual SMC proliferation/apoptosis relationship and potentially causes long-term IH formation.

1.4.3 Role of Immediate Early Genes

Immediate early genes such as c-fos, c-jun and early growth response factor-1 (egr-1) are linked to both increased proliferation and apoptosis of surrounding cells, although they affect these processes to varying degrees [39]. These IEG are also expressed in endothelial cells (EC) in response to biochemical or biomechanical stimuli [40-45]. Certain IEG have been shown to be differentially expressed in human arteriovenous fistulas [32] and human saphenous veins that have been manipulated for use as bypass grafts [31, 46, 47]. Therefore, expression of certain IEG may upset the normal balance between cell proliferation and apoptosis and could play a vital role in IH formation in vascular bypass grafts.

IEG play key roles in the mechanotransduction processes responsible for proliferation and apoptosis as illustrated in Figure 1.7 and explained in detail in other publications [27, 28, 48-50]. For example, when EC are exposed to shear stress, the tyrosine kinases in the focal adhesion sites relay the signal to downstream Ras proteins. These proteins further activate multiple kinase phosphorylations pathways including extra-cellular signal-regulated kinase (ERK) and Jun N-terminal kinase (JNK) pathways. Activated ERKs

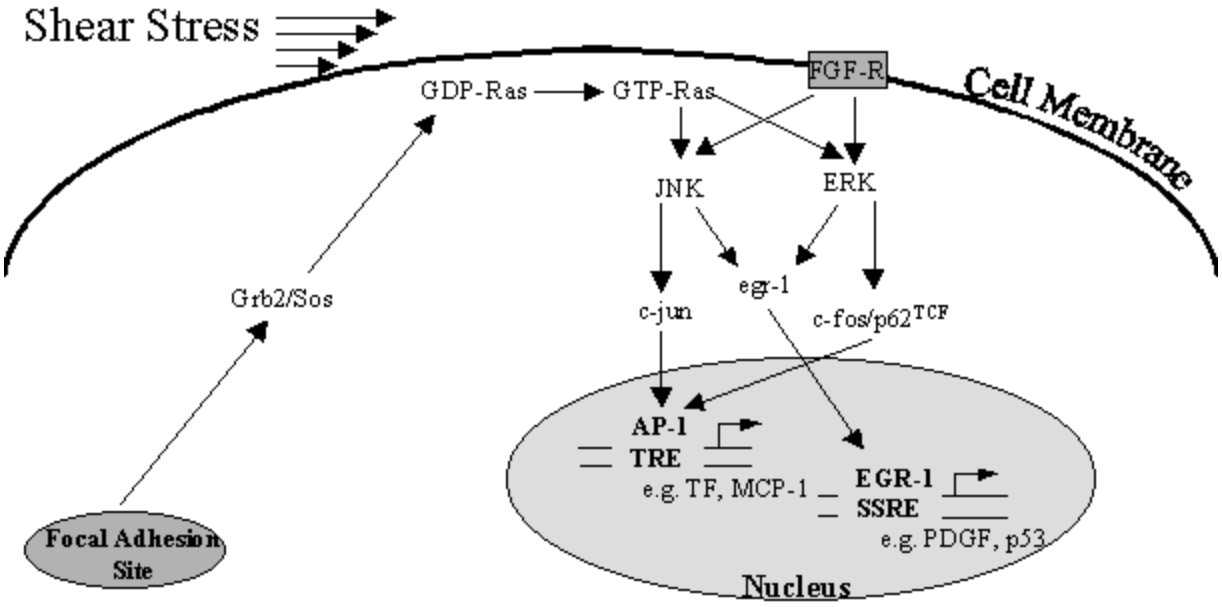

Figure 1.7 The cell signaling pathways involved in the mechanotransduction of shear stress on an endothelial cell that ultimately leads to changes in gene expression. Diagram adapted from [27,28].

phosphorylate factors that activate the c-fos gene, leading to synthesis of the c-fos protein. Similarly, activated JNKs phosphorylate factors that activate the c-jun gene, leading to synthesis of the c-jun protein. Other products of the ERK and JNK pathways induce expression of the egr-1 gene and lead to the synthesis of the egr-1 protein. The c-fos and c-jun proteins then translocate from the cytoplasm to the nucleus and form the transcription factor, activator protein-1 (AP-1) which can either be a c-jun/c-jun or a c-fos/c-jun dimer complex. AP-1 then binds with the tissue 12-O-tetradecanoylphorbol 13-acetate (TPA)- responsive element (TRE) of the promoter for genes including tissue factor (TF) and monocyte chemotactic protein (MCP-1) and mediate their expression [27, 49, 50]. Similarly, egr-1 protein translocates to the nucleus and alters the transcription of several genes implicated in proliferation and apoptosis including TF, platelet derived growth factor (PDGF), fibroblast growth factor (FGF), apolipoprotein A1, intracellular adhesion molecule-1 (ICAM-1), tumor necrosis factor-alpha (TNF-) and p53 [28]. Therefore, IEG expression, protein production and translocation are key elements of the signal transduction system and result in the regulation of genes implicated in cardiovascular disease.

A number of IEG (e.g., c-fos, c-myc, egr-1) have been shown to increase SMC proliferation [51]. Sylvester *et al.* demonstrated that rat vascular SMC proliferation is associated with the expression of c-fos [52]. In both *in vitro* and *in vivo* models, the expression of c-fos occurred before the onset of proliferation and remained elevated during the proliferative response. Cirillo *et al.* exposed rabbit SMC in culture to activated platelets and leukocytes [40]. These cells released products that resulted in increased c-fos expression and subsequently enhanced SMC proliferation. They found a correlation between the intensity of c-fos expression and the degree of SMC proliferation. Further evidence using antisense oligonucleotides (ASO) to IEG demonstrate that these genes are involved in the process of SMC proliferation and migration [53]. ASO are single-stranded DNA molecules synthesized with a base pair sequence complementary to the mRNA sequence of the target gene. They bind to the native RNA and thereby inhibit translation of the target gene (i.e. IEG) [45]. Ebbecke *et al.* [54] and Shi *et al.* [55] exposed cultured human SMC (from the ascending aorta and saphenous vein) to ASO targeted to c-myc (an IEG) and found that the SMC

proliferation rate was strongly inhibited in a concentration–dependent manner. Similarly, Biro *et al.* [56], Bennett *et al.* [57] and Edelman *et al.* [58] exposed cultured rat SMC to c-myc ASO and found a decrease in both SMC proliferation and migration that was dependent on the concentration of the ASO. Sachinidis *et al.* performed a similar experiment except they used an ASO directed to egr-1 and found that the oligonucleotide inhibited proliferation of aortic SMC [59]. These studies demonstrate that IEG expression is linked to increased SMC proliferation and migration and these cellular processes are suppressed when the genes are blocked.

Similarly, a number of IEG (e.g., c-fos, c-jun, c-myc) have been implicated in vascular cell apoptosis [31, 60-64]. Li *et* al. exposed rat vascular SMC to hydrogen peroxide and found that this chemical increased c-fos gene expression and subsequently resulted in SMC apoptosis [60]. Preston *et al.* have demonstrated that c-fos protein induces apoptosis in hamster embryo cells [61] and Smeyne *et al.*, using a transgenic mouse model, provided evidence that the continuous expression of c-fos was associated with subsequent apoptosis [62]. Bossy-Wetzel *et al.* demonstrated that c-jun induces apoptosis in fibroblasts and they determined that this process is separate from c-jun induction of proliferation [63]. Evan *et al.* determined that deregulated c-myc expression leads to fibroblast apoptosis [64]. Galea *et al.* subjected human saphenous veins to a pressure distention of 350-400 mmHg for 2 minutes in order to simulate the surgical trauma that occurs when preparing these veins as coronary artery bypass grafts [31]. They found a peak in c-fos expression 1 hour after removal from the venous circulation in non-distended veins, which was elevated in distended veins. They determined that the expression of c-fos correlated with the level of vascular cell apoptosis, not the level of proliferation. These studies demonstrate that IEG expression is linked to vascular cell apoptosis.

From these and other studies, it is apparent that IEG upregulation can lead to an increase in both vascular cell proliferation and apoptosis [31]. Table 1.1 summarizes the research relating IEG expression with proliferation and apoptosis discussed in this section. Although it is still unclear how the interaction between these two processes leads to IH formation, both are intricately involved in the disease process and the expression of IEG are an important unifying component [24].

Table 1.1 Summary table of research determining the effect of increased IEG expression on cell proliferation and apoptosis.

IEG	Proliferation	Apoptosis
c-fos	⇑[40,52]	⇑[31, 60-62]
c-jun	⇑[63]	⇑[63]
c-myc	⇑[54-58]	⇑[64]
egr-1	⇑ [59]	N/A

1.5 Previous Research on the Role of Hemodynamics in Intimal Hyperplasia

The hemodynamic environment present in the vascular system appears to be a crucial element in the formation of IH. In native arteries, IH tends to form at curves, branches and bifurcations (i.e. coronary artery branch and the carotid bifurcation) where uniform flow is diverted or split [65, 66]. In canine vascular reconstructions, IH occurs preferentially in the ETS anastomotic configuration as opposed to the ETE configuration where the flow is essentially unchanged from the original situation [67]. Clinically, IH is more prevalent at the distal anastomosis of an ETS graft, where the flow is more disturbed, than at the proximal anastomosis, where the flow is more uniform [68, 69]. Since IH is one of the primary causes of bypass graft failure, accounting for 20-50% of bypass graft occlusion [18, 70, 71], it is important to determine which features of the hemodynamic environment cause this pathological condition and how the process is triggered.

To accomplish this goal, previous researchers have characterized the hemodynamic environment present at the distal anastomosis of ETS vascular bypass grafts as well as the cellular response associated with IH. The studies focusing on the distal anastomosis hemodynamics have included *in vivo* human or animal models, physical flow models or computational simulations. The studies focusing on the cellular response to hemodynamics (i.e. vascular cell proliferation, apoptosis and IEG expression) have included cell culture studies, animal or human *in vivo* models. These studies are summarized in the subsections below.

1.5.1 Human Studies

A number of human tissue or clinical studies have demonstrated that hemodynamics affect IH formation. Porter *et al.* filleted open human saphenous veins and exposed the luminal surface to venous and arterial wall shear stress (WSS) for 14 days using an *ex vivo* perfusion system [72]. They found that the veins exposed to venous levels of WSS (~1 dynes/cm^2) developed significantly thicker neointimas than veins exposed to arterial levels of WSS (~9 dynes/cm^2) and the veins cultured in static conditions developed significantly thicker neointimas than those exposed to venous or arterial conditions. Kornet *et al.* measured the mean WSS in the common femoral and superficial femoral arteries in 54 presumed healthy patients using noninvasive ultrasound [73]. They found a significantly lower WSS in the common femoral artery compared to the superficial artery (see Figure 1.8). This significantly decreased WSS correlated with significantly increased intima-media thicknesses present on the common femoral artery (see Figure 1.8). Hofstra *et al.* studied the relationship between flow velocity and IH formation at the distal ETS anastomosis in arteriovenous fistulas of 24 patients receiving hemodialysis [74]. They found that grafts with extensive IH at the distal anastomosis had high initial flow rates suggesting that high WSS (~3 times higher than physiological levels) leads to IH formation. Taylor *et al.* have developed an improved prosthetic bypass graft

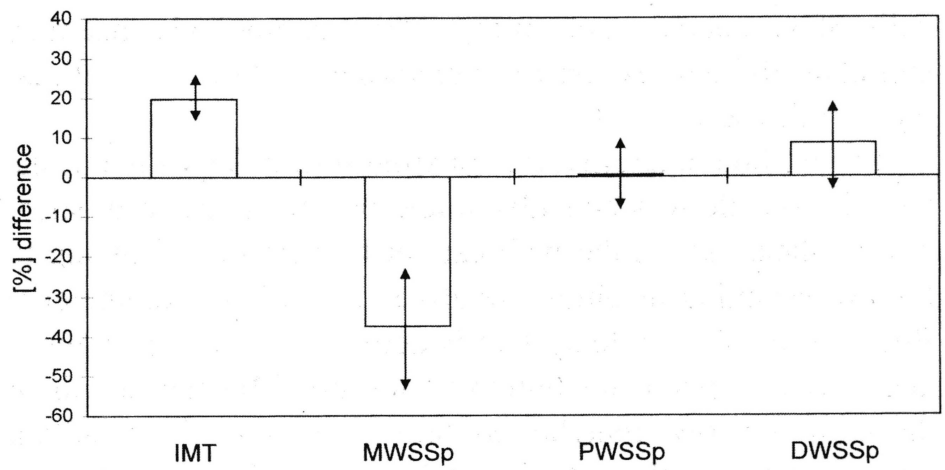

Figure 1.8 Figure from [73] showing the decrease in mean WSS (MWSSp) and corresponding increase in intima-media thickness (IMT) of the common femoral artery relative to the superficial artery. No correlation was found between IMT and peak systolic WSS (PWSSp) or the maximum cyclic change in WSS (DWSSp).

configuration that incorporates a vein patch at the distal ETS anastomosis [75, 76]. The Taylor patch design has significantly increased prosthetic bypass graft patency rates one and five years after placement and they attribute this improvement to the modified hemodynamic environment at the anastomosis.

These studies demonstrate that the hemodynamic environment, particularly non-physiologic (low or high) levels of WSS, influences the formation of IH in human tissue.

1.5.2 Animal Studies

A number of animal studies have demonstrated a correlation between the hemodynamics and IH formation in ETS bypass grafts. Dobrin *et al*. compared the mechanical and histologic changes in ETE verses ETS femoral vein bypass grafts of the femoral artery in dogs [67]. They found that IH occurs preferentially in the ETS grafts, where the flow is dramatically altered from normal physiologic conditions, as opposed to ETE configurations. LoGerfo *et al.* placed Dacron femoro-femoral grafts in dogs and compared the amount of IH occurring at the proximal and distal anastomoses [68]. They found a significant increase in IH at the distal anastomosis of an ETS graft where the flow is more disturbed than at the proximal anastomosis where the flow is more uniform. Sottiurai *et al.* and Bassiouny *et al.*have also used dog models of ilio-femoral ETS bypass grafts [77, 78]. They found that IH forms exclusively at the heel and toe (recall Figure 1.4) of the distal ETS anastomosis and on the floor of the native artery. These areas include flow separation and stagnation zones characterized by low WSS. [77, 78]. Similarly, Keynton *et* al. found increased incidence of IH in the toe and floor regions of PTFE grafts implanted in dogs [79]. They also observed that over 75% of the IH occurred at or below a mean wall shear rate of 100 s^{-1} while approximately 92% occurred at or below a mean WSS equal to one half that of the native artery. Rittgers *et al.* placed iliofemoral vein grafts with various proximal anastomotic angles to provide a wide range of flow conditions in the dog grafts [80]. They used hot-film velocity measurements to determine the velocity profiles and WSS in the grafts. They found an inverse correlation between the WSS and the degree of intimal proliferation. Similarly, Mattsson *et al.* found that baboon prosthetic ETS grafts exposed to elevated WSS (by creating a downstream AV fistula) exhibited significantly less IH proliferation than grafts exposed to normal WSS [81].

These animal studies provide additional evidence that the formation of IH is affected by the flow and WSS present at the distal anastomosis of ETS bypass grafts. In particular, IH formation in animal models occurs in regions of flow separation, flow stagnation and low WSS.

1.5.3 Physical Flow Models

Several researchers have focused on visualizing the hemodynamic phenomena at the distal anastomosis of a vascular bypass graft. Typically, transparent, rigid models made either from idealized representations of the anastomosis (intersecting tubes) or based on casts made from animal models have been studied using flow visualization to determine the flow patterns. Bassiouny *et al.* accompanied their *in vivo* study with a scaled-up, transparent, Sylgard model of the ETS anastomosis [78]. They determined from flow visualization that a stagnation zone existed along the floor of the artery and separation regions and secondary flows existed at the heel and toe of the graft. They concluded that low WSS corresponds to regions of intimal thickening in the animal model. Similarly, Loth *et al.* created a scaled-up, Sylgard model from a canine ilio-femoral graft cast [82]. They used laser Doppler anemometry to determine the flow field and resulting WSS at the anastomosis during steady flow. They found a region of low WSS on the floor of the native artery that extended up the sidewalls to the hood and conclude that this large region of low WSS would induce IH formation. Ojha *et al.* used the photochromic tracer technique to visualize flow in an idealized Plexiglas model of an ETS anastomosis [83]. They found regions of low WSS at the heel and toe along with sharp temporal and spatial variations of WSS gradient (WSSG) along the floor of the artery, including a stagnation zone. They determined that these regions correlated with areas of IH formation demonstrated by others. Zarins *et al.* [66] and Ku *et al.* [84] studied the flow in a carotid artery bifurcation that has disturbed flow similar to an ETS graft. They used laser Doppler velocimetry and found a quantitative correlation between the areas of intimal thickening in human cadavers and areas of low or oscillating WSS found in the Plexiglas model.

These physical models give detailed information about the hemodynamics present in ETS bypass grafts and demonstrate that regions of flow separation, secondary flow, low and oscillating WSS and WSSG correlate with areas of IH formation.

1.5.4 Computational Simulations

A number of research groups have utilized computational fluid dynamics (CFD) to understand the precise local hemodynamics at the distal anastomosis of an ETS vascular graft. Steinman *et al.* developed a two dimensional CFD model, which demonstrated elevated WSS at the toe and heel (recall Figure 1.4) of the anastomosis and along the floor of the host artery [85]. Additionally, they noted highly variable WSS over the cardiac cycle and elevated WSSG. Hofer *et al.* developed a CFD model of an ETS anastomosis with distensible vessel walls [86]. Their results demonstrate large secondary motion, flow separation and recirculation along the artery floor and along the inner wall downstream from the toe. They concluded that regions of low WSS correlated with areas of IH formation. Similarly, Henry *et al.* developed a three dimensional CFD model and demonstrated that regions of the ETS anastomosis corresponding to IH formation had low WSS but were also sites of increased spatial WSSG [87]. Fei *et al.* used a three dimensional CFD model to study the effect of graft angle on the flow in an ETS anastomosis [88]. They concluded that grafts should be placed with a minimal angle (<20 degrees) so as to decrease the amount of flow separation and WSS extremes experienced by the artery walls. Ethier *et al*. developed a three dimensional CFD model to study the effect of various flow waveforms on the hemodynamics at the distal ETS anastomosis [89]. The spatial distribution of normalized, average WSS was different depending on the imposed flow waveform as shown in Figure 1.9. They found larger regions of temporal and spatial WSSG for the femoral waveform than for the coronary waveform and suggest that this may lead to more IH formation. Lei and Kleinstreuer *et al.* used a three dimensional CFD model to optimize the anastomosis geometry in order to eliminate severe WSSG [90, 91]. They hypothesize that the increased success of Taylor patch anastomoses, which have a more gradual transition from the straight graft segment to the native artery,

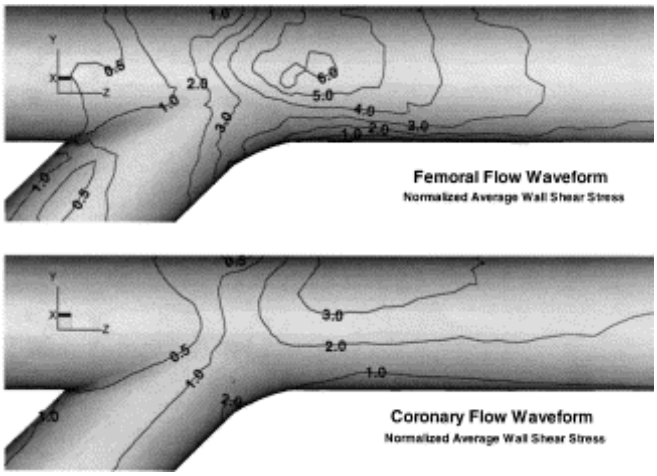

Figure 1.9 Figure from [89] showing the different patterns of WSS depending on the imposed flow waveform.

versus standard anastomoses is due to the decrease in temporal and spatial WSSG in the Taylor patch geometry.

Other researchers have reconstructed three dimensional geometries from *in vivo* data of different regions of the vascular system and incorporated this information into a CFD model. Chandran *et al.* used intravascular ultrasound to obtain the cross-sectional images needed to reconstruct a segment of the abdominal aorta in a dog [92]. They determined the WSS distribution at peak systole in normal caliber vessels and in artificially stenosed vessels (25 and 40% lumen area reduction). Krams *et al.* used a combination of intravascular ultrasound and angiography to reconstruct human coronary arteries [93]. They applied steady flow through the reconstructions and found an inverse correlation between wall thickness and WSS using this minimally invasive technique. Perktold *et al.* obtained a human heart at autopsy and created a cast of the bifurcation of the left anterior descending coronary artery [94]. This cast was both digitized and reconstructed into a CFD model (shown in Figure 1.10) and a transparent model was made for flow visualization and verification of the CFD results. They determined the flow field and WSS distribution for pulsatile flow through the bifurcation and concluded that low and oscillating WSS occurs in the same regions as atherosclerotic lesions. Xu *et al.* used a non-invasive, magnetic resonance angiographic and velocity

Figure 1.10 Figure from [94] showing the CFD model of the reconstructed left anterior descending coronary artery bifurcation.

imaging technique to reconstruct a human aortic bifurcation and developed a CFD model [95]. They found that the geometry, velocity profiles and resulting WSS patterns were highly non-planar. Another research group has used magnetic resonance to reconstruct complex vascular geometries and develop CFD models of the carotid artery bifurcation and ETS anastomosis [96-101]. They have demonstrated that it is feasible to reconstruct these complex geometries in a patient-specific manner using non-invasive magnetic resonance techniques and emphasized the importance of applying the appropriate amount of surface smoothing to the reconstructed geometry in order to accurately determine the hemodynamics. Specifically, in the ETS anastomosis studies, they found that simplified models, with a lot of smoothing, captured the qualitative aspects of the hemodynamic environment that can be correlated to general disease states. However, more complex models with less smoothing are necessary for correlating quantitative hemodynamic and pathophysiologic data, as long as the geometry itself is not so rough that it induces error [99]. Therefore

there is an optimal degree of smoothing which must be applied to three dimensional reconstructions of complex vascular geometries in order to accurately recreate the quantitative hemodynamic environment.

These CFD studies demonstrate that the hemodynamic environment at the distal ETS anastomosis is complex and the hemodynamic variables (i.e. WSS, WSSG) can be calculated quantitatively and correlated with regional data of IH formation. Additionally, three dimensional *in vivo* geometries can be reconstructed using minimally or non-invasive techniques (i.e. intravascular ultrasound and magnetic resonance) and developed into a CFD model to elucidate patient-specific patterns of WSS and WSSG that may lead to IH formation.

From these and other studies, it is apparent that hemodynamic parameters affect the formation of IH. Table 1.2 summarizes the research relating hemodynamics and IH discussed in this section.

Table 1.2 Summary table of research determining the effect of hemodynamics on IH formation.

Hemodynamic Parameter	**Intimal Hyperplasia**
flow separation, stagnation	⇑[77, 78, 83, 102]
low WSS	⇑[72, 73, 77-83, 86, 87, 93, 94, 102]
high WSS	⇑[74]
oscillatory WSS	⇑[66, 84, 89, 94]
spatial WSSG	⇑[66, 93, 85, 87, 89-91, 102]
temporal WSSG	⇑[84, 94]

1.6 Previous Research on the Hemodynamic Response of Vascular Cells Leading to IH

The previous research presented above demonstrates that the altered hemodynamic environment influences the formation of IH. However, this research does not explain how and why the vessel wall responds in this fashion. A separate line of research has focused on determining the mechanism by which vascular cells sense the hemodynamic environment and then initiate a hyperplastic response. Studies on

vascular cell proliferation, apoptosis and IEG expression in response to hemodynamic stimuli have been conducted, and are summarized in this section.

1.6.1 Vascular Cell Proliferation in Response to Hemodynamic Stimuli

SMC proliferation is one of the key processes in IH formation. It leads to the increase of intimal mass and eventual occlusion of the affected vessel. Since there is evidence of a correlation between hemodynamics and IH formation, researchers have studied the specific effect of hemodynamic parameters on SMC proliferation using cell culture models, animal models and human tissue. These are discussed separately below.

1.6.1.1 Cell Culture Studies

Cell culture studies have demonstrated that SMC proliferation is affected by the application of WSS and WSSG. Nackman *et al.* used an *in vitro* co-culture model to determine SMC proliferation in response to EC stimulation by WSS [103]. They cultured bovine aortic EC (BAEC) and SMC (BASMC) on opposite sides of a semi-permeable membrane that allowed for cell-to-cell contact and then exposed the EC side of the membrane to laminar WSS of 0, 1 or 10 dynes/cm^2 for 24 hours. They found a dramatic decrease in SMC proliferation for membranes exposed to 1 and 10 dynes/cm^2 compared to the static controls. Sterpetti *et al.* performed a number of studies using cultured BASMC on fibronectin-coated polystyrene cylinders and exposed them to WSS values of 0, 3, 6, and 9 dynes/cm^2 for 24 hours [104-106]. In all studies, they found a significant reduction in SMC proliferation that was proportional to the level of WSS applied. Ueba *et al.* exposed cultured human vascular SMC to WSS of 14 or 28 dynes/cm^2 for 24 hours using a cone-and-plate viscometer [107]. They also found a significant decrease in SMC proliferation that was dependent on the magnitude of applied WSS (see Figure 1.11). DePaola *et al.* exposed BAEC to a disturbed flow environment for 48 hours using a modified cone-and-plate flow chamber [108]. EC proliferation decreased in the region with high WSSG while high cell densities were observed downstream of the disturbance indicating EC migration away from the region of high WSSG.

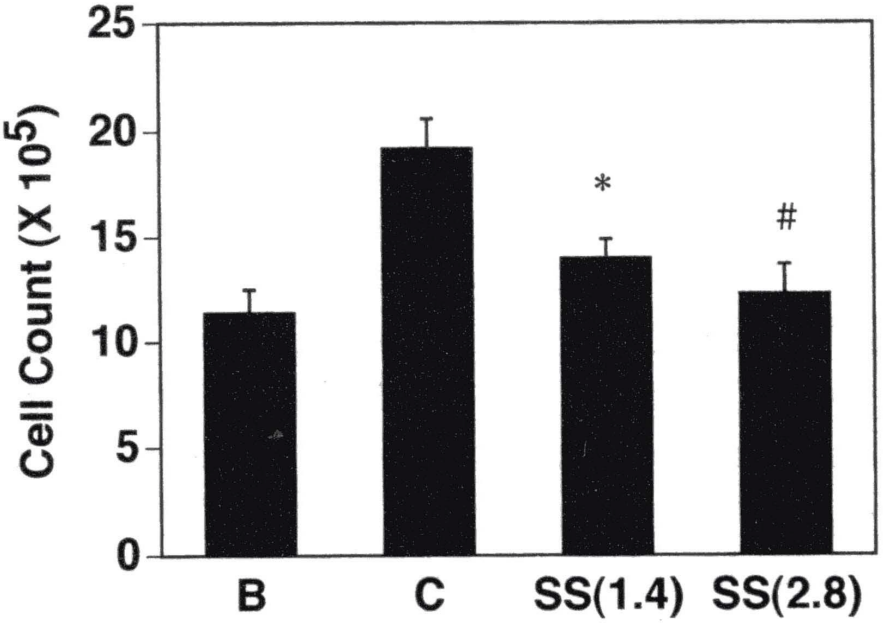

Figure 1.11 Figure from [107] showing the decrease in the number of SMC for cultures exposed to no flow (C), WSS of 14 dynes/cm^2 (SS(1.4)) and WSS of 18 dynes/cm^2 (SS(2.8)) for 24 hours. B denotes the cell count before the initiation of the experiment.

These studies demonstrate that SMC in culture have increased proliferation when they are exposed to decreased WSS and have increased proliferation when exposed to increased WSSG. This data is consistent with the IH data presented in section 1.5 and Table 1.2 that demonstrated an increase in IH formation in regions exposed to low WSS and high WSSG.

1.6.1.2 <u>Animal Studies</u>

Animal models of vascular bypass grafts have demonstrated that the amount of blood flow and hence WSS applied to the graft affects SMC proliferation. Zwolak *et al.* used a rabbit model to determine the time course of SMC proliferation in jugular vein grafts placed in the carotid artery circulation [109]. They found a dramatic increase in SMC proliferation in vein grafts compared to vein and artery controls that peaked 1 week after surgery. SMC proliferation decreased from this maximal value by 4 weeks and returned to baseline 12 weeks post-op [109]. Kraiss, Geary and colleagues determined the effect of WSS on SMC proliferation in prosthetic grafts implanted in baboons [110, 111]. In one study, they created 3 ETS bypass

grafts: one superceliac to the infarenal aorta and two aorto-iliac grafts [110]. The aorta was ligated so that flow from the proximal aorto-aortic graft would go directly to the two aorto-iliac grafts allowing twice as much blood flow in the proximal graft (~40 cm/sec) compared to each of the distal aorto-iliac grafts (~17 cm/sec). They found a significant decrease in SMC proliferation in the high-flow grafts that were exposed to a WSS of approximately 24 dynes/cm^2 compared to the low-flow grafts that were exposed to a WSS of approximately 11 dynes/cm^2. In another study, they placed bilateral aortoiliac PTFE grafts into baboons with bilateral femoral AV fistulas [111]. Eight weeks later, they ligated one fistula, which caused high blood flow in the graft with the corresponding open AV fistula and normal flow in the graft with the ligated fistula. They found a significant decrease in SMC proliferation in the high flow grafts on days 4 and 7 after the ligation of one AV fistula. Additionally, they found a progressive increase in SMC in the neointima of the normal flow grafts throughout the 28 day study. Yamamura *et al.* used a canine "poor run-off" model to determine the effect of WSS on SMC proliferation [112]. They ligated all tributary arteries distal to the saphenous artery in one limb and allowed the animal to recover for 4 weeks. Then they placed the femoral vein from the "poor run-off" limb in the femoral artery circulation of the same limb and performed the same grafting procedure on the normal limb. This provided a WSS of approximately 31 dynes/cm^2 in the "poor run-off" graft and 77 dynes/cm^2 in the control graft. They found a significant increase in SMC proliferation in the intima of the "poor run-off" graft compared to the control graft indicating that the decrease in WSS initiated SMC proliferation. Liu determined the effect of disturbed blood flow on the proliferation of SMC, assessed immunohistochemically with 5-bromo-2'-deoxyuridine labeling, using a canine ETE vein graft model [113]. The diameter of the vein graft (jugular vein) was larger than the host artery (aorta) and therefore caused the formation of eddy blood flow at the anastomosis. In some experiments, he eliminated this diameter mismatch (and eddy flow) by wrapping the vein with a piece of fixative-treated intestine. Liu found a significant increase in SMC proliferation in leading and trailing regions of the grafts with eddy flow (nonengineered) compared to the same regions in grafts without eddy flow (engineered) (see Figure 1.12 A and C). These results suggested that disturbed flow (e.g. increased WSSG) caused the upregulation of SMC

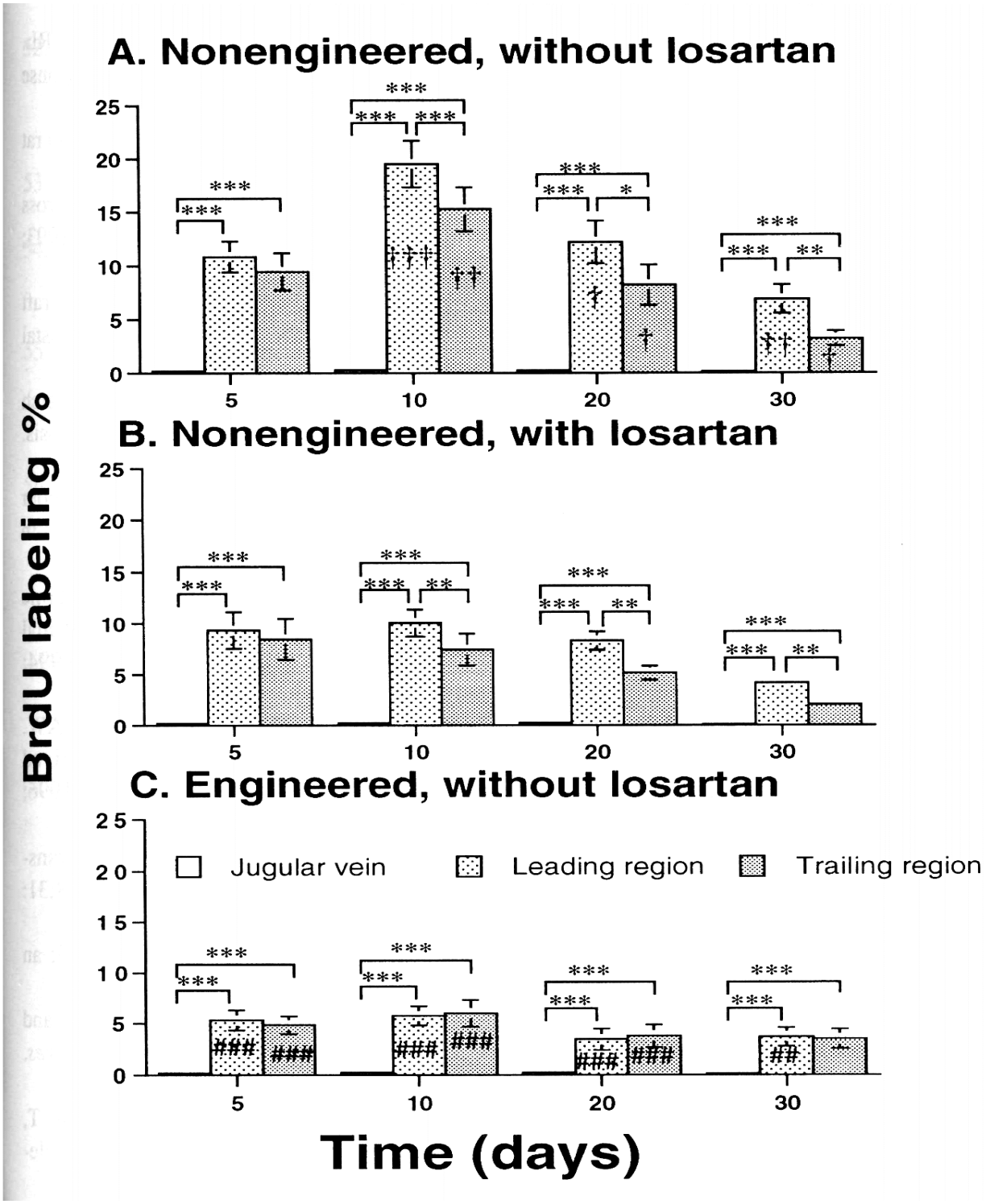

Figure 1.12 Figure from [113] showing the increase in SMC proliferation (BrdU labeling) in the leading and trailing regions of nonengineered grafts with disturbed flow as compared to the same regions in engineered grafts without disturbed flow. An angiotensin II type I receptor agonist, Losartan, partially blocked the proliferative response.

proliferation. He also examined the effect of the angiotensin II type 1 receptor on SMC proliferation by using Losartan, an angiotensin II type 1 receptor antagonist and found that this agonist partially blocked the increase in SMC proliferation in the nonengineered grafts (see Figure 1.12 B).

Taken together, these animal models demonstrate that SMC proliferation is increased in bypass grafts exposed to low WSS and high WSSG conditions. This is consistent with the data in section 1.5 and Table 1.2 that demonstrated an inverse correlation between WSS and IH formation and a positive correlation between WSSG and IH formation.

1.6.1.3 Human Studies

Alterations of SMC proliferation due to the hemodynamic environment have also been seen in studies of human vascular tissue. Because flow conditions can not be altered and regulated safely *in vivo* for humans, studies on the hemodynamic effect of vascular grafts have been performed in *ex vivo* perfusion systems. For example, Mavromatis *et al.* perfused matched pairs of freshly isolated human saphenous vein under arterial and venous flow conditions for three days [114]. They found an increase in cell proliferation in the veins exposed to pulsatile, increased pressure and flow conditions. Porter *et al.* found similar results when perfusing human saphenous veins for 14 days [115]. Other researchers have studied cellular proliferation in human atheromas present at branch points in the vasculature and in coronary arteries. Yoshida *et al.* studied the difference between SMC proliferation in regions of branching arteries exposed to different WSS environments and found an increase in SMC proliferation in the areas of low, turbulent WSS relative to those exposed to high, laminar WSS [116]. Wentzel *et al.* used intravascular ultrasound and CFD techniques to determine the effect of shear stress on neointimal growth in human coronary arteries six months after stent placement [117]. As shown in Figure 1.13, regions of decreased shear stress resulted in increased neointimal thickness and they concluded that the degree of neointimal proliferation was inversely proportional to the shear stress.

These studies demonstrate that when human vascular tissue is exposed to altered hemodynamic forces, vascular cell proliferation occurs and is a precursor of IH.

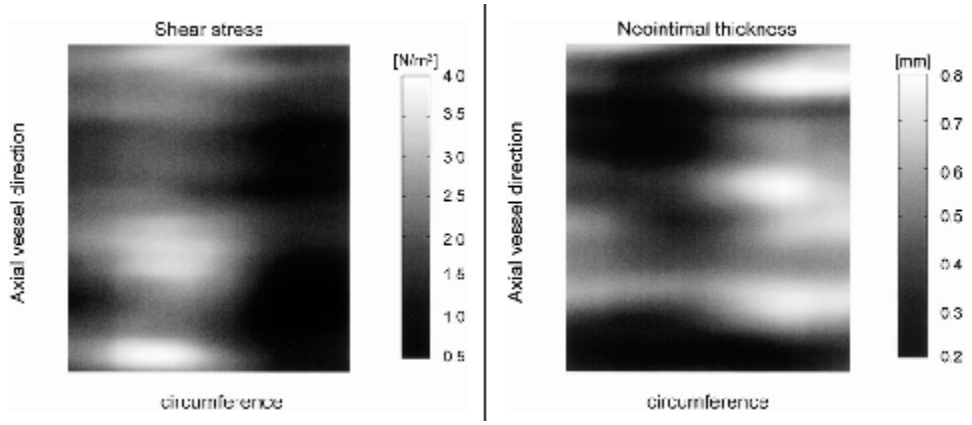

Figure 1.13 Figure from [117] suggesting a relationship between decreased shear stress and increased neointimal thickness in human coronary arteries.

1.6.2 Vascular Cell Apoptosis in Response to Hemodynamic Stimuli

Vascular cell apoptosis is involved in the formation of IH. Since there is evidence of a correlation between hemodynamics and IH formation, researchers have studied the specific effect of hemodynamic parameters on vascular cell apoptosis using cell culture models, animal models and human tissue. These are discussed separately below.

1.6.2.1 Cell Culture Studies

There have not been any studies on the effect of hemodynamics on the apoptosis of SMC in culture. However, there have been a number of studies on cultured EC apoptosis in response to hemodynamics [37, 118-121]. EC apoptosis has been implicated in vascular disease including atherosclerosis and restenosis and may be associated with IH formation [36, 38, 122, 123]. Kaiser *et al.* cultured human umbilical vein EC under static or dynamic (0.05-0.1 dynes/cm^2) conditions for up to 10 days [118]. On days 1-4, 6 and 10, they found a significant increase in the number of apoptotic cells in the plates cultured under static conditions and concluded that the lack of hemodynamic forces is directly responsible for the increased apoptosis. Hu *et al.* exposed BAEC to a laminar WSS of 12 dynes/cm^2 in a rectangular flow chamber [37]. They found that the application of WSS for 12 hours did not cause apoptosis. Dimmeler *et al.* performed a number of experiments in which they subjected apoptotic human umbilical vein EC cultures to laminar WSS of 15 dynes/cm^2 using a cone-and-plate flow apparatus [119-121]. Apoptosis was induced in the EC cultures by

stimulating them with either TNF-α, H_2O_2 or xanthine/xanthine oxidase in order to determine if a biomechanical stimulus (WSS) could reverse this biochemical induction of apoptosis. In all cases, they found a significant decrease in the number of apoptotic cells in the cultures exposed to shear stress for 18 hours compared to the static controls.

These studies demonstrate that cells in static culture are more prone to apoptotic cell death than those exposed to WSS for hours or days. Since increased apoptosis occurs in cells exposed to little or no WSS and low WSS typically increases IH formation, these studies suggest a positive correlation between apoptosis and IH.

1.6.2.2 Animal Studies

Although animal studies relating particular hemodynamic parameters to the degree of apoptosis have not been completed, vascular injury models have demonstrated that mechanical forces cause apoptosis in SMC [26, 124-126]. Malik *et al.* used a porcine model of coronary angioplasty and determined the degree of SMC apoptosis and proliferation [26]. In the media, they found a significant increase in apoptotic cells as early as 1 hour after injury, a peak at 6 and 18 hours and return to baseline by 14 days as shown in Figure 1.14 C. Interestingly, they did not find an increase SMC proliferation until 3 days post-surgery. There was a quantitative difference between the amount apoptosis and proliferation that favored apoptosis at early time-points (1, 6 and 18 hours) and proliferation at later time-points (3, 7, 14, and 28 days) leading to long-term IH formation. Perlman *et al.* determined SMC apoptosis in both a rat carotid and rabbit external iliac arterial injury model [124]. In both models, there was a peak in the number of apoptotic cells 30 minutes after injury that declined sharply by 4 hours and led to a 65% reduction in medial cell density. Pollman *et al.* performed balloon angioplasty on rabbit carotid arteries [125]. They observed apoptotic nuclei in the media as early as 30 minutes after injury that persisted for 24 hours. In addition, they performed a second balloon injury 4 weeks after the initial trauma to determine the degree of apoptosis experienced by vessels that have already been injured and remodeled. Surprisingly, they found that the intimal cells were more resistant to apoptosis

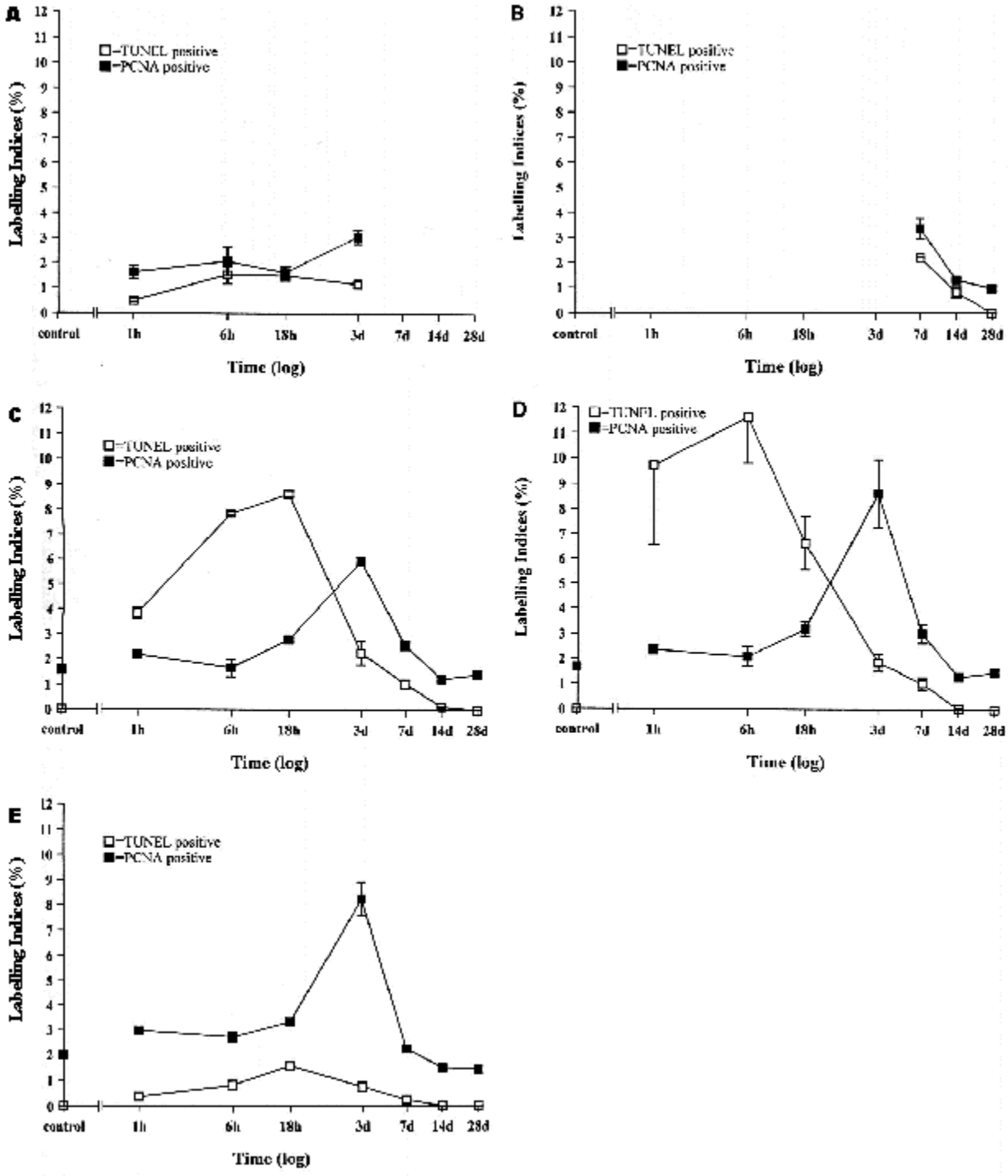

Figure 1.14 Figure from [26] showing the temporal variation of proliferation (PCNA) and apoptosis (TUNEL) in the A) adherent thrombus, B) neointima, C) media, D) adventitia and E) loose connective tissue of injured porcine arteries.

after the second injury. Kamenz *et al.* determined the degree of apoptosis after balloon angioplasty of atherosclerotic rabbit carotid arteries [126]. Although there was a peak in the number of apoptotic cells 7 days after injury, the number of proliferating cells was much greater at this and all other time-points leading to the IH formation.

These animal models demonstrate that SMC undergo apoptosis within hours of mechanical stimulation of whole tissue. This alters the normal balance between SMC proliferation and apoptosis and correlates with long-term IH formation.

1.6.2.3 Human Studies

Alterations of SMC apoptosis, related to hemodynamics, have also been seen in human studies of vascular pathogenesis [118, 127-129]. Wang *et* al. obtained sections of saphenous vein grafts at repeat CABG surgeries and found evidence of apoptosis in the hyperplastic intima and adjacent media [127]. Tricot *et al.* determined the effect of blood flow on EC apoptosis in human carotid plaques [128]. They found a 7-fold increase in EC apoptosis in the downstream sections of the plaques exposed to low shear stress in comparison with the upstream regions exposed to high shear stress. Isner *et al.* performed histological studies on hyperplastic lesions in human peripheral and coronary arteries [129]. They found evidence of apoptosis in over 85% of specimen obtained from regions from repeat procedures compared to less than 45% of specimen obtained from initial procedures indicating that the hemodynamic alterations caused by the initial procedures increases vascular cell apoptosis. Kaiser *et al.* exposed human umbilical veins to steady shear stress and found a decrease in apoptosis in the perfused segment versus nonperfused controls [118]. They concluded that physiologic levels of shear stress reduce cell death.

Taken together, these human studies demonstrate that apoptosis is evident in regions of vascular disease where the concurrent hemodynamics are altered from the normal, physiologic environment.

1.6.3 Immediate Early Gene Expression in Response to Hemodynamic Stimuli

IEG, such as c-fos, c-jun and egr-1, provide an immediate response to an external signal that results in a long-term alteration in the expression of other genes [130]. As discussed in section 1.4.3, IEG expression

occurs in response to a number of different chemical and mechanical stimuli, including shear stress [43-45]. This latter stimulus appears to be regulated by the shear stress responsive element (SSRE), a cis-acting element originally discovered in the 5'promoter region of platelet-derived growth factor B (PDGF-B) and found to be responsible for the upregulation of PDGF-B in response to physiological levels of WSS [131]. This same SSRE, consisting of the core sequence of nucleic acids GAGACC, has been found in other genes regulated by shear stress including PDGF-A, tissue plasminogen activator (tPA), ICAM-1, TGF- and MCP-1 [132-137]. The SSRE is also present in IEG including c-fos and c-jun and regulates their expression in the presence of shear stress [138]. Because IEG expression is a key component of the signal transduction systems which may initiate IH, a number of cell culture, animal and human studies have been conducted to determine how these genes/proteins are regulated by hemodynamic stimuli. These studies are summarized separately below.

1.6.3.1 Cell Culture Studies

Cell culture studies have demonstrated an upregulation of IEG expression in response to WSS and WSSG [43-45, 139]. Hsieh *et al.* placed cultured human umbilical vein EC in a parallel plate apparatus and applied a steady or pulsatile WSS for 4 hours [43]. A steady WSS of 16 dynes/cm^2 resulted in a 24-fold increase in c-fos expression 30 minutes after the onset of flow. An average pulsatile WSS of 16 dynes/cm^2 caused a 62-fold increase in c-fos expression 30 minutes after the onset of flow. The expression of c-fos returned to the initial zero value of expression at all subsequent time-points. In addition, a direct relationship existed between the magnitude of WSS and the expression of c-fos. Stationary cultures of human umbilical vein EC had a detectable level of c-jun expression that doubled or tripled when exposed to either steady or pulsatile flow for 0.5-4 hours. Stationary cultures also had a basal expression of c-myc, which increased slightly to a peak at 2 hours and decreased during the following 2 hours of exposure to either steady or pulsatile flow. Ranjan and Diamond exposed human umbilical vein EC cultures to low (4 dynes/cm^2) and arterial levels (25 dynes/cm^2) of steady laminar WSS for 1 hour and determined the amount of c-fos protein present in the nuclei of sheared cells [44]. They found a 5.4-fold increase in intracellular c-fos protein in the

nuclei of cells exposed to arterial levels of WSS compared to stationary controls. In contrast, cells exposed to low levels of WSS demonstrated only a slight increase in intracellular c-fos protein that was not localized in the nucleus. Nagel *et al.* exposed cultured human umbilical vein EC for 30 minutes to well-defined flow consisting of both uniform and disturbed flow regions [45]. They used a modified cone-and-plate flow apparatus and quantified the amount of nuclear localized IEG protein using image analysis. They found a significant increase in c-fos, c-jun and egr-1 protein in the nuclei of cells exposed to uniform flow (increased WSS) versus static cultures as shown in Figure 1.15. They also found a significant further increase in c-fos, c-jun and egr-1 expression in cells exposed to disturbed flow (WSSG).

Taken together, these studies demonstrate that WSS and WSSG regulate the expression of IEG such as c-fos, c-jun and egr-1 at time points less than 6 hours after stimulation. Specifically, there is an increase in IEG expression in cells exposed to arterial levels of WSS and in cells exposed to WSSG.

1.6.3.2 Animal Studies

In vivo animal studies have also illustrated IEG expression caused by the insertion of bypass grafts and the implication of these genes in IH formation [46, 140, 141]. Ramirez *et al.* determined the amount of c-myc protein present in rat epigastric vein grafts inserted into the femoral artery circulation [46]. They found a steady increase in c-myc protein that peaked 1 week after surgery. The high levels of c-myc protein coincided with increased SMC proliferation. Suggs *et al.* used the same rat vein graft model to determine the time course of c-fos and c-jun expression and the effect of antisense oligonucleotides to these IEG [140]. They found an increase in the amount of c-fos and c-jun protein 15 minutes after graft insertion, which increased dramatically and peaked at 2 hours. The amount of c-fos protein remained at its peak level until 24 hours after surgery and then decreased until 48 hours. The amount of c-jun protein decreased from its peak level but remained elevated up to 48 hours after surgery. Some grafts were treated with a gel containing antisense oligonucleotides to c-fos or c-jun and were explanted 2 weeks after surgery. The antisense oligonucleotides treated grafts had a 30% decrease in intimal and wall thicknesses that was significant compared to the untreated control grafts. Mannion *et al.* placed saphenous vein incubated *ex vivo* with c-myc

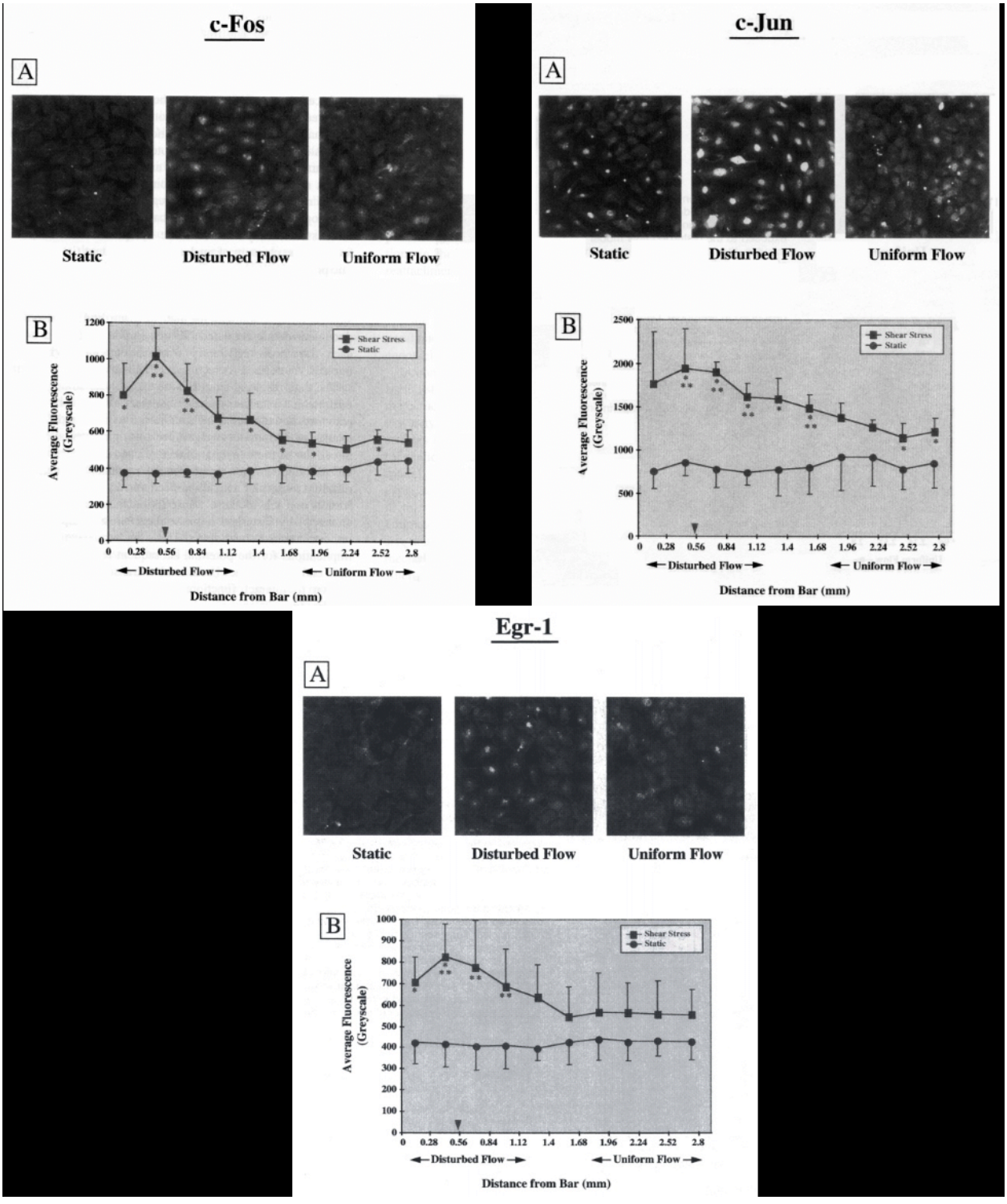

Figure 1.15 Figure from [45] showing the expression of IEG proteins in cultured EC exposed to no flow, uniform flow (arterial WSS) and disturbed flow (WSSG).

antisense oligonucleotides as carotid artery interposition grafts in pigs [141]. Three months after surgery, they found a significant decrease in neointimal and wall thickness in grafts treated with c-myc antisense oligonucleotides than in untreated controls indicating that the early inhibition of c-myc expression caused a long-term, beneficial effect on IH formation.

These animal models demonstrate that IEG expression is increased in vessels inserted as bypass grafts within minutes after insertion and this increase in IEG expression correlates with SMC proliferation. There is a further correlation between the expression of IEG and IH formation since treating vessels with antisense oligonucleotides inhibited both the IEG expression and IH formation at time points weeks and months after surgery.

1.6.3.3 Human Studies

Vascular grafting procedures in humans have also been demonstrated to alter the expression of IEG [31, 47, 142]. Moggio *et al.* studied the expression of c-fos and c-myc in human saphenous veins harvested for coronary bypass operations [47]. They found a dramatic increase in c-fos expression from 30 minutes to 2 hours after harvest, which decreased by 4 to 6 hours and reinitiated 8 to 10 hours after manipulation. The expression of c-myc was elevated 30 minutes after harvest and remained high up to 10 hours later. Galea *et al*. subjected human saphenous veins to a pressure distention of 350-400 mmHg for 2 minutes in order to simulate the surgical trauma that occurs when preparing these veins as coronary artery bypass grafts [31]. They found a peak in c-fos expression 1 hour after removal from the venous circulation in non-distended veins, which was even greater for distended veins. Gan *et al.* exposed human umbilical veins to different levels of WSS for 1.5 to 6 hours and determined the gene and protein levels of c-jun and c-fos [142]. The expression of c-jun was higher in the vessels exposed to high (25 dynes/cm^2) WSS compared to those exposed to low (<4 dynes/cm^2) WSS at all time points studied (as shown in Figure 1.16a) and the level of protein also increased over time. They also found an increase in c-fos gene expression in the vessels exposed to high WSS for 6 hours as shown in Figure 1.16c but the protein level remained unchanged.

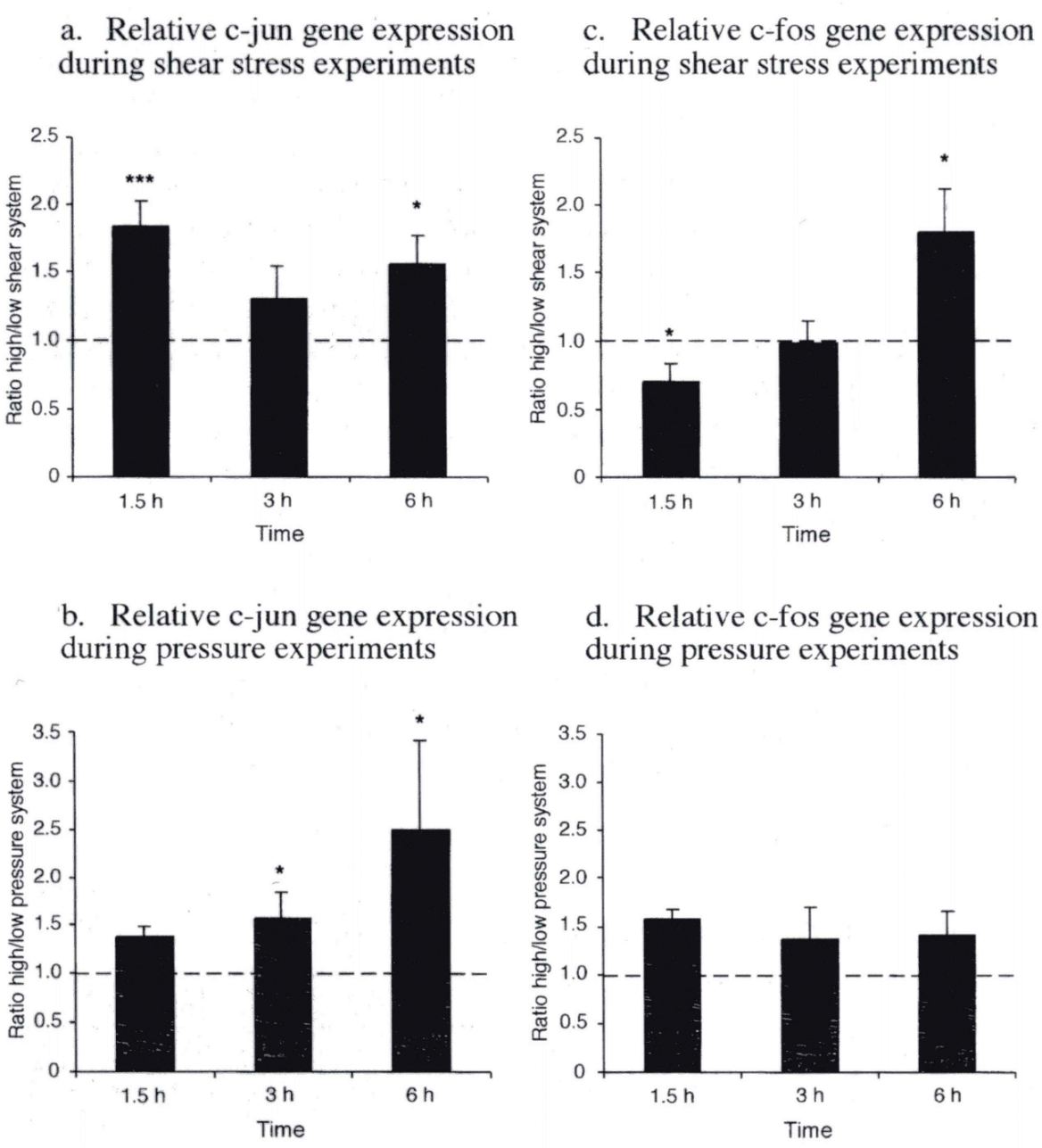

Figure 1.16 Figure from [142] showing the increase in c-jun (a) and c-fos (c) gene expression in human veins exposed to high WSS relative to veins exposed to low WSS.

These studies of human veins demonstrate an increase in IEG expression minutes and hours after mechanical stimulation, which may explain why these vessels frequently fail due to long-term IH formation.

From the studies reviewed in this section and others, it is apparent that hemodynamic parameters affect the formation of IH. Table 1.3 summarizes the research relating hemodynamics and the biologic response of vascular cells discussed in this section.

Table 1.3 Summary table of research determining the effect of hemodynamics on vascular cell response leading to IH. There is no information available in the literature on the relationship between WSS and apoptosis.

Hemodynamic Parameter	EC Proliferation	SMC Proliferation	EC Apoptosis	EC IEG Expression	SMC IEG Expression
static (no flow)	N/A	⇑[104-107, 112, 116, 117]	⇑[128]	⇓[44, 142]	⇓[142]
low WSS	N/A	⇓[110, 111]	N/A	⇑[43, 139, 142]	⇑[142]
high WSS	⇑[108]	⇑[113]	N/A	⇑[45]	N/A
spatial WSSG	N/A	⇑[103]	⇑[118-121]	⇓[43-45, 139]	N/A

1.7 Summary and Limitations of Previous Research

Although there is a significant amount of research on the hemodynamic implications in IH, the results of these studies are not conclusive. Most studies have demonstrated a correlation between low WSS and IH (recall Table 1.2) [72, 73, 77-83, 86, 87, 94, 102], however, others have suggested that high WSS or WSS outside a prescribed "safe range" initiates IH formation [74, 85]. Still others have demonstrated a correlation between spatial and/or temporal wall shear stress gradient (WSSG) and IH formation (recall Table 1.2) [66, 84, 85, 87, 89-91, 94]. In addition to these global studies of hemodynamics and IH, a number of *in vitro* and *in vivo* experimental models have demonstrated that both high and low WSS cause a pathophysiologic response in vascular cells including changes in SMC proliferation, apoptosis and IEG expression (recall Table 1.3). For example, a number of cell culture and animal models demonstrate that increased WSS leads to decreased SMC proliferation [103-107, 110-112, 143]. However, studies of human saphenous vein tissue

demonstrate that exposing the vein to increased WSS causes an increase in SMC proliferation and IH formation [114, 115]. Other studies have demonstrated that disturbed flow and increased WSSG causes increased SMC proliferation [108, 113] while exposing cells and vascular tissue to physiologic WSS conditions decreases apoptosis [37, 118-121]. Finally, cell culture and human tissue studies have demonstrated that IEG expression is upregulated in response to WSS [43-45, 139, 142] and disturbed flow [45] and that genetically blocking the expression of IEG decreased IH formation [140, 141].

Although a significant amount of research has attempted to isolate the influence of hemodynamics on IH formation, no study has determined a quantitative correlation between a specific hemodynamic parameter and a particular cellular response that leads to IH. In previous studies there has been at least one of three key limitations that prevented this correlation:

1) no direct coupling between quantitative biologic and hemodynamic measurements

2) the values of these parameters were not continuously known or regulated

3) the biologic model was not complete

For example, physical flow and CFD models, such as those discussed in sections 1.5.3 and 1.5.4, only give information about the hemodynamic environment and do not include any biologic measurements. Findings from these studies about the influence of hemodynamics on IH formation are based on qualitative or general quantitative biologic data from separate studies and are not conclusive. For *in vivo* human and animal investigations, such as those discussed in sections 1.5.1 and 1.5.2, the biologic endpoints (i.e. intimal thickness) and hemodynamic parameters (i.e. WSS) are measured either at the start of the experiment or after the chosen time period (i.e. days, weeks, months) during which the hemodynamic parameters can not be tightly regulated. Therefore, the findings from these studies do not include any knowledge of how the hemodynamic parameters vary over time and the results from these could be misleading. Most of the previous studies on the vascular cell response to hemodynamic stimuli have been limited to cell culture studies, such as those discussed in sections 1.6.1.1, 1.6.2.1 and 1.6.3.1, which do not include the effects of surrounding vascular cells and the structure of the vessel wall. *In vivo* animal and human models, such as those discussed

in sections 1.6.1.2, 1.6.1.3, 1.6.2.2, 1.6.2.3, 1.6.3.2 and 1.6.3.3, give more applicable results to the clinical environment but the effect of hemodynamics can not be isolated. For example, the use of prosthetic grafts or saphenous veins impose a compliance mismatch at the anastomosis.

Given these limitations of previous studies, there is a need for research that exposes an intact vessel to a well-controlled hemodynamic environment and quantifies the resulting biologic and hemodynamic parameters in a directly coupled manner.

1.8 Specific Aims

The proposed work is designed to test the following hypothesis:

A quantitative correlation exists between the hemodynamic phenomena at the distal anastomosis of a vascular bypass graft and carefully selected, acute biological markers of intimal hyperplasia.

The specific aims that were executed to address this hypothesis are as follows:

Specific Aim #1: Utilize experimental methods to determine the spatial variation of acute biological markers related to IH formation (c-fos, c-jun, egr-1 protein expression and apoptosis) in artery-artery, end-to-side anastomoses exposed to well-controlled *ex vivo* perfusion.

Specific Aim #2: Utilize computational methods to determine the spatial variation of wall shear stress (WSS) and wall shear stress gradient (WSSG) in three-dimensional, reconstructed models of each experimental distal anastomosis perfusion.

Specific Aim #3: Determine whether a quantitative correlation exists between the spatial variation of IH-related molecular endpoints and the spatial variation of WSS and/or WSSG in order to understand the precise hemodynamic factors that lead to IH formation.

This research project involved two main components: the perfusion of intact vessels *ex vivo* (Specific Aim #1) and the estimation of precise hemodynamic parameters using a CFD model incorporating the perfusion conditions and a realistic geometry (Specific Aim #2). The perfusion experiments allowed us to assess the regional variation of IEG protein expression and vascular cell apoptosis associated with the acute

intimal hyperplastic response of an artery-artery, ETS anastomosis. Since the pressure and flow rate in the *ex vivo* perfusion model were precisely known, the CFD model utilized this information along with the anastomotic geometry to accurately estimate WSS and WSSG. This process allowed for a distinct and unique coupling between the perfusion experiment and the computational simulation that has not been achieved previously. The final step was to assess the possible quantitative correlation between the IEG protein expression and/or apoptosis in the perfused vessels and the local WSS and WSSG acting on the vessel walls (Specific Aim #3).

The overall goal of this research was to provide specific evidence of the influence of hemodynamics on the acute, pathological mechanisms that result in IH. In the long-term, this research may help improve the clinical success rate of vascular bypass grafts. That is, once the important hemodynamic variables that cause a pathologic response at the distal anastomosis are determined, surgeons may be able to tailor the anastomosis to achieve optimal hemodynamics. Specifically, surgeons have some control over the geometry of the anastomosis, and therefore have the ability to alter the hemodynamics in order to minimize the pathologic variables leading to IH formation. Additionally, once the important hemodynamically induced molecular players are identified, clinicians could treat the surrounding tissue pharmaceutically or genetically to reduce the production of these molecules at the time of bypass grafting.

2 .0 *EX VIVO* PERFUSION EXPERIMENTS

2.1 Introduction

2.1.1 Advantages of an *Ex Vivo* Perfusion System

The experimental aspect of this research utilizes a whole-vessel, *ex vivo* perfusion system because of the advantages of this system over other models. As demonstrated in sections 1.5 and 1.6, most of the previous research on the biologic response of vascular cells to hemodynamic stimuli has been conducted in cell culture models or *in vivo* animal models. Although cell monolayer and co-culture models allow for the precise control over imposed the biomechanical environment, they do not incorporate the true vessel structure. Therefore the results can not be extrapolated to the clinical setting. *In vivo* animal models do incorporate the complete vascular structure but do not allow for the precise control over individual hemodynamic parameters (i.e. pressure and flow) over the duration of the experiment, which can last days, weeks or months for IH studies. Therefore, this research utilizes a whole-vessel *ex vivo* perfusion system that allows for the precise and individual regulation of pressure and flow within the vessels and maintains these values throughout the experiment.

2.1.2 Previous Research Utilizing an *Ex Vivo* Perfusion System

A number of research groups have studied the effect of biomechanical stimulation on intact vascular tissue using *ex vivo* perfusion systems [72, 144-150]. Specifically, our group and its predecessors at the University of Pittsburgh have developed a system and utilized it extensively for a variety of applications [144, 146, 147, 150-153]. Berceli *et al.* developed paired perfusion systems to expose human saphenous vein segments to arterial or venous flow and pressure conditions for 20 hours [144]. They found alterations in endothelial cell morphology and low-density lipoprotein metabolism in the veins exposed to arterial conditions. Labadie *et al.* improved this system by incorporating a computer-controlled in-line gate valve that allowed for the generation of physiologic, arterial pressure waveforms as seen in Figure 2.1 [146]. They validated the system by evaluating vascular homeostasis *ex vivo* using vasomotor bioassays after one, 24 and

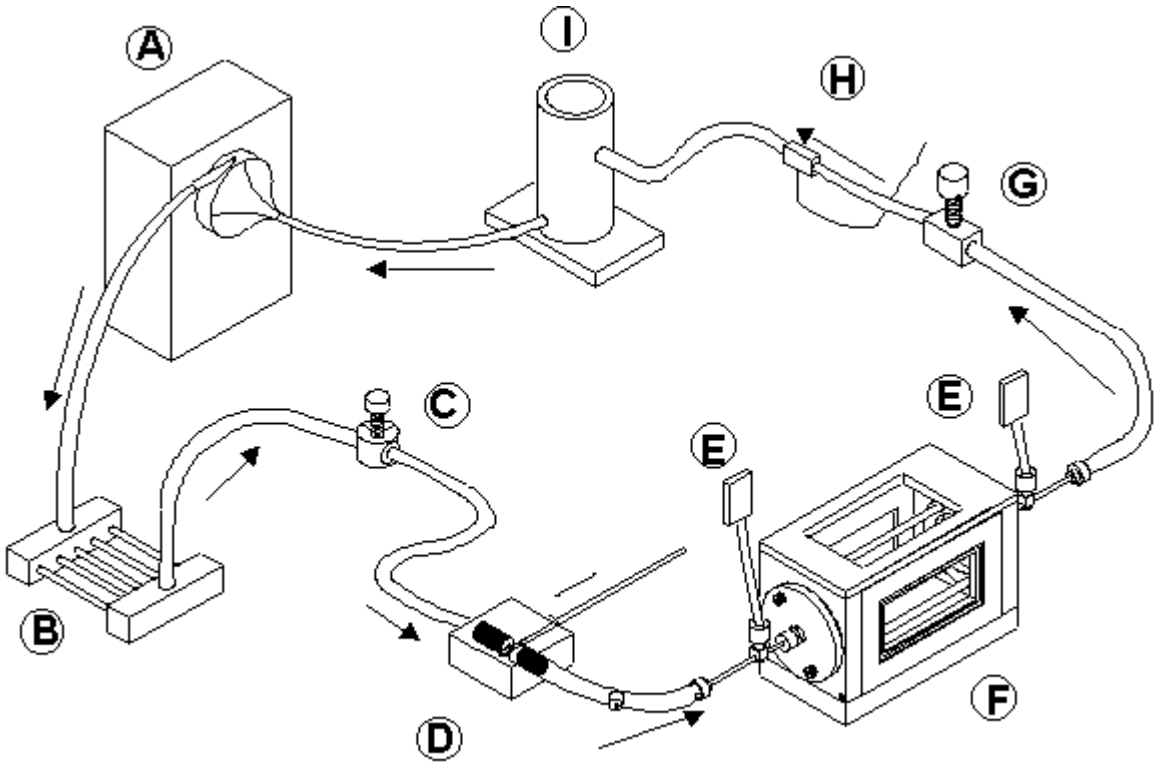

Figure 2.1 Schematic of the arterial perfusion system used by Labadie *et al.* where tissue culture medium is pumped by a centrifugal pump (A) through a heat exchanger (B) and past a pressure regulator (C). A gate valve (D) creates pulsatility and the pressure is measured with pressure transducers (E). The vessel is secured in the vessel housing chamber (F). The flow rate is maintained with a needle valve flow resistor (G) and measured with an in-line flow probe (H). The perfusate is then collected in the reservoir for recirculation through the system. Figure from [146].

48 hours of perfusion. Additionally, human saphenous vein segments were perfused for 24 hours and the resulting confocal and transmission electron micrographs demonstrated typical vascular morphology. Vorp *et al.* further modified the system so that cyclic strains, consistent with those found in native blood vessels, could be applied to intact vessels using a combination of twisting and axial stretching as shown in Figure 2.2 [147]. This apparatus, called the dynamic vascular testing (DVT) device, was successfully utilized by Severyn *et al.* [151] and Muluk *et al.*[150] to study the effect of coronary and lower extremity arterial biomechanics on the thrombogenicity of porcine and human vascular segments. Muluk *et al.* found a significant enhancement of TF expression in veins exposed to coronary arterial vein graft conditions

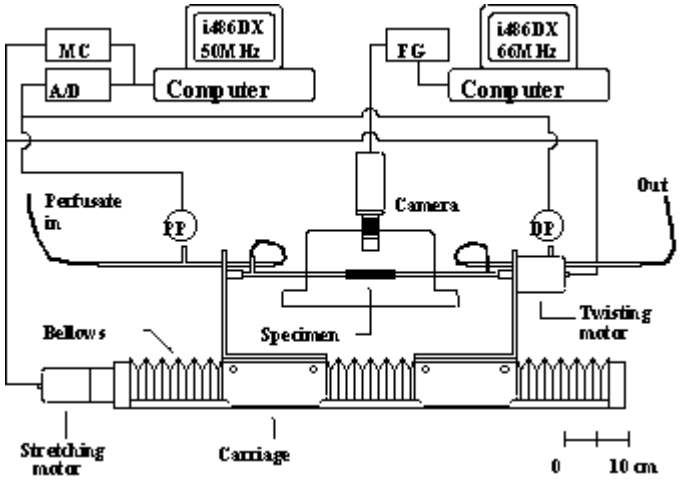

Figure 2.2 Schematic of the DVT system showing the twisting and stretching motors. Figure from [147].

compared to those exposed to venous conditions. In a similar study, Vorp *et al.* exposed porcine arteries to cyclic bending consistent with that found in coronary arteries in vivo [152]. Their results demonstrated a consistent and significant downregulation of E-selectin and matrix metalloproteinase-1 (MMP-1) in the specimens subjected to cyclic bending as compared to the non-bending control. Kute *et al.* also used this *ex vivo* perfusion system to determine the effect of disturbed flow on TF and IEG expression in porcine femoral arteries [153]. Before the initiation of flow, umbilical tape was used to constrict each vessel at its center for approximately 1/3 the length of the vessel, resulting in a 30% reduction in the local diameter. The constricted arteries were then perfused under steady flow and pressure conditions (100 mmHg and 100 cc/min). These flow conditions resulted in a normal wall shear rate (WSR) distribution (~480 sec^{-1}) in the constricted region and low WSR in the proximal and distal segments (~80 sec^{-1}). They found a significant increase in c-fos, c-jun and TF gene expression in the constricted regions compared to the proximal, non-constricted segments of the same vessels. Additionally, TF surface activity in the constricted segments was significantly higher than in the distal, non-constricted segments.

These studies demonstrate that the *ex vivo* perfusion system developed and modified by our research group at the University of Pittsburgh can apply a wide range of well-controlled physiologic and pathologic

biomechanical forces on intact vascular tissue, while preserving the basic structural and phenotypic characteristics of the vessels.

2.2 Methods

2.2.1 Modification of the *Ex Vivo* Perfusion System

The basic *ex vivo* perfusion system, shown in Figure 2.1 and used for numerous research projects in the past [146, 147, 150-153], was modified slightly in order to accommodate the distal ETS bypass graft geometry (see Figures 2.3 and 2.4). Because these perfusions did not require pulsatility, the gate valve was removed from the system. The removable spool in the vascular housing chamber was modified to accommodate the graft segment; i.e., another tee entered the chamber at a 30 degree angle. Also, the flow path was altered to allow for two different flow condition in the proximal artery. For perfusions with no flow entering through the proximal artery, the tubing connected to this tee was simply clamped as shown in Figure 2.3. For perfusions with retrograde flow in the proximal artery, tubing was attached to the proximal artery tee, and a flow probe, pressure transducer and flow resistor were inserted in this branch of tubing as shown

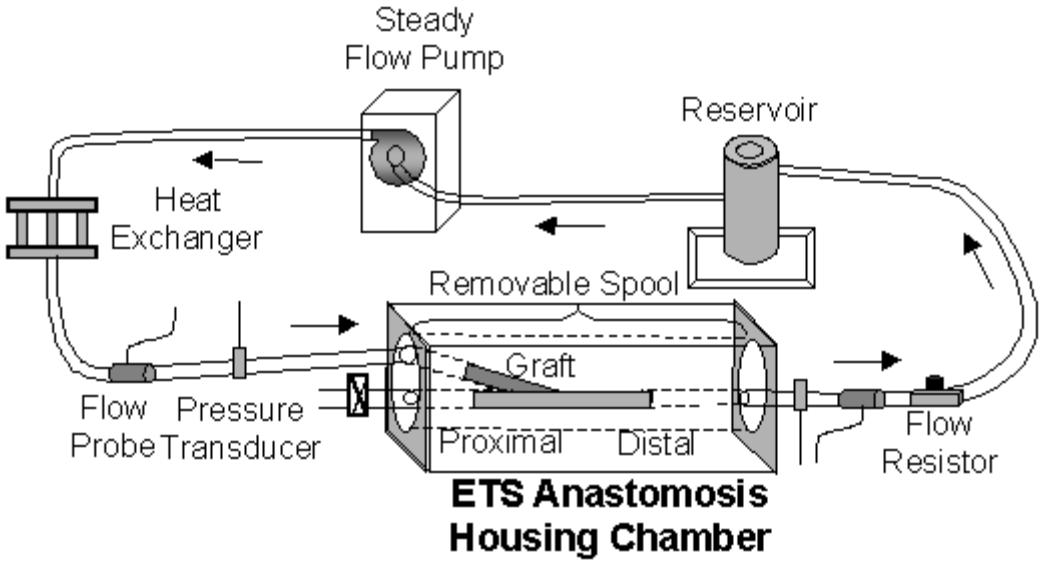

Figure 2.3 Schematic diagram of the Zero Flow Perfusion System. Note the occluded tubing proximal to the anastomosis in the arterial (host) segment.

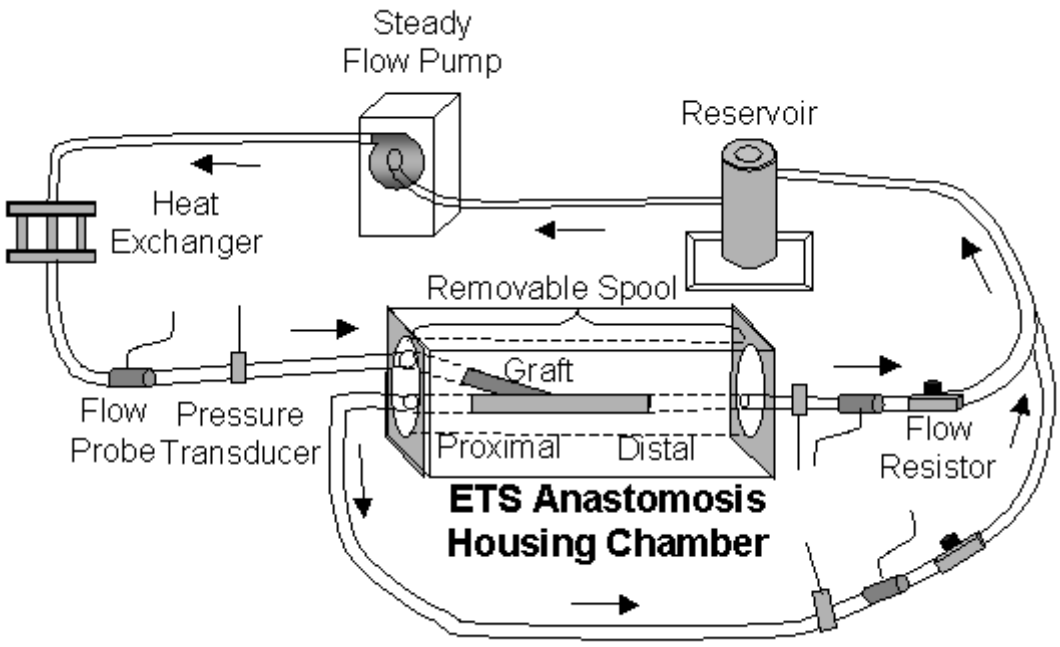

Figure 2.4 Schematic diagram of the Retrograde Flow Perfusion System.

in Figure 2.4. This allowed for independent control of pressure and flow in all three inlets/outlets of the distal, ETS anastomosis (graft, proximal and distal artery).

2.2.2 Tissue Source and Harvest

The right and left femoral arteries were harvested under semi-sterile conditions from ~230 kg pigs at Green Valley Packing Company, an abattoir in Claysville, PA. Care was taken to ligate any visible tributaries before removal of the vessel to limit handling of the tissue in the laboratory. The vessels were maintained at *in situ* length using two custom vascular clamps [144, 146] and the vessels were transported to our laboratory in a cold, Ringer's solution supplemented with antibiotics (Mefoxin, 0.5 g/liter) in order to prevent infection, papaverine (60 mg/liter) in order to prevent spasm and Heparin (500 units/liter) to prevent blood clot formation.

2.2.3 Experimental Design

For each experiment, an ETE and an ETS anastomosis was constructed and each was perfused in a separate perfusion system. The ETE anastomosis was used a control since it received the same surgical

trauma and mechanical forces induced by the vascular clips as the ETS anastomosis but did not experience disturbed flow. This allowed us to attribute any significant regional variations in biologic parameter in the ETS anastomosis to hemodynamic parameters as long as a regional variation in the same biologic parameters was not present in the ETE anastomosis. For a second control, a small segment of the vessel used for the ETE anastomosis was removed before creating the anastomosis. This nonperfused control was used to determine the baseline biologic values for each animal and to as sure that the perfusion was responsible for an alteration in biologic parameters.

2.2.4 Construction of ETE and ETS Distal Anastomoses

After transporting the vessels to the laboratory, one artery was arbitrarily chosen for the ETE anastomosis and the other was used for the ETS anastomosis. For the ETE anastomosis, the procedure described in section 1.2.2 was utilized. Specifically, the chosen artery was secured with 2-0 suture proximally and distally to two in-line perfusion tees supported within the removable spool. Media-199 was perfused through the vessel to check for previously undetected leaks, which were ligated with 4-0 suture. The vessel was then cut at the midsection and the intima-to-intima contact method was used to create the ETE anastomosis with VCS™ vascular clips under loupe magnification. This protocol causes the least amount of damage to the native vessels during the creation of the anastomosis and allows for a leak-free anastomosis [12]. A completed ETE anastomosis is shown in Figure 2.5.

For the ETS anastomosis, the procedure described in section 1.2.2 was utilized. Specifically, the proximal 1/3 of the other femoral artery was cut and designated as the “graft” segment and sutured at its proximal end to a tee entering the spool proximally at a 30 degree angle to the two in-line tees (see Figure 2.3). The remaining 2/3 of the same femoral artery was attached proximally and distally to two in-line perfusion tees using purse string sutures and a leak check was performed. A slit was cut in the midsection of the in-line vessel segment and the edges were everted and approximated to the everted edges of the distal end of the graft segment. Under loupe magnification, a few VCS™ vascular clips were placed at the toe and

heel of the ETS anastomosis to stabilize the vessels and then VCS™ vascular clips were placed continually from heel to toe on both sides of the anastomosis. A completed ETS anastomosis is shown in Figure 2.6.

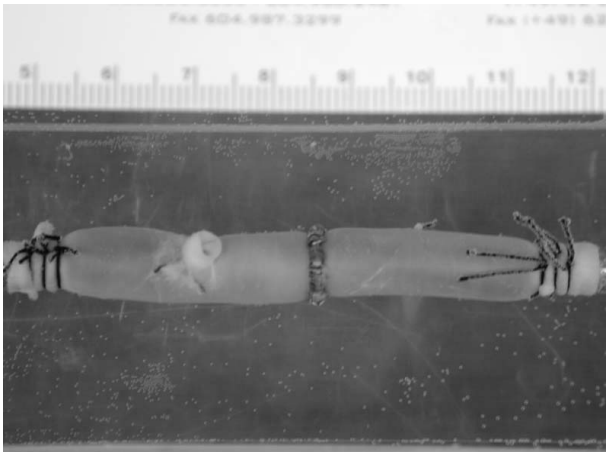

Figure 2.5 Completed ETE anastomosis.

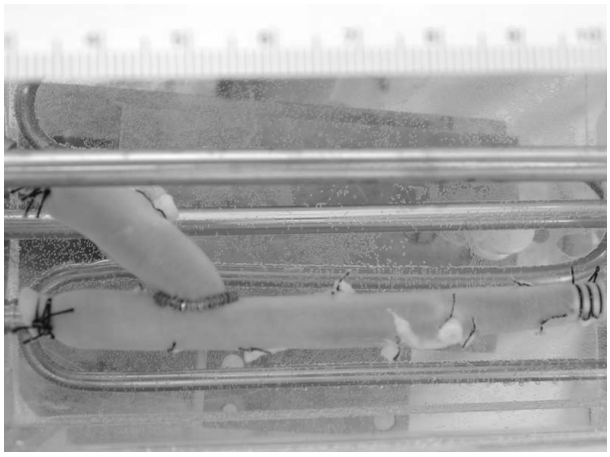

Figure 2.6 Completed ETS anastomosis.

The vessels were irrigated during anastomosis construction to assure vessel viability and the completed anastomosis were placed in the perfusion system within 3 hours of harvest and within 30 minutes of the anastomosis construction initiation. After the completion of each anastomosis, the tees were locked in place so that the vessels were maintained at *in vivo* length and the removable spool was placed into the vessel housing chamber. Flow of perfusion media was slowly initiated to reintroduce fluid into the anastomoses, and pressure and flow rate were gradually increased to the experimental levels described in sections 2.2.6 and 2.2.7.

2.2.5 General Perfusion Conditions

Vessels mounted into the *ex vivo* perfusion systems were exposed to precisely controlled hemodynamics. The closed-loop perfusion systems (recall Figure 2.3) allowed the circulation of perfusate (tissue culture Media-199 supplemented with 0.5 g/liter antibiotic/antimycotic) through the anastomosis contructions. All components of both perfusion systems that came in contact with the sterile perfusate (i.e. centrifugal pump head, Tygon™ tubing, connectors, flow resistors, tees, heat exchanger, vessel housing

chamber, reservoir, etc) were sterilized with ethylene-oxide before the experiment in order to minimize vessel contamination.

A Bio-Medicus™ centrifugal flow pump provided steady flow and variable needle-valve flow resistors in the flow circuit allowed for the independent adjustment of pressure and flow rates in the graft, proximal and distal artery segments. The pressures at each vessel segment were measured with standard pressure transducers attached to ports on the tees and the flow rate was measured with an ultrasonic flow transducer.

In a separate loop, a roller pump circulated a sterile adventitial bath solution (Media-199 supplemented with 0.5 g/liter antibiotic/antimycotic) around the specimen mounted in the sealed vessel housing chamber. Both the perfusate and adventitial bath media were maintained at 37°C, oxygenated and the pO_2 levels were measured every hour and the oxygen level was adjusted, if necessary, in order to maintain physiologic conditions. A pH indicator (phenol red) was present in the perfusate media to allow for the identification of any leaks in the vessels into the clear adventitial bath. Phenol red also allowed for continual visual inspection of the pH level which was measured in the perfusate and adventitial bath with a hand-held probe every hour and adjusted, if necessary.

The anastomoses were exposed for six hours to the well-controlled flow and pressure levels explained in the following sections. This time point was chosen based on previous research of the shear-induced alteration of IEG protein levels in both cell culture and *in vivo* models [44, 140, 142], and because apoptosis can occur over this time period [38].

2.2.6 Perfusion Conditions for the ETS Anastomoses

Three flow conditions in the proximal artery of the distal ETS anastomosis can occur clinically when bypassing a blocked region of the native artery. A partial stenosis of a bypassed arterial segment may allow residual prograde flow through the proximal artery entering the distal anastomosis of the graft. A complete stenosis may allow for zero flow in the proximal artery segment or retrograde flow due to the presence of small collateral vessels upstream. In a computational model of a three-dimensional, idealized ETS anastomosis, we examined the effect of the proximal artery flow condition (i.e. prograde, zero and retrograde

flow) on the hemodynamics at the distal ETS anastomosis [154]. We found a marked difference in both the magnitude and spatial distribution of WSS and WSSG between the three conditions (see Figure 2.7). For example, as shown in Figure 2.8, the maximum WSS magnitude on the floor of the artery proximal to the anastomosis for the prograde and zero flow cases is 1.8 and 3.9 dynes/cm^2, respectively, while it is increased to 10.3 dynes/cm^2 in the retrograde flow case. Similarly, the maximum value of WSSG magnitude on the floor of the artery proximal to the anastomosis for the prograde flow case is 4.9 dynes/cm^3 while it is increased to 13.6 and 24.2 dynes/cm^3, respectively, in the zero and retrograde flow cases. We also calculated the severity parameter (SP), a quantification of hemodynamic variation [90, 155], at the anastomosis and the value of SP is highest for the retrograde flow case (13.7 dynes/cm^3) and 8.1% and 12.1% lower than this for the prograde (12.6 dynes/cm^3) and zero (12.0 dynes/cm^3) flow cases, respectively. Therefore, our model results indicated that a wide range of hemodynamic parameters could be imposed by varying the flow condition in the proximal artery. Because the largest difference in the maximum WSS and WSSG magnitude

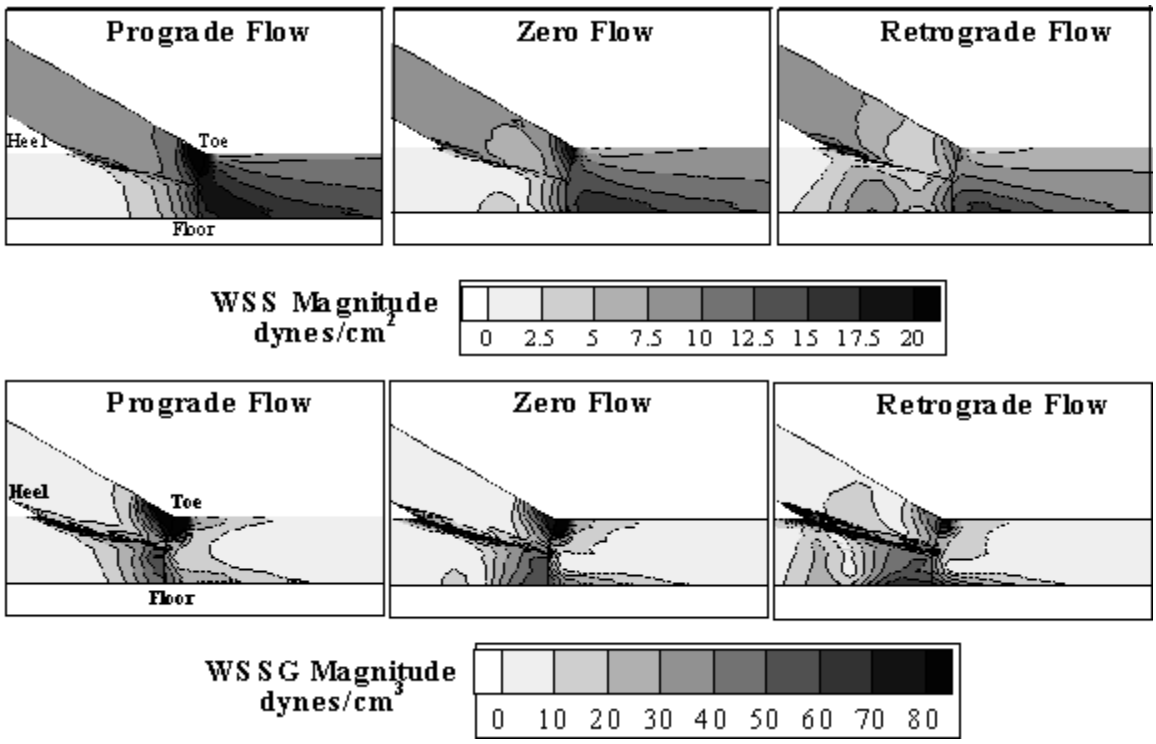

Figure 2.7 Contour plots of WSS and WSSG magnitude for each flow case (prograde, zero and retrograde). Figure from [154].

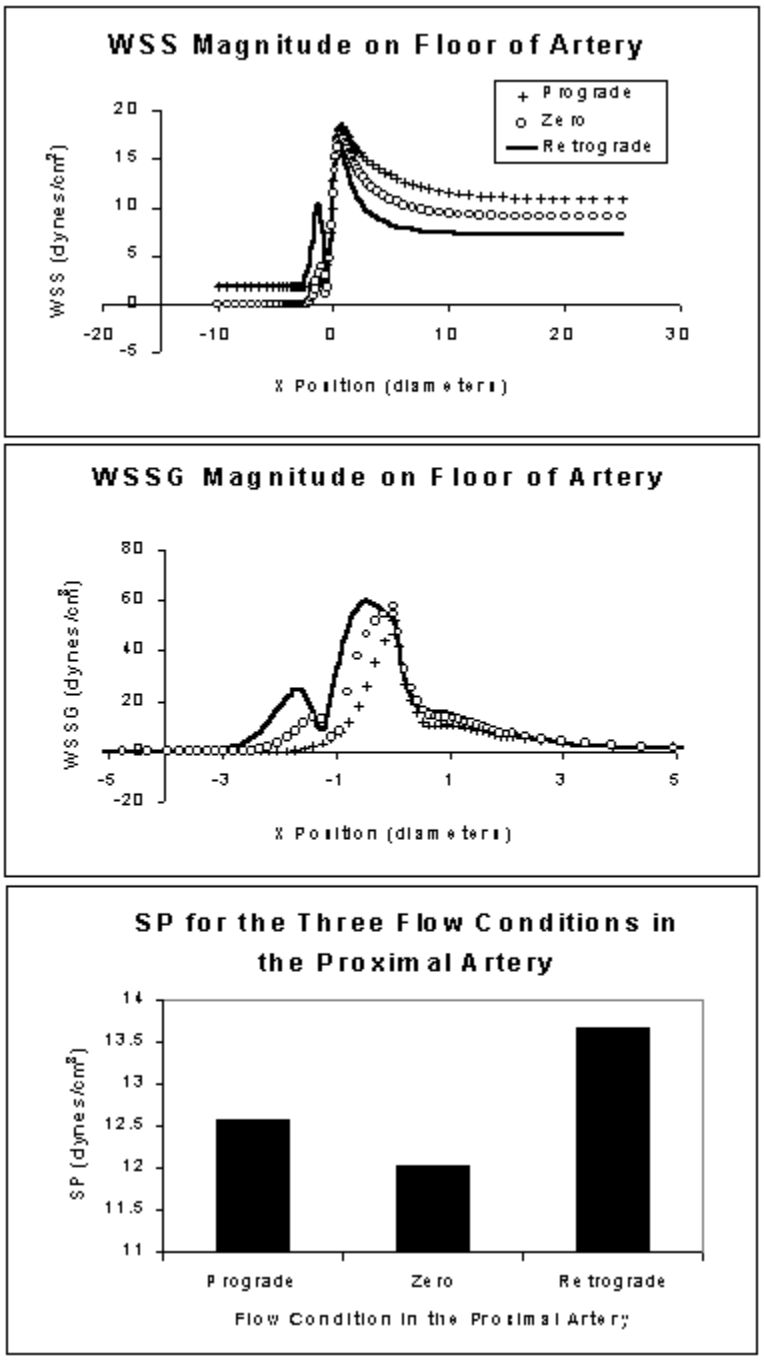

Figure 2.8 Comparison of WSS and WSSG magnitude along the artery floor and the value of SP at the anastomosis for the three flow cases (prograde, zero, retrograde). Figure from [154].

on the floor of the artery proximal to the anastomosis, and in the value of SP at the anastomosis, occurred between the zero and retrograde flow conditions, we simulated these conditions for the ETS anastomoses perfused *ex vivo*. Accordingly, each ETS anastomosis was exposed to one of two flow protocols described below and shown schematically in Figure 2.9.

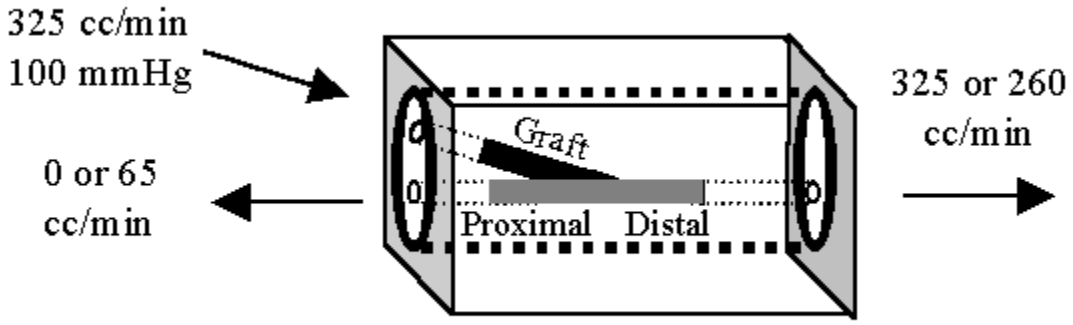

Figure 2.9 Perfusion conditions for the ETS anastomosis. Each anastomosis was exposed to one of two flow protocols; zero (n=5) or retrograde (n=5) flow in the proximal artery.

2.2.6.1 Zero Flow in the Proximal Artery

For the zero flow protocol, the tubing attached to the proximal artery branch tee of the ETS anastomosis was clamped so that all flow entered the graft and exited through the distal artery segment. The graft inlet and distal artery outlet flow rates were maintained at 325 cc/min and the graft inlet pressure was maintained at 100 mmHg. This flow rate was chosen so that, based on the inner diameter of the vessels and tees (approximately 5mm), a WSR of approximately 440 sec^{-1} was imposed on the graft segment[1].

A total of five ETS anastomoses were perfused under these conditions. Based on previous studies of IEG expression in constricted porcine femoral arteries in our laboratory, we initially estimated the sample

[1] Arteries *in vivo* maintain a WSS of approximately 15-20 dynes/cm^2 [156]. Based on the viscosity of blood (i.e., 3.5 cP), a physiologic arterial WSR is 430-570 sec^{-1}.

size based on the formula for comparing two means of two groups with equal sample size using a two-sided test with significance level α and power 1 - β [157]:

$$N_{per\ group} \geq 2(Z_{1-\alpha/2}+Z_{1-\beta})^2(\sigma/\Delta)^2 \quad [2.1]$$

where σ is the standard deviation for the desired measurement in the control group and Δ is the expected change in means. The average ratio for the previous IEG studies was 0.26/0.55 = 0.47. Assuming that α = 0.05 and β = 0.025 so that $Z_{1-\alpha/2} = Z_{1-\beta}$ =1.96, this gave a sample size of seven. However, after analyzing the biologic data from the first set of zero flow ETS experiments, statistical significance (see section 2.2.13) was reached after only three experiments. Therefore, a total of five experiments was determined sufficient.

2.2.6.2 Retrograde Flow in the Proximal Artery

For the retrograde flow protocol, the tubing attached the proximal artery tee was not clamped so that flow could exit through this branch of tubing as well as the distal artery outlet. For this protocol, the graft inlet flow rate (325 cc/min) and pressure (100 mmHg) were maintained the same as in the zero flow protocol, but the outlet flow rates were adjusted to allow for the retrograde flow through the proximal artery. Specifically, the flow resistors downstream of the proximal and distal artery segments were adjusted so that 20% of the graft inlet flow rate (65 cc/min) exited through the proximal artery segment with the remaining flow (260 cc/min) exiting through the distal artery. This division of outflow rates was chosen based on the results of the computational study of the idealized ETS anastomosis that demonstrated elevated WSS, WSSG and SP in the retrograde flow model with a 5:1 division of flow (recall Figures 2.7 and 2.8) [154]. Based on similar arguments as presented in section 2.2.6.1, a total of five ETS anastomoses were perfused under these conditions.

2.2.7 Perfusion Conditions for the ETE Anastomosis

All distal ETE anastomoses were exposed to the same perfusion conditions as shown in Figure 2.10. The graft inlet flow rate (325 cc/min) and pressure (100 mmHg) were the same as both ETS flow protocols and since an ETE construction consists essentially of a straight tube, all flow exited through the distal artery.

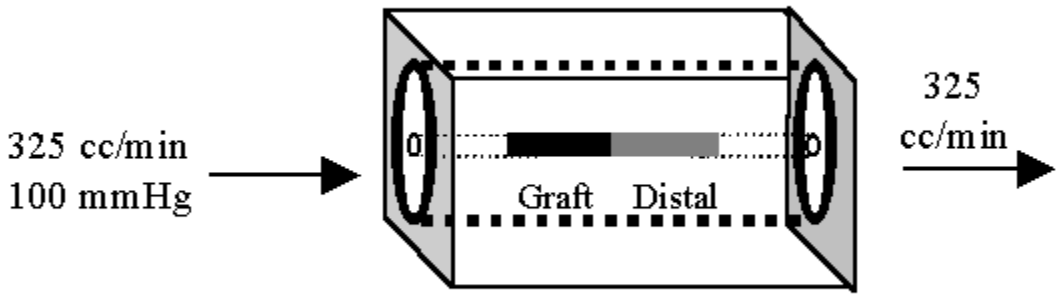

Figure 2.10 Perfusion condition for all ETE anastomoses (n=10).

A total of ten ETE anastomoses (5 paired with the zero flow ETS experiments and 5 paired with the retrograde flow ETS experiments) were perfused under these conditions.

2.2.8 Post-Perfusion Processing of the Tissue

2.2.8.1 Pressure Fixation

At the completion of the six hour perfusion, the ETE and ETS anastomoses were pressure fixed as follows. The adventitial bath media was first drained from the vessel housing chambers for each anastomosis and replaced with 2% paraformaldehyde. This fixative was also flushed through the anastomoses, the distal artery (for ETE and ETS) and proximal artery (for ETS only) outlets were clamped off and a pressure infusion bag attached to the graft inlet tubing maintained the pressure of the fixative at 100mmHg for one hour. The nonperfused control tissue was simply immersed in fixative for one hour at the beginning of the experiment. After fixation, the anastomoses were removed from the housing chambers and all tissue was placed in 30 % sucrose overnight at 4°C.

2.2.8.2 Cryopreservation

For further processing of the anastomosis tissue, the VCS™ vascular clips had to be removed but the original anastomosis geometry needed to be maintained. Therefore, a few VCS™ vascular clips were removed at a time using a VCS™ universal clip remover under loupe magnification and the clips were

replaced by continuous suturing with 6-0 prolene suture as shown in Figure 2.11. This was repeated until all clips were removed and replaced with suture. The anastomoses were then placed on filter paper and submerged in liquid-nitrogen-cooled isopentane for 20 seconds as shown in Figure 2.12. The vessels were immediately transferred to liquid nitrogen for 5 seconds to complete the freezing process and then set on a rack above liquid nitrogen so they would remain frozen. Next, they were embedded in TBS/TFM tissue freezing medium (Fisher Scientific) using a custom mold (Figure 2.12 C). The Teflon® mold was lined with aluminum foil and placed on a rack over liquid nitrogen. Tissue freezing medium was placed in the frozen mold and the vessels were submerged, careful to eliminate any air bubbles. Once the vessels were frozen, they were stored at -80°C until further processing.

2.2.8.3 Slicing

A custom vessel cutter was machined from a block of aluminum and had the same geometry as the freezing mold with the addition of thin grooves that allowed the penetration of a cryostat blade (see Figure 2.13). One by one, parallel slices were made every 2mm along the length of the vessel in the cold environment of a cryostat chamber. The orientation of the vessel slices were noted and the slices were stored

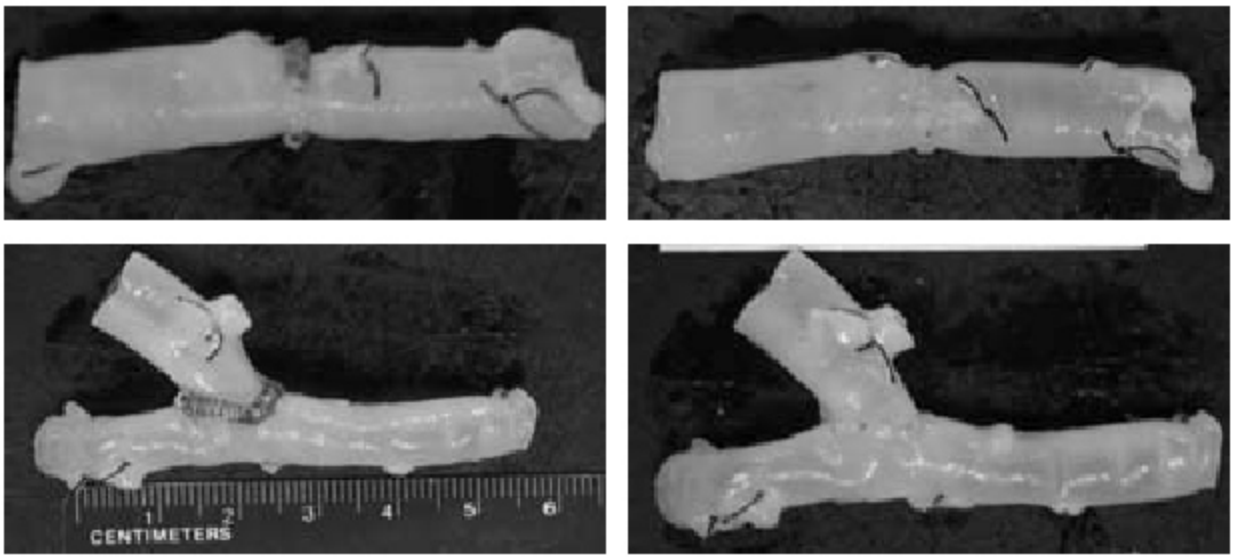

Figure 2.11 Photographs of ETE and ETS anastomoses from Retrograde Flow Experiment #4 before complete clip removal (left column) and after replacing clips with suture (right column).

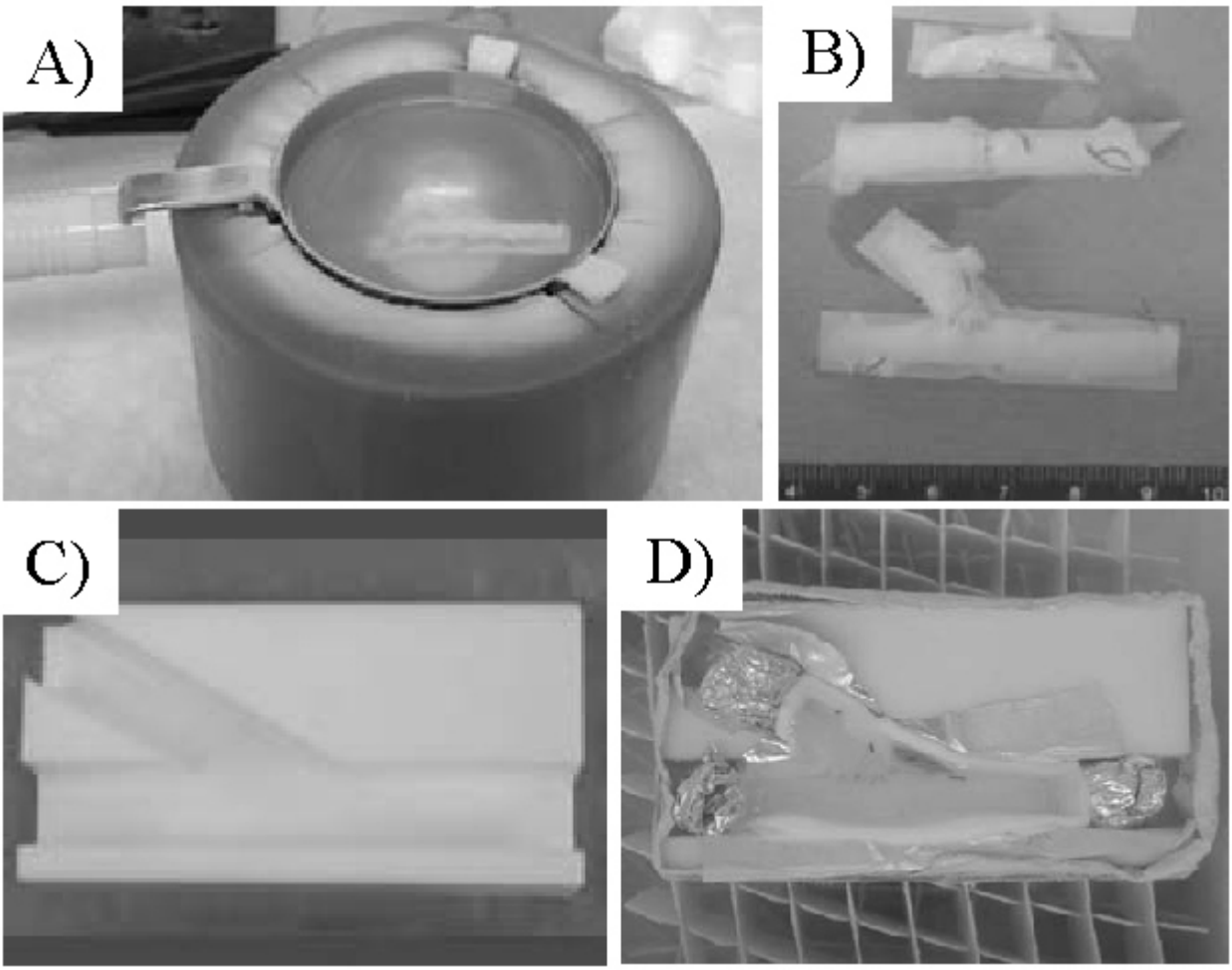

Figure 2.12 Photographs showing the freezing process A) ETS anastomosis submerged in liquid-cooled isopentane. B) All vessels from one experiment (nonperfused segment, ETE and ETS) after the freezing process. C) Custom mold. D) ETS anastomosis submerged in freezing medium in the mold lined with aluminum foil.

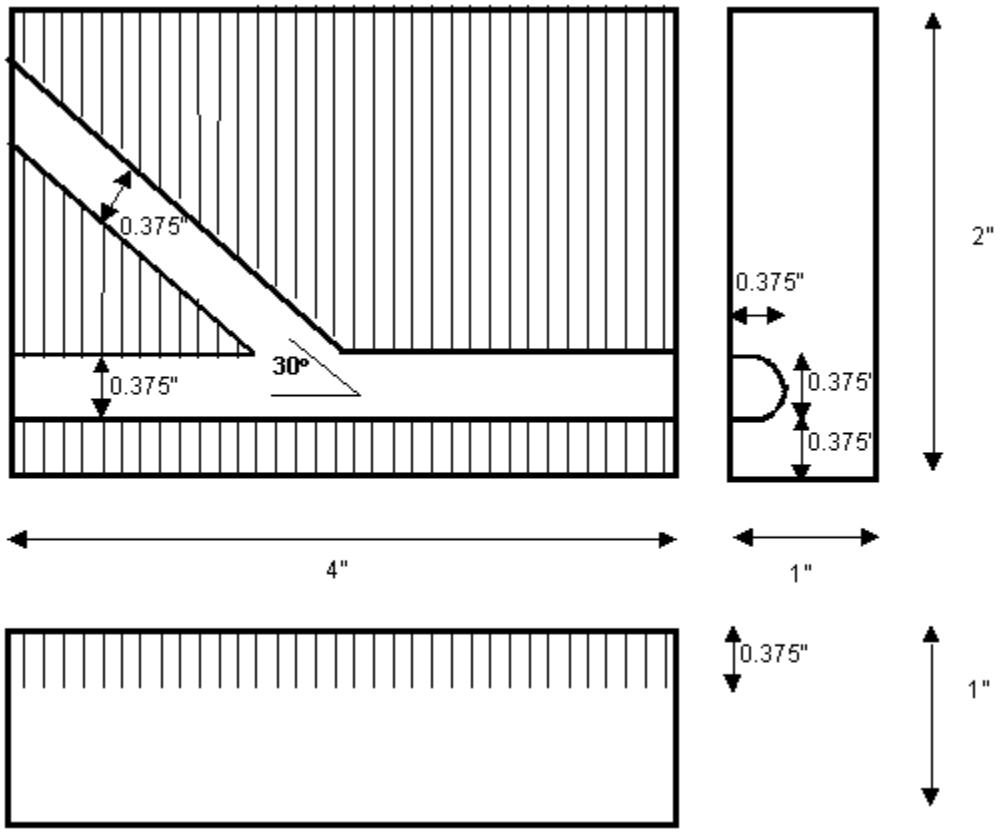

Figure 2.13 Diagram of the custom vessel cutter showing the three orthogonal views.

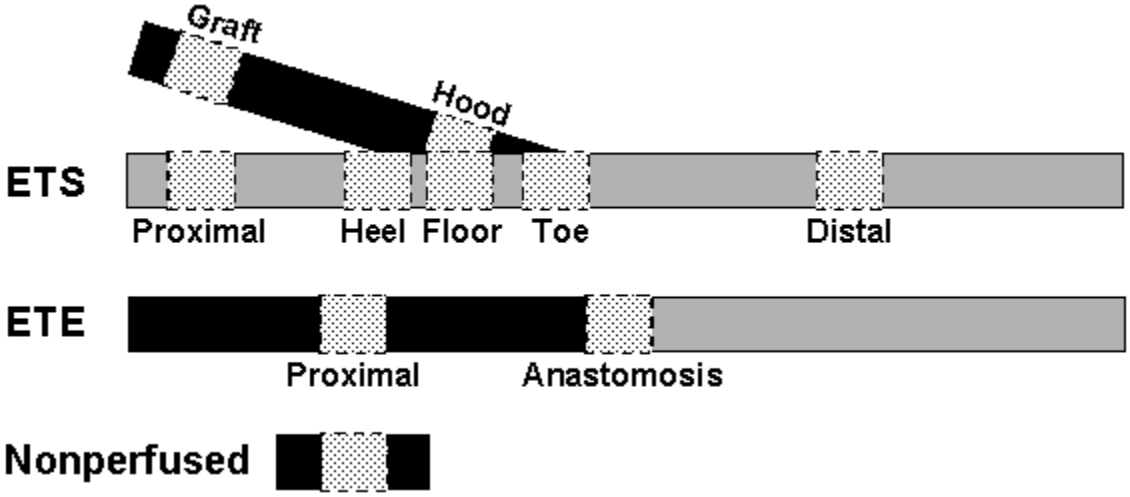

Figure 2.14 Schematic diagram of the ten regions of interest for each experiment including ETS graft, proximal artery, distal artery, heel, toe, hood and floor, ETE proximal and anastomosis, and the nonperfused segment.

in separate cassettes at -80°C. A total of ten regions of interest were studied in detail including seven regions from the ETS anastomosis (graft, proximal artery, distal artery, heel, toe, hood and floor), two regions from the ETE anastomosis (proximal and anastomosis) and the nonperfused segment as shown in Figure 2.14. Cross-sections from these regions of interest were cut with four micron thickness using a cryostat and mounted on gelatin coated microscope slides. The slides were stored at -80°C until staining.

2.2.9 Immunohistochemistry Technique for IEG Protein Staining

Immunofluorescence on serial slides was used to identify c-fos, c-jun and egr-1 protein expression. The slides were removed from the -80°C freezer and 2% paraformaldehyde was immediately placed on the sections for one hour at room temperature in order to fix the tissue to the slide. The slides were blocked with 5% goat serum for 45 minutes and incubated with the primary antibody (mouse anti-human c-fos monoclonal (sc-7481), rabbit anti-human c-jun polyclonal (sc-1694) or rabbit anti-human egr-1 polyclonal (sc-189), all from Santa Cruz Biotechnology) at a 1:100 dilution in bovine serum albumin for one hour. Next, the sections were incubated in the dark with the corresponding fluorescent secondary antibody (goat anti-mouse CY3 (115-165-003) for c-fos and goat anti-rabbit CY3 (111-165-003) for c-jun and egr-1, all from Jackson Immunoresearch Labs) at a 1:3000 dilution for one hour. Nuclei were counterstained with Hoechst (Molecular Probes H-1398) for 30 seconds and the slides were coverslipped using gel mount-Biomeda mounting medium (Fisher Scientific). Negative control slides received all incubation steps except the primary antibody. All slides were stored in the dark at 4°C until microscopy.

2.2.10 TUNEL Technique for Apoptosis Staining

To identify apoptosis, the terminal deoxynucleotidyl transferase (TdT)-mediated dUTP-biotin nick-end labeling (TUNEL) technique was used which fluorescently labels genomic DNA that is cleaved by an endonuclease selectively activated during apoptosis [36, 158]. Immediately after the slides were removed from the -80°C freezer, they were submerged in cold methanol for 30 minutes at -20°C to fix the tissue to the slide. The TUNEL mixture consisting of deionized water, TdT buffer, TdT, $CoCl_2$ (all from Roche Molecular Biochemicals #220582) and biotin-16-2'-deoxyuridine-5'-triphosphate (Roche Molecular

Biochemicals #1093070) was placed on the slides, which were then coverslipped. The slides were incubated with the TUNEL mixture for 1 hour in a humidified chamber at 37°C. The coverslips were removed and the streptavidin CY3 secondary antibody (Jackson ImmunoResearch #016-160-064) placed on the sections for one hour at room temperature. Nuclei were counterstained with Hoechst (Molecular Probes H-1398) for 30 seconds and the slides were coverslipped using gel mount-Biomeda mounting medium (Fisher Scientific). Positive control slides were incubated with DNAse1 to induce DNA fragmentation before the TUNEL mixture was applied. Negative control slides were incubated in deionized water and biotin only. All slides were stored in the dark at 4°C until microscopy.

2.2.11 Fluorescent Microscopy

Fluorescent images were digitally captured from an Olympus Provis microscope in the Center for Biologic Imaging at the University of Pittsburgh. The images were taken at 40X magnification with high numerical aperture, color corrected, oil immersion objectives and a high sensitivity, integrating three chip Sony color camera, (700X600 pixels) and Corecco frame grabber board. Multicolor cubes were used as filters to visualize the CY3 and Hoechst staining and separate images were taken so that one image showed the IEG protein or TUNEL (apoptosis) staining, and one showed all nuclei. For each region of interest, twelve images were taken around the circumference of the cross-section. Because the ETS hood and floor regions are not complete circles, as many images as possible (typically 6-8) were taken at regular, non-overlapping intervals. Images were saved in the 24-bit TIFF format.

2.2.12 Quantification of IEG Protein and Apoptosis Staining

The amount of IEG protein expression and apoptosis was quantified on a dedicated PC using the image analysis software Bioquant Nova (Version 5.00.8, R&M Biometrics, Nashville, TN). Because IEG proteins must translocate to the nucleus to affect transcription, CY3 staining was considered positive only if it overlapped nuclear (Hoechst) staining. Similarly, TUNEL fluorescently labels DNA fragments in the nucleus so CY3 staining for these slides was also only considered positive if it overlapped nuclear (Hoechst) staining. IEG protein staining was almost exclusively limited to the endothelium so only the amount of EC staining

was quantified for the IEG proteins. Apoptosis was present in both the endothelial and medial layers so the amount of apoptotic EC and SMC staining was quantified.

The step-by-step process for quantifying EC staining is demonstrated in Figure 2.15. For each paired set of images, the number of nuclei was first quantified as follows. The area of interest was drawn freehand along the internal elastic lamina to isolate the endothelium. The image was then thresholded by the user to highlight the bright nuclear staining. The software automatically determined the outline of nuclear staining based on this threshold level (Figure 2.15A). Some user intervention was required to split cells that were close to each other and to delete erroneous tracings in order to get an accurate cell count. Once the nuclear tracings and cell count were complete, the degree of staining was quantified as follows. The corresponding CY3 image was opened and the same area of interest as used in the cell count was utilized. The threshold for the bright CY3 staining was set by the user who utilized the tracings from the nuclei image as a guide. The outlines of CY3 staining was automatically determined by the software and adjusted by the user as necessary (Figure 2.15B). These tracings were overlapped with the nuclei tracings (Figure 2.15C) so that the user could determine which CY3 stainings were positive (Figure 2.15D). The false CY3 positive counts and tracings were then discarded. As a final check, the positive tracings were compared to an color overlay image (Figure 2.15E) of the CY3 (red) and nuclei staining (blue) in which only the pink/purple regions are positive for nuclear IEG protein or apoptosis. This process yielded the total number of EC nuclei and the total number of IEG protein positive or apoptotic EC for each set of paired images. This was repeated for all images taken for each cross-section. Care was used to ensure that at least 100 EC were counted for each region of interest in order to have a representative count.

An analogous process was used to quantify the degree of SMC apoptosis. The only difference was that the region of interest for each image included the media defined as the area between the internal elastic lamina and clearly distinguishable fibrous tissue of the adventitia. The number of SMC per image was much greater than the number of EC so the total number of SMC counted per region of interest was at least 1000.

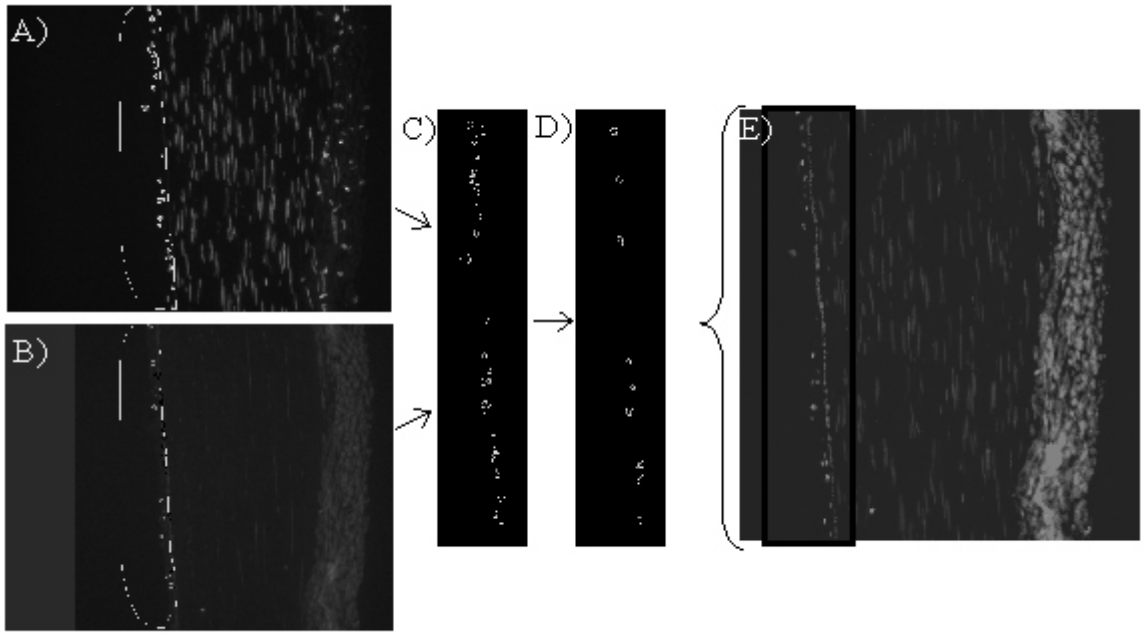

Figure 2.15 Process of EC staining quantification, using a c-fos example. EC region of interest is highlighted and the tracings of A) nuclei staining and B) CY3 staining are created. These tracings are overlapped (C) and only the ones that match are considered positive (D). These are compared to a color overlay image (E) that shows positive nuclear staining as pink or purple.

For each region of interest, the staining index (i.e. percentage of positive staining) was calculated by taking the total number of positive stained cells divided by the total number of nuclei for the entire cross-section.

$$Staining\,Index_{ROI} = \frac{Number\,of\,Positive\,Stained\,Cells_{ROI}}{Number\,of\,Nuclei_{ROI}} \qquad [2.2]$$

Therefore, five quantitative, biological parameters were calculated for each region of interest; i.e., staining indices for c-fos (EC), c-jun (EC), egr-1 (EC) and apoptosis (both EC and SMC). A mean staining index for

$$Mean\,Staining\,Index_{ROI} = \frac{\sum_{i=1}^{n} (Staining\,Index_{ROI})_i}{n} \quad [2.3]$$

Finally, the Mean Staining Index was calculated, which represented the percent of staining in all tissue exposed to one flow condition. This single, quantitative value was calculated by averaging the Mean Staining Index $_{ROI}$ over all regions of interest (m).

$$Mean\,Staining\,Index = \frac{\sum_{j=1}^{m} (Mean\,Staining\,Index_{ROI})_j}{m} \quad [2.4]$$

These data are presented as the mean ± standard error of the mean (SEM).

2.2.13 Statistical Analysis

To compare Mean Staining Indices between flow conditions (e.g., c-fos for the zero flow experiments versus c-fos for the retrograde flow experiments), unpaired Student's t-tests were performed using the mean staining indices for each region of interest calculated for the five experiments. A difference was considered significant if this test rendered a p-value less than 0.05. To compare the mean staining indices between types of staining (e.g., c-fos versus c-jun for the zero flow experiments), one-way ANOVA was performed [157]. If a significant ($p < 0.05$) F value was obtained, a post-hoc paired comparisons test was completed to determine which staining indices were significantly ($p < 0.05$) different from each other.

When assessing the regional variation of IEG protein expression and apoptosis, a normalized staining index was used to eliminate experiment to experiment variability. The normalized staining index for each region of interest in one experiment (Normalized Staining Index $_{ROI}$) was calculated by dividing the Staining Index $_{ROI}$ by the Mean Staining Index $_{ROI}$ averaged over all regions of interest for the same experiment (Mean Staining Index $_{Experiment}$).

$$Normalized\,Staining\,Index_{ROI} = \frac{Staining\,Index_{ROI}}{Mean\,Staining\,Index_{Experiment}} \quad [2.5]$$

Similar to the non-normalized data, a mean normalized staining index for each region of interest (Mean Normalized Staining Index $_{ROI}$) was calculated for all experiments with the same flow condition as:

$$Mean\,Normalized\,Staining\,Index_{ROI} = \frac{\sum_{i=1}^{n} (Normalized\,Staining\,Index_{ROI})_i}{n} \quad [2.6]$$

The data are presented as mean ± SEM.

One-way ANOVA was used to determine if the Mean Normalized Staining Index$_{ROI}$ for each stain (i.e., c-fos (EC), c-jun (EC), egr-1 (EC) and apoptosis (both EC and SMC)) varied between regions of interest for each flow condition. If a significant ($p < 0.05$) F value was obtained, a post-hoc paired comparisons test was completed to determine which regions of interest were significantly ($p < 0.05$) different from each other.

To compare the Mean Normalized Staining Indices $_{ROI}$ between flow conditions (e.g., c-fos in the toe region for the zero flow experiments versus c-fos in the toe region for the retrograde flow experiments), unpaired Student's t-tests were performed using the Mean Normalized Staining Indices for each region of interest calculated for the five experiments. A difference was considered significant if this test rendered a p-value less than 0.05.

2.2.14 Reliability

In order to minimize error, a single user performed the quantification protocol for one stain for all regions of interest of a particular experiment. To determine if there was a significant difference in the staining quantification completed by different users, the normalized staining indices for all regions of interest were quantified by two users for one experiment. Using a paired Student's t-test, there was no significant difference between the normalized staining index for c-fos ($p = 0.98$), c-jun ($p = 0.99$), egr-1 ($p = 0.63$), EC apoptosis ($p = 0.62$) or SMC apoptosis ($p = 0.42$). Therefore, the results shown below are independent of which user performed the quantification.

2.3 Results

2.3.1 Mean Staining Index

The Mean Staining Indices (mean ± SEM), calculated as per Equation 2.4, for c-fos, c-jun, egr-1, EC and SMC apoptosis for both flow conditions are presented in Figure 2.16. Note that negative control slides for all markers were devoid of nuclear staining. For the zero flow experiments, the c-jun (44.76% ± 5.98) and egr-1 (39.38% ± 5.12) Mean Staining Indices were significantly higher than the c-fos (21.91% ± 6.36), EC apoptosis (15.59% ± 4.93) and SMC apoptosis (5.7% ± 2.29) Mean Staining Indices. The SMC apoptosis Mean Staining Index (5.7% ± 2.29) was significantly lower than the c-fos (21.91% ± 6.36), c-jun (44.76% ± 5.98), egr-1 (39.38% ± 5.12) and EC apoptosis (15.59% ± 4.93) Mean Staining Indices. For the retrograde flow experiments, both c-jun (45.36% ± 5.47) and egr-1 (39.16% ± 7.5%) were significantly higher than the EC and SMC apoptosis Mean Staining Indices (32.21% ± 7.36 and 5.99% ± 1.89,

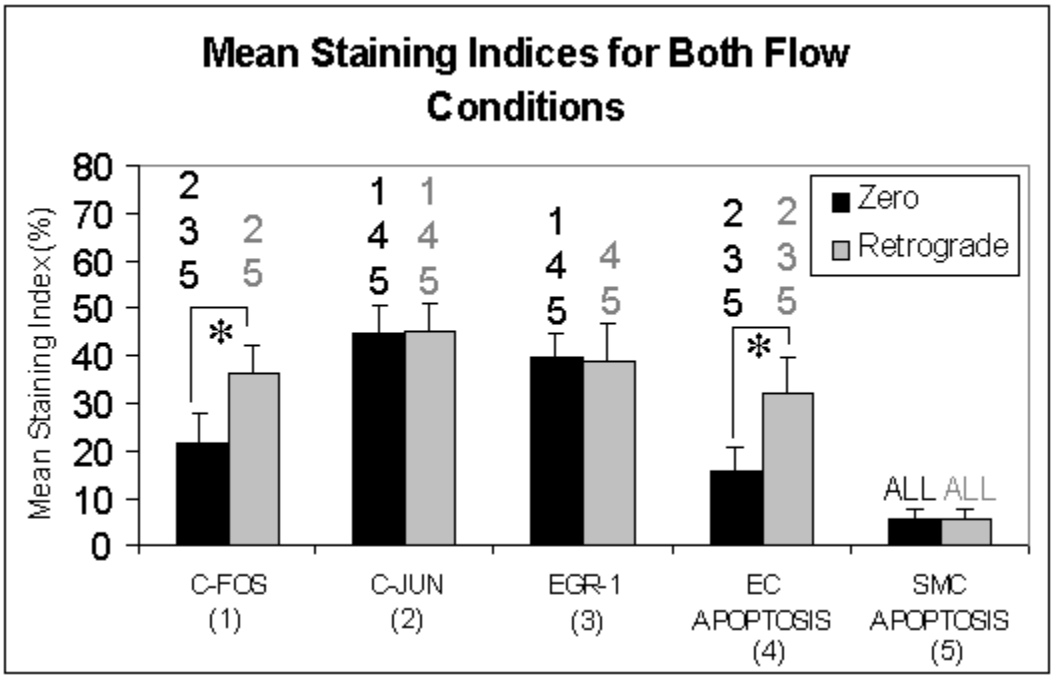

Figure 2.16 Mean Staining Indices (see Equation 2.4) for 1) c-fos, 2) c-jun, 3) egr-1, 4) EC apoptosis and 5) SMC apoptosis for the zero flow (black) and retrograde flow (grey) experiments. The numbers above each data point indicate which indices are significantly different from that index. An asterisk (*) indicates a significant difference between flow conditions for that index.

respectively) while only the c-jun Mean Staining Index (45.36% ± 5.47) was significantly higher than the c-fos Mean Staining Index (36.27% ± 5.77). Similar to the zero flow experiments, the SMC apoptosis Mean Staining Index (5.99% ± 1.89) was significantly lower than the c-fos (36.27% ± 5.77), c-jun (45.36% ± 5.47), egr-1 (39.16% ± 7.5%) and EC apoptosis (32.21% ± 7.36) Mean Staining Indices. The c-fos and EC apoptosis Mean Staining Indices for the zero flow condition (21.91% ± 6.36 and 15.59% ± 4.93, respectively) were significantly lower than the same indices for the retrograde flow experiments (36.27% ± 5.77 and 32.21% ± 7.36, respectively).

2.3.2 Mean Normalized Staining Index $_{ROI}$

The Mean Normalized Staining Indices $_{ROI}$ (mean ± SEM), calculated as per Equation 2.6, for c-fos, c-jun, egr-1, EC and SMC apoptosis are presented for each region of interest and both flow conditions in Figures 2.17, 2.18, 2.19 and 2.20, respectively. Additionally, similar graphs incorporating all the data (zero and retrograde flow experiments) are shown in Figures 2.21 (c-fos and c-jun) and 2.22(egr-1 and apoptosis).

2.3.2.1 Regional Variation of C-fos Protein

The regional variation of c-fos protein expression followed the same trend for both flow conditions (Figure 2.17). In the zero flow experiments, the regions that were significantly different from the highest number of other regions were ETS proximal and ETS toe. The ETS proximal region (1.62 ± 0.203) had the highest c-fos Mean Normalized Staining Index $_{ROI}$ and this value was significantly higher than the c-fos Mean Normalized Staining Index $_{ROI}$ for the ETS heel (0.873 ± 0.058), toe (0.713 ± 0.175), floor (0.824 ± 0.147) and hood (0.772 ± 0.195) regions. The ETS toe region (0.713 ± 0.175) had the lowest c-fos Mean Normalized Staining Index $_{ROI}$ of the perfused regions and this value was significantly lower than the c-fos Mean Normalized Staining Index $_{ROI}$ for the ETS proximal (1.62 ± 0.203), distal (1.261 ± 0.339) and ETE proximal (1.290 ± 0.176) and anastomosis (1.334 ± 0.170) regions.

In the retrograde flow experiments, the regions that were significantly different from the highest number of other regions were ETS distal and ETS hood. The ETS distal region (1.345 ± 0.157) had the highest c-fos Mean Normalized Staining Index $_{ROI}$ and this value was significantly higher than the c-fos Mean Normalized

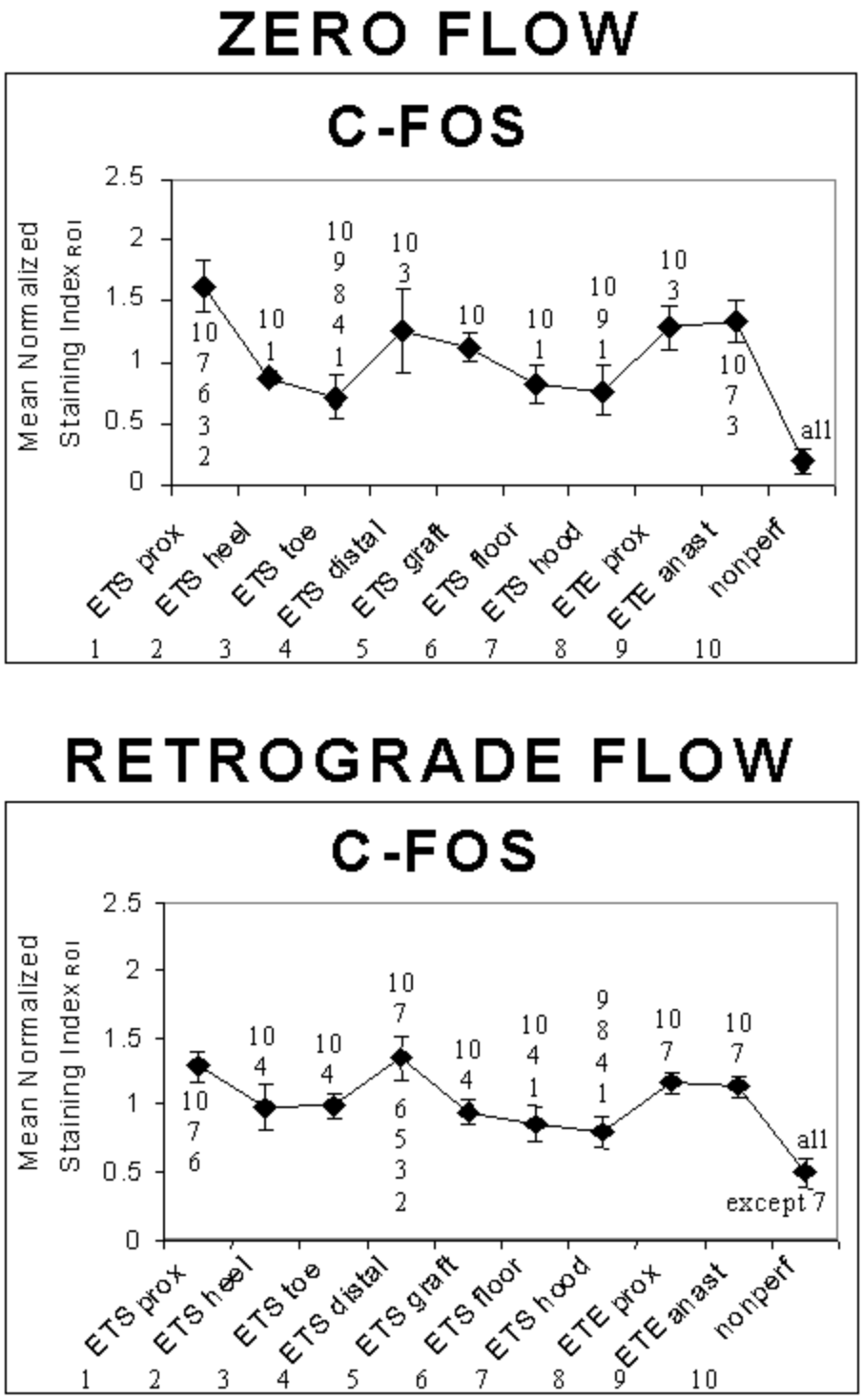

Figure 2.17 Mean Normalized Staining Index $_{ROI}$ (see Equation 2.6) for c-fos for the zero flow (top) and retrograde flow (bottom) experiments. The numbers above or below each data point indicate which regions (1-ETS proximal artery, 2-ETS heel, 3-ETS toe, 4-ETS distal artery, 5-ETS graft, 6-ETS floor, 7-ETS hood, 8-ETE proximal, 9-ETE anastomosis and 10-nonperfused segment) are significantly different from that region.

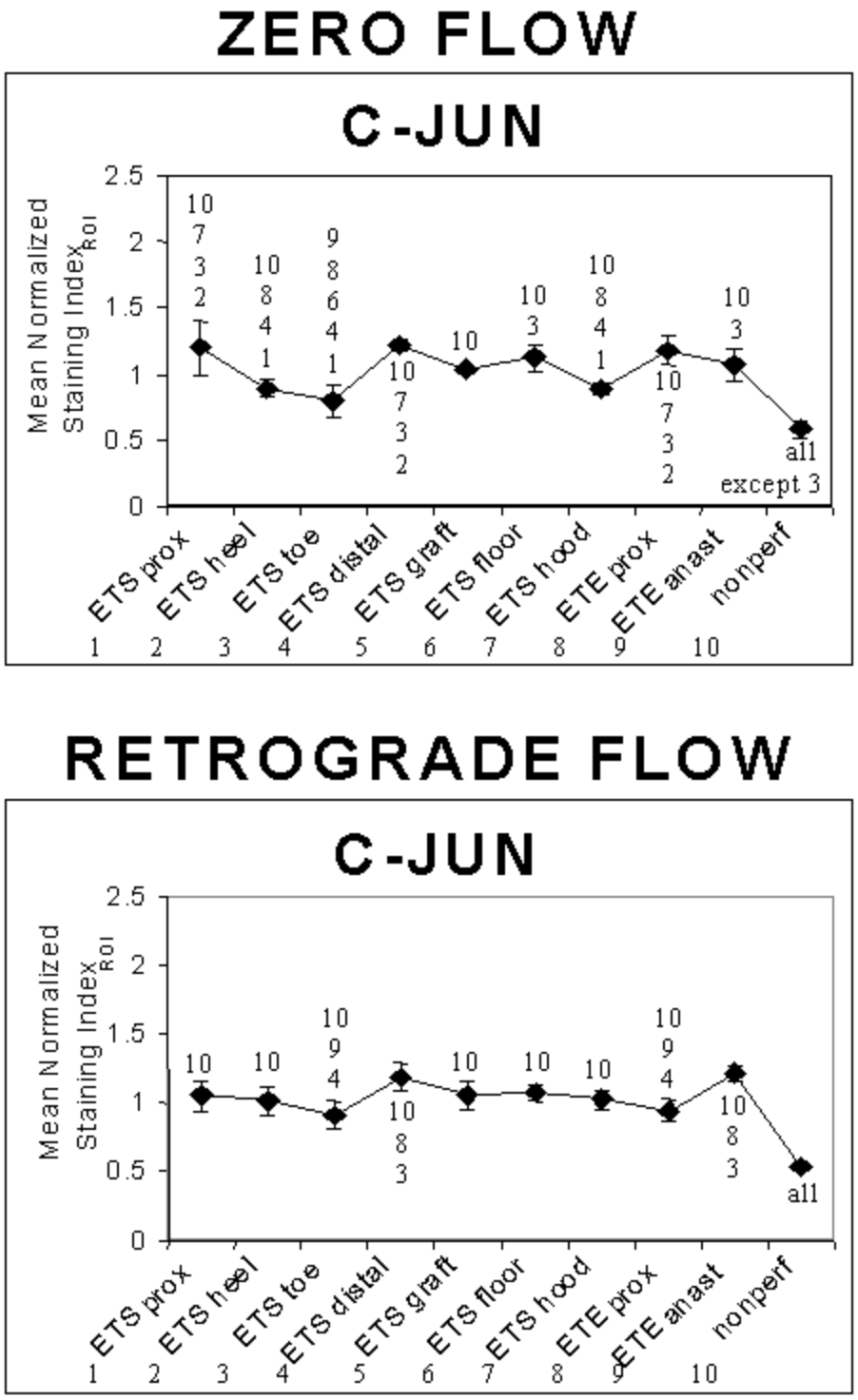

Figure 2.18 Mean Normalized Staining Index $_{ROI}$ (see Equation 2.6) for c-jun for the zero flow (top) and retrograde flow (bottom) experiments. The numbers above or below each data point indicate which regions (1-ETS proximal artery, 2-ETS heel, 3-ETS toe, 4-ETS distal artery, 5-ETS graft, 6-ETS floor, 7-ETS hood, 8-ETE proximal, 9-ETE anastomosis and 10-nonperfused segment) are significantly different from that region.

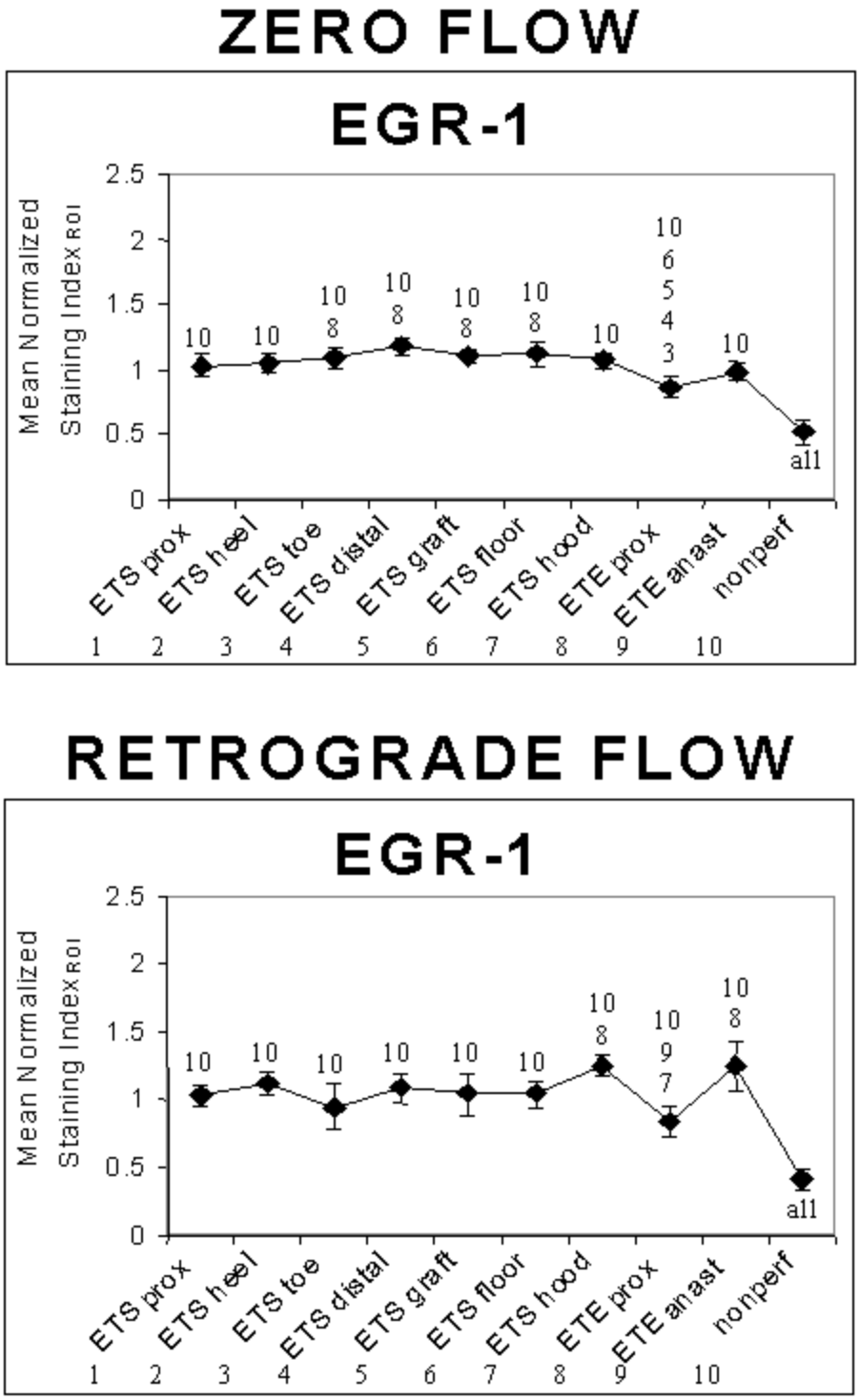

Figure 2.19 Mean Normalized Staining Index $_{ROI}$ (see Equation 2.6) for egr-1 for the zero flow (top) and retrograde flow (bottom) experiments. The numbers above or below each data point indicate which regions (1-ETS proximal artery, 2-ETS heel, 3-ETS toe, 4-ETS distal artery, 5-ETS graft, 6-ETS floor, 7-ETS hood, 8-ETE proximal, 9-ETE anastomosis and 10-nonperfused segment) are significantly different from that region.

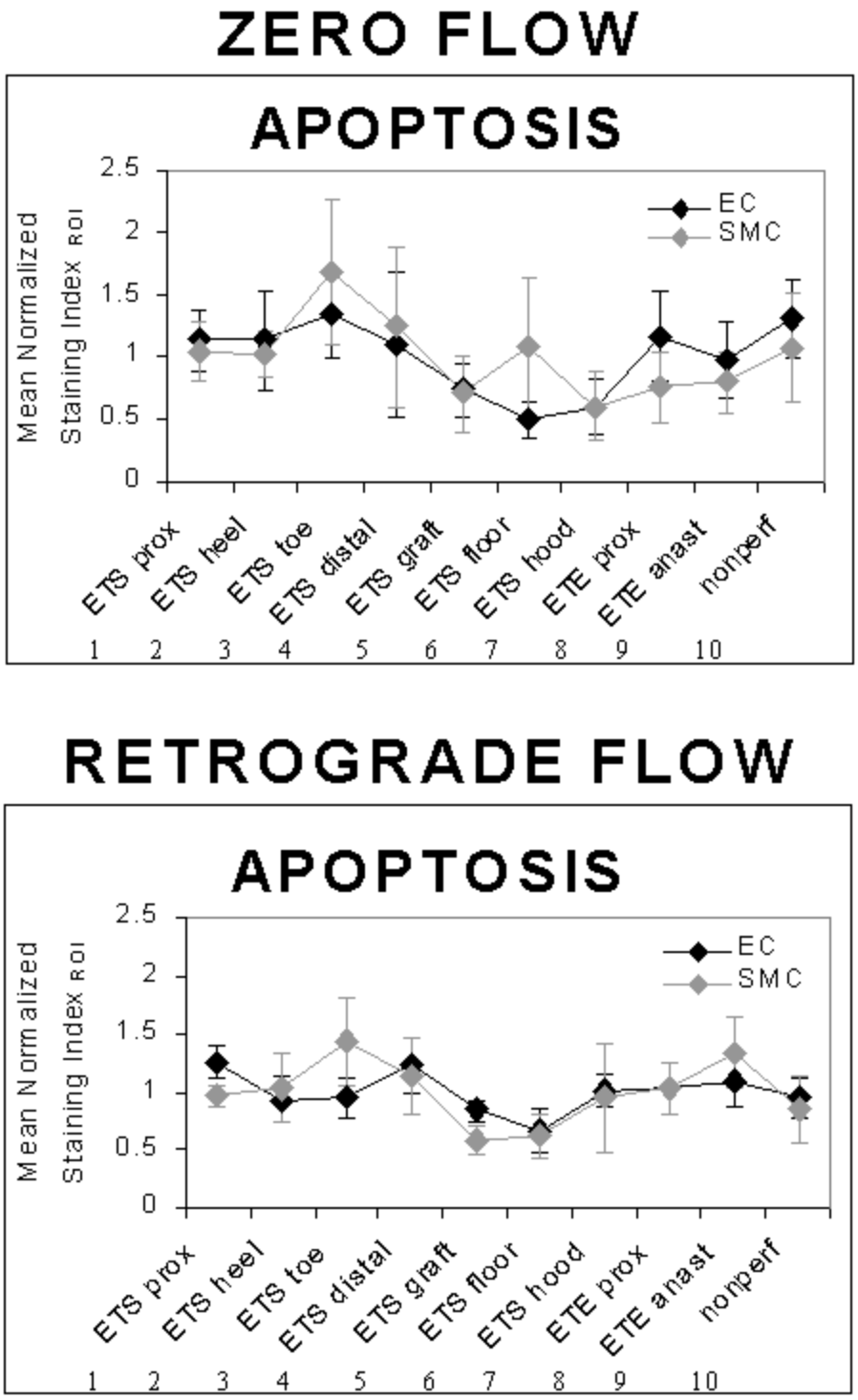

Figure 2.20 Mean Normalized Staining Index $_{ROI}$ (see Equation 2.6) for apoptosis (EC-black, SMC-grey) for the zero flow (top) and retrograde flow (bottom) experiments. The numbers above or below each data point indicate which regions (1-ETS proximal artery, 2-ETS heel, 3-ETS toe, 4-ETS distal artery, 5-ETS graft, 6-ETS floor, 7-ETS hood, 8-ETE proximal, 9-ETE anastomosis and 10-nonperfused segment) are significantly different from that region.

ALL EXPERIMENTS

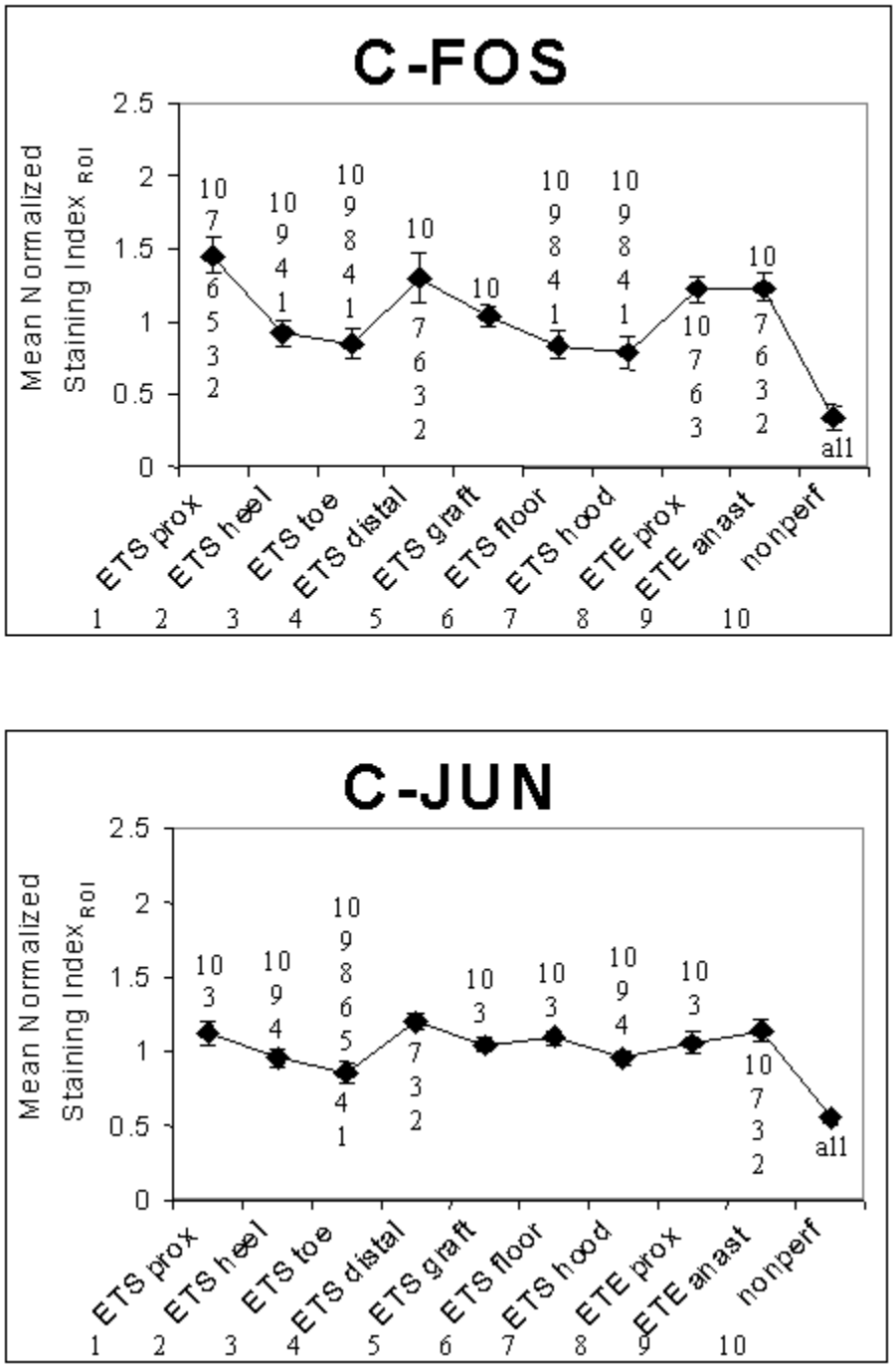

Figure 2.21 Mean Normalized Staining Indices $_{ROI}$ (see Equation 2.6) for c-fos and c-jun for all experiments. The numbers above or below each data point indicate which regions (1-ETS proximal artery, 2-ETS heel, 3-ETS toe, 4-ETS distal artery, 5-ETS graft, 6-ETS floor, 7-ETS hood, 8-ETE proximal, 9-ETE anastomosis and 10-nonperfused segment) are significantly different from that region.

ALL EXPERIMENTS

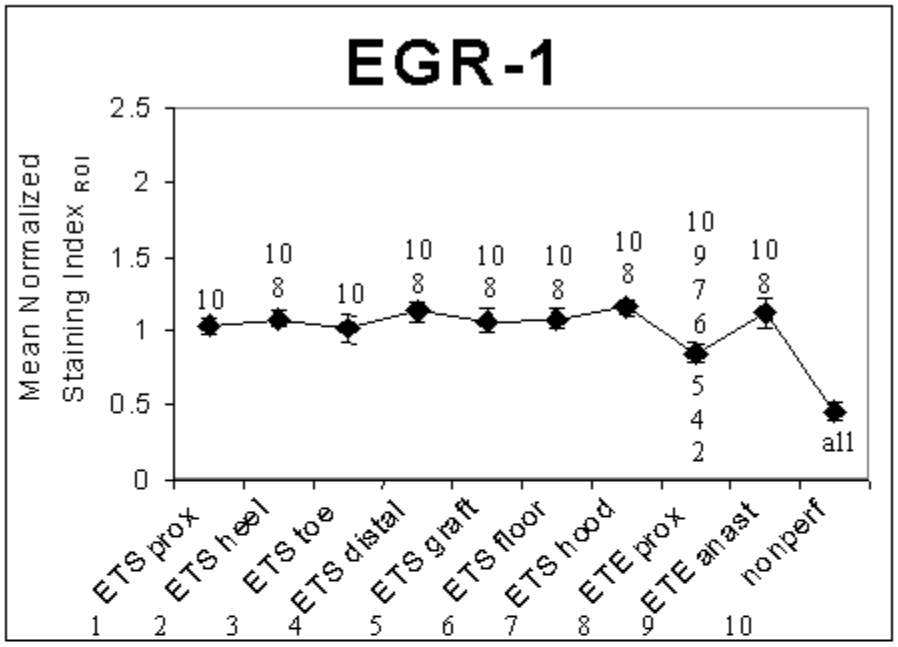

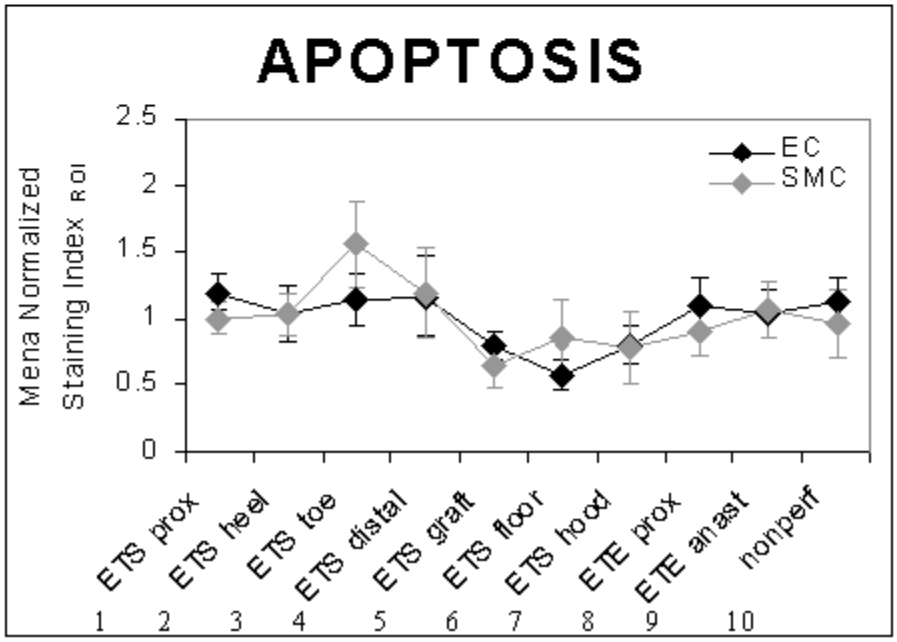

Figure 2.22 Mean Normalized Staining Indices $_{ROI}$ (see Equation 2.6) for egr-1 and apoptosis (EC-black, SMC- grey) for all experiments. The numbers above or below each data point indicate which regions (1-ETS proximal artery, 2-ETS heel, 3-ETS toe, 4-ETS distal artery, 5-ETS graft, 6-ETS floor, 7-ETS hood, 8-ETE proximal, 9-ETE anastomosis and 10-nonperfused segment) are significantly different from that region.

Staining Index $_{ROI}$ for the ETS heel (0.981 ± 0.171), toe (0.988 ± 0.088), graft (0.95 ± 0.088), floor (0.855 ±0.132) and hood (0.795 ± 0.115) regions. The ETS hood region (0.795 ± 0.115) had the lowest c-fos Mean Normalized Staining Index $_{ROI}$ of the perfused regions and this value was significantly lower than the c-fos Mean Normalized Staining Index $_{ROI}$ for the ETS proximal (1.285 ± 0.109), distal (1.345 ± 0.157), ETE proximal (1.162 ± 0.081) and anastomosis (1.134 ± 0.077) regions.

Although the regional variation of c-fos Mean Normalized Staining Index $_{ROI}$ depended on the flow condition in the proximal artery, there were no statistically significant differences for any of the regions of interest due to the imposed flow condition. For example, even though the c-fos Mean Normalized Staining Index $_{ROI}$ in the ETS proximal artery region was higher in the zero flow experiments (1.62 ± 0.203) as opposed to the retrograde flow experiments (1.285 ± 0.109), this difference was not statistically significant ($p = 0.183$).

When the data from both flow conditions were pooled together (Figure 2.21), a global understanding of the regional variation of c-fos protein levels in vascular bypass grafts can be determined. The ETS proximal region (1.452± 0.122) had the highest c-fos Mean Normalized Staining Index $_{ROI}$ followed by the ETS distal region (1.303 ± 0.177). These protein levels were significantly higher than those of the ETS heel (0.927 ± 0.087), toe (0.850 ± 0.103), floor (0.840 ± 0.093) and hood (0.783 ± 0.107). The ETS proximal c-fos Mean Normalized Staining Index $_{ROI}$ (1.452 ± 0.122) was also significantly higher than the ETS graft (1.039 ± 0.072) region. The ETE proximal (1.226 ± 0.094) and anastomosis (1.234 ± 0.094) regions had the next highest c-fos Mean Normalized Staining Indices $_{ROI}$ and these were significantly higher than the ETS toe (0.850 ± 0.103), floor (0.840 ± 0.093) and hood (0.783 ± 0.107) regions.

For all experiments, the ETE proximal and anastomosis regions were not significantly different from each other indicating that surgical trauma and use of the VCS™ clips does not induce appreciable nuclear c-fos protein expression. Further evidence that the regional variation of c-fos protein levels was caused by hemodynamics is the fact that all regions of interest from perfused vessels (except ETS hood for the

retrograde flow experiments) showed significantly higher c-fos protein levels compared to the nonperfused segment.

2.3.2.2 Regional Variation of C-jun Protein

The c-jun Mean Normalized Staining Indices $_{ROI}$ followed the same trend for both flow conditions, however, more significant regional variation occurred in the zero flow experiments (Figure 2.18). In the zero flow experiments, the regions that were significantly different from the highest number of other regions were ETS proximal, toe, distal and ETE proximal. The ETS proximal region (1.198 ± 0.203) had the highest c-jun Mean Normalized Staining Index $_{ROI}$ followed by the ETE proximal (1.181 ± 0.109) and ETS distal (1.219 ± 0.046) regions. These c-jun indices were significantly higher than those for the ETS heel (0.896 ± 0.065), toe (0.804 ± 0.119) and hood (0.888 ± 0.052) regions. The ETS toe region (0.804 ± 0.119) had the lowest c-jun Mean Normalized Staining Index $_{ROI}$ of the perfused regions and this value was significantly lower than the c-jun Mean Normalized Staining Index $_{ROI}$ for the ETS proximal (1.198 ± 0.203), distal (1.219 ± 0.046), floor (1.124 ± 0.100) and ETE proximal (1.181 ± 0.109) and anastomosis (1.066 ± 0.124) regions.

In the retrograde flow experiments, the regions that were significantly different from the highest number of other regions were ETS distal, toe, ETE proximal and anastomosis. The ETS distal (1.191 ± 0.100) and ETE anastomosis (1.211 ± 0.062) regions had the highest c-jun Mean Normalized Staining Indices $_{ROI}$. These values were significantly higher than the c-jun Mean Normalized Staining Index $_{ROI}$ for the ETS toe (0.916 ± 0.100) and ETE proximal (0.946 ± 0.076) regions, which had the lowest c-jun indices of the perfused regions.

Although the regional variation of c-jun Mean Normalized Staining Index $_{ROI}$ depended on the flow condition in the proximal artery, there were no statistically significant differences for any of the regions of interest due to the imposed flow condition. For example, even though the c-jun Mean Normalized Staining Index $_{ROI}$ in the ETS hood region was lower in the zero flow experiments (0.888 ± 0.052) as opposed to the retrograde flow experiments (1.021 ± 0.061), this difference was not statistically significant ($p = 0.136$).

When the data from both sets of experiments were pooled (Figure 2.21), the region that had the most significantly different c-jun Mean Normalized Staining Index $_{ROI}$ was the ETS toe region. The c-jun Mean Normalized Staining Index $_{ROI}$ for ETS toe (0.860 ± 0.075) was significantly less than the c-jun Mean Normalized Staining Index $_{ROI}$ for the ETS proximal (1.126 ± 0.081), distal (1.205 ± 0.052), graft (1.047 ± 0.050), floor (1.095 ± 0.055), ETE proximal (1.064 ± 0.074) and anastomosis (1.138 ± 0.070) regions. The highest c-jun Mean Normalized Staining Indices $_{ROI}$ occurred for the ETS distal (1.205 ± 0.052) and ETE proximal (1.064 ± 0.074) regions. These values were significantly higher than those for the ETS heel (0.957 ± 0.060), toe (0.860 ± 0.075) and hood (0.955 ± 0.044) regions.

Similar to the c-fos data, there was evidence that the regional variation of c-jun protein levels was due to hemodynamic forces. The ETE proximal and anastomosis regions were not significantly different from each other indicating that surgical trauma and use of the VCS™ clips did not induce nuclear c-jun protein expression. Additionally, all regions of interest from perfused vessels (except ETS toe for the zero flow experiments) showed significantly higher c-jun protein levels compared to the nonperfused segment indicating that the perfusion was responsible for the nuclear c-jun protein expression.

2.3.2.3 <u>Regional Variation of Egr-1 Protein</u>

The egr-1 Mean Normalized Staining Indices $_{ROI}$ followed the same trend for both flow conditions (Figure 2.19). In the zero flow experiments, the ETE proximal region was the only region that was significantly different from others. The ETE proximal region (0.865 ±0.082) had the lowest egr-1 Mean Normalized Staining Index $_{ROI}$ of the perfused regions and this value was significantly lower than the egr-1 Mean Normalized Staining Index $_{ROI}$ for the ETS toe (1.086 ± 0.078), distal (1.175 ± 0.073), graft (1.102 ± 0.042) and floor (1.121 ± 0.095) regions.

In the retrograde flow experiments, the ETE proximal region (0.839 ± 0.116) again had the lowest egr-1 Mean Normalized Staining Index $_{ROI}$. This value was statistically significant with respect to the ETS hood (1.248 ± 0.077) and ETE anastomosis (1.245 ± 0.180) regions, which had the highest egr-1 expression.

Although the regional variation of egr-1 Mean Normalized Staining Index $_{ROI}$ depended on the flow condition in the proximal artery, there were no statistically significant differences for any of the regions of interest due to the imposed flow condition. For example, even though the egr-1 Mean Normalized Staining Index $_{ROI}$ in the ETS hood region was lower in the zero flow experiments (1.067 ± 0.059) as opposed to the retrograde flow experiments (1.248 ± 0.077), this difference was not statistically significant (p = 0.097).

When the data from both sets of experiments are pooled (Figure 2.22), the significant reduction in egr-1 expression in the ETE proximal region becomes even more pronounced. The egr-1 Mean Normalized Staining Index $_{ROI}$ for ETE proximal (0.852 ± 0.067) is significantly lower than that of the ETS heel (1.082 ± 0.052), distal (1.129 ± 0.065), graft (1.070 ± 0.075), floor (1.080 ± 0.065), hood (1.158 ± 0.055) and ETE anastomosis (1.117 ± 0.101).

Contrary to the c-fos and c-jun data, there is not clear evidence that the regional variation of egr-1 protein expression is caused by hemodynamic forces. Although all regions of interest from perfused vessels showed significantly higher egr-1 protein levels compared to the nonperfused segment, the expression of egr-1 in the ETE proximal and anastomosis regions was significantly different from each other. Therefore it is possible that the surgical manipulation necessary to construct the anastomoses or other factors induced a larger amount of nuclear egr-1 protein expression than the regional variation of hemodynamics.

2.3.2.4 Regional Variation of EC and SMC Apoptosis

Contrary to the IEG protein data, the EC and SMC apoptosis Mean Normalized Staining Indices $_{ROI}$ did not vary significantly between regions (Figure 2.20). In the zero flow experiments, the ETS toe region (1.349 ± 0.363) had the highest EC apoptosis Mean Normalized Staining Index $_{ROI}$ and the ETS floor region (0.498 ± 0.135) had the lowest although neither of these were significantly different from any other region, including the nonperfused segment. The ETS toe region (1.675 ± 0.578) also had the highest SMC apoptosis Mean Normalized Staining Index $_{ROI}$, while the ETS hood region (0.604 ± 0.277) had the lowest level of SMC apoptosis. However, these were not significantly different from any other region, including the nonperfused segment.

In the retrograde flow experiments, the EC apoptosis Mean Normalized Staining Indices $_{ROI}$ qualitatively followed the same trend as the c-fos Mean Normalized Staining Indices $_{ROI}$ for the same flow condition. However, the highest levels of EC apoptosis, occurring in the ETS proximal (1.263 ± 0.138) and distal artery (1.235 ± 0.230) regions, were not significantly higher than that of the region with the lowest EC apoptosis Mean Normalized Staining Index $_{ROI}$, the ETS floor (0.672 ± 0.174). The SMC apoptosis Mean Normalized Staining Index $_{ROI}$ was again highest in the ETS toe region (1.439 ± 0.375) and the lowest level of SMC apoptosis occurred in the ETS graft region (0.593 ± 0.284) yet neither of these were significantly different from the other regions.

Although the regional variation of EC and SMC apoptosis Mean Normalized Staining Indices $_{ROI}$ depended on the flow condition in the proximal artery, there were no statistically significant differences for any of the regions of interest due to the imposed flow condition. For example, even though the EC apoptosis Mean Normalized Staining Index $_{ROI}$ in the ETS hood region was lower in the zero flow experiments (0.597 ± 0.215) as opposed to the retrograde flow experiments (1.011 ± 0.139), this difference was not statistically significant ($p = 0.145$). Similarly, even though the SMC apoptosis Mean Normalized Staining Index $_{ROI}$ in the ETS floor region was higher in the zero flow experiments (1.082 ± 0.567) as opposed to the retrograde flow experiments (0.627 ± 0.190), this difference was not statistically significant ($p = 0.469$).

When the data from both sets of experiments were pooled (Figure 2.22), the reduction in EC apoptosis Mean Normalized Staining Index $_{ROI}$ in the ETS floor region becomes more pronounced. However, the EC apoptosis Mean Normalized Staining Index $_{ROI}$ for ETS floor (0.585 ± 0.108) was still not significantly lower than that of any region including those with the highest EC apoptosis Mean Normalized Staining Indices $_{ROI}$, the ETS proximal (1.198 ± 0.137), toe (1.148 ± 0.200), and distal (1.168 ± 0.296). The pooled SMC apoptosis data showed an enhanced increase in the SMC apoptosis Mean Normalized Staining Index $_{ROI}$ in the ETS toe region (1.557 ± 0.327) and the ETS graft region had the lowest SMC apoptosis Mean Normalized Staining Index $_{ROI}$ (0.647 ± 0.498) but neither of these were significantly different from the other regions.

For all experiments, the EC and SMC apoptosis Mean Normalized Staining Index $_{ROI}$ in the perfused regions were not significantly different from the EC and SMC apoptosis Mean Normalized Staining Index $_{ROI}$ found in the nonperfused segment. Therefore, the surgical manipulation of the vessels during anastomosis construction does not induce regulated EC death. In addition, the use of the VCS™ clips to secure the anastomosis did not induce EC or SMC apoptosis since there was no significant difference between the EC and SMC apoptosis Mean Normalized Staining Indices $_{ROI}$ for the proximal and anastomosis regions of the ETE construct.

2.4 Discussion

2.4.1 Regional Variation of IEG Protein

A significant, regional variation of IEG protein existed in ETS anastomoses perfused *ex vivo* but the degree of EC and SMC apoptosis did not vary regionally. In our experiments, nuclear protein staining for c-fos, c-jun and egr-1 was localized primarily to the endothelial layer while both EC and SMC exhibited apoptosis. For the zero flow experiments, the c-fos and EC apoptosis Mean Staining Indices were significantly lower than the c-jun and egr-1 Mean Staining Indices. For the retrograde flow experiments, the c-fos and EC apoptosis Mean Staining Indices increased significantly compared to their levels for the zero flow condition but these levels were still lower than the c-jun Mean Staining Index. The c-jun Mean Staining Index was also significantly higher than the egr-1 Mean Staining Index. For all experiments, the SMC apoptosis Mean Staining Index was significantly lower than all other Mean Staining Indices.

The ETS regions of interest that had significantly different Mean Normalized Staining Indices $_{ROI}$ as compared to the ETE proximal artery segment (i.e., control) for all of the experiments are presented in Table 2.1. The arrows indicate a significantly increased or decreased Mean Normalized Staining Index $_{ROI}$ in that region compared to the ETE proximal artery segment.

The regions with the most number of significant differences relative to the ETE proximal artery segment were the ETS toe and hood regions. For the ETS toe region, the c-fos and c-jun Mean Normalized Staining

Table 2.1 Summary of the Mean Normalized Staining Indices $_{ROI}$ in the ETS regions of interest for the two flow conditions (zero and retrograde) in the proximal artery. The arrows indicate a significantly ($p < 0.05$) increased or decreased value of the Mean Normalized Hemodynamic Index $_{ROI}$ in that region compared to the ETE proximal artery segment (i.e., control) for the same flow condition.

	C-fos		**C-jun**		**Egr-1**		**EC/SMC Apoptosis**	
	Zero	Retro	Zero	Retro	Zero	Retro	Zero	Retro
ETS proximal	-	-	-	-	-	-	-	-
ETS heel	-	-	⇓	-	-	-	-	-
ETS toe	⇓	-	⇓	-	⇑	-	-	-
ETS distal	-	-	-	⇑	⇑	-	-	-
ETS graft	-	-	-	-	⇑	-	-	-
ETS floor	-	-	-	-	⇑	-	-	-
ETS hood	-	⇓	⇓	-	-	⇑	-	-

Indices $_{ROI}$ were significantly decreased in the zero flow experiments while the egr-1 Mean Normalized Staining Index $_{ROI}$ was significantly increased. It is expected that c-fos and c-jun protein expression may follow the same trend since they bind together to form the AP-1 transcription factor that regulates downstream gene expression [27, 49, 51]. For the ETS hood region, the c-jun Mean Normalized Staining Index $_{ROI}$ was significantly decreased in the zero flow experiments. The c-fos Mean Normalized Staining Index $_{ROI}$ in the ETS hood was significantly decreased for the retrograde flow experiments while the egr-1 Mean Normalized Staining Index $_{ROI}$ was significantly increased.

The Mean Normalized Staining Indices $_{ROI}$ with the most number of regions with significant differences were the c-jun and egr-1 Mean Normalized Staining Indices $_{ROI}$. For the zero flow experiments, the c-jun Mean Normalized Staining Index $_{ROI}$ was significantly decreased in the ETS heel, toe and hood regions. The egr-1 Mean Normalized Staining Index $_{ROI}$ was significantly increased in the ETS toe, distal, graft and floor regions. For the retrograde flow experiments, the c-jun Mean Normalized Staining Index $_{ROI}$ was significantly increased in the ETS distal region while no significant differences existed for the egr-1 Mean Normalized Staining Index $_{ROI}$.

In all cases where the Mean Normalized Staining Indices $_{ROI}$ for a particular region of interest was significantly different for one flow condition, it was not significant for the other flow condition. For example, the c-fos and c-jun Mean Normalized Staining Indices $_{ROI}$ for the ETS toe region were significantly decreased in the zero flow experiments but there were no significant differences in these indices for the retrograde flow experiments. Similarly, the egr-1 Mean Normalized Staining Index $_{ROI}$ was significantly increased in the ETS toe, distal, graft and floor regions for the zero flow experiments while there were no significant differences for these regions in the retrograde flow experiments. In fact, 8 of the 11 significant differences occurred for the zero flow experiments while only 3 occurred for the retrograde flow experiments.

In most cases, the Mean Normalized Staining Index $_{ROI}$ for the ETE proximal artery segment and the ETE anastomosis region were not significantly different (see Figures 2.17 - 2.20). These data indicate that the significant differences for the ETS regions of interest are due to the altered hemodynamics in the ETS anastomosis as opposed to the surgical manipulation of the vessels and use of the VCS™ clips to secure the anastomosis. However, there were significant differences in the c-jun and egr-1 Mean Normalized Staining Indices $_{ROI}$ in the ETE anastomosis region compared to the ETE proximal artery region for the retrograde flow experiments. Therefore the significant increases in the c-jun Mean Normalized Staining Index $_{ROI}$ for the ETS distal region and the egr-1 Mean Normalized Staining Index $_{ROI}$ in the ETS hood region for the retrograde flow experiments may not solely be due to the altered hemodynamic environment in the ETS anastomosis.

While there were significant differences in the Mean Normalized Staining Index $_{ROI}$ for c-fos, c-jun and egr-1 in the ETS regions of interest, the EC apoptosis and SMC apoptosis Mean Normalized Staining Indices $_{ROI}$ were not significantly different from the control segment. In addition, the levels of EC and SMC apoptosis Mean Normalized Staining Indices $_{ROI}$ in the perfused regions were not significantly different from that found in the nonperfused segments (see Figure 2.20). Because there was no significant difference between the EC apoptosis indices for the proximal and anastomosis regions of the ETE construct, the surgical

manipulation of the vessels and use of the VCS™ clips to secure the anastomosis does not induce regulated EC death.

2.4.2 Limitations

We chose an *ex vivo* perfusion model so that we could control the pressure and flow conditions in ETS and ETE anastomoses in a precise manner. Although an *in vivo* model would be more physiologically relevant, we would not be able to regulate or even continuously measure the pressure and flow over time. Therefore, the *ex vivo* perfusion model allows us to isolate the hemodynamic influence on IEG protein expression and EC apoptosis while providing a simulated physiologic environment (i.e. pH, oxygen, temperature, nutrients, etc.) for the vessels. However, we have neglected one main physiological component, pulsatility. We chose to complete these experiments under steady flow conditions because of the technical difficulties in creating and perfusing anastomoses *ex vivo*. Future studies in our laboratory could easily incorporate pulsatility since the perfusion system already has these capabilities and we have now had extensive experience in creating the anastomoses.

2.5 Conclusion

We have shown that a significant regional variation of IEG proteins (c-fos, c-jun and egr-1) exists in ETS and ETE anastomoses perfused *ex vivo* under two flow conditions imposed in the proximal artery (zero and retrograde flow). The levels of c-fos and c-jun protein are highest in the ETS proximal and distal artery segments while the lowest levels of c-fos and c-jun protein occur in the regions in and near the anastomosis including the ETS heel, toe, floor and hood. There was no significant difference between the ETE proximal and anastomosis regions indicating that the surgical manipulation and use of vascular clips to create an anastomosis do not contribute to differences in c-fos and c-jun protein expression. In contrast, the only region showing consistently different egr-1 protein expression was the ETE anastomosis segment, which was lower than almost all other regions. This indicates that the surgical trauma associated with the creation of the anastomosis may be the primary cause of egr-1 protein expression. EC/SMC apoptosis did not vary

significantly between any regions and therefore does not appear to be important regionally at this acute time point.

3 .0 COMPUTATIONAL FLUID DYNAMIC MODELS

3.1 Introduction

Computational fluid dynamics is a method for solving the flow field in a complex geometry. Although analytical equations can be solved for a small set of idealized geometries, most realistic geometries require the use of CFD. For CFD models, the geometry is discretized into many smaller domains (a grid) over which the basic governing equations can be solved and, through an iterative technique, a solution for the entire domain can be determined. There are a number of discretization techniques including the finite volume method, the finite element method, the finite difference method and the boundary element method. The models for this project were developed using the finite volume method.

3.1.1 Finite Volume Method

The finite volume method is a discretization technique that is useful for fluid flow solutions because it conserves flow quantities. The large, complex geometry is first sectioned into smaller domains known as finite volumes which comprise the computational grid. Once this grid, or mesh, is constructed, the governing equations can be solved for each finite volume, or cell. The governing equations for incompressible flow (neglecting gravity) are the conservation of linear momentum (Equation 3.1) and continuity (Equation 3.2):

$$\frac{\partial(\rho \boldsymbol{V})}{\partial t} + (\rho \boldsymbol{V} \cdot \nabla)\boldsymbol{V} = -\nabla p + \nabla \cdot \underline{\underline{\tau}} \qquad [3.1]$$

$$\nabla \cdot \boldsymbol{V} = 0 \qquad [3.2]$$

where t is time, ρ is the density of the fluid, **V** is the velocity vector (**V** = u**i** + v**j** + w**k**), ∇ is the gradient operator given by

$$\nabla = \frac{\partial}{\partial x}\boldsymbol{i} + \frac{\partial}{\partial y}\boldsymbol{j} + \frac{\partial}{\partial z}\boldsymbol{k} \qquad [3.3]$$

p is the pressure and $\underline{\underline{\tau}}$ is the viscous stress tensor. For a Newtonian fluid, the viscous stress tensor is given by:

$$\underline{\tau}=\mu(\nabla \boldsymbol{V}+(\nabla \boldsymbol{V})^T) \qquad [3.4]$$

where μ is the dynamic viscosity of the fluid .

These partial differential equations are discretized on the computational grid, forming a corresponding set of algebraic equations. For illustration purposes, the finite volume discretization of the governing equations for steady flow for a two-dimensional cell on a uniform grid (shown in Figure 3.1) is derived. For more detailed information, the interested reader is referred to [159]. The cell of interest, P, is surrounded by its neighbors, east (E), west (W), north (N) and south (S). Discrete values of velocity are stored at the

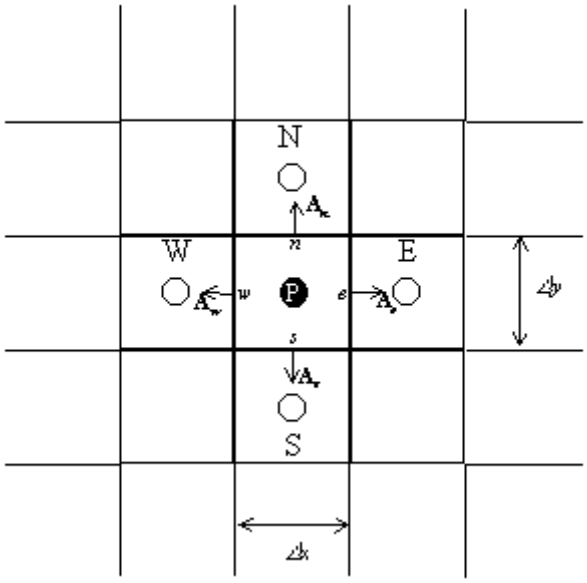

Figure 3.1 Two dimensional, uniform grid used for finite volume discretization.

cell centroids along with the fluid viscosity. The cell faces *e, w, n, s* are associated with area vectors $\mathbf{A}_e$, $\mathbf{A}_w$, $\mathbf{A}_n$ and $\mathbf{A}_s$ that are positive pointing outwards from cell P. The volume of the cell (per unit thickness) is given by $\Delta\forall = \Delta x\, \Delta y$. Each of the x and y components of the linear momentum equation (Equation 3.1) for steady flow of a Newtonian fluid can be written in the form of a general transport equation as:

$$\nabla \cdot \boldsymbol{J}=\boldsymbol{S} \qquad [3.5]$$

where, for the x-component, S is given by

$$S = -\frac{\partial p}{\partial x} \qquad [3.6]$$

and **J** is given by

$$\boldsymbol{J} = \rho \boldsymbol{V}\Phi - \Gamma \nabla \Phi \qquad [3.7]$$

and $\Phi = u$, $\Gamma = \mu$. Note that for the y-component, $S = -\partial p/dy$ and $\Phi = v$. Since similar methods are used for the discretization of the equations for the x and y components, we will focus only on the x-component for this demonstration. Equation 3.5 is integrated over $\Delta\forall$ to obtain

$$\int_{\Delta\forall} \nabla \cdot \boldsymbol{J}\, \partial \forall = \int_{\Delta\forall} S\, \partial \forall \qquad [3.8]$$

Applying the divergence theorem to the first integral results in

$$\int_{A} \boldsymbol{J} \cdot \partial \boldsymbol{A} = \int_{\Delta\forall} S\, \partial \forall \qquad [3.9]$$

where A is the perimeter of the cell P. In the finite volume discretization technique, **J** is assumed to vary linearly over each face of the cell P. Therefore, the value of **J** on each face may be represented by its value at the face centroid. Assuming that the mean value of the source term over the control volume is S*, integrating Equation 3.9 over cell P yields

$$(\boldsymbol{J}\cdot\boldsymbol{A})_e + (\boldsymbol{J}\cdot\boldsymbol{A})_w + (\boldsymbol{J}\cdot\boldsymbol{A})_n + (\boldsymbol{J}\cdot\boldsymbol{A})_s = S^* \Delta\forall \qquad [3.10]$$

where S* is given by

$$S^* = \frac{-(p_e - p_w)}{\Delta x} \qquad [3.11]$$

and p_e and p_w are the pressures at the east and west faces of cell P. Then, Equation 3.10 can be written as

$$\boldsymbol{J}_e \cdot \boldsymbol{A}_e + \boldsymbol{J}_w \cdot \boldsymbol{A}_w + \boldsymbol{J}_n \cdot \boldsymbol{A}_n + \boldsymbol{J}_s \cdot \boldsymbol{A}_s = -(p_e - p_w)\Delta y \qquad [3.12]$$

where for unit thickness of the cell, the area vectors are given by

$$\begin{aligned} \boldsymbol{A}_e &= \Delta y\, \boldsymbol{i} \\ \boldsymbol{A}_w &= -\Delta y\, \boldsymbol{i} \\ \boldsymbol{A}_n &= \Delta x\, \boldsymbol{j} \\ \boldsymbol{A}_s &= -\Delta x\, \boldsymbol{j} \end{aligned} \qquad [3.13]$$

Using Equations 3.7 and 3.13, the flux term for the east face has the following form:

$$\boldsymbol{J}_e \cdot \boldsymbol{A}_e = (\rho u \Phi)_e \Delta y - \Gamma_e \Delta y \left(\frac{\partial \Phi}{\partial x}\right)_e \qquad [3.14]$$

and the terms for the other faces are analogous. Assuming that Φ varies linearly between cell centroids, the flux term for the east face becomes

$$\boldsymbol{J}_e \cdot \boldsymbol{A}_e = \rho_e u_e \left(\frac{\Phi_E + \Phi_P}{2}\right) \Delta y - \Gamma_e \Delta y \left(\frac{\Phi_E - \Phi_P}{\Delta x}\right) \qquad [3.15]$$

and the terms for the other faces are analogous. We also assume that p varies linearly between cell centroids, so that the pressure term becomes

$$(p_W - p_E)\Delta y \qquad [3.16]$$

Rearranging Equation 3.12 and using the flux terms analogous to Equation 3.15 for all faces along with Equation 3.16, we may write the following discrete equation for the cell P:

$$a_P \Phi_P = a_E \Phi_E + a_W \Phi_W + a_N \Phi_N + a_S \Phi_S + b \qquad [3.17]$$

where

$$a_E=\Gamma_e\frac{\Delta y}{\Delta x}-\frac{(\rho u)_e\Delta y}{2}$$

$$a_W=\Gamma_w\frac{\Delta y}{\Delta x}+\frac{(\rho u)_w\Delta y}{2}$$

$$a_N=\Gamma_n\frac{\Delta x}{\Delta y}-\frac{(\rho v)_n\Delta x}{2} \qquad [3.18]$$

$$a_S=\Gamma_s\frac{\Delta x}{\Delta y}+\frac{(\rho v)_s\Delta x}{2}$$

$$a_P=a_E+a_W+a_N+a_S+(\rho u_e\Delta y-\rho u_w\Delta y+\rho v_n\Delta x-\rho v_s\Delta x)$$

$$b=(p_W-p_E)\Delta y$$

As mentioned previously, the y-component of linear momentum is discretized for each cell in the same manner and the resulting equation has the same form as Equations 3.17 and 3.18 except that Φ = v and b = $(p_S - p_N)\Delta y$. In addition, the continuity equation is also discretized for each cell and has the following form:

$$u_E\Delta y-u_W\Delta y+v_N\Delta x-v_S\Delta x=0 \qquad [3.19]$$

The following set of algebraic equations, consisting of the discretized forms of the x and y components of the linear momentum equations (Equation 3.20) and the continuity equation (Equation 3.21), are developed for each cell in the grid and are then solved numerically:

$$\begin{aligned} a_P u_P &= a_E u_E + a_W u_W + a_N u_N + a_S u_S + (p_W - p_E)\Delta y \\ a_P v_P &= a_E v_E + a_W v_W + a_N v_N + a_S v_S + (p_S - p_N)\Delta x \end{aligned} \qquad [3.20]$$

$$u_E\Delta y-u_W\Delta y+v_N\Delta x-v_S\Delta x=0 \qquad [3.21]$$

A velocity-pressure coupling technique is used to determine the components of velocity and the pressure term as shown schematically in Figure 3.2. An initial guess for the pressure term is determined and then the set of algebraic equations corresponding to the linear momentum equation is solved numerically, yielding

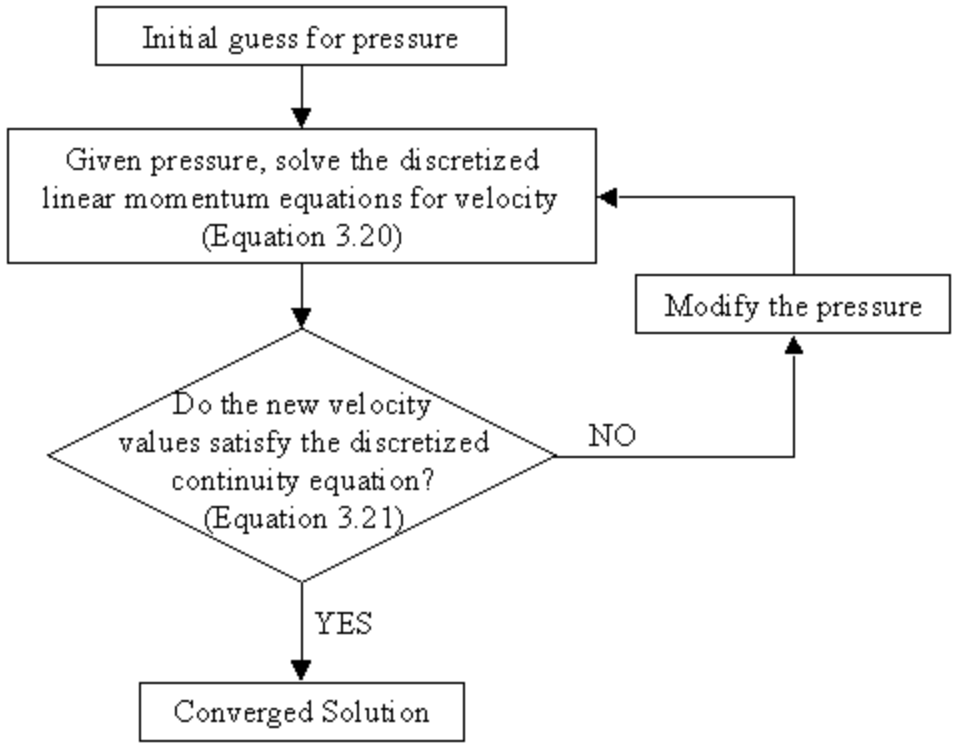

Figure 3.2 Flowchart of the iterative algorithm used to solve for the pressure and velocity fields.

the components of velocity. This velocity field is placed into the set of equations corresponding to the continuity equation to determine if continuity is satisfied. If not, another iteration is performed with a modified guess for the pressure term. An iterative solution scheme is utilized so that the solution for each grid point is improved for each iteration until the error for the entire domain is acceptably small.

There are a number of commercially-available CFD software programs that utilize the finite volume method, including CFD-ACE™ (CFD Research Corporation, Huntsville, AL). These programs allow the user to create a desired complex geometry, create a computational grid, apply desired boundary conditions and solve for the velocity and pressure field within the domain. Hemodynamic parameters such as WSS and WSSG can be calculated from the resulting velocity field, providing a continuous representation of these parameters.

3.1.2 Advantages of CFD

There are a number of advantages to using CFD as opposed to relying on analytical or experimental determinations of hemodynamic parameters. Most striking is the ability to identify the velocity field in a complex, physiologically realistic geometry. Analytical equations can only be used for simple, idealized geometries that have closed form solutions [159] such as cylindrical tubes. However, such geometries do not capture the reality of bending and branching vasculature. CFD also provides a complete definition of the flow field. Experimental flow visualization models can be used to understand the general flow dynamics in a complex geometry but the velocity measurements are made at discrete points and do not allow for the determination of the entire velocity field. Additionally, there are severe limitations in the resolution and accuracy of the velocity measurements and these errors are magnified for quantities such as WSS and WSSG that are derived from the flow field. These same problems occur for *in vivo* studies using velocity transducers.

Because CFD allows for the continuous representation of the flow field and derived hemodynamic parameters in complex geometries, it is ideal for characterizing blood flow. The progressive increase in computational power, speed and the development of commercially-available CFD packages, have allowed this technology to be used extensively for studies of the cardiovascular system as detailed in section 1.5 [66, 78, 83-87, 89-102, 154].

3.2 Methods

To obtain an accurate and precise measurement of the hemodynamic environment present in each of the experimental anastomoses described in Chapter 2, three dimensional reconstructions of each ETS and ETE anastomosis were created. Since the pressure and flow rate in the *ex vivo* perfusions were set and maintained throughout the experiment, CFD models utilized this information along with the anastomotic geometry to accurately estimate WSS and WSSG. This process allows for a distinct and unique coupling

between the perfusion experiment (i.e., the spatial distribution of biologic end points) and the computational simulation (i.e., the spatial distribution of WSS and WSSG) that has not been previously achieved.

3.2.1 Three Dimensional Reconstruction

3.2.1.1 Ellipse Fitting

As explained in section 2.2.8.3., the anastomoses were sliced into 2mm segments. High resolution, digital photographs of the frozen slices were taken with a Nikon Coolpix 950 digital camera as seen in Figures 3.3, 3.4 and 3.5. These JPEG images were converted to TIFF images using Adobe Photoshop. Using Scion Image, the best-fit ellipse for each cross-section was determined. Each TIFF image was scaled based on the ruler included in the photograph. For each cross-section, the binary threshold level was optimized to reveal the inner wall and the automatic boundary detection algorithm was implemented as shown in Figure 3.5. This highlighted the outline of the inner wall and, by using the analyze-measure command, the best-fit ellipse parameters (major axis, minor axis, angle of orientation) were recorded. This was repeated for all cross-sections for the ETS graft, proximal and distal artery regions as well as for all cross-sections of the ETE anastomosis. For the ETS anastomosis cross-sections, two separate ellipses were fit to the hood and floor.

3.2.1.2 Surface Creation

A three dimensional surface was created by stacking the two dimensional ellipses fit to each cross-section as follows. Note that the detailed protocol can be found in Appendix A. The models were assumed to be symmetric since the experimental apparatus held the vessels in a plane of symmetry. To impose symmetry, the ellipse angle of orientation was forced to be either 0, 90, 180 or 270 degrees with respect to the plane of symmetry. Ellipses with measured angles of orientation between 0 and 45 degrees were set to 0 degrees. Ellipses with measured angles of orientation between 45 and 90 degrees were set to 90 degrees and so on. These modified ellipses were input into CFD-GEOM, the preprocessor for CFD-ACE™.

For the ETE models, a lofted surface was created whereby the surface was extruded from one cross-section to the next, using splines to smooth the portion of the surface between the cross-sections. The lofted

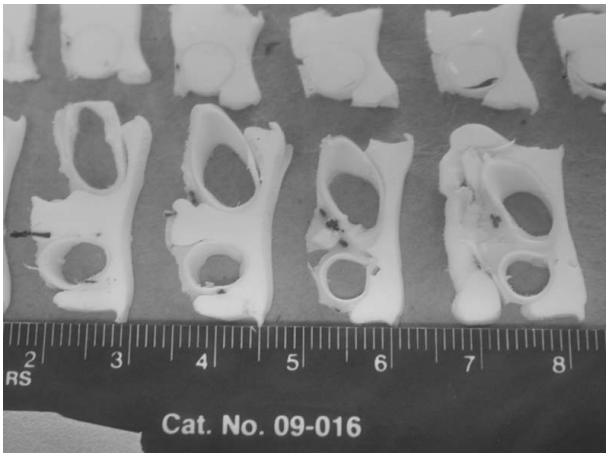

Figure 3.3 Frozen cross-sections of the graft and proximal artery regions from an ETS anastomosis.

Figure 3.4 Frozen cross-sections of the distal artery regions from an ETS anastomosis.

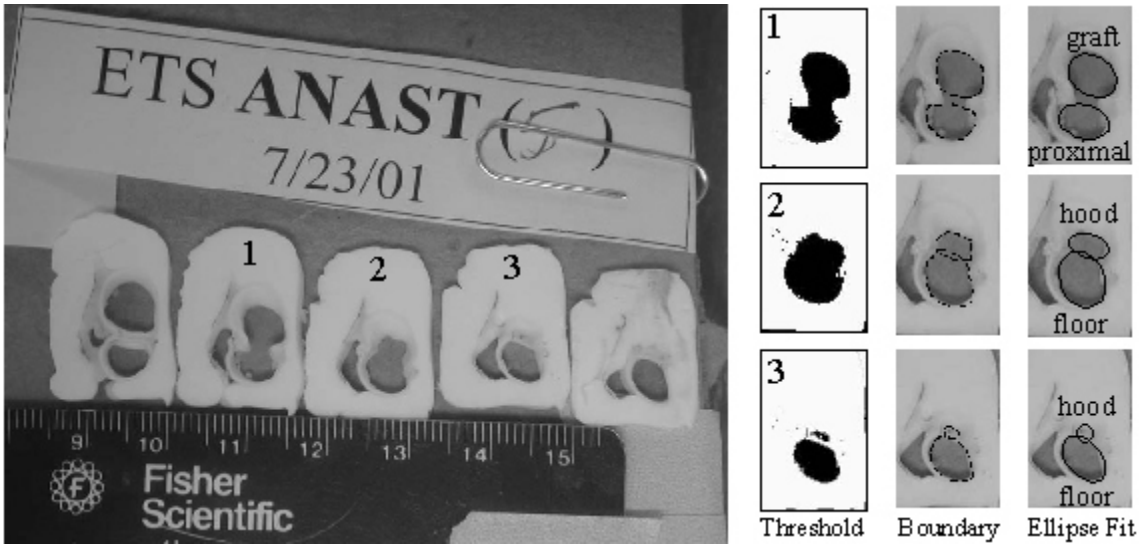

Figure 3.5 Procedure for determining the best-fit ellipse for each cross-section The original image (left) is scaled and the threshold level is optimized for the cross-sections of interest (left center). The boundary is automatically detected (right center) and the best-fit ellipse parameters are determined by Scion Image (right).

surface was created by connecting the most proximal ellipse to the next ellipse in line until the surface was complete (see Figure 3.6). Note that the X = 0 plane was defined as the cross-section where the VCS™ clips were placed and the centroids of all ellipses determined the Y = 0 and Z = 0 planes. For the ETS models, the first or second set (depending on the individual geometry) of overlapping ellipses was chosen as the intersection point for the graft, proximal and distal artery surfaces. A lofted proximal artery surface was created by connecting the most proximal ellipse to the next ellipse in line until the intersection point was reached (see Figure 3.7). A similar method was used to create the graft surface. To construct the distal artery surface, the remaining overlapping ellipses were intersected and trimmed to create a figure-eight shape. These figure-eight shapes were lofted in succession and the surface continued by lofting the single distal artery ellipses. This allowed for a smooth surface along the toe of the ETS anastomosis. Note that the X = 0 plane was defined as the most distal cross-section with double ellipses and the centroids of all proximal artery, floor and distal artery ellipses determined the Y = 0 and Z = 0 planes.

To allow for fully developed flow at the inlets and outlets of the models, additional straight tube surfaces were created upstream of the proximal artery segments and downstream of the distal artery segment for all models as shown in Figures 3.8A and 3.9A. The ETS models had an additional straight tube extension upstream from the graft (see Figure 3.9A). For the ETE proximal artery extension, a circular cross-section with a diameter equal to the average of the minor and major axis dimensions of the most proximal elliptical cross-section was placed ~20 diameters upstream from the most proximal elliptical cross-section. A lofted surface was created by connecting the upstream circular cross-section to the most proximal elliptical cross-section. The ETE distal artery and ETS extensions were created in a similar manner. The lengths of all extensions were based on the dimensions used in our previous studies of idealized ETS anastomosis models and those of other research groups [89, 96, 154]. Each extension had a different length depending on the magnitude of disturbed flow expected in that region. For example, the extensions for the ETE proximal artery and ETS graft were ~20 diameters because these were inlet regions where uniform plug flow was prescribed upstream and the flow needed a length of approximately 10 diameters to fully develop, depending

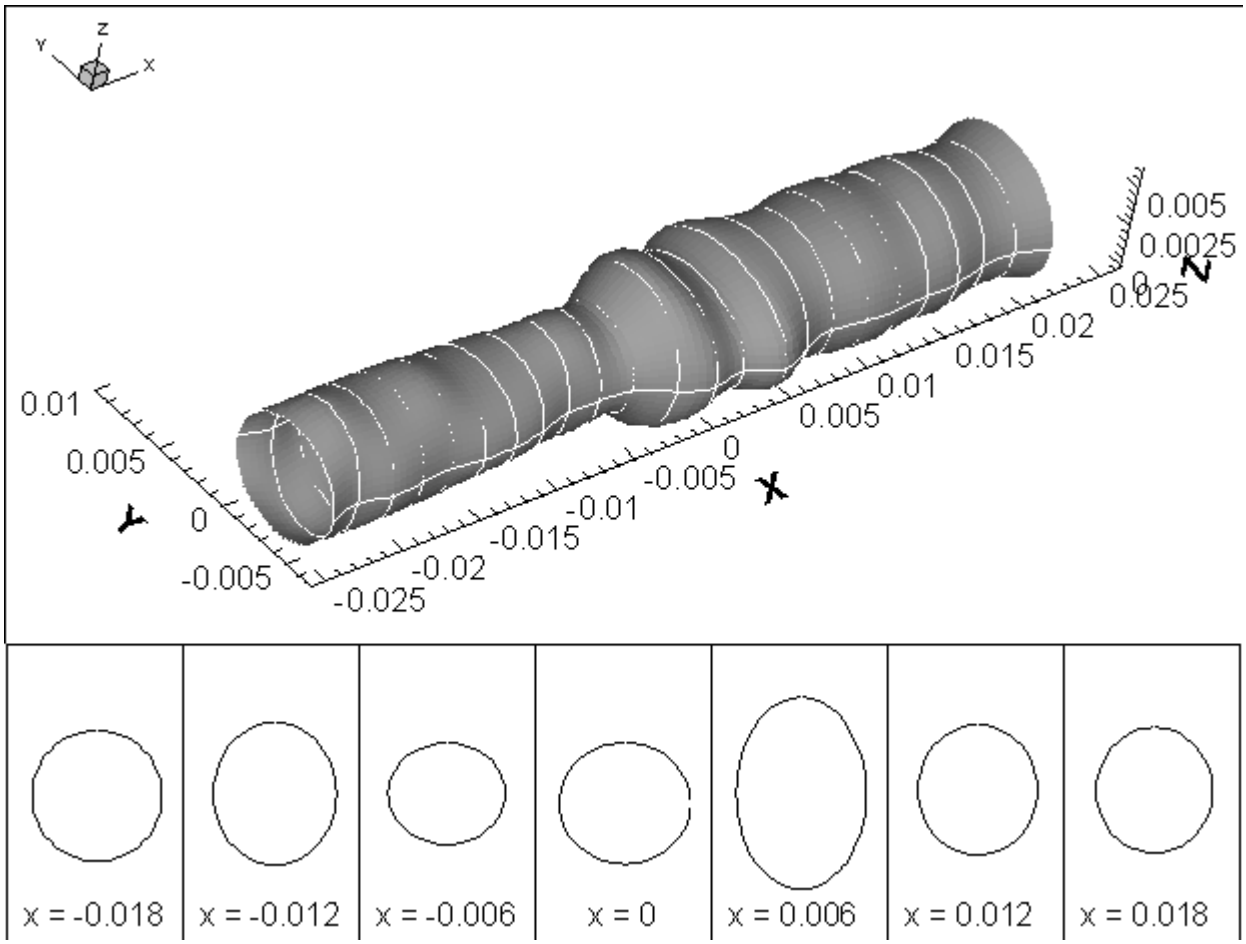

Figure 3.6 Three dimensional ETE surface reconstruction technique. The ETE surface is created by lofting single ellipses along the length of the anastomosis.

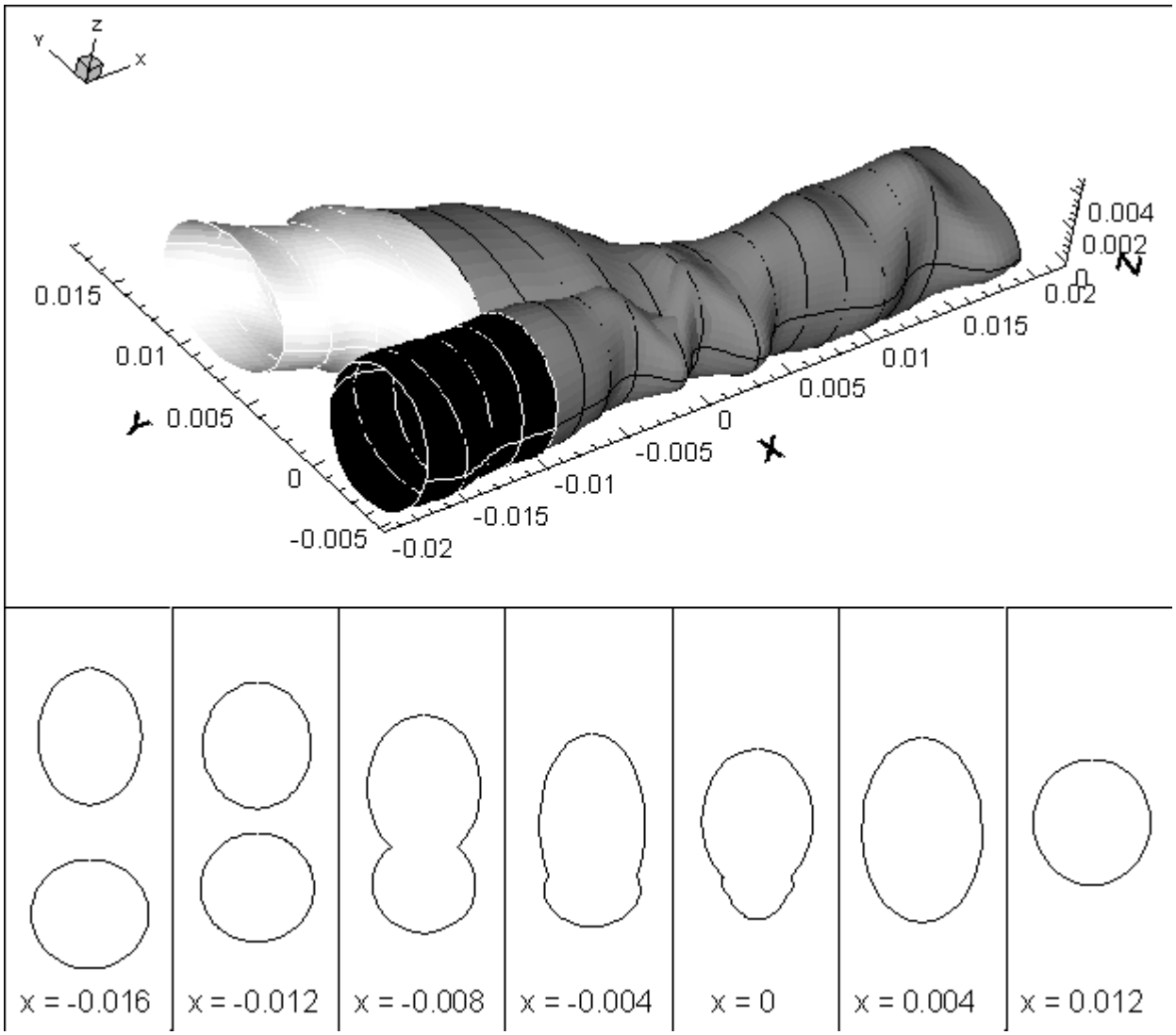

Figure 3.7 Three dimensional ETS surface reconstruction technique. Each surface is created by lofting either single ellipses (black=proximal artery, light grey=graft) and intersecting and single ellipses (dark grey = distal artery).

on the velocity magnitude [219]. The extension for the ETE distal region was also ~20 diameters because the flow exiting the ETE model was expected to be fairly uniform. However, the flow exiting the ETS models was not expected to be uniform so the distal artery extension was much longer, ~75 diameters. For the zero flow ETS models, no flow exited the proximal artery so the extension was short, ~5 diameters. For the retrograde flow ETS models, some flow exited the proximal artery region so the extension was slightly longer, ~10 diameters, but still much shorter than the ETS distal artery extension since only 20% of the flow exited this segment. For each model, it was confirmed that the resulting flow field was fully developed (i.e., parabolic velocity profile) before entering the reconstructed region and before exiting the distal artery. Additionally, for the ETS models, it was confirmed that the proximal artery boundary did not interfere with the recirculation region in the proximal artery.

3.2.2 Mesh Creation

In order to numerically solve the governing equations using CFD, it was necessary to discretize the three dimensional geometry. This physical discretization is known as grid, or mesh, development. For these models, a body-fitted, structured grid was created using CFD-GEOM™. Body-fitted meshes conform to the boundaries of the surface geometry and are required for irregularly-shaped geometries. Structured grids have a specific layout such that the control volumes, or cells, are arranged in rows, columns and layers. A structured grid was chosen because of the ability to tightly regulate the spacing of the grid which is particularly important when calculating derived, near-wall quantities such as WSS. All cells in these models were hexahedrals, or six-sided blocks.

The ETE models consisted of 6 interconnecting blocks: an outer and inner block for the reconstructed region and the two straight tube extensions (see Figure 3.8 B, C). Similarly, the mesh for the ETS models consisted of 12 interconnecting blocks: an outer and inner block for the graft, proximal and distal artery segments as well as the three straight tube extensions (see Figure 3.9 B, C). The inner block mesh allowed for well-aligned cells along the wall, crucial for accurate WSS calculation. The cells were ordered such that the I direction generally followed along the long axis of the vessel, the J direction generally followed the

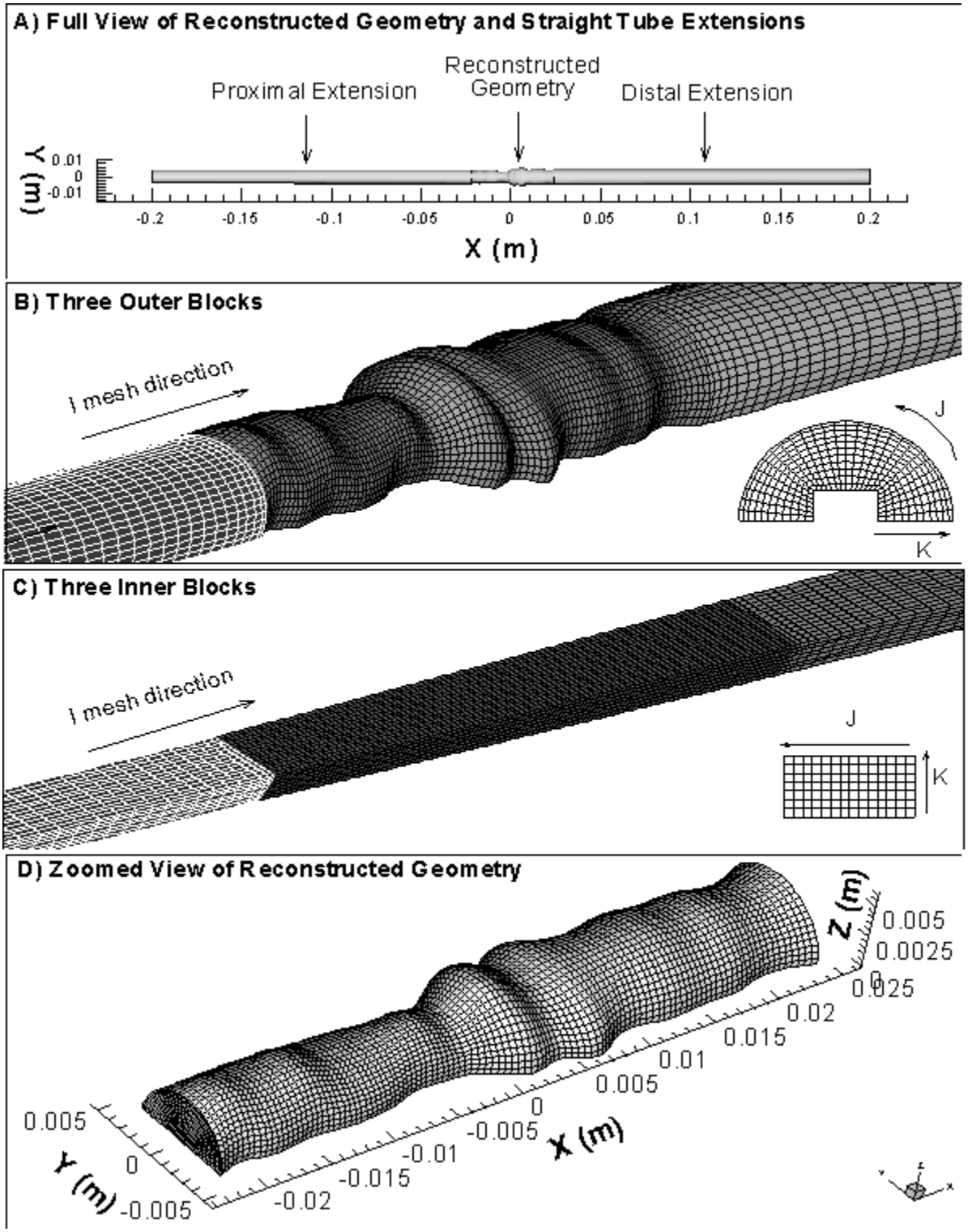

Figure 3.8 Body-fitted, structured mesh for the complete ETE anastomosis model. The top figure (A) shows the complete model including the reconstructed region and the straight extensions. Perspective views of the mesh illustrating the B) outer and C) inner blocks are shown in the center figures where I, J and K refer to the mesh direction. The bottom figure (D) shows a perspective view of the reconstructed region.

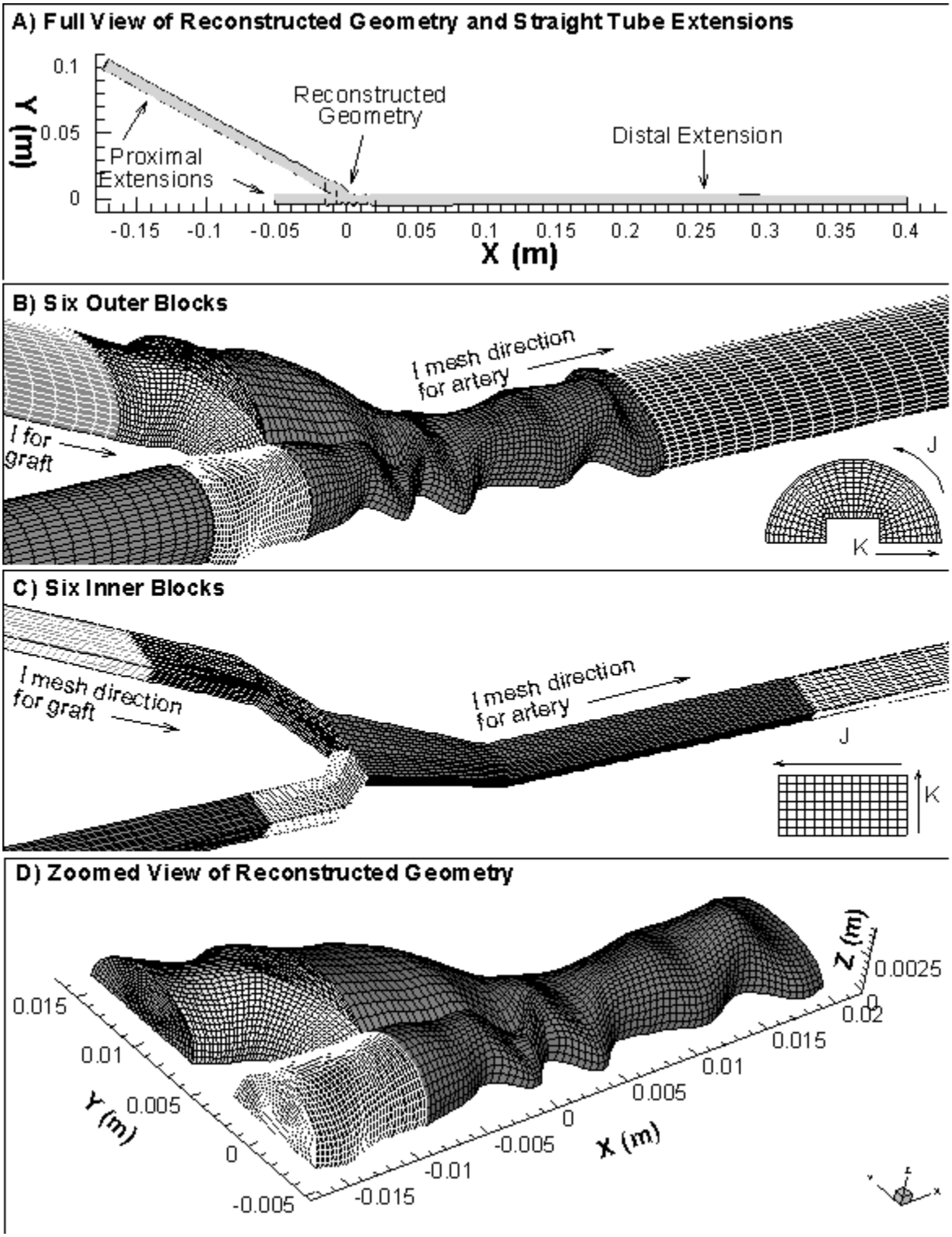

Figure 3.9 Body-fitted, structured mesh for the complete ETS anastomosis model. The top figure (A) shows the complete model including the reconstructed region and the straight extensions. Perspective views of the mesh illustrating the B) outer and C) inner blocks are shown in the center figures where I, J and K refer to the mesh direction. The bottom figure (D) shows a perspective view of the reconstructed region.

circumferential direction around the vessel and the K direction was radial in orientation; i.e., from the innermost layer of the vessel to the outer wall (see Figures 3.8 B, C and 3.9 B, C). Figures 3.8D and 3.9D show a close-up view of the high density mesh in the reconstructed region. The mesh for the straight tube extensions was not as dense because the flow field was not complex in these regions.

3.2.3 Mesh Independence

To determine the mesh density needed for all simulations, four different grids were created for one model each for the ETS zero flow case, ETS retrograde flow case and the ETE case. The initial mesh distribution and density was based on the mesh used in our previous studies of idealized ETS anastomosis models [154]. For each ETS and ETE case, a mesh with approximately twice as many cells as the initial mesh was developed, as well as meshes with half and a quarter number of the cells, where the change in density was uniform in all three dimensions. This is a well-established method for determining mesh independence [94, 160]. Table 3.1 shows the number of cells for each mesh. The ETS zero flow meshes ranged from 33920 to 285714 cells. The number of cells in the ETS retrograde flow meshes ranged from 36320 to 305694 cells. The number of cells in the ETE meshes ranged from 27360 to 221112 cells. The most dense mesh (mesh 4) was used as the standard for comparison for the other grid densities, since a mesh with the highest density should result in the most accurate solution [159]. The spatial averages of WSS and WSSG magnitude were calculated at the seven regions of interest for the ETS models and the two regions of interest in the ETE models. The percent differences between the WSS and WSSG values obtained in meshes 1-3 and the WSS and WSSG values obtained in mesh 4 were determined and averaged for all regions of interest.

Table 3.1 Number of cells in the ETS zero flow, ETS retrograde flow and ETE models used to determine mesh independence.

	Mesh 1	Mesh 2	Mesh 3	Mesh4
ETS zero	33920	78624	138852	285714
ETS retrograde	36320	84096	148596	305694
ETE	27360	61056	106372	221112

3.2.4 Boundary Conditions

The pressure and flow rate boundary conditions for the models were determined by the conditions prescribed in each experimental perfusion that was modeled (see Chapter 2). The graft inlet boundary condition for the ETS models and the proximal artery inlet condition for the ETE models were assigned as a plug flow (flat velocity profile) equal to the experimentally applied value in each case. Table 3.2 shows that experimental flow rate values for the inlets/outlets for each anastomosis and the corresponding velocity imposed in the CFD models. The ETS graft and ETE proximal artery domains were long enough (>10 vessel diameters), both in the experiments and the CFD models, to ensure fully-developed flow before reaching the anastomosis. For the retrograde flow ETS models, the proximal artery extension outlet had a plug flow rate equal to the experimentally applied value in each case. The proximal and distal artery segments were long enough to avoid any interference between the flow at the anastomosis and the prescribed outlet conditions. Finite volume methods require that a reference pressure be prescribed for at least one grid point. Therefore, for all models, a fixed pressure (arbitrarily chosen as zero) was prescribed at the distal artery outlet. All boundaries other than the symmetry plane had the no-slip boundary condition.

3.2.5 Solution Parameters

CFD-ACE™ was used to solve the full Navier-Stokes equations for steady flow of a Newtonian fluid (perfusion media) with a dynamic viscosity of 1 cP and density of 1000 kg/m^3. The Reynold's number for each simulation was between 600 and 1400, based on the density and viscosity of the fluid, mean velocity in the graft and the graft diameter for the ETS models and on the mean velocity and diameter of the proximal artery for the ETE models (see Table 3.2). The advection scheme was second-order upwind, the linear equation solver was conjugate gradient and the pressure correction term was calculated using the SIMPLEC algorithm. The velocity and pressure under-relaxation values were 0.02 and 0.2, respectively. The iterations continued until the residuals were reduced by five orders of magnitude, which required typically ~1000 iterations. An example of the output file from CFD-ACE™ is shown in the Appendix B.

Table 3.2 Experimental flow rate values for the inlets/outlets for each anastomosis and the corresponding velocity imposed in the CFD models. The Reynold's number for each ETS anastomosis is based on the density (1000 kg/m^3) and viscosity (1 cP) of the perfusate, mean velocity prescribed at the graft inlet and the graft diameter. For the ETE anastomoses, the Reynold's number is based on the mean velocity prescribed at the proximal artery inlet and the proximal artery diameter.

	Inlet/Outlet	Experimental Flow Rate (cc/min)	CFD Velocity (m/s)	Diameter (m)	Reynold's Number
Zero Flow Expt #1	ETS graft	300	0.10450	0.00781	816
	ETS proximal	0	0	0.00739	-
	ETE	300	0.12665	0.00709	898
Zero Flow Expt #2	ETS graft	300	0.06520	0.00988	644
	ETS proximal	0	0	0.00548	-
	ETE	300	0.05970	0.01033	616
Zero Flow Expt #3	ETS graft	300	0.28010	0.00477	1335
	ETS proximal	0	0	0.00818	-
	ETE	300	0.17835	0.00597	1066
Zero Flow Expt #4	ETS graft	315	0.11290	0.00770	869
	ETS proximal	0	0	0.00548	-
	ETE	315	0.28970	0.00480	1392
Zero Flow Expt #5	ETS graft	315	0.09500	0.00839	797
	ETS proximal	0	0	0.00560	-
	ETE	315	0.11648	0.00758	882
Retrograde Flow Expt #1	ETS graft	326	0.08860	0.00883	782
	ETS proximal	62	0.04200	0.00560	-
	ETE	325	0.12097	0.00755	913
Retrograde Flow Expt #2	ETS graft	323	0.07190	0.00976	702
	ETS proximal	55	0.02250	0.00720	-
	ETE	320	0.16486	0.00642	1058
Retrograde Flow Expt #3	ETS graft	333	0.06930	0.01010	700
	ETS proximal	68	0.02780	0.00718	-
	ETE	328	0.16558	0.00648	1074
Retrograde Flow Expt #4	ETS graft	325	0.06766	0.01010	683
	ETS proximal	60	0.01980	0.00800	-
	ETE	320	0.24344	0.00528	1286
Retrograde Flow Expt #5	ETS graft	325	0.05835	0.01087	634
	ETS proximal	65	0.01990	0.00830	-
	ETE	325	0.17040	0.00636	1084

3.2.6 Calculation of Hemodynamic Parameters

Post-processing of the results included plotting the velocity vectors output from CFD-ACE™ as well as calculating secondary flow, WSS and spatial WSSG, three parameters shown to be associated with IH formation [78, 85, 90, 91, 138, 161-163]. The velocity at each cell was output directly from CFD-ACE™ and we plotted the velocity vectors on the symmetry plane in order to get a general understanding of the flow field throughout the anastomosis. In each cell, we then calculated the magnitude of secondary flow, ψ:

$$\psi = \sqrt{(v^2 + w^2)} \qquad [3.22]$$

and plotted it on various cross-sections along the length of the anastomosis to visualize the degree of nonuniform flow throughout the model.

The axial (i.e., along the I direction of the structured grid; see Figures 3.8 B, C and 3.9 B, C) and circumferential (i.e., perpendicular to the I direction) components of WSS, along with the WSS magnitude were calculated using custom FORTRAN code and Tecplot (Version 9.0, Amtec Engineering, Bellevue, WA) as follows. Note that the detailed protocol can be found in Appendix C. The normal vector (n_i) on the outer face of each cell was calculated with the CFD Analyzer add-in for Tecplot and was used to calculate the vectors in the axial and circumferential directions using the custom FORTRAN program. The first step in determining the vector in the axial direction was to calculate the length and direction between the normal vector of the current cell ($\mathbf{n}_i$) and the normal vector of the next cell ($\mathbf{n}_{i+1}$) in the axial direction (see Figure 3.10). This calculated vector (dashed line arrow) was projected onto the cell surface and normalized, resulting in the tangent vector in the axial direction, $\mathbf{t}_{ax}$. The vector in the circumferential direction, $\mathbf{t}_{circ}$ was calculated orthogonal to both the normal ($\mathbf{n}_i$) and axial vectors ($\mathbf{t}_{ax}$). In order to calculate the axial and circumferential components of WSS, the stress vector (τ) was first calculated by multiplying the viscous stress tensor, $\underline{\underline{\tau}}$ (Equation 3.4), by the normal vector ($\mathbf{n}_i$). Then the axial WSS was calculated as the dot product between the stress vector (τ) and the axial tangent vector ($\mathbf{t}_{ax}$). Similarly, the circumferential WSS was calculated as the dot product between the stress vector (τ) and the circumferential tangent vector ($\mathbf{t}_{circ}$).

The WSS magnitude was computed as the square root of the sum of the axial and circumferential components squared. The equations for the axial and circumferential components of WSS (τ_{ax} and τ_{circ}) and WSS magnitude, $|\tau|$, are:

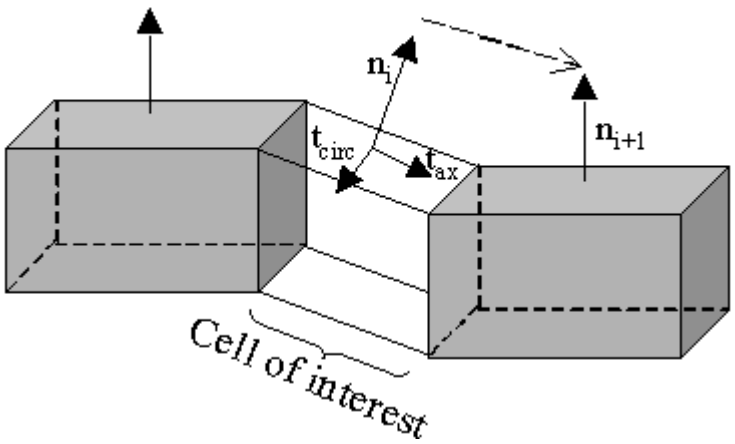

Figure 3.10 Vector used to calculate the axial and circumferential components of WSS.

$$\tau_{ax} = \underline{\underline{\tau}} \cdot \boldsymbol{t}_{ax}$$

$$\tau_{circ} = \underline{\underline{\tau}} \cdot \boldsymbol{t}_{circ} \qquad [3.23]$$

$$|\tau| = \sqrt{\tau_{ax}^2 + \tau_{circ}^2}$$

For the calculation of the axial and circumferential components and magnitude of WSSG, the gradients of τ_{ax} and τ_{circ}, $\nabla\tau_{ax}$ and $\nabla\tau_{circ}$, were computed in Tecplot:

$$\nabla\tau_{ax} = \left(\frac{\partial\tau_{ax}}{\partial x}, \frac{\partial\tau_{ax}}{\partial y}, \frac{\partial\tau_{ax}}{\partial z}\right)$$

$$\nabla\tau_{circ} = \left(\frac{\partial\tau_{circ}}{\partial x}, \frac{\partial\tau_{circ}}{\partial y}, \frac{\partial\tau_{circ}}{\partial z}\right) \qquad [3.24]$$

Another FORTRAN program calculated the axial component of WSSG as the dot product between the normalized axial gradient of τ_{ax}, $\nabla\tau_{ax}$, and axial tangent vector, $\mathbf{t}_{ax}$. Similarly, the circumferential component

of WSSG was calculated as the dot product between the normalized circumferential gradient of τ_{circ}, $\nabla\tau_{circ}$, and the circumferential tangent vector, $\mathbf{t}_{circ}$. The WSSG magnitude was computed as the square root of the sum of the axial and circumferential components squared. The equations for the axial and circumferential components of WSSG ($WSSG_{ax}$ and $WSSG_{circ}$) and WSSG magnitude, |WSSG|, are:

$$WSSG_{ax} = \nabla\tau_{ax} \cdot \boldsymbol{t}_{ax}$$

$$WSSG_{circ} = \nabla\tau_{circ} \cdot \boldsymbol{t}_{circ} \qquad [3.25]$$

$$|WSSG| = \sqrt{WSSG_{ax}^2 + WSSG_{circ}^2}$$

To determine a single, quantitative value for each hemodynamic parameter at the same regions of interest chosen for the biologic endpoints (see section 2.2.8.3), each hemodynamic parameter was spatially averaged over the region of interest. Using the Tecplot CFD Analyzer add-in, a hemodynamic index was calculated for each region of interest (Hemodynamic Index $_{ROI}$) using the following formula:

$$Hemodynamic\ Index_{ROI} = \frac{\int_A Hemodynamic\ Index\ \partial A}{\int_A \partial A} \qquad [3.26]$$

Because the integration required a continuous mesh, each region of interest was defined as the mesh on the outer wall (see Figure 3.11) that most closely corresponded to the 2mm slice used for the biologic endpoints. For example, if the second axial slice was used for the biologic quantification for the proximal artery segment, the mesh that overlapped the region between the second and third elliptical cross-sections was used to define the computational proximal artery region of interest. This process was used to determine six Mean Hemodynamic Indices (i.e., axial, circumferential and magnitude of both WSS and WSSG) at the nine regions of interest (i.e., ETS graft, proximal artery, distal artery, heel, toe, hood, floor, ETE proximal and anastomosis regions). A mean hemodynamic index for each region of interest (Mean Hemodynamic Index $_{ROI}$) was calculated by averaging the Hemodynamic Index $_{ROI}$ over all experiments (n) with the same flow condition.

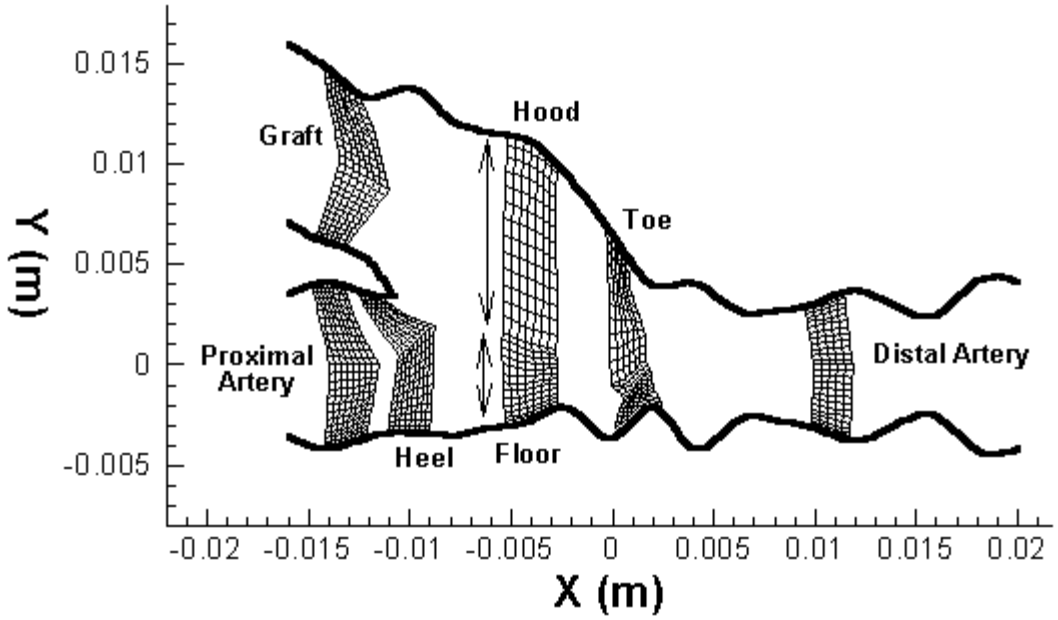

Figure 3.11 The CFD regions of interest for a representative ETS model.

$$Mean\ Hemodynamic\ Index_{ROI} = \frac{\sum_{i=1-n} (Hemodynamic\ Index_{ROI})_i}{n} \quad [3.27]$$

Finally, the Mean Hemodynamic Index was calculated, which represented the mean value of the hemodynamic parameter in all tissue exposed to one flow condition. This single, quantitative value was calculated by averaging the Hemodynamic Index $_{ROI}$ over all regions of interest (m).

$$Mean\ Hemodynamic\ Index = \frac{\sum_{j=1-m} (Mean\ Hemodynamic\ Index_{ROI})_j}{m} \quad [3.28]$$

These data are presented as mean ± standard error of the mean (SEM).

3.2.7 Statistical Analysis

To compare Mean Hemodynamic Indices between flow conditions (i.e., axial WSS for the zero flow experiments versus axial WSS for the retrograde flow experiments), unpaired Student's t-tests were

performed using the mean hemodynamic indices for each region of interest calculated for the five experiments. A difference was considered significant if this test rendered a p-value less than 0.05.

To be consistent with the Normalized Staining Index $_{ROI}$ used for the statistical analysis of the biologic data, a Normalized Hemodynamic Index $_{ROI}$ was computed. The normalized hemodynamic index for each region of interest in one experiment (Normalized Hemodynamic Indices $_{ROI}$) was calculated by dividing by the corresponding mean hemodynamic index averaged over all regions of interest for the same experiment (Mean Hemodynamic Index $_{Experiment}$).

$$Normalized\ Hemodynamic\ Index_{ROI} = \frac{Hemodynamic\ Index_{ROI}}{Mean\ Hemodynamic\ Index_{Experiment}} \quad [3.29]$$

Similar to the non-normalized data, a mean normalized hemodynamic index for each region of interest (Mean Normalized Hemodynamic Index $_{ROI}$) was calculated for all experiments (n) with the same flow condition as:

$$MeanNormalized\ Hemodynamic\ Index_{ROI} = \frac{\sum_{i=1}^{n} (Hemodynamic\ Index_{ROI})_i}{n} \quad [3.30]$$

The data are presented as mean ± SEM.

One-way ANOVA was used to determine if the Mean Normalized Hemodynamic Index $_{ROI}$ for each hemodynamic parameter (i.e., axial, circumferential and magnitude of both WSS and WSSG) varied between regions of interest for each flow condition [157]. If a significant ($p < 0.05$) F value was obtained, a post-hoc paired comparisons test was completed to determine which regions of interest were significantly ($p < 0.05$) different from each other.

To compare the Mean Normalized Hemodynamic Indices $_{ROI}$ between flow conditions (e.g. axial WSS in the toe region for the zero flow experiments versus axial WSS in the toe region for the retrograde flow experiments), unpaired Student's t-tests were performed using the Mean Normalized Hemodynamic Indices

for each region of interest calculated for the five experiments. A difference was considered significant if this test rendered a p-value less than 0.05.

3.3 Results

3.3.1 Mesh Independence

The results of the mesh independence studies are shown in Figure 3.12 where the meshes were as defined in Table 3.1. For all models, the percent difference for WSSG was higher than for WSS since the calculation of WSSG requires taking another derivative of the velocity field, thus magnifying errors. The highest percent differences occurred for the ETS zero flow models.

For the ETS zero flow models, there was a dramatic decrease in the average percent difference when increasing the grid density from mesh 1 (33920 cells) to mesh 2 (78624 cells). The average percent difference for WSS decreased from 50% to 23%. The average percent difference for WSSG decreased from 74% to 35%. When using mesh 3 (138852 cells), the decrease in the average percent difference was less pronounced, decreasing to 14% for WSS and 18% for WSSG. Because the slope of the average percent difference for both WSS and WSSG decreased markedly when using mesh 3, we determined that the substantial increase in CPU resources needed to calculate the results for all the simulations using mesh 4 (approximately 1 week versus 1 day) was not warranted.

For the ETS retrograde flow models, there was a decrease in the average percent difference when increasing the grid density from mesh 1 (36320 cells) to mesh 2 (84096 cells). The average percent difference for WSS decreased from 14% to 8%. The average percent difference for WSSG decreased from 26% to 15%. When using mesh 3 (148596 cells), the decrease in the average percent difference was less pronounced, decreasing to 5% for WSS and 10% for WSSG. Because the average percent difference for both WSS and WSSG was less than 11% when using mesh 3, this mesh density was chosen, again in light of the computational savings.

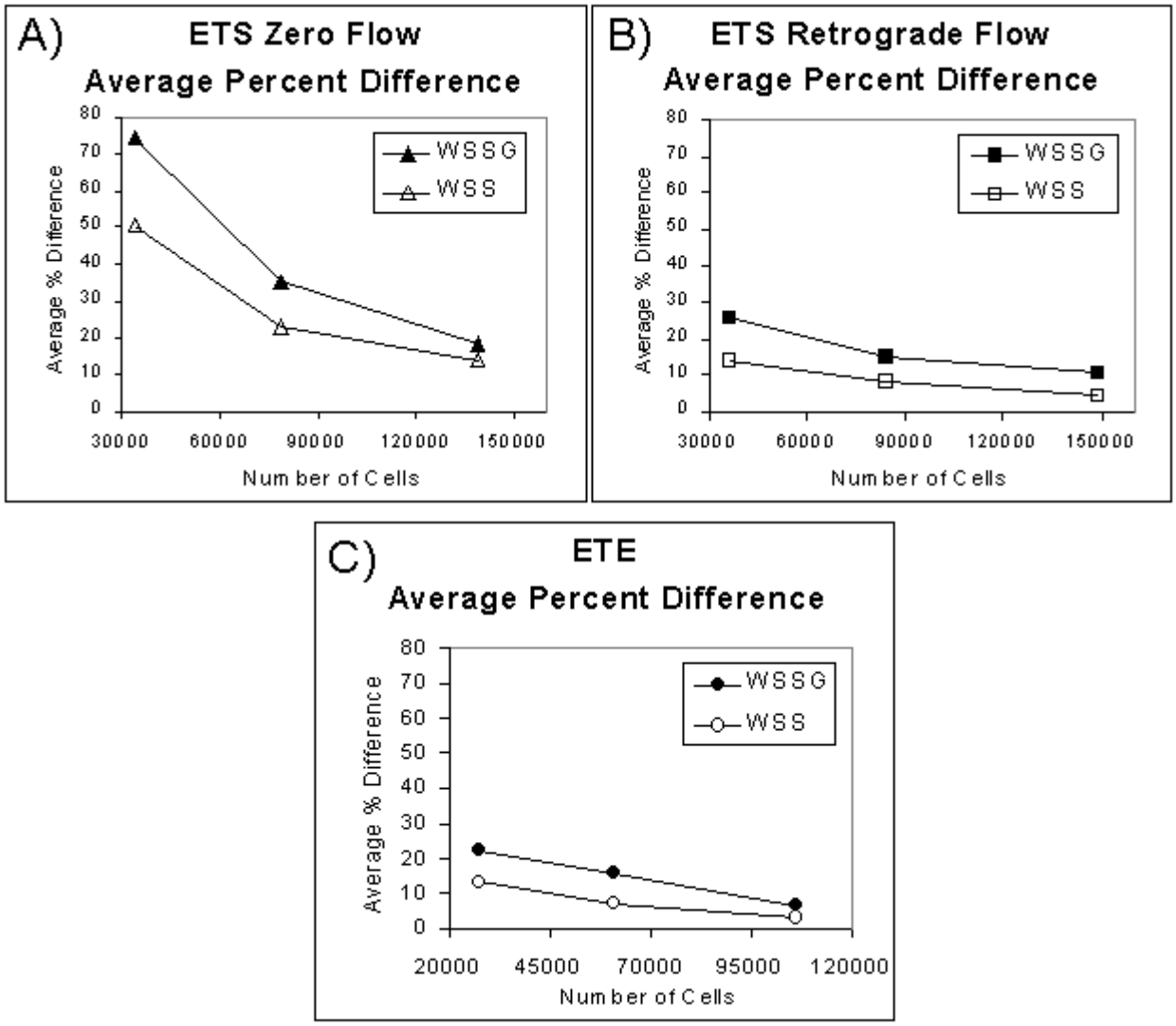

Figure 3.12 WSS and WSSG magnitude percent differences (with respect to the most dense mesh, mesh 4) averaged over the anastomosis regions of interest for the three types of simulations: A) ETS zero flow, B) ETS retrograde flow and C) ETE models.

The mesh independence studies for the ETE models had similar results as those from the retrograde flow models. The average percent difference in WSS decreased from 13% to 7% when increasing the mesh density from mesh 1 (27360 cells) to mesh 2 (61056 cells)and the average percent difference in WSSG decreased from 22% to 15%. A similar decrease in differences occurred when using mesh 3 (106372 cells) where the average percent difference in WSS and WSSG decreased to 3% and 7%, respectively. Because the average percent difference for both WSS and WSSG was less than or equal to 7% when using mesh 3, this mesh density was again chosen.

Therefore, all subsequent results are from the models with mesh 3. Each ETS zero flow model consisted of 138852 cells. Each ETS retrograde flow model consisted of 148956 cells and each ETE model consisted of 106372 cells.

3.3.2 Geometry

For clarity, the five ETS zero flow models will be referred to here as ETS-Z1, ETS-Z2, ..., ETS-Z5, and the ETE control models as ETE-Z1, ETE-Z2, ..., ETE-Z5. Similarly, the five ETS retrograde flow models will be referred to as ETS-R1, ETS-R2, ..., ETS-R5, and the ETE control models as ETE-R1, ETE-R2, ..., ETE-R5. The geometry of each anastomosis is shown in the top panel (A) of Figures 3.13 - 3.17 (ETS-Z1 to ETS-Z5), 3.18 - 3.22 (ETS-R1 to ETS-R5), 3.23 - 3.27 (ETE-Z1 to ETE-Z5) and 3.28 - 3.32 (ETE-R1 to ETE-R5), where all models are shown on the same scale for comparison. Note that vessel caliber and degree of tapering along the vessels varies between anastomoses. For example, ETS-Z3 had a much smaller caliber vessel segment used for the graft compared to the other experiments (see Figure 3.15). The corresponding ETE anastomosis, ETE-Z3, also had a smaller caliber vessel (see Figure 3.25). Along the length of all anastomoses, there was a variation in size and orientation of the elliptical cross-sections used to create the reconstructions. These changes in shape and size occurred because of the ligation of branching vessels present along the native vessels as well as due to the tension caused by connecting the vessels together with the vascular clips. These variations in native vessels and anastomosis construction, underscore the necessity of individual three dimensional reconstructions for each experiment.

3.3.3 Velocity Vectors

The velocity vectors on the symmetry plane for each reconstructed anastomosis are shown in the center panel (B) of Figures 3.13 - 3.17 (ETS-Z1 to ETS-Z5), 3.18 - 3.22 (ETS-R1 to ETS-R5), 3.23 - 3.27 (ETE-Z1 to ETE-Z5) and 3.28 - 3.32 (ETE-R1 to ETE-R5). Note that the dimension and velocity scales are different in this panel of each figure in order to optimize visualization. There are a number of features of the flow field which occur in all of the ETS models (see Figures 3.13 - 3.22). Most notably, there is significant skewing of the velocity towards the floor of the artery due to the entrance of the flow from the graft. There is also a recirculation region in the proximal artery near the heel that is intensified in the retrograde flow simulations. Additionally, regions of local geometric constriction leads to increased velocity while regions of expansion develop recirculation zones. Although these phenomena also occur in the ETE models (see Figures 3.23 - 3.32), in general, the flow is more uniform for these than in the ETS models.

3.3.4 Secondary Flow

The contours of secondary flow magnitude and streamlines on cross-sections at axial positions along the anastomoses (i.e., proximal artery, graft, heel, hood, floor, toe and distal artery) are shown in the bottom panels of Figures 3.13 - 3.17 (ETS-Z1 to ETS-Z5), 3.18 - 3.22 (ETS-R1 to ETS-R5), 3.23 - 3.27 (ETE-Z1 to ETE-Z5) and 3.28 - 3.32 (ETE-R1 to ETE-R5). Note that the dimension scales are different in these panels for each figure in order to optimize visualization. The ETS models have regions of significant secondary flow magnitude (see Figures 3.13 - 3.22). The magnitude of the secondary flow is much lower in the ETE models, as expected, although some recirculation regions do exist (see Figures 3.23 - 3.32). Note that for all models, the streamlines are projected onto the cross-section and are numerically drawn even if the variations in secondary flow magnitude are close to zero. This causes streamlines to appear to originate or terminate at a wall. Therefore, the most important information to be taken from the streamlines in the areas of recirculation.

Similarities exist in the secondary flow present in the ETS zero and retrograde flow models (Figures 3.13 - 3.22). All models have at least one region of secondary flow magnitude reaching 0.05 m/s. All models

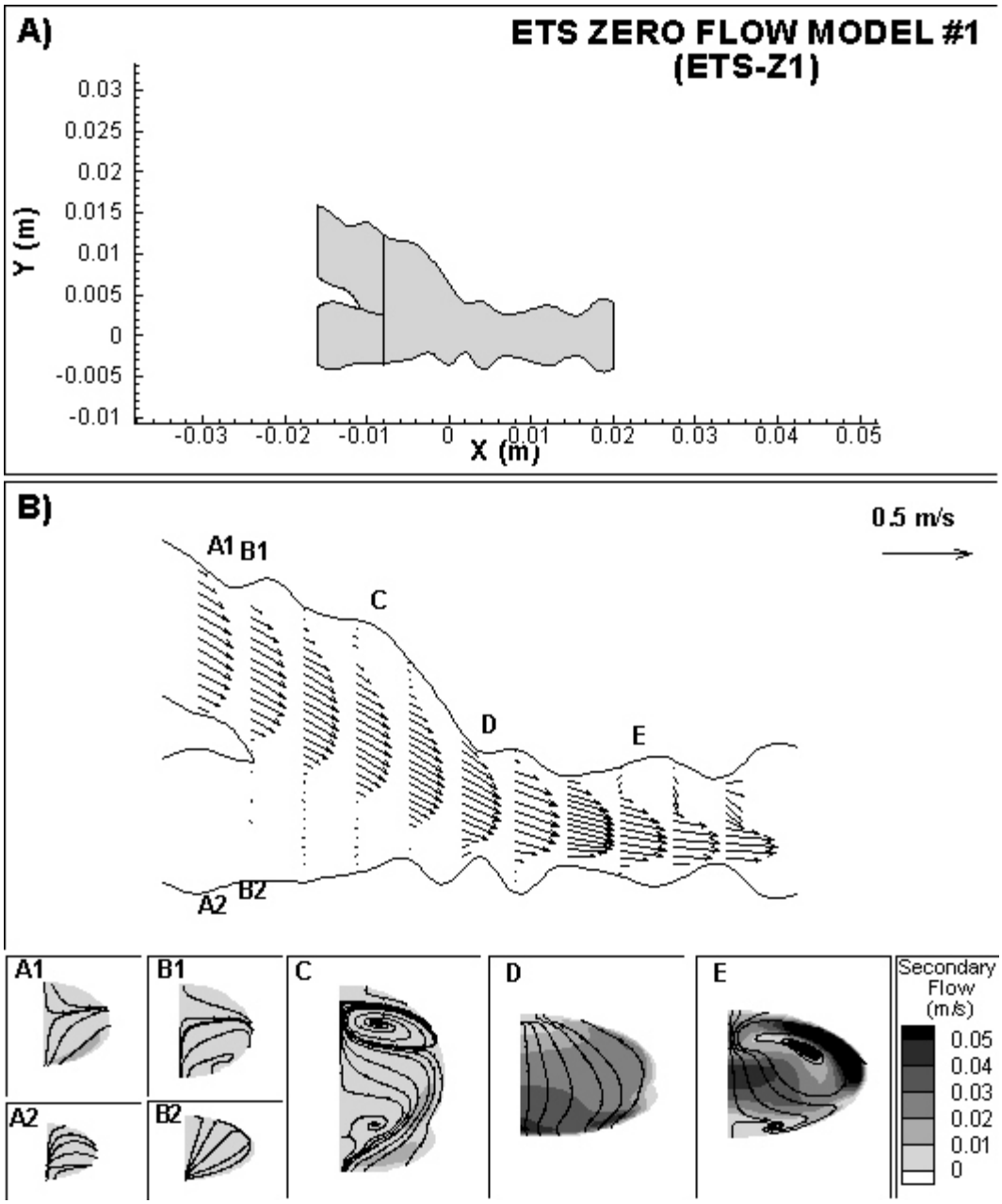

Figure 3.13 Geometry and velocity fields for ETS-Z1. A) Profile of the outer walls of the reconstructed geometry. The solid outlines indicate the proximal artery, graft and distal artery surfaces. Note that the scale is the same for all ETS and ETE models. B) Zoomed view of the model showing the velocity vectors on the symmetry plane at different axial positions. The bottom panels show the contour plots of the secondary flow magnitude and streamlines at the axial positions denoted in panel B: A1) graft, A2) proximal artery, B1) heel (in graft segment), B2) heel (in artery segment), C) hood and floor, D) toe and E) distal artery. Note that each panel illustrates a half cross-section and the view is as if standing at the end of the proximal artery and looking downstream. A small recirculation region is present upstream of the heel and the velocity vectors distal to the anastomosis are skewed toward the floor of the artery.

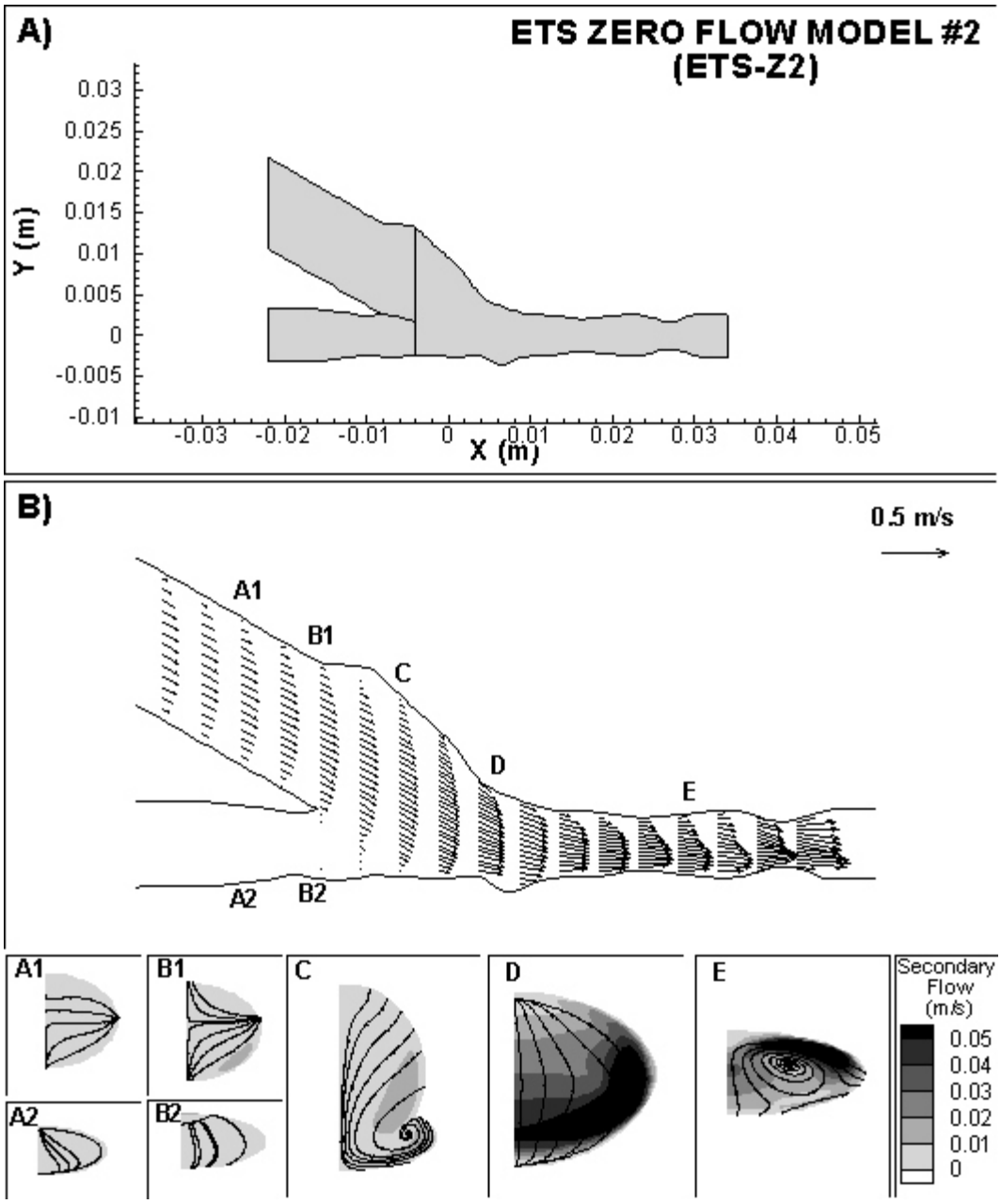

Figure 3.14 Geometry and velocity fields for ETS-Z2. A) Profile of the outer walls of the reconstructed geometry. The solid outlines indicate the proximal artery, graft and distal artery surfaces. Note that the scale is the same for all ETS and ETE models. B) Zoomed view of the model showing the velocity vectors on the symmetry plane at different axial positions. The bottom panels show the contour plots of the secondary flow magnitude and streamlines at the axial positions denoted in panel B: A1) graft, A2) proximal artery, B1) heel (in graft segment), B2) heel (in artery segment), C) hood and floor, D) toe and E) distal artery. Note that each panel illustrates a half cross-section and the view is as if standing at the end of the proximal artery and looking downstream. A small recirculation region is present upstream of the heel and the velocity vectors distal to the anastomosis are skewed toward the floor of the artery.

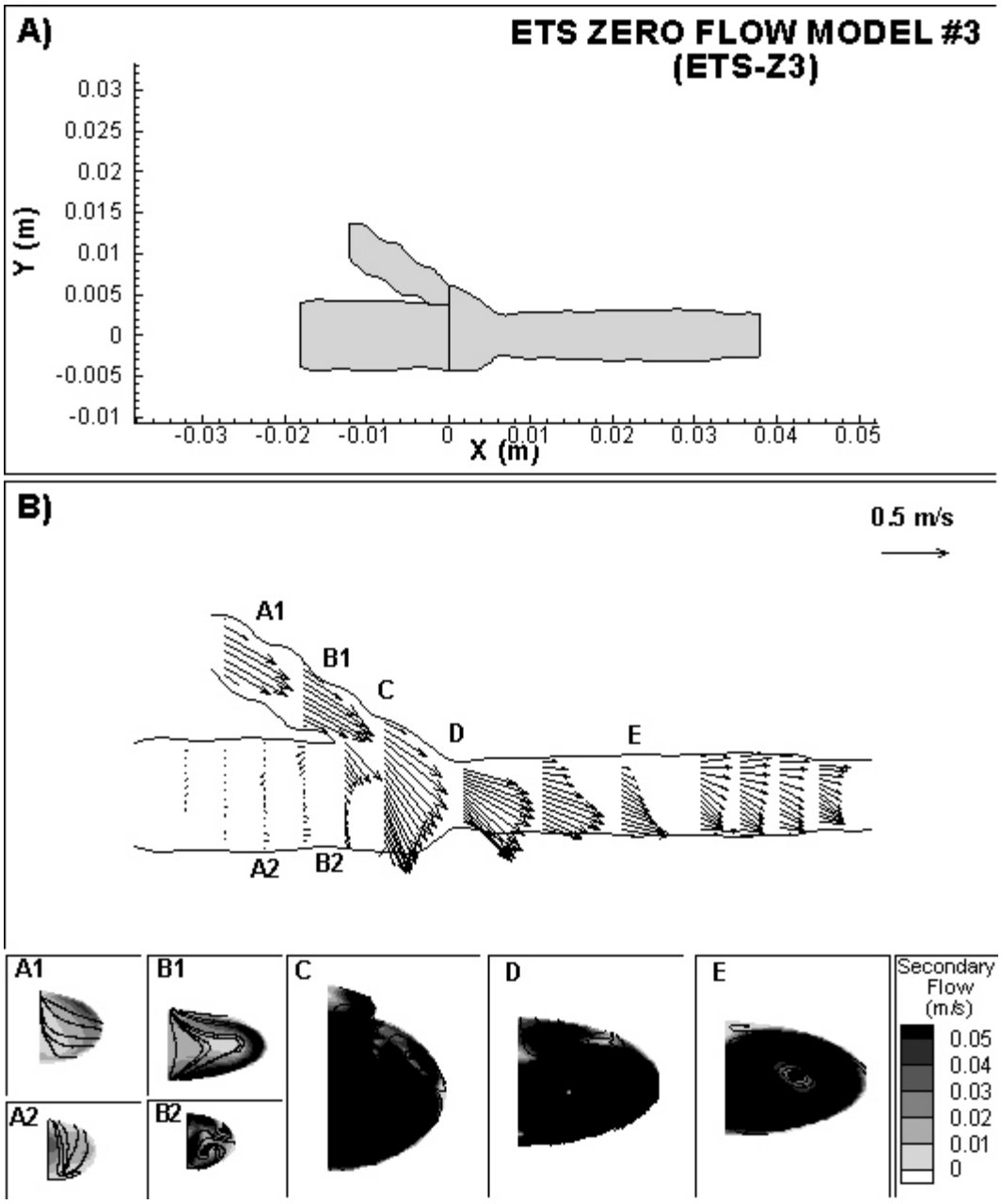

Figure 3.15 Geometry and velocity fields for ETS-Z3. A) Profile of the outer walls of the reconstructed geometry. The solid outlines indicate the proximal artery, graft and distal artery surfaces. Note that the scale is the same for all ETS and ETE models. B) Zoomed view of the model showing the velocity vectors on the symmetry plane at different axial positions. The bottom panels show the contour plots of the secondary flow magnitude and streamlines at the axial positions denoted in panel B: A1) graft, A2) proximal artery, B1) heel (in graft segment), B2) heel (in artery segment), C) hood and floor, D) toe and E) distal artery. Note that each panel illustrates a half cross-section and the view is as if standing at the end of the proximal artery and looking downstream. A small recirculation region is present upstream of the heel and the velocity vectors distal to the anastomosis are skewed toward the floor of the artery.

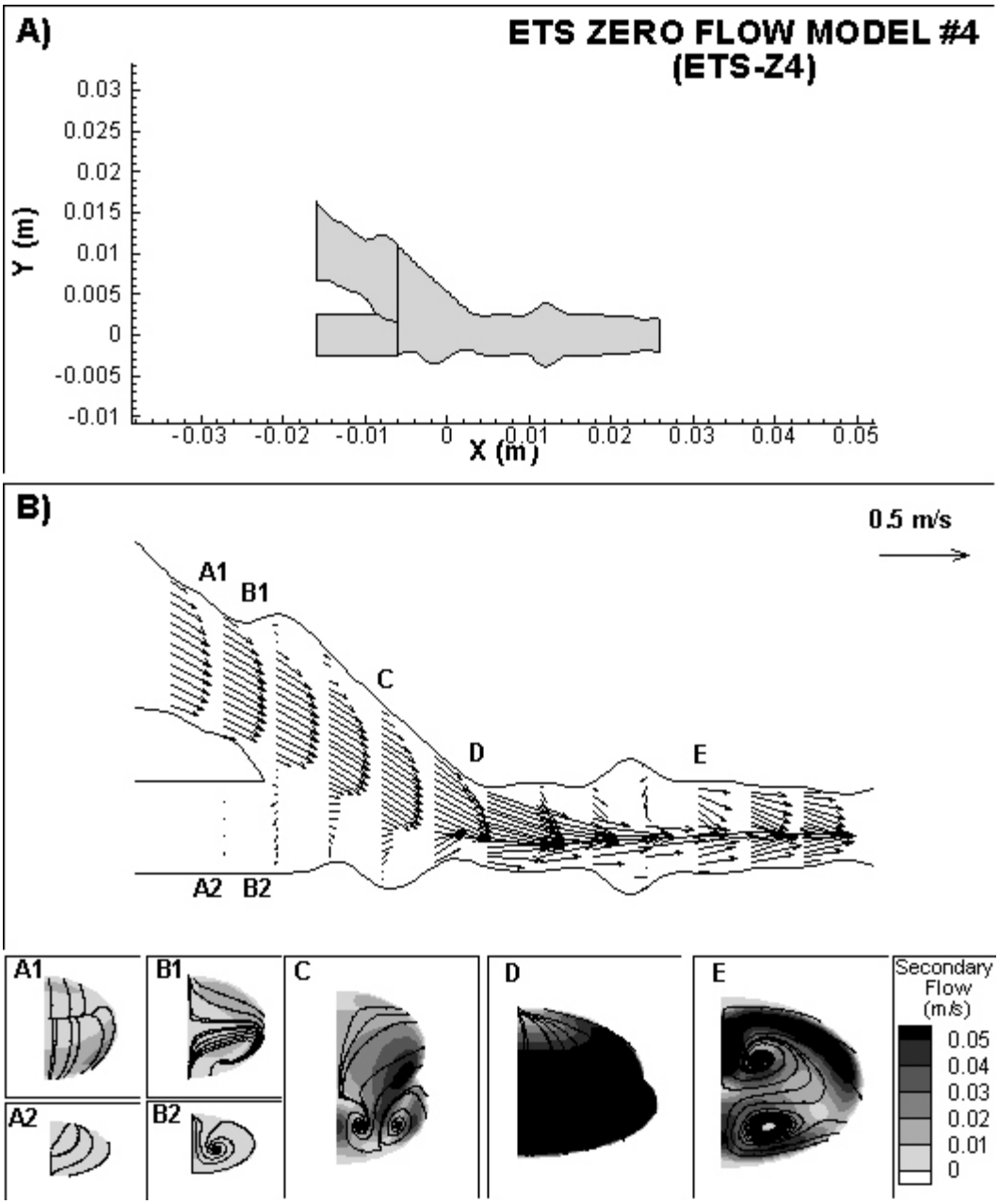

Figure 3.16 Geometry and velocity fields for ETS-Z4. A) Profile of the outer walls of the reconstructed geometry. The solid outlines indicate the proximal artery, graft and distal artery surfaces. Note that the scale is the same for all ETS and ETE models. B) Zoomed view of the model showing the velocity vectors on the symmetry plane at different axial positions. The bottom panels show the contour plots of the secondary flow magnitude and streamlines at the axial positions denoted in panel B: A1) graft, A2) proximal artery, B1) heel (in graft segment), B2) heel (in artery segment), C) hood and floor, D) toe and E) distal artery. Note that each panel illustrates a half cross-section and the view is as if standing at the end of the proximal artery and looking downstream. A small recirculation region is present upstream of the heel and the velocity vectors distal to the anastomosis are skewed toward the floor of the artery.

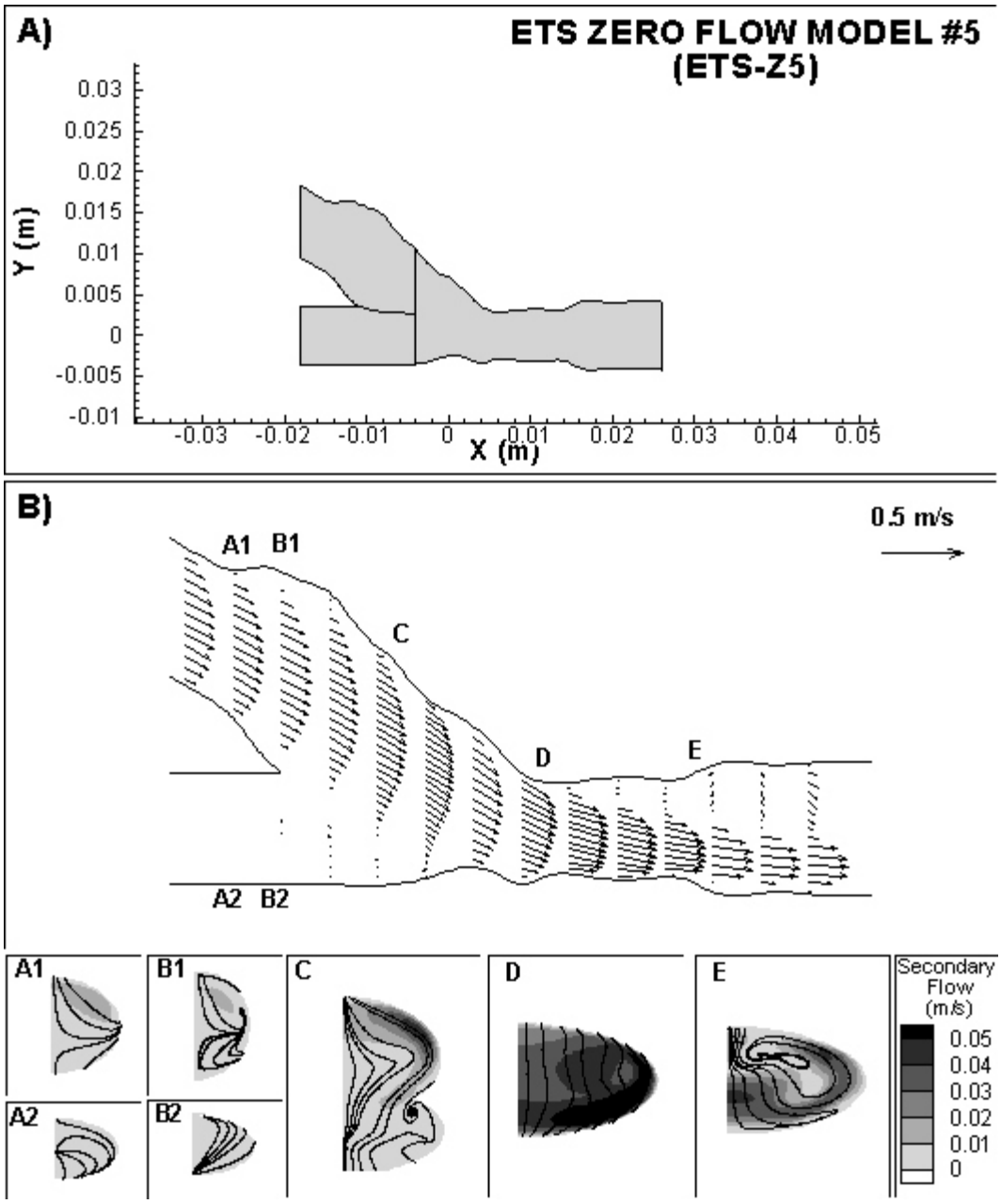

Figure 3.17 Geometry and velocity fields for ETS-Z5. A) Profile of the outer walls of the reconstructed geometry. The solid outlines indicate the proximal artery, graft and distal artery surfaces. Note that the scale is the same for all ETS and ETE models. B) Zoomed view of the model showing the velocity vectors on the symmetry plane at different axial positions. The bottom panels show the contour plots of the secondary flow magnitude and streamlines at the axial positions denoted in panel B: A1) graft, A2) proximal artery, B1) heel (in graft segment), B2) heel (in artery segment), C) hood and floor, D) toe and E) distal artery. Note that each panel illustrates a half cross-section and the view is as if standing at the end of the proximal artery and looking downstream. A small recirculation region is present upstream of the heel and the velocity vectors distal to the anastomosis are skewed toward the floor of the artery.

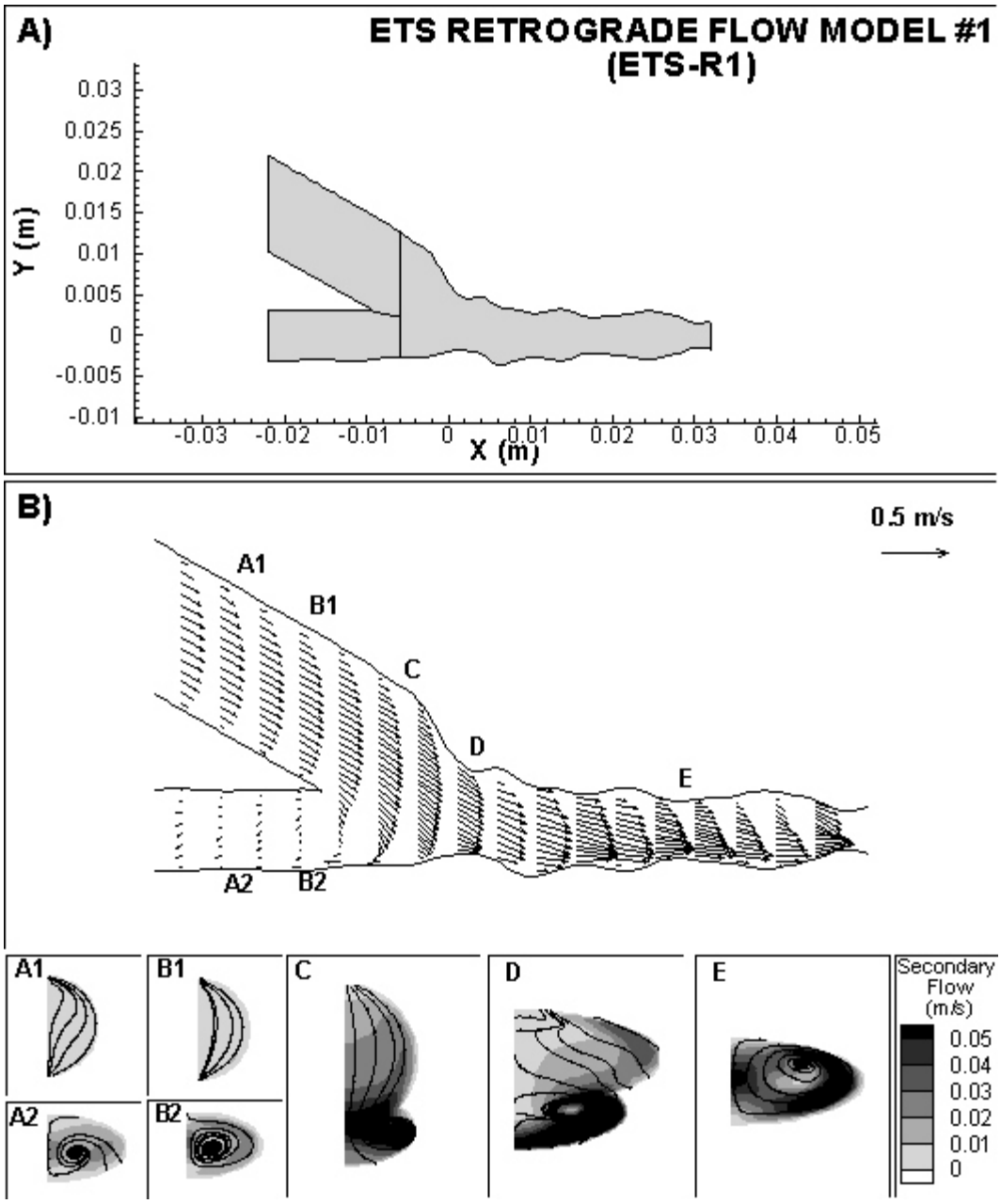

Figure 3.18 Geometry and velocity fields for ETS-R1. A) Profile of the outer walls of the reconstructed geometry. The solid outlines indicate the proximal artery, graft and distal artery surfaces. Note that the scale is the same for all ETS and ETE models. B) Zoomed view of the model showing the velocity vectors on the symmetry plane at different axial positions. The bottom panels show the contour plots of the secondary flow magnitude and streamlines at the axial positions denoted in panel B: A1) graft, A2) proximal artery, B1) heel (in graft segment), B2) heel (in artery segment), C) hood and floor, D) toe and E) distal artery. Note that each panel illustrates a half cross-section and the view is as if standing at the end of the proximal artery and looking downstream. As with the zero flow cases, the velocity vectors distal to the anastomosis are skewed toward the floor of the artery, though a larger recirculation region is present upstream of the heel than in those cases.

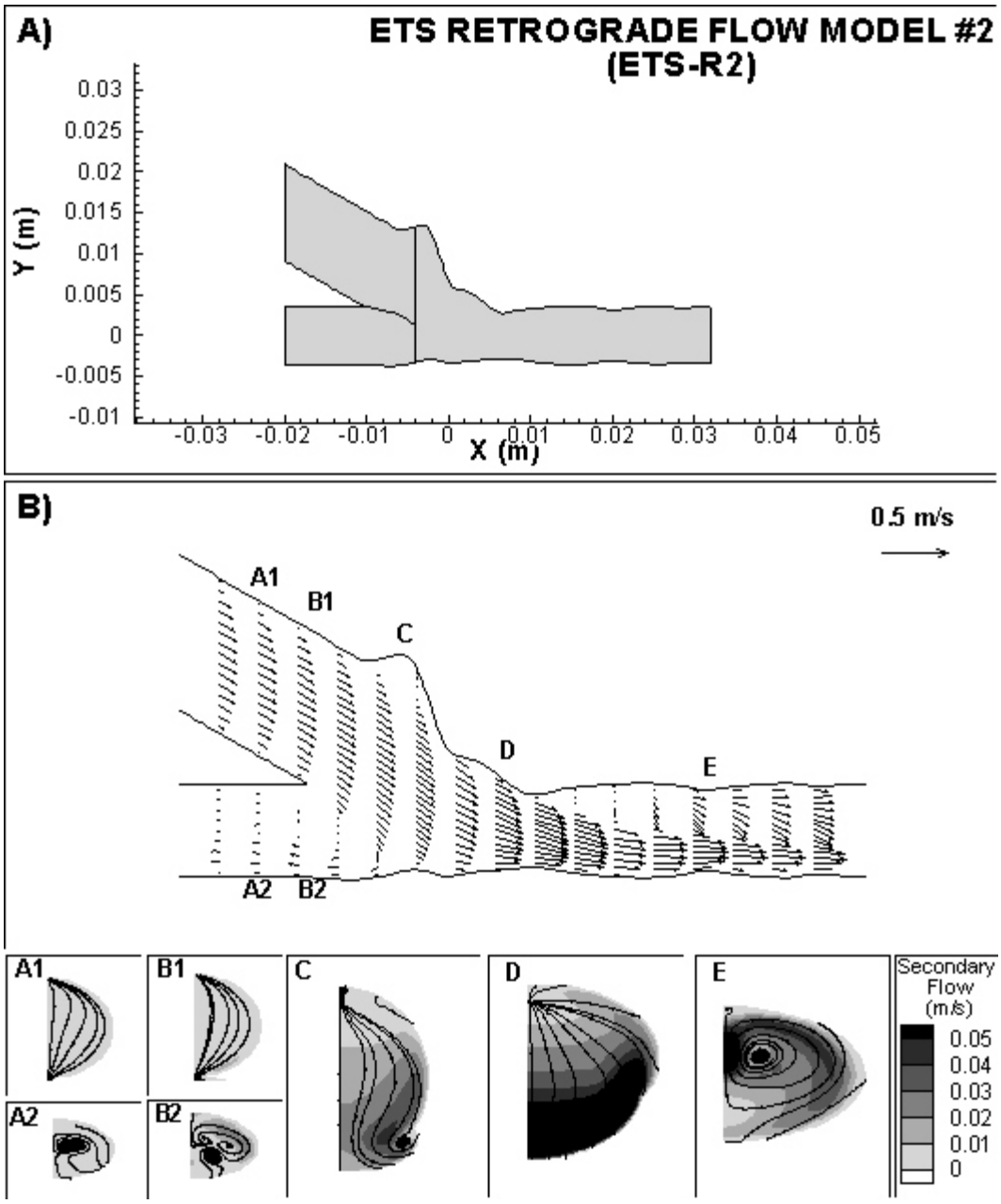

Figure 3.19 Geometry and velocity fields for ETS-R2. A) Profile of the outer walls of the reconstructed geometry. The solid outlines indicate the proximal artery, graft and distal artery surfaces. Note that the scale is the same for all ETS and ETE models. B) Zoomed view of the model showing the velocity vectors on the symmetry plane at different axial positions. The bottom panels show the contour plots of the secondary flow magnitude and streamlines at the axial positions denoted in panel B: A1) graft, A2) proximal artery, B1) heel (in graft segment), B2) heel (in artery segment), C) hood and floor, D) toe and E) distal artery. Note that each panel illustrates a half cross-section and the view is as if standing at the end of the proximal artery and looking downstream. As with the zero flow cases, the velocity vectors distal to the anastomosis are skewed toward the floor of the artery, though a larger recirculation region is present upstream of the heel than in those cases.

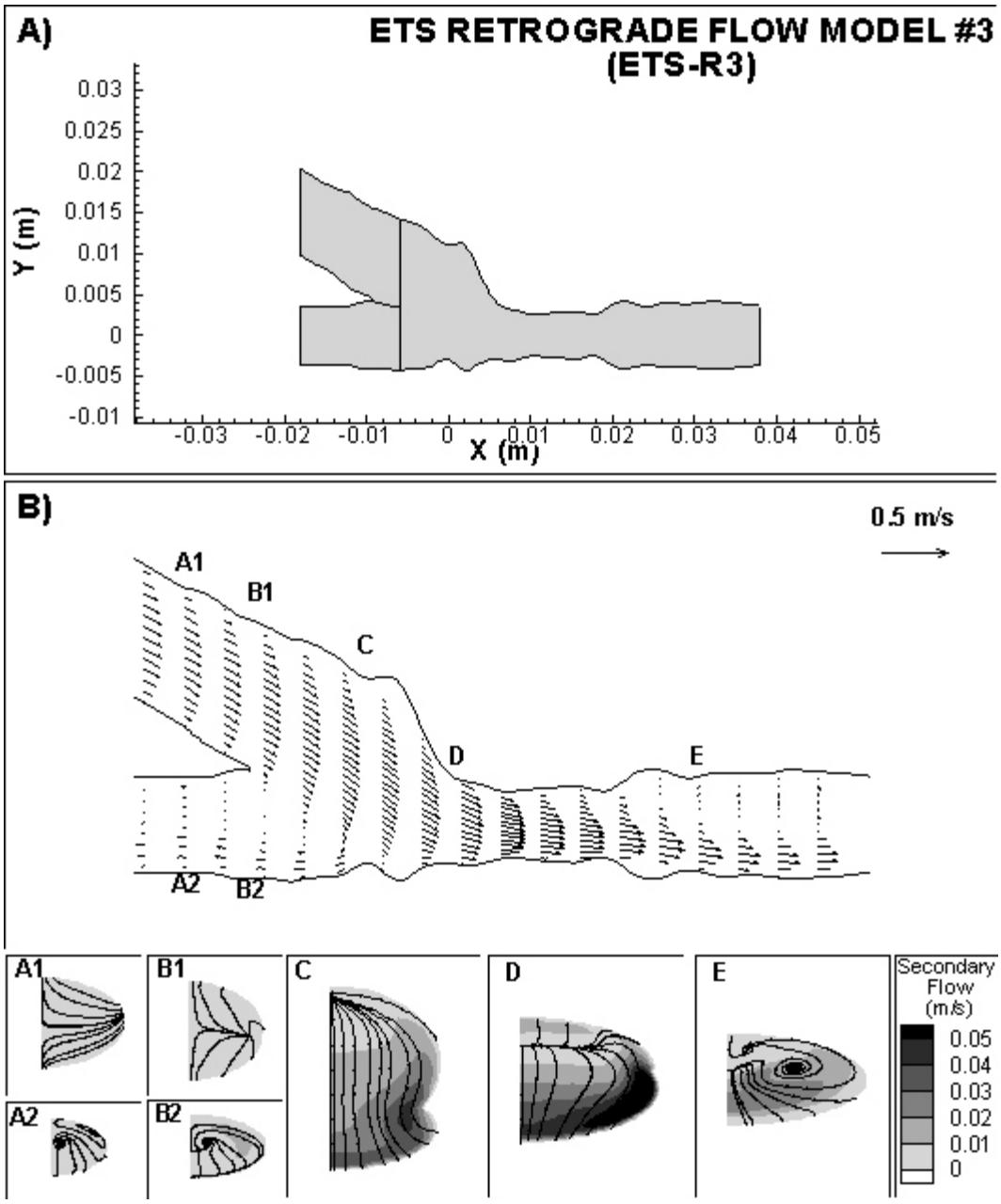

Figure 3.20 Geometry and velocity fields for ETS-R3. A) Profile of the outer walls of the reconstructed geometry. The solid outlines indicate the proximal artery, graft and distal artery surfaces. Note that the scale is the same for all ETS and ETE models. B) Zoomed view of the model showing the velocity vectors on the symmetry plane at different axial positions. The bottom panels show the contour plots of the secondary flow magnitude and streamlines at the axial positions denoted in panel B: A1) graft, A2) proximal artery, B1) heel (in graft segment), B2) heel (in artery segment), C) hood and floor, D) toe and E) distal artery. Note that each panel illustrates a half cross-section and the view is as if standing at the end of the proximal artery and looking downstream. As with the zero flow cases, the velocity vectors distal to the anastomosis are skewed toward the floor of the artery, though a larger recirculation region is present upstream of the heel than in those cases.

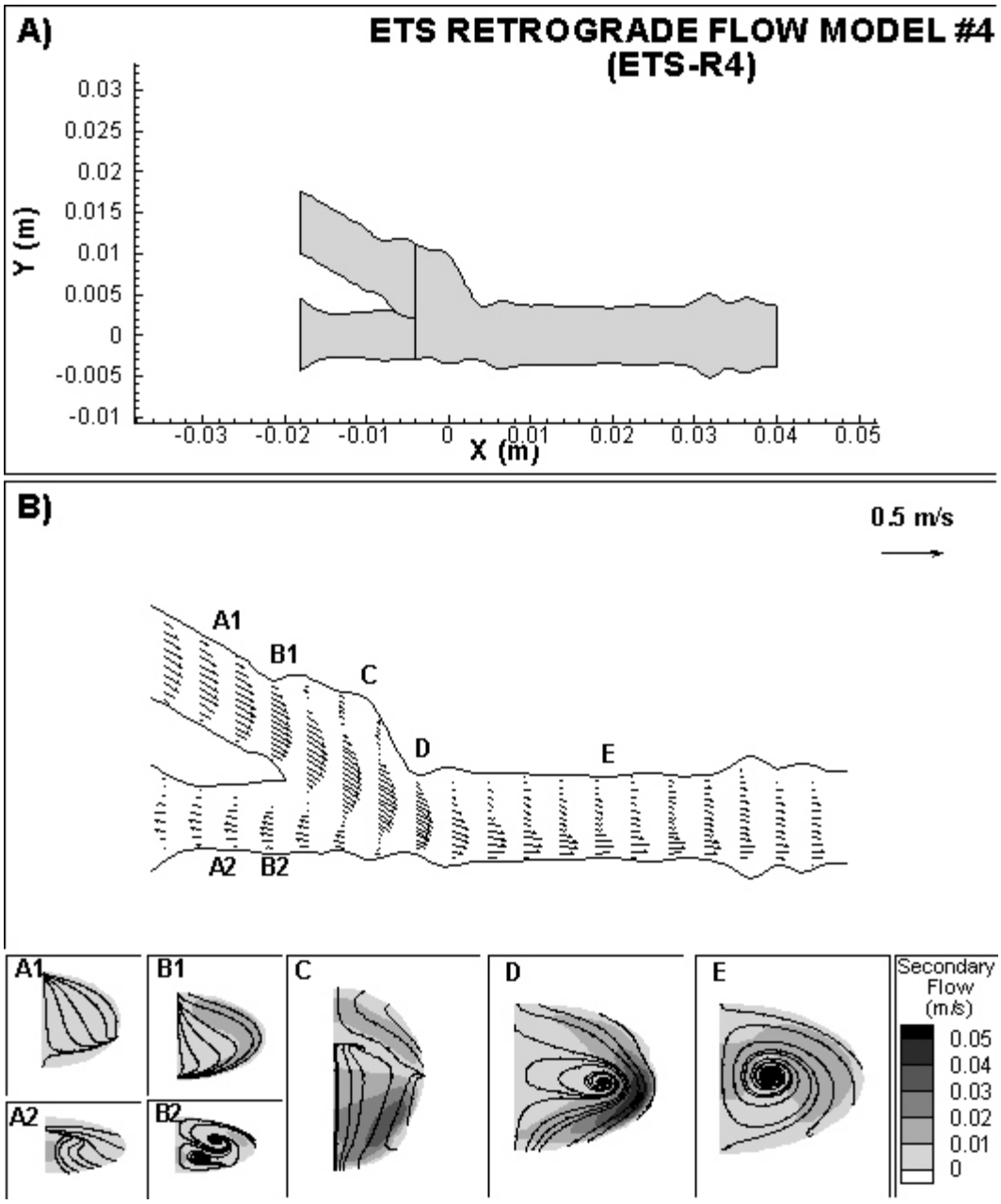

Figure 3.21 Geometry and velocity fields for ETS-R4. A) Profile of the outer walls of the reconstructed geometry. The solid outlines indicate the proximal artery, graft and distal artery surfaces. Note that the scale is the same for all ETS and ETE models. B) Zoomed view of the model showing the velocity vectors on the symmetry plane at different axial positions. The bottom panels show the contour plots of the secondary flow magnitude and streamlines at the axial positions denoted in panel B: A1) graft, A2) proximal artery, B1) heel (in graft segment), B2) heel (in artery segment), C) hood and floor, D) toe and E) distal artery. Note that each panel illustrates a half cross-section and the view is as if standing at the end of the proximal artery and looking downstream. As with the zero flow cases, the velocity vectors distal to the anastomosis are skewed toward the floor of the artery, though a larger recirculation region is present upstream of the heel than in those cases.

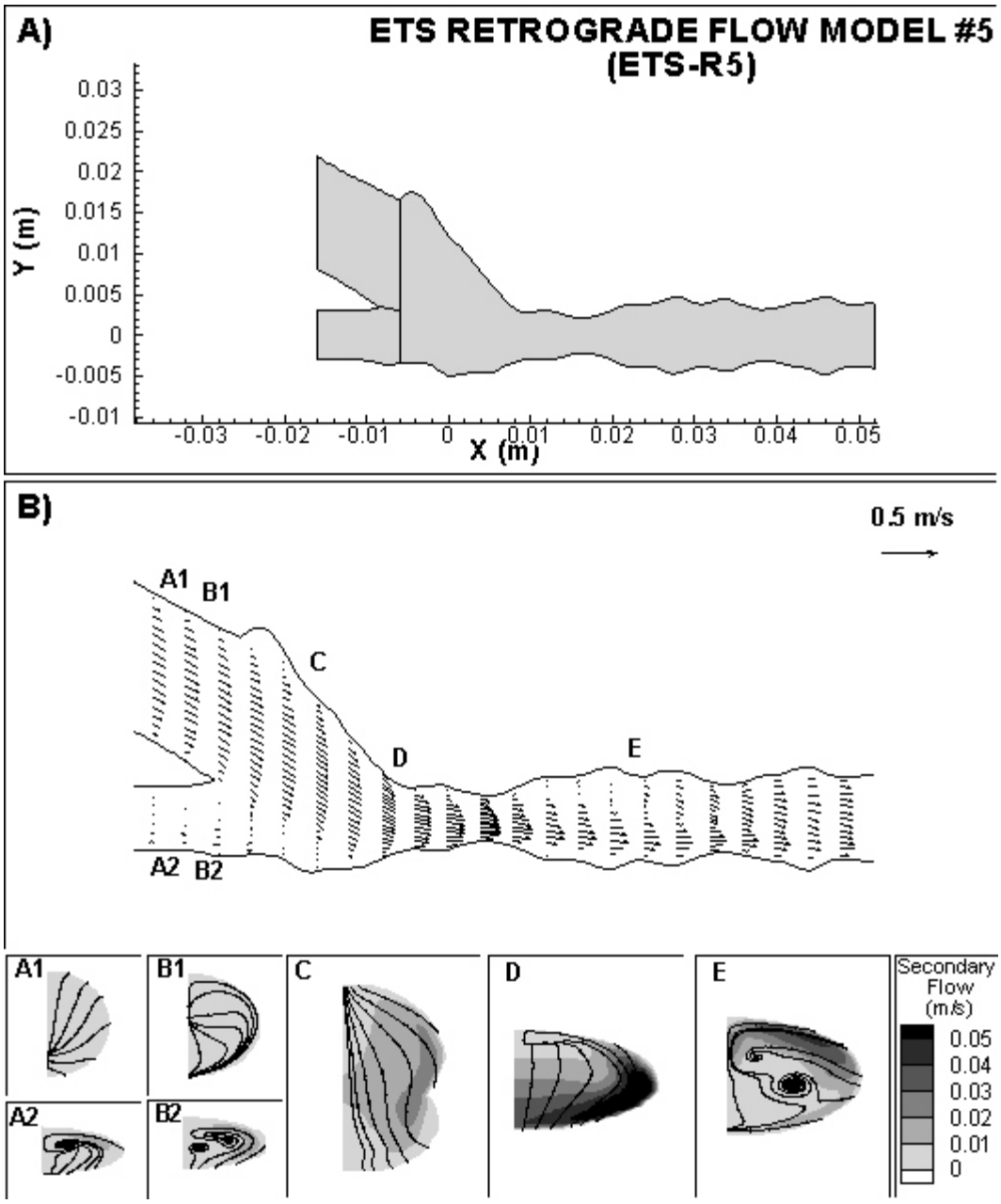

Figure 3.22 Geometry and velocity fields for ETS-R5. A) Profile of the outer walls of the reconstructed geometry. The solid outlines indicate the proximal artery, graft and distal artery surfaces. Note that the scale is the same for all ETS and ETE models. B) Zoomed view of the model showing the velocity vectors on the symmetry plane at different axial positions. The bottom panels show the contour plots of the secondary flow magnitude and streamlines at the axial positions denoted in panel B: A1) graft, A2) proximal artery, B1) heel (in graft segment), B2) heel (in artery segment), C) hood and floor, D) toe and E) distal artery. Note that each panel illustrates a half cross-section and the view is as if standing at the end of the proximal artery and looking downstream. As with the zero flow cases, the velocity vectors distal to the anastomosis are skewed toward the floor of the artery, though a larger recirculation region is present upstream of the heel than in those cases.

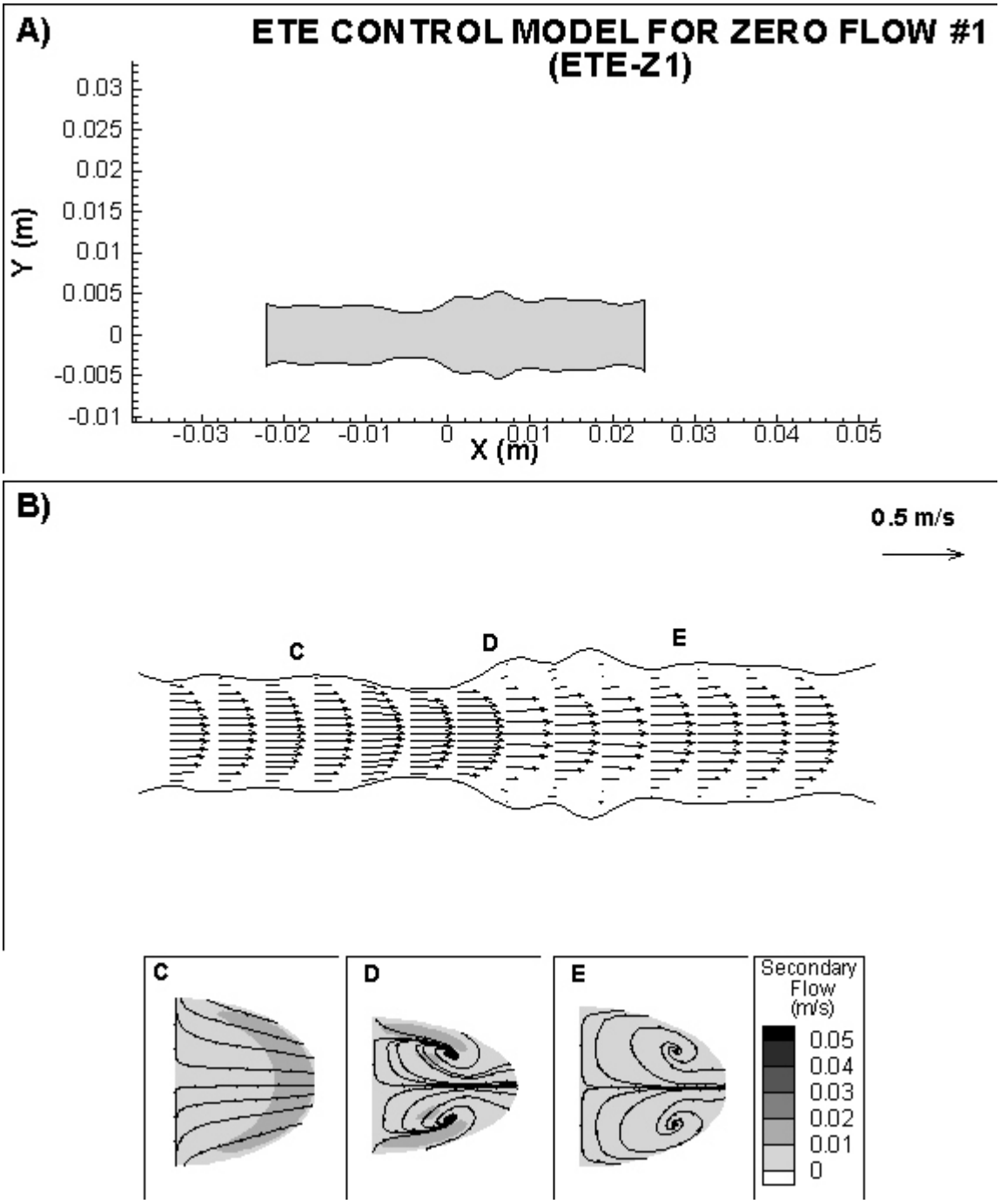

Figure 3.23 Geometry and velocity fields for ETE-Z1. A) Profile of the outer wall of the reconstructed geometry. Note that the scale is the same for all ETS and ETE models. B) Zoomed view of the model showing the velocity vectors on the symmetry plane at different axial positions. The bottom panels show the contour plots of the secondary flow magnitude and streamlines at the axial positions denoted in panel B: C) proximal artery, D) anastomosis and E) distal artery. Note that each panel illustrates a half cross-section and the view is as if standing at the end of the proximal artery and looking downstream. Velocity increases in regions of constriction and recirculation occurs in expansions.

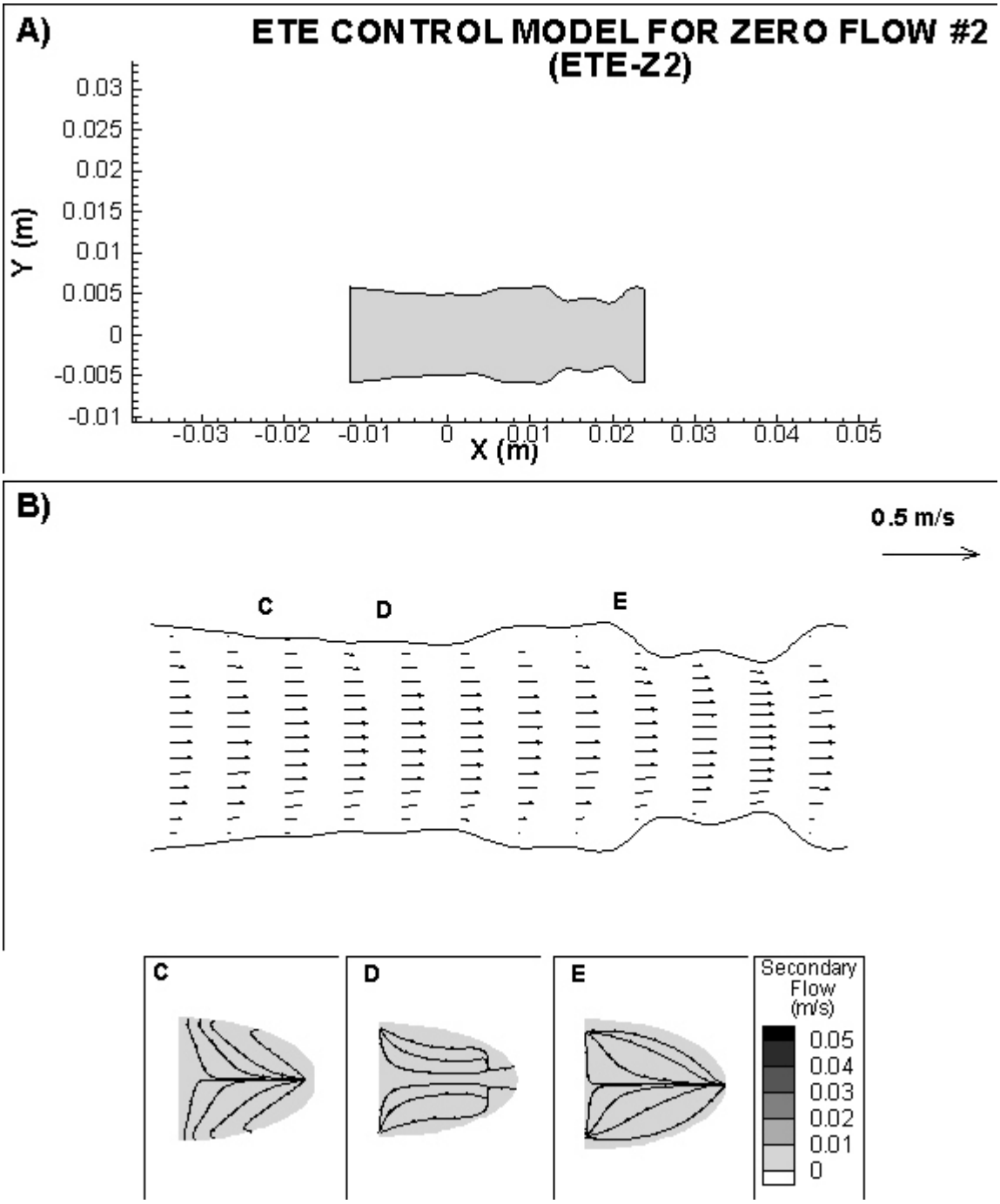

Figure 3.24 Geometry and velocity fields for ETE-Z2. A) Profile of the outer wall of the reconstructed geometry. Note that the scale is the same for all ETS and ETE models. B) Zoomed view of the model showing the velocity vectors on the symmetry plane at different axial positions. The bottom panels show the contour plots of the secondary flow magnitude and streamlines at the axial positions denoted in panel B: C) proximal artery, D) anastomosis and E) distal artery. Note that each panel illustrates a half cross-section and the view is as if standing at the end of the proximal artery and looking downstream. Velocity increases in regions of constriction and recirculation occurs in expansions.

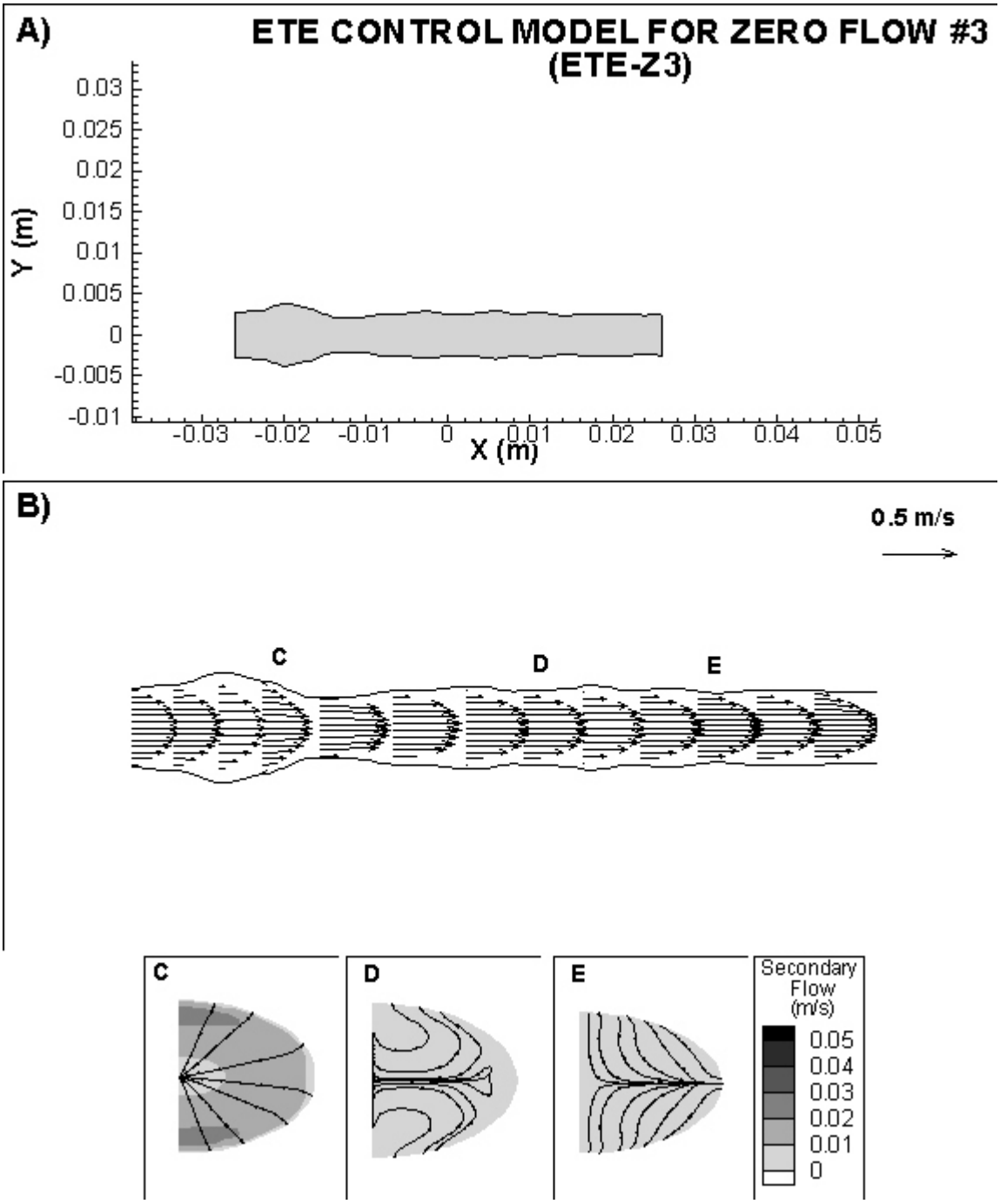

Figure 3.25 Geometry and velocity fields for ETE-Z3. A) Profile of the outer wall of the reconstructed geometry. Note that the scale is the same for all ETS and ETE models. B) Zoomed view of the model showing the velocity vectors on the symmetry plane at different axial positions. The bottom panels show the contour plots of the secondary flow magnitude and streamlines at the axial positions denoted in panel B: C) proximal artery, D) anastomosis and E) distal artery. Note that each panel illustrates a half cross-section and the view is as if standing at the end of the proximal artery and looking downstream. Velocity increases in regions of constriction and recirculation occurs in expansions.

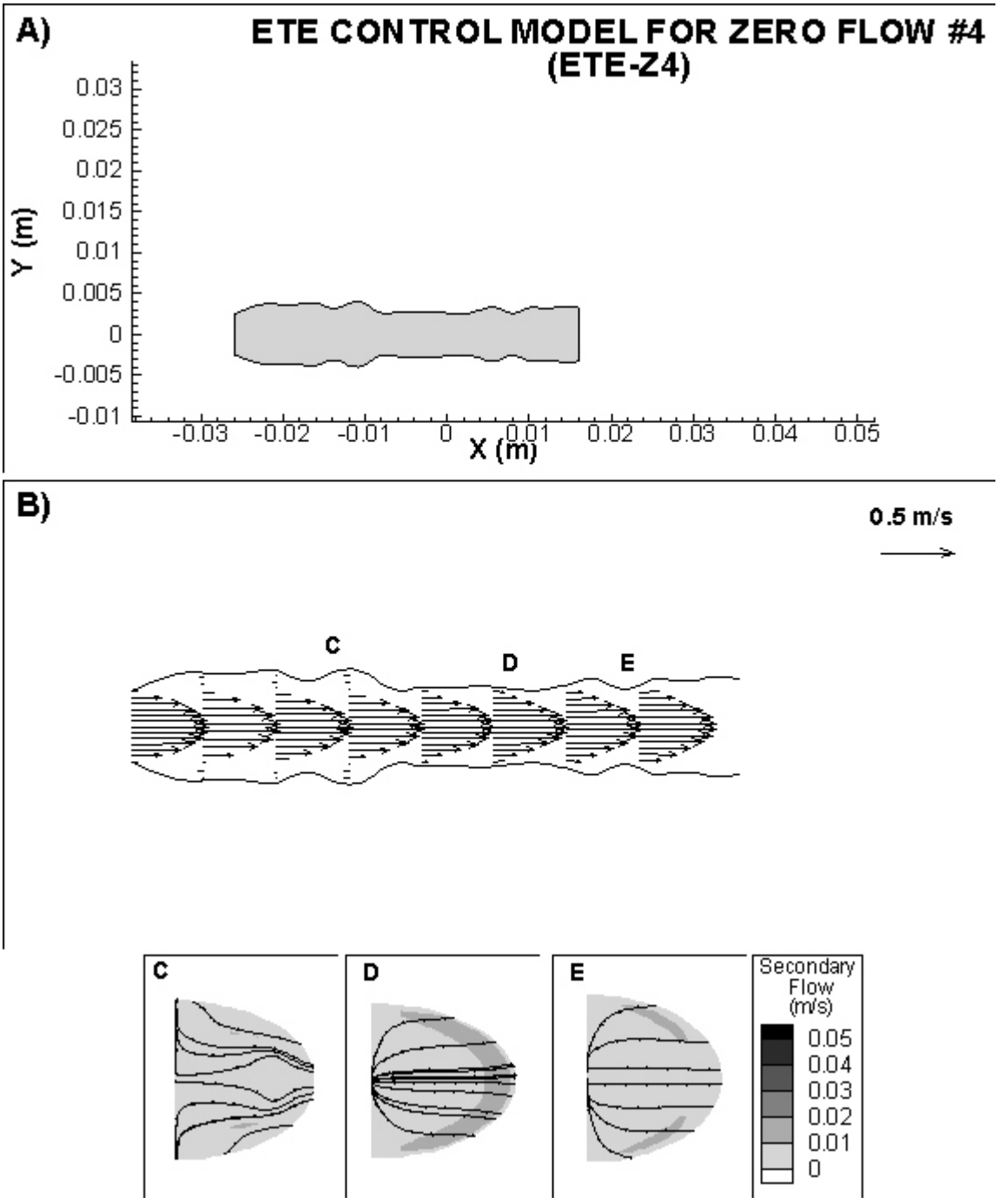

Figure 3.26 Geometry and velocity fields for ETE-Z4. A) Profile of the outer wall of the reconstructed geometry. Note that the scale is the same for all ETS and ETE models. B) Zoomed view of the model showing the velocity vectors on the symmetry plane at different axial positions. The bottom panels show the contour plots of the secondary flow magnitude and streamlines at the axial positions denoted in panel B: C) proximal artery, D) anastomosis and E) distal artery. Note that each panel illustrates a half cross-section and the view is as if standing at the end of the proximal artery and looking downstream. Velocity increases in regions of constriction and recirculation occurs in expansions.

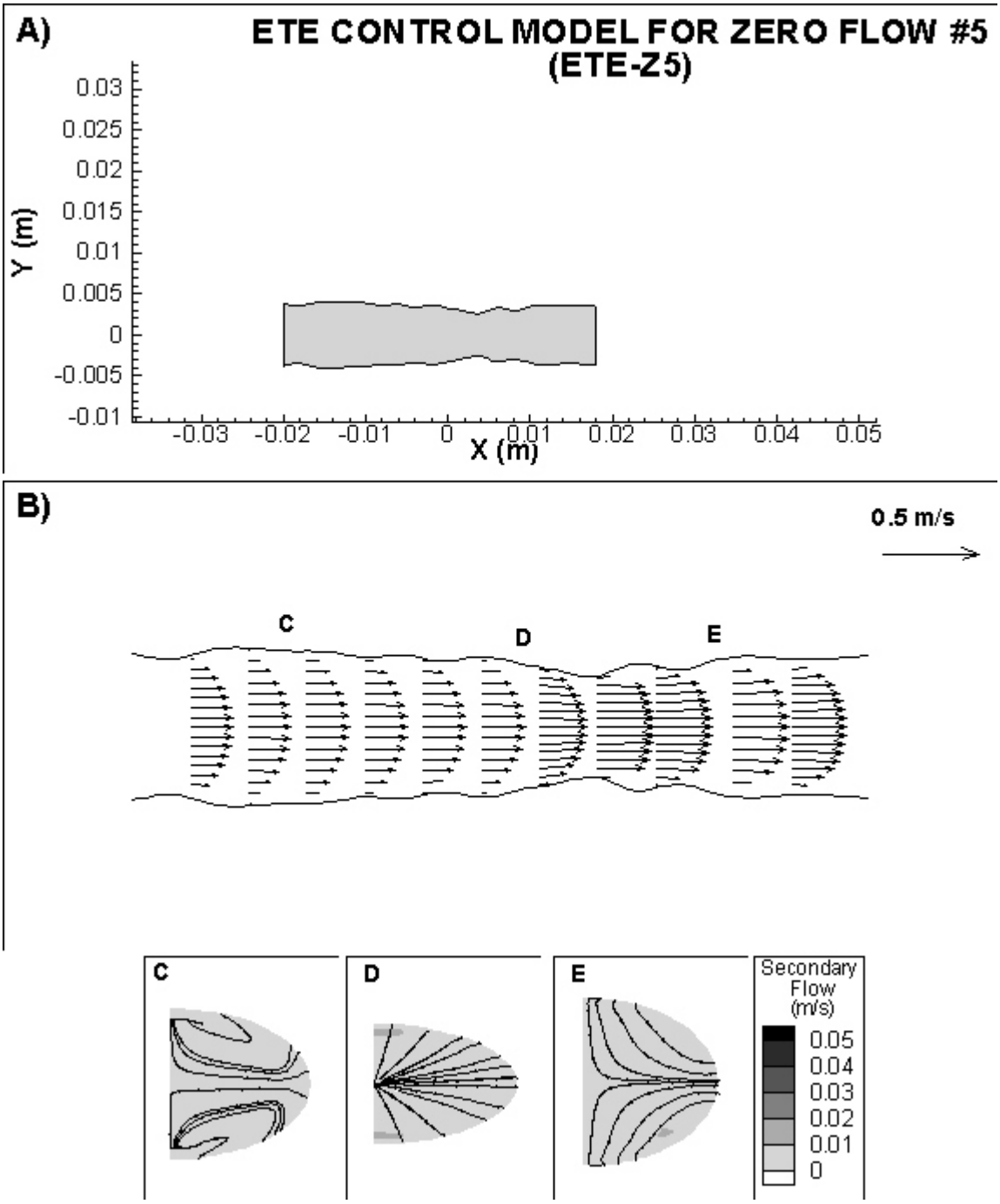

Figure 3.27 Geometry and velocity fields for ETE-Z5. A) Profile of the outer wall of the reconstructed geometry. Note that the scale is the same for all ETS and ETE models. B) Zoomed view of the model showing the velocity vectors on the symmetry plane at different axial positions. The bottom panels show the contour plots of the secondary flow magnitude and streamlines at the axial positions denoted in panel B: C) proximal artery, D) anastomosis and E) distal artery. Note that each panel illustrates a half cross-section and the view is as if standing at the end of the proximal artery and looking downstream. Velocity increases in regions of constriction and recirculation occurs in expansions.

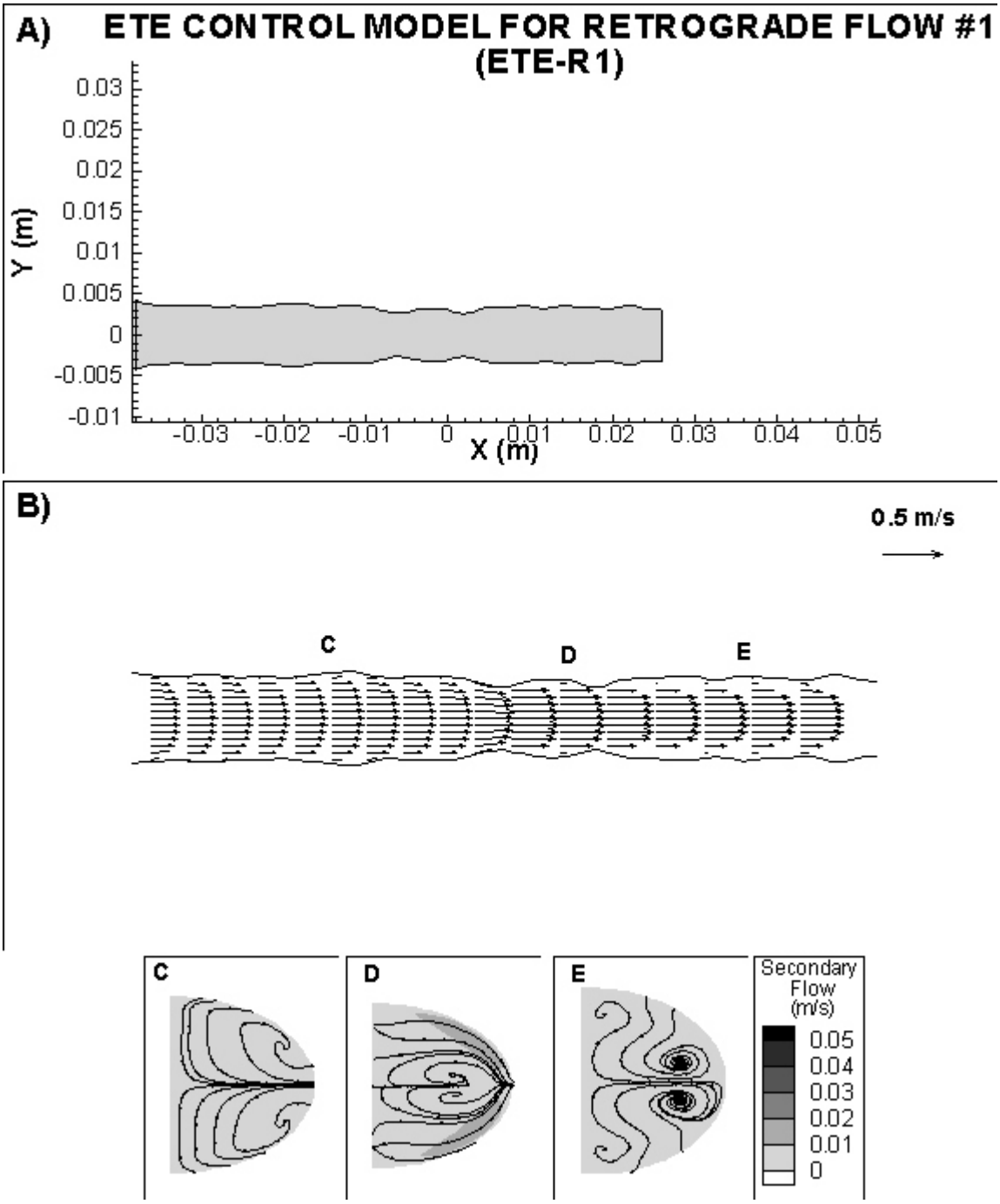

Figure 3.28 Geometry and velocity fields for ETE-R1. A) Profile of the outer wall of the reconstructed geometry. Note that the scale is the same for all ETS and ETE models. B) Zoomed view of the model showing the velocity vectors on the symmetry plane at different axial positions. The bottom panels show the contour plots of the secondary flow magnitude and streamlines at the axial positions denoted in panel B: C) proximal artery, D) anastomosis and E) distal artery. Note that each panel illustrates a half cross-section and the view is as if standing at the end of the proximal artery and looking downstream. Velocity increases in regions of constriction and recirculation occurs in expansions.

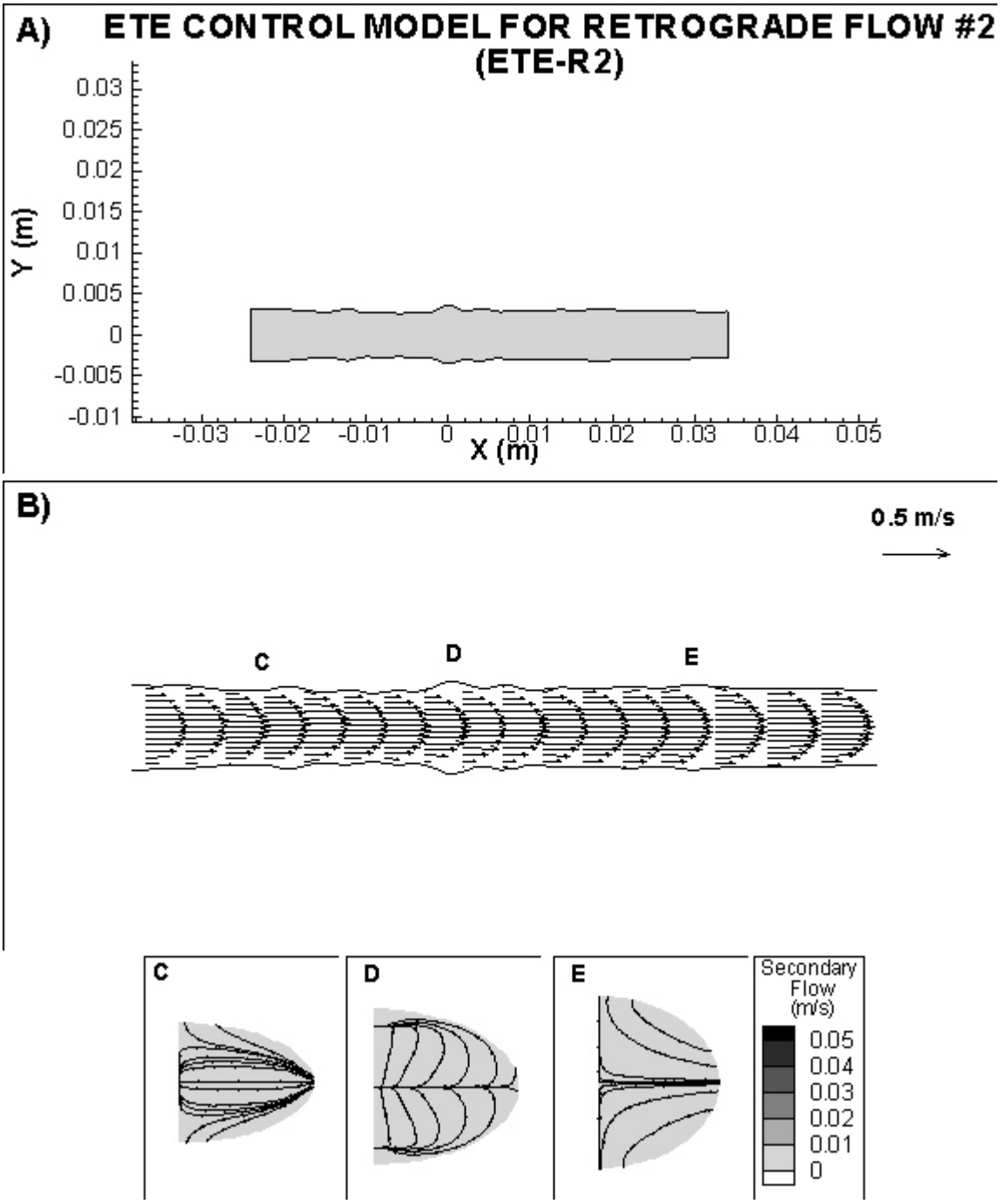

Figure 3.29 Geometry and velocity fields for ETE-R2. A) Profile of the outer wall of the reconstructed geometry. Note that the scale is the same for all ETS and ETE models. B) Zoomed view of the model showing the velocity vectors on the symmetry plane at different axial positions. The bottom panels show the contour plots of the secondary flow magnitude and streamlines at the axial positions denoted in panel B: C) proximal artery, D) anastomosis and E) distal artery. Note that each panel illustrates a half cross-section and the view is as if standing at the end of the proximal artery and looking downstream. Velocity increases in regions of constriction and recirculation occurs in expansions.

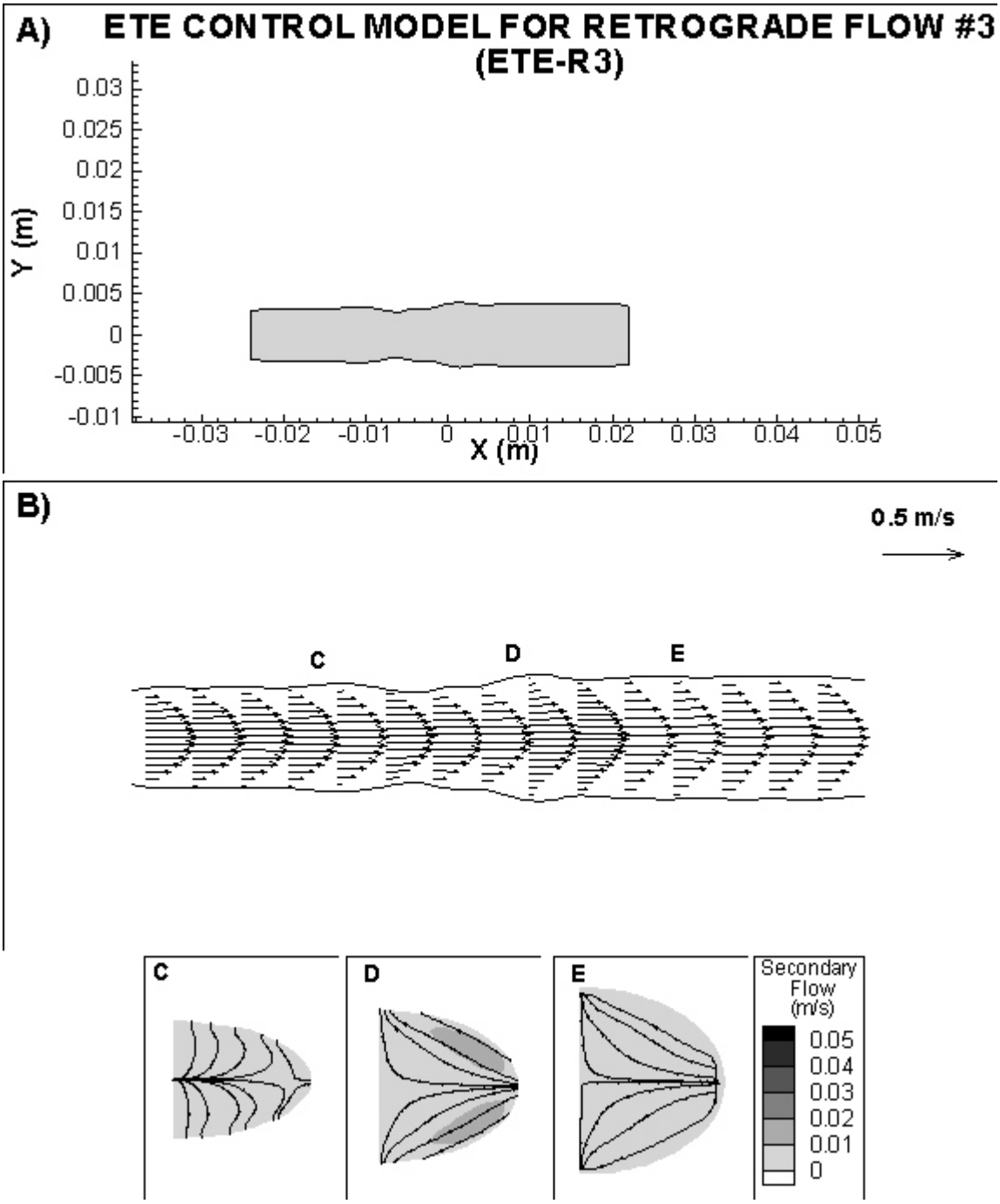

Figure 3.30 Geometry and velocity fields for ETE-R3. A) Profile of the outer wall of the reconstructed geometry. Note that the scale is the same for all ETS and ETE models. B) Zoomed view of the model showing the velocity vectors on the symmetry plane at different axial positions. The bottom panels show the contour plots of the secondary flow magnitude and streamlines at the axial positions denoted in panel B: C) proximal artery, D) anastomosis and E) distal artery. Note that each panel illustrates a half cross-section and the view is as if standing at the end of the proximal artery and looking downstream. Velocity increases in regions of constriction and recirculation occurs in expansions.

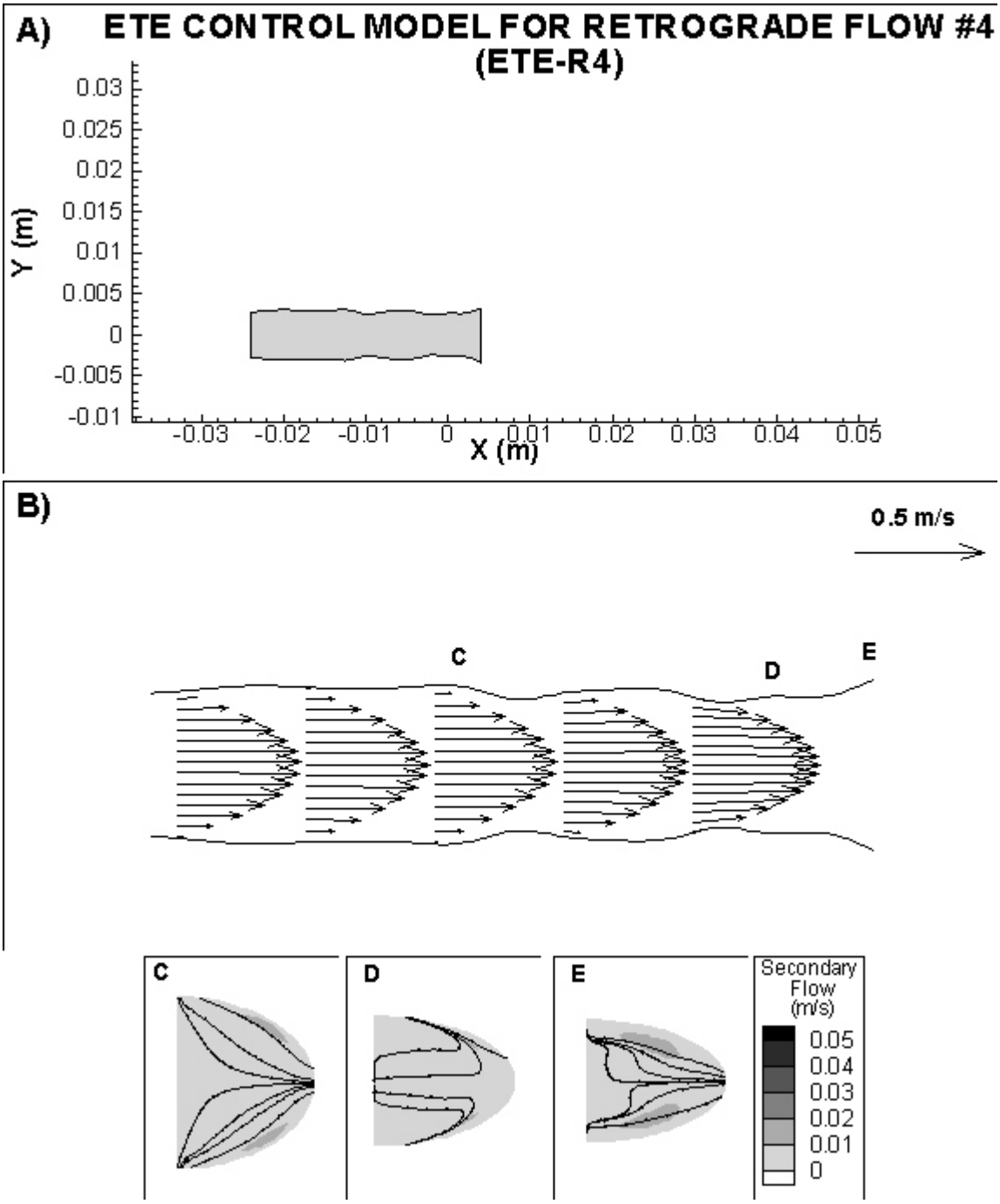

Figure 3.31 Geometry and velocity fields for ETE-R4. A) Profile of the outer wall of the reconstructed geometry. Note that the scale is the same for all ETS and ETE models. B) Zoomed view of the model showing the velocity vectors on the symmetry plane at different axial positions. The bottom panels show the contour plots of the secondary flow magnitude and streamlines at the axial positions denoted in panel B: C) proximal artery, D) anastomosis and E) distal artery. Note that each panel illustrates a half cross-section and the view is as if standing at the end of the proximal artery and looking downstream. Velocity increases in regions of constriction and recirculation occurs in expansions.

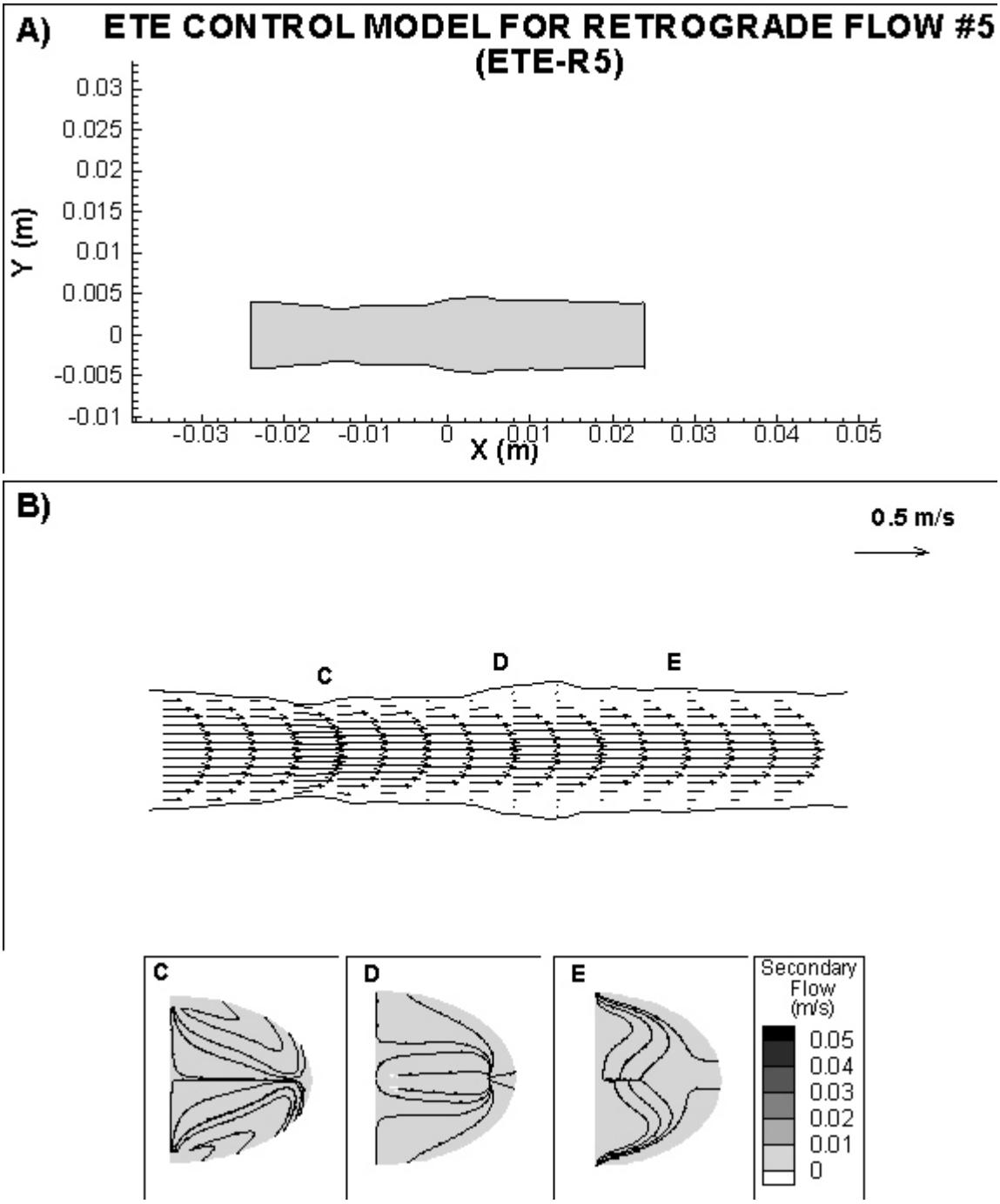

Figure 3.32 Geometry and velocity fields for ETE-R5. A) Profile of the outer wall of the reconstructed geometry. Note that the scale is the same for all ETS and ETE models. B) Zoomed view of the model showing the velocity vectors on the symmetry plane at different axial positions. The bottom panels show the contour plots of the secondary flow magnitude and streamlines at the axial positions denoted in panel B: C) proximal artery, D) anastomosis and E) distal artery. Note that each panel illustrates a half cross-section and the view is as if standing at the end of the proximal artery and looking downstream. Velocity increases in regions of constriction and recirculation occurs in expansions.

have recirculation regions half-way down the distal artery along the lateral wall. In most cases, this recirculation region flows counter-clockwise according to the view shown in the figures.

There are also differences in the secondary flow between the ETS zero flow, ETS retrograde flow and ETE models. In all of the ETS zero flow models (see Figures 3.13 - 3.17), recirculation regions exist in the floor cross-section while recirculation in this region is only present in ETS retrograde flow models ETS-R1 (Figure 3.18) and ETS-R2 (Figure 3.19). In all of the ETS retrograde flow models (Figures 3.18 - 3.22), recirculation regions exist in the heel cross-sections while this recirculation region is only present in ETS-Z3 (Figures 3.15) and ETS-Z4 (Figure 3.16). Additionally, in four of the five retrograde flow models (ETS-R1 (Figure 3.18), ETS-R2 (Figure 3.19), ETS-R3 (Figure 3.20) and ETS-R5 (Figure 3.22)), recirculation regions exist in the proximal artery while recirculation does not occur in this region for any of the ETS zero flow models (see Figures 3.13 - 3.17). For the ETE models, the magnitude of the secondary flow is quite small (see Figures 3.23 - 3.32). Recirculation regions only occur in regions of expansions and contractions since the flow is not coming in at an angle as it is in the ETS models.

In addition to the differences between the ETS zero flow, ETS retrograde flow and ETE models, there are differences within the groups. For example, the ETS-Z3 has very high magnitudes of secondary flow due to its small graft diameter (see Figure 3.15). This causes large recirculation regions in the floor, toe and distal regions as well as recirculation at the heel. In three of the ETS zero flow models, dual recirculation regions occur in the same cross-section. This happens in the hood/floor cross-section in ETS-Z1 (see Figure 3.13), the heel, hood/floor and toe cross-sections in ETS-Z3 (see Figure 3.15) as well as the hood/floor cross-section in ETS-Z4 (see Figure 3.16). For the ETS retrograde flow models, recirculation regions in the toe cross-section occur in ETS-R1 (see Figure 3.18) and ETS-R4 (Figure 3.21), but not in the other three models (see Figures 3.19, 3.20 and 3.22). Dual recirculation regions are present in four of the ETS retrograde flow although they occur in different cross-sections. Dual recirculation regions exist in the heel segment in ETS-R2 (Figure 3.19), ETS-R4 (Figure 3.21) and ETS-R5 (Figure 3.22) and exist in the distal cross-section in ETS-R3 (Figure 3.20) and ETS-R5 (Figure 3.22). For the ETE models, there is not as much variation, since

there is not much secondary flow (see Figures 3.23 - 3.32). However, recirculation regions do exist in three of the ETE models. In ETE-Z1 (Figure 3.23), dual recirculation regions occur in the anastomosis and distal cross-sections which are regions of expansion. Similarly, in ETE-R1 (Figure 3.28), dual recirculation regions occur in the distal artery cross-sections although the direction of these recirculation regions is opposite to those in ETE-Z1 (Figure 3.23). Weak dual recirculation also exists in proximal segment of the ETE-Z5 (Figure 3.27) as well as the proximal segment of ETE-R1 (Figure 3.28). Therefore, differences in secondary flow exist for all models due to the imposed flow conditions and the global and local variations in geometry.

3.3.5 Wall Shear Stress

The axial component of WSS for all models are shown in Figures 3.33 - 3.36, the circumferential component of WSS for all models are shown in Figures 3.37 - 3.40 and the magnitude of WSS for all models are shown in Figures 3.41 - 3.44. Note that the dimension scales are different for each anastomosis in order to optimize visualization. All models exhibit regional variation of WSS due to the alteration in diameter along the length of the vessels. In addition, the ETS models have WSS variations due to the disturbed flow caused by the angled insertion of the graft. In particular, there are regions (e.g. toe) where the circumferential WSS (see Figures 3.37 and 3.38) is the same order of magnitude as the axial component of WSS (see Figures 3.33 and 3.34) due to the secondary flow in these regions. This does not occur in the ETE models (see Figures 3.39 and 3.40) because the secondary flow is almost zero. Note that the upper range of the contour levels for WSS magnitude in these simulations is 7 dynes/cm^2 (see Figures 3.41 - 3.44). Although the WSS magnitude did reach as high as 30 dynes/cm^2 in some regions (i.e., toe region of ETS-Z3), in general, the levels of WSS in these simulations were lower than the normal physiologic value of 15 dynes/cm^2. This is because the experiments were designed to match normal physiologic wall shear rate (440 sec^{-1}) based on an assumed vessel inner diameter of 5 mm, yielding a WSS of 4.3 dynes/cm^2. Therefore, all subsequent comments on WSS levels as "high" or "low" is relative to the WSS range present in these models.

Similarities exist in the values of axial and circumferential WSS as well as the magnitude of WSS present in the ETS zero and retrograde flow models. In all ETS models, except ETS-Z3 and ETS-Z4, the

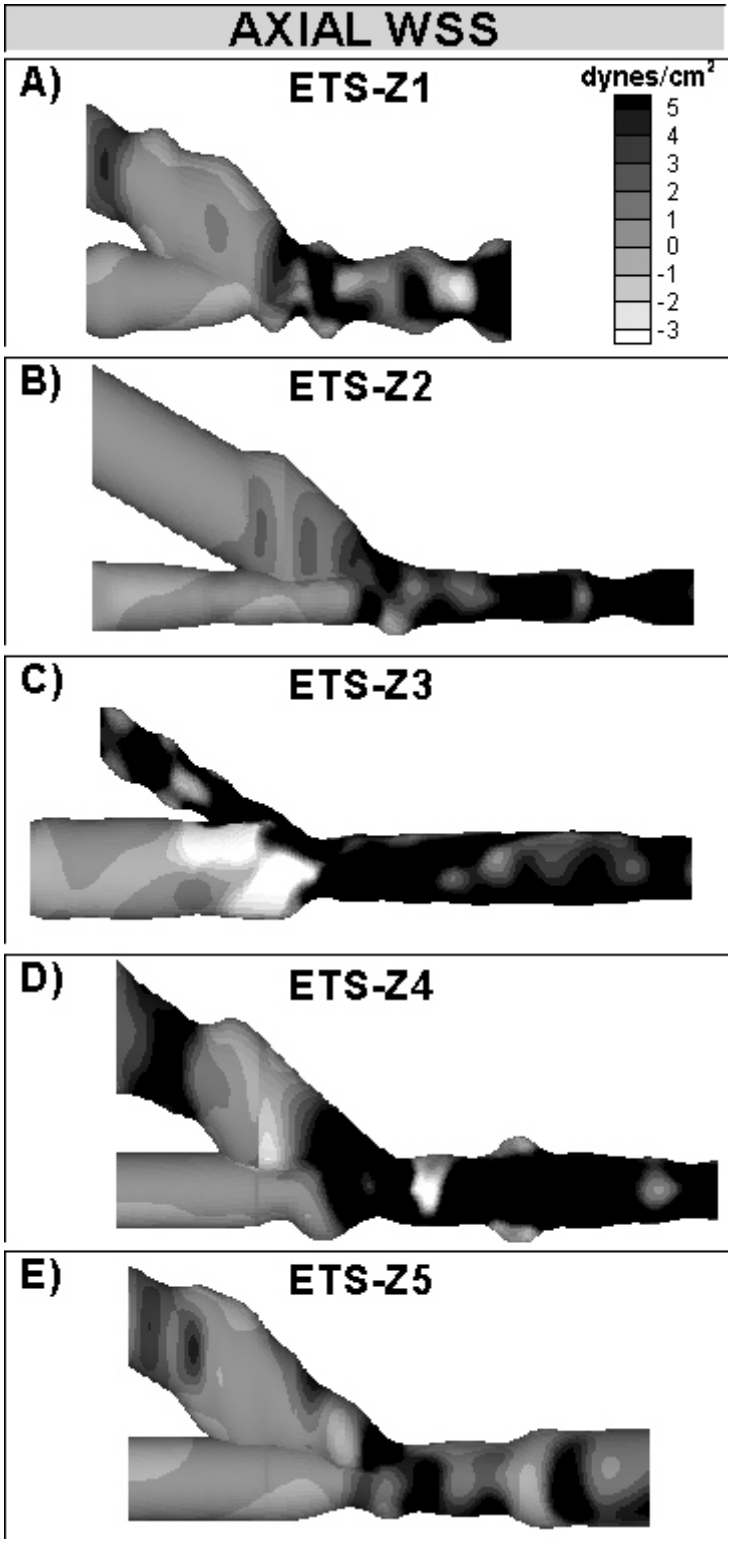

Figure 3.33 Contour plot of the axial component of WSS for each of the ETS zero flow models.

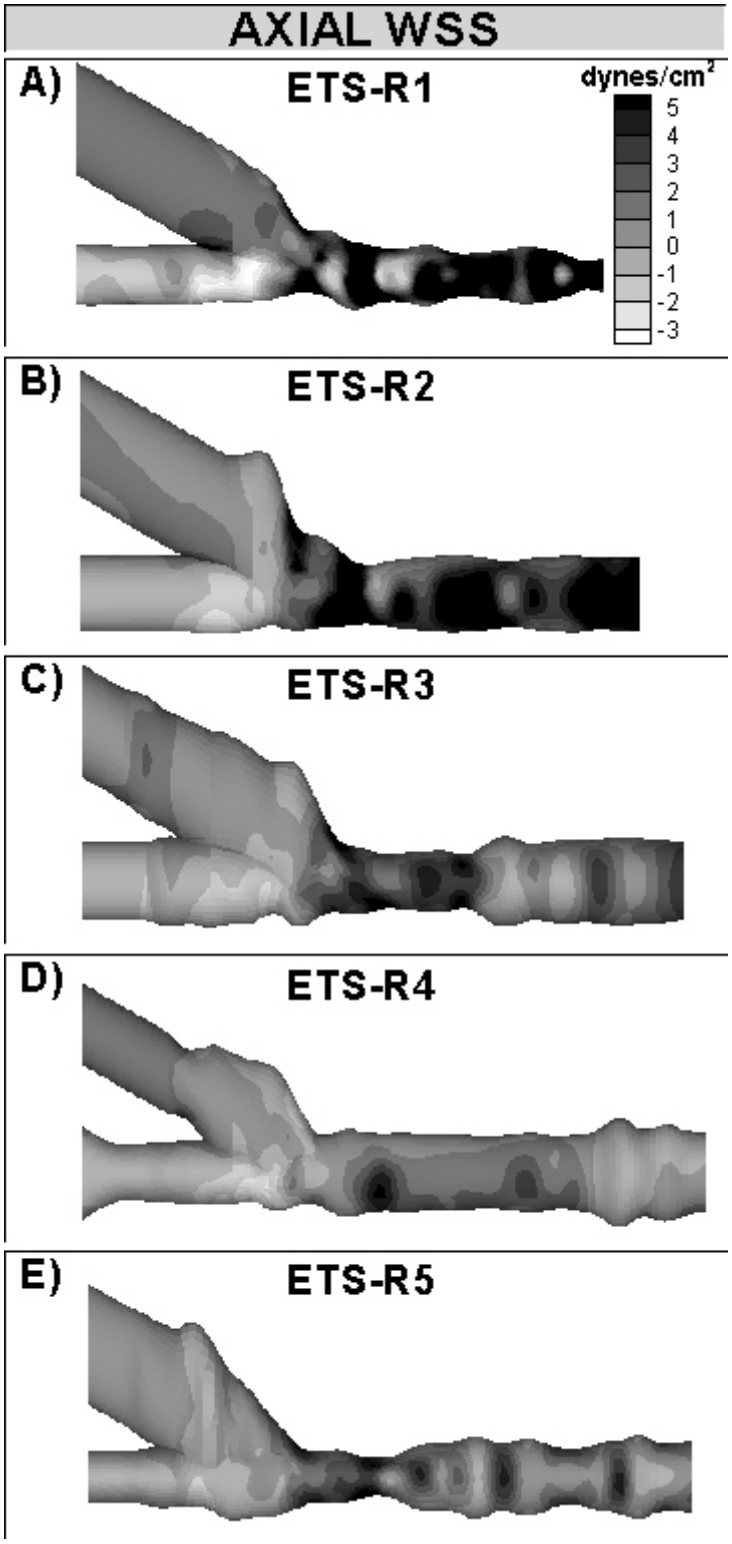

Figure 3.34 Contour plot of the axial component of WSS for each of the ETS retrograde flow models.

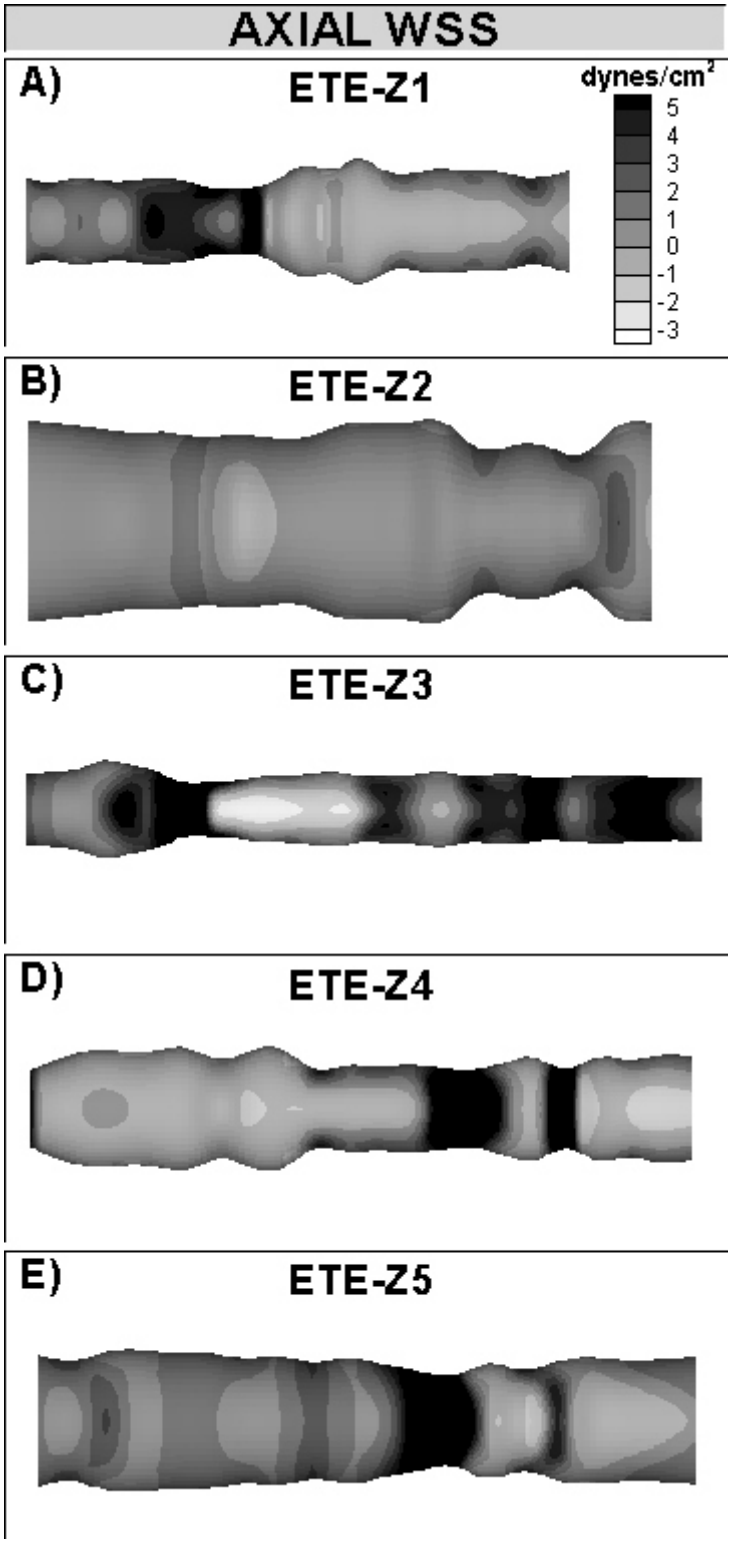

Figure 3.35 Contour plot of the axial component of WSS for each of the ETE models corresponding to the ETS zero flow experiments.

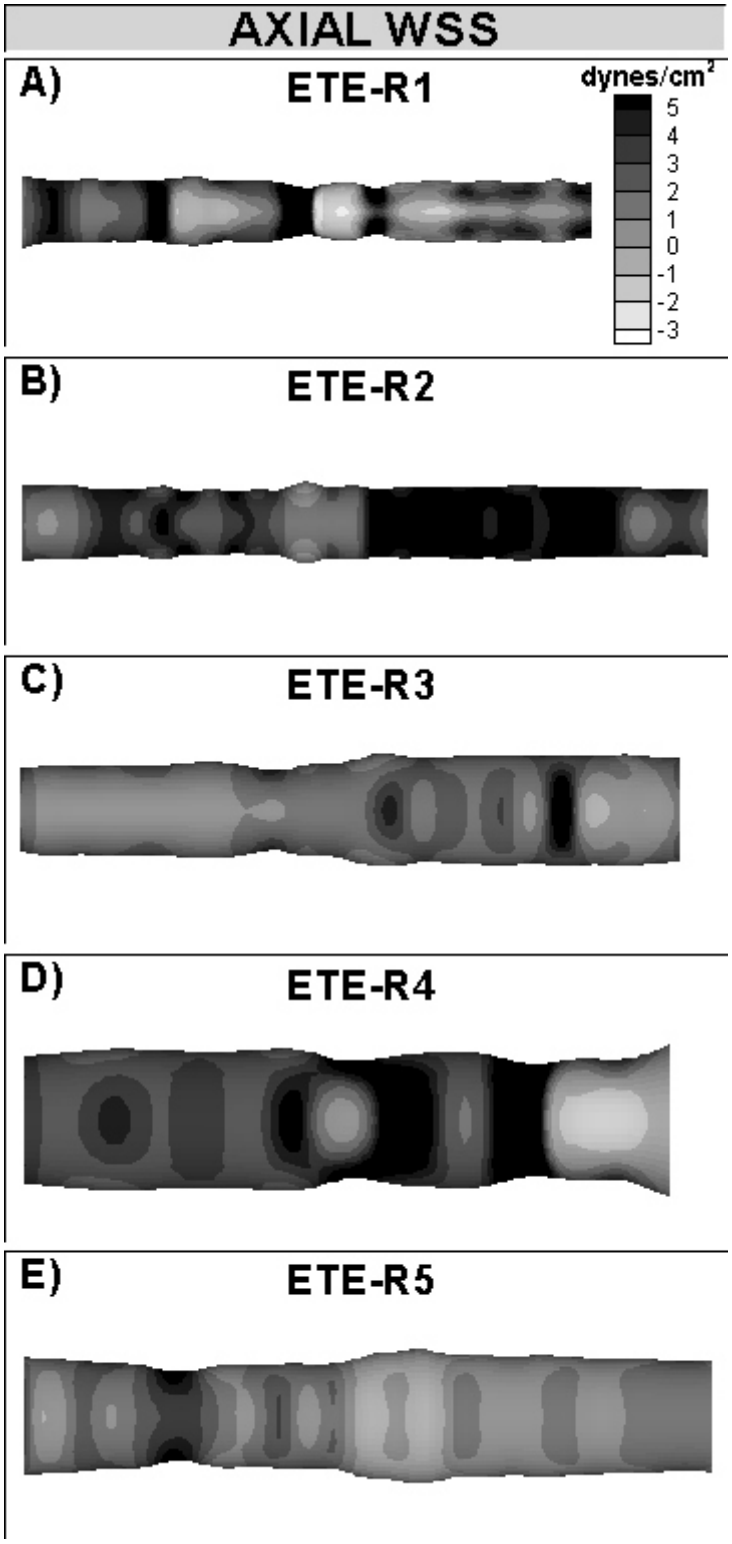

Figure 3.36 Contour plot of the axial component of WSS for each of the ETE models corresponding to the ETS retrograde flow experiments.

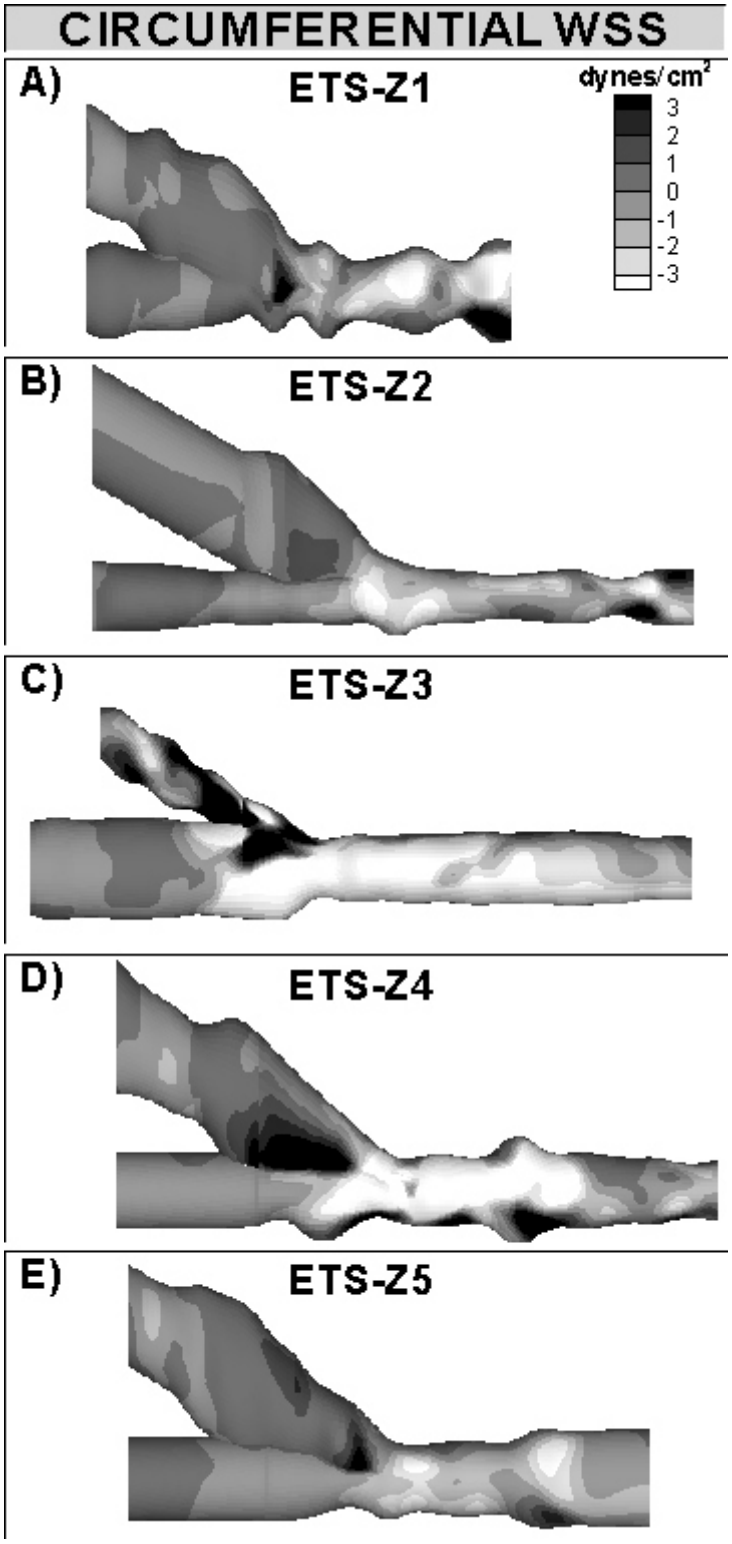

Figure 3.37 Contour plot of the circumferential component of WSS for each of the ETS zero flow models.

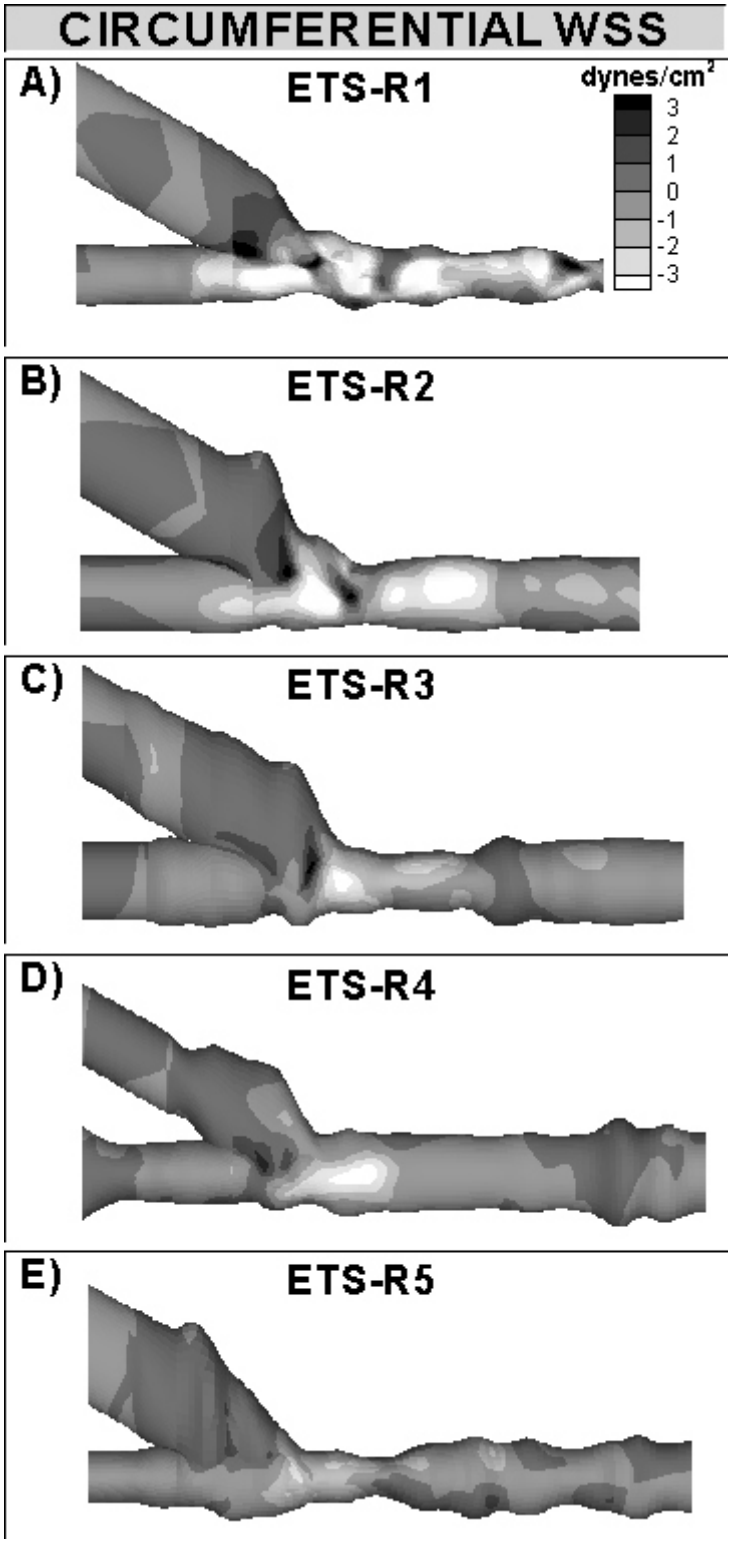

Figure 3.38 Contour plot of the circumferential component of WSS for each of the ETS retrograde flow models.

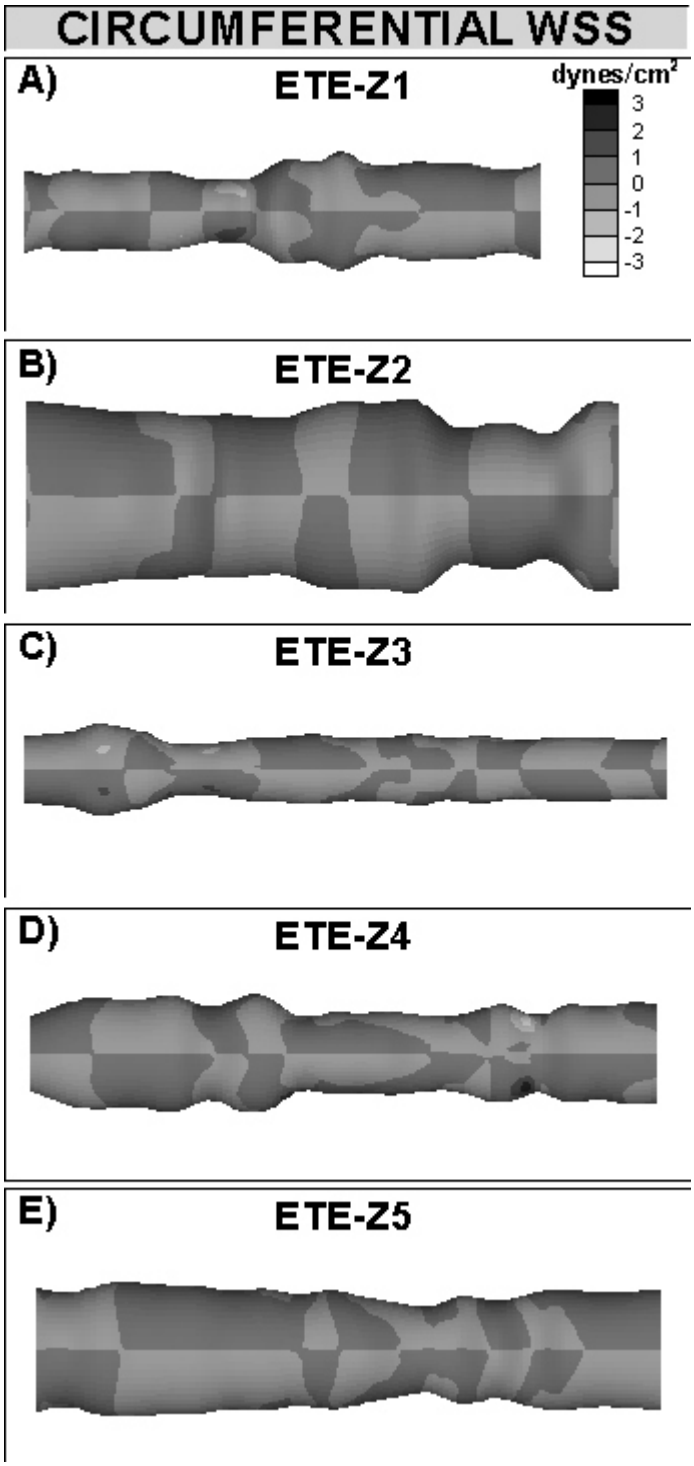

Figure 3.39 Contour plot of the circumferential component of WSS for each of the ETE models corresponding to the ETS zero flow experiments. The patchy appearance is an artifact due to the change in contour level at 0 dynes/cm^2, which is the value for most of the vessel.

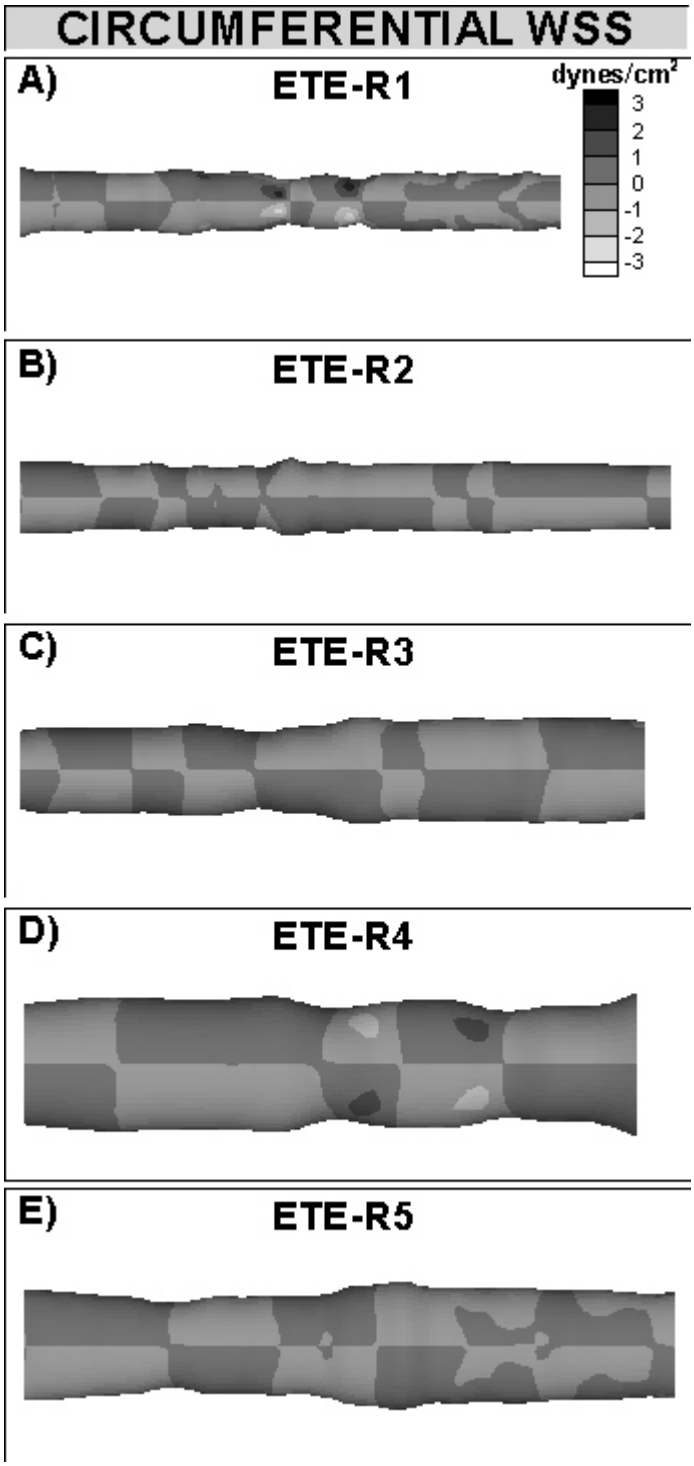

Figure 3.40 Contour plot of the circumferential component of WSS for each of the ETE models corresponding to the ETS retrograde flow experiments. The patchy appearance is an artifact due to the change in contour level at 0 dynes/cm^2, which is the value for most of the vessel.

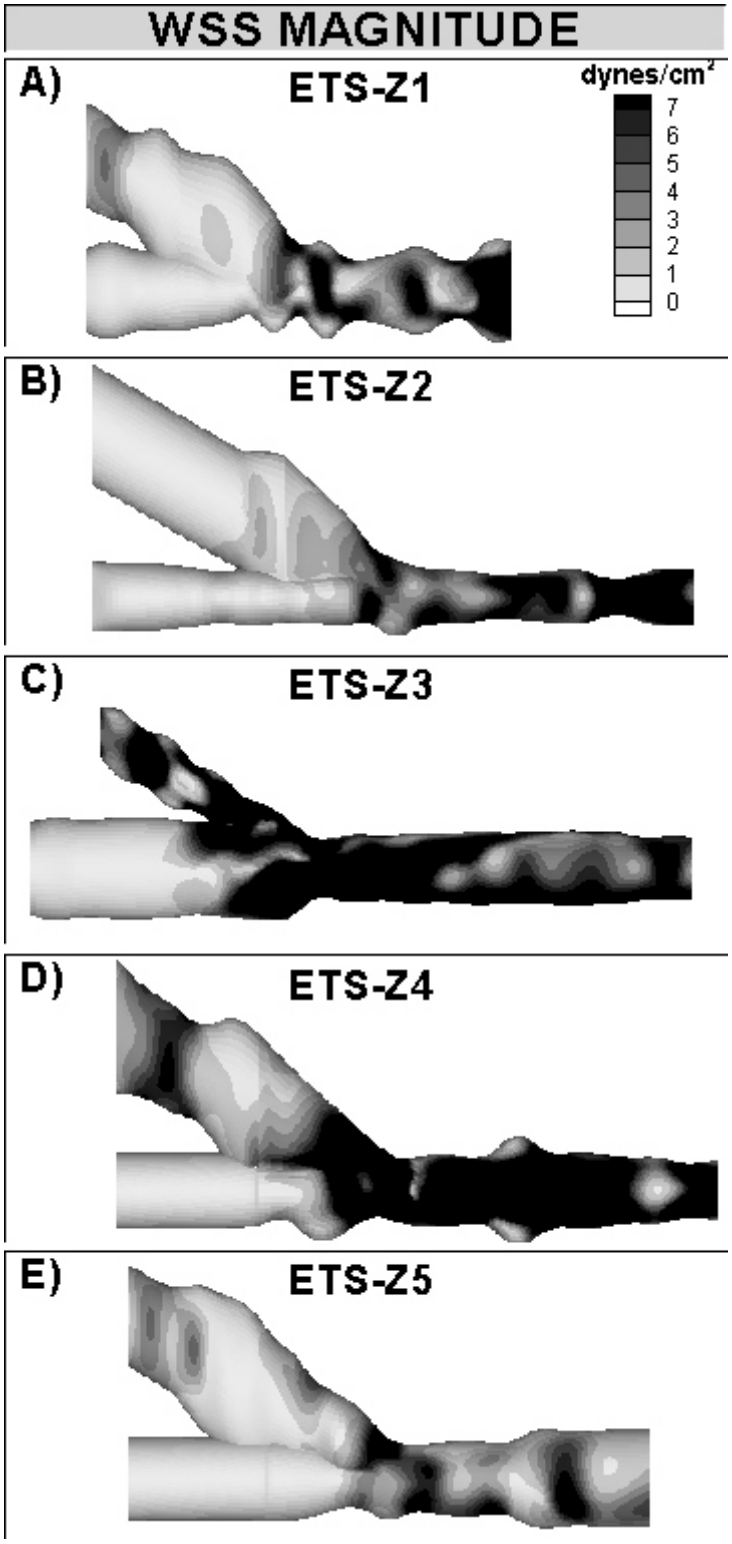

Figure 3.41 Contour plot of WSS magnitude for each of the ETS zero flow models.

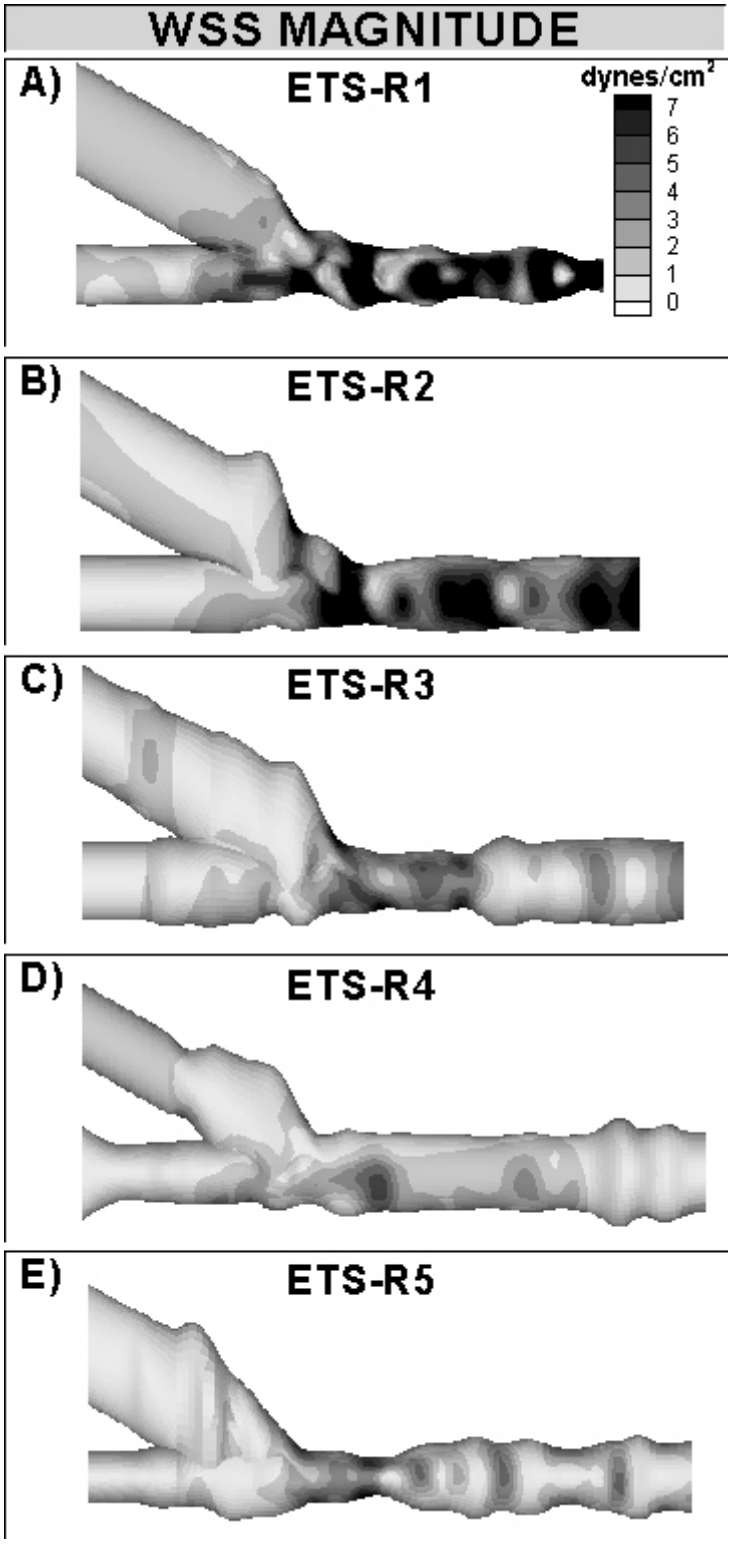

Figure 3.42 Contour plot of WSS magnitude for each of the ETS retrograde flow models.

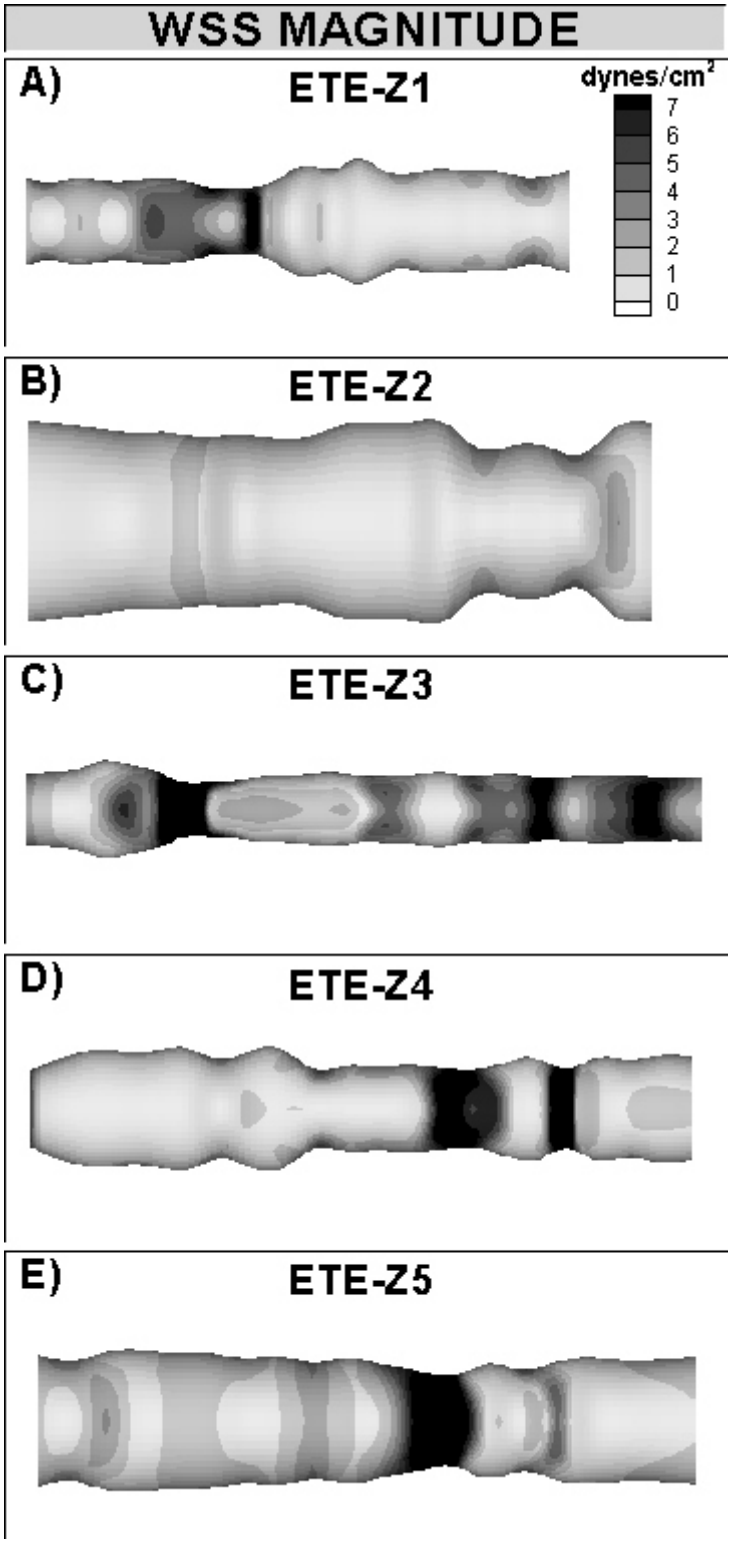

Figure 3.43 Contour plot of WSS magnitude for each of the ETE models corresponding to the ETS zero flow experiments.

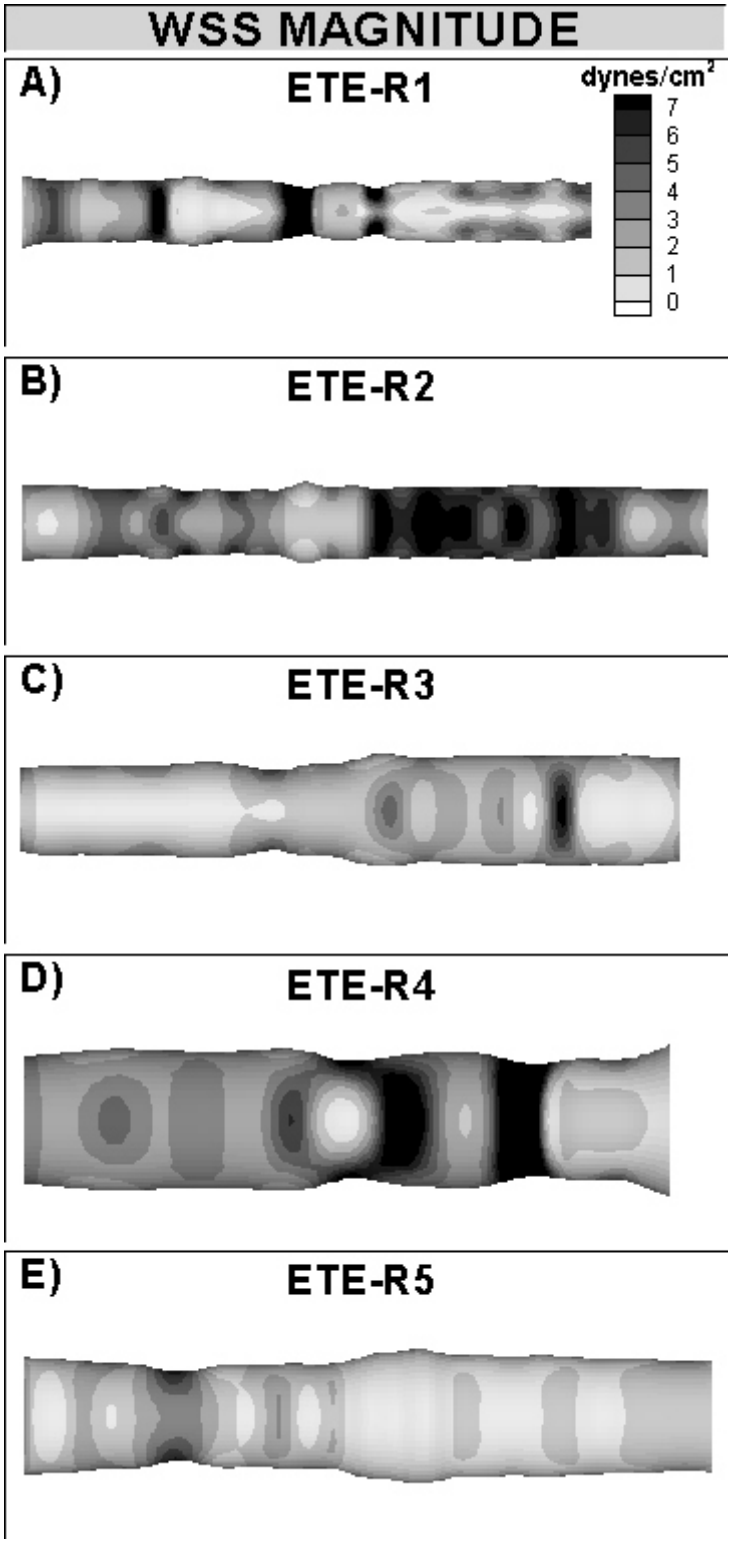

Figure 3.44 Contour plot of WSS magnitude for each of the ETE models corresponding to the ETS retrograde flow experiments.

axial (Figures 3.33 and 3.34) and circumferential (Figures 3.37 and 3.38) components and magnitude of WSS (Figures 3.41 and 3.42) were small in the graft and proximal artery segments. Also, the circumferential WSS in the distal artery of all models was predominantly negative, due to the secondary flow in the counter-clockwise direction discussed in the previous section (see Figures 3.37 and 3.38).

There are also differences in the components and magnitude of WSS between the ETS zero flow, ETS retrograde flow and ETE models. In the ETS zero flow models, the axial component of WSS (Figure 3.33) as well as the magnitude of WSS (Figure 3.41) appears to be increased in the distal artery segment compared to the ETS retrograde flow models, most likely because all of the fluid is exiting through the distal artery in the zero flow models. In the ETS retrograde models, there is a region of negative axial WSS along the floor near the heel of the anastomosis due to the increased recirculation region caused by the exit of flow from the proximal artery (see Figure 3.34). This also leads to an increased WSS magnitude in the same region for the ETS retrograde flow models (see Figure 3.42). All ETS retrograde flow models (Figure 3.38), except ETS-R1, appear to have lower circumferential WSS than the ETS zero flow models (Figure 3.37). Similarly, ETS-R3, ETS-R4 and ETS-R5 appear to have lower magnitudes of WSS (Figure 3.42) throughout the models compared to the ETS zero flow models (Figure 3.41), although the region on the floor across from the heel appears to be relatively increased. The ETE models have very little circumferential WSS since there is little secondary flow in these straight-tube models (see Figures 3.39 and 3.40). The WSS values vary spatially due to the expansion and constriction of the artery along its length.

In addition to the noted differences between the ETS zero flow, ETS retrograde flow and ETE models, there are marked differences within the groups. For the ETS zero flow models, ETS-Z3 and ETS-Z4 appear to have increased values of axial (Figure 3.33) and circumferential components (Figure 3.37), and magnitude of WSS (Figure 3.41) in the graft and distal artery regions. This is likely due to the relatively small vessel diameters and resulting increased velocity magnitude. ETS-Z3 also has a more extensive region of negative circumferential WSS in the distal artery due to the stronger secondary flow caused by the increased graft flow impinging on the flow of the artery (see Figure 3.37). ETS-Z4 has a larger region of increase

circumferential WSS along the anastomosis due to the secondary flow caused by the expansion of the hood. For the ETS retrograde flow cases, ETS-R1 and ETS-R2 appear to have increased axial WSS (Figure 3.34) as well as WSS magnitude (Figure 3.42), likely due to their decreased vessel diameters. The increased secondary flow in these models appears to also cause more extensive regions of circumferential WSS. For the ETE models, ETE-Z2 appears to have decreased axial component (Figure 3.35) and therefore WSS magnitude (Figure 3.43), most likely due to its increased vessel diameter. Analogous to this, ETE-Z3 and the ETE-R2 appear to have increased axial component (Figures 3.35 and 3.36, respectively) and WSS magnitude (Figures 3.43 and 3.44, respectively), likely due to their decreased vessel diameters. Therefore, differences in axial, circumferential WSS as well as WSS magnitude appear to exist for all models due to the imposed flow conditions and the global and local variations in geometry.

3.3.6 Wall Shear Stress Gradient

The axial component of WSSG for all models are shown in Figures 3.45 - 3.48, the circumferential component of WSSG for all models are shown in Figures 3.49 - 3.52 and the magnitude of WSSG for all models are shown in Figures 3.53 - 3.56. Note that the dimension scales are different for each anastomosis in order to optimize visualization. All models exhibit regional variation of WSSG due to the alteration in diameter along the length of the vessels. In addition, the ETS models have WSSG variations due to the disturbed flow caused by the angled insertion of the graft. Note that in a purely uniform flow region, the magnitude of WSSG would be zero so any non-zero value of WSSG denotes a nonuniform hemodynamic environment.

Similarities exist in the values of axial and circumferential WSSG as well as the magnitude of WSSG present in the ETS zero and retrograde flow models. In all ETS models, there appears to be an increased level of axial (see Figures 3.45 and 3.46) and circumferential (see Figures 3.49 and 3.50) components, and magnitude of WSSG (see Figures 3.53 and 3.54) at the toe of the anastomosis. Additionally, there are alternating regions of positive and negative axial components of WSS along the distal artery segment (see Figures 3.33 and 3.34). This causes large regions of increased WSSG magnitude in the distal artery for all

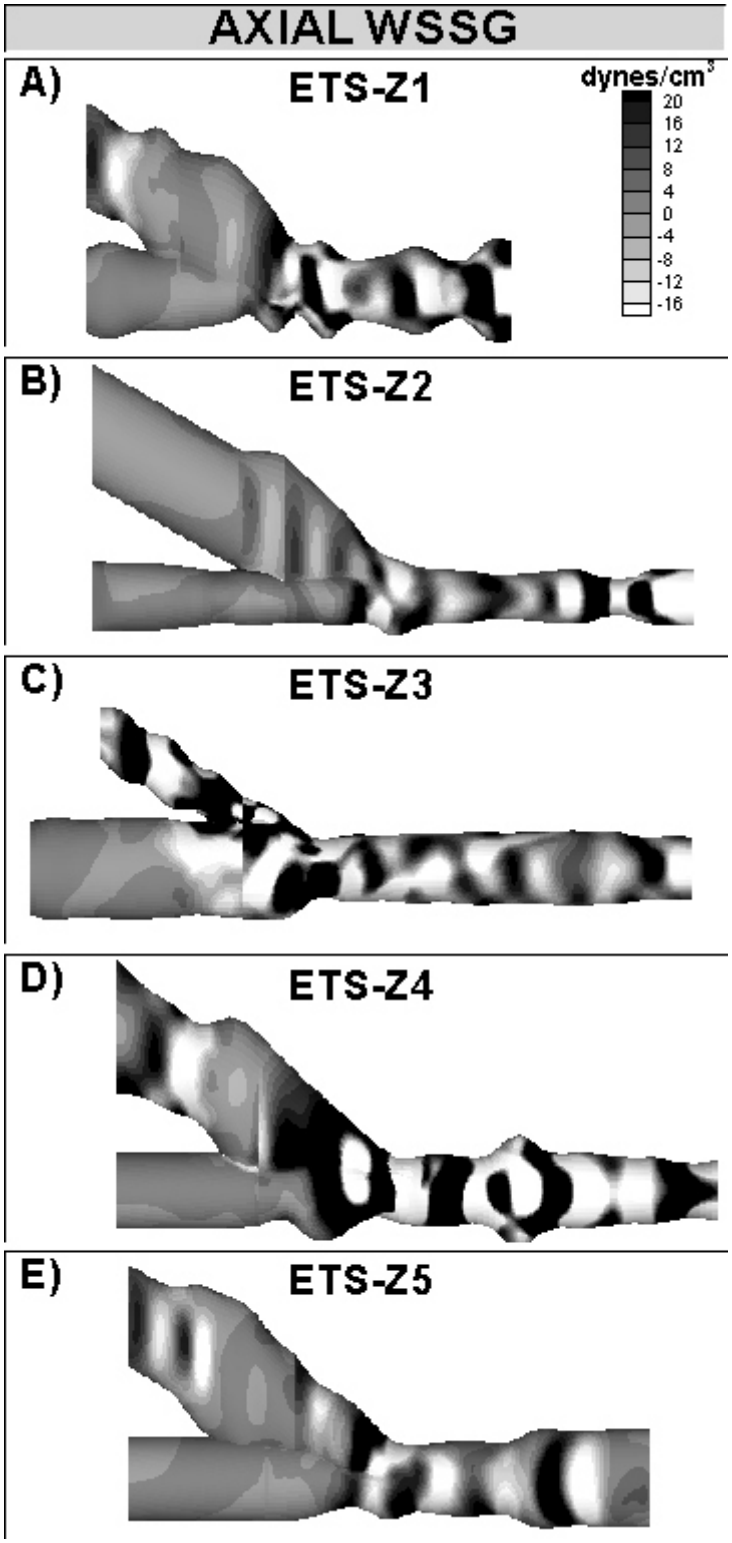

Figure 3.45 Contour plot of the axial component of WSSG for each of the ETS zero flow models.

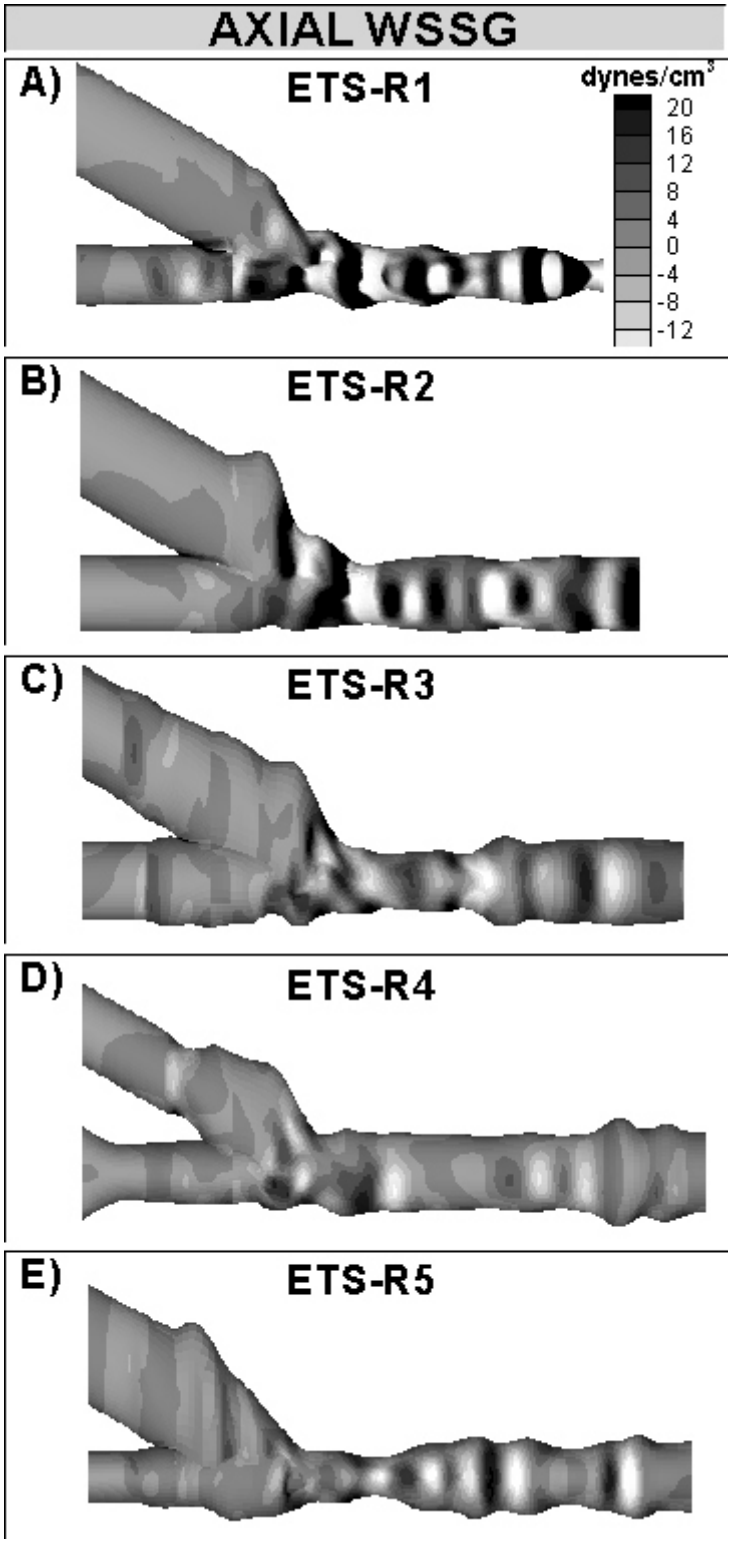

Figure 3.46 Contour plot of the axial component of WSSG for each of the ETS retrograde flow models.

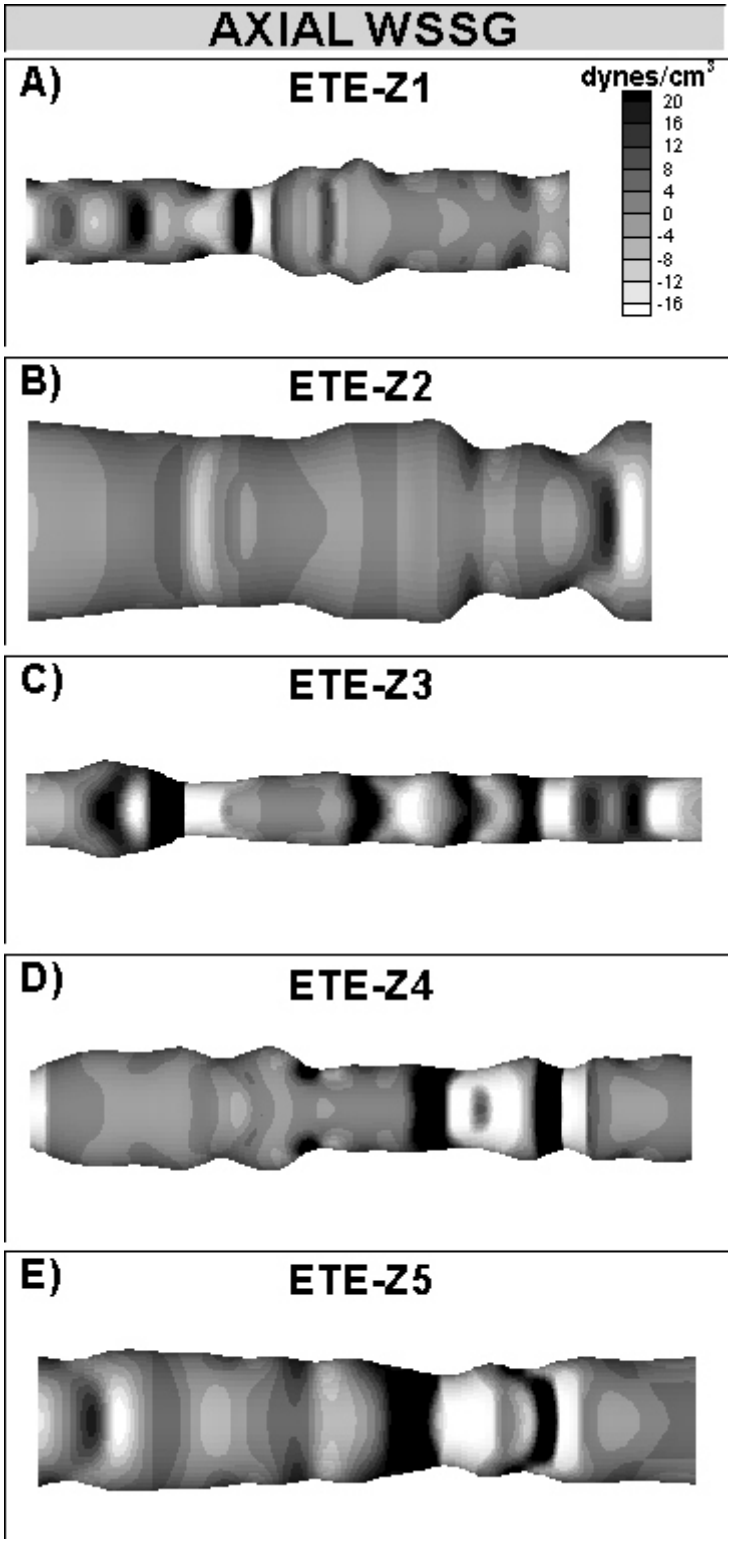

Figure 3.47 Contour plot of the axial component of WSSG for each of the ETE models corresponding to the ETS zero flow experiments.

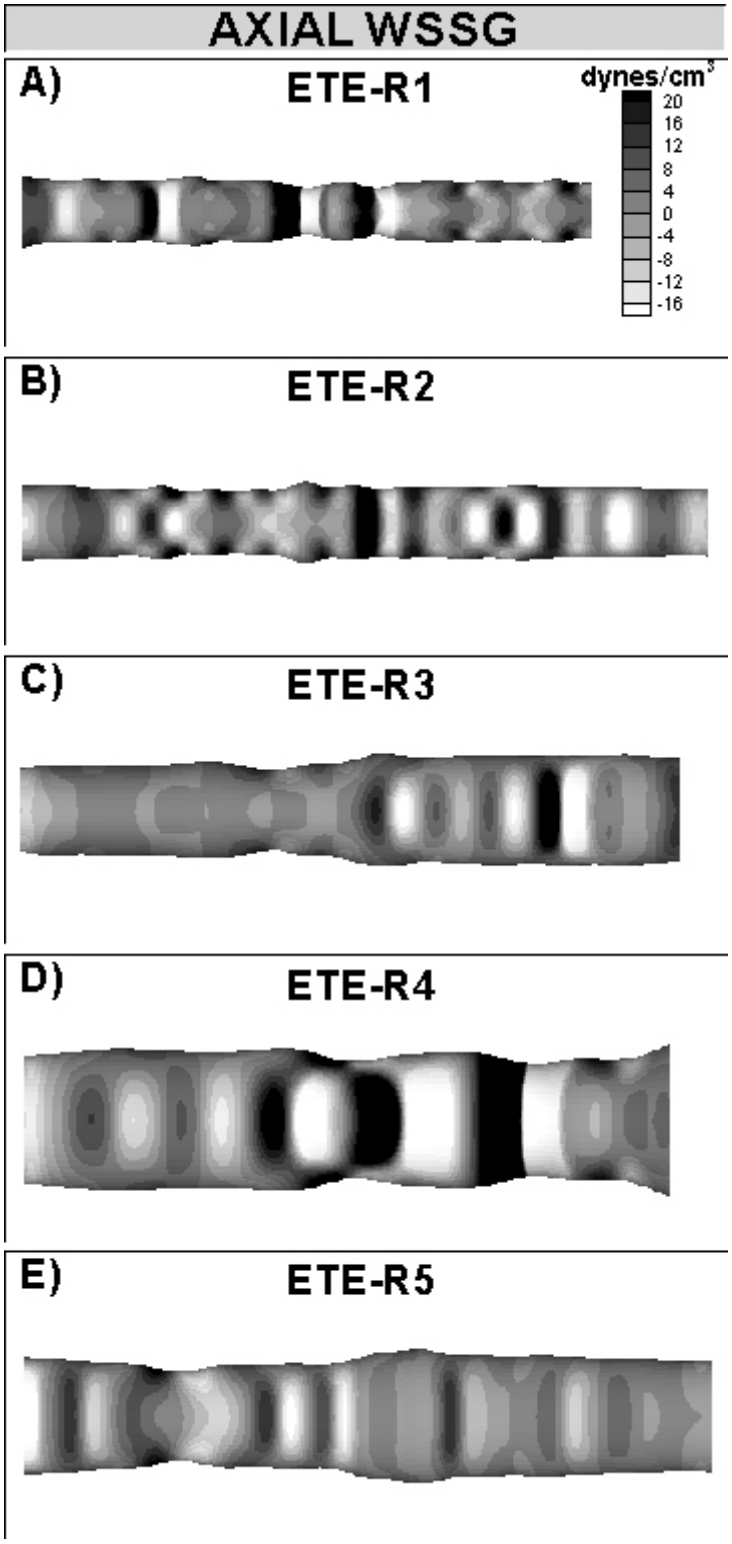

Figure 3.48 Contour plot of the axial component of WSSG for each of the ETE models corresponding to the ETS retrograde flow experiments.

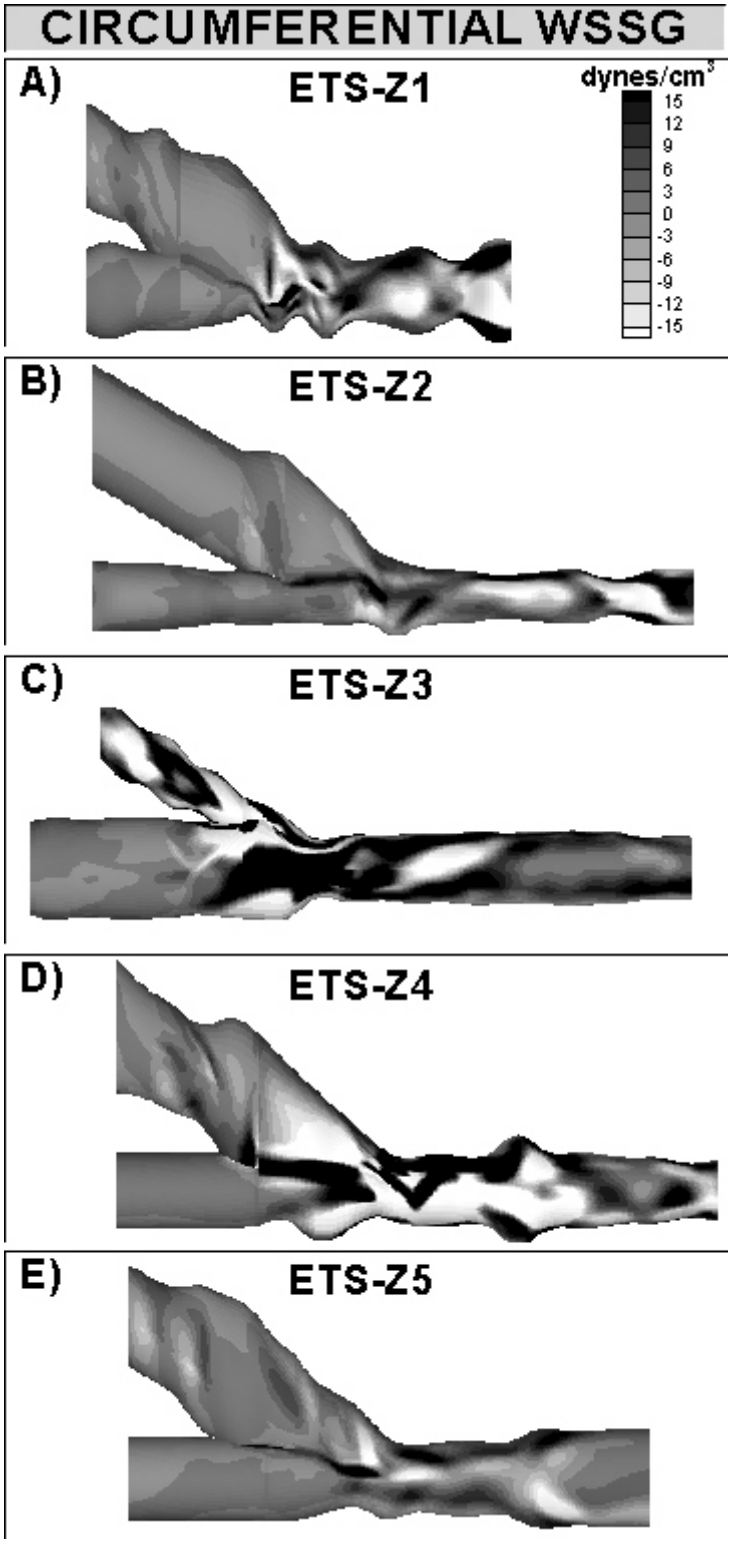

Figure 3.49 Contour plot of the circumferential component of WSSG for each of the ETS zero flow models.

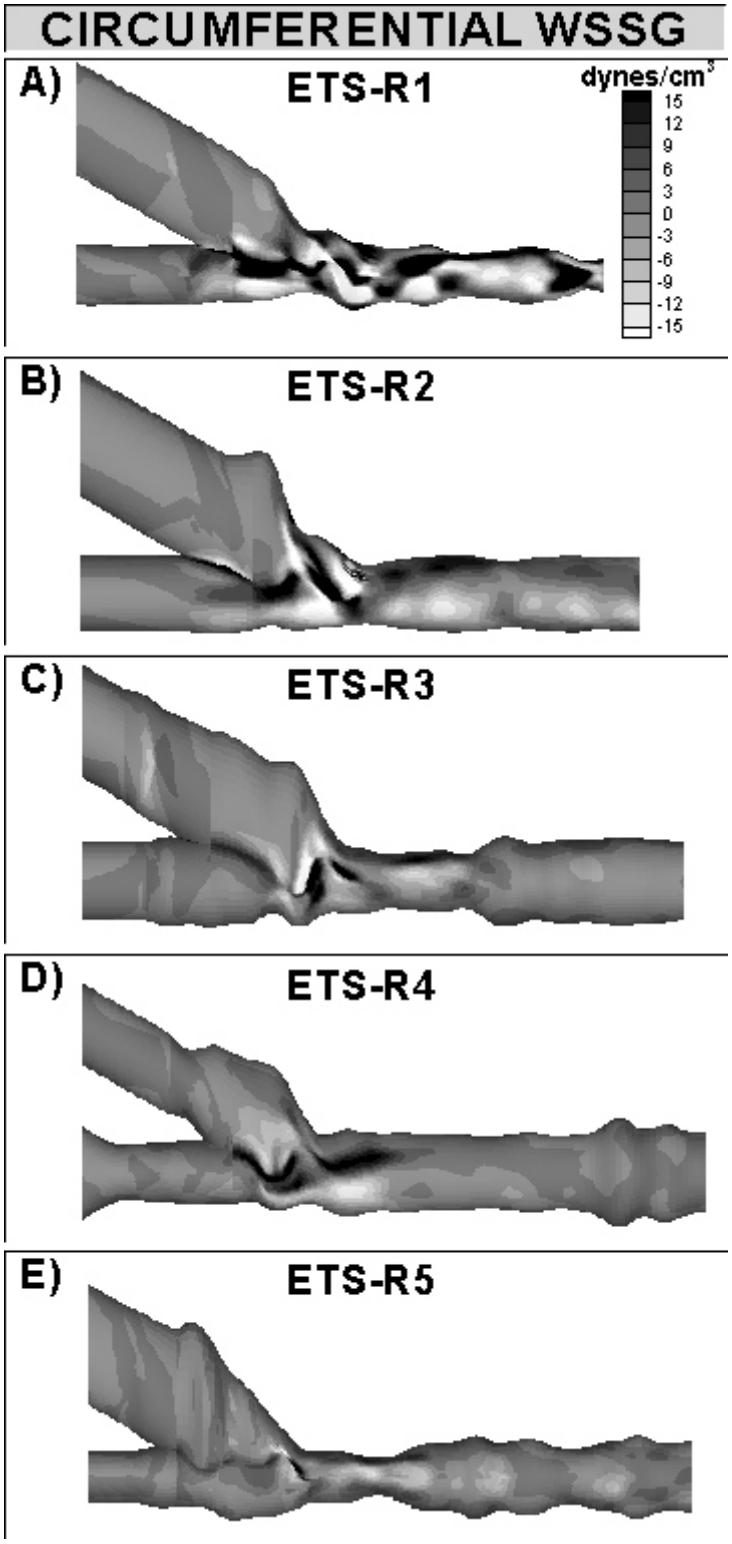

Figure 3.50 Contour plot of the circumferential component of WSSG for each of the ETS retrograde flow models.

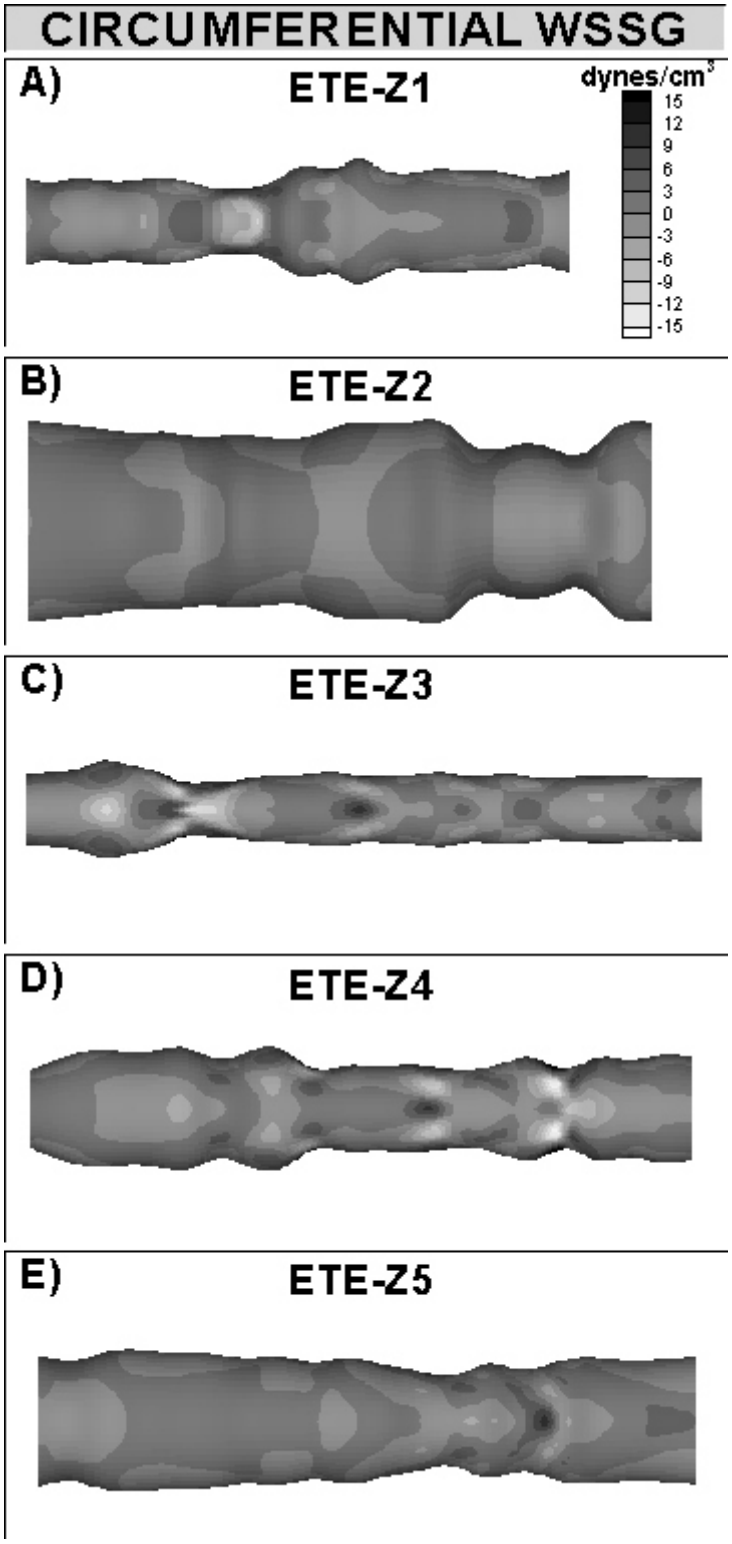

Figure 3.51 Contour plot of the circumferential component of WSSG for each of the ETE models corresponding to the ETS zero flow experiments.

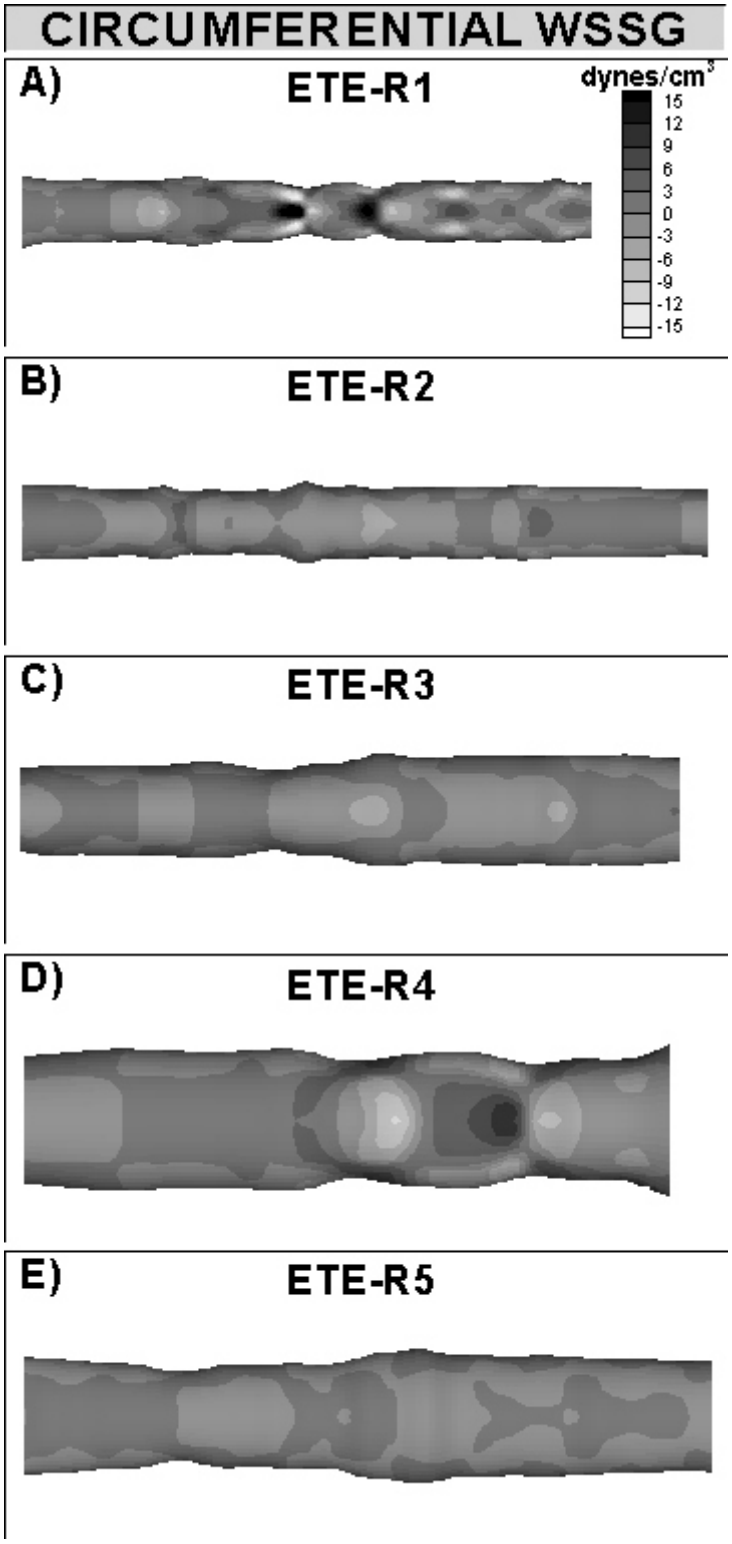

Figure 3.52 Contour plot of the circumferential component of WSSG for each of the ETE models corresponding to the ETS retrograde flow experiments.

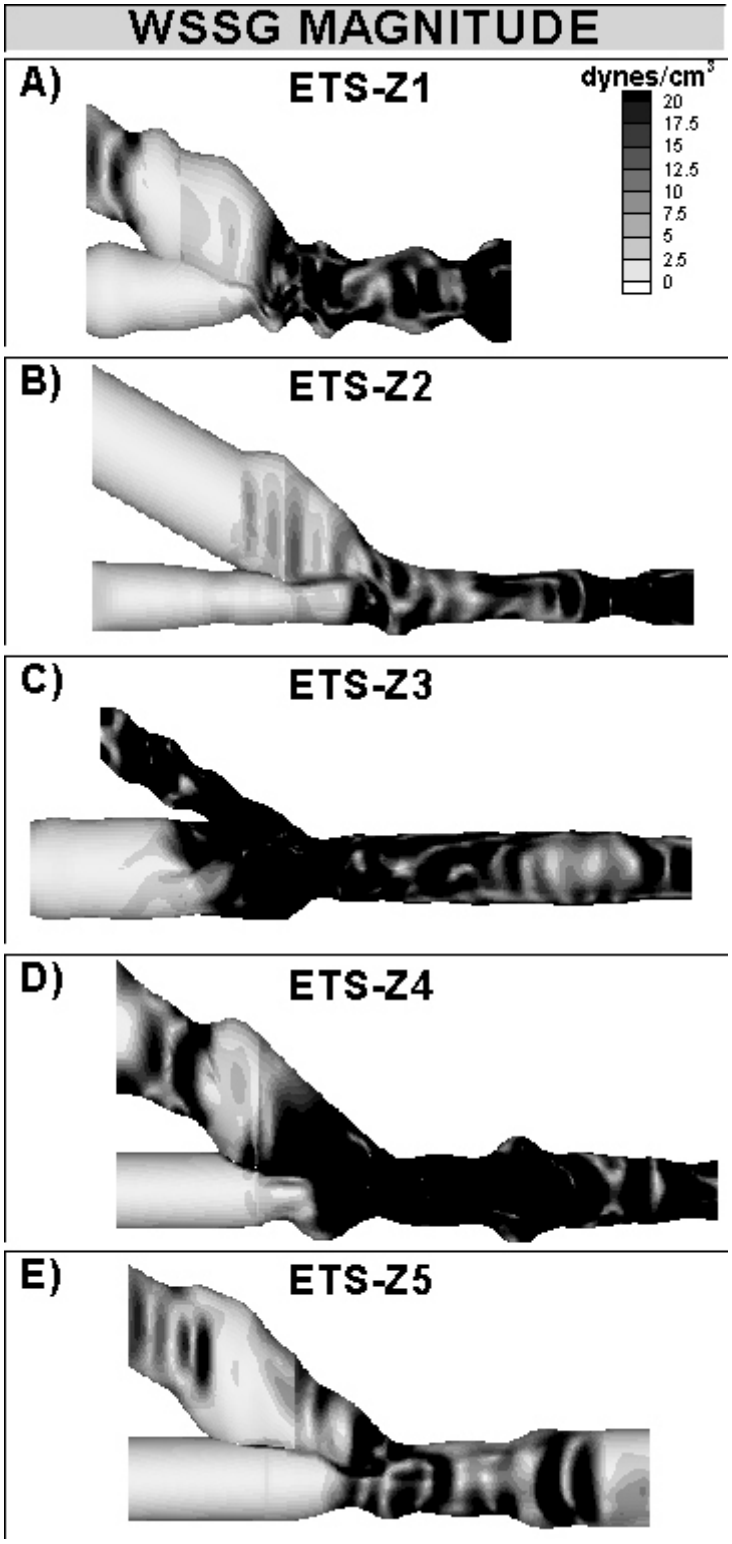

Figure 3.53 Contour plot of WSSG magnitude for each of the ETS zero flow models.

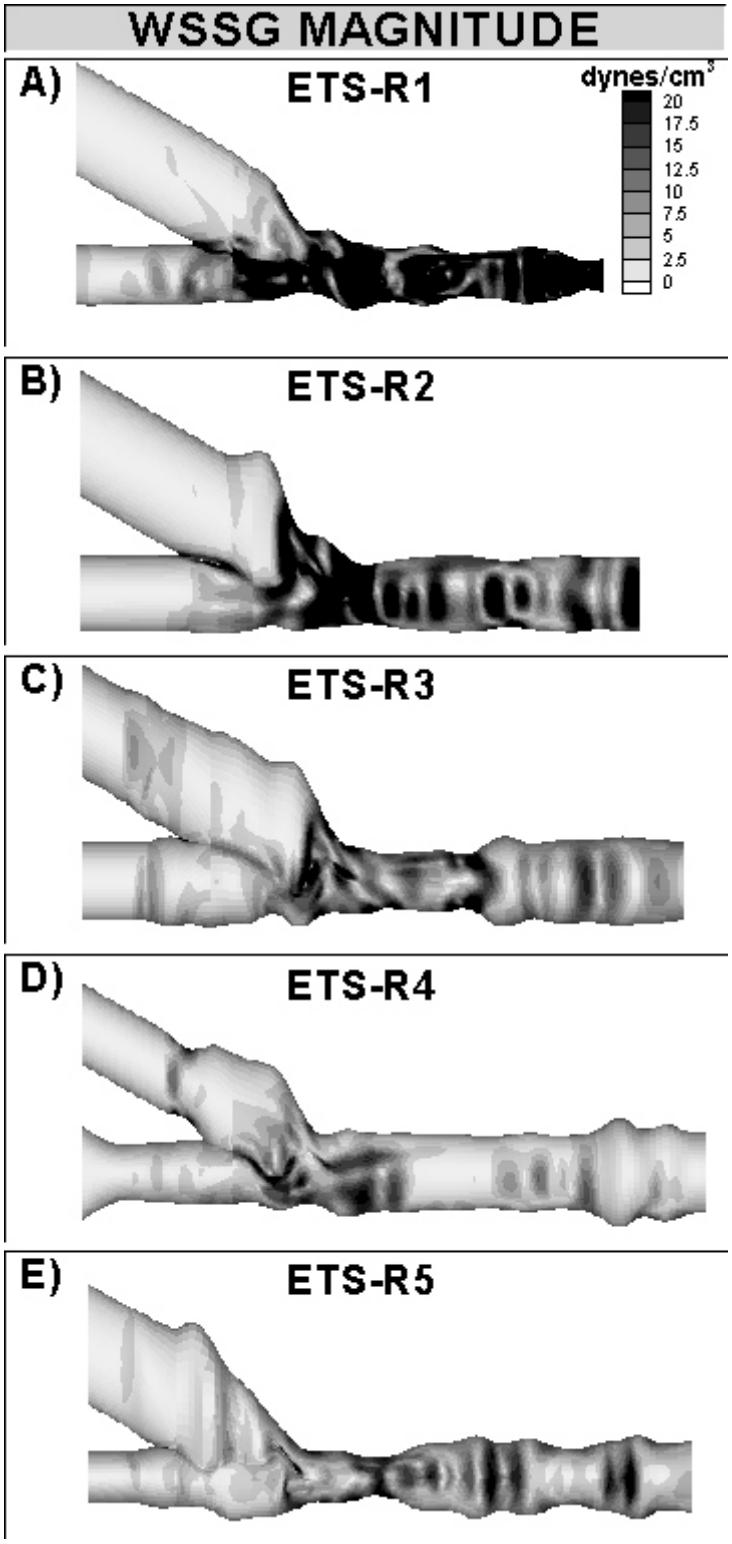

Figure 3.54 Contour plot of WSSG magnitude for each of the ETS retrograde flow models.

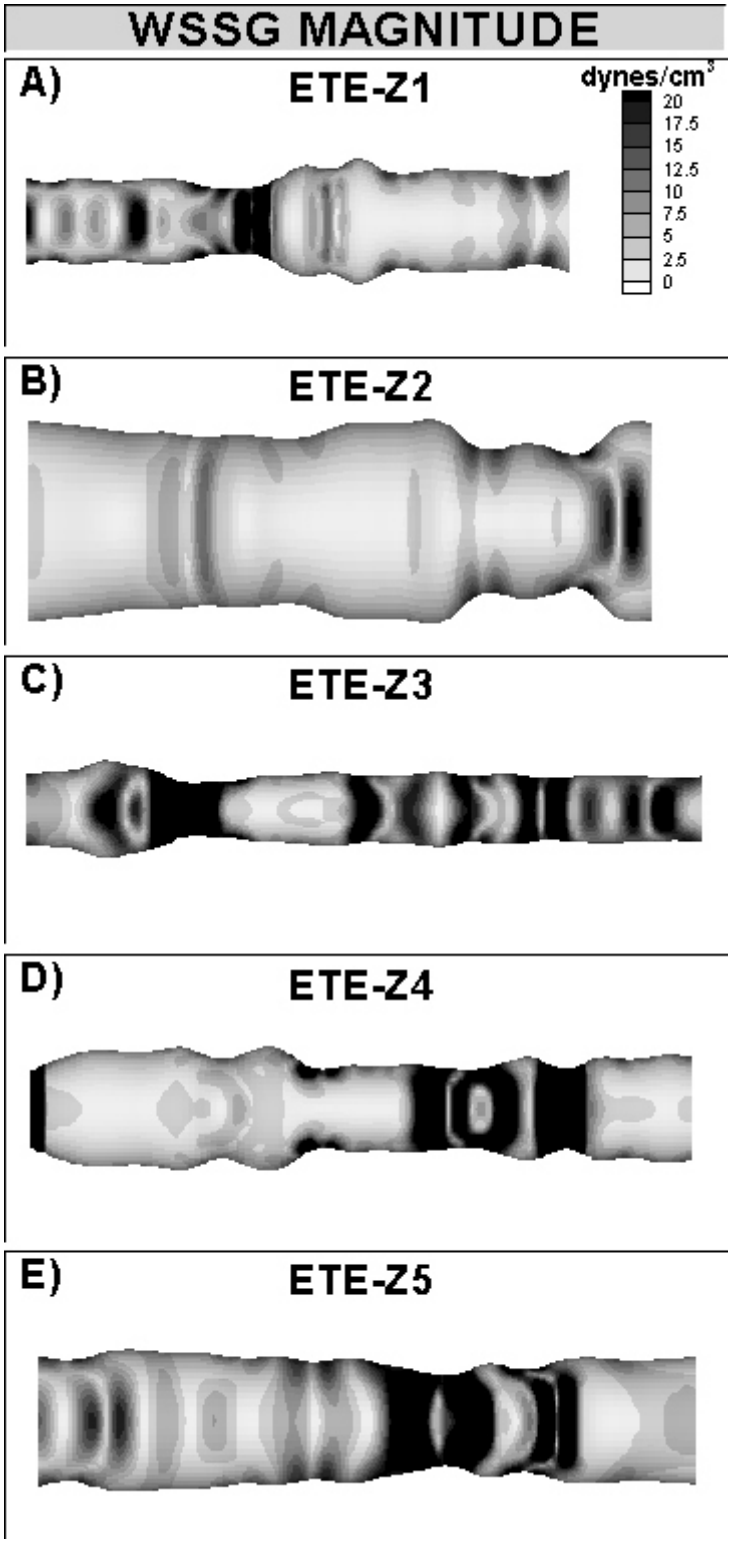

Figure 3.55 Contour plot of WSSG magnitude for each of the ETE models corresponding to the ETS zero flow experiments.

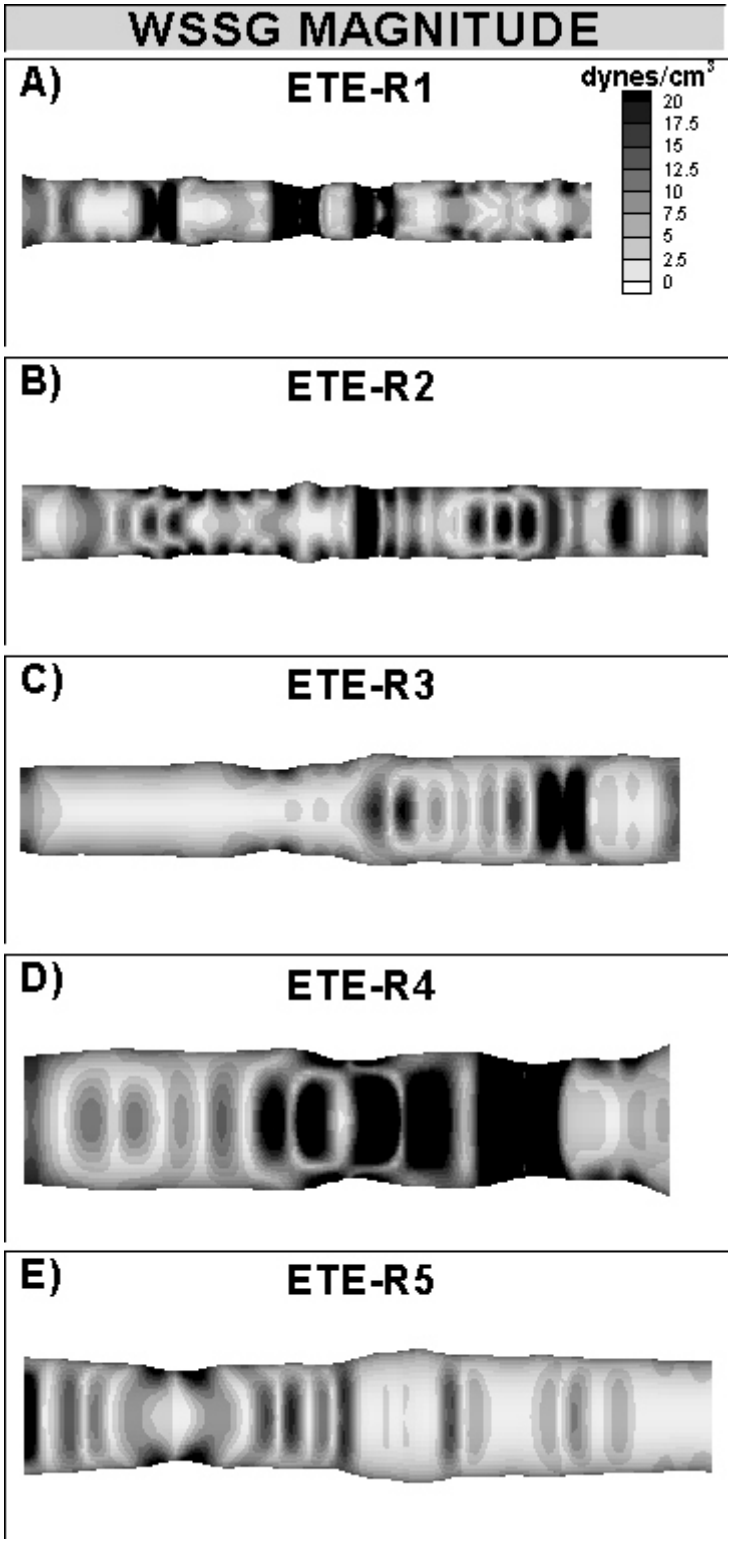

Figure 3.56 Contour plot of WSSG magnitude for each of the ETE models corresponding to the ETS retrograde flow experiments.

models (see Figures 3.53 and 3.54). The ETE models have alternating regions of high and low axial WSSG (see Figures 3.47 and 3.48) and high WSSG (see Figures 3.55 and 3.56) magnitude that appears to be comparable to those present in the ETS models.

There are also differences in the components and magnitude of WSSG between the ETS zero flow, ETS retrograde flow and ETE models. In the ETS zero flow models, there are more regions of positive and negative axial WSSG in the distal artery (see Figure 3.45) compared to last three ETS retrograde flow models, ETS-R3, ETS-R4 and ETS-R5 (see Figure 3.46). This appears to be due to the increased range of axial WSS present in the ETS zero flow models (see Figure 3.33) allowing for the possibility of increased axial WSSG. All of the ETS zero flow models, except ETS-Z5, also appear to have more regions of circumferential WSSG (Figure 3.49) than the last three ETS retrograde flow models, ETS-R3, ETS-R4 and ETS-R5 (see Figure 3.50) and this again appears to be due to the increased range of circumferential WSS present in the ETS zero flow models (see Figure 3.37). The increase in axial and circumferential WSSG in the ETS zero flow models appears to lead to an increase in the magnitude of WSSG in these models (see Figure 3.53) compared to the last three ETS retrograde flow models, ETS-R3, ETS-R4 and ETS-R5 (see Figure 3.54). In contrast to the ETS models, the ETE models did not have regions of high or low circumferential WSSG (see Figure 3.51 and 3.52), most likely because the value of the circumferential component of WSS (see Figures 3.39 and 3.40) appeared to be very low in these models.

In addition to the differences between the ETS zero flow, ETS retrograde flow and ETE models, there are differences within the groups. For the ETS zero flow models, ETS-Z3 appears to have more extensive regions of positive and negative circumferential WSSG (see Figure 3.49), which appear to lead to increased WSSG magnitude that extends across the entire model except for the proximal artery segment (see Figure 3.53). ETS-Z4 also appears to have more extensive increased circumferential WSSG (see Figure 3.49) that appears to lead to increased WSSG magnitude (see Figure 3.53) that covers most of the anastomosis but does not extend up into the graft. For the ETS retrograde flow models, ETS-R1 and ETS-R2 appear to have more extensive regions of alternating positive and negative axial (see Figure 3.46) and circumferential components

of WSSG (see Figure 3.50) that appear to lead to higher levels of WSSG magnitude along the floor of the anastomosis and the distal artery (see Figure 3.54). For the ETE models, ETE-Z2 appears to have very small regions of positive or negative axial WSSG (see Figure 3.47), likely due to the smaller values of axial WSS in this model (see Figure 3.35) and therefore appears to lead to low WSSG magnitude along the entire model (see Figure 3.55). ETE-Z3 and ETE-R2 appear to have the most number of regions of high WSSG magnitude (see Figures 3.55 and 3.56), likely due to the increased levels of WSS along the models (see Figures 3.43 and 3.44). Therefore, differences in axial, circumferential WSSG as well as WSSG magnitude appear to exist for all models due to the imposed flow conditions and the global and local variations in geometry.

3.3.7 Regional Variation of Hemodynamic Parameters

The Mean Hemodynamic Indices (mean ± SEM), calculated as per Equation 3.28, including the axial and circumferential components and magnitude of WSS and WSSG for both flow conditions are presented in Figure 3.57. The Mean Axial WSS Index for the zero flow experiments (3.11 ± 2.27) was significantly higher ($p < 0.05$) than the same index for the retrograde flow experiments (0.87 ± 0.91). The Mean WSS Magnitude Index was also significantly higher ($p < 0.05$) for the zero flow experiments (4.31 ± 2.77) as

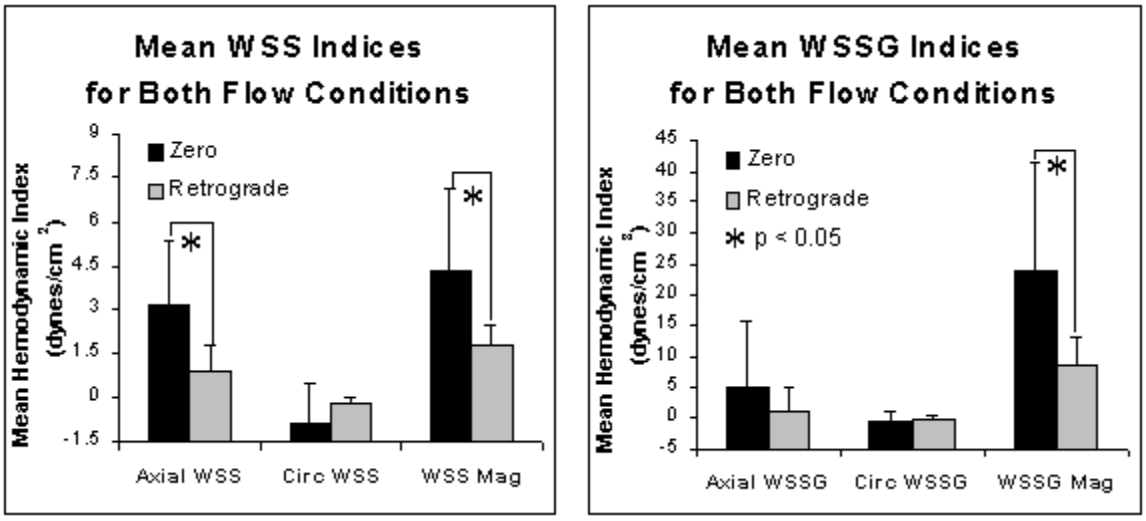

Figure 3.57 Mean Hemodynamic Indices (see Equation 3.28) for axial and circumferential components and magnitude of WSS (left) and WSSG (right) for the zero and retrograde flow experiments. An asterisk (*) indicates a significant difference between flow conditions for that index.

compared to the retrograde flow experiments (1.75 ± 0.75). Similarly, the Mean WSSG Magnitude Index was significantly higher ($p < 0.05$) for the zero flow experiments (23.88 ± 17.36) than for the retrograde flow experiments (8.45 ± 4.51).

The Mean Normalized Hemodynamic Indices $_{ROI}$ (mean ± SEM), calculated as per Equation 3.30, for both flow conditions are presented in Figures 3.58 (axial WSS), 3.59 (circumferential WSS), 3.60 (WSS magnitude), 3.61 (axial WSSG), 3.62 (circumferential WSSG) and 3.63 (WSSG magnitude). Additionally, similar graphs incorporating all the data (zero and retrograde flow experiments) are shown in Figures 3.64 (axial WSS and WSSG), 3.65 (circumferential WSS and WSSG) and 3.66 (WSS and WSSG magnitude).

3.3.7.1 Regional Variation of Mean Normalized Axial WSS $_{ROI}$

The regional variation of Mean Normalized Axial WSS Index $_{ROI}$ followed the same trend for both flow conditions although it was more pronounced in the retrograde flow experiments (see Figure 3.58). In the zero flow experiments, the ETS toe, distal artery, graft and ETE proximal artery regions had the highest values of Mean Normalized Axial WSS Index $_{ROI}$. These regions had significantly higher Mean Normalized Axial WSS Index $_{ROI}$ than the regions with the lowest values of Mean Normalized Axial WSS Index $_{ROI}$, which included the ETS proximal artery, heel and floor regions. Specifically, the ETS toe region (2.6 ± 0.4) was significantly higher than the ETS proximal artery (0.0 ± 0.01, $p = 0.0001$), heel (0.0 ± 0.05, $p = 0.0001$) and floor (-0.1 ± 0.2, $p = 0.0001$) regions. The ETS distal artery region (2.0 ± 0.8) was also significantly higher than the ETS proximal artery (0.0 ± 0.01, $p = 0.002$), heel (0.0 ± 0.05, $p = 0.002$) and floor (-0.1 ± 0.2, $p = 0.002$) regions. The ETS graft region (1.3 ± 0.2) was significantly higher than the ETS proximal artery (0.0 ± 0.01, $p = 0.032$), heel (0.0 ± 0.05, $p = 0.026$) and floor (-0.1 ± 0.2, $p = 0.025$) regions. The ETE proximal artery region (1.5 ± 0.7) was also significantly higher than the ETS proximal artery (0.0 ± 0.01, $p = 0.021$), heel (0.0 ± 0.05, $p = 0.017$) and floor (-0.1 ± 0.2, $p = 0.016$) regions. In addition, the ETS toe (2.6 ± 0.4) region was significantly higher than the ETS graft (1.3 ± 0.2, $p = 0.049$) , hood (1.0 ± 0.2, $p = 0.012$) and ETE anastomosis (0.8 ± 0.4, $p = 0.005$) regions.

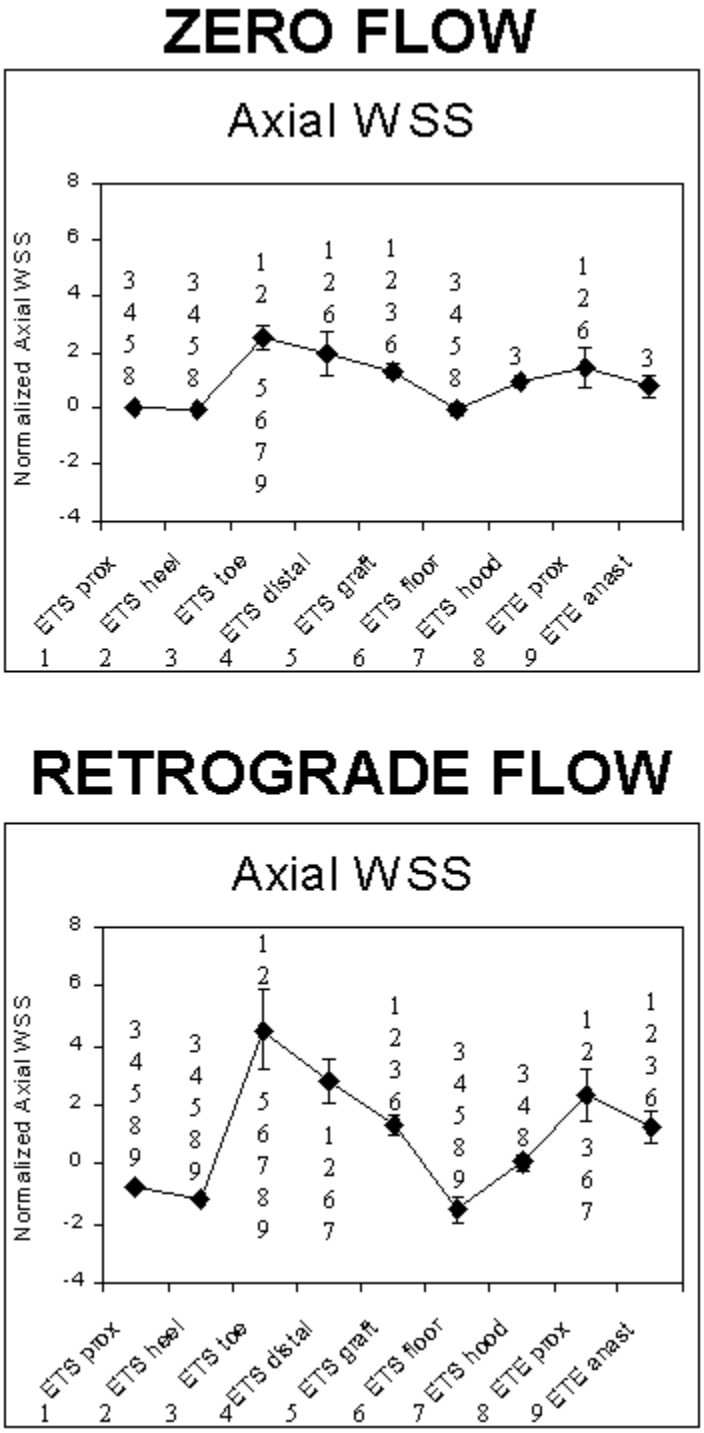

Figure 3.58 Mean Normalized Axial WSS Index $_{ROI}$ (see Equation 3.30) for the zero (top) and retrograde (bottom) flow experiments. The data for each region of interest of one experiment are normalized by the mean hemodynamic index for the same experiment. The numbers above and/or below each data point indicate which regions (1-ETS proximal artery, 2-ETS heel, 3-ETS toe, 4-ETS distal artery, 5-ETS graft, 6-ETS floor, 7-ETS hood, 8-ETE proximal, 9-ETE anastomosis) are significantly different from that region.

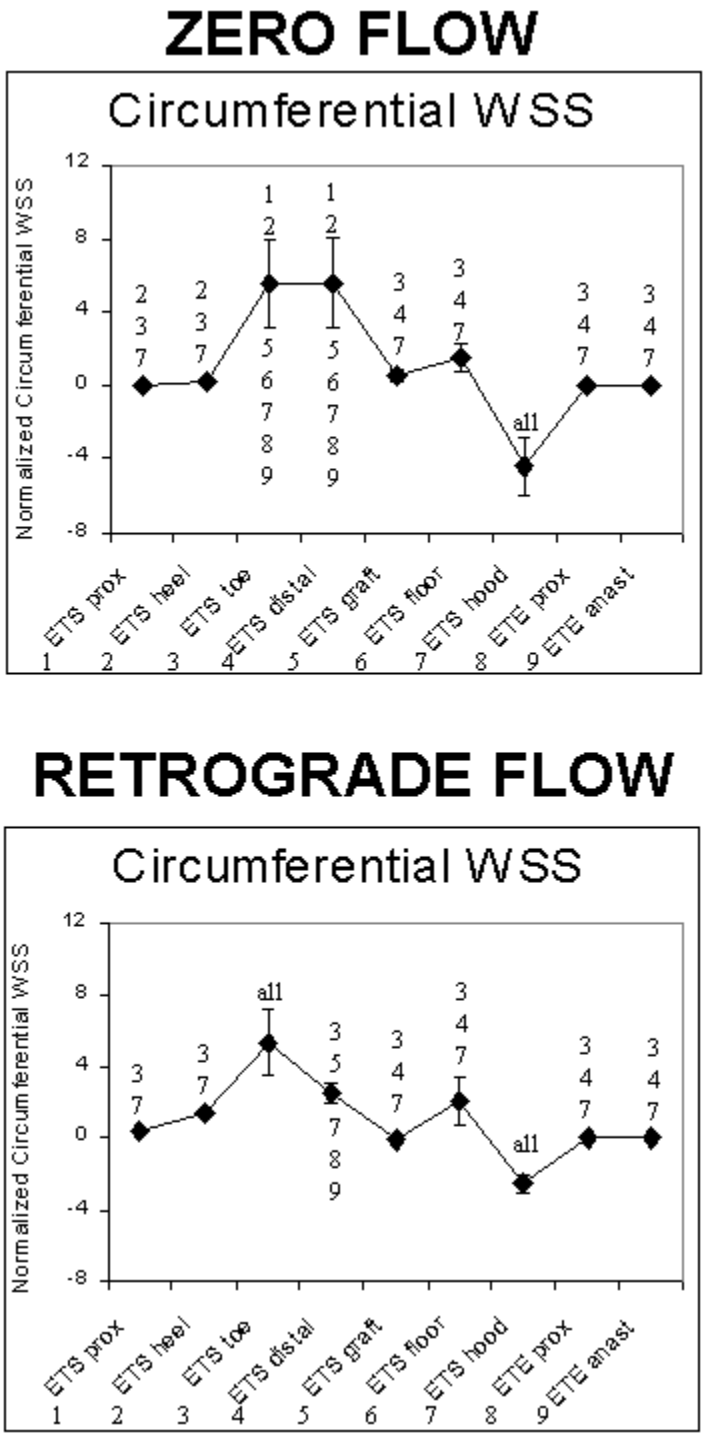

Figure 3.59 Mean Normalized Circumferential WSS Index $_{ROI}$ (see Equation 3.30) for the zero (top) and retrograde (bottom) flow experiments. The data for each region of interest of one experiment are normalized by the mean hemodynamic index for the same experiment. The numbers above and/or below each data point indicate which regions (1-ETS proximal artery, 2-ETS heel, 3-ETS toe, 4-ETS distal artery, 5-ETS graft, 6-ETS floor, 7-ETS hood, 8-ETE proximal, 9-ETE anastomosis) are significantly different from that region.

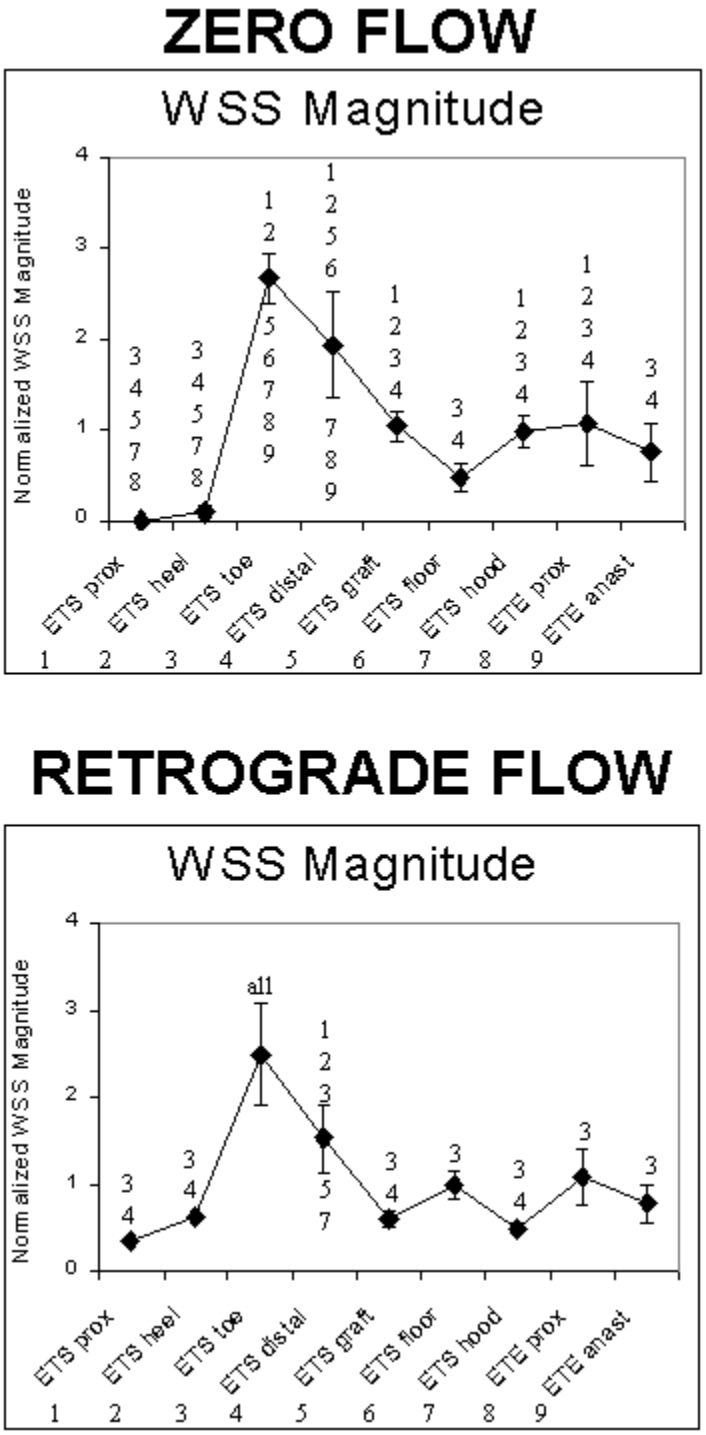

Figure 3.60 Mean Normalized WSS Magnitude Index $_{ROI}$ (see Equation 3.30) for the zero (top) and retrograde (bottom) flow experiments. The data for each region of interest of one experiment are normalized by the mean hemodynamic index for the same experiment. The numbers above and/or below each data point indicate which regions (1-ETS proximal artery, 2-ETS heel, 3-ETS toe, 4-ETS distal artery, 5-ETS graft, 6-ETS floor, 7-ETS hood, 8-ETE proximal, 9-ETE anastomosis) are significantly different from that region.

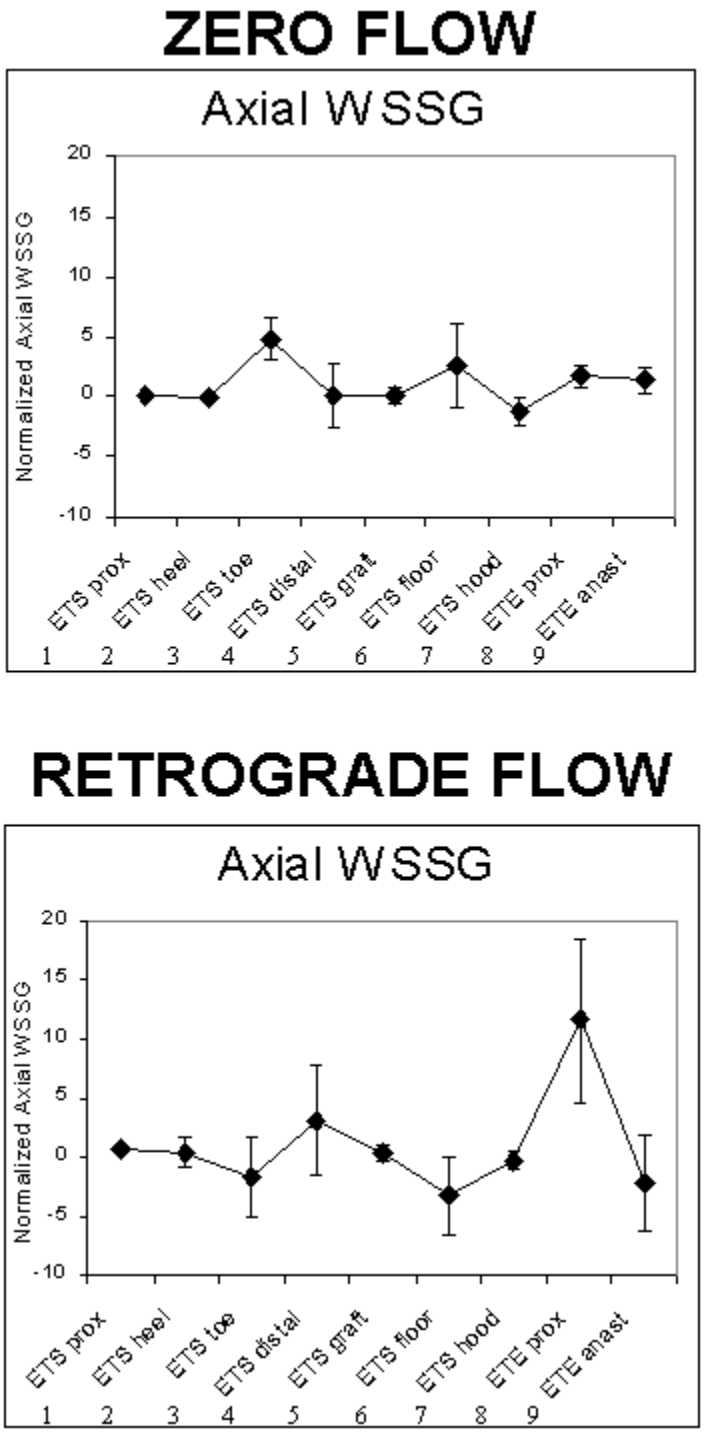

Figure 3.61 Mean Normalized Axial WSSG Index $_{ROI}$ (see Equation 3.30) for the zero (top) and retrograde (bottom) flow experiments. The data for each region of interest of one experiment are normalized by the mean hemodynamic index for the same experiment. The numbers above and/or below each data point indicate which regions (1-ETS proximal artery, 2-ETS heel, 3-ETS toe, 4-ETS distal artery, 5-ETS graft, 6-ETS floor, 7-ETS hood, 8-ETE proximal, 9-ETE anastomosis) are significantly different from that region.

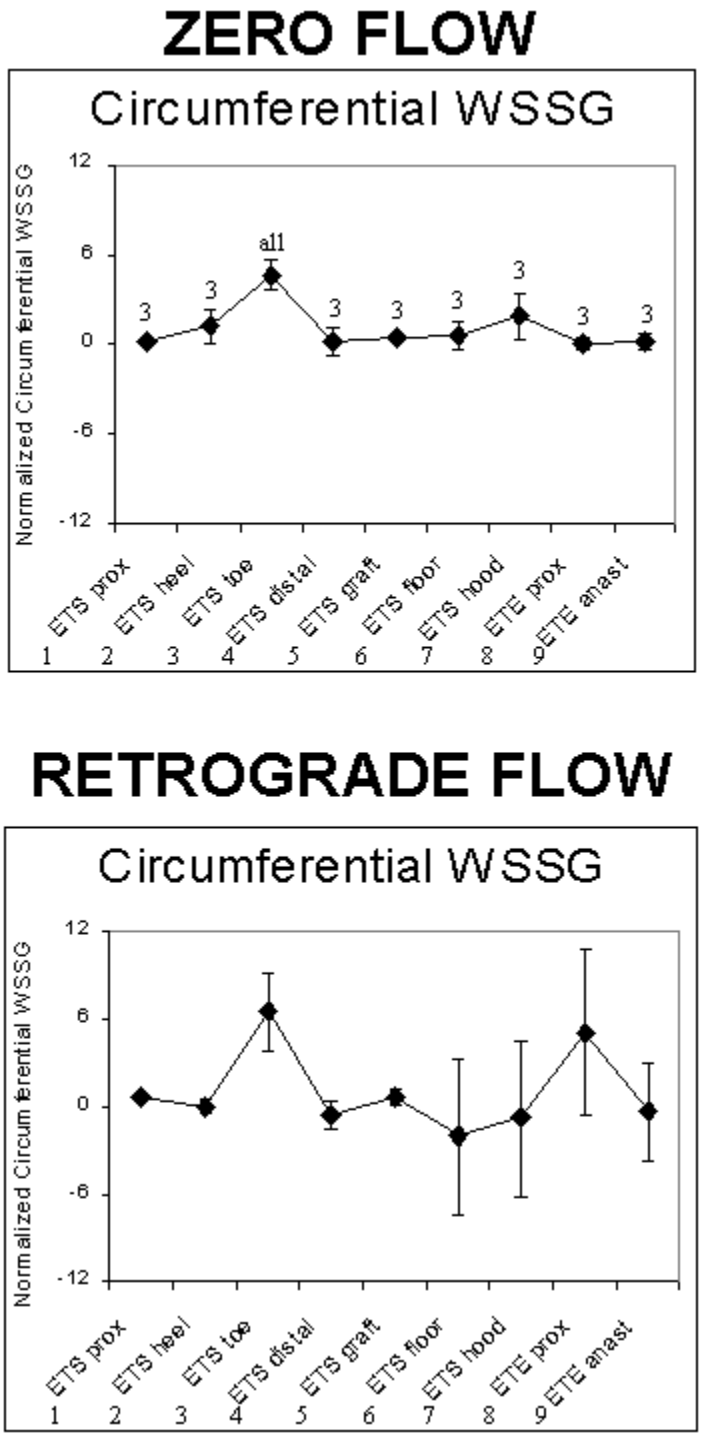

Figure 3.62 Mean Normalized Circumferential WSSG Index $_{ROI}$ (see Equation 3.30) for the zero (top) and retrograde (bottom) flow experiments. The data for each region of interest of one experiment are normalized by the mean hemodynamic index for the same experiment. The numbers above and/or below each data point indicate which regions (1-ETS proximal artery, 2-ETS heel, 3-ETS toe, 4-ETS distal artery, 5-ETS graft, 6-ETS floor, 7-ETS hood, 8-ETE proximal, 9-ETE anastomosis) are significantly different from that region.

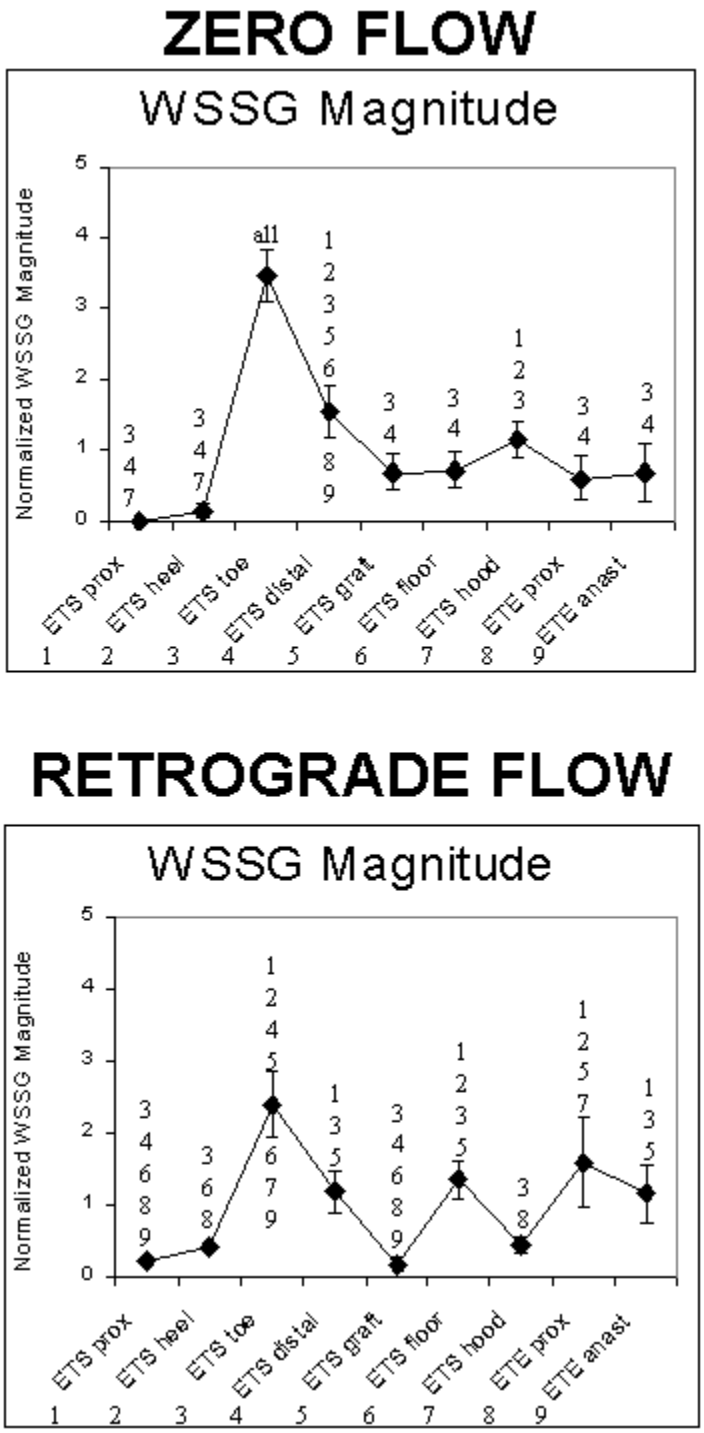

Figure 3.63 Mean Normalized WSSG Magnitude Index$_{ROI}$ (see Equation 3.30) for the zero (top) and retrograde (bottom) flow experiments. The data for each region of interest of one experiment are normalized by the mean hemodynamic index for the same experiment. The numbers above and/or below each data point indicate which regions (1-ETS proximal artery, 2-ETS heel, 3-ETS toe, 4-ETS distal artery, 5-ETS graft, 6-ETS floor, 7-ETS hood, 8-ETE proximal, 9-ETE anastomosis) are significantly different from that region.

ALL EXPERIMENTS

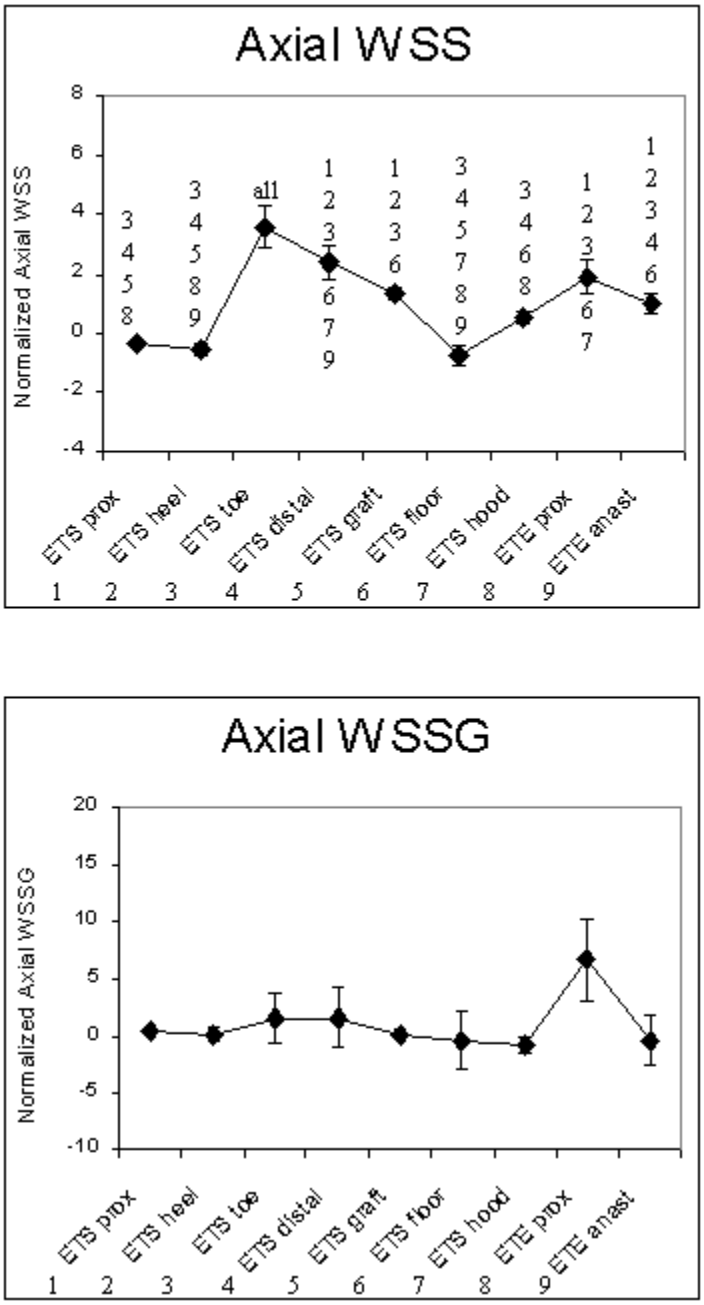

Figure 3.64 Mean Normalized Axial WSS and WSSG Index $_{ROI}$ (see Equation 3.30) for the pooled data from all experiments. The data for each region of interest of one experiment are normalized by the mean hemodynamic index for the same experiment. The numbers above and/or below each data point indicate which regions (1-ETS proximal artery, 2-ETS heel, 3-ETS toe, 4-ETS distal artery, 5-ETS graft, 6-ETS floor, 7-ETS hood, 8-ETE proximal, 9-ETE anastomosis) are significantly different from that region.

ALL EXPERIMENTS

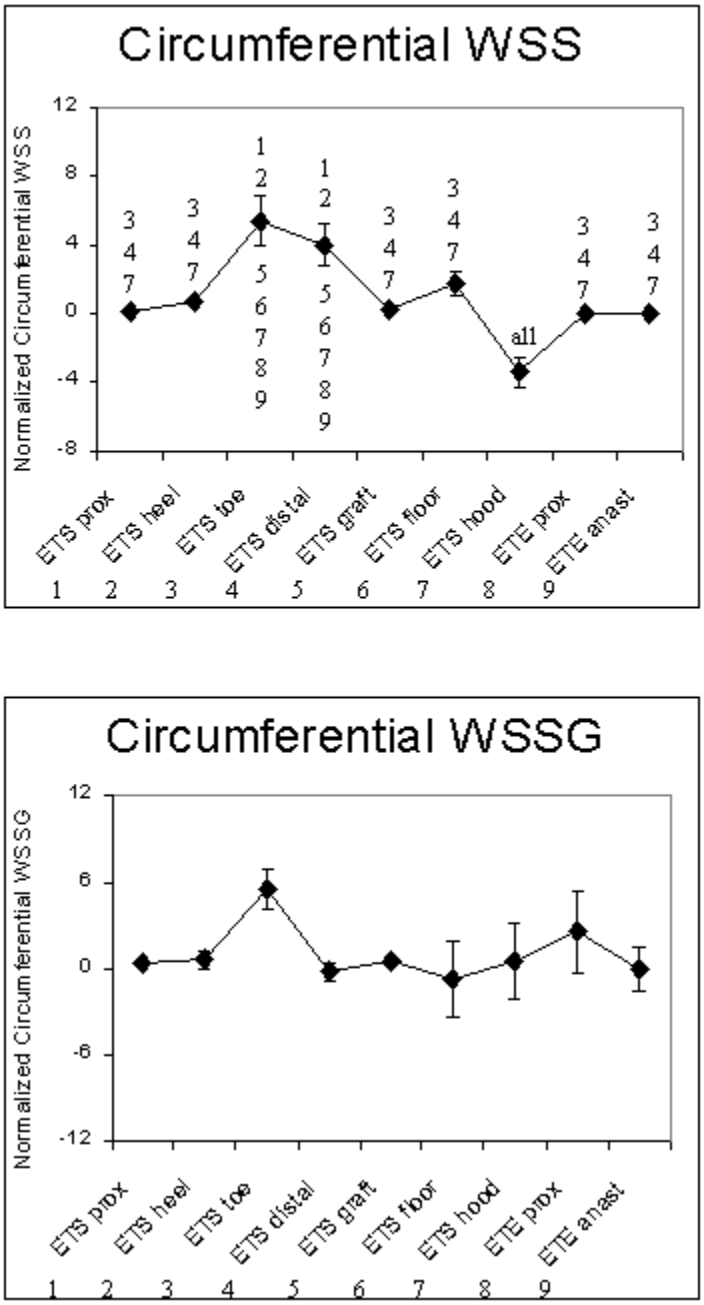

Figure 3.65 Mean Normalized Circumferential WSS and WSSG Index $_{ROI}$ (see Equation 3.30) for the pooled data from all experiments. The data for each region of interest of one experiment are normalized by the mean hemodynamic index for the same experiment. The numbers above and/or below each data point indicate which regions (1-ETS proximal artery, 2-ETS heel, 3-ETS toe, 4-ETS distal artery, 5-ETS graft, 6-ETS floor, 7-ETS hood, 8-ETE proximal, 9-ETE anastomosis) are significantly different from that region.

ALL EXPERIMENTS

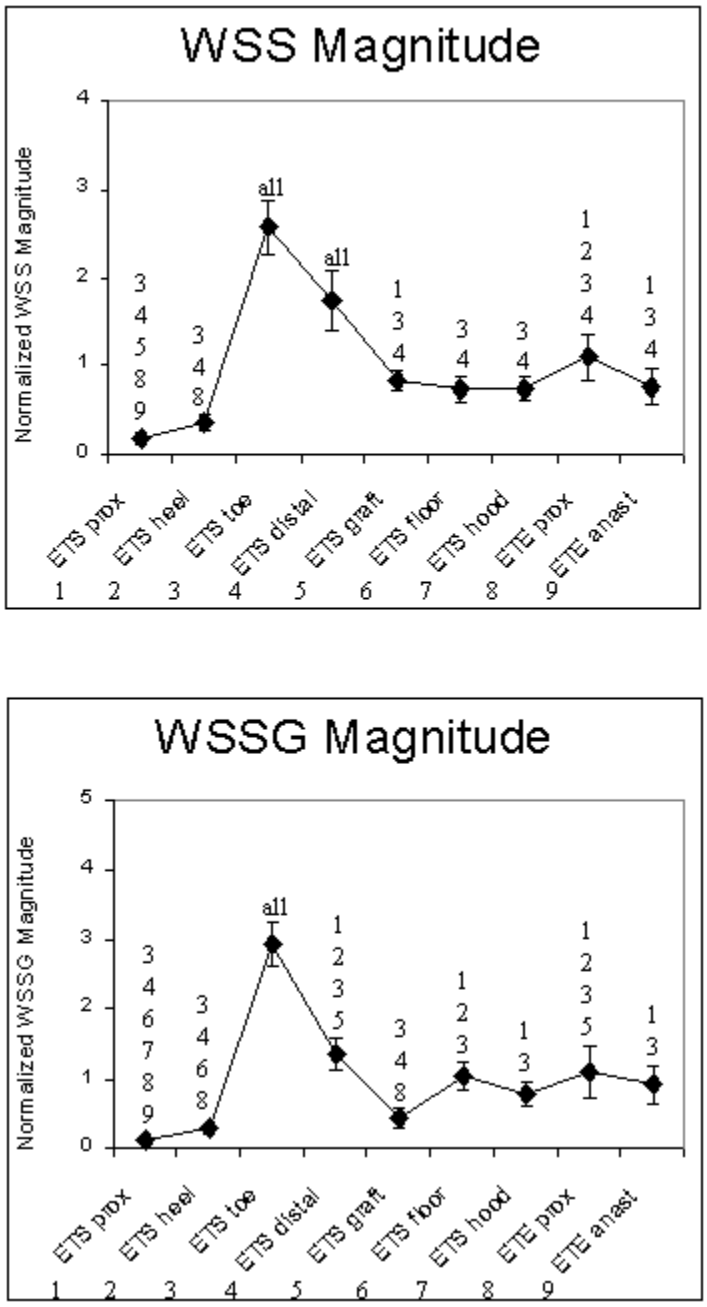

Figure 3.66 Mean Normalized WSS and WSSG Magnitude Index $_{ROI}$ (see Equation 3.30) for the pooled data from all experiments. The data for each region of interest of one experiment are normalized by the mean hemodynamic index for the same experiment. The numbers above and/or below each data point indicate which regions (1-ETS proximal artery, 2-ETS heel, 3-ETS toe, 4-ETS distal artery, 5-ETS graft, 6-ETS floor, 7-ETS hood, 8-ETE proximal, 9-ETE anastomosis) are significantly different from that region.

In the retrograde flow experiments (Figure 3.58), the ETS toe and distal artery regions also had the highest values of Mean Normalized Axial WSS Index $_{ROI}$ and these values were higher than in the zero flow experiments. Similar to the zero flow experiments, these values were significantly higher than the Mean Normalized Axial WSS Index $_{ROI}$ for the regions with the lowest values of Mean Normalized Axial WSS Index $_{ROI}$ which included the ETS proximal artery, heel and floor regions. Specifically, the ETS toe region (4.6 ± 1.1) was significantly higher than the ETS proximal artery (-0.7 ± 0.1, $p < 0.0001$), heel (-1.1 ± 0.1, $p < 0.0001$) and floor (-1.5 ± 0.4, $p < 0.0001$) regions. Similarly, the ETS distal artery region (2.8 ± 0.8) was significantly higher than the ETS proximal artery (-0.7 ± 0.1, $p = 0.0004$), heel (-1.1 ± 0.1, $p = 0.0001$) and floor (-1.5 ± 0.4, $p < 0.0001$) regions. In addition, the ETS toe (4.6 ± 1.1) region was significantly higher than the ETS graft (1.3 ± 0.3, $p = 0.001$), hood (0.0 ± 0.2, $p < 0.0001$), ETE proximal artery (2.4 ± 0.9, $p = 0.023$) and anastomosis (1.2 ± 0.6, $p = 0.001$) regions.

When the Mean Normalized Axial WSS Index $_{ROI}$ for each region of interest exposed to the zero flow condition was compared to the same region of interest exposed to retrograde flow, statistically significant differences were found. For example, the Mean Normalized Axial WSS Index $_{ROI}$ in the ETS proximal, heel, floor and hood regions were higher in the zero flow experiments (0.0 ± 0.01, 0.0 ± 0.05, -0.1 ± 0.2, 1.0 ± 0.2, respectively) as opposed to the retrograde flow experiments (-0.7 ± 0.1, -1.1 ± 0.1, -1.5 ± 0.4, 0.0 ± 0.2, respectively). These differences were statistically significant ($p = 0.0002$, $p = 0.0001$, $p = 0.018$, $p = 0.024$, respectively) while the other regions of interest did not vary significantly due to the imposed flow condition in the proximal artery.

When the data from both flow conditions were pooled together (Figure 3.64), an understanding of the regional variation of axial WSS in vascular bypass grafts can be determined. The ETS toe (3.6 ± 0.7) region had significantly higher Mean Normalized Axial WSS Index $_{ROI}$ than all the other regions of interest including the ETS proximal (-0.4 ± 0.1, $p < 0.0001$), heel (-0.6 ± 0.2, $p < 0.0001$), distal (2.4 ± 0.5, $p = 0.046$), graft (1.3 ± 0.2, $p = 0.0002$), floor (-0.8 ± 0.3, $p < 0.0001$), hood (0.5 ± 0.2, $p < 0.0001$), ETE proximal (1.9 ± 0.6, $p = 0.005$) and anastomosis (1.0 ± 0.3, $p < 0.0001$) regions. The ETS proximal, heel and

floor regions had the lowest level of Mean Normalized Axial WSS Index $_{ROI}$. The ETS proximal region (-0.4 ± 0.1) was significantly lower than the ETS toe (3.6 ± 0.7, $p < 0.0001$), distal (2.4 ± 0.5, $p < 0.0001$), graft (1.3 ± 0.2, $p = 0.004$), ETE proximal artery (1.9 ± 0.6, $p = 0.0002$) and anastomosis (1.0 ± 0.3, $p = 0.018$) regions. Similarly, the ETS heel region (-0.6 ± 0.2) was significantly lower than the ETS toe (3.6 ± 0.7, $p < 0.0001$), distal (2.4 ± 0.5, $p < 0.0001$), graft (1.3 ± 0.2, $p = 0.0001$), ETE proximal artery (1.9 ± 0.6, $p < 0.0001$) and anastomosis (1.0 ± 0.3, $p = 0.007$) regions. The ETS floor region (-0.8 ± 0.3) was also significantly lower than the ETS toe (3.6 ± 0.7, $p < 0.0001$), distal (2.4 ± 0.5, $p < 0.0001$), graft (1.3 ± 0.2, $p = 0.0004$), ETE proximal artery (1.9 ± 0.6, $p < 0.0001$) and anastomosis (1.0 ± 0.3, p = 0.0.003) regions.

3.3.7.2 <u>Regional Variation of Mean Normalized Circumferential WSS $_{ROI}$</u>

In the zero flow experiments (Figure 3.59), only three regions exhibited significant levels of Mean Normalized Circumferential WSS Index $_{ROI}$. The ETS toe and distal artery regions had the highest level of Mean Normalized Circumferential WSS Index $_{ROI}$. These values were significantly higher than those of all of the other regions of interest. Specifically, the ETS toe region (5.6 ± 2.4) was significantly higher than the ETS proximal (0.0 ± 0.01, $p = 0.004$), heel (0.2 ± 0.1, $p = 0.005$), graft (0.6 ± 0.3, $p = 0.009$), floor (1.5 ± 0.8, $p = 0.033$), hood (-4.4 ± 1.5, $p < 0.0001$), ETE proximal (0.0 ± 0.003, $p = 0.004$) and anastomosis (0.0 ± 0.004, $p = 0.004$) regions. Similarly, the ETS distal artery region (5.6 ± 2.4) had significantly higher Mean Normalized Circumferential WSS Index $_{ROI}$ than the ETS proximal (0.0 ± 0.01, $p = 0.004$), heel (0.2 ± 0.1, $p = 0.005$), graft (0.6 ± 0.3, $p = 0.009$), floor (1.5 ± 0.8, $p = 0.031$), hood (-4.4 ± 1.5, $p < 0.0001$), ETE proximal (0.0 ± 0.003, $p = 0.004$) and anastomosis (0.0 ± 0.004, $p = 0.004$) regions. The region with the lowest Mean Normalized Circumferential WSS Index $_{ROI}$ was the ETS hood (-4.4 ± 1.5) and this value was significantly lower than all other regions of interest including the ETS proximal (0.0 ± 0.01, $p = 0.020$), heel (0.2 ± 0.1, $p = 0.015$), toe (5.6 ± 2.4, $p < 0.0001$), graft (0.6 ± 0.3, $p = 0.009$), floor (1.5 ± 0.8, $p = 0.002$), ETE proximal (0.0 ± 0.003, $p = 0.020$) and anastomosis (0.0 ± 0.004, $p = 0.020$) regions. Because the value for the hood region was negative, the direction of the normalized circumferential WSS was in the opposite direction of the other regions but the hood region still exhibited a relatively large magnitude of Mean

Normalized Circumferential WSS Index $_{ROI}$. Therefore the regions with low magnitudes of Mean Normalized Circumferential WSS Index $_{ROI}$ were the ETS proximal (0.0 ± 0.01), heel (0.2 ± 0.1), graft (0.6 ± 0.3), floor (1.5 ± 0.8), ETE proximal (0.0 ± 0.003) and anastomosis (0.0 ± 0.004) regions, which were shown above to have significantly lower Mean Normalized Circumferential WSS Index $_{ROI}$ compared to the ETS toe and distal artery regions.

In the retrograde flow experiments (see Figure 3.59), the ETS toe (5.4 ± 1.9) again had the highest level of Mean Normalized Circumferential WSS Index $_{ROI}$. This value was significantly higher than the Mean Normalized Circumferential WSS Index $_{ROI}$ present in all other regions of interest including the ETS proximal (0.3 ± 0.2, $p < 0.0001$), heel (1.3 ± 0.1, $p = 0.001$), distal artery (2.5 ± 0.5, $p = 0.017$), graft (-0.1 ± 0.04, $p < 0.0001$), floor (2.1 ± 1.3, $p = 0.006$), hood (-2.5 ± 0.5, $p > 0.0001$), ETE proximal (0.0 ± 0.03, $p < 0.0001$) and anastomosis (0.0 ± 0.01, $p < 0.0001$) regions. Similar to the zero flow experiments, the ETS hood (-2.5 ± 0.5) region had the lowest value of Mean Normalized Circumferential WSS Index $_{ROI}$ and this was significantly lower than the same value for all other regions including the ETS proximal (0.3 ± 0.2, $p = 0.017$), heel (1.3 ± 0.1, $p = 0.002$), toe (5.4 ± 1.9, $p < 0.0001$), distal artery (2.5 ± 0.5, $p = 0.0001$), graft (-0.1 ± 0.04, $p = 0.040$), floor (2.1 ± 1.3, $p = 0.0003$), ETE proximal (0.0 ± 0.03, $p = 0.033$) and anastomosis (0.0 ± 0.01, $p = 0.035$) regions. Again, although this value was negative, it indicates that the hood region had a large magnitude of Mean Normalized Circumferential WSS Index $_{ROI}$ that was in the opposite direction of the other regions. Therefore, similar to the zero flow experiments, the regions with significantly low magnitudes of Mean Normalized Circumferential WSS Index $_{ROI}$ were the ETS proximal (0.3 ± 0.2), heel (1.3 ± 0.1), graft (-0.1 ± 0.04), floor (2.1 ± 1.3), ETE proximal (0.0 ± 0.03) and anastomosis (0.0 ± 0.01) regions, which were shown above to be significantly lower than the ETS toe region (5.4 ± 1.9).

When the Mean Normalized Circumferential WSS Index $_{ROI}$ for each region of interest exposed to the zero flow condition was compared to the same region of interest exposed to retrograde flow, statistically significant differences were found. For example, the Mean Normalized Circumferential WSS Index $_{ROI}$ in the ETS heel region was lower in the zero flow experiments (0.19 ± 0.14) as opposed to the retrograde flow

experiments (1.33 ± 0.3). This difference was statistically significant ($p = 0.0003$) while the other regions of interest did not vary significantly due to the imposed flow condition in the proximal artery.

When the data from all experiments were pooled together (Figure 3.65), the ETS toe and distal artery regions have significantly higher Mean Normalized Circumferential WSS Index $_{ROI}$ than all other regions of interest. Specifically, the ETS toe region (5.5 ± 1.4) was significantly higher than the ETS proximal (0.2 ± 0.1, $p < 0.0001$), heel (0.8 ± 0.2, $p < 0.0001$), graft (0.2 ± 0.2, $p < 0.0001$), floor (1.8 ± 0.7, $p = 0.0008$), hood (-3.5 ± 0.8, $p < 0.0001$), ETE proximal (0.0 ± 0.01, $p < 0.0001$) and anastomosis (0.0 ± 0.004, $p < 0.0001$) regions. Similarly, the ETS distal artery region (4.1 ± 1.3) was significantly higher than the ETS proximal (0.2 ± 0.1, $p = 0.0004$), heel (0.8 ± 0.2, $p = 0.003$), graft (0.2 ± 0.2, $p = 0.0005$), floor (1.8 ± 0.7, $p = 0.035$), hood (-3.5 ± 0.8, $p < 0.0001$), ETE proximal (0.0 ± 0.01, $p = 0.0003$) and anastomosis (0.0 ± 0.004, $p = 0.0002$) regions. The ETS hood (-3.5 ± 0.8) region had significantly lower Mean Normalized Circumferential WSS Index $_{ROI}$ than all other regions of interest including the ETS proximal (0.2 ± 0.1, $p = 0.001$), heel (0.8 ± 0.2, $p = 0.0001$), toe (5.5 ± 1.4, $p < 0.0001$), distal (4.1 ± 1.3, $p < 0.0001$), graft (0.2 ± 0.2, $p < 0.0007$), floor (1.8 ± 0.7, $p < 0.0001$), ETE proximal (0.0 ± 0.01, $p = 0.001$) and anastomosis (0.0 ± 0.004, $p = 0.002$) regions. Once again, the negative value means that the ETS hood region had a large magnitude of Mean Normalized Circumferential WSS Index $_{ROI}$ but the direction was opposite to the other regions. Therefore, the regions with significantly low magnitudes of Mean Normalized Circumferential WSS Index $_{ROI}$ were the ETS proximal (0.2 ± 0.1), heel (0.8 ± 0.2), graft (0.2 ± 0.2), floor (1.8 ± 0.7), ETE proximal (0.0 ± 0.01) and anastomosis (0.0 ± 0.004) regions, which were shown above to have significantly lower Mean Normalized Circumferential WSS Index $_{ROI}$ compared to the ETS toe and distal artery regions.

3.3.7.3 Regional Variation of Mean Normalized WSS Magnitude $_{ROI}$

In the zero flow experiments (Figure 3.60), the ETS toe and distal artery regions had the largest Mean Normalized WSS Magnitude Index $_{ROI}$ and these values were significantly higher than all other regions of interest. Specifically, the Mean Normalized WSS Magnitude Index $_{ROI}$ for the ETS toe region (2.7 ± 0.3) was significantly higher than the ETS proximal artery (0.0 ± 0.01, $p < 0.0001$), heel (0.1 ± 0.1, $p < 0.0001$), graft

(1.0 ± 0.2, p = 0.0005), floor (0.5 ± 0.2, p < 0.0001), hood (1.0 ± 0.2, p = 0.0004) and ETE proximal (1.1 ± 0.5, p = 0.001) and anastomosis (0.7 ± 0.3, p < 0.0001) segments. Similarly, the ETS distal artery (1.9 ± 0.6) region had a significantly higher Mean Normalized WSS Magnitude Index $_{ROI}$ than the ETS proximal artery (0.0 ± 0.01, p = 0.0001), heel (0.1 ± 0.1, p = 0.0001), graft (1.0 ± 0.2, p = 0.041), floor (0.5 ± 0.2, p = 0.001), hood (1.0 ± 0.2, p = 0.0030) and ETE proximal (1.1 ± 0.5, p = 0.049) and anastomosis (0.7 ± 0.3, p = 0.008) segments. The ETS proximal artery and heel regions had the smallest Mean Normalized WSS Magnitude Index $_{ROI}$. Specifically, the Mean Normalized WSS Magnitude Index $_{ROI}$ for the ETS proximal artery region (0.0 ± 0.01) was significantly lower than the ETS toe (2.7 ± 0.3, p < 0.0001), distal (1.9 ± 0.6, p = 0.0001), graft (1.0 ± 0.2, p = 0.022), hood (1.0 ± 0.2, p = 0.030) and ETE proximal (1.1 ± 0.5, p = 0.018) segments. Similarly, the ETS heel region (0.1 ± 0.1) was significantly lower than the ETS toe (2.7 ± 0.3, p < 0.0001), distal (1.9 ± 0.6, p = 0.0001), graft (1.0 ± 0.2, p = 0.034), hood (1.0 ± 0.2, p = 0.046) and ETE proximal (1.1 ± 0.5, p = 0.028) segments.

In the retrograde flow experiments (Figure 3.60), the ETS toe and distal artery segments had the highest values of Mean Normalized WSS Magnitude Index $_{ROI}$, similar to the zero flow experiments. The value of the Mean Normalized WSS Magnitude Index $_{ROI}$ for the ETS toe (2.5 ± 0.6) region was significantly higher than all other regions of interest, including the ETS proximal (0.4 ± 0.1, p < 0.0001), heel (0.6 ± 0.04, p < 0.0001), distal (1.5 ± 0.4, p = 0.019), graft (0.6 ± 0.1, p < 0.0001), floor (1.0 ± 0.2, p = 0.0005), hood (1.0 ± 0.2, p < 0.0001), ETE proximal (1.1 ± 0.3, p = 0.001) and anastomosis (0.8 ± 0.2, , p = 0.0001) regions. The value for the ETS distal artery (1.5 ± 0.4) segment was significantly higher than the ETS proximal (0.4 ± 0.1, p = 0.005), heel (0.6 ± 0.04, p = 0.029), graft (0.6 ± 0.1, p = 0.019) and hood (1.0 ± 0.2, p = 0.013) regions.

When the Mean Normalized WSS Magnitude Index $_{ROI}$ for each region of interest exposed to the zero flow condition was compared to the same region of interest exposed to retrograde flow, statistically significant differences were found. For example, the Mean Normalized WSS Magnitude Index $_{ROI}$ in the ETS proximal, heel, floor and hood regions were higher in the zero flow experiments (0.0 ± 0.01, 0.1 ± 0.1, 0.5

± 0.2, 1.0 ± 0.2, respectively) as opposed to the retrograde flow experiments (0.4 ± 0.1, 0.6 ± 0.04, 1.0 ± 0.2, 1.0 ± 0.2, respectively). These differences were statistically significant ($p < 0.0001$, $p = 0.0001$, $p = 0.043$, $p = 0.041$, respectively) while the other regions of interest did not vary significantly due to the imposed flow condition in the proximal artery.

When the data from all experiments were pooled together (Figure 3.66), the ETS toe and distal artery (1.7 ± 0.3) regions again had the highest Mean Normalized WSS Magnitude Index $_{ROI}$ and these values were significantly higher than all other regions. Specifically, the ETS toe region (2.6 ± 0.3) was significantly higher than the ETS proximal artery (0.2 ± 0.06, $p < 0.0001$), heel (0.4 ± 0.1, $p < 0.0001$), distal (1.7 ± 0.3, $p = 0.005$), graft (0.8 ± 0.1, $p < 0.0001$), floor (0.7 ± 0.1, $p < 0.0001$), hood (0.7 ± 0.1, $p < 0.0001$), ETE proximal (1.1 ± 0.3, $p < 0.0001$) and anastomosis (0.8 ± 0.2, $p < 0.0001$) regions. Similarly, the ETS distal artery region (1.7 ± 0.3) was significantly higher than the ETS proximal artery (0.2 ± 0.06, $p < 0.0001$), heel (0.4 ± 0.1, $p < 0.0001$), toe (2.6 ± 0.3, $p = 0.005$), graft (0.8 ± 0.1, $p = 0.002$), floor (0.7 ± 0.1, $p = 0.001$), hood (0.7 ± 0.1, $p = 0.001$), ETE proximal (1.1 ± 0.3, $p = 0.027$) and anastomosis (0.8 ± 0.2, $p = 0.001$) regions. The ETS proximal artery (0.2 ± 0.06) region had the lowest Mean Normalized WSS Magnitude Index $_{ROI}$ and this was significantly lower than that of the ETS toe (2.6 ± 0.3, $p < 0.0001$), distal (1.7 ± 0.3, $p < 0.0001$), graft (0.8 ± 0.1, $p = 0.030$), ETE proximal (1.1 ± 0.3, $p = 0.002$) and anastomosis (0.8 ± 0.2, $p = 0.048$) regions.

3.3.7.4 Regional Variation of Mean Normalized Axial WSSG $_{ROI}$

In the zero flow experiments (Figure 3.61), there was no significant regional variation of Mean Normalized Axial WSSG Index $_{ROI}$. The highest levels of Mean Normalized Axial WSSG Index $_{ROI}$ occurred in the ETS toe (4.8 ± 1.7) and floor (2.5 ± 3.6) segments but these values were not significantly higher than any other region. The ETS hood (-1.3 ± 1.1) region had the lowest level of Mean Normalized Axial WSSG Index $_{ROI}$ but this was not significantly different from the other regions of interest.

Similarly, in the retrograde flow experiments (Figure 3.61), no significant regional variation of normalized axial WSSG existed. The ETS distal (3.2 ± 4.6) and ETE proximal (11.6 ± 6.9) regions had the

highest levels of Mean Normalized Axial WSSG Index $_{ROI}$. The ETS floor (-3.3 ± 3.3) region had the lowest value of Mean Normalized Axial WSSG Index $_{ROI}$. However, none of these values were significantly different from the other regions of interest.

When the Mean Normalized Axial WSSG Index $_{ROI}$ for each region of interest exposed to the zero flow condition was compared to the same region of interest exposed to retrograde flow, statistically significant differences were found. For example, the Mean Normalized Axial WSSG Index $_{ROI}$ in the ETS proximal artery region was lower in the zero flow experiments (0.01 ± 0.02) as opposed to the retrograde flow experiments (0.78 ± 0.3). This difference was statistically significant ($p = 0.049$) while the other regions of interest did not vary significantly due to the imposed flow condition in the proximal artery.

When the data from all experiments were pooled together (Figure 3.64), there was still no significant regional variation of normalized axial WSSG. The ETE proximal (6.6 ± 3.7) segment had the highest level of Mean Normalized Axial WSSG Index $_{ROI}$ but this value was not significantly different from the other regions of interest.

3.3.7.5 Regional Variation of Mean Normalized Circumferential WSSG$_{ROI}$

In the zero flow experiments (Figure 3.62), the ETS toe region was the only region that had a significantly different Mean Normalized Circumferential WSSG Index $_{ROI}$. The ETS toe (4.6 ± 1.1) region had significantly higher Mean Normalized Circumferential WSSG Index $_{ROI}$ than all other regions of interest including the ETS proximal (0.1 ± 0.1, $p = 0.001$), heel (1.2 ± 1.2, $p = 0.009$), distal (0.1 ± 0.9, $p = 0.001$), graft (0.4 ± 0.2, $p = 0.002$), floor (0.6 ± 0.9, $p = 0.003$), hood (1.9 ± 1.6, $p = 0.033$), ETE proximal (0.0 ± 0.4, $p = 0.001$) and anastomosis (0.2 ± 0.5, $p = 0.001$) regions.

In the retrograde flow experiments (Figure 3.62), there was no regional variation of Mean Normalized Circumferential WSSG Index $_{ROI}$. The ETS toe (6.5 ± 2.8) and ETE proximal (5.1 ± 5.7) segments had the highest levels of Mean Normalized Circumferential WSSG Index $_{ROI}$. The ETS floor (-2.1 ± 5.4) segment had the lowest level of Mean Normalized Circumferential WSSG Index $_{ROI}$. However, none of these values were significantly different from the other regions of interest.

When the Mean Normalized Circumferential WSSG Index $_{ROI}$ for each region of interest exposed to the zero flow condition was compared to the same region of interest exposed to retrograde flow, statistically significant differences were found. For example, the Mean Normalized Circumferential WSSG Index $_{ROI}$ in the ETS proximal artery region was lower in the zero flow experiments (0.08 ± 0.08) as opposed to the retrograde flow experiments (0.59 ± 0.3). This difference was statistically significant ($p = 0.025$) while the other regions of interest did not vary significantly due to the imposed flow condition in the proximal artery.

When the data from all experiments were pooled together (Figure 3.65), no region of interest had a significantly different value of Mean Normalized Circumferential WSSG Index $_{ROI}$. The ETS toe (5.6 ± 1.4) and ETS floor (-0.7 ± 2.6) regions had the highest and lowest levels of Mean Normalized Circumferential WSSG Index $_{ROI}$, respectively, but these values were not significantly different from the other regions of interest.

3.3.7.6 Regional Variation of Normalized WSSG Magnitude $_{ROI}$

The regional variation of Mean Normalized WSSG Magnitude Index $_{ROI}$ (see Figure 3.63) followed the same trend as the regional variation in Mean Normalized WSS Magnitude Index $_{ROI}$ (see Figure 3.60). In the zero flow experiments, the ETS toe and distal artery segments had the highest Mean Normalized WSSG Magnitude Index $_{ROI}$. Specifically, the value for the ETS toe (3.5 ± 0.4) region was significantly higher than all other regions of interest including the ETS proximal (0.0 ± 0.01, $p < 0.0001$), heel (0.1 ± 0.1, $p < 0.0001$), distal (1.5 ± 0.4 , $p < 0.0001$), graft (0.7 ± 0.2, $p < 0.0001$), floor (0.7 ± 0.3, $p < 0.0001$), hood (1.1 ± 0.2, $p < 0.0001$), ETE proximal (0.6 ± 0.3 , $p < 0.0001$) and anastomosis (0.7 ± 0.4, $p < 0.0001$) regions. The value for the ETS distal region (1.5 ± 0.4) was significantly higher than the ETS proximal (0.0 ± 0.01, $p = 0.0004$), heel (0.1 ± 0.1, $p = 0.001$), toe (3.5 ± 0.4, $p < 0.0001$), graft (0.7 ± 0.2, $p = 0.037$), floor (0.7 ± 0.3, $p = 0.045$), ETE proximal (0.6 ± 0.3 , $p = 0.024$) and anastomosis (0.7 ± 0.4, $p = 0.036$) regions.

In the retrograde flow experiments (Figure 3.63), the ETS toe region (2.4 ± 0.5) had the highest Mean Normalized WSSG Magnitude Index $_{ROI}$ and this value was significantly higher than the ETS proximal (0.2 ± 0.1, $p < 0.0001$), heel (0.4 ± 0.1, $p = 0.0001$), distal (1.2 ± 0.3, $p = 0.013$), graft (0.2 ± 0.1, $p < 0.0001$),

floor (1.4 ± 0.3, p = 0.029), hood (0.5 ± 0.1, p = 0.0001) and ETE anastomosis (1.2 ± 0.4, p = 0.010) regions. The ETS proximal and graft regions had the lowest levels of normalized WSSG magnitude. The Mean Normalized WSSG Magnitude Index $_{ROI}$ for the ETS proximal region (0.2 ± 0.1) was significantly lower than that of the ETS toe (2.4 ± 0.5, p < 0.0001), distal (1.2 ± 0.3, p = 0.040), floor (1.4 ± 0.3, p = 0.018), ETE proximal (1.6 ± 0.6, p = 0.005) and anastomosis (1.2 ± 0.4, p = 0.047) regions. The ETS graft region (0.2 ± 0.1) had lower Mean Normalized WSSG Magnitude Index $_{ROI}$ than the ETS toe (2.4 ± 0.5, p < 0.0001), distal (1.2 ± 0.3, p = 0.033), floor (1.4 ± 0.3, p = 0.014), ETE proximal (1.6 ± 0.6, p = 0.004) and anastomosis (1.2 ± 0.4, p = 0.039) regions.

When the Mean Normalized WSSG Magnitude Index $_{ROI}$ for each region of interest exposed to the zero flow condition was compared to the same region of interest exposed to retrograde flow, statistically significant differences were found. For example, the Mean Normalized WSSG Magnitude Index $_{ROI}$ in the ETS proximal artery region was lower in the zero flow experiments (0.01 ± 0.01) as opposed to the retrograde flow experiments (0.22 ± 0.06). This difference was statistically significant (p = 0.007) while the other regions of interest did not vary significantly due to the imposed flow condition in the proximal artery.

When the data from all experiments were pooled together (Figure 3.66), the ETS toe (3.0 ± 0.3) region had significantly higher Mean Normalized WSSG Magnitude Index $_{ROI}$ than all other regions of interest including the ETS proximal (0.1 ± 0.04, p < 0.0001), heel (0.3 ± 0.1, p < 0.0001), distal (1.4 ± 0.2, p < 0.0001), graft (0.4 ± 0.1, p < 0.0001), floor (1.0 ± 0.2, p < 0.0001), hood (0.8 ± 0.2, p < 0.0001), ETE proximal (1.1 ± 0.4, p < 0.0001) and anastomosis (0.9 ± 0.3, p < 0.0001) regions. The ETS proximal (0.1 ± 0.04) region had the lowest level of Mean Normalized WSSG Magnitude Index $_{ROI}$ and this value was significantly lower than the ETS toe (3.0 ± 0.3, p < 0.0001), distal (1.4 ± 0.2, p = 0.0002), floor (1.0 ± 0.2, p = 0.005), hood (0.8 ± 0.2, p = 0.039), ETE proximal (1.1 ± 0.4, p = 0.003) and anastomosis (0.9 ± 0.3, p = 0.015) regions.

3.4 Discussion

3.4.1 CFD Models of ETS and ETE Bypass Graft Anastomoses

Because the geometries (i.e., vessel caliber, number and placement of ligated branching vessels, size and shape of the anastomosis) varied greatly from experiment to experiment, a general, idealized model could not be used to determine the flow field and calculate the resulting hemodynamic parameters. Therefore, we developed three-dimensional reconstructions of each ETS and ETE anastomosis perfused *ex vivo* for the purposes of CFD analysis. The computational results illustrate that although some similarities could be determined, the mapping of hemodynamic parameters varied greatly between the type of anastomosis (ETS versus ETE) as well as between the individual anastomoses. In all ETS models, the velocity vectors in the distal artery were skewed toward the floor due to the impingement of flow from the angled graft which also caused secondary flow (Figures 3.13 - 3.22). The degree of the skewing and magnitude of the secondary flow depended on the geometry of the anastomosis and the imposed flow rate into the graft. For example, the skewing of the velocity vectors and the magnitude and extent of secondary flow was especially high in ETS-Z3 (Figure 3.15) because the graft had a small diameter, which increased the velocity of the fluid in the graft. In all ETS models, a recirculation zone occurred near the heel (Figures 3.13 - 3.22). The size and magnitude of this recirculation depended on which flow condition was prescribed in the proximal artery (zero or retrograde) as well as the geometry of the anastomosis. For example, the strength of the recirculation zone at the heel ranged from relatively weak in ETS-Z1 (Figure 3.13) to strong in ETS-R4 (Figure 3.21). Flow in the ETE models (Figures 3.23 - 3.32) was generally more uniform than in the ETS models, although disturbances did occur due to local changes in vessel diameter along the length of the anastomosis. This was most prominent in ETE-Z3 (Figure 3.25) and ETE-R1 (Figure 3.28). All of these differences in the flow field resulted in local variations of WSS and WSSG. Therefore, computational reconstructions were necessary to quantify the hemodynamic parameters at regions of interest along each anastomosis.

3.4.2 Regional Variation of Hemodynamic Parameters

Our results showed that there exists a significant, regional variation of all normalized hemodynamic parameters examined in the three-dimensional reconstructions of vascular bypass graft anastomoses. The ETS regions of interest that had significantly different Mean Normalized Hemodynamic Indices $_{ROI}$ as compared to the ETE proximal artery segment (i.e., control) for all of the experiments are presented in Table 3.3. The arrows indicate a significantly increased or decreased Mean Normalized Hemodynamic Index $_{ROI}$ in that region compared to the ETE proximal artery segment.

The region with the most number of significant differences relative to the ETE proximal artery segment was the ETS toe region. The Mean Normalized Circumferential WSS and WSS Magnitude Indices $_{ROI}$ for the ETS toe region were significantly increased in this region for both flow conditions. The same region had increased Mean Normalized Hemodynamic Indices $_{ROI}$ for circumferential WSSG and WSSG magnitude only for the zero flow condition, while the Mean Normalized Axial WSS Magnitude Index $_{ROI}$ for the ETS toe region was increased only for the retrograde flow models. The Mean Normalized Axial WSSG Index $_{ROI}$

Table 3.3 Summary of the Mean Normalized Hemodynamic Indices $_{ROI}$ in the ETS regions of interest for the two flow conditions (zero and retrograde) in the proximal artery. The arrows indicate a significantly ($p < 0.05$) increased or decreased value of the Mean Normalized Hemodynamic Index $_{ROI}$ in that region compared to the ETE proximal artery segment (i.e., control) for the same flow condition.

	Axial WSS		**Circ WSS**		**Mag WSS**		**Axial WSSG**		**Circ WSSG**		**Mag WSSG**	
	Zero	Retro	Zero	Retro	Zero	Retro	Zero	Retro	Zero	Retro	Zero	Retro
ETS proximal	⇓	⇓	-	-	⇓	-	-	-	-	-	-	⇓
ETS heel	⇓	⇓	-	-	⇓	-	-	-	-	-	-	⇓
ETS toe	-	⇑	⇑	⇑	⇑	⇑	-	-	⇑	-	⇑	-
ETS distal	-	-	⇑	⇑	⇑	-	-	-	-	-	⇑	-
ETS graft	-	-	-	-	-	-	-	-	-	-	-	⇓
ETS floor	⇓	⇓	-	-	-	-	-	-	-	-	-	-
ETS hood	-	⇓	⇓	⇓	-	-	-	-	-	-	-	⇓

in the ETS toe region was not statistically different from the ETE proximal artery segment for either flow condition.

The Mean Normalized Hemodynamic Indices $_{ROI}$ with the most number of regions with significant differences were those for axial WSS and WSSG magnitude. For the zero flow models, the Mean Axial WSS Index $_{ROI}$ for the ETS proximal artery, heel and floor regions were significantly decreased. The Mean WSSG Magnitude Index $_{ROI}$ for the ETS toe and distal artery regions were significantly increased compared to the ETE proximal artery segment. For the retrograde flow models, the Mean Axial WSS Index $_{ROI}$ for the ETS proximal artery, heel, floor and hood regions were significantly decreased and the index for the ETS toe region was significantly increased. The Mean WSSG Magnitude Index $_{ROI}$ for the ETS proximal artery, heel, graft and hood regions were significantly decreased compared to the ETE proximal artery segment.

The Mean Normalized Hemodynamic Indices $_{ROI}$ for circumferential WSS and WSS magnitude also had a number of regions with significant differences relative to the ETE proximal artery. The Mean Normalized Circumferential WSS $_{ROI}$ was significantly increased in the ETS toe and distal regions and significantly decreased in the hood region for both flow conditions. For the zero flow models, the Mean Normalized WSS Magnitude $_{ROI}$ was significantly decreased in the ETS proximal artery and heel regions, and significantly increased in the ETS toe and distal regions. For the retrograde flow models, the only significant difference for the Mean Normalized WSS Magnitude $_{ROI}$ was an increase for the ETS toe segment.

The Mean Normalized Axial and Circumferential WSSG Indices $_{ROI}$ did not have many regions with significant differences relative to the ETE proximal segment. The Mean Normalized Axial WSSG Index $_{ROI}$ was not significantly different for any region of interest for either flow condition. The Mean Normalized Circumferential WSSG was significantly increased only in the ETS toe region for the zero flow models.

The statistical differences between the Mean Normalized Hemodynamic Indices $_{ROI}$ for the ETS regions of interest and the ETE proximal artery segment depended on the imposed flow condition for 12 of the 19 hemodynamic parameter and region combinations that exhibited significant differences. For example, for the retrograde flow models, the Mean Normalized Axial WSS Index $_{ROI}$ was significantly increased for the

ETS toe region and significantly decreased for the ETS hood region, but there were no significant differences for these regions in the zero flow models. The Mean Normalized WSS Magnitude Index $_{ROI}$ for the ETS proximal artery and heel regions was significantly decreased while the ETS distal region had a significant increase in this index for the zero flow models. However, none of these regions had significant differences in the Mean Normalized WSS Magnitude Index $_{ROI}$ for the retrograde flow models. The Mean Normalized Circumferential WSSG Index $_{ROI}$ for the ETS toe region was significantly increased as was the Mean Normalized WSSG Magnitude Index $_{ROI}$ for the ETS toe and distal regions in the zero flow models but there was no significant difference for the retrograde flow models. The Mean Normalized WSSG Magnitude Index$_{ROI}$ was significantly decreased in the ETS proximal artery, heel, graft and hood regions only for the retrograde flow experiments.

In general, the regions with the most number of significant variations in Mean Normalized Hemodynamic Indices$_{ROI}$ occurred in the ETS proximal artery, heel, toe, distal artery and hood regions. In general, the ETS proximal artery, heel and hood segments had low axial WSS and WSS magnitude (compared to at least four other regions of interest). The ETS toe and distal segments had high axial WSS, circumferential WSS and magnitudes of WSS and WSSG. Because these regions, particularly the toe and heel, have previously been shown to be prone to intimal hyperplasia formation [77, 78], these data suggest that low and/or high values of axial WSS and magnitudes of WSS and WSSG may play key roles in the formation of intimal hyperplasia.

3.4.3 Comparison to Other Research

Other researchers have developed three dimensional reconstructions of cardiovascular structures including single vessels, the carotid bifurcation and ETS anastomoses [92, 93, 95-101, 164]. Although our reconstruction methodology differs from the many types used in these studies, mostly due to their need for non-invasive *in vivo* imaging techniques, some similarities exist. Krams *et al.* reconstructed human coronary arteries using a combination of angiography and intravascular ultrasound imaging techniques [93]. The reconstructed surface shown in their publication exhibits a non-uniform diameter along the length of the

vessel as shown in Figure 3.67. This is similar to the non-uniform diameter present in the vessels of our ETS and ETE models although our models have more variations due to the ligation of branching vessels (see Figures 3.13 - 3.32). Leuprecht *et* al. developed computational models from castings of sheep end-to-side bypass grafts [164]. In a pulsatile, deformable wall simulation of a conventional ETS anastomosis with no flow in the proximal artery, they found counter-rotating recirculation zones on a cross-section of the hood and floor regions as shown in Figure 3.68 (panel a, cross-section B). This is similar to the dual recirculation zones present in the hood/floor cross-section in ETS-Z1 (see Figure 3.13). They also found a recirculation zone in the distal cross-section (Figure 3.68, panel a, cross-section D) similar to those present in all of our ETS zero flow models Figures (3.13 - 3.17). These previous studies show that the general geometric and flow features of our models are realistic and comparable to other reconstructed models.

To our knowledge, these are the first data showing a regional variation of hemodynamic parameters in three dimensional reconstructions of ETS and ETE bypass grafts perfused *ex vivo*. However, a number of other computational and flow visualization studies of idealized ETE and ETS anastomoses have been completed [66, 78, 83-87, 89-91, 102, 165-167]. Although the details of their anastomosis geometries and

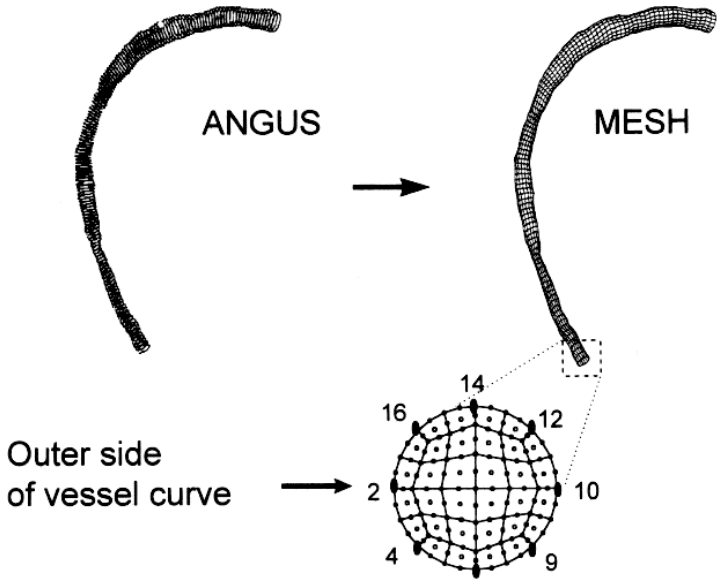

Figure 3.67 Reconstruction of a human coronary artery by Krams *et al.* [93].

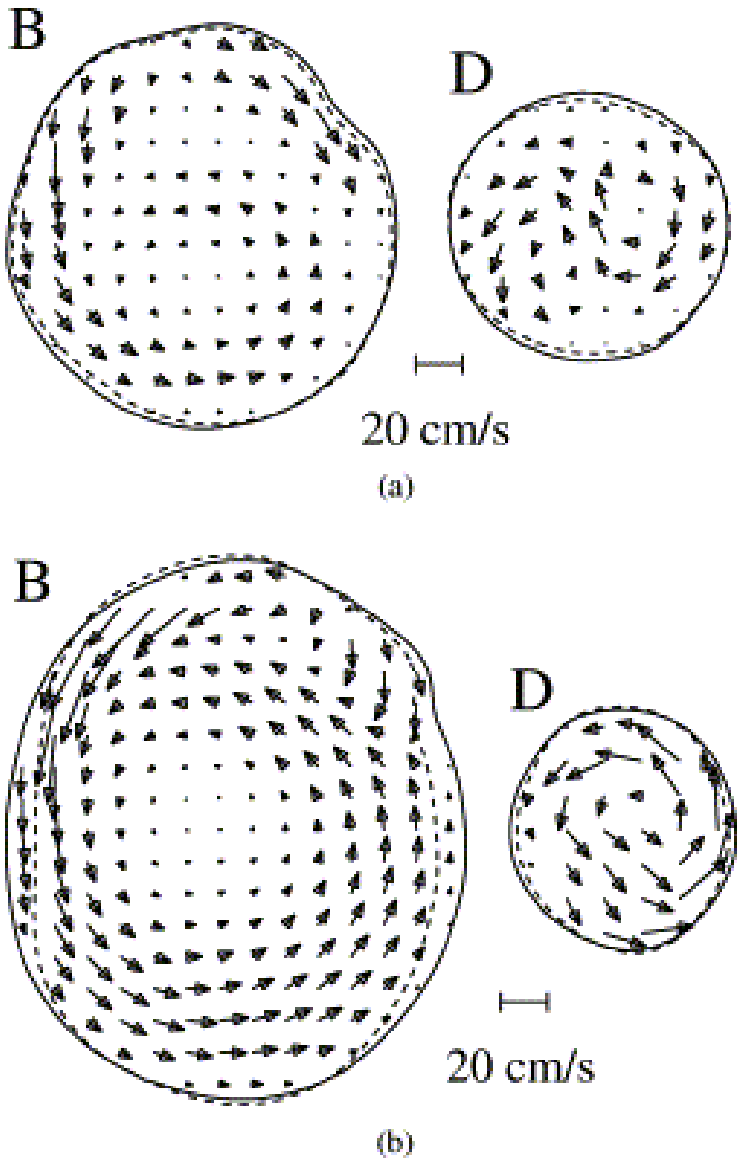

Figure 3.68 Results from Leuprecht, *et al.* [164]. In-plane velocity vectors in cross-sections B (hood/floor) and D (distal artery) during systolic deceleration for (a) conventional type anastomosis and (b) Miller-cuff type; dashed lines denote cross-section of rigid wall model corresponding to diastolic pressure.

imposed flow conditions are different than the models we presented, general characteristics of the flow field and resulting hemodynamic parameters of the most closely related models can be compared to our results.

The computational work of Hyun *et al.* on arterial expansions can be compared to our ETE models [165]. They found that smooth, symmetric enlargements in the diameter of the artery produce regions of flow reversal and recirculation as shown in Figure 3.69. This is similar to the flow reversal and recirculation regions present in our ETE models due to the variation in diameter along the length of the vessels (see Figures 3.23 - 3.32).

The computational work presented by Henry *et al.* [87] offers a comparison to our ETS zero flow simulations. They modeled a 30 degree anastomosis formed from vessels of the same diameter and a fully occluded proximal artery so that no flow entered from this region. As we did, they imposed a steady flow in this three dimensional model. Similar to our findings in the ETS zero flow models (see Figures 3.13 -

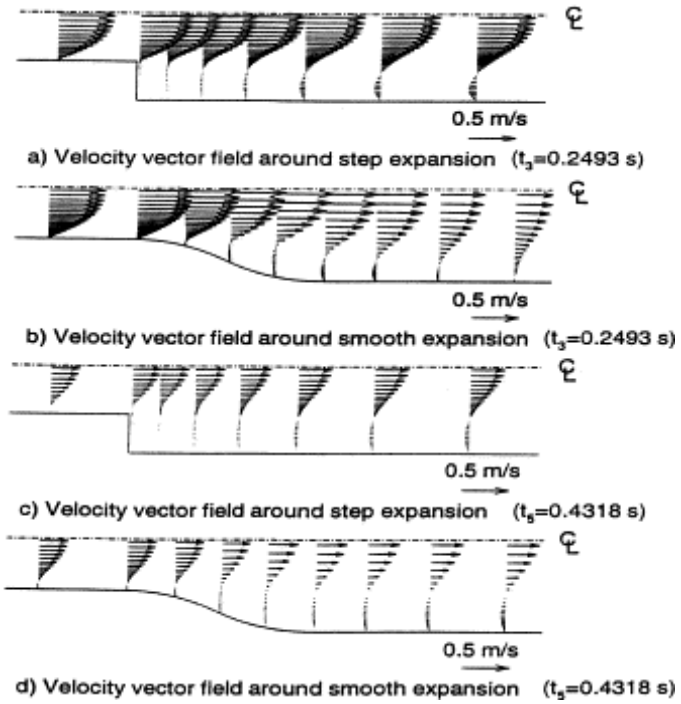

Figure 3.69 Results from Hyun, *et al.*[165] showing the velocity vector fields for axisymmetric expansion geometries at representative time steps. Note the regions of flow reversal and recirculation immediately following the smooth expansions in panels b and d.

3.17), they showed that the proximal artery flow was essentially quiescent with a small region of recirculation at the heel.

The flow visualization work presented by Hughes and How [166] offers a comparison to our ETS zero and retrograde flow models. They used transparent polyurethane models to study various distal anastomoses idealized as 8mm tubes intersecting at various angles under steady and pulsatile flow conditions. A particle tracking technique was utilized to qualitatively determine the flow field at the anastomosis for different flow rate ratios for the graft versus the proximal artery. A 30 degree model with zero flow in the proximal artery showed a small recirculation region at the heel as shown in Figure 3.70A, similar to the results of Henry *et al.* and our ETS zero flow models (Figures 3.13 - 3.17). Retrograde flow with a magnitude of 1/4 of graft flow (comparative to our 1/5 value) caused a captive vortex at the heel of the anastomosis and a region of flow reversal formed at the toe as shown in Figure 3.70B. These results are consistent with our ETS retrograde flow models, as recirculation zones and secondary flow were present at the heel for all ETS retrograde flow models (see Figures 3.18 - 3.22) and flow reversal occurred near the toe for ETS-R4 (Figure 3.21) and ETS-R5 (Figure 3.22).

Li and Rittgers used a pulsatile flow model to study the effect of zero and retrograde flow in the proximal artery [167]. They used flow visualization to determine the general flow patterns in a compliant anastomosis. They also used laser Doppler anemometry (LDA) to measure velocity at discrete intervals along the artery floor and graft hood regions. From these measurements, they derived the WSS magnitude

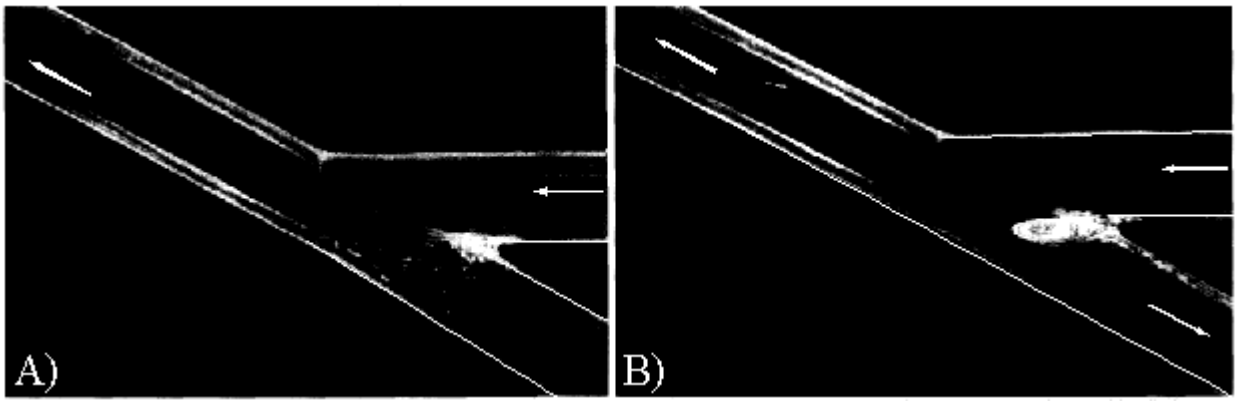

Figure 3.70 Flow visualization results from Hughes *et al.* showing a small recirculation region at the heel for the zero flow model (A) and a captive vortex at the heel for the retrograde flow model (B) [166].

and spatial WSSG magnitude. They showed a statistical difference between the mean WSS magnitude along the hood of the graft for both flow cases. Specifically, the mean WSS magnitude in the hood of the graft was higher in the zero flow case as compared to the retrograde flow case but there was no statistically significant difference in spatial WSSG. We also determined that the normalized WSS magnitude in the hood region for the ETS zero flow models (1.0 ± 0.2) was higher than in the retrograde flow models (0.5 ± 0.1, see Figure 3.60). In order to compare our results to theirs, we performed an unpaired Student's t-test on the data. We also determined that this difference in WSS magnitude for the hood region was statistically significant ($p = 0.041$). However, contrary to Li and Rittgers, we determined that the difference in the normalized WSSG magnitude in the hood region between the zero (1.1 ± 0.2) and retrograde (0.5 ± 0.1) flow models was also significant ($p = 0.039$).

Taken together, comparison of our results to those of the previous studies indicate that the general flow features found in our CFD models are realistic.

3.4.4 Limitations

We have developed relatively simplistic CFD models in that they do not incorporate physiologically relevant features such as pulsatility (i.e., unsteady flow), compliant walls and non-Newtonian fluid mechanics. In addition, our models considered only planar ETS geometries; i.e., the graft and artery lied within the same plane. Although other research groups have developed CFD models incorporating some or all of these complexities [86, 89, 96, 99, 164, 168, 169], the ultimate goal of this research was to recreate the experimental conditions. The experimental anastomoses were perfused with steady flow of a Newtonian fluid (i.e., cell culture media). The anastomoses were held fixed in space in a planar configuration. Because the flow was steady, a compliant wall model would not have made a difference; the rigid wall model would provide the same results. Therefore, our CFD models did not incorporate all the complexities computationally possible because the goal of these CFD models was to reconstruct the hemodynamic environment present in the accompanying experimental studies.

The reconstruction techniques used in this study were novel and, to our knowledge, have not been used previously. Because of the tissue processing required for the biologic endpoints in the experimental studies, certain possible limitations existed in the reconstruction technique. Arterial tissue is naturally under longitudinal tension *in vivo*. Therefore, care was taken during the extraction of the vessels, construction and perfusion of the anastomoses to maintain the vessels at the *in vivo* length. To maintain the vessel geometry after removing the anastomoses from the housing chamber, vessels were first pressure fixed by filling the vessels with 2% paraformaldehyde and maintaining the internal pressure at the same value used during the perfusion experiment. Additionally, the bath around the vessels was filled with paraformaldehyde to enhance the cross-linking process. This fixation process lasted for one hour, which is the maximum length of time recommended for optimal immunohistochemical staining. Even though these techniques were used to maintain the anastomosis geometry when removing it from the housing chamber, the vessels may have shortened slightly causing the lumen to expand due to the incompressibility of the tissue. This longitudinal contraction and circumferential expansion would occur uniformly along the anastomosis with the clips acting as a stabilization point. In the reconstruction process, this would result in artificially large cross-sectional diameters and consequently, artificially decreased WSS values. These decreased WSS values would be uniform along the anastomosis and would results in a decrease in the average hemodynamic values for the entire anastomosis. Therefore, any error associated with circumferential expansion would be accounted for in the normalization of hemodynamic parameters since the values at each region are normalized by the average value in the experiment.

For the reconstruction process, we chose to assume that the cross-sections were symmetric ellipses. We believe that this assumption is reasonable since we used healthy arterial segments that did not have luminal pathologies (e.g., asymmetric plaque) and the experimental apparatus held the anastomoses in a plane of symmetry. This assumption could be a limitation since the full three dimensional surface was not incorporated into the models. However, other studies have shown that incorporating this level of detail into the model may actually cause more errors than avoid them. For instance, Moore *et al.* developed six models

of a single human femoral-popliteal ETS bypass graft with varying degrees of detail in order to determine the complexity needed to faithfully reconstruct patient-specific geometries [99]. The most detailed model (Model 1) was based on smoothed contours obtained from computerized tomography (CT) images. The first simplification they made (Model 2) was to fit ellipses to the contours obtained from the CT images. The next level of simplification was to develop Model 3 which used circular cross-sections of constant diameter. In Model 4, the out-of-plane curvature was removed and in Model 5 the graft and host artery diameters were set equal. Model 6 consisted of a completely idealized intersection of two intersecting uniform cylinders. The largest differences in hemodynamic parameters occurred for models 4-6 as compared to model 1. Little variation in WSS was observed for model 3 (circular cross-sections) and even less occurred for Model 2 (ellipse cross-sections) as compared to model 1. They concluded that the most important feature required for accurate representation for ETS anastomoses is the ratio between the graft and host artery diameters, while the local arterial caliber and out-of-plane geometry were of secondary importance and the small-scale surface topology was least critical. We performed a similar sensitivity analysis by creating three models each for three separate experiments: one using asymmetric ellipses, one using symmetric ellipses and the third using circular cross-sections (see Section 4.2.2). Because the overall goal of this research was to determine if a correlation exists between the biologic and hemodynamic data, we determined if the different computational models resulted in a correlation that would lead to a different conclusion about the relative importance of a biologic or hemodynamic parameter. The results of these sensitivity analyses (see Section 4.3.4) showed that the use of the asymmetric or symmetric ellipse did not significantly affect the correlation between the biologic and hemodynamic data although there was a difference between these models and the circular cross-section reconstructions. Therefore, we chose the symmetric ellipse cross-section because it allowed us to take advantage computationally of the geometric symmetry without over-generalizing the shape of the cross-section.

To determine the mesh density needed for our simulations, we performed a mesh independence study by creating four grids for one model each for the ETS zero flow case, ETS retrograde flow case and the ETE

case (see Sections 3.2.3 and 3.3.1). Ideally, it would be best to perform this same type of study for each of the 20 reconstructions. However, this was not feasible due to the computational time required to solve the highest density mesh (approximately 1 week). Because similar mesh densities were found to be ideal for the three models (ETS zero flow, ETS retrograde flow and ETE) that we studied, we believe that this mesh density is adequate for all models.

3.5 Conclusion

We have developed three-dimensional reconstructions and CFD models of the ETS and ETE anastomoses perfused *ex vivo* in the accompanying experimental study (Chapter 2). From these models, we have determined that a regional variation of hemodynamic parameters, most notably axial WSS and the magnitudes of WSS and WSSG, exist in these anastomoses. Although a number of other studies have alluded to this regional variation of hemodynamic parameters, particularly in ETS anastomoses, to our knowledge this is the first study to quantify these parameters in varying regions along the anastomoses and illustrate that these differences are statistically significant.

The regions with the most hemodynamic parameters that were significantly different from other regions of interest were the ETS proximal, distal, toe and heel segments. These regions, particularly the toe and heel, have previously been shown to be prone to IH formation. In addition, the hemodynamic parameters which varied significantly in these regions, particularly the WSS magnitude, have been implicated in IH formation. Therefore, a correlation between the biologic response of these regions due to the hemodynamic parameters present in these regions may exist and will be explored in the next chapter.

4 .0 CORRELATION BETWEEN BIOLOGICAL DATA AND HEMODYNAMIC PARAMETERS

4.1 Introduction

Although a number of previous studies have attempted to determine the role of hemodynamics in intimal hyperplasia formation, a quantitative correlation between a specific hemodynamic parameter and a particular cellular response leading to intimal thickening has not been established. There are a number of reasons why a single hemodynamic predictor of IH has not yet been determined. Most importantly, many of the previous studies have not obtained directly-coupled biologic and hemodynamic data. Most studies focused on either a detailed analysis of the formation of IH or the hemodynamic environment, and then made a qualitative comparison to the other. For example, studies have determined that IH in animal and human ETS anastomoses occurs preferentially in the heel, toe and floor regions, but there were no quantitative measurements of hemodynamic parameters in these studies [18, 68, 69, 77, 170, 171]. Idealized and geometrically realistic physical flow [78, 82, 83] and computational models [86, 87, 89-91, 154] have shown that the flow field in an ETS anastomosis is complex and causes variations of WSS and WSSG along the anastomosis. In particular, the regions of low WSS, oscillating WSS and high spatial and temporal gradients of WSS occurred in the same general regions (i.e. heel, toe, floor) that IH forms, however these models did not have any direct, quantitative, biological data.

Although some studies do obtain directly-coupled biologic and hemodynamic data, the correlation between the data may not be valid. For example, developments in ultrasound technology allow for the simultaneous, noninvasive measurement of intimal thickness and WSS. Studies that have used this technology to determine the relationship between IH and WSS in human carotid arteries have found that intimal thickness is increased in regions of lower WSS [172, 173]. However, the hemodynamic data is not strictly appropriate because the hemodynamic measurements were made after the formation of disease and therefore do not necessarily indicate the hemodynamic conditions that caused the disease. Instead, they are the resulting hemodynamics due to IH formation and do not have predictive value. Similarly, the

hemodynamic measurements in casts of human tissue obtained at autopsy are not necessarily predictive of disease formation [65, 66, 84] .

Another limitation of previous studies with coupled biologic and hemodynamic data is that the hemodynamic parameters are not rigorously regulated throughout the experiment. For example, *in vivo* animal models allow for the measurement of hemodynamic parameters and IH formation in ETE and ETS anastomoses [79, 164, 174-176]. However, the formation of IH takes days, weeks or months during which time it is impossible to regulate the hemodynamics. In these studies, the hemodynamics are only measured at a single time point, usually at the time of graft insertion while the animal is under anesthesia. Therefore, the hemodynamic parameters are measured at a snapshot in time and there is no information about how these change during the course of the study as the animal recovers from surgery and becomes active. Additionally, even if these studies were able to continuously measure the hemodynamics, they would still be changing over time and correlations would require the use of averaged hemodynamic data.

Ex vivo models allow for the collection of directly-coupled biologic and hemodynamic data while also providing a well-controlled hemodynamic environment that remains constant over the duration of the study. Additionally, they allow for the perfusion of intact vascular segments, an improvement over cell culture studies that do not incorporate the effect of the multi-cellular and matrix environment present in the vasculature. Although previous *ex vivo* perfusion studies of vascular graft tissue have been completed, they did not isolate the effect of hemodynamics in ETS anastomoses. For example, most *ex vivo* perfusion studies related to bypass grafts have documented the pathologic changes in saphenous vein segments exposed to arterial levels of pressure and flow [72, 148-150]. Therefore the cause of the observed biologic alterations can not be isolated to just hemodynamics. Some studies have separated the effects of pressure and flow on vein grafts but have not incorporated the complex geometry and resulting hemodynamics in ETS bypass grafts [142, 145, 177]. The only *ex vivo* study of bypass graft anastomoses found in the literature did not perfuse the anastomoses [178]. The ETS anastomoses were simply incubated under standard cell culture conditions and, therefore, this study did not elicit any hemodynamic data.

Due to the limitations of previous studies, it was necessary to develop a novel study that allows for the collection of directly-coupled, quantitative biologic and hemodynamic data where the hemodynamics are well-controlled over time. We have developed a coupled approach involving the *ex vivo* perfusion of ETE and ETS vascular constructs (to obtain quantitative biologic data) and the reconstruction of the flow field in these anastomoses using computational fluid dynamics (to obtain quantitative hemodynamic data). Because the experiments were performed with an *ex vivo* perfusion system, the hemodynamic parameters were well-controlled throughout the experiment and could be directly correlated with the resulting biologic response measured at the end of the experiment. Because the anastomoses consisted of artery-artery junctions, there was no compliance mismatch and the pressure conditions used were in the physiologic range for porcine femoral arteries. Therefore the hemodynamics within the anastomoses was the only variable. This allowed us to determine if a specific biologic response related to IH (i.e., either c-fos, c-jun, egr-1 protein expression or apoptosis) correlated with a. particular hemodynamic parameter (i.e., either axial, circumferential components or magnitude of WSS or WSSG).

4.2 Methods

4.2.1 Regression and Statistics

To determine if a correlation existed between any biologic endpoint (c-fos, c-jun, egr-1 protein expression and apoptosis) and any hemodynamic parameter (axial and circumferential components and magnitude of WSS and WSSG), linear regression was performed and the Pearson correlation coefficient, r, was calculated as:

$$r = \frac{L_{xy}}{\sqrt{L_{xx}L_{yy}}} = \frac{\sum (x_i - \bar{x})(y_i - \bar{y})}{\sqrt{\sum (x_i - \bar{x})^2 \sum (y_i - \bar{y})^2}} \qquad [4.1]$$

where L_{xx} and L_{yy} are the corrected sum of squares for x and y, L_{xy} is the corrected sum of cross products, x_i are the hemodynamic parameter values, y_i are the corresponding biologic parameter values and $\bar{x}$ and $\bar{y}$

are the mean values of the hemodynamic and biologic parameters, respectively [157]. The Pearson correlation coefficient is a quantitative measure of whether or not there is a relationship between two variables. Specifically, $-1 < r < 1$ such that a negative value of r indicates a negative correlation and a positive value of r indicates a positive correlation [157]. To determine if the correlation between two variables was significant, a one-sample t-test was performed where t is calculated as:

$$t = \frac{r\sqrt{n-2}}{\sqrt{1-r^2}} \qquad [4.2]$$

where n is the number of data points and (n-2) are the degrees of freedom. A correlation is considered significant if the t value is greater than or equal to the t distribution value for the given degrees of freedom and for the desired p level. For example, the t distribution value for 7 degrees of freedom (n=9) and $p < 0.05$ is 2.365 [157].

Linear regression was performed on the raw biologic data and hemodynamic data for all regions of interest for each set of experiments (zero or retrograde flow). For these analyses, the correlation was based on a total of 45 data points (5 experiments, 9 regions of interest because the nonperfused segment was not included) and the correlation was significant ($p < 0.05$) if $t \geq 2.021$. Similarly, linear regression was performed on the pooled data from both sets of flow conditions. For these analyses, the correlation was based on a total of 90 data points (10 experiments, 9 regions of interest) and the correlation was significant ($p < 0.05$) if $t \geq 2.000$.

Linear regression was also performed on the normalized biologic and hemodynamic data (and absolute values of the normalized data) for all regions of interest for each set of experiments (zero or retrograde flow). This correlation is more relevant than using the raw data since the data from a number of experiments are used for linear regression and normalization accounts for the experiment to experiment variation in biologic and hemodynamic parameters. For these analyses, the t-distribution values were the same as above for the raw data correlations.

Nonlinear regression analysis was also performed on the normalized biologic and hemodynamic data for the pooled data from all experiments. The following nonlinear models were used to investigate functional relationships:

$$\begin{aligned}
&\textit{Reciprocal}: && y = a + \frac{b}{x} \\
&\textit{Reciprocal}\,(\textit{Absolute Value}): && y = a + \frac{b}{|x|} \\
&\textit{Exponential}: && y = a e^{bx} \\
&\textit{Exponential}\,(\textit{Absolute Value}): && y = a e^{b|x|} \\
&\textit{Power}\,(\textit{Absolute Value}): && y = a|x|^{b} \\
&\textit{Logarithmic}\,(\textit{Absolute Value}): && y = a + b\log(|x|)
\end{aligned} \qquad [4.3]$$

where x and y are the values of the biologic (y) and hemodynamic (x) parameter sets for each region of interest and a and b are parameters determined from the regression analysis. These functions were transformed into their linear counterparts so that linear regression analysis could be applied [179]. The transformed data (x' and y' values) were calculated from the original data (x and y values) as follows:

$$\begin{aligned}
&\textit{Reciprocal}: && x' = \frac{1}{x},\ y' = y \\
&\textit{Reciprocal}\,(\textit{Absolute Value}): && x' = \frac{1}{|x|},\ y' = y \\
&\textit{Exponential}: && x' = x,\ y' = \ln(y) \\
&\textit{Exponential}\,(\textit{Absolute Value}): && x' = |x|,\ y' = \ln(y) \\
&\textit{Power}\,(\textit{Absolute Value}): && x' = \log(|x|),\ y' = \log(y) \\
&\textit{Logarithmic}\,(\textit{Absolute Value}): && x' = \ln(|x|),\ y' = y
\end{aligned} \qquad [4.4]$$

which resulted in corresponding linear regression models:

$$
\begin{aligned}
&\textit{Reciprocal}: && y' = a + bx' \\
&\textit{Reciprocal}(\textit{Absolute Value}): && y' = a + bx' \\
&\textit{Exponential}: && y' = \ln(a) + bx' \\
&\textit{Exponential}(\textit{Absolute Value}): && y' = \ln(a) + bx' \\
&\textit{Power}(\textit{Absolute Value}): && y' = \log(a) + bx' \\
&\textit{Logarithmic}(\textit{Absolute Value}): && y' = a + bx'
\end{aligned}
\qquad [4.5]
$$

Therefore, the transformed, normalized data for c-fos, c-jun, egr-1 and EC and SMC apoptosis at each region of interest were correlated with the transformed, normalized data for the axial, circumferential and magnitudes of WSS and WSSG for the same region of interest using each of the above regression models. For the reciprocal and exponential regression models, both the normalized data and absolute values of the normalized data were transformed. This could not be done for the power and logarithmic models since they necessarily require positive values for the linear transformation. The Pearson correlation coefficient, r, and t-test parameter were calculated in the same manner as shown in Equations 4.1 and 4.2 except that transformed data (x' and y') were used instead of the original data (x and y). Note that the goodness of fit parameter, R^2, for the nonlinear models is equal to the square of the Pearson correlation coefficient, r^2, for the transformed models due to the linear transformation procedure [179].

4.2.2 Sensitivity Analysis

To determine the sensitivity of the correlation results to the three dimensional reconstruction technique, the following technique was used as depicted in the flowchart in Figure 4.1. First, the geometry of an ETS anastomosis was reconstructed using three different cross-sectional shapes. The symmetric ellipse model used for the above correlations was compared to a more complex, asymmetric ellipse model and a more simple model constructed from circular cross-sections. The asymmetric ellipse reconstructions used the same elliptical cross-sections as the symmetric cross-section technique, however the orientation of the cross-sections were taken directly from the digitized data and not rotated to the 0 or 90° axis which was done for

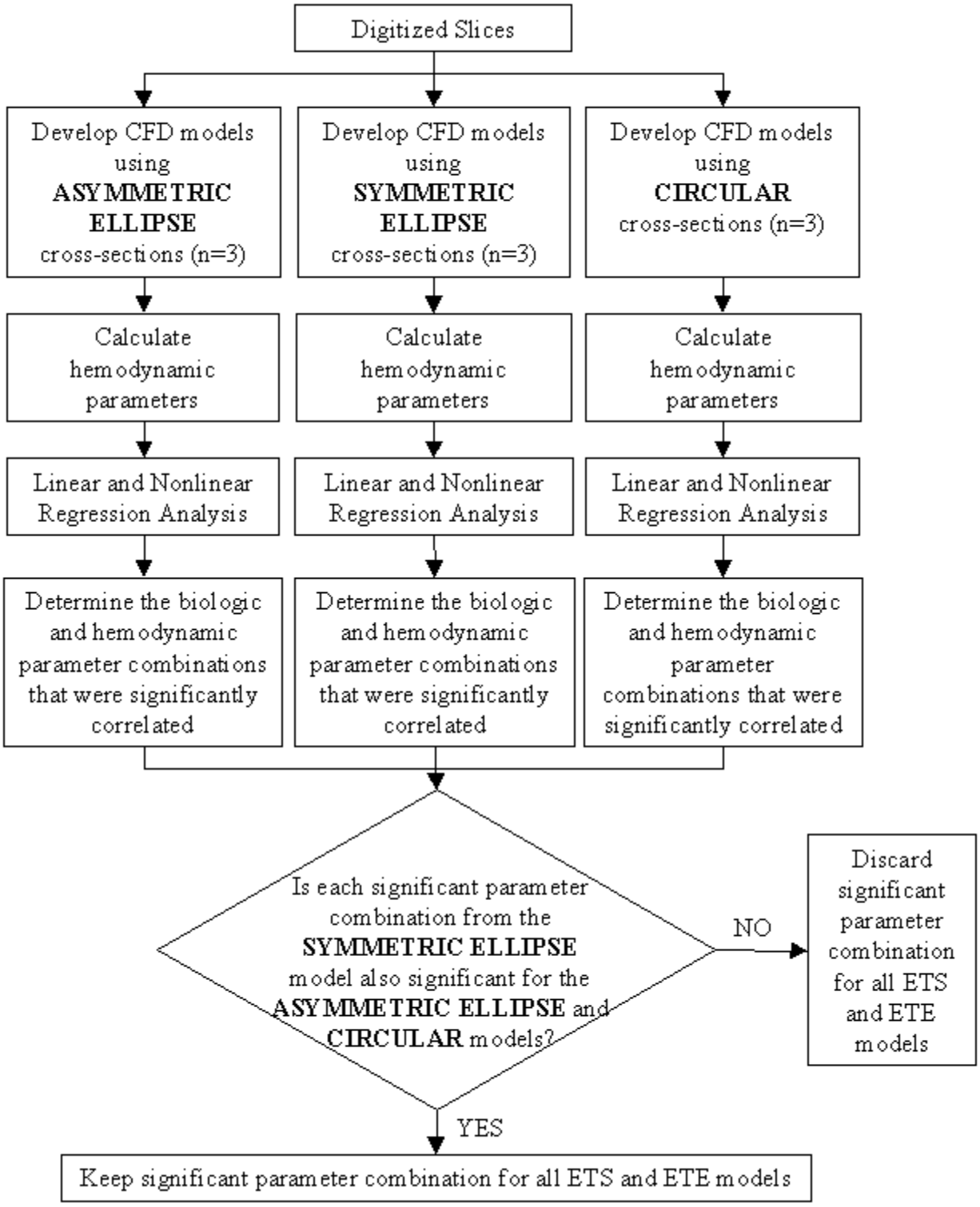

Figure 4.1 Flowchart depicting the sensitivity analysis procedure.

the symmetric ellipse models (see Section 3.2.1.2). The circular cross-section reconstructions used a best fit circle instead of a ellipse to represent each cross-section. The subsequent surface creation, meshing, solving and post-processing procedures were identical to those described for the symmetric ellipse models (see Sections 3.2.1 - 3.2.6). The only difference was that the asymmetric ellipse models could not take the advantage of symmetry so the entire volume had to be reconstructed and meshed. Twice as many cells were used to mesh the asymmetric model in order to maintain the same cell density as the symmetric ellipse and circular models. The multiple reconstruction techniques were repeated for three separate (zero flow) experiments and the normalized hemodynamic parameters were calculated for each anastomosis model. Linear and nonlinear regression were performed using the normalized biologic parameters. This yielded three sets of correlation coefficients, one for each reconstruction technique. The linear and nonlinear regressions for each reconstruction type were based on a total of 21 data points (3 experiments, 7 regions of interest because the ETE regions of interest were not included) and the correlation was significant ($p < 0.05$) if $t \geq 2.093$. The parameter combinations (e.g., c-fos and axial WSS) found to be significant for each reconstruction technique were compared to confirm that the symmetric ellipse technique would not result in a false positive correlation. Any parameter combination that resulted in a significant correlation for the symmetric model but not for the asymmetric and/or circular models was eliminated for the final analysis of the data from all of the symmetric models.

4.3 Results

4.3.1 Raw Data - Linear Regression

Table 4.1 shows the correlation coefficient value (r) from the linear regression analysis on the raw biologic and hemodynamic data for each set of experiments (zero and retrograde) and for the pooled data from all experiments. Significant correlations ($p < 0.05$) are highlighted in grey. Graphs of the data that exhibited a significant correlation ($p < 0.05$) between the raw biologic and hemodynamic parameters for the zero flow, retrograde flow and all experiments are shown in Figures 4.2 , 4.3 and 4.4, respectively.

Table 4.1 Correlation coefficient (r) values for the raw data parameter combinations for the zero flow, retrograde flow and for the data from all experiments pooled together. Significant correlations ($p < 0.05$) are highlighted in grey.

ZERO FLOW	CFOS	CJUN	EGR1	EC APOPTOSIS	SMC APOPTOSIS
Axial WSS	0.12	-0.17	-0.20	-0.12	-0.07
Circ WSS	0.13	0.15	-0.08	0.09	0.14
WSS Mag	-0.05	-0.20	-0.06	-0.20	-0.18
Axial WSSG	-0.01	-0.14	-0.06	-0.28	-0.22
Circ WSSG	0.03	-0.12	-0.14	0.10	0.33
WSSG Mag	-0.12	-0.27	-0.05	-0.19	-0.14
RETROGRADE FLOW	CFOS	CJUN	EGR1	EC APOPTOSIS	SMC APOPTOSIS
Axial WSS	0.13	-0.25	-0.16	0.03	0.04
Circ WSS	0.09	0.21	0.04	-0.11	-0.10
WSS Mag	-0.07	-0.40	-0.09	0.14	0.02
Axial WSSG	-0.04	0.14	0.01	-0.19	-0.19
Circ WSSG	0.04	0.04	-0.03	-0.08	0.19
WSSG Mag	-0.01	-0.31	-0.08	0.16	0.05
ALL EXPERIMENTS	CFOS	CJUN	EGR1	EC APOPTOSIS	SMC APOPTOSIS
Axial WSS	-0.05	-0.18	-0.15	-0.19	-0.05
Circ WSS	0.16	0.14	-0.03	0.10	0.10
WSS Mag	-0.18	-0.22	-0.05	-0.21	-0.14
Axial WSSG	-0.07	-0.07	-0.03	-0.22	-0.21
Circ WSSG	0.04	-0.07	-0.08	0.03	0.28
WSSG Mag	-0.21	-0.25	-0.04	-0.20	-0.10

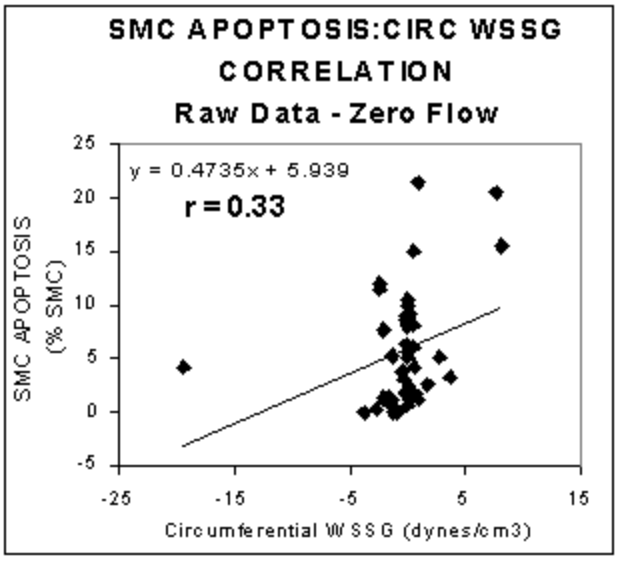

Figure 4.2 Plot showing the only significant correlation ($p < 0.05$) for the raw data from the zero flow experiments.

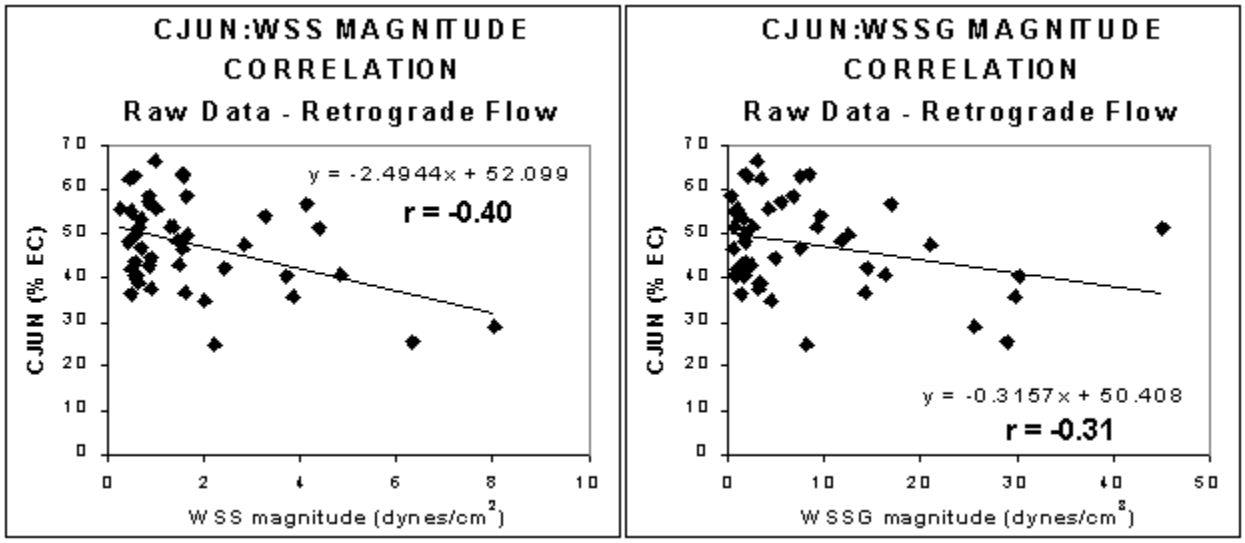

Figure 4.3 Plots showing the linear regression for biologic and hemodynamic parameter combinations with significant ($p < 0.05$) correlation coefficients (r) for the raw data from the retrograde flow experiments.

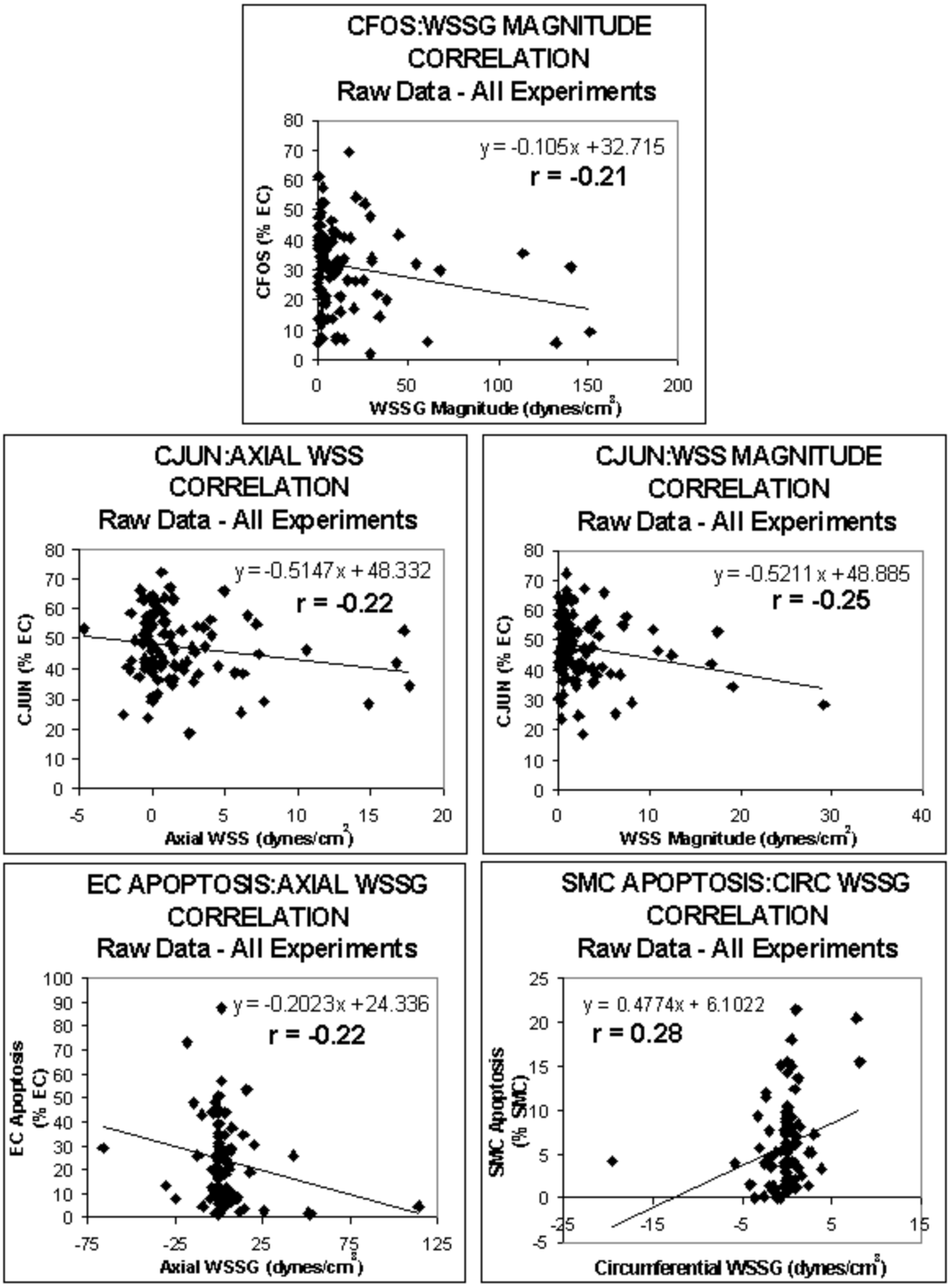

Figure 4.4 Plots showing the linear regression for biologic and hemodynamic parameter combinations with significant ($p < 0.05$) correlation coefficients (r) for the raw, pooled data from all experiments.

For the zero flow experiments, only one combination of parameters had a significant correlation as shown in Figure 4.2. The level of SMC apoptosis was positively correlated with circumferential WSSG ($r = 0.33$, $p = 0.028$). For the retrograde flow experiments, two combinations of parameters yielded a significant correlation as shown in Figure 4.3. The level of EC c-jun protein expression was inversely correlated with the magnitude of WSS ($r = -0.40$, $p = 0.006$) and WSSG ($r = -0.31$, $p = 0.040$). When the data from all experiments were pooled together, a large number of significant correlations were found as shown in Figure 4.4. The level of EC c-fos protein expression correlated inversely with the magnitude of WSSG ($r = -0.21$, $p = 0.045$). The level of EC c-jun protein expression was inversely correlated with the magnitude of WSS ($r = -0.22$, $p = 0.040$) and WSSG ($r = -0.25$, $p = 0.017$). The level of EC apoptosis was inversely correlated with axial WSSG ($r = -0.22$, $p = 0.036$) and the level of SMC apoptosis was positively correlated with circumferential WSSG ($r = 0.28$, $p = 0.007$). The level of egr-1 protein was the only biologic parameter to not have a significant correlation with any hemodynamic parameter for any of the analyses.

4.3.2 Normalized Data - Linear Regression

Table 4.2 shows the correlation coefficient value (r) from the linear regression analysis on the normalized biologic and hemodynamic data for each set of experiments (zero and retrograde) and for the pooled data from all experiments. Significant correlations ($p < 0.05$) are highlighted in grey. Graphs of the data that exhibited a significant correlation ($p < 0.05$) between the normalized biologic and hemodynamic parameters for the zero flow, retrograde flow and all experiments are shown in Figures 4.5, 4.6 and 4.7, respectively.

For the zero flow experiments, four combinations of parameters had significant correlations as shown in Figure 4.5. The level of EC c-fos protein expression was inversely correlated with the magnitude of WSS ($r = -0.31$, $p = 0.036$) and WSSG ($r = -0.41$, $p = 0.005$). The level of EC egr-1 protein expression was positively correlated with circumferential WSS ($r = 0.38$, $p = 0.010$) and the degree of SMC apoptosis was positively correlated with circumferential WSSG ($r = 0.31$, $p = 0.036$). For the retrograde flow experiments, the only biologic parameter with a significant hemodynamic correlation was egr-1 as shown in Figure 4.6.

Table 4.2 Correlation coefficient (r) values for the normalized data parameter combinations for the zero flow, retrograde flow and for the data from all experiments pooled together. Significant correlations ($p < 0.05$) are highlighted in grey.

ZERO FLOW	CFOS	CJUN	EGR1	EC APOPTOSIS	SMC APOPTOSIS
Axial WSS	-0.18	-0.11	0.00	-0.08	-0.04
Circ WSS	-0.10	0.15	0.38	-0.03	-0.01
WSS Mag	-0.31	-0.11	0.17	-0.10	-0.04
Axial WSSG	0.12	-0.01	-0.10	0.19	0.25
Circ WSSG	-0.20	-0.24	-0.14	0.21	0.31
WSSG Mag	-0.41	-0.25	0.21	0.05	0.16
RETROGRADE FLOW	CFOS	CJUN	EGR1	EC APOPTOSIS	SMC APOPTOSIS
Axial WSS	0.12	-0.18	-0.35	0.00	0.17
Circ WSS	0.02	-0.08	-0.27	-0.12	0.20
WSS Mag	-0.05	-0.23	-0.42	-0.18	0.09
Axial WSSG	0.18	-0.09	-0.15	0.10	0.18
Circ WSSG	0.13	-0.03	-0.01	-0.12	0.04
WSSG Mag	0.00	-0.19	-0.41	-0.12	0.16
ALL EXPERIMENTS	CFOS	CJUN	EGR1	EC APOPTOSIS	SMC APOPTOSIS
Axial WSS	-0.02	-0.14	-0.27	-0.03	0.08
Circ WSS	-0.06	0.06	0.03	-0.06	0.06
WSS Mag	-0.22	-0.16	-0.16	-0.12	0.01
Axial WSSG	0.13	-0.05	-0.14	0.12	0.18
Circ WSSG	0.02	-0.07	-0.03	0.00	0.09
WSSG Mag	-0.26	-0.22	-0.14	0.00	0.16

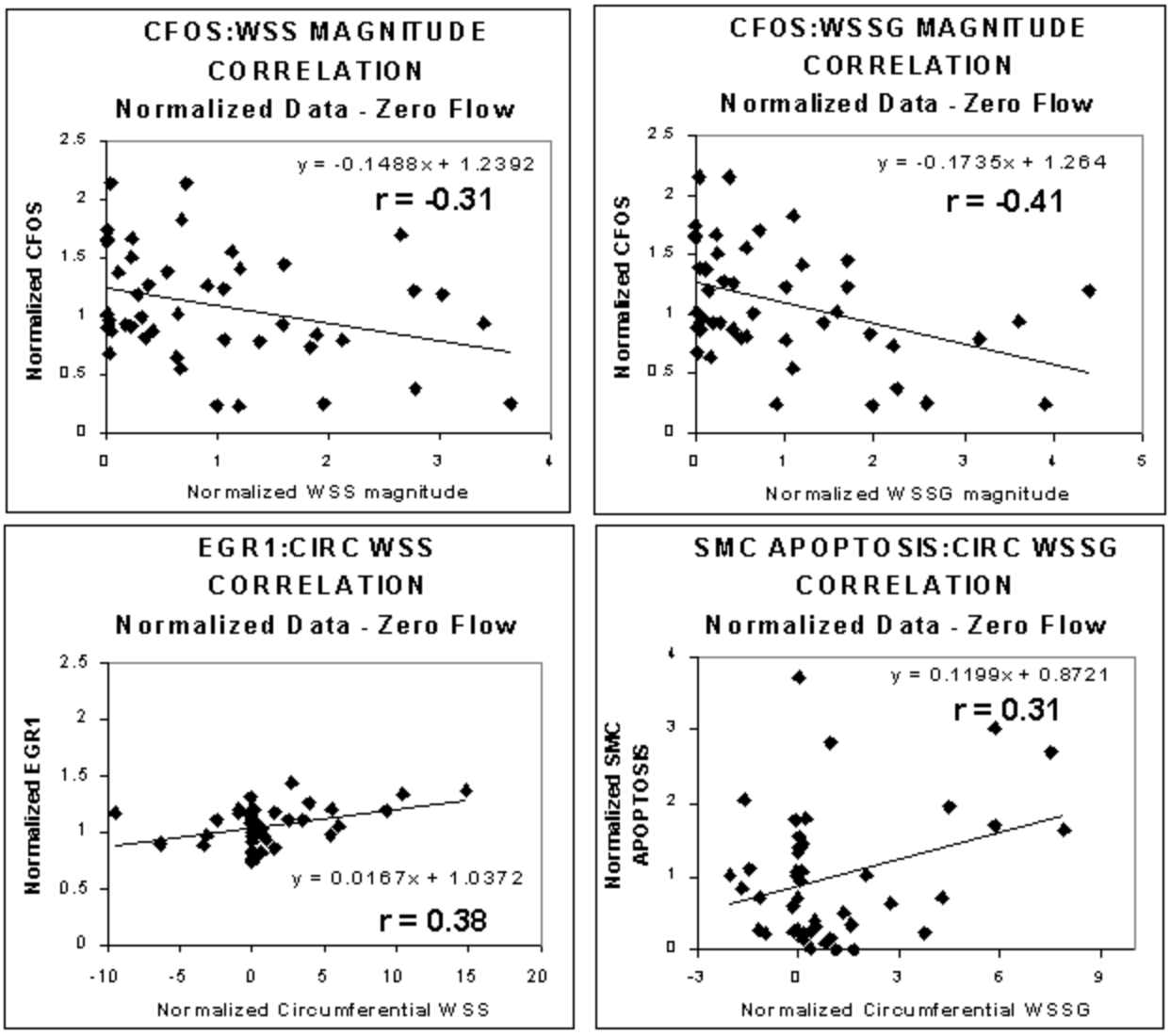

Figure 4.5 Plots showing the linear regression for biologic and hemodynamic parameter combinations with significant ($p < 0.05$) correlation coefficients (r) for the normalized data from the zero flow experiments.

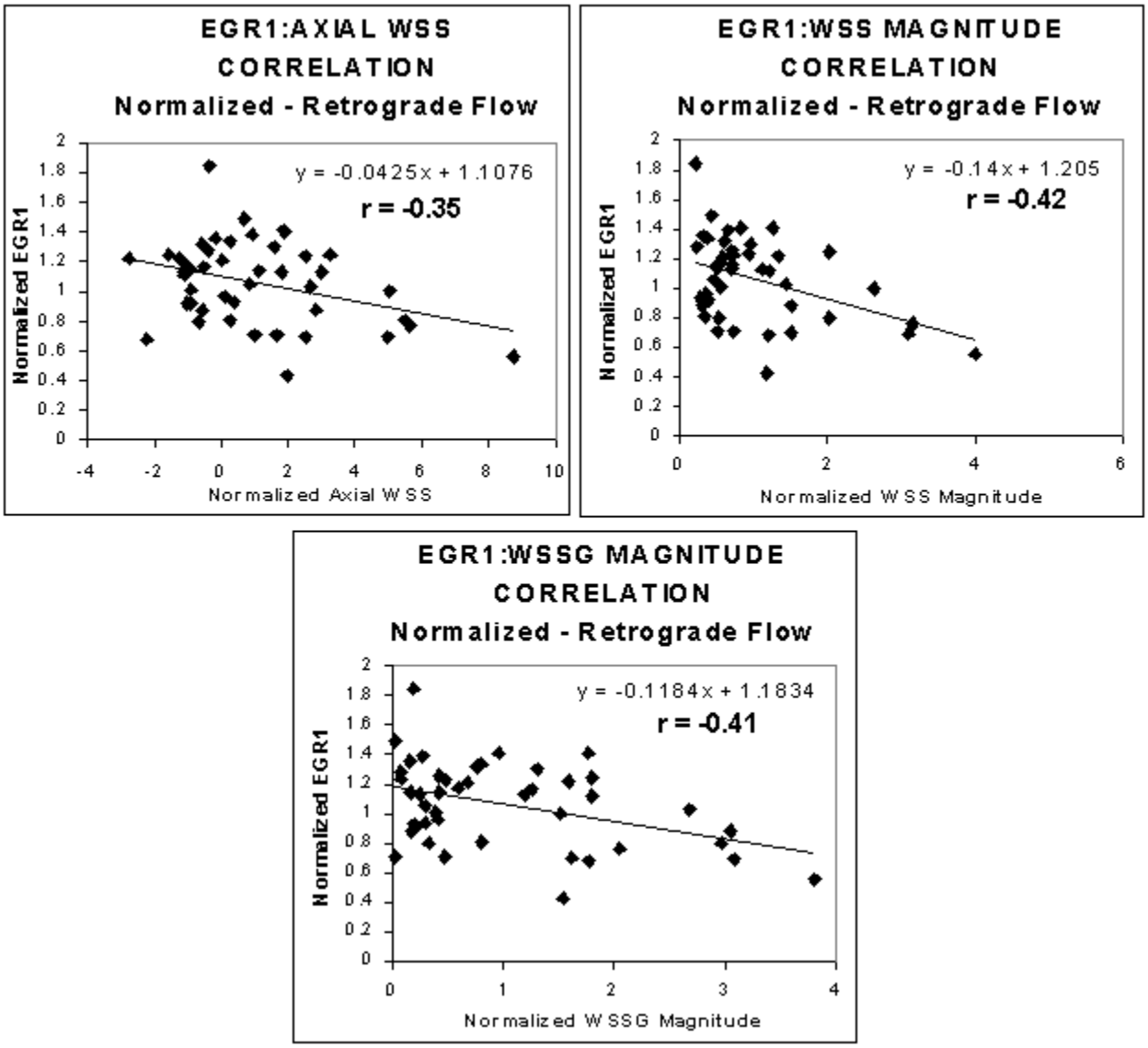

Figure 4.6 Plots showing the linear regression for biologic and hemodynamic parameter combinations with significant ($p < 0.05$) correlation coefficients (r) for the normalized data from the retrograde flow experiments.

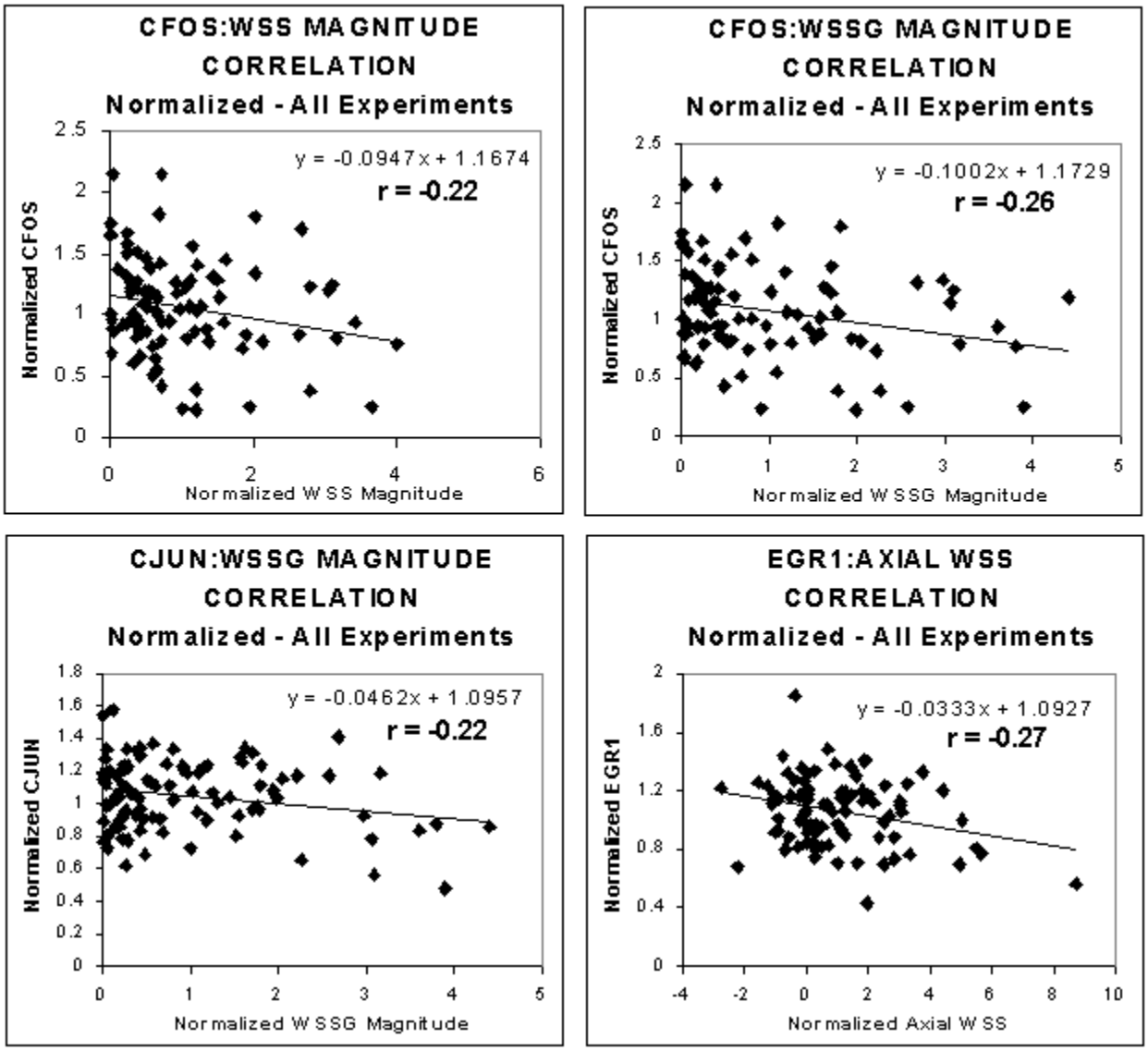

Figure 4.7 Plots showing the linear regression for biologic and hemodynamic parameter combinations with significant ($p < 0.05$) correlation coefficients (r) for the normalized data from the pooled data from all experiments.

The level of EC egr-1 protein expression was inversely correlated with axial WSS ($r = -0.35$, $p = 0.017$), the magnitude of WSS ($r = -0.42$, $p = 0.004$) and WSSG ($r = -0.41$, $p = 0.005$). When the data from all experiments were pooled together, four combinations of parameters had significant correlations as shown in Figure 4.7. The level of EC c-fos protein expression was inversely correlated with the magnitude of WSS ($r = -0.22$, $p = 0.037$) and WSSG ($r = -0.26$, $p = 0.012$). The level of EC c-jun protein expression was inversely correlated with WSSG magnitude ($r = -0.22$, $p = 0.034$). The level of EC egr-1 protein expression was inversely correlated with axial WSS ($r = -0.27$, $p = 0.011$). The degree of EC and SMC apoptosis did not have a significant correlation with a hemodynamic parameter.

Table 4.3 shows the correlation coefficient value (r) for the linear regression analysis on the normalized biologic data and the absolute value of the normalized hemodynamic data for each set of experiments (zero and retrograde) and for the pooled data from all experiments. Significant correlations ($p < 0.05$) are highlighted in grey. Graphs of the data that exhibited a significant correlation ($p < 0.05$) between the normalized biologic and hemodynamic parameters for the zero flow, retrograde flow and all experiments are shown in Figures 4.8, 4.9 and 4.10/4.11, respectively.

For the zero flow experiments, the same four combinations of parameters that had significant correlations for the original, normalized data (see Table 4.2) had significant correlations for the absolute value of the normalized data as shown in Figure 4.8. Because the absolute value of the magnitude parameters did not change, the level of EC c-fos protein expression had the same inverse correlation with the magnitude of WSS ($r = -0.31$, $p = 0.036$) and WSSG ($r = -0.41$, $p = 0.005$). The level of EC egr-1 protein expression was more strongly positively correlated with circumferential WSS ($r = 0.41$, $p = 0.005$) and the degree of SMC apoptosis was more strongly positively correlated with circumferential WSSG ($r = 0.35$, $p = 0.020$). For the retrograde flow experiments, the only biologic parameter with a significant hemodynamic correlation was egr-1 as shown in Figure 4.9. As seen for the original, normalized data, the level of EC egr-1 protein expression was inversely correlated with axial WSS ($r = -0.43$, $p = 0.003$), the magnitude of WSS ($r = -0.42$, $p = 0.004$) and WSSG ($r = -0.41$, $p = 0.005$). In addition, the level of EC egr-1 protein expression was

Table 4.3 Correlation coefficient (r) values for the absolute values of the normalized data parameter combinations for the zero flow, retrograde flow and for the data from all experiments pooled together. Significant correlations ($p < 0.05$) are highlighted in grey.

ZERO FLOW	CFOS	CJUN	EGR1	EC APOPTOSIS	SMC APOPTOSIS
Axial WSS	-0.24	-0.10	0.06	-0.10	-0.05
Circ WSS	-0.29	0.20	0.41	-0.09	0.05
WSS Mag	-0.31	-0.11	0.17	-0.10	-0.04
Axial WSSG	0.23	-0.04	0.06	-0.09	0.00
Circ WSSG	-0.23	-0.24	-0.01	0.23	0.35
WSSG Mag	-0.41	-0.25	0.21	0.05	0.16
RETROGRADE FLOW	CFOS	CJUN	EGR1	EC APOPTOSIS	SMC APOPTOSIS
Axial WSS	0.00	-0.22	-0.43	-0.20	0.08
Circ WSS	-0.23	-0.08	-0.15	-0.17	0.18
WSS Mag	-0.05	-0.23	-0.42	-0.18	0.09
Axial WSSG	0.08	-0.10	-0.33	0.13	0.23
Circ WSSG	-0.21	-0.03	-0.28	-0.28	-0.22
WSSG Mag	0.00	-0.19	-0.41	-0.12	0.16
ALL EXPERIMENTS	CFOS	CJUN	EGR1	EC APOPTOSIS	SMC APOPTOSIS
Axial WSS	-0.12	-0.15	-0.27	-0.12	0.02
Circ WSS	-0.27	-0.16	0.10	-0.11	0.09
WSS Mag	-0.22	-0.16	-0.16	-0.12	0.01
Axial WSSG	-0.06	-0.07	-0.23	0.03	0.12
Circ WSSG	-0.17	-0.07	-0.21	-0.06	-0.04
WSSG Mag	-0.26	-0.22	-0.14	0.00	0.16

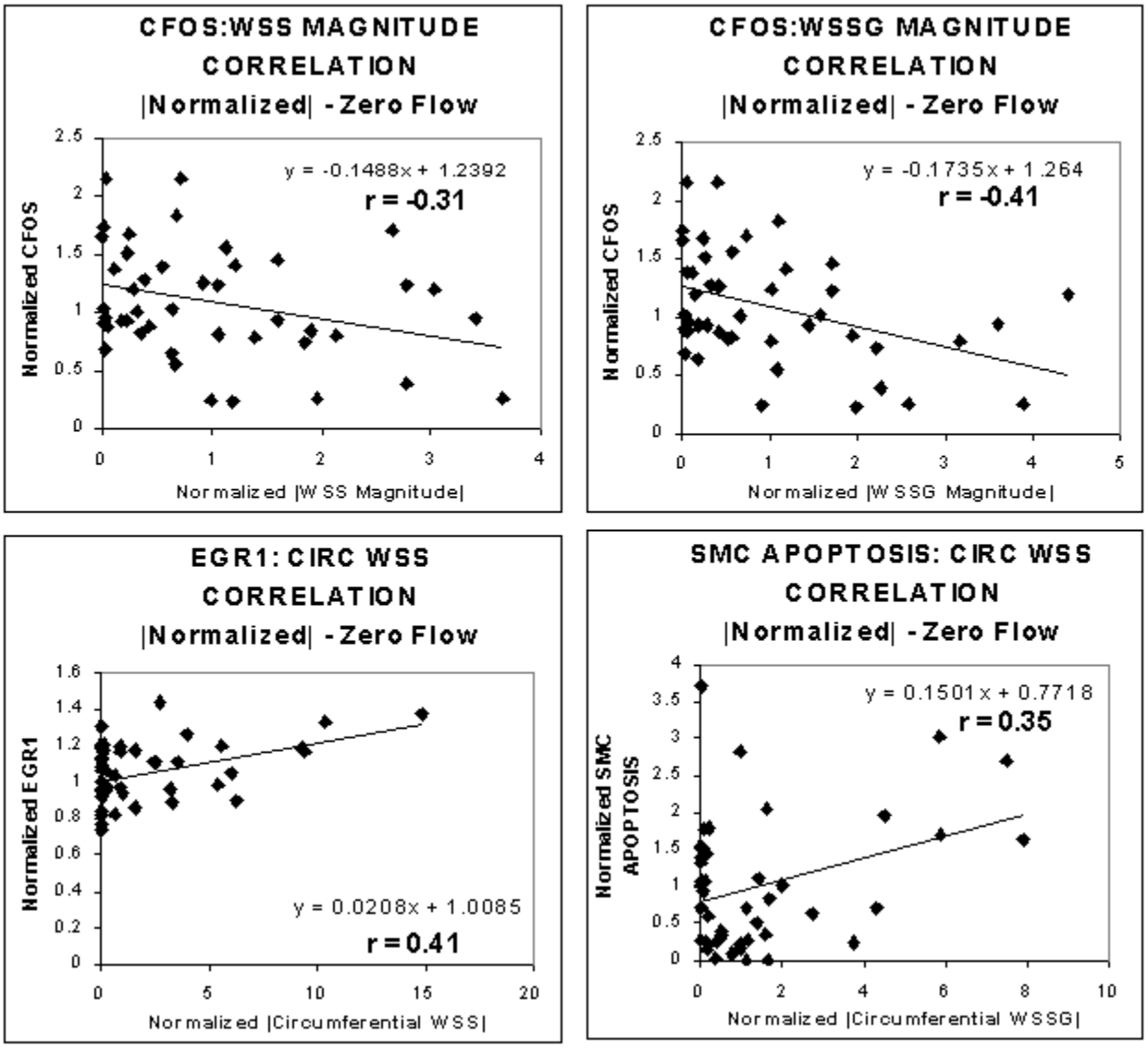

Figure 4.8 Plots showing the linear regression for biologic and hemodynamic parameter combinations with significant ($p < 0.05$) correlation coefficients (r) for the absolute value of the normalized data from the zero flow experiments.

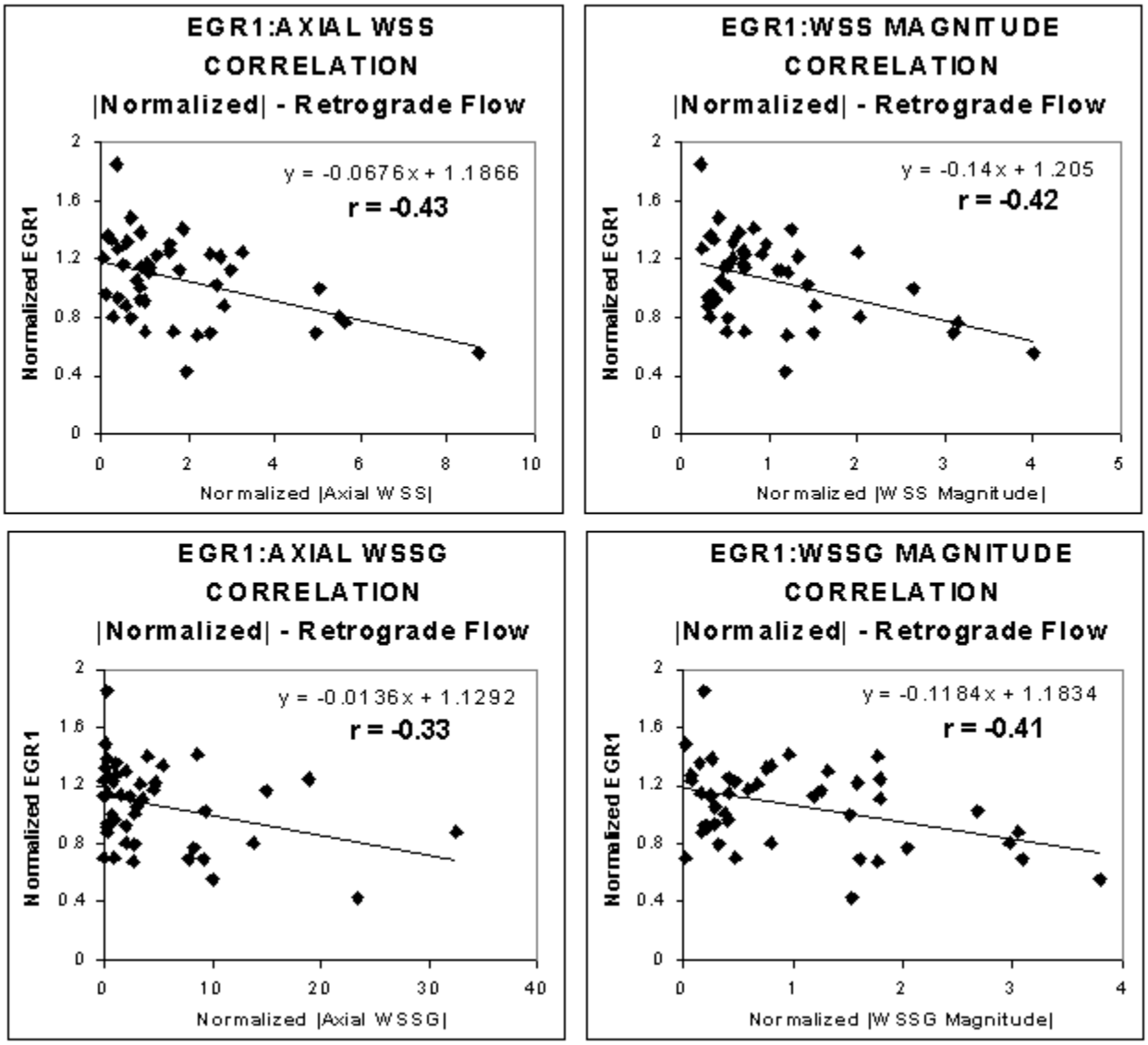

Figure 4.9 Plots showing the linear regression for biologic and hemodynamic parameter combinations with significant ($p < 0.05$) correlation coefficients (r) for the absolute value of the normalized data from the retrograde flow experiments.

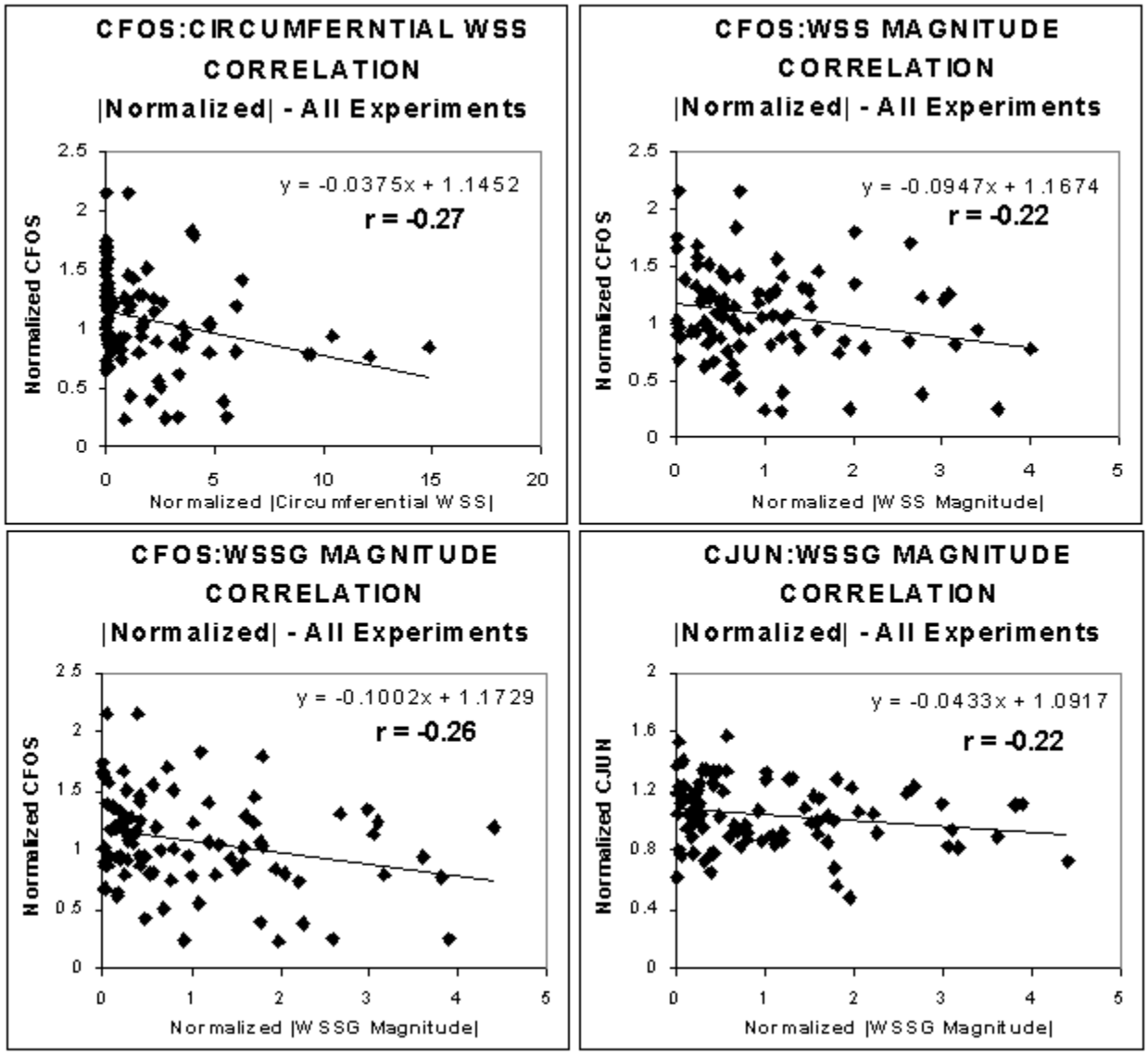

Figure 4.10 Plots showing the linear regression for biologic and hemodynamic parameter combinations with significant ($p < 0.05$) correlation coefficients (r) for the absolute value of the normalized data from the pooled data from all experiments. Note that only the graphs for c-fos and c-jun are shown in this figure. The graphs for egr-1 are shown in the following figure.

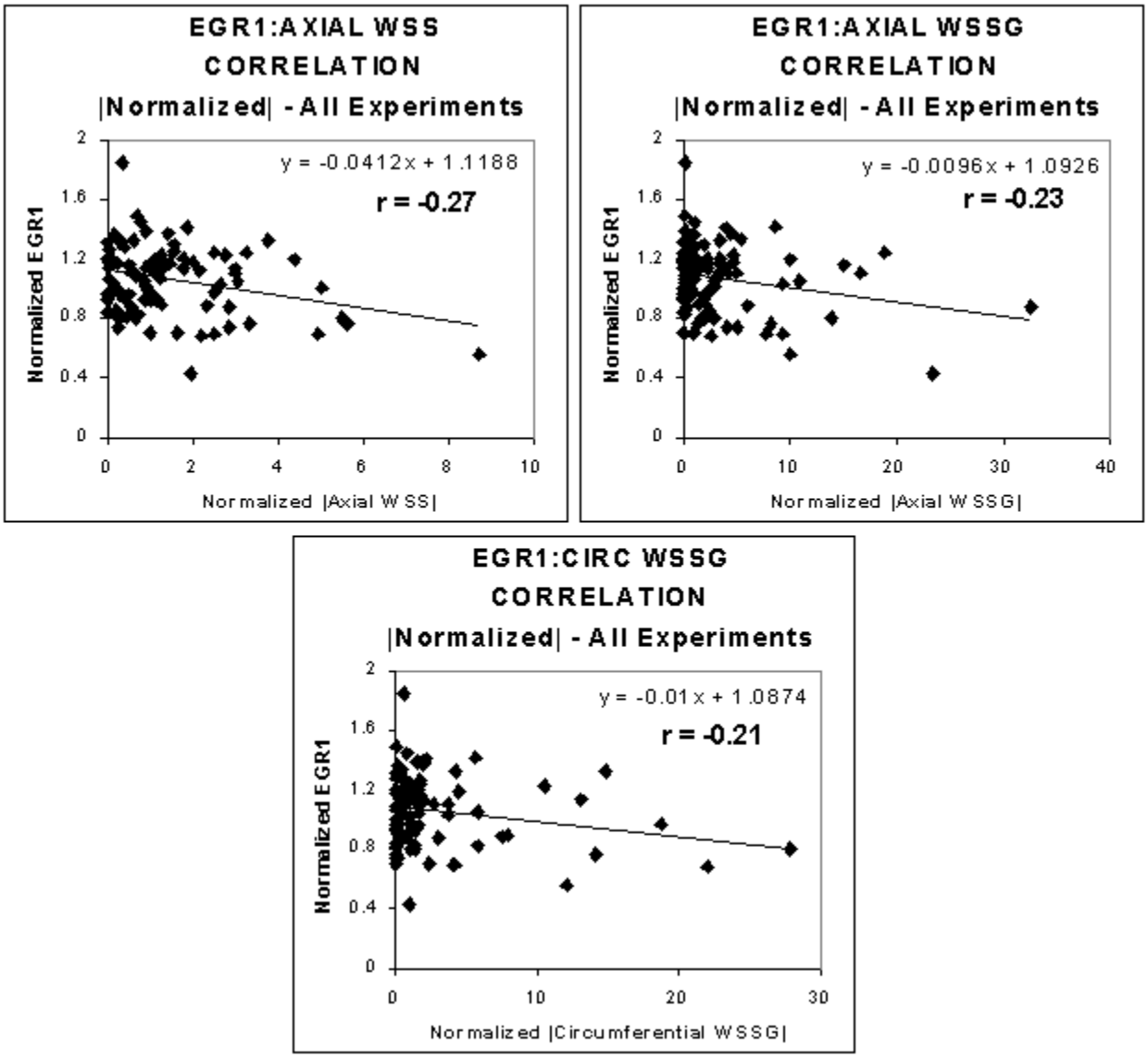

Figure 4.11 Plots showing the linear regression for biologic and hemodynamic parameter combinations with significant ($p < 0.05$) correlation coefficients (r) for the absolute value of the normalized data from the pooled data from all experiments. Note that only the graphs for egr-1 are shown in this figure. The graphs for c-fos and c-jun are shown in the previous figure.

inversely correlated with axial WSSG ($r = -0.33$, $p = 0.027$). When the data from all experiments were pooled together, seven combinations of parameters had significant correlations (as shown in Figures 4.10 and 4.11) compared to the four parameter combinations for the original, normalized data. The same four combinations had significant correlations including the level of EC c-fos protein expression with the magnitude of WSS ($r = -0.22$, $p = 0.037$) and WSSG ($r = -0.26$, $p = 0.012$), the level of EC c-jun protein expression with WSSG magnitude ($r = -0.22$, $p = 0.034$) and the level of EC egr-1 protein with axial WSS ($r = -0.27$, $p = 0.009$). In addition, the level of EC c-fos protein expression was inversely correlated with circumferential WSS ($r = -0.27$, $p = 0.010$) and the level of EC egr-1 protein was inversely correlated with axial WSSG ($r = -0.23$, $p = 0.032$) and circumferential WSSG ($r = -0.21$, $p = 0.042$). The degree of EC and SMC apoptosis did not have a significant correlation with a hemodynamic parameter.

4.3.3 Normalized Data - Nonlinear Regression

Table 4.4 shows the correlation coefficient value (r) for the reciprocal nonlinear regression analysis on the normalized biologic and hemodynamic data for the pooled data from all experiments. Tables 4.5, 4.6 and 4.7 show the correlation coefficient values (r) for the exponential, power and logarithmic nonlinear regression analyses on the same data. Significant correlations ($p < 0.05$) are highlighted in grey. Graphs of the data that exhibited a significant correlation ($p < 0.05$) between the normalized biologic and hemodynamic parameters for the reciprocal, reciprocal absolute value, exponential, exponential absolute value, power and logarithmic regression analyses are shown in Figures 4.12, 4.13, 4.14/4.15, 4.16/4.17/4.18, 4.19/4.20 and 4.21/4.22, respectively. The graphs in the left column of the figures show the regressions for the linearly transformed data and the graphs in the right column show the corresponding nonlinear regression.

For the reciprocal nonlinear regression model, three combinations of parameters had significant correlations for the original, normalized data and the absolute value of the normalized data as shown in Table 4.4 and Figures 4.12 and 4.13. Using the linear transformation of the reciprocal model, the level of EC c-fos protein expression was positively correlated with axial WSS ($r = 0.21$, $p = 0.045$) and the magnitude of WSS ($r = 0.21$, $p = 0.044$) and WSSG ($r = 0.23$, $p = 0.027$). Because the absolute value of the magnitude

Table 4.4 Correlation coefficient (r) values for the reciprocal nonlinear regression for the parameter combinations using the original, normalized data and the absolute value of the normalized data from all experiments. Significant correlations ($p < 0.05$) are highlighted in grey.

RECIPROCAL	CFOS	CJUN	EGR1	EC APOPTOSIS	SMC APOPTOSIS
Axial WSS	0.21	0.06	-0.10	-0.02	0.03
Circ WSS	0.04	0.09	-0.05	-0.08	-0.04
WSS Mag	0.21	0.08	-0.08	-0.01	0.03
Axial WSSG	-0.05	-0.15	-0.05	-0.07	-0.06
Circ WSSG	-0.17	-0.05	0.06	-0.02	-0.04
WSSG Mag	0.23	0.10	-0.09	-0.04	0.01
RECIPROCAL ABS VALUE	CFOS	CJUN	EGR1	EC APOPTOSIS	SMC APOPTOSIS
Axial WSS	0.21	0.06	-0.09	-0.02	0.03
Circ WSS	0.06	0.09	-0.07	-0.09	-0.04
WSS Mag	0.21	0.08	-0.08	-0.01	0.03
Axial WSSG	-0.05	-0.15	-0.05	-0.07	-0.06
Circ WSSG	0.18	0.06	-0.06	0.02	0.05
WSSG Mag	0.23	0.10	-0.09	-0.04	0.01

parameters did not change, using the absolute value of the data did not change the correlation coefficients for the parameter combinations with WSS and WSSG magnitude but the correlation coefficients did change for all other combinations. However, similar to the correlation using the original, normalized data, the level of EC c-fos protein expression was still positively correlated with axial WSS ($r = 0.21$, $p = 0.044$) and this was the only significant combination of parameters other than positive correlation between the level of EC c-fos protein expression with the magnitude of WSS ($r = 0.21$, $p = 0.044$) and WSSG ($r = 0.23$, $p = 0.027$).

For the exponential nonlinear regression model, there were a number of combinations of parameters that had significant correlations for the original, normalized data which were different from the significant parameter combinations for the absolute value of the normalized data as shown in Table 4.5 and Figures 4.14/4.15 and 4.16/4.17/4.18. Using the linear transformation of the exponential model, the level of EC c-fos protein expression was inversely correlated with the magnitude of WSS ($r = -0.25$, $p = 0.020$) and WSSG ($r = -0.29$, $p = 0.006$). The level of EC c-jun protein expression was also inversely correlated with the magnitude of WSSG ($r = -0.25$, $p = 0.018$). The level of EC egr-1 protein expression was inversely

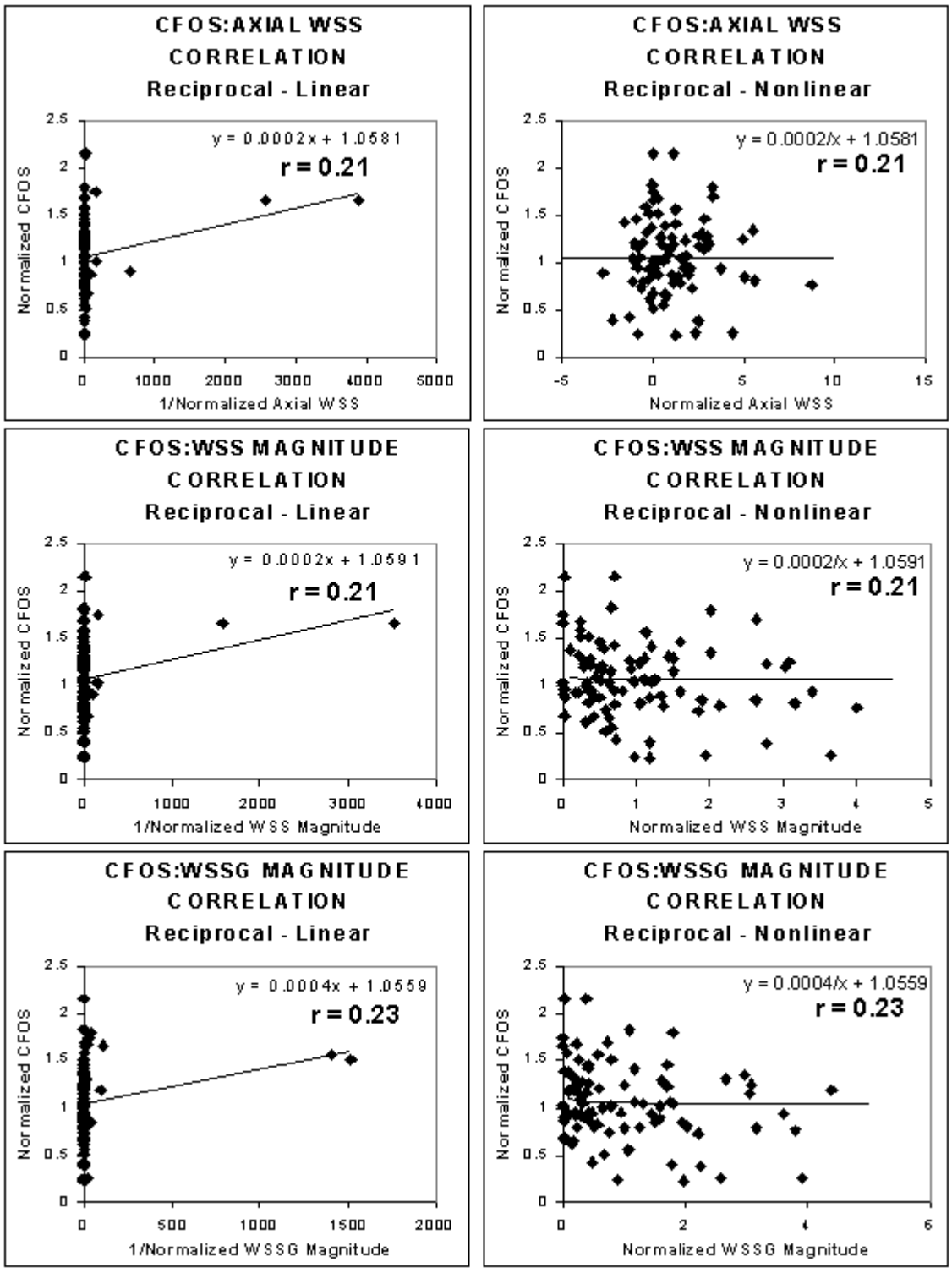

Figure 4.12 Plots showing the reciprocal regression for biologic and hemodynamic parameter combinations with significant ($p < 0.05$) correlation coefficients (r) for the normalized data from all experiments. The graphs in the left column show the linear regressions using the transformed data and the graphs in the right column show the corresponding nonlinear regressions.

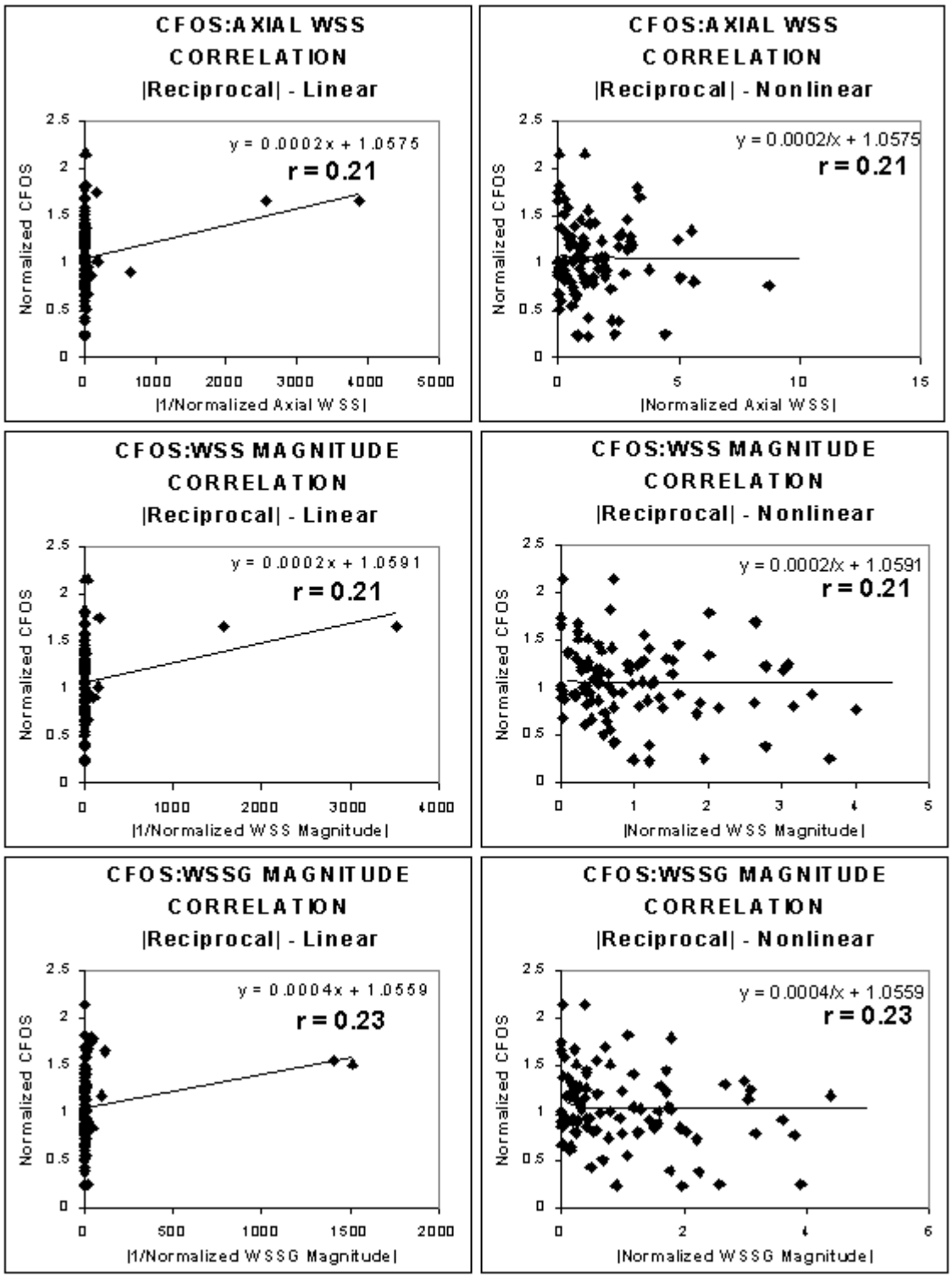

Figure 4.13 Plots showing the reciprocal nonlinear regression for biologic and hemodynamic parameter combinations with significant ($p < 0.05$) correlation coefficients (r) for the absolute value of the normalized data from all experiments. The graphs in the left column show the linear regressions using the transformed data and the graphs in the right column show the corresponding nonlinear regressions.

Table 4.5 Correlation coefficient (r) values for the exponential nonlinear regression for the parameter combinations using the original, normalized data and the absolute value of the normalized data from all experiments. Significant correlations ($p < 0.05$) are highlighted in grey.

EXPONENTIAL	CFOS	CJUN	EGR1	EC APOPTOSIS	SMC APOPTOSIS
Axial WSS	-0.02	-0.15	-0.29	-0.04	-0.11
Circ WSS	-0.05	0.08	0.01	-0.05	-0.12
WSS Mag	-0.25	-0.17	-0.18	-0.16	-0.27
Axial WSSG	0.13	-0.06	-0.17	0.12	0.18
Circ WSSG	0.03	-0.08	-0.04	0.02	0.04
WSSG Mag	-0.29	-0.25	-0.16	-0.05	-0.10
EXPONENTIAL ABS VALUE	CFOS	CJUN	EGR1	EC APOPTOSIS	SMC APOPTOSIS
Axial WSS	-0.12	-0.16	-0.31	-0.11	-0.13
Circ WSS	-0.25	-0.15	0.09	-0.09	-0.09
WSS Mag	-0.25	-0.17	-0.18	-0.16	-0.27
Axial WSSG	-0.03	-0.07	-0.27	0.04	0.02
Circ WSSG	-0.15	-0.06	-0.23	-0.02	0.00
WSSG Mag	-0.29	-0.25	-0.16	-0.05	-0.10

correlated with axial WSS ($r = -0.29$, $p = 0.005$) and the degree of SMC apoptosis was inversely correlated with WSS magnitude ($r = -0.27$, $p = 0.009$). Because the absolute value of the magnitude parameters did not change, the level of EC c-fos protein expression had the same inverse correlations with the magnitude of WSS ($r = -0.25$, $p = 0.020$) and WSSG ($r = -0.29$, $p = 0.006$) when using the absolute value of the data. The same is true for the inverse correlations between the level of EC c-jun protein expression was also inversely correlated with the magnitude of WSSG ($r = -0.25$, $p = 0.018$) and the degree of SMC apoptosis was inversely correlated with WSS magnitude ($r = -0.27$, $p = 0.009$). Similar to the exponential regression using the original, normalized data, the level of EC egr-1 protein expression was inversely correlated with axial WSS ($r = -0.31$, $p = 0.005$). However, three additional parameter combinations were significant for the absolute value of the normalized data including the inverse correlation between the level of EC c-fos protein expression with circumferential WSS ($r = -0.25$, $p = 0.018$) and the inverse correlation between the level of EC egr-1 protein expression with axial WSSG ($r = -0.27$, $p = 0.010$) and circumferential WSSG ($r = -0.23$, $p = 0.033$).

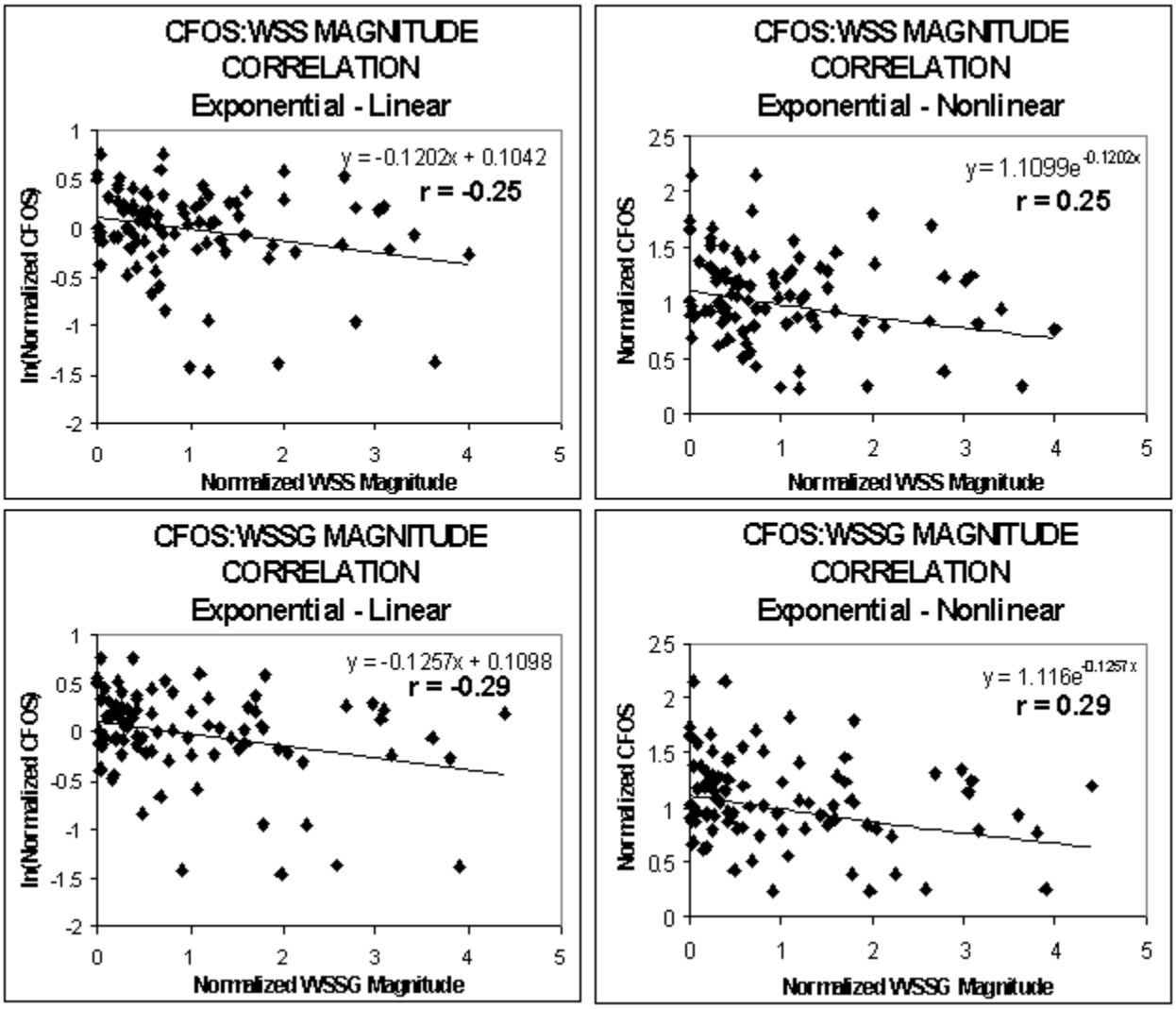

Figure 4.14 Plots showing the exponential nonlinear regression for biologic and hemodynamic parameter combinations with significant ($p < 0.05$) correlation coefficients (r) for the normalized data from all experiments. The graphs in the left column show the linear regressions using the transformed data and the graphs in the right column show the corresponding nonlinear regressions. Note that only the graphs for c-fos are shown in this figure. The graphs for c-jun, egr-1 and SMC apoptosis are shown in the following figure.

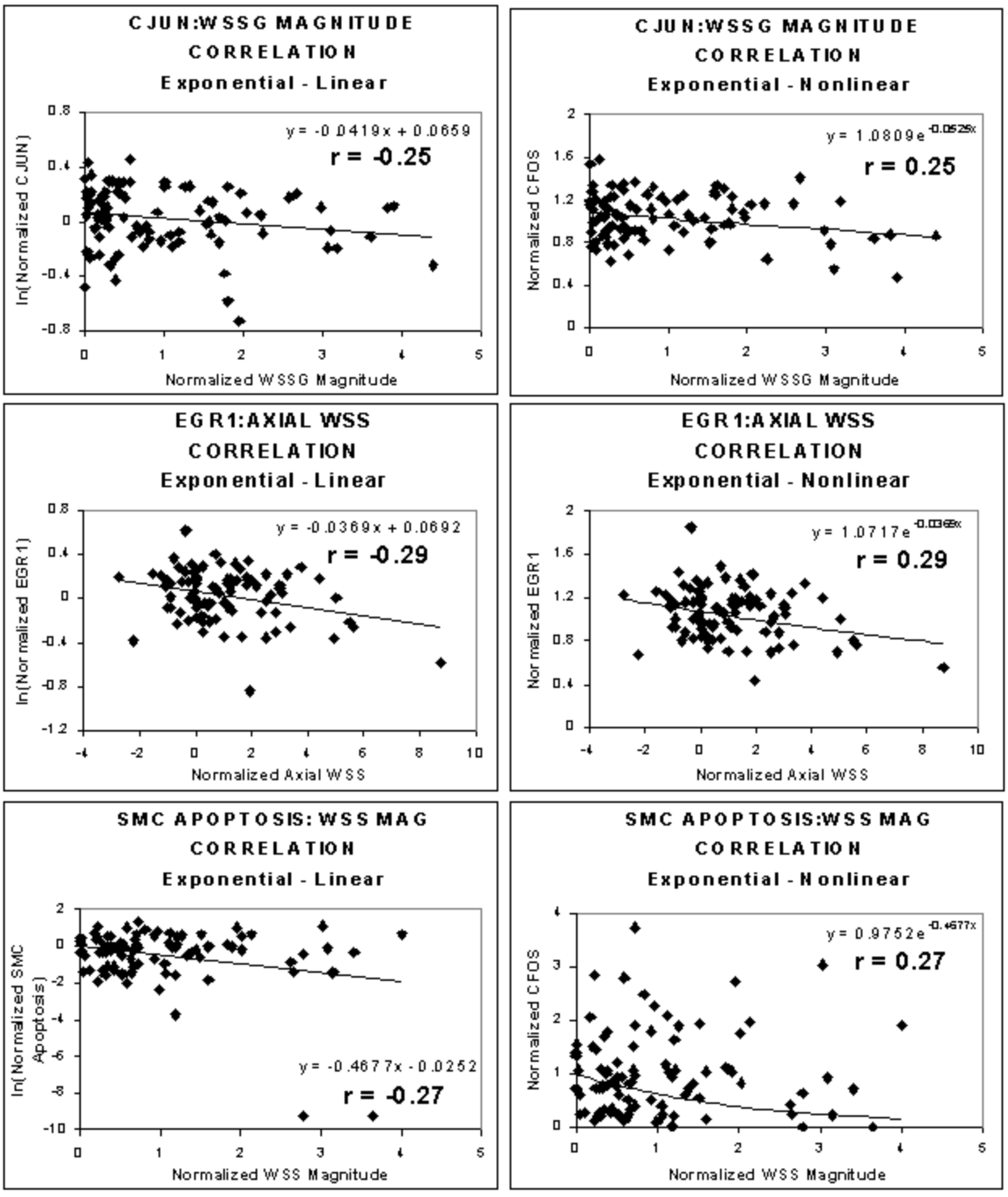

Figure 4.15 Plots showing the exponential nonlinear regression for biologic and hemodynamic parameter combinations with significant ($p < 0.05$) correlation coefficients (r) for the normalized data from all experiments. The graphs in the left column show the linear regressions using the transformed data and the graphs in the right column show the corresponding nonlinear regressions. Note that only the graphs for c-jun, egr-1 and SMC apoptosis are shown in this figure. The graphs for c-fos are shown in the previous figure.

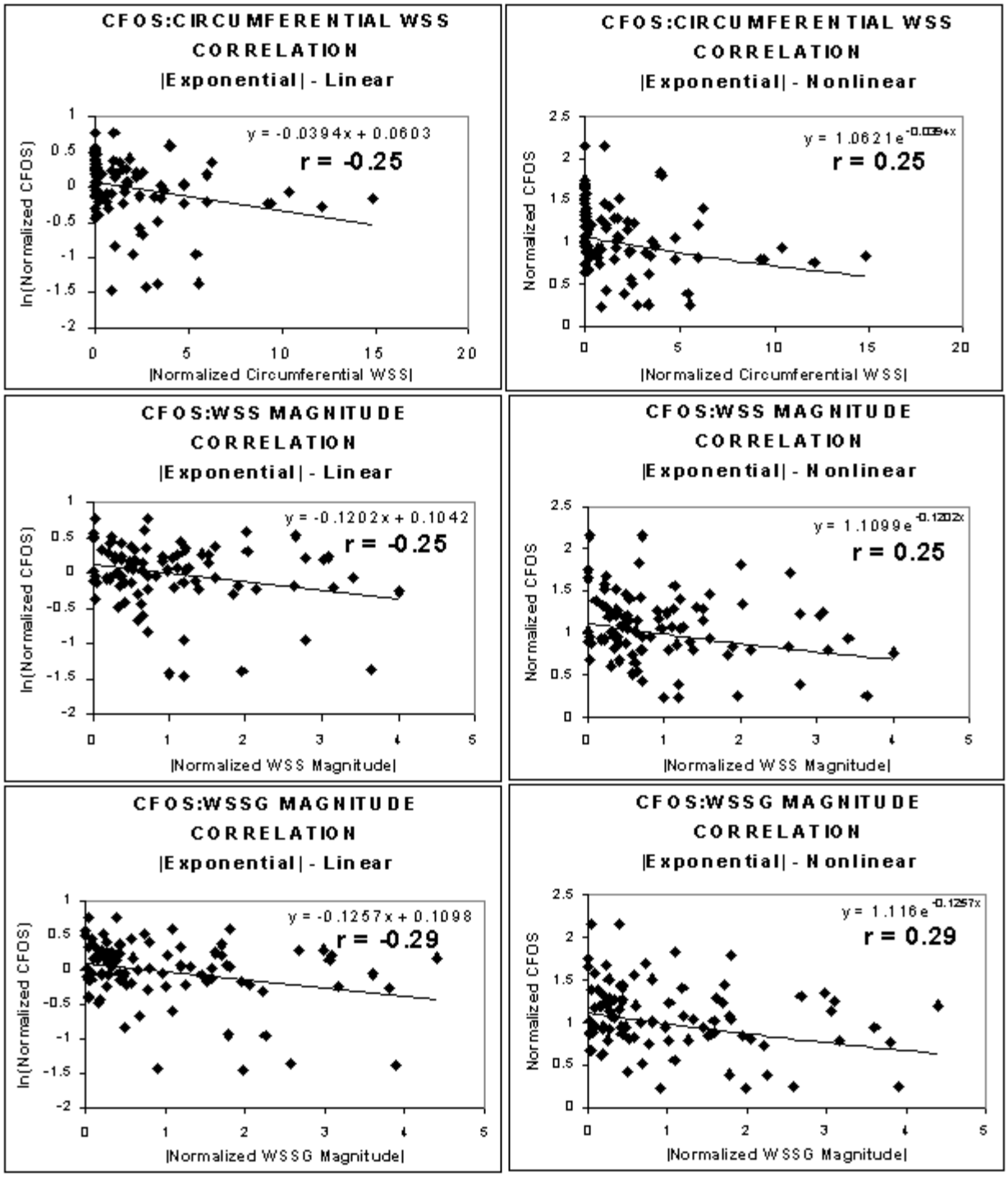

Figure 4.16 Plots showing the exponential nonlinear regression for biologic and hemodynamic parameter combinations with significant ($p < 0.05$) correlation coefficients (r) for the absolute value of the normalized data from all experiments. The graphs in the left column show the linear regressions using the transformed data and the graphs in the right column show the corresponding nonlinear regressions. Note that only the graphs for c-fos are shown in this figure. The graphs for c-jun, egr-1 and SMC apoptosis are shown in the two following figures.

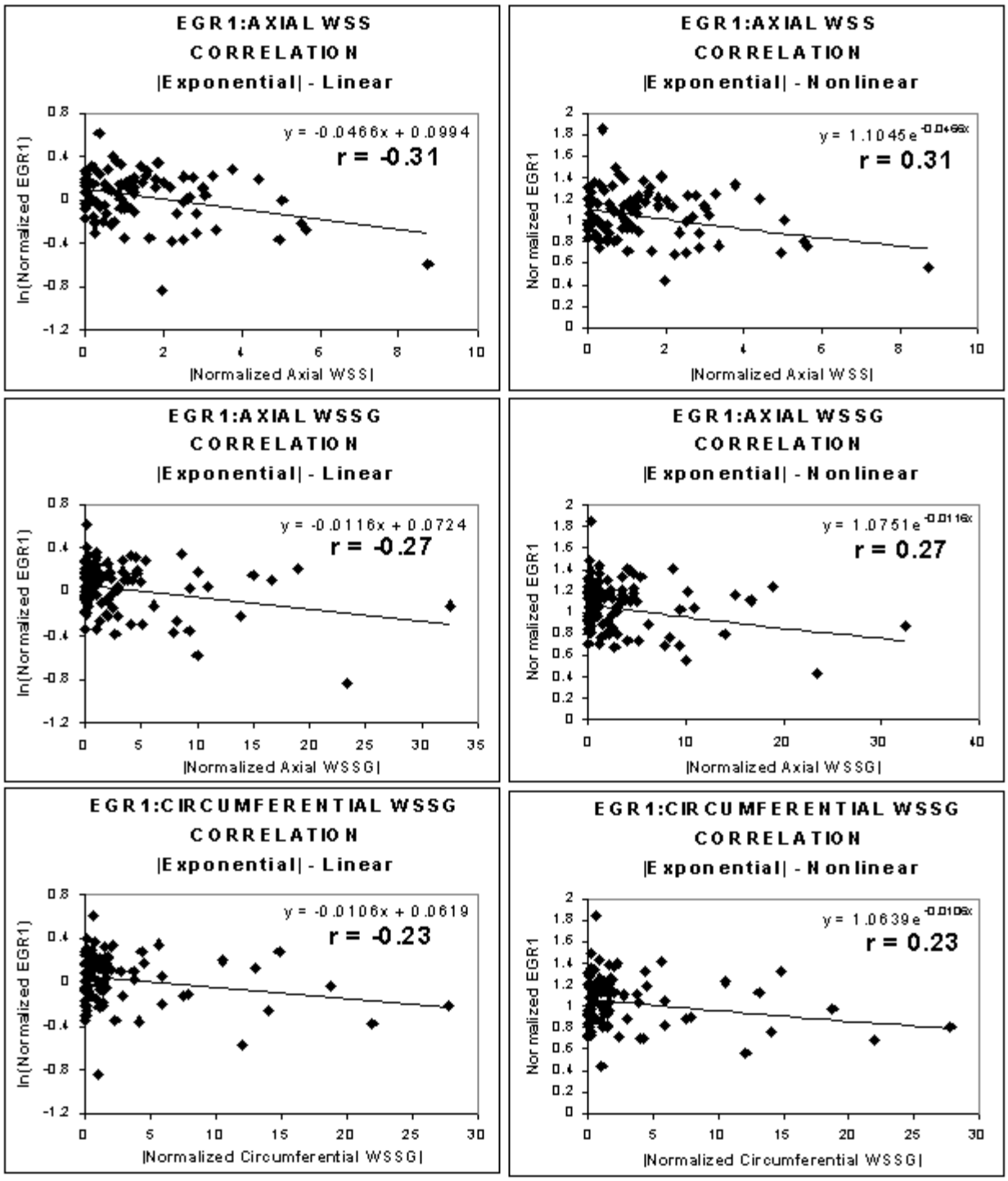

Figure 4.17 Plots showing the exponential nonlinear regression for biologic and hemodynamic parameter combinations with significant ($p < 0.05$) correlation coefficients (r) for the absolute value of the normalized data from all experiments. The graphs in the left column show the linear regressions using the transformed data and the graphs in the right column show the corresponding nonlinear regressions. Note that only the graphs for egr-1 are shown in this figure. The graphs for c-fos are shown in the previous figure and the graphs for c-jun and SMC apoptosis are shown in the following figure.

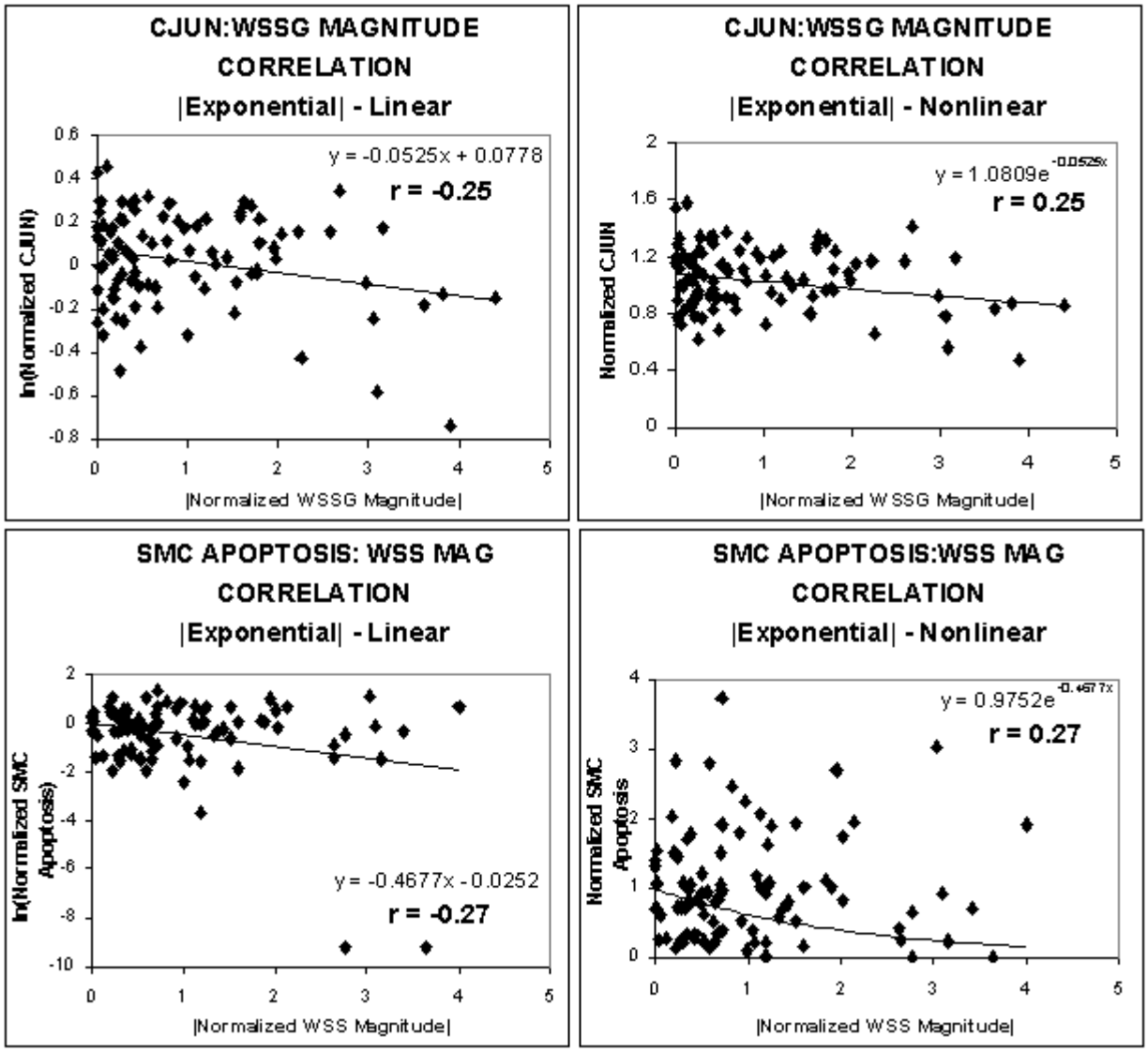

Figure 4.18 Plots showing the exponential nonlinear regression for biologic and hemodynamic parameter combinations with significant ($p < 0.05$) correlation coefficients (r) for the absolute value of the normalized data from all experiments. The graphs in the left column show the linear regressions using the transformed data and the graphs in the right column show the corresponding nonlinear regressions. Note that only the graphs for c-jun and SMC apoptosis are shown in this figure. The graphs for c-fos and egr-1 are shown in the two previous figures.

For the power nonlinear regression model, the only biologic parameter that had significant correlations was the level of EC c-fos protein expression as shown in Table 4.6 and Figures 4.19 and 4.20. Using the linear transformation of the power model, the level of EC c-fos protein expression was inversely correlated with circumferential WSS ($r = -0.34$, $p = 0.001$) and WSS magnitude ($r = -0.27$, $p = 0.011$). Additionally, the level of EC c-fos protein expression was inversely correlated with circumferential WSSG ($r = -0.26$, $p = 0.015$) and WSSG magnitude ($r = -0.29$, $p = 0.006$).

For the logarithmic nonlinear regression model, the same four parameter combinations had significant correlations as the power nonlinear regression mode as shown in Table 4.7 and Figures 4.21 and 4.22. Using the linear transformation of the logarithmic model, the level of EC c-fos protein expression was inversely correlated with circumferential WSS ($r = -0.34$, $p = 0.001$) and WSS magnitude ($r = -0.29$, $p = 0.006$). Additionally, the level of EC c-fos protein expression was inversely correlated with circumferential WSSG ($r = -0.31$, $p = 0.003$) and WSSG magnitude ($r = -0.30$, $p = 0.004$).

4.3.4 Sensitivity Analysis

The correlation coefficients for the linear regression model are presented in Tables 4.8 and 4.9 for each parameter combination for each reconstruction technique. For the symmetric elliptical cross-section reconstruction technique, four parameter combinations had significant correlations. The level of EC c-fos protein expression was inversely correlated with the axial WSS ($r = -0.56$, $p = 0.009$) and the magnitudes of WSS ($r = -0.54$, $p = 0.012$) and WSSG ($r = -0.50$, $p = 0.022$). The level of EC egr-1 protein expression was positively correlated with circumferential WSS ($r = 0.61$, $p = 0.004$). These same parameter combinations yielded significant correlations in the asymmetric elliptical and circular cross-section reconstructions.

The asymmetric ellipse and circle reconstructions also had significant correlations that did not occur for the other reconstruction techniques. The asymmetric ellipse reconstruction showed a significant positive correlation for EC c-jun protein expression and circumferential WSSG ($r = 0.44$, $p = 0.048$). The degree of EC apoptosis was inversely correlated with circumferential WSSG ($r = -0.54$, $p = 0.011$) as was the degree of SMC apoptosis and circumferential WSS ($r = -0.57$, $p = 0.007$). The circular reconstruction showed a

Table 4.6 Correlation coefficient (r) values for the power nonlinear regression for the parameter combinations using the absolute value of the normalized data from all experiments. Significant correlations ($p < 0.05$) are highlighted in grey.

POWER	CFOS	CJUN	EGR1	EC APOPTOSIS	SMC APOPTOSIS
Axial WSS	-0.18	-0.07	-0.11	-0.04	-0.13
Circ WSS	-0.34	-0.19	0.15	-0.05	-0.12
WSS Mag	-0.27	-0.12	-0.07	-0.05	-0.16
Axial WSSG	-0.17	-0.10	-0.11	-0.05	-0.07
Circ WSSG	-0.26	-0.10	-0.03	0.04	-0.05
WSSG Mag	-0.29	-0.17	-0.08	-0.08	-0.13

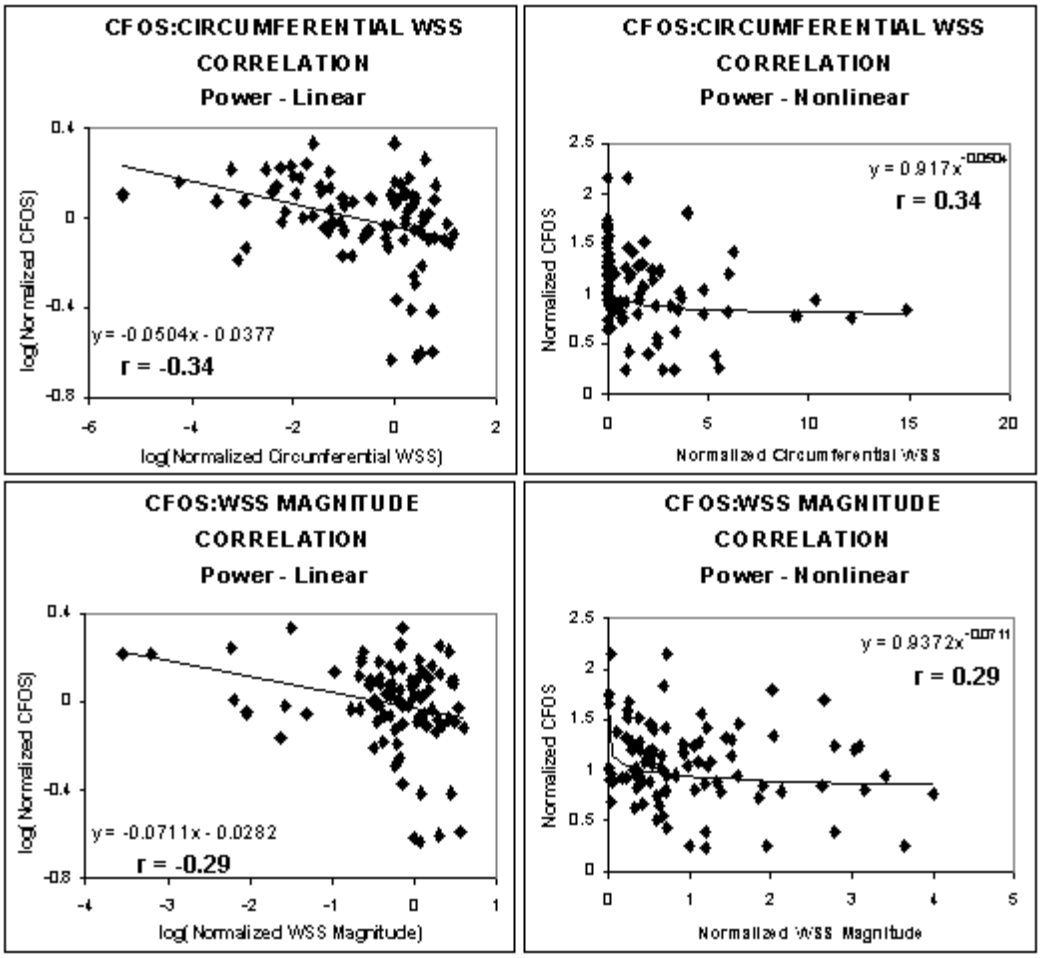

Figure 4.19 Plots showing the power nonlinear regression for biologic and hemodynamic parameter combinations with significant ($p < 0.05$) correlation coefficients (r) for the absolute value of the normalized data from all experiments. The graphs in the left column show the linear regressions using the transformed data and the graphs in the right column show the corresponding nonlinear regressions. Note that only the graphs for WSS are shown in this figure. The graphs for WSSG are shown in the following figure.

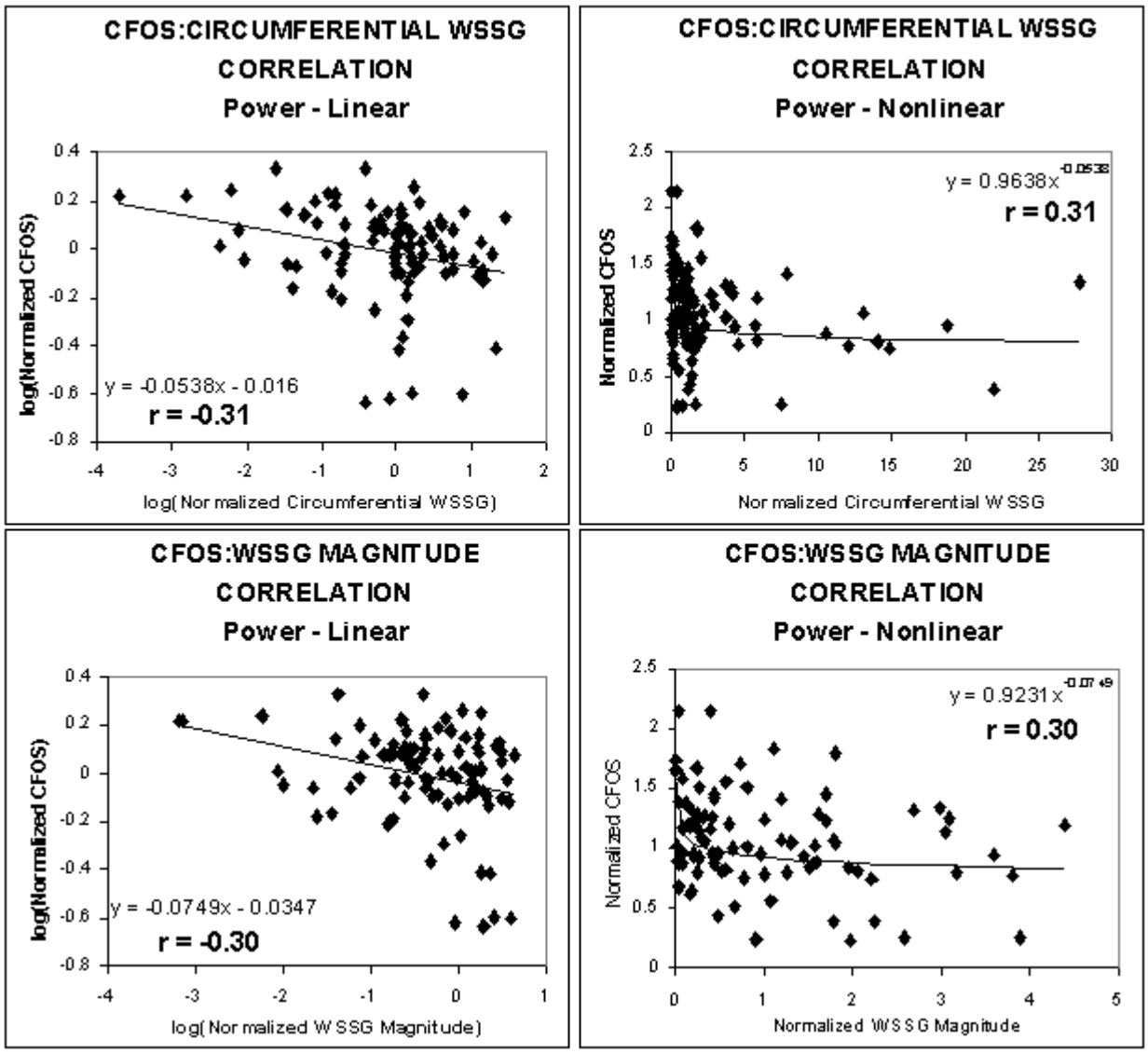

Figure 4.20 Plots showing the power nonlinear regression for biologic and hemodynamic parameter combinations with significant ($p < 0.05$) correlation coefficients (r) for the absolute value of the normalized data from all experiments. The graphs in the left column show the linear regressions using the transformed data and the graphs in the right column show the corresponding nonlinear regressions. Note that only the graphs for WSSG are shown in this figure. The graphs for WSS are shown in the previous figure.

Table 4.7 Correlation coefficient (r) values for the logarithmic nonlinear regression for the parameter combinations using the absolute value of the normalized data from all experiments. Significant correlations ($p < 0.05$) are highlighted in grey.

LOGARITHMIC	CFOS	CJUN	EGR1	EC APOPTOSIS	SMC APOPTOSIS
Axial WSS	-0.21	-0.07	-0.08	-0.05	-0.02
Circ WSS	-0.34	-0.19	0.15	-0.04	0.09
WSS Mag	-0.29	-0.12	-0.04	-0.06	0.01
Axial WSSG	-0.19	-0.11	-0.08	-0.08	0.03
Circ WSSG	-0.31	-0.10	-0.01	-0.04	0.00
WSSG Mag	-0.30	-0.17	-0.06	-0.06	0.06

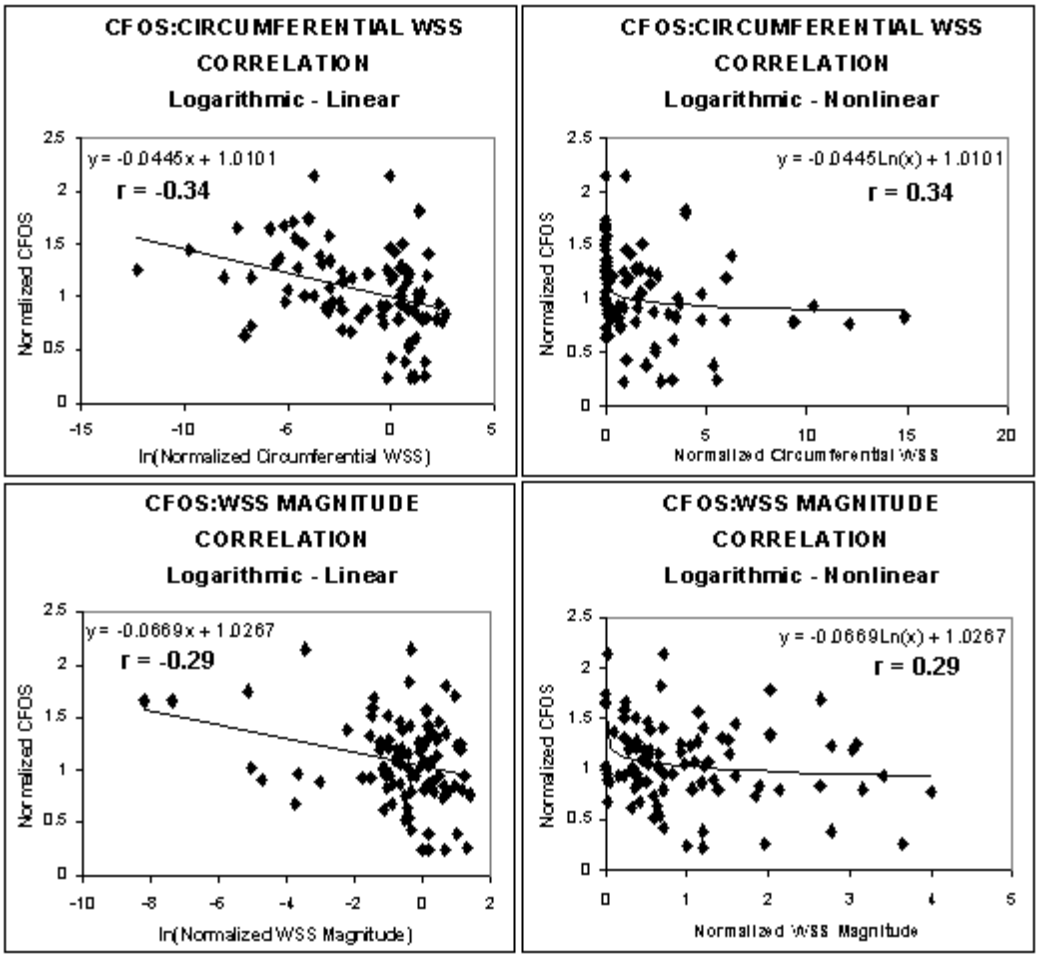

Figure 4.21 Plots showing the logarithmic nonlinear regression for biologic and hemodynamic parameter combinations with significant ($p < 0.05$) correlation coefficients (r) for the absolute value of the normalized data from all experiments. The graphs in the left column show the linear regressions using the transformed data and the graphs in the right column show the corresponding nonlinear regressions. Note that only the graphs for WSS are shown in this figure. The graphs for WSSG are shown in the following figure.

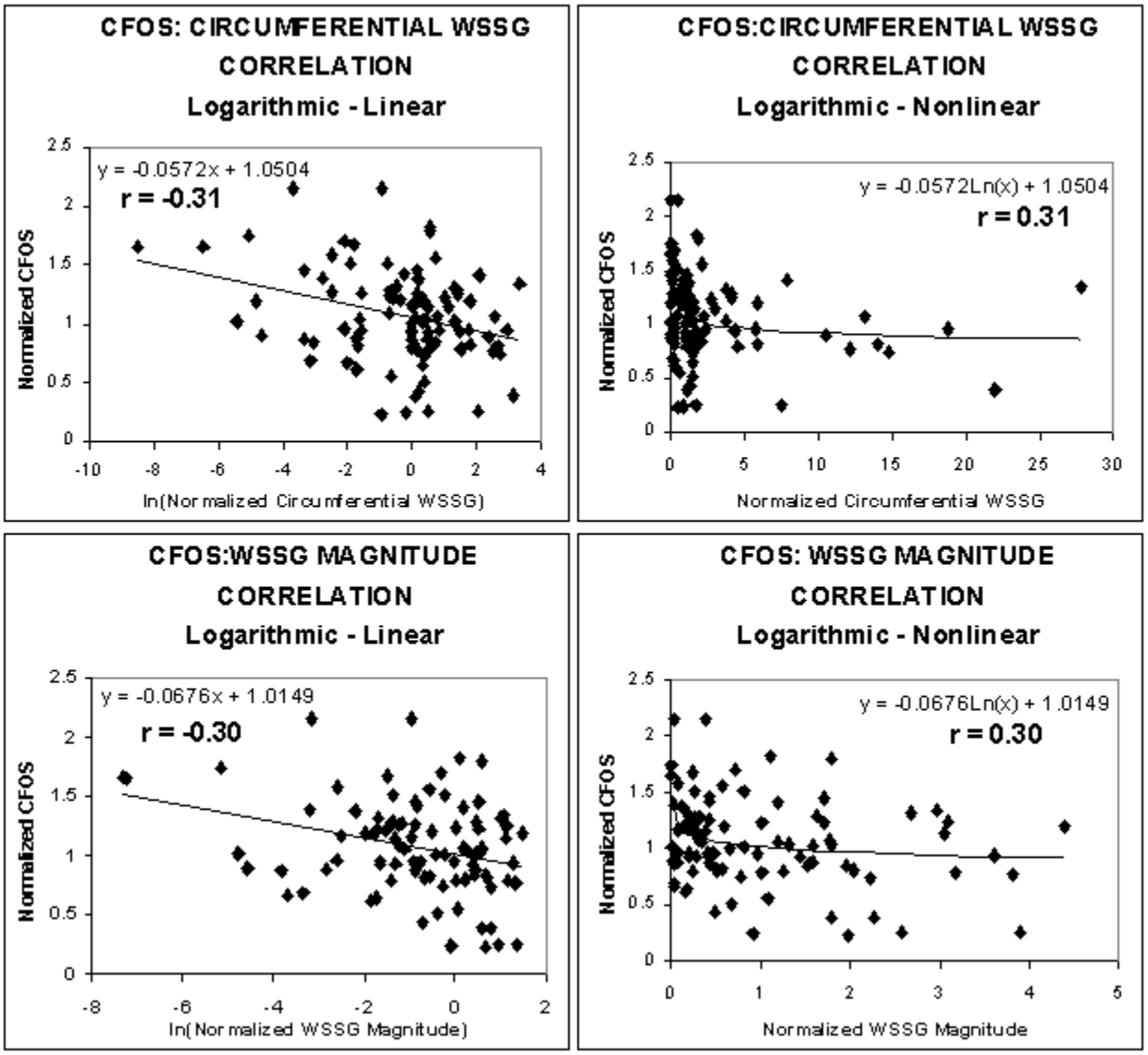

Figure 4.22 Plots showing the logarithmic nonlinear regression for biologic and hemodynamic parameter combinations with significant ($p < 0.05$) correlation coefficients (r) for the absolute value of the normalized data from all experiments. The graphs in the left column show the linear regressions using the transformed data and the graphs in the right column show the corresponding nonlinear regressions. Note that only the graphs for WSSG are shown in this figure. The graphs for WSS are shown in the previous figure.

Table 4.8 IEG correlation coefficients (r) using the linear regression model for the normalized data and the absolute value of the normalized data for the three reconstruction techniques. Significant correlations ($p < 0.05$) are highlighted in grey.

		CFOS			CJUN			EGR1	
LINEAR	SYMM ELLIPSE	ASYMM ELLIPSE	CIRCLE	SYMM ELLIPSE	ASYMM ELLIPSE	CIRCLE	SYMM ELLIPSE	ASYMM ELLIPSE	CIRCLE
Axial WSS	-0.56	-0.55	-0.46	-0.38	-0.39	-0.42	0.14	0.07	0.07
Circ WSS	-0.09	-0.06	-0.05	0.32	0.08	0.26	0.61	0.58	0.64
WSS Mag	-0.54	-0.54	-0.47	-0.31	-0.33	-0.40	0.27	0.17	0.09
Axial WSSG	-0.33	-0.24	-0.16	-0.18	-0.15	-0.45	0.11	0.14	-0.17
Circ WSSG	-0.28	0.25	-0.12	-0.31	0.44	-0.40	-0.37	0.33	-0.09
WSSG Mag	-0.50	-0.46	-0.47	-0.38	-0.30	-0.44	0.14	0.19	0.02

		CFOS			CJUN			EGR1	
LINEAR ABS VALUE	SYMM ELLIPSE	ASYMM ELLIPSE	CIRCLE	SYMM ELLIPSE	ASYMM ELLIPSE	CIRCLE	SYMM ELLIPSE	ASYMM ELLIPSE	CIRCLE
Axial WSS	-0.57	-0.53	-0.43	-0.37	-0.37	-0.41	0.15	0.09	0.09
Circ WSS	-0.29	-0.26	0.07	-0.19	-0.23	-0.26	0.44	0.14	0.05
WSS Mag	-0.54	-0.54	-0.47	-0.31	-0.33	-0.40	0.27	0.17	0.09
Axial WSSG	-0.41	-0.27	-0.52	0.15	-0.02	-0.45	0.12	0.16	-0.07
Circ WSSG	-0.27	-0.37	-0.30	-0.41	-0.41	-0.02	-0.23	-0.24	-0.11
WSSG Mag	-0.50	-0.46	-0.47	-0.38	-0.30	-0.44	0.14	0.19	0.02

Table 4.9 Apoptosis correlation coefficients (r) using the linear regression model for the normalized data and the absolute value of the normalized data for the three reconstruction techniques. Significant correlations ($p < 0.05$) are highlighted in grey.

	EC APOPTOSIS			SMC APOPTOSIS		
LINEAR	SYMM ELLIPSE	ASYMM ELLIPSE	CIRCLE	SYMM ELLIPSE	ASYMM ELLIPSE	CIRCLE
Axial WSS	0.08	0.26	0.22	-0.17	0.06	0.09
Circ WSS	-0.09	-0.10	-0.04	-0.14	-0.57	-0.21
WSS Mag	0.05	0.21	0.17	-0.09	0.10	0.09
Axial WSSG	0.12	0.33	0.38	0.21	0.41	0.37
Circ WSSG	0.31	-0.54	0.19	0.29	-0.42	0.42
WSSG Mag	0.26	0.26	0.22	0.14	0.18	0.16

	EC APOPTOSIS			SMC APOPTOSIS		
LINEAR ABS VALUE	SYMM ELLIPSE	ASYMM ELLIPSE	CIRCLE	SYMM ELLIPSE	ASYMM ELLIPSE	CIRCLE
Axial WSS	0.05	0.25	0.21	-0.13	0.10	0.09
Circ WSS	-0.07	-0.08	-0.04	-0.04	0.17	0.09
WSS Mag	0.05	0.21	0.17	-0.09	0.10	0.09
Axial WSSG	-0.10	0.24	0.15	-0.18	0.24	0.06
Circ WSSG	0.26	0.26	-0.14	0.37	0.29	-0.08
WSSG Mag	0.26	0.26	0.22	0.14	0.18	0.16

significant inverse correlation between EC c-jun protein expression and axial WSSG ($r = -0.45$, $p = 0.040$) and WSSG magnitude ($r = -0.44$, $p = 0.049$).

For the sensitivity analysis, the most important biologic and hemodynamic parameter combinations are those that resulted in significant correlations for the data from the symmetric ellipse models for all experiments shown in section 4.3.2. Specifically, significant correlations existed for c-fos and WSS magnitude, c-fos and WSSG magnitude, c-jun and WSSG magnitude, and egr-1 and axial WSS (see Table 4.2 - all experiments). The data presented in this sensitivity analysis section showed the same results (i.e., significant or insignificant correlation coefficients) for the symmetric ellipse, asymmetric ellipse and circle models for all of these parameter combinations except c-jun and WSSG. For this parameter combination, the symmetric and asymmetric models had the same results (i.e., insignificant correlation coefficient) while the circular model resulted in a significant correlation. Therefore, it is possible that this parameter combination is sensitive to the reconstruction technique and may not be a valid significant correlation.

The results of the linear regression of the absolute value of the normalized data are also shown in Tables 4.8 and 4.9. For the symmetric elliptical cross-section reconstruction technique, the same four parameter combinations had significant correlations using the absolute value of the normalized data. The level of EC c-fos protein expression was inversely correlated with the axial WSS ($r = -0.57$, $p = 0.007$) and the magnitudes of WSS ($r = -0.54$, $p = 0.012$) and WSSG ($r = -0.50$, $p = 0.022$). The level of EC egr-1 protein expression was positively correlated with circumferential WSS ($r = 0.44$, $p = 0.049$). The inverse correlations between c-fos and the magnitudes of WSS and WSSG were also significant for the asymmetric elliptical and circular cross-section reconstructions. However, the correlation between c-fos and axial WSS was not significant for the circular cross-section reconstruction and the correlation between egr-1 and circumferential WSS was not significant for either the asymmetric ellipse or circular cross-section reconstruction.

For the sensitivity analysis, the most important biologic and hemodynamic parameter combinations are those that resulted in significant correlations for the data from the symmetric ellipse models for all

experiments shown in section 4.3.2. Specifically, significant correlations existed for c-fos and circumferential WSS, c-fos and WSS magnitude, c-fos and WSSG magnitude, c-jun and WSSG magnitude, egr-1 and axial WSS, egr-1 and axial WSSG, and egr-1 and WSSG magnitude (see Table 4.3 - all experiments). The data presented in this sensitivity analysis section showed the same results (i.e., significant or insignificant correlation coefficients) for the symmetric ellipse, asymmetric ellipse and circle models for all of these parameter combinations except c-jun and WSSG. For this parameter combination, the symmetric and asymmetric models had the same results (i.e., insignificant correlation coefficient) while the circular model resulted in a significant correlation. Therefore, it is possible that this parameter combination is sensitive to the reconstruction technique and may not be a valid significant correlation.

The correlation coefficients for the linear transformation of the reciprocal nonlinear regression model using the original, normalized data and the absolute value of the normalized data are shown in Tables 4.10 and 4.11. For the symmetric elliptical cross-section reconstruction technique, eight parameter combinations had significant correlations using the original, normalized data. Four of these parameter combinations were significant for all reconstruction techniques. The level of EC c-fos protein expression was positively correlated with axial WSS ($r = 0.65$, $p = 0.002$, symmetric ellipse), WSS magnitude ($r = 0.59$, $p = 0.005$, symmetric ellipse) and WSSG magnitude ($r = 0.60$, $p = 0.004$, symmetric ellipse). The level of EC egr-1 protein expression was inversely correlated with circumferential WSS ($r = -0.56$, $p = 0.008$, symmetric ellipse). Four parameter combinations were significant for the symmetric ellipse model but not for the asymmetric ellipse and/or circle cross-section techniques. For the symmetric ellipse model, the level of EC c-fos protein expression was directly correlated with axial WSSG ($r = 0.50$, $p = 0.020$) and the degree of SMC apoptosis was positively correlated with axial WSS ($r = 0.47$, $p = 0.033$) and axial WSSG ($r = 0.50$, $p = 0.021$), but these correlations were not significant for the other reconstruction techniques. Similarly, for the symmetric ellipse model, the level of EC c-jun protein expression was positively correlated with WSS magnitude ($r = 0.65$, $p = 0.002$, symmetric ellipse) but this correlation was not significant for the asymmetric ellipse model. For the symmetric elliptical cross-section reconstruction technique, eight parameter

Table 4.10 IEG correlation coefficients (r) using the linear transformation of the reciprocal regression model for the normalized data and the absolute value of the normalized data for the three reconstruction techniques. Significant correlations ($p < 0.05$) are highlighted in grey.

		CFOS			CJUN			EGR1	
RECIPROCAL	SYMM ELLIPSE	ASYMM ELLIPSE	CIRCLE	SYMM ELLIPSE	ASYMM ELLIPSE	CIRCLE	SYMM ELLIPSE	ASYMM ELLIPSE	CIRCLE
Axial WSS	0.65	0.60	0.53	0.42	0.46	0.47	-0.10	-0.04	-0.02
Circ WSS	0.02	-0.12	-0.02	-0.35	-0.19	-0.27	-0.56	-0.55	-0.63
WSS Mag	0.59	0.60	0.58	0.34	0.40	0.46	-0.22	-0.13	-0.05
Axial WSSG	0.50	0.22	0.17	0.19	0.19	0.61	-0.08	-0.10	0.21
Circ WSSG	0.38	-0.51	0.29	0.42	-0.63	0.40	0.39	-0.37	0.12
WSSG Mag	0.60	0.47	0.57	0.49	0.37	0.54	-0.09	-0.15	0.02

		CFOS			CJUN			EGR1	
RECIPROCAL ABS VALUE	SYMM ELLIPSE	ASYMM ELLIPSE	CIRCLE	SYMM ELLIPSE	ASYMM ELLIPSE	CIRCLE	SYMM ELLIPSE	ASYMM ELLIPSE	CIRCLE
Axial WSS	0.65	0.60	0.52	0.41	0.46	0.47	-0.12	-0.06	-0.04
Circ WSS	0.15	0.06	-0.04	0.13	0.20	0.18	-0.37	-0.11	0.01
WSS Mag	0.59	0.60	0.58	0.34	0.40	0.46	-0.22	-0.13	-0.05
Axial WSSG	0.46	0.16	0.64	-0.07	0.09	0.60	-0.13	-0.15	0.09
Circ WSSG	0.37	0.48	0.22	0.50	0.58	0.08	0.28	0.24	0.07

Table 4.11 Apoptosis correlation coefficients (r) using the linear transformation of the reciprocal regression model for the normalized data and the absolute value of the normalized data for the three reconstruction techniques. Significant correlations ($p < 0.05$) are highlighted in grey.

	EC APOPTOSIS			SMC APOPTOSIS		
RECIPROCAL	SYMM ELLIPSE	ASYMM ELLIPSE	CIRCLE	SYMM ELLIPSE	ASYMM ELLIPSE	CIRCLE
Axial WSS	0.09	-0.06	-0.04	0.47	0.25	0.25
Circ WSS	0.05	-0.09	0.02	0.18	0.02	0.07
WSS Mag	0.05	-0.04	-0.03	0.42	0.29	0.31
Axial WSSG	0.22	-0.16	-0.39	0.50	-0.02	-0.41
Circ WSSG	-0.11	0.16	0.03	0.03	0.02	0.18
WSSG Mag	-0.08	-0.13	-0.11	0.23	0.14	0.17

	EC APOPTOSIS			SMC APOPTOSIS		
RECIPROCAL ABS VALUE	SYMM ELLIPSE	ASYMM ELLIPSE	CIRCLE	SYMM ELLIPSE	ASYMM ELLIPSE	CIRCLE
Axial WSS	0.12	-0.05	-0.05	0.47	0.25	0.25
Circ WSS	-0.09	-0.13	-0.18	0.11	-0.15	-0.05
WSS Mag	0.05	-0.04	-0.03	0.42	0.29	0.31
Axial WSSG	0.19	-0.23	-0.05	0.49	-0.09	0.20
Circ WSSG	-0.21	-0.11	-0.06	-0.03	-0.08	0.08
WSSG Mag	-0.08	-0.13	-0.11	0.23	0.14	0.17

combinations had significant correlations using the absolute value of the normalized data. Three of these parameter combinations were significant for all reconstruction techniques. The level of EC c-fos protein expression was positively correlated with axial WSS ($r = 0.65$, $p = 0.001$, symmetric ellipse), WSS magnitude ($r = 0.59$, $p = 0.005$, symmetric ellipse) and WSSG magnitude ($r = 0.60$, $p = 0.004$, symmetric ellipse). Five parameter combinations were significant for the symmetric ellipse model but not for the asymmetric ellipse and/or circle cross-section techniques. For the symmetric ellipse model, the level of EC c-fos protein expression was directly correlated axial WSSG ($r = 0.46$, $p = 0.035$), the level of EC c-jun protein expression was directly correlated with circumferential WSSG ($r = 0.50$, $p = 0.020$) and WSSG magnitude ($r = 0.49$, $p = 0.025$) but these correlations were not significant for either the asymmetric ellipse or the circle cross-section reconstruction technique. Similarly, for the symmetric ellipse model, the degree of SMC apoptosis was positively correlated with axial WSS ($r = 0.47$, $p = 0.031$) and axial WSSG ($r = 0.49$, $p = 0.025$) but these correlations were not significant for the other reconstruction techniques.

For the sensitivity analysis, the most important biologic and hemodynamic parameter combinations are those that resulted in significant correlations for the data from the symmetric ellipse models for all experiments shown in section 4.3.3. Specifically, significant correlations existed for c-fos and axial WSS, c-fos and WSS magnitude, and c-fos and WSSG magnitude (see Table 4.4) for both the original, normalized data and the absolute value of the normalized data. The data presented in this sensitivity analysis section showed the same results (i.e., significant or insignificant correlation coefficients) for the symmetric ellipse, asymmetric ellipse and circle models for all of these parameter combinations. Therefore, these parameter combinations are not sensitive to the reconstruction technique and all significant correlations using the reciprocal nonlinear regression model found in section 4.3.3 are valid.

The correlation coefficients for the linear transformation of the exponential nonlinear regression model using the original, normalized data and the absolute value of the normalized data are shown in Tables 4.12 and 4.13. For the symmetric elliptical cross-section reconstruction technique, seven parameter combinations had significant correlations using the original, normalized data. Four of these parameter combinations were

Table 4.12 IEG correlation coefficients (r) using the linear transformation of the exponential regression model for the normalized data and the absolute value of the normalized data for the three reconstruction techniques. Significant correlations ($p < 0.05$) are highlighted in grey.

		CFOS			CJUN			EGR1	
EXPONENTIAL	SYMM ELLIPSE	ASYMM ELLIPSE	CIRCLE	SYMM ELLIPSE	ASYMM ELLIPSE	CIRCLE	SYMM ELLIPSE	ASYMM ELLIPSE	CIRCLE
Axial WSS	-0.63	-0.60	-0.52	-0.40	-0.43	-0.45	0.12	0.05	0.04
Circ WSS	-0.06	0.03	-0.02	0.35	0.14	0.28	0.58	0.56	0.64
WSS Mag	-0.59	-0.60	-0.55	-0.33	-0.37	-0.44	0.25	0.15	0.07
Axial WSSG	-0.45	-0.25	-0.17	-0.19	-0.17	-0.54	0.10	0.12	-0.19
Circ WSSG	-0.34	0.41	-0.23	-0.37	0.54	-0.41	-0.38	0.35	-0.11
WSSG Mag	-0.58	-0.49	-0.55	-0.43	-0.33	-0.49	0.11	0.17	0.00

		CFOS			CJUN			EGR1	
EXPONENTIAL ABS VALUE	SYMM ELLIPSE	ASYMM ELLIPSE	CIRCLE	SYMM ELLIPSE	ASYMM ELLIPSE	CIRCLE	SYMM ELLIPSE	ASYMM ELLIPSE	CIRCLE
Axial WSS	-0.64	-0.60	-0.50	-0.39	-0.42	-0.45	0.13	0.07	0.07
Circ WSS	-0.23	-0.16	0.06	-0.16	-0.22	-0.23	0.41	0.12	0.02
WSS Mag	-0.59	-0.60	-0.55	-0.33	-0.37	-0.44	0.25	0.15	0.07
Axial WSSG	-0.46	-0.22	-0.61	0.12	-0.05	-0.53	0.13	0.15	-0.08
Circ WSSG	-0.33	-0.44	-0.27	-0.46	-0.50	-0.05	-0.26	-0.24	-0.09
WSSG Mag	-0.58	-0.49	-0.55	-0.43	-0.33	-0.49	0.11	0.17	0.00

Table 4.13 Apoptosis correlation coefficients (r) using the linear transformation of the exponential regression model for the normalized data and the absolute value of the normalized data for the three reconstruction techniques. Significant correlations ($p < 0.05$) are highlighted in grey.

	EC APOPTOSIS			SMC APOPTOSIS		
EXPONENTIAL	SYMM ELLIPSE	ASYMM ELLIPSE	CIRCLE	SYMM ELLIPSE	ASYMM ELLIPSE	CIRCLE
Axial WSS	-0.01	0.17	0.13	-0.47	-0.21	-0.17
Circ WSS	-0.06	0.02	-0.02	-0.18	-0.28	-0.14
WSS Mag	0.00	0.13	0.10	-0.38	-0.21	-0.22
Axial WSSG	-0.05	0.27	0.39	-0.22	0.23	0.47
Circ WSSG	0.21	-0.36	0.09	0.06	-0.24	0.13
WSSG Mag	0.17	0.21	0.16	-0.15	-0.05	-0.10

	EC APOPTOSIS			SMC APOPTOSIS		
EXPONENTIAL ABS VALUE	SYMM ELLIPSE	ASYMM ELLIPSE	CIRCLE	SYMM ELLIPSE	ASYMM ELLIPSE	CIRCLE
Axial WSS	-0.04	0.15	0.13	-0.46	-0.19	-0.17
Circ WSS	0.02	0.01	0.10	-0.06	0.10	0.11
WSS Mag	0.00	0.13	0.10	-0.38	-0.21	-0.22
Axial WSSG	-0.16	0.26	0.08	-0.49	0.15	-0.18
Circ WSSG	0.24	0.15	-0.05	0.16	0.07	-0.18
WSSG Mag	0.17	0.21	0.16	-0.15	-0.05	-0.10

significant for all reconstruction techniques. The level of EC c-fos protein expression was inversely correlated with axial WSS ($r = -0.63$, $p = 0.002$, symmetric ellipse), WSS magnitude ($r = -0.59$, $p = 0.004$, symmetric ellipse) and WSSG magnitude ($r = -0.58$, $p = 0.006$, symmetric ellipse). The level of EC egr-1 protein expression was positively correlated with circumferential WSS ($r = 0.58$, $p = 0.005$, symmetric ellipse). Three parameter combinations were significant for the symmetric ellipse model but not for the asymmetric ellipse and/or circle cross-section techniques. For the symmetric ellipse model, the level of EC c-fos protein expression was inversely correlated axial WSSG ($r = -0.50$, $p = 0.041$) and the degree of SMC apoptosis was inversely correlated with axial WSS ($r = -0.47$, $p = 0.032$) but these correlations were not significant for either the asymmetric ellipse or the circle cross-section reconstruction technique. Similarly, for the symmetric ellipse model, the level of EC c-jun protein expression was inversely correlated with WSSG magnitude ($r = -0.43$, $p = 0.049$) but this correlation was not significant for the asymmetric ellipse model. For the symmetric elliptical cross-section reconstruction technique, eight parameter combinations had significant correlations using the absolute value of the normalized data. Three of these parameter combinations were significant for all reconstruction techniques. The level of EC c-fos protein expression was inversely correlated with axial WSS ($r = -0.64$, $p = 0.002$, symmetric ellipse), WSS magnitude ($r = -0.59$, $p = 0.004$, symmetric ellipse) and WSSG magnitude ($r = -0.58$, $p = 0.006$, symmetric ellipse). Five parameter combinations were significant for the symmetric ellipse model but not for the asymmetric ellipse and/or circle cross-section techniques. For the symmetric ellipse model, the level of EC c-fos protein expression was inversely correlated axial WSSG ($r = -0.46$, $p = 0.038$) and the level of EC c-jun protein expression was inversely correlated with circumferential WSSG ($r = -0.46$, $p = 0.036$) and WSSG magnitude ($r = -0.43$, $p = 0.049$) but these correlation were not significant for either the asymmetric ellipse or the circular cross-section reconstruction techniques. Similarly, for the symmetric ellipse model, the degree of SMC apoptosis was inversely correlated with axial WSS ($r = -0.46$, $p = 0.037$) and axial WSSG ($r = -0.49$, $p = 0.023$) but these correlations were not significant for either the asymmetric ellipse or the circle cross-section reconstruction technique.

For the sensitivity analysis, the most important biologic and hemodynamic parameter combinations are those that resulted in significant correlations for the data from the symmetric ellipse models for all experiments shown in section 4.3.3. Specifically, significant correlations existed for c-fos and WSS magnitude, c-fos and WSSG magnitude, c-jun and WSSG magnitude, egr-1 and axial WSS, SMC apoptosis and WSS magnitude (see Table 4.5) for both the original, normalized data and the absolute value of the normalized data. The data presented in this sensitivity analysis section showed the same results (i.e., significant or insignificant correlation coefficients) for the symmetric ellipse, asymmetric ellipse and circle models for all of these parameter combinations except c-jun and WSSG. For this parameter combination, the symmetric and circular models had the same results (i.e., significant correlation coefficient) while the asymmetric model resulted in an insignificant correlation. Therefore, it is possible that this parameter combination is sensitive to the reconstruction technique and may not be a valid significant correlation.

The correlation coefficients for the linear transformation of the power nonlinear regression model using the absolute value of the normalized data are shown in Tables 4.14 and 4.15. For the symmetric elliptical cross-section reconstruction technique, six parameter combinations had significant correlations. Three of these parameter combinations were significant for all reconstruction techniques. The level of EC c-fos protein expression was inversely correlated with axial WSS ($r = -0.56$, $p = 0.009$, symmetric ellipse), WSS magnitude ($r = -0.50$, $p = 0.021$, symmetric ellipse) and WSSG magnitude ($r = -0.54$, $p = 0.012$, symmetric ellipse). Three parameter combinations were significant for the symmetric ellipse model but not for the asymmetric ellipse and/or circle cross-section techniques including the inverse correlation of the level of EC c-fos protein expression with circumferential WSS ($r = -0.51$, $p = 0.019$, symmetric ellipse), axial WSSG ($r = -0.46$, $p = 0.034$, symmetric ellipse) and circumferential WSSG ($r = -0.54$, $p = 0.012$, symmetric ellipse).

For the sensitivity analysis, the most important biologic and hemodynamic parameter combinations are those that resulted in significant correlations for the data from the symmetric ellipse models for all experiments shown in section 4.3.3. Specifically, significant correlations existed for c-fos and circumferential WSS, c-fos and WSS magnitude, c-fos and circumferential WSSG, and c-fos and WSSG

Table 4.14 IEG correlation coefficients (r) using the linear transformation of the power and logarithmic regression models for the absolute value of the normalized data for the three reconstruction techniques. Significant correlations ($p < 0.05$) are highlighted in grey.

		CFOS			CJUN			EGR1	
POWER	SYMM ELLIPSE	ASYMM ELLIPSE	CIRCLE	SYMM ELLIPSE	ASYMM ELLIPSE	CIRCLE	SYMM ELLIPSE	ASYMM ELLIPSE	CIRCLE
Axial WSS	-0.56	-0.44	-0.50	-0.34	-0.29	-0.34	0.23	0.11	0.30
Circ WSS	-0.46	-0.46	-0.40	-0.27	-0.26	-0.39	0.32	0.32	0.21
WSS Mag	-0.50	-0.51	-0.51	-0.30	-0.31	-0.36	0.28	0.23	0.26
Axial WSSG	-0.51	-0.31	-0.56	-0.25	-0.21	-0.34	0.24	0.23	0.29
Circ WSSG	-0.46	-0.50	-0.42	-0.34	-0.47	-0.23	0.16	0.02	0.11
WSSG Mag	-0.54	-0.50	-0.53	-0.34	-0.32	-0.34	0.25	0.22	0.27

		CFOS			CJUN			EGR1	
LOG	SYMM ELLIPSE	ASYMM ELLIPSE	CIRCLE	SYMM ELLIPSE	ASYMM ELLIPSE	CIRCLE	SYMM ELLIPSE	ASYMM ELLIPSE	CIRCLE
Axial WSS	-0.62	-0.47	-0.53	-0.34	-0.28	-0.34	0.23	0.11	0.30
Circ WSS	-0.52	-0.58	-0.46	-0.27	-0.26	-0.41	0.33	0.32	0.22
WSS Mag	-0.55	-0.56	-0.56	-0.31	-0.32	-0.37	0.27	0.23	0.26
Axial WSSG	-0.53	-0.33	-0.59	-0.24	-0.20	-0.33	0.23	0.23	0.29
Circ WSSG	-0.52	-0.58	-0.47	-0.33	-0.47	-0.24	0.16	0.00	0.10
WSSG Mag	-0.59	-0.55	-0.58	-0.34	-0.32	-0.34	0.25	0.22	0.26

Table 4.15 Apoptosis correlation coefficients (r) using the linear transformation of the power and logarithmic regression models for the absolute value of the normalized data for the three reconstruction techniques. No significant correlations were found.

	EC APOPTOSIS			SMC APOPTOSIS		
POWER	SYMM ELLIPSE	ASYMM ELLIPSE	CIRCLE	SYMM ELLIPSE	ASYMM ELLIPSE	CIRCLE
Axial WSS	-0.02	-0.01	0.01	-0.29	-0.24	-0.23
Circ WSS	-0.03	-0.03	0.00	-0.19	-0.06	-0.15
WSS Mag	-0.01	-0.01	0.01	-0.26	-0.24	-0.23
Axial WSSG	0.01	0.01	0.01	-0.29	-0.13	-0.24
Circ WSSG	0.05	0.08	-0.20	-0.11	-0.05	-0.20
WSSG Mag	-0.01	0.02	0.00	-0.23	-0.21	-0.20

	EC APOPTOSIS			SMC APOPTOSIS		
LOG	SYMM ELLIPSE	ASYMM ELLIPSE	CIRCLE	SYMM ELLIPSE	ASYMM ELLIPSE	CIRCLE
Axial WSS	-0.04	-0.10	0.02	-0.07	-0.01	-0.01
Circ WSS	-0.08	-0.03	-0.09	0.00	0.12	-0.01
WSS Mag	-0.05	-0.05	-0.02	-0.06	-0.02	-0.02
Axial WSSG	-0.03	-0.05	0.00	-0.02	-0.03	-0.01
Circ WSSG	0.00	0.07	-0.23	0.12	0.18	0.04
WSSG Mag	-0.05	-0.04	-0.04	-0.02	0.01	0.03

magnitude (see Table 4.6). The data presented in this sensitivity analysis section showed the same results (i.e., significant or insignificant correlation coefficients) for the symmetric ellipse, asymmetric ellipse and circle models for c-fos and WSS as well as c-fos and WSSG. However, for c-fos and circumferential WSS as well as c-fos and circumferential WSSG, the symmetric and asymmetric models had the same results (i.e., significant correlation coefficient) while the circular model resulted in an insignificant correlation. Therefore, it is possible that this parameter combination is sensitive to the reconstruction technique and may not be a valid significant correlation.

The correlation coefficients for the linear transformation of the logarithmic nonlinear regression model using the absolute value of the normalized data are shown in Tables 4.14 and 4.15. For the symmetric elliptical cross-section reconstruction technique, six parameter combinations had significant correlations. Five of these parameter combinations were significant for all reconstruction techniques. The level of EC c-fos protein expression was inversely correlated with axial WSS ($r = -0.62$, $p = 0.003$, symmetric ellipse), circumferential WSS ($r = -0.52$, $p = 0.016$, symmetric ellipse), WSS magnitude ($r = -0.55$, $p = 0.009$, symmetric ellipse), circumferential WSSG ($r = -0.52$, $p = 0.015$, symmetric ellipse) and WSSG magnitude ($r = -0.59$, $p = 0.005$, symmetric ellipse). Only one parameter combination was significant for the symmetric ellipse model but not for the asymmetric ellipse reconstruction technique including the inverse correlation of the level of EC c-fos protein expression with axial WSSG ($r = -0.53$, $p = 0.013$, symmetric ellipse).

For the sensitivity analysis, the most important biologic and hemodynamic parameter combinations are those that resulted in significant correlations for the data from the symmetric ellipse models for all experiments shown in section 4.3.3. Specifically, significant correlations existed for c-fos and circumferential WSS, c-fos and WSS magnitude, c-fos and circumferential WSSG, and c-fos and WSSG magnitude (see Table 4.7). The data presented in this sensitivity analysis section showed the same results (i.e., significant or insignificant correlation coefficients) for the symmetric ellipse, asymmetric ellipse and circle models for all of these parameter combinations. Therefore, these parameter combinations are not

sensitive to the reconstruction technique and all significant correlations using the logarithmic nonlinear regression model found in section 4.3.3 are valid.

4.4 Discussion

4.4.1 Correlation Between Biologic and Hemodynamic Parameters

We have determined significant correlations between immediate early gene protein expression and hemodynamic parameters using directly-coupled data. For each region of interest in ETS and ETE anastomoses, biologic data were obtained from *ex vivo* perfusion experiments and hemodynamic data were obtained from CFD models of each experimental anastomosis. Linear regression was performed on these data and three combinations of parameters yielded significant correlations when using either the raw or normalized data. For the zero flow experiments, the degree of SMC apoptosis was positively correlated with circumferential WSSG. For the pooled data from all experiments, the levels of EC c-fos and c-jun protein expression were inversely correlated with WSSG magnitude. A number of other parameter combinations elicited significant correlations depending on whether raw or normalized data was used and which flow condition was considered.

The data with the most impact are the normalized data from all experiments. These correlations are based on the largest number of data points since all experiments (zero and retrograde flow) are included and normalization of the data accounts for experiment to experiment variability. When analyzed with linear regression, four combinations of parameters yielded significant correlations. The level of EC c-fos protein expression was inversely correlated with WSS and WSSG magnitude. The level of EC c-jun protein expression was also inversely correlated with WSSG magnitude. The level of EC egr-1 protein expression was inversely correlated with axial WSS. These data suggest that low levels of various WSS and WSSG parameters cause the upregulation of immediate early gene proteins as shown in Table 4.16. In addition, the relationships between low WSS and WSSG magnitude and the increase in EC c-fos protein level were found when using all three reconstruction techniques. Therefore, the strongest linear relationship between

Table 4.16 Hemodynamic influence on IEG protein expression as suggested by this study.

⇓ Axial WSS	⇑ EGR1
⇓ WSS Mag	⇑ CFOS
⇓ WSSG Mag	⇑ CFOS ⇑ CJUN

hemodynamic stimuli and IEG expression in these studies is that decreased WSS and WSSG caused an increase in the level of EC c-fos protein expression.

The relationship between the hemodynamic parameters and IEG protein expression shown in Table 4.16, specifically the strength of the correlation between WSS/WSSG magnitude with c-fos, was further validated when nonlinear regression models (reciprocal, exponential, power and logarithmic) were used to analyze the normalized data from all experiments. Table 4.17 summarizes the linear and nonlinear regression results for these parameter combinations. The linear transformation of the exponential nonlinear regression model based on the original, normalized data or the absolute value of the normalized data resulted in significant inverse correlations between the level of EC egr-1 protein expression and axial WSS as well as the level of EC c-jun protein expression and WSSG. For the egr-1 and WSS relationship, the same results were obtained when using any of the three reconstruction techniques indicating that this relationship is independent of the reconstruction technique. However, this was not true for the c-jun and WSSG relationship since the asymmetric ellipse reconstruction technique failed to reach significance. The linear transformation of the all of the nonlinear regression models (reciprocal, exponential, power and logarithmic) based on the original, normalized data or the absolute value of the normalized data resulted in significant inverse correlations between the level of EC c-fos protein expression and the magnitudes of WSS and WSSG. Again, the same results were obtained when using any of the three reconstruction techniques. Because all of the linear and nonlinear regressions used to analyze these combinations of normalized data resulted in significant correlations, the strongest relationship between hemodynamic stimuli and IEG expression in these studies is that decreased WSS and WSSG caused an increase in the level of EC c-fos protein expression.

Table 4.17 Parameter combinations with the most number of significant correlations using linear and nonlinear regression models. The regression equations, correlation coefficients and associated p values are shown as well as an indication of whether or not the correlation was significant for all reconstruction techniques.

Parameter Combination	Regression Equation	Correlation Coefficient	P Value	All reconstructions have same results?
EGR-1 and Axial WSS	$y = ax + b$	-0.27	0.011	yes
EGR-1 and Axial WSS	$y = a\|x\| + b$	-0.27	0.009	yes
EGR-1 and Axial WSS	$y = ae^{bx}$	0.29	0.005	yes
EGR-1 and Axial WSS	$y = ae^{b\|x\|}$	0.31	0.003	yes
CJUN and WSSG Mag	$y = ax + b$	-0.22	0.034	no
CJUN and WSSG Mag	$y = a\|x\| + b$	-0.22	0.034	no
CJUN and WSSG Mag	$y = ae^{bx}$	0.25	0.018	no
CJUN and WSSG Mag	$y = ae^{b\|x\|}$	0.25	0.018	no
CFOS and WSS Mag	$y = ax + b$	-0.22	0.037	yes
CFOS and WSS Mag	$y = a\|x\| + b$	-0.22	0.037	yes
CFOS and WSS Mag	$y = a + b/x$	0.21	0.044	yes
CFOS and WSS Mag	$y = a + b/\|x\|$	0.21	0.044	yes
CFOS and WSS Mag	$y = ae^{bx}$	0.25	0.020	yes
CFOS and WSS Mag	$y = ae^{b\|x\|}$	0.25	0.020	yes
CFOS and WSS Mag	$y = a\|x\|^b$	0.27	0.011	yes
CFOS and WSS Mag	$y = a + b \ln\|x\|$	0.29	0.006	yes
CFOS and WSSG Mag	$y = ax + b$	-0.26	0.012	yes
CFOS and WSSG Mag	$y = a\|x\| + b$	-0.26	0.012	yes
CFOS and WSSG Mag	$y = a + b/x$	0.23	0.027	yes
CFOS and WSSG Mag	$y = a + b/\|x\|$	0.23	0.027	yes
CFOS and WSSG Mag	$y = ae^{bx}$	0.29	0.006	yes
CFOS and WSSG Mag	$y = ae^{b\|x\|}$	0.29	0.006	yes
CFOS and WSSG Mag	$y = a\|x\|^b$	0.29	0.006	yes
CFOS and WSSG Mag	$y = a + b \ln\|x\|$	0.30	0.004	yes

4.4.2 Comparison to Other Research

To our knowledge, these are the first directly-coupled data demonstrating significant correlations between immediate early gene protein expression and specific hemodynamic parameters at the end-to-side vascular anastomosis. Most of the previous research on the biological effect of hemodynamics on IEG expression has been conducted in endothelial cell culture models. As discussed in Section 1.6.3.1, studies conducted by Hsieh *et al.* [43], Ranjan and Diamond [44] and Nagel *et al.* [45] exposed human umbilical vein EC to various levels of WSS for 30 minutes to 4 hours and measured the resulting gene and protein expression of various IEG. They found that c-fos, c-jun and egr-1 expression correlates directly with WSS. In contrast, in vascular bypass grafts perfused *ex vivo*, we found that egr-1 protein expression was inversely correlated with axial WSS and c-fos protein expression was inversely correlated with WSS. Our results also showed that c-fos and c-jun protein expression was inversely correlated with WSSG magnitude. However, Nagel *et al.* prescribed disturbed flow in their cell culture experiments for 30 minutes and found that the expression of c-fos, c-jun and egr-1 protein correlated directly with spatial WSSG.

There are a number reasons that could account for the discrepancy between our results and those of previous cell culture studies. The most striking is that cell culture studies can not incorporate the multiple cellular and extracellular matrix interactions and the effects of the three-dimensional structure and mechanical environment on the vascular EC that is accounted for in a whole-vessel preparation [177, 180-182]. For cell culture studies, the cells are grown on a non-physiologic substrate in a monolayer configuration, which can affect their phenotype and response to external stimuli [180, 183]. Additionally, the cells used in such cell culture studies are often EC derived from human umbilical veins while the EC population in our study was from intact porcine femoral arteries. Vein and artery cells are normally exposed to very different biomechanical environments and may respond differently to hemodynamic stimuli [7, 184, 185]. Finally, cells obtained from different species may also exhibit varied responses [185]. Therefore, although the correlations between IEG protein expression and hemodynamic parameters in our study are different than the correlations found previously in cell culture models, we believe that our experimental

design is more physiologically relevant and may come closer to determining the correlations that exist *in vivo*.

Previous research by Gan *et al.* is most closely related to our study [142]. They perfused intact human umbilical veins *ex vivo* for 6 hours at low (< 4 dynes/cm^2) or high (<25 dynes/cm^2) levels of WSS. They found a significant increase in the amount of c-fos and c-jun gene expression, as well as c-jun protein expression, for the vessels exposed to high WSS c-jun protein compared to the low WSS vessels (see Figure 1.16a). They did not find a significant difference in the level of c-fos protein expression due to the level of WSS. We found, however, that low levels of WSS significantly increased EC c-fos protein expression. There are a number of possible reasons for the discrepancy in our results including the type of vessel used for the experiment and the techniques for calculating WSS and quantifying c-fos protein expression. In their study, Gan *et al.* used human umbilical veins so the discrepancy could be due to the fact that we used arterial segments from swine. Also, in the study by Gan *et al.,* only a generalized WSS (τ) was calculated for the entire vessel using a modified form of the Poiseuille equation:

$$\tau = \frac{1}{2}\left(\frac{\Delta P}{L}\right)^{3/4}\left(\frac{8\eta Q}{\pi}\right)^{1/4} \qquad [4.6]$$

where ΔP is the pressure drop over the vessel, L is the vessel length, η is the kinematic viscosity of the fluid and Q is the flow rate through the vessel. This calculation assumes that the vessel has a uniform diameter along its length which may not be realistic, as seen in the diameter variations along the length of our vessels even in the regions away from the anastomosis. Finally, Gan *et al.* based their quantification of c-fos protein expression on regions of the entire vessel wall so the quantitative value they report includes the expression of c-fos by SMC whereas our measurements focus solely on the expression of c-fos by the EC. Therefore, there are a number of factors that could account for the fact that we found a significant, inverse correlation between c-fos protein expression and WSS while the study by Gan *et al.* did not find a significant change in c-fos protein expression due to different levels of WSS.

As discussed in Section 1.4.3, although a direct correlation between IEG expression and IH has not been determined previously, there is a large body of evidence leading to the conclusion that IEG expression precedes and is related to IH. For example, c-fos expression has been shown to lead to increased SMC proliferation, a defining characteristic of IH [40, 51, 52]. C-fos expression has also been shown to result in SMC apoptosis which may upset the balance between proliferation and apoptosis and lead to IH formation [60]. The most striking evidence that IEG are related to IH is that gene therapy blocking c-fos, c-jun or egr-1 expression inhibits IH formation *in vivo* [59, 140].

As discussed in Sections 1.5 and 1.7, previous research has not been conclusive on the hemodynamic implications in IH. However, many studies have shown that low WSS leads to IH formation [72, 73, 77-83, 86, 87, 94, 102]. If we assume that the level of IEG expression correlates with IH formation, then we can relate the results of our studies to the previous research on the role of hemodynamics in IH formation. For example, our results show that low levels of WSS (specifically axial WSS and WSS magnitude) would result in increased IH, a similar finding to previous research. Other studies have previously shown that spatial WSSG correlates with IH formation [66, 85, 87, 89-91]. However, our study found the opposite result. We determined that spatial WSSG magnitude inversely correlates with IH, assuming that IEG expression is directly related to IH formation. The discrepancy in our results is most likely due to the fact that the previous studies focusing on WSSG did not utilize quantitative, directly-coupled hemodynamic and biologic data. It may initially seem counterintuitive that WSSG would be protective since the hemodynamics in a physiological, non-diseased state is assumed to be uniform. However, in reality, the vasculature is constantly branching and curving and the blood flow is pulsatile which innately causes spatial as well as temporal WSSG. Therefore, at least hypothetically, it is conceivable that vessels may be prone to IH formation if the level of WSSG normally found in the vasculature is decreased.

Previous research by Keynton *et al.* is most closely related to our study in that they obtained hemodynamic and biologic data in distal ETS anastomoses as shown in Figure 4.23 [79]. The main difference between their study and ours is that they used an *in vivo* dog model and measured wall shear rate

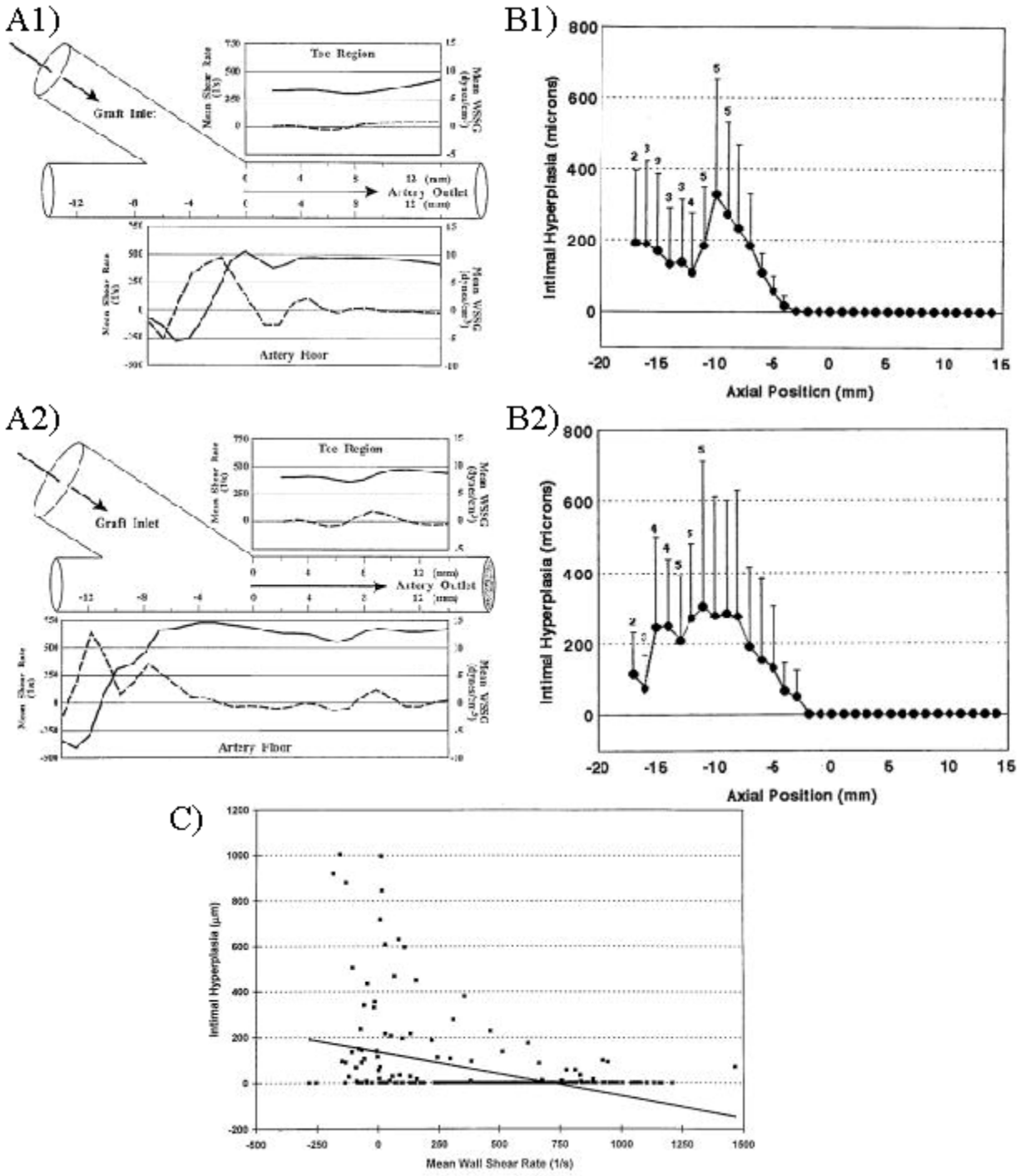

Figure 4.23 Results from [79] studying correlating WSR and IH formation in ETS vascular bypass grafts. Mean WSR (solid line) and spatial WSSG (dashed line) distributions for the toe region and the artery floor are shown for graft-host artery diameter ratios of A1) 1.0 and A2) 1.5. The corresponding distribution of IH formation (mean ± standard deviation) along the floor are shown for graft-host artery diameter ratios of B1) 1.0 and B2) 1.5. The pooled data for both diameter ratios were analyzed and the linear regression with the best correlation, mean WSR and IH, is shown in C).

(WSR) at the time of insertion of a prosthetic graft and the degree of IH formation along the anastomosis 12 weeks after anastomosis construction. From the WSR measurements, Keynton *et al.* were able to calculate a number of hemodynamic parameters including mean, peak, pulse amplitude, absolute mean and absolute peak WSS and WSSG as well as the oscillatory shear index. Their linear regression analysis showed that the best relationship was an inverse correlation between the mean WSR and IH formation ($r = -0.406$, $p < 0.05$). This is analogous to our results showing a significant inverse correlation between WSS magnitude and c-fos protein expression ($r = -0.22$, $p < 0.05$), which, again, could be extrapolated to IH formation assuming that IEG expression correlates directly with IH. Keynton *et al.* did not, however, find a significant correlation between spatial WSSG and IH formation while we found a significant inverse correlation between WSSG magnitude and c-fos ($r = -0.26$, $p < 0.05$) and c-jun ($r = -0.22$, $p < 0.05$) protein expression), which could be extrapolated to IH formation assuming that IEG expression correlates directly with IH. One possible reason that our WSSG results do not match those of Keynton *et al.* is that their dog model necessarily incorporated pulsatility and while we imposed steady flow in porcine arteries. Another possible reason for the discrepancy could be due their inability to obtained directly-coupled biologic and hemodynamic data. Because of extensive tissue encapsulation, they could not measure the hemodynamic data at the end of the experiment when the biologic data was measured and there is no way to regulate the hemodynamics in a conscious dog over the 12 week period. In contrast, our use of an *ex vivo* model allowed for tight regulation of the hemodynamics such that the resulting biologic parameter can be correlated with the hemodynamic value imposed throughout the experiment. Another possible reason that we found a significant correlation based on WSSG is that we obtained biologic data from regions in the entire anastomosis, including the graft and hood while the IH measurements of Keynton *et al.* were only taken along the host artery since a prosthetic graft was used. Also, since a prosthetic graft was used, compliance mismatch occurs at the anastomosis, increasing the number of parameters that may be responsible for IH formation whereas our artery-artery constructs do not have compliance mismatch and therefore isolate the hemodynamics as the cause of the resulting biologic response.

4.4.3 Limitations

In order to obtain directly-coupled biologic and hemodynamic data, we chose to obtain the biologic data from *ex vivo* perfusion of ETS anastomoses and then reconstruct these anastomoses to determine the hemodynamic data from CFD analyses. The main drawback of this approach is that it involves a lot of steps in the process, which potentially introduce error and are time-consuming. To obtain the biologic data for each anastomosis, the perfusion must be completed, the tissue processed, frozen and sliced before cryosectioning can occur. For each region of interest, the slides are stained, microscopy images are taken and then quantified. The error up to this point in the process is approximately 29% based on the repeatability studies of the staining quantification (see Appendix D.1). In addition, if any of these steps is performed incorrectly, it is possible to lose all the data for a given experiment. To obtain the hemodynamic data, the tissue cross-sections are digitized to obtain the luminal boundary and the error associated with the luminal digitization is approximately 20% (see Appendix D.2). These two-dimensional shapes are lofted to create a three-dimensional surface that is meshed and the boundary conditions are applied based on the experimental flow conditions. The flow rate and viscosity values used in the CFD simulations have a potential error of approximately 5% and 1.5%, respectively, based on the sensitivity of the flow meter and the range of media viscosity. The hemodynamic parameters of interest are derived from the resulting velocity field and then averaged over the region of interest. The mesh independence analysis (see sections 3.2.3 and 3.3.1) illustrated that the CFD results can have an error ranging up to 20% depending on the imposed flow condition, type of anastomosis and hemodynamic parameter being calculated. Because there are so many steps in determining the biologic and hemodynamic parameters, there is the potential to introduce error, as outlined above, as well as the potential for this error to propagate throughout the process. Therefore, we have focused on the normalized biologic and hemodynamic data in order to account for, and minimize, these errors (explained in detail in sections 2.2.13 and 3.4.4). Finally, even if all steps required for the measurement of biologic parameters and calculation of hemodynamic parameters are performed correctly and in a timely manner, it takes approximately three weeks to determine the single, quantitative values for the biologic and

hemodynamic parameters for each region of interest for a given experiment. However, the ability to obtain the directly-coupled, quantitative data is unique and an important tool for determining the hemodynamic parameter responsible for IEG protein expression in vascular bypass grafts.

Because we obtained directly-coupled data, we were able to correlate the biologic endpoints with the hemodynamic environment in vascular bypass grafts. We chose to perform the correlation analyses using parametric statistical tests which assume that the underlying distribution of the data follows the normal distribution. Figures 4.24, 4.25, 4.26 and 4.27 show the raw and normalized biologic (IEG and apoptosis) and hemodynamic (WSS and WSSG) data compared to the normal distribution. Qualitatively, the data follow the normal distribution. The main difference between the data and the normal distribution is that most of the data have higher peaks indicating less variance compared the normal distribution [157]. For almost all of the parameters, the peak of the curve for the data occurs at the same point as the normal distribution. The only parameters showing any evidence of skewness are the normalized axial WSS, WSS and WSSG magnitude data. Therefore, based on these plots of the data for each biologic and hemodynamic parameter compared to the normal distribution, we believe that it is valid assume that the data follow the normal distribution. However, further statistical analyses could be completed using the nonparametric analogues to the parametric tests we used: e.g., the Spearman rank-correlation coefficient could be calculated instead of the Pearson correlation coefficient [157]. As an example, we calculated the Spearman rank-correlation coefficient for the linear regression analyses of the normalized data pooled from all experiments. The parameter combinations with statistically significant correlations using this nonparametric analysis were c-fos and WSS (inverse correlation), c-fos and WSSG (inverse correlation), and SMC apoptosis and axial WSSG (direct correlation), while the parameter combinations found using the parametric tests were c-fos and WSS, c-fos and WSSG, c-jun and WSSG, and egr-1 and axial WSS (all inverse correlations, see Table 4.2). Therefore, although the results were slightly different depending on whether parametric or nonparametric analyses were performed, it did not affect our final conclusion that the strongest relationship

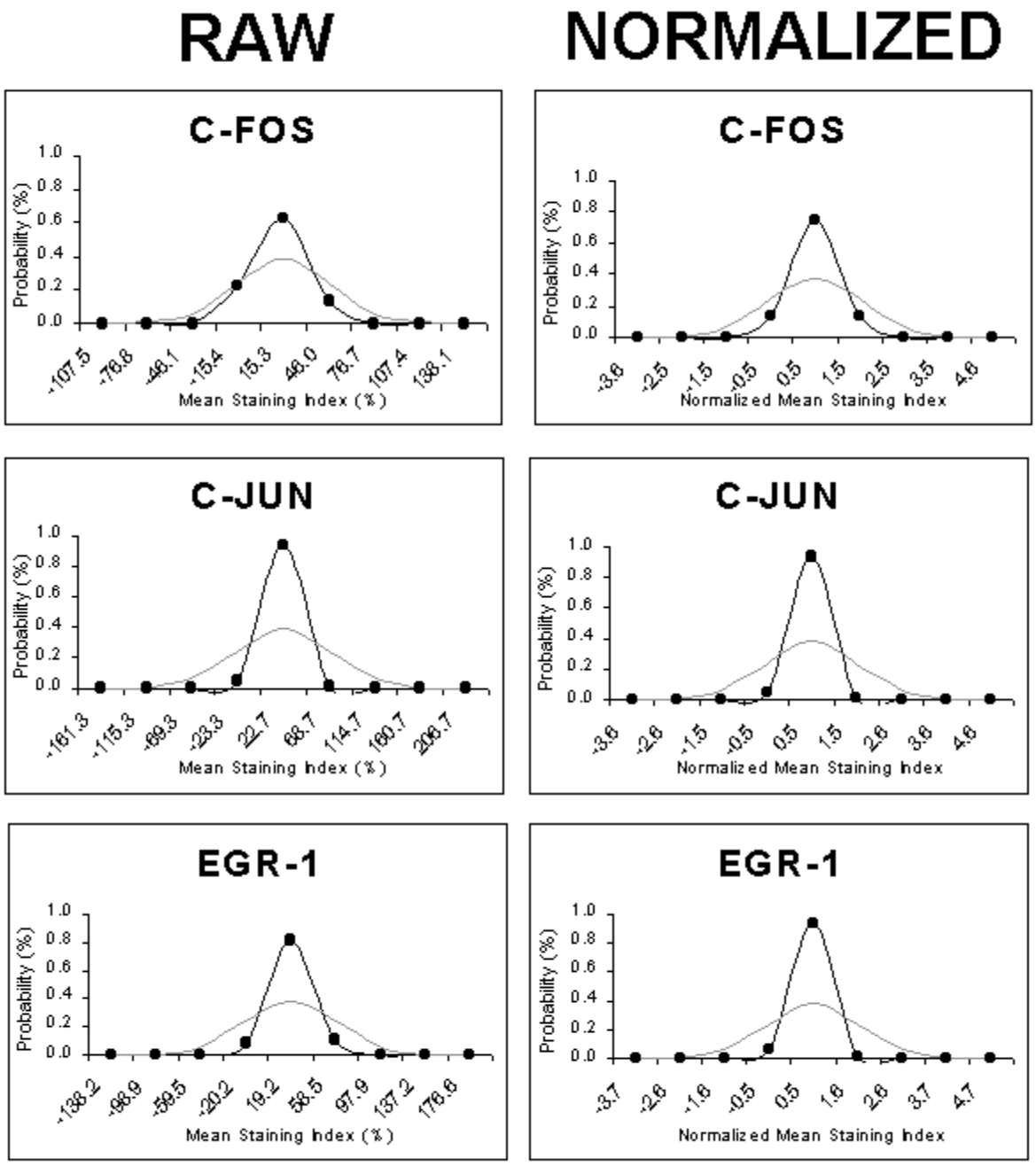

Figure 4.24 Plot of the raw (left) and normalized (right) data for c-fos, c-jun and egr-1. The data were separated into 9 even intervals (-4 standard deviations from the mean to +4 standard deviations from the mean) and the percentage of data points present in each interval were plotted as filled circles connected by a black curve. The normal distribution was plotted as the grey curve for comparison where the mean occurs at the peak and the height is inversely proportional to the standard deviation. Note that increased height of the curve indicates less variance in the data.

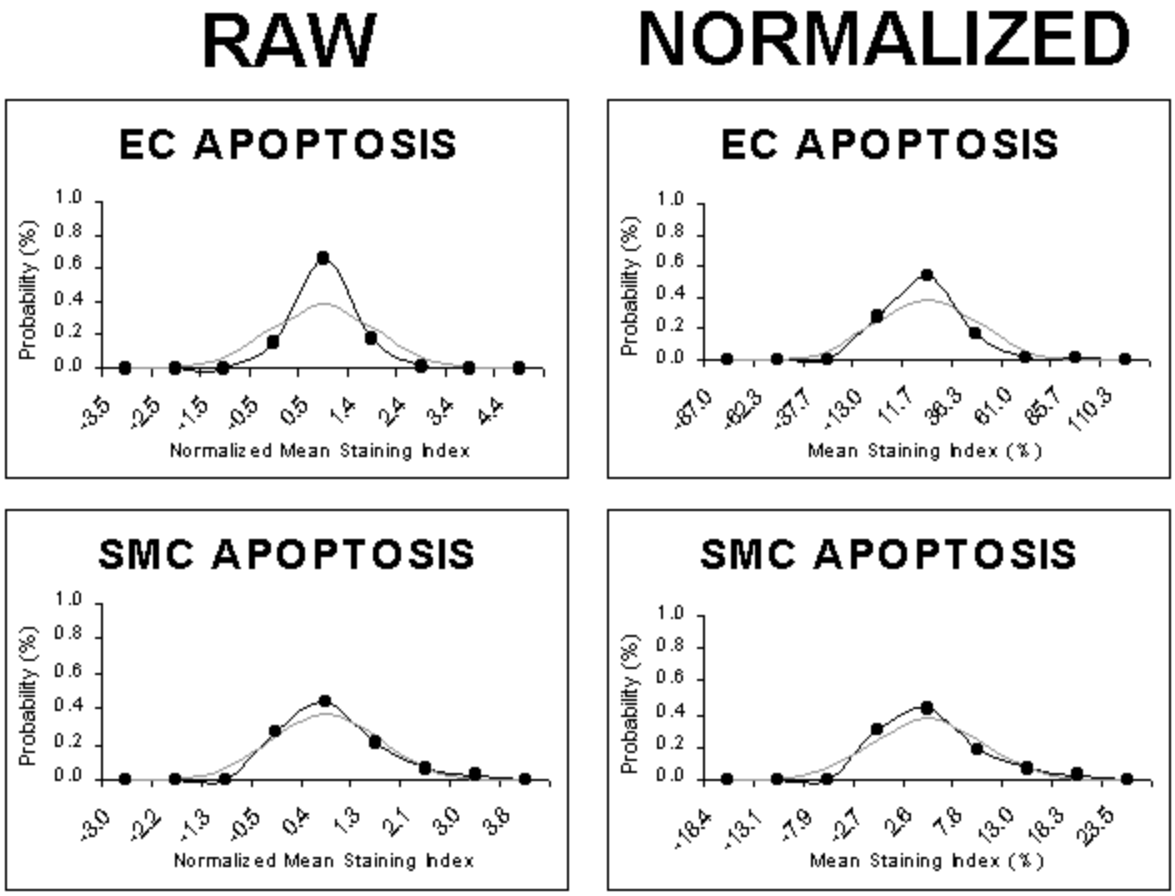

Figure 4.25 Plot of the raw (left) and normalized (right) data for EC and SMC apoptosis. The data were separated into 9 even intervals (-4 standard deviations from the mean to +4 standard deviations from the mean) and the percentage of data points present in each interval were plotted as filled circles connected by a black curve. The normal distribution was plotted as the grey curve for comparison where the mean occurs at the peak and the height is inversely proportional to the standard deviation. Note that increased height of the curve indicates less variance in the data.

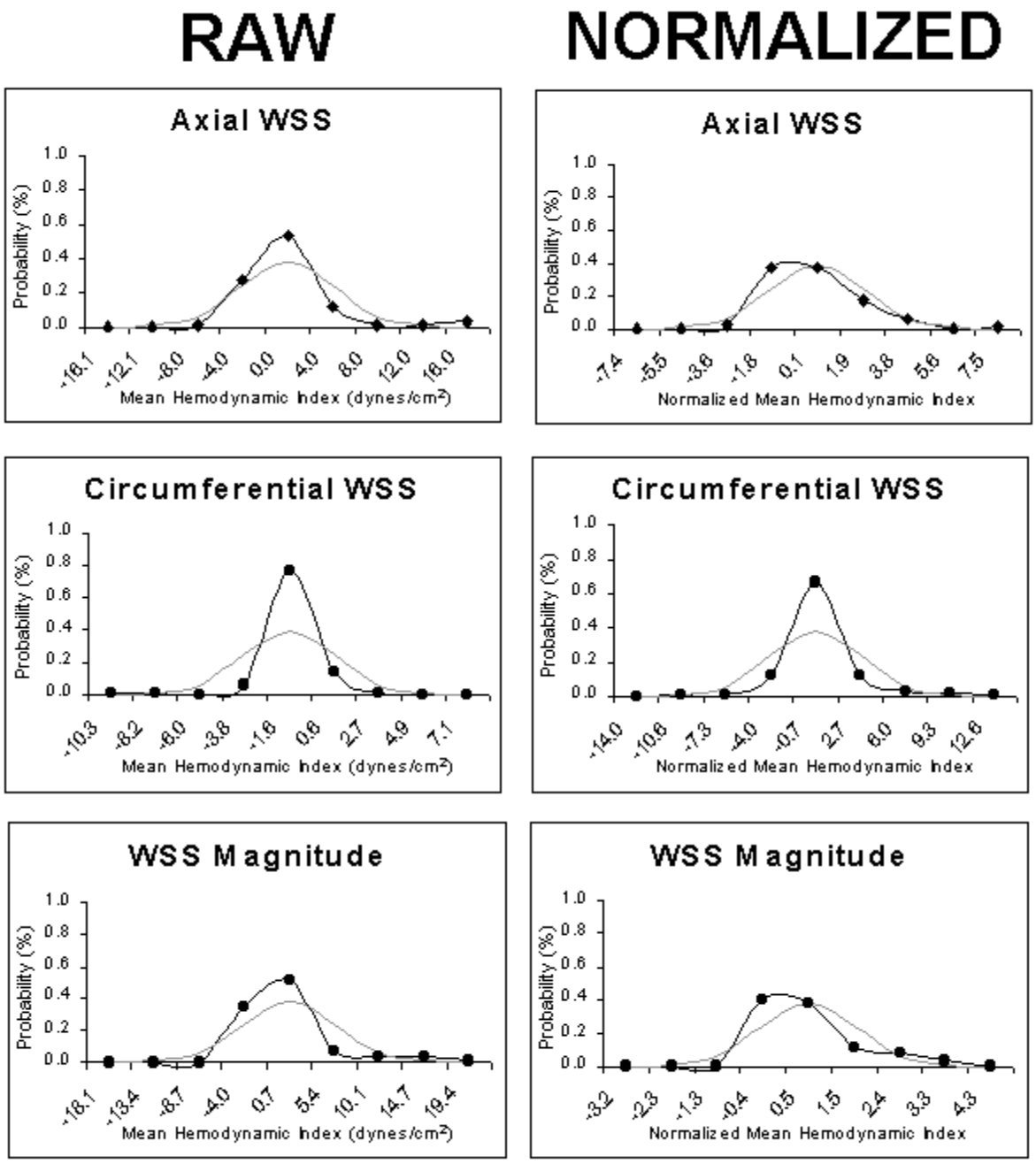

Figure 4.26 Plot of the raw (left) and normalized (right) data for axial WSS, circumferential WSS and WSS magnitude. The data were separated into 9 even intervals (-4 standard deviations from the mean to +4 standard deviations from the mean) and the percentage of data points present in each interval were plotted as filled circles connected by a black curve. The normal distribution was plotted as the grey curve for comparison where the mean occurs at the peak and the height is inversely proportional to the standard deviation. Note that increased height of the curve indicates less variance in the data.

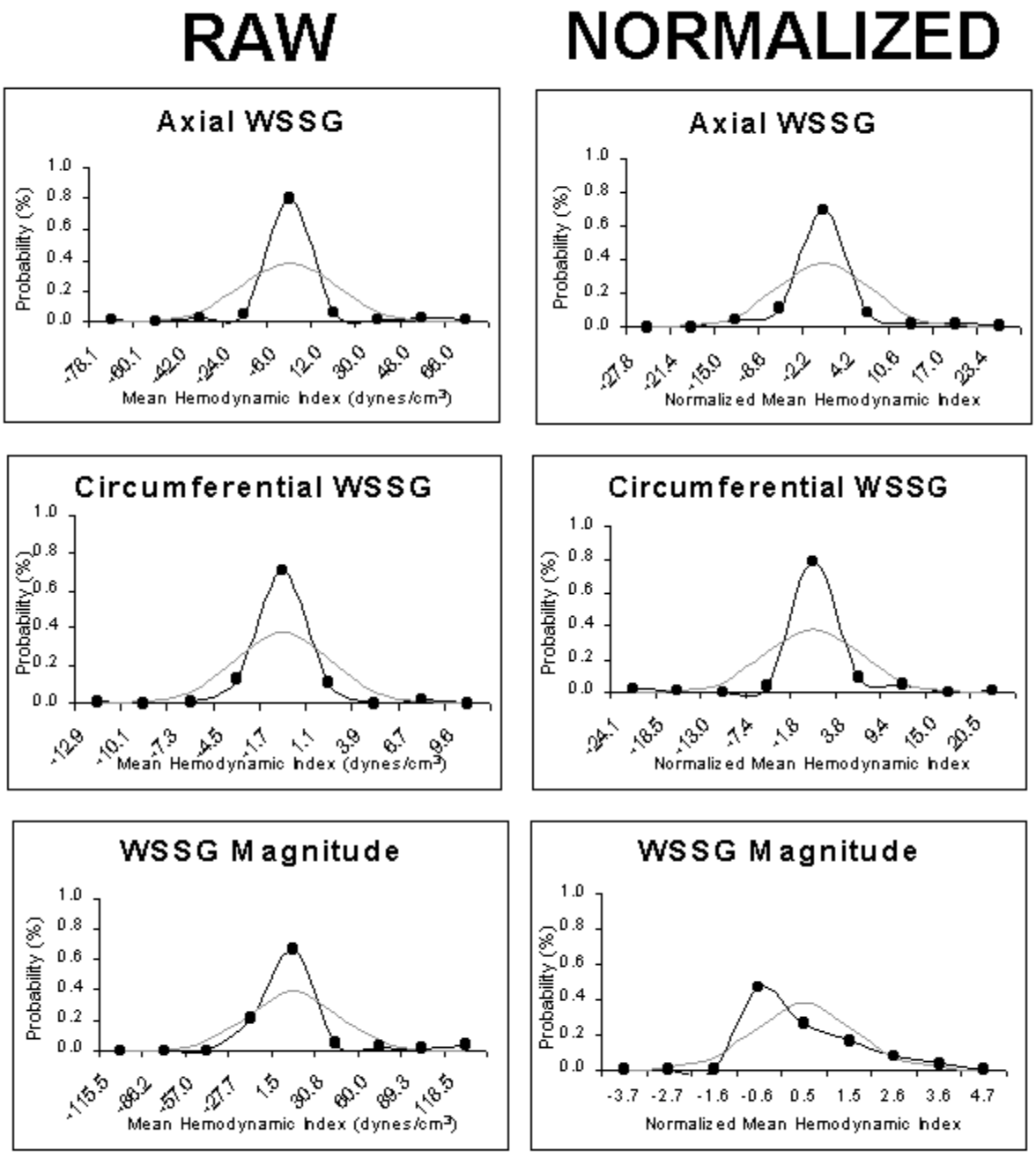

Figure 4.27 Plot of the raw (left) and normalized (right) data for axial WSSG, circumferential WSSG and WSSG magnitude. The data were separated into 9 even intervals (-4 standard deviations from the mean to +4 standard deviations from the mean) and the percentage of data points present in each interval were plotted as filled circles connected by a black curve. The normal distribution was plotted as the grey curve for comparison where the mean occurs at the peak and the height is inversely proportional to the standard deviation. Note that increased height of the curve indicates less variance in the data.

between hemodynamic stimuli and IEG expression in these studies is that decreased WSS and WSSG caused an increase in the level of EC c-fos protein expression.

We utilized all data obtained from the experiments and CFD models for the regression analyses and did not examine the data for any possible outliers. Potential outliers can be detected by determining if any of the data points is more than four standard deviations from the mean [157]. The plots in Figures 4.24, 4.25, 4.26 and 4.27 illustrate that there were no outliers based on this criteria for the raw and normalized biologic and hemodynamic data. However, transformation of the data for the nonlinear regression analyses could have resulted in outliers. For example, when transforming the hemodynamic data for the reciprocal regression analyses, the data were inverted so that WSS magnitude values close to zero became very large. Therefore, these large reciprocal values (i.e., more than four standard deviations from the mean) may be outliers for the reciprocal nonlinear regression analysis even though the original data did not have any outliers. However, potential outliers should not be removed without careful consideration including a physical reason for their removal (e.g., experimental mishap). Because the original data did not contain outliers and there was no experimental or physical reason for removing outliers just for the nonlinear regression analyses, we did not believe that removing potential outliers was valid. An alternative approach for accounting for potential outliers is to analyze the data using nonparametric methods (as discussed in the previous paragraph) which minimize the effects of outliers on the overall result [157]. As an example, we calculated the Spearman rank-correlation coefficient for the reciprocal nonlinear regression analyses of the normalized data pooled from all experiments. The two parameter combinations with statistically significant direct correlations using this nonparametric analysis were c-fos and WSS, and c-fos and WSSG, while the parameter combinations found using the parametric tests were c-fos and axial WSS, c-fos and WSS, c-fos and WSSG (see Table 4.4). Therefore, although the results were slightly different depending on whether parametric or nonparametric analyses were performed, this comparison illustrates that potential outliers do not affect our final conclusion that the strongest relationship between hemodynamic stimuli and IEG

expression in these studies is that decreased WSS and WSSG caused an increase in the level of EC c-fos protein expression.

We chose to complete these studies using steady flow which does not capture the pulsatility found physiologically. Due to the technical difficulties in creating the anastomoses *ex vivo*, we decided to simplify the protocol and only include steady flow. To incorporate pulsatility into the CFD models, each reconstructed anastomosis would have taken approximately sixty times longer to complete since a full steady flow simulation would essentially have to be solved for each time step of an input waveform sampled at 1 Hertz. This would have required approximately 120 days to complete each pulsatile simulation with our current computational resources and was therefore not feasible. To maintain the ability to obtain directly-coupled data, we chose to perform the experiments under steady flow conditions. Therefore, the correlations were found are only relevant for steady flow. As part of his cell culture study, Hsieh *et al.* found that although EC respond differently to steady and pulsatile flow, the response is simply more pronounced under pulsatile flow conditions and not radically altered [43]. Therefore, our results may still be valid when applying them to the pulsatile flow situation but this will have to be validated by future studies that incorporate pulsatility. These studies could be completed in our lab with our current experimental equipment and increased computational resources which are readily available.

4.5 Conclusion

We have determined a significant correlation between the hemodynamic stimuli and biologic response of the EC layer in ETS and ETE anastomoses. Vascular bypass graft constructs were exposed to well-controlled hemodynamics using an *ex vivo* perfusion system and the expression of IEG proteins in EC as well as EC and SMC apoptosis were quantified at 9 regions of interest along the anastomoses. CFD models of each anastomosis were developed based on the geometry and imposed pressure and flow conditions in each experiment. From these models, we determined the axial and circumferential components and magnitude of WSS and WSSG in the same regions of interest. Through linear and nonlinear regression analysis on this

directly-coupled data, we found that low levels of various WSS and WSSG parameters cause the upregulation of certain IEG proteins. Although a number of other studies have attempted to determine the influence of hemodynamics on biologic precursors of IH formation, to our knowledge this is the first study to determine a quantitative correlation between directly-coupled hemodynamic and biologic data.

Further studies need to be completed in order to determine if the same correlations exist in a pulsatile environment, but if these correlations remain valid, there are a number of options that could be investigated to decrease the amount of IH formation in vascular bypass grafts. The hemodynamics of graft construction, particularly the geometry, could be optimized to exclude low levels of axial WSS and magnitudes of WSS and WSSG. Alternatively, since surgeons are frequently unable to influence the graft geometry due to local constraints, regions known to have low levels of WSS or WSSG could be treated locally with gene therapy or pharmacological agents that would reduce the expression of c-fos, c-jun and/or egr-1. These treatments could potentially lead to decreased IH formation and increase the success of vascular bypass grafts.

5 .0 DISCUSSION

5.1 Summary of Results

We have developed a technique for collecting regional, quantitative biologic and hemodynamic data in ETS and ETE vascular bypass graft anastomoses. These data were correlated to determine a quantitative relationship between acute precursors of IH (IEG protein expression, EC and SMC apoptosis) and the hemodynamic parameters (axial and circumferential components and magnitude of WSS and WSSG) that cause this biologic response. To our knowledge, this is the first time that such a directly-coupled approach has been utilized. It has allowed for the determination of the association of certain hemodynamic parameters with the expression of IEG, and possibly with IH formation and eventual bypass graft failure.

5.1.1 Spatial Variation of IEG and Apoptosis

To accomplish Specific Aim #1, we created ETS and ETE anastomoses of porcine femoral arteries using vascular clips and perfused them *ex vivo* under steady flow conditions for six hours. We found a significant regional variation of IEG proteins (c-fos, c-jun and egr-1) within the ETS anastomosis (Figures 2.21 and 2.22). The levels of c-fos and c-jun protein were highest in the ETS proximal and distal artery segments while the lowest levels of c-fos and c-jun protein occurred in the regions in and near the anastomosis including the ETS heel, toe, floor and hood. There was no significant difference between the ETE proximal and anastomosis regions indicating that the surgical manipulation and use of vascular clips to create an anastomosis do not contribute to differences in c-fos and c-jun protein expression. In contrast, the only region showing consistently different egr-1 protein expression was the ETE anastomosis segment, which was lower than almost all other regions. Although we found a significant spatial variation in IEG protein expression, there was no significant regional variation of EC or SMC apoptosis. To our knowledge, these are the first data showing a regional variation of IEG protein expression along ETS and ETE anastomoses of vascular bypass grafts.

5.1.2 Spatial Variation of Hemodynamic Parameters

To accomplish Specific Aim #2, we reconstructed the three-dimensional inner surface of each experimental ETS and ETE anastomosis and developed computational fluid dynamics models. For each CFD model, the hemodynamic parameters of interest (axial and circumferential components and magnitude of WSS and WSSG) were calculated everywhere within the three-dimensional domain and the average hemodynamic parameters were determined for the same regions of interest used for the biologic endpoints. We determined that a regional variation of hemodynamic parameters, most notably axial WSS and the magnitudes of WSS and WSSG, exist in these anastomoses (Figures 3.64 - 3.66). The regions with the most variation in hemodynamic parameters were the ETS proximal artery, heel, toe and distal artery segments. The ETS proximal artery and heel regions exhibited significantly lower axial WSS and WSSG magnitude compared to other regions of interest. The ETS toe and distal artery segments had significantly higher axial and circumferential components as well as magnitude of WSS compared to other regions. Although a number of other studies have alluded to a regional variation of hemodynamic parameters, particularly in ETS anastomoses, to our knowledge this is the first study to quantify these difference and illustrate that they are statistically significant.

5.1.3 Correlation of Biologic and Hemodynamic Data

For Specific Aim #3, we determined if any significant correlations existed between the biologic and hemodynamic data acquired in Specific Aims #1 and #2. Through linear and nonlinear regression analyses on this directly-coupled data, we found four significant correlations:

1) EC egr-1 protein expression was inversely correlated with axial WSS.

2) EC c-fos protein expression was inversely correlated with WSS magnitude.

3) EC c-fos protein expression was inversely correlated with WSSG magnitude.

4) EC c-jun protein expression was inversely correlated with WSSG magnitude.

Therefore, our data suggest that low levels of WSS and WSSG cause the upregulation of IEG proteins. Based on previous research showing that increased levels of IEG expression correlate with IH formation [40,

51, 52, 59, 60, 140], our results suggest that low levels of WSS and WSSG ultimately lead to increased IH formation. Although a number of other studies have attempted to determine the influence of hemodynamics on IH formation, to our knowledge this is the first study to determine a quantitative correlation between directly-coupled hemodynamic and biologic data in ETS and ETE anastomoses of vascular bypass grafts.

Although a significant amount of previous research has attempted to isolate the influence of hemodynamics on IH formation, a quantitative correlation between a specific hemodynamic parameter and a particular cellular response leading to IH had not been elucidated. With the intent of clarifying this mechanism, we exposed ETS and ETE anastomoses created from intact vascular segments to a well-controlled hemodynamic environment. We then quantified the resulting biologic and hemodynamic parameters in a directly coupled manner and determined the parameters with a significant correlation. By determining that low levels of axial WSS and magnitudes of WSS and WSSG correlate with upregulation of IEG protein, we believe that we have taken a significant step toward determining a mechanistic understanding of how hemodynamic parameters cause the upregulation of biologic precursors of IH formation.

5.2 Clinical Significance

There are a number of treatments that may improve the clinical success rate of vascular bypass grafts based on the correlations we found between low levels of WSS and WSSG and the subsequent increase in IEG protein expression. For example, in order to exclude the pathologically low levels of axial WSS and magnitudes of WSS and WSSG, the hemodynamics of graft construction could be optimized. Geometric features of the anastomosis such as the angle of insertion, diameter ratio between the graft and host artery and flow split between the proximal and distal outflow segments have previously been shown to alter the hemodynamics [79, 88, 91, 154, 155, 166, 175, 186-189] and could potentially be manipulated to produce the optimal pattern of WSS and WSSG. For example, Lei *et al.* used CFD models to calculate the WSSG magnitude in ETS distal anastomoses with different geometries [91, 155]. They concluded that the increased

patency of the Taylor patch anastomosis compared to a conventional anastomosis was at least partially due to the altered geometry, which resulted in lower WSSG along the anastomosis. Moreover, they determined an optimal graft geometry that minimized the WSSG along the anastomosis. However, surgeons are frequently limited in determining the graft geometry due to local constraints. In this case, regions known to have low levels of WSS or WSSG based on the configuration they are forced to use, could be treated locally with gene therapy or pharmacological agents that would reduce the expression of c-fos, c-jun and/or egr-1. Such treatments have previously shown potential in decreasing the extent of IH [53, 57, 58, 140, 190] and having the added knowledge of where to focus these treatments locally could further decrease IH formation and increase the success of vascular bypass grafts.

5.3 Advantages of Methodology

In previous studies there was either no direct coupling between quantitative biologic and hemodynamic measurements, the values of these parameters were not continuously known or regulated, or the biologic model was not complete. Our coupled experimental and computational approach has allowed us to collect and correlate directly-coupled biologic and hemodynamic data. The advantages of our methodology are summarized below.

5.3.1 *Ex Vivo* Perfusions

Much of the previous research on the effect of WSS and WSSG has been conducted in cell culture or *in vivo* models. Cell culture models are advantageous because they allow for the tight regulation and alteration of a single hemodynamic parameter. However, the results may not be relevant to *in vivo* conditions. Cell culture studies can not incorporate the multiple cellular and extracellular matrix interactions and the effects of the three-dimensional structure and mechanical environment on the vascular EC that occurs *in vivo* [177, 180-182]. On the other hand, *in vivo* models are not ideal because the hemodynamic parameters can not be regulated over the time course of the experiment which can last for weeks or months, in the case of intimal hyperplasia formation. Additionally, it is not possible to alter a single hemodynamic parameter

at a time since, for example, changing the blood flow will affect the blood pressure and other physiological functions. Therefore, we chose to utilize an *ex vivo* perfusion system which allows us to study intact vascular segments while also regulating the imposed hemodynamics independent of other parameters, such as pressure.

5.3.2 Artery-Artery Anastomoses

Most of the previous vascular graft research has used prosthetic conduits or veins as vascular grafts since these are used most often clinically. However, when these types of grafts are used, the biologic response of the vascular cells can not be solely attributed to an alteration in hemodynamics due to the creation of the anastomosis. For example, the biologic response of the vascular cells in a vein graft are complicated by the fact that the venous cells are suddenly placed in the high pressure, high flow, pulsatile environment of the arterial system. This alone could lead to a biologic response by the venous cells [7, 184, 185], which could not be separated from the response due to the altered hemodynamics at the anastomosis. In addition, the use of prosthetic or vein grafts causes a compliance mismatch to occur at the anastomosis, which has been shown to affect vascular cells. Because our studies were conducted under steady flow conditions, compliance mismatch was not an issue. However, artery-artery anastomoses would be critical for future studies incorporating pulsatility in order to isolate the hemodynamic effects from the compliance mismatch effects. Therefore, we have chosen to create artery-artery anastomoses to isolate the effect of altered hemodynamic parameters on the vascular cells.

5.3.3 Continuous Mapping of Hemodynamic Parameters

Physical models and *in vivo* studies of the hemodynamics in ETS and ETE anastomoses are not able to obtain a three-dimensional flow field and therefore are not able to continuously map the hemodynamic parameters along the entire inner surface of the anastomosis. In physical flow models, laser Doppler anemometry (LDA) measures the velocity at a single point and particle image velocimetry (PIV) measures the velocity within a single, two-dimensional slice. Ultrasonic and electromagnetic transducers can directly measure the flow rate or wall shear rate *in vivo*, but only at discrete points along the anastomosis. Therefore,

we chose to obtain our hemodynamic data from CFD models that allow for the determination of the three-dimensional flow field based on the geometry of the anastomosis and the imposed flow conditions.

5.3.4 Directly-Coupled Approach

One of the most important advantages of our methodology is that the biologic and hemodynamic data are measured in the same regions of the same anastomoses. Most previous work that has measured both biologic and hemodynamic data has assumed a generalized measurement for one of the data sets. For example, in many reports, biologic measurements were made in multiple bypass grafts but the hemodynamic measurements were made in a single graft reconstruction with global geometric traits similar to the average of the grafts used to obtain the biologic data [78, 164, 176]. The primary reason this is done is because the geometry of the anastomosis is lost due to the required tissue processing for the determination of biologic data. To avoid this problem, we developed a protocol for processing the tissue so that the IEG protein expression and EC and SMC apoptosis could be measured while also allowing for the reconstruction of each ETS and ETE anastomosis to develop CFD models for the calculation of hemodynamic parameters. This allowed us to obtain biologic and hemodynamic data from the same regions of the same anastomoses and resulted in a directly-coupled data set. Therefore, the results of this study illustrate a cause and effect relationship between the hemodynamic stimuli (i.e., low WSS and WSSG) and biologic response (IEG protein expression) in intact vascular bypass grafts that had not been established previously.

5.4 Disadvantages of Methodology

Although our methodology resulted in directly-coupled data from intact vascular bypass graft constructs exposed to *ex vivo* perfusion where the effect of hemodynamics could be isolated, there are some issues that should be kept in mind when interpreting our data, and should be addressed before the results of this study can be applied clinically. These potential limitations are outlined below.

5.4.1 *Ex Vivo* Perfusion

We chose an *ex vivo* perfusion model so that we could control the pressure and flow conditions in ETS and ETE anastomoses in a precise manner. This system allowed us to alter the hemodynamics independent of other parameters and we were able to isolate the hemodynamic influence on IEG protein expression and EC and SMC apoptosis while providing a simulated physiologic environment (i.e. pH, oxygen, temperature, nutrients, etc.) for the vessels. However, this simulated environment does not incorporate all the conditions that occur *in vivo*. For example, we perfused the vessels with cell culture media so the effect of blood cells and coagulation factors, which have been shown to affect EC and SMC response, were not present in our system [191-201]. In addition, we isolated the effect of hemodynamics on vascular cell response but in reality, a number of factors change simultaneously when inserting a vascular graft, and isolating one parameter may not give a good indication of the complex interaction that actually occurs *in vivo*. Therefore, caution must be used when applying the results of an *ex vivo* model to the *in vivo* situation.

5.4.2 Level of Shear Stress

The data used for the correlation of the WSS parameters with biologic end points included axial and circumferential components of WSS ranging from -18 to 18 dynes/cm^2 and the magnitude of WSS ranged from 0 to 30 dynes/cm^2 (see section 3.3.5). Because the normal physiologic value of WSS is 15 dynes/cm^2, the data used for the correlation include both low (<10 dynes/cm^2) and high (>20 dynes/cm^2) shear stress values. However, because the flow rate into the graft was prescribed such that it was exposed to a physiologic shear rate (~ 440 sec^{-1}, see section 2.2.6.1), the average applied shear stress (viscosity * shear rate) in the anastomosis was low due to the decreased viscosity of the perfusate. Cell culture media has the same dynamic viscosity as water, which is approximately 3.5 times lower than blood, so the resulting WSS was expected to be 4.3 dynes/cm^2. As expected, the average level of WSS measured in the regions of interest was ~ 3 dynes/cm^2, a low level of WSS (see Figure 3.57).

To provide a physiologic level of shear stress, either the viscosity of the perfusate needs to be enhanced or the shear rate needs to be increased. We chose not to use either of these methods because of the

complicating factors involved with each. To match the viscosity, the perfusate could either be blood or viscosity enhanced tissue culture media. We did not perfuse the vessels with blood because of the immediate thrombosis which would occur when placing it in the perfusion system and because it would cause difficulty in maintaining and cleaning the perfusion system components. Anticoagulating the blood would have introduced unknown factors and would affect the vascular cells' biologic response. Some previous studies have supplemented non-blood perfusate with glycerol or dextran to match the viscosity of blood [138, 202-204]. However, this also introduces the possibility of an unknown biologic effect of the viscosity supplement on the cells. Therefore, because we chose to perfuse the vessels with low viscosity media, the only other method for achieving physiologic levels of WSS is to apply a high (nonphysiologic) wall shear rate. However, previous studies have shown that vascular cells respond differently to the same level of WSS caused by increasing the viscosity or the flow rate of the perfusate [202, 203, 205]. In addition, limitations in the inherent resistance of our system and the maximum capacity of the flow pump did not allow us to increase the flow enough to achieve physiologic levels of WSS. Therefore, we chose to match the physiologic level of wall shear rate in these experiments.

5.4.3 Steady Flow

We chose to complete these experiments under steady flow conditions because of the technical difficulties in perfusing anastomoses *ex vivo* and the large increase in computational time required to simulate each anastomosis using pulsatile flow. Previous studies have shown that vascular cells respond differently when exposed to steady or pulsatile flow [43, 206-211]. Of particular relevance is the study by Hsieh *et al.* who placed cultured human umbilical vein endothelial cells in a parallel plate apparatus and applied a steady or pulsatile WSS for 4 hours [43]. Steady WSS resulted in an increase of c-fos and c-jun gene expression compared to static controls. Pulsatile WSS caused a higher increase in c-fos expression than the steady WSS but the c-jun gene expression for the pulsatile experiments were comparable to the steady flow results. Therefore, steady and pulsatile WSS caused the same gene expression results, just different magnitude of gene expression for c-fos. Similar studies of the differential gene response to steady and

pulsatile shear stress were summarized in the review by Malek and Izumo [138]. In all of these studies, although the magnitude of the response may have varied between the steady and pulsatile experiments, the same basic correlation existed; i.e., if steady WSS increased gene expression so did pulsatile WSS. In addition, previous CFD studies have studied both steady and pulsatile flows in bypass models and have shown that the WSS results are qualitatively similar for both conditions [85, 102, 166, 212]. Therefore, we believe that the correlation results we found for steady flow are valid. Future studies could be completed in our laboratory to verify this by repeating the experiments using the pulsatile element of our perfusion system and developing the corresponding pulsatile CFD models using more advanced computational resources.

5.4.4 Three Dimensional Reconstruction

We used a novel reconstruction technique to develop the CFD models of each anastomosis. Accurate reconstruction of the anastomoses is dependent on both the processing of the tissue after the experimental procedure and the techniques used to represent the geometry. Although care was taken to maintain the dimensions of the tissue when removing the anastomoses from the perfusion system and during the subsequent freezing and slicing procedures, the resulting configuration of each cross-section may have been altered. When removing the fixed vessels from the perfusion system, it is possible that they shortened slightly causing the lumen to expand due to the incompressibility of the tissue. In the reconstruction process, this would result in artificially large cross-sectional diameters and consequently, artificially decreased WSS values. However, these decreased WSS values would be uniform along the anastomosis and would result in a decrease in the average hemodynamic values for the entire anastomosis. Therefore, any error associated with circumferential expansion would be accounted for in the normalization of hemodynamic parameters since the values at each region are normalized by the average value in the experiment.

For the reconstruction process, we chose to assume that the cross-sections were symmetric ellipses. We believe that this assumption is reasonable since we are using healthy arterial segments that do not have disease formation (i.e. asymmetric plaque) and the experimental apparatus held the anastomoses in a plane

of symmetry. This assumption could be a limitation since the full, three-dimensional topology was not incorporated into the models. However, Moore *et al.* studied the effect of incorporating different levels of detail in three dimensional models of ETS anastomoses and found that incorporating specific three dimensional details may actually cause more errors than avoid them [99]. They concluded that the most important feature required for accurate representation of ETS anastomoses is the ratio between the graft and host artery diameters, while the local arterial caliber and out-of-plane geometry were of secondary importance and the small-scale surface topology was least critical. Similar to that study, we completed a sensitivity analysis by creating ETS models using asymmetric ellipses, symmetric ellipses and circular cross-sections for three separate experiments. We determined if there were any instances when the asymmetric ellipse and/or circular cross-section models resulted in significant correlations that were different from the ones we found using the symmetric ellipse reconstructions of all the anastomoses. The results of these sensitivity analyses (see Sections 4.2.2 and 4.3.4) showed that the choice of cross-section shape (asymmetric ellipse, symmetric ellipse or circular) did not significantly affect the correlation between the level of EC c-fos protein expression and the magnitudes of WSS and WSSG magnitude. Similarly, the correlation between the level of EC egr-1 protein expression and axial WSS was unaffected by the reconstruction technique. The correlation between the level of EC c-jun protein expression and WSSG magnitude was affected by the reconstruction technique, however. The linear correlation was only significant for the circular reconstruction indicating that this model had the potential for resulting in a false positive correlation. Therefore, we chose the symmetric ellipse cross-section technique because it allowed us to take advantage computationally of the geometric symmetry without over-generalizing the shape of the cross-section.

5.4.5 Multiple Steps

In order to obtain directly-coupled biologic and hemodynamic data, we chose to obtain the biologic data from *ex vivo* perfusion of ETS anastomoses and then reconstruct these anastomoses to determine the hemodynamic data. The main drawback of this approach is that it involves a lot of steps in the process and is time-consuming. To obtain the biologic data for each anastomosis, the perfusion must be completed, the

tissue processed, frozen and sliced before cryosectioning can occur. For each region of interest, the slides are stained, microscopy images are taken and then quantified. Improper handling of the tissue during any of these steps could result in the loss of all biologic data from the perfusion, rendering the experiment unusable. To obtain the hemodynamic data, the tissue cross-sections are digitized to obtain the luminal boundary and these two-dimensional shapes are lofted to create a three-dimensional surface. This surface is then meshed and the CFD model is solved. The hemodynamic parameters of interest are derived from the resulting velocity field and then averaged over the region of interest. The reconstruction requires a lot of technical skill and experience using the CFD pre-processor, solver and post-processor and there is little automation in the current methodology. Because there are so many steps in handling the tissue and reconstructing the anastomosis, there is the potential to introduce error during any of the steps at these errors may be magnified as the process continues. Additionally, even if all steps are performed correctly and in a timely manner, it takes approximately three weeks to determine the single, quantitative values for the biologic and hemodynamic parameters for each region of interest for a given experiment. Therefore this process is very time-consuming. Although this methodology results in coupled data, the number of steps required to complete the process have the potential for losing data, introducing error and require a large amount of time to obtain both the biologic and hemodynamic data.

5.5 Future Work

Future work related to this research could address some of the current limitations or extend the model to address the issue of how IEG expression leads to IH formation. Two limitations previously mentioned are the nonphysiologic viscosity of the perfusate and lack of pulsatility. These issues could easily be addressed in future studies. The viscosity of the cell culture media could be enhanced with supplements such as glycerol or dextran. Preliminary studies would need to be completed before conducting an anastomosis experiment to determine if these supplements have any toxic effects on the vascular cells, interfere with any of the tissue processing steps or affect the perfusion system equipment. Once this is confirmed, the same

perfusion experiments as those in the current study could be repeated using this more viscous perfusate. The only necessary change in the computational protocol would be the appropriate increase in the viscosity value of the fluid. Using the enhanced viscosity perfusate would allow for the application of physiologic levels of WSS and wall shear rate and the results could be compared to the present study that was only able to match wall shear rate values.

Another study could incorporate pulsatility into the experimental and computational models. The perfusion system is already equipped to provide a pulsatile waveform. Because of the experience now gained from using the vascular clips, the introduction of pulsatility should not cause any leaking at the anastomosis, which was a concern for these studies. To maintain the process of obtaining directly coupled data, the boundary conditions for the computational models would need to be altered to allow for pulsatile pressure and flow. These models would require an extensive increase in computational resources. In addition, the hemodynamic variables of interest would change and could include parameters such as peak, mean and pulse amplitude WSS, temporal and spatial WSSG and oscillating shear index. The correlation combinations involving mean WSS and spatial WSSG could be compared to the steady flow data and this information, along with the potential correlations with time dependent hemodynamic parameters, would determine the effect of pulsatility.

Other studies could focus on improving the computational limitations present in this study. It would be beneficial to directly validate the reconstruction technique. In the present study, the reconstruction technique is indirectly validated using the correlation results from three experiments in which the ETS anastomosis was reconstructed using three different cross-section shapes. However, a direct validation could be done using an ETS anastomosis model of known dimensions created by a process such as stereo lithography. The key to this study would be creating the physical model out of a material that could accurately mimic the material properties of tissue. This physical model could be frozen and sliced according to the same protocol currently used and the resulting reconstruction could be compared to the known geometry of the physical model. Additionally, CFD analysis could be performed for the actual and

reconstructed models. The hemodynamic parameters could be calculated for each model in the regions of interest to determine a quantitative comparison between the actual and reconstructed models. This would give a more direct indication of the error associated with the reconstruction technique.

Future computational work could also focus on developing a more automated reconstruction technique. The current protocol requires a lot of user interface to determine the luminal boundary. The threshold of the image must be adjusted for each individual cross-section which is time-consuming since there are up to 40 cross-sections per anastomosis. This also requires that all cross-sections are digitized at the same time by the same person in order to provide continuity in judgement of the appropriate threshold level. Once the cross-section digitization is complete, the three dimensional surfaces for the graft, proximal artery and distal artery must be created. These individual surfaces are intersected to determine the surface of the entire anastomosis and the model is meshed. Because the overall geometry and mesh distribution for each anastomosis is generally the same, it is conceivable that this process could be at least partially automated. For example, each of these steps could be automatically completed but since the details of the geometry and mesh do vary from anastomosis to anastomosis, it would be useful to give the user the opportunity to adjust the reconstruction after each step. This could potentially save a lot of time on the reconstruction process while not losing any accuracy.

Future studies could also extend the current study by directly determining the effect of hemodynamic parameters on IH formation. This could be accomplished by perfusing the anastomoses *ex vivo* for days or weeks. In this study, we were not able to assess cell proliferation since this can only be measured after 24 hours of stimulation and our experiments were conducted for only six hours. If the anastomoses were perfused for 24 to 72 hours, the regional variation in the balance between SMC proliferation and apoptosis could be determined and could be correlated with hemodynamic parameters. Additionally, the regional variation in the proliferation/apoptosis balance found at this later time point could be compared to the regional variation in IEG expression found at six hours to determine if a correlation exists. Furthermore, if the experiments were extended to 2 to 3 weeks, it would be possible to directly measure the degree of IH

formation. The regional variation of IH formation could be correlated with hemodynamic parameters. Additionally, the regional variation in IH could be compared to the regional variation in IEG expression found at six hours to determine if a correlation exists. By exposing anastomoses to well-controlled pressure and flow for a period of weeks, the hemodynamic parameter(s) that cause IH formation could be determined directly for the first time. In addition, if a correlation existed between the acute IEG expression and the chronic IH formation, then further studies could be completed to determine the effectiveness of local genetic or pharmacologic treatments to block the early induction of IEG protein in the susceptible regions.

6 .0 CONCLUSIONS

Determining a quantitative relationship between the effect of hemodynamics on IH formation will significantly advance the field of cardiovascular surgery, particularly the success of bypass grafts. As many as 20-50% of bypass grafts fail due to the formation of intimal hyperplasia (IH) [18, 70, 71]. Studies as early as 1933 [213] noted that blood vessels could respond to changes in blood flow rate and by the 1970's, researchers hypothesized that the endothelium was modulating the vessel's response [162, 214]. By the 1980's, it was theorized that decreased blood flow caused intimal hyperplasia formation in vascular grafts [68, 215, 216] and further studies determined that low WSS was related to IH formation [8, 217, 218]. However, these and many other subsequent studies have failed to determine a quantitative correlation between a specific hemodynamic parameter and a particular cellular response that leads to IH formation.

Using a combined experimental and computational approach, we have determined a quantitative correlation between specific hemodynamic parameters (axial WSS, WSS and WSSG magnitude) and the expression of IEG protein in vascular bypass graft anastomoses. Compared to previous studies of the hemodynamic implication of IH formation, this research represents a significant advancement in this field. We used a whole-vessel, *ex vivo* perfusion model to obtain quantitative values for biologic end points in specific regions along ETS and ETE anastomoses along with a CFD reconstruction technique to obtain quantitative, hemodynamic data in the same regions of interest. This allowed for a direct correlation between quantitative biologic and hemodynamic data that has not been achieved previously. However, the methodology used for this study does have some limitations. The tissue processing protocol for obtaining the biologic data and the reconstruction protocol for calculating the hemodynamic parameters are complicated, time-consuming and have the possibility of incorporating error into the correlation. In addition, this study has not accounted for physiologic characteristics such as pulsatility and the viscous and biochemical influences of blood flow. However, future research could address these issues and build upon the results of this study.

If the correlation results from future research support the results of this study, there are a number of treatments that may improve the clinical success rate of vascular bypass grafts based on the correlations we found between low levels of WSS and WSSG and the subsequent increase in IEG protein expression. For example, the hemodynamics of graft construction could be optimized or targeted gene therapy or pharmacological agents could be employed to reduce the expression of c-fos, c-jun and/or egr-1. Such treatments have the potential of decreasing the level of IEG protein expression and thereby may decrease IH formation and increase the success of vascular bypass grafts.

APPENDICES

APPENDIX A

3D Reconstruction Protocol using CFD-GEOM

1) Put ellipse data from NIH Image analysis of digital photo into the correct input.dat format:

Prox Anast Distal Graft
4 3 7 2
NOTE: Major, Minor refer to DIAMETERS in METERS and ANGLE is in DEGREES measured from image x-axis (output from NIH)
NOTE: Order of the info goes Prox, Anast Floor, Dist, Graft, Anast Hood
Major Minor Angle
0.0028 0.0027 41.03
0.0031 0.0025 59.59
etc

2) Use ellipse_symm.f and ellipses.f (attached at the end of the protocol) to output curves to be read by CFD-GEOM (ellipses.TAB)

3) Choose double ellipse to be used for the block intersection (close to proximal end).

4) Loft proximal artery surface using full ellipses.

Loft graft surgery using full ellipses.

5) Intersect ellipse segments from final graft and proximal artery ellipses and trim.

Intersect double ellipses and trim.

Cut single ellipses in half.

6) Loft upper distal artery surface using upper halves of intersected double ellipses and upper halves of single ellipses.

Repeat for lower distal artery surface.

7) Create z=0 surface (x = -0.2, 0.42 and y = -0.025, 0.12)

Create y=0 surface (x = -0.2, 0.42 and z = -0.01, 0.01)

Create y=30˚ angle surface by duplicate/rotating y=0 surface

8) To get outline of the model, intersect all anastomosis surfaces with z=0 surface

9) Intersect the graft and proximal artery outlines and TRIM

10) Intersect the graft and proximal artery surfaces.

11) To get top lines for graft and proximal proximal artery and distal distal artery, intersect surfaces with y=0 and y=30˚ angle plane

12) Intersect all lines with ellipses and TRIM to get interim block sections.

13) To make inner blocks, start at the block intersection at the anastomosis. Draw a line between the intersections of the 2 ellipses. A 0.3 cut is used for the height dimension (z-direction). The interim block ellipses use a height equal to the 0.3 double-ellipse cut and the lengths are 0.3 cuts. The end circles are all 0.3 cut.

14) Create edges, faces and blocks. Be sure inner box blocks stay along the center of the geometry (can redraw if needed).

15) Project all outer faces to appropriate surface.

16) Check the cell volumes under grid tools to be sure there aren't any degenerate cells.

17) Once the proximal artery, graft and distal artery blocks are completed, make vessel extensions (upstream of graft and proximal artery and downstream of distal artery) by using a circle with radius=(major+minor)/4 of closest ellipse (dimensions from input.dat text file)

For proximal artery: x = -0.0515

For graft: x = -0.2

For distal artery x = 0.4

18) Loft each surface using the ¼ ellipses from previous surfaces and full circles just created

19) Create edges, faces, blocks for the extensions.

20) In total, there should be 6 main areas (proximal proximal artery, proximal artery, proximal graft, graft, distal artery, distal distal artery) with inner and outer blocks each for a total of 12 blocks.

21) Save as .DTF and CAREFULLY check grid and surface projection in CFD-VIEW before proceeding to CFD-ACE.

```
      PROGRAM ELLIPSE_SYMM
      implicit double precision(a-h,o-z)
      character*30 outfile,infile
      parameter(outfile='input_symm.dat')
      parameter(infile='input.dat')
      parameter(mxcrvs=200)
      dimension d1(mxcrvs),d2(mxcrvs),angle(mxcrvs)

C     This code takes the input from the original ellipse file and
C     and outputs the corresponding SYMMETRICAL ellipse file to be used in
C     ellipses.f to create a CFD-GEOM input file of curves (*.TAB)

C     Ncrvs = # of ellipses to be output
C     This rotates all ellipses with an angle of orientation between 0 and 45 to 0,
C      between 45 and 90 to 45, between 90 and 135 to 90 and between 135 and 180 to 135

      open(90,file=infile)
      read(90,*)
      read(90,*) nprox,nanast,ndist,ngraft
      ncrvs=nprox + ndist + 2*nanast + ngraft
      read(90,*)
      read(90,*)
      read(90,*)
      do i=1,ncrvs
        read(90,*) d1(i),d2(i),a
        if((a.ge.0.0d0).and.(a.le.45.0d0)) then
          angle(i)=0.0d0
          write(*,*)i,a,angle(i)
        elseif((a.gt.45.0d0).and.(a.le.135.0d0)) then
          angle(i)=90.0d0
          write(*,*)i,a,angle(i)
        elseif((a.gt.135.0d0).and.(a.le.225.0d0)) then
          angle(i)=180.0d0
```

```
          write(*,*)i,a,angle(i)
        elseif((a.gt.225.0d0).and.(a.le.315.0d0)) then
          angle(i)=270.0d0
          write(*,*)i,a,angle(i)
        elseif((a.gt.315.0d0).and.(a.le.360.0d0)) then
          angle(i)=0.0d0
          write(*,*)i,a,angle(i)
        else
          write(*,*) "Angle problem - STOPPING",a
          STOP
        endif
      enddo
      close(90)

C     Output newly rotated, symmetric ellipses to file

      open(99,file=outfile)
      write(99,*) 'Prox Anast   Distal  Graft'
      write(99,*) nprox,nanast,ndist,ngraft
      write(99,*) 'NOTE: Major, Minor refer to DIAMETERS in METERS and
     *     ANGLE is in DEGREES measured from image x-axis (output from
     *     NIH)'
      write(99,*) 'NOTE: Order of the info goes Prox, Anast Floor, Dist,
     *     Graft, Anast Hood'
      write(99,*) 'Major        Minor   Angle'
      do i=1,ncrvs
        write(99,*) d1(i),d2(i),angle(i)
      enddo
      close(99)
      stop
      end

------------------------------------------------------------------------------------------------------------------------

      PROGRAM ELLIPSES
      implicit double precision(a-h,o-z)
      character*30 outfile,infile
      parameter(outfile='ellipses.TAB')
      parameter(infile='input.dat')
      parameter(mxpts=100,mxcrvs=200)
      dimension x(mxcrvs,mxpts),y(mxcrvs,mxpts),
     *     z(mxcrvs,mxpts),npts(mxcrvs),r(mxcrvs)
```

```
      dimension rmax(mxcrvs),rmin(mxcrvs),angle(mxcrvs)
      dimension xc(mxcrvs),yc(mxcrvs)

C     This code assumes full elliptical cross-sections with
C     4 segments each - floor to outer, outer to hood, hood
C     to inner and inner to floor - 19 points on each cs
C     Anastomosis c-s split into 2 ellipses (floor and hood)
C     Outputs discrete points along curve to be read into CFD-GEOM

C     Input file has max diameter, min diameter (meters) and angle of orientation (degrees) info

      pi=ACOS(-1.0d0)
      open(90,file=infile)
      read(90,*)
      read(90,*) nprox,nanast,ndist,ngraft
      ncrvs=nprox + ndist + 2*nanast + ngraft

C     Read in diameter and angle of orientation info
C     Convert diameter to radius and angle to radians

      read(90,*)
      read(90,*)
      read(90,*)
      do i=1,ncrvs
        read(90,*) d1,d2,a
        rmax(i)=d1/2.0d0
        rmin(i)=d2/2.0d0
        angle(i)=a*pi/180.0d0
      enddo

C     output to screen as double check

      write(*,*)  nprox,nanast,ndist,ngraft
      do i=1,ncrvs
        write(*,*) rmax(i),rmin(i),angle(i)
      enddo

C     Check dimensions of arrays to be sure not overwriting anything

      if(ncrvs*4.gt.mxcrvs) then
        write(*,*)"WARNING!!!!! Number of Circles exceeds Maximum",
```

```
*    "Change mxcrvs dimension","*******EXITING*******"
     stop
    endif

C    Set number of points to be calculated per curve

    nptscrv=19
    do i=1,ncrvs
     npts(i)=nptscrv
    enddo

C    Check array dimensions WRT # points per curve

    if(nptscrv*4.gt.mxpts) then
     write(*,*)"WARNING!!!!! Number of Points exceeds Maximum",
*       "Change mxpts dimension","*******EXITING*******"
     stop
    endif

C    Create points for all artery ellipses (prox, anast floor, dist) - 2mm apart (slice thickness)

    numcirc=0
    do i=1,nprox+ndist+nanast
     numcirc=numcirc+1
     xshift=float(i-nprox-1)*0.002d0
     xc(i)=xshift
     yc(i)=0.0d0
     start=ATAN(-rmax(i)/rmin(i)*TAN(angle(i)))
     ytemp=rmin(i)*sin(start*pi/180.0d0)
     ztemp=rmax(i)*cos(start*pi/180.0d0)
     ztemp=ztemp*cos(angle(i))-ytemp*sin(angle(i))
     if(ztemp.lt.0.0d0) then
      start=start+pi
     endif
     do j=1,4*npts(i)-3
      x(i,j)=xshift
      y(i,j)=rmin(i)*sin(start+float(j-1)*2.0d0*pi/
*          (4*npts(i)-4))
      z(i,j)=rmax(i)*cos(start+float(j-1)*2.0d0*pi/
*          (4*npts(i)-4))
      yhold=y(i,j)
```

```
          zhold=z(i,j)
          y(i,j)=zhold*sin(angle(i))+yhold*cos(angle(i))
          z(i,j)=zhold*cos(angle(i))-yhold*sin(angle(i))
          if(j.eq.1) then
            write(*,100) i,x(i,j),y(i,j),z(i,j)
 100          format(' ',i6,f12.5,f12.5,f12.5)
          endif
        enddo
      enddo

C     Create points for all graft ellipses (graft + anast hood) - 2mm apart (slice thickness)
C     30 degree angle (pi/6) vessel

      do i=nprox+ndist+nanast+1,nprox+ndist+nanast+ngraft+nanast
        xshift=float(i-(nprox+ndist+nanast+ngraft+1))*0.002d0
        ycenter=(x(nprox+nanast+1,1)-xshift)*tan(pi/6.0d0)
        zcenter=0.0d0
        xc(i)=xshift
        yc(i)=ycenter
        start=ATAN(-rmax(i)/rmin(i)*TAN(angle(i)))
        ytemp=rmin(i)*sin(start*pi/180.0d0)
        ztemp=rmax(i)*cos(start*pi/180.0d0)
        ztemp=ztemp*cos(angle(i))-ytemp*sin(angle(i))
        if(ztemp.lt.0.0d0) then
          start=start+pi
        endif
        do j=1,4*npts(i)-3
          x(i,j)=xshift
          y(i,j)=ycenter+rmin(i)*sin(start+float(j-1)*2.0d0*pi/
     *          (4*npts(i)-4))
          z(i,j)=zcenter+rmax(i)*cos(start+float(j-1)*2.0d0*pi/
     *          (4*npts(i)-4))
          yhold=y(i,j)-ycenter
          zhold=z(i,j)
          y(i,j)=zhold*sin(angle(i))+yhold*cos(angle(i))+ycenter
          z(i,j)=zhold*cos(angle(i))-yhold*sin(angle(i))
          if(j.eq.1) then
            write(*,100) i,x(i,j),y(i,j),z(i,j)
          endif
        enddo
      enddo
```

```
C     Write output file to be read by CFD-GEOM (file.TAB)
      open(99,file=outfile)
      write(99,*)nprox+ndist+2*nanast+ngraft+5
      do i=1, nprox+ndist+2*nanast+ngraft
        write(99,*) npts(i)*4-3
      enddo
      write(99,*) npts(ncrvs)*4-3
      write(99,*) nprox+nanast+ndist
      write(99,*) nprox+nanast+ndist
      write(99,*) nanast+ngraft+1
      write(99,*) nanast+ngraft+1

      do i=1,nprox+ndist+2*nanast+ngraft
        do j=1,npts(i)*4-3
          write(99,50) x(i,j),y(i,j),z(i,j)
 50       format(' ',f12.6,f12.6,f12.6)
        enddo
      enddo
      do j=1,npts(ncrvs)*4-3              !extra anast c-s
        write(99,50) xc(nprox+nanast+1),y(ncrvs,j)-yc(ncrvs),z(ncrvs,j)
      enddo
      do i=1,nprox+nanast+ndist
        write(99,50) xc(i),yc(i),0.0d0
      enddo
      do i=1,nprox+nanast+ndist
       write(99,50) x(i,1),y(i,1),z(i,1)
      enddo
      do i=nprox+nanast+ndist+1,ncrvs
        write(99,50) xc(i),yc(i),0.0d0
      enddo
C  ***EXTRA ANAST CS:
      write(99,50) xc(nprox+nanast+1),yc(nprox+nanast+1),0.0d0
      do i=nprox+nanast+ndist+1,ncrvs
        write(99,50) x(i,1),y(i,1),z(i,1)
      enddo
C  ***EXTRA ANAST CS:
      write(99,50) x(nprox+nanast+1,1),y(ncrvs,1)-yc(ncrvs),z(ncrvs,1)
      close(99)
      stop
      end
```

APPENDIX B

Example output file from CFD-ACEU

```
   ************************************************************
**                                                            **
**  CCCCC  FFFFF DDDD          AAA    CCCCC  EEEEE     U  U    **
**  C      F     D   D       A   A  C      E     U  U     **
**  C      FFFF  D    D  ==  AAAAA  C      EEEE    U  U    **
**  C      F     D   D      A   A  C      E       U  U    **
**  CCCCC  F     DDDD       A   A  CCCCC  EEEEE    UUU     **
**                                                            **
**     Version         :  6. 6. 8                             **
**     Build Date      : Wed Jul 25 11:15:07 CDT 2001         **
**     Build OS        : SunOS                                **
**     Build OS Release : 5.6                                 **
**     Build OS Version : Generic                             **
**     Build Machine    : pepper                              **
**                                                            **
**    Copyright (c) 2000, CFD Research Corporation,           **
**               All Rights Reserved                          **
   ************************************************************

============================================================
  CFD-ACEU Run Platform Information :
============================================================
  Run Date          : 02/22/2002 16:01:55
  Run OS            : SunOS
  Run OS Release    : 5.8
  Run OS Version    : Generic_108528-07
  Run Machine       : graft
============================================================
```

```
 ========================================
 Summary of Input Information
 ========================================
 Title           :
 Modules         : FLOW
DTF File Name    : symm_4_25_01_half.DTF
 Model Name      : symm_4_25_01_half
 Simulation Number :  1
 Diagnostic      : Basic
 Iterations      :  1000
 Output Frequency :   25
 Time Dependence  : Steady

========================================
 Summary of 3D Grid Data
========================================

 Total No. of nodes :  150787
 No. of quad faces  :  428109
 Total No. of faces :  428109
 No. of hexa. cells :  138852
 Total No. of cells :  138852

 ========================================
 Summary of Properties
 ========================================
 Total No. of Property VCs :     12
 ========================================
  ----------------------------
  Key No.         :    2531
  Zone No.        :     1
  VC Name.        : NoName
  No. of Cells    :  3038
  Material  Type  : Fluid
  Density   method : Constant      = 1.00E+03
  Viscosity method : Constant_Dyn  = 1.00E-03
  Sp. Heat  method : Constant      = 1.00E+03
  ----------------------------
  ----------------------------
  Key No.         :    2538
  Zone No.        :     2
```

VC Name. : NoName
No. of Cells : 9548
Material Type : Fluid
Density method : Constant = 1.00E+03
Viscosity method : Constant_Dyn = 1.00E-03
Sp. Heat method : Constant = 1.00E+03

Key No. : 2643
Zone No. : 3
VC Name. : NoName
No. of Cells : 3038
Material Type : Fluid
Density method : Constant = 1.00E+03
Viscosity method : Constant_Dyn = 1.00E-03
Sp. Heat method : Constant = 1.00E+03

Key No. : 2650
Zone No. : 4
VC Name. : NoName
No. of Cells : 9548
Material Type : Fluid
Density method : Constant = 1.00E+03
Viscosity method : Constant_Dyn = 1.00E-03
Sp. Heat method : Constant = 1.00E+03

Key No. : 2733
Zone No. : 5
VC Name. : NoName
No. of Cells : 7742
Material Type : Fluid
Density method : Constant = 1.00E+03
Viscosity method : Constant_Dyn = 1.00E-03
Sp. Heat method : Constant = 1.00E+03

Key No. : 2740
Zone No. : 6
VC Name. : NoName

No. of Cells : 24332
Material Type : Fluid
Density method : Constant = 1.00E+03
Viscosity method : Constant_Dyn = 1.00E-03
Sp. Heat method : Constant = 1.00E+03

Key No. : 2848
Zone No. : 7
VC Name. : NoName
No. of Cells : 2254
Material Type : Fluid
Density method : Constant = 1.00E+03
Viscosity method : Constant_Dyn = 1.00E-03
Sp. Heat method : Constant = 1.00E+03

Key No. : 2862
Zone No. : 8
VC Name. : NoName
No. of Cells : 7084
Material Type : Fluid
Density method : Constant = 1.00E+03
Viscosity method : Constant_Dyn = 1.00E-03
Sp. Heat method : Constant = 1.00E+03

Key No. : 2923
Zone No. : 9
VC Name. : NoName
No. of Cells : 5782
Material Type : Fluid
Density method : Constant = 1.00E+03
Viscosity method : Constant_Dyn = 1.00E-03
Sp. Heat method : Constant = 1.00E+03

Key No. : 2930
Zone No. : 10
VC Name. : NoName
No. of Cells : 18172

Material Type : Fluid
Density method : Constant = 1.00E+03
Viscosity method : Constant_Dyn = 1.00E-03
Sp. Heat method : Constant = 1.00E+03

Key No. : 2991
Zone No. : 11
VC Name. : NoName
No. of Cells : 11662
Material Type : Fluid
Density method : Constant = 1.00E+03
Viscosity method : Constant_Dyn = 1.00E-03
Sp. Heat method : Constant = 1.00E+03

Key No. : 2998
Zone No. : 12
VC Name. : NoName
No. of Cells : 36652
Material Type : Fluid
Density method : Constant = 1.00E+03
Viscosity method : Constant_Dyn = 1.00E-03
Sp. Heat method : Constant = 1.00E+03

==========

Exited input_A Elapsed Time= 3.999869E+01 Delta-time= 3.999869E+01
Exited input_A DBM Memory = 2.943405E+01 MAX_DBM Memory= 2.943405E+01
Exited input_B Elapsed Time= 4.000828E+01 Delta-time= 9.471893E-03
Exited input_B DBM Memory = 2.943405E+01 MAX_DBM Memory= 2.943405E+01

==========

Summary of Initial Conditions
Total No. of Initial Condition VCs : 12

==========

Zone No. : 1
Key No. : 2531
VC Name. : NoName
No. of Cells : 3038
Material Type : Fluid

Variable	Evaluation Method	Value
X-Direction Velocity (U)	Constant	1.045E-01
Y-Direction Velocity (V)	Constant	0.000E+00
Z-Direction Velocity (W)	Constant	0.000E+00
Pressure	Constant	0.000E+00
Temperature	Constant	3.000E+02

Zone No. : 2
Key No. : 2538
VC Name. : NoName
No. of Cells : 9548
Material Type : Fluid

Variable	Evaluation Method	Value
X-Direction Velocity (U)	Constant	1.045E-01
Y-Direction Velocity (V)	Constant	0.000E+00
Z-Direction Velocity (W)	Constant	0.000E+00
Pressure	Constant	0.000E+00
Temperature	Constant	3.000E+02

Zone No. : 3
Key No. : 2643
VC Name. : NoName
No. of Cells : 3038
Material Type : Fluid

Variable	Evaluation Method	Value
X-Direction Velocity (U)	Constant	1.045E-01
Y-Direction Velocity (V)	Constant	0.000E+00
Z-Direction Velocity (W)	Constant	0.000E+00
Pressure	Constant	0.000E+00
Temperature	Constant	3.000E+02

Zone No. : 4
Key No. : 2650
VC Name. : NoName
No. of Cells : 9548
Material Type : Fluid

Variable	Evaluation Method	Value
X-Direction Velocity (U)	Constant	1.045E-01
Y-Direction Velocity (V)	Constant	0.000E+00
Z-Direction Velocity (W)	Constant	0.000E+00
Pressure	Constant	0.000E+00
Temperature	Constant	3.000E+02

Zone No. : 5
Key No. : 2733
VC Name. : NoName
No. of Cells : 7742
Material Type : Fluid

Variable	Evaluation Method	Value
X-Direction Velocity (U)	Constant	1.045E-01
Y-Direction Velocity (V)	Constant	0.000E+00
Z-Direction Velocity (W)	Constant	0.000E+00
Pressure	Constant	0.000E+00
Temperature	Constant	3.000E+02

Zone No. : 6
Key No. : 2740
VC Name. : NoName
No. of Cells : 24332
Material Type : Fluid

Variable	Evaluation Method	Value
X-Direction Velocity (U)	Constant	1.045E-01
Y-Direction Velocity (V)	Constant	0.000E+00
Z-Direction Velocity (W)	Constant	0.000E+00

Pressure	Constant	0.000E+00
Temperature	Constant	3.000E+02

Zone No. : 7
Key No. : 2848
VC Name. : NoName
No. of Cells : 2254
Material Type : Fluid

Variable	Evaluation Method	Value
X-Direction Velocity (U)	Constant	1.045E-01
Y-Direction Velocity (V)	Constant	0.000E+00
Z-Direction Velocity (W)	Constant	0.000E+00
Pressure	Constant	0.000E+00
Temperature	Constant	3.000E+02

Zone No. : 8
Key No. : 2862
VC Name. : NoName
No. of Cells : 7084
Material Type : Fluid

Variable	Evaluation Method	Value
X-Direction Velocity (U)	Constant	1.045E-01
Y-Direction Velocity (V)	Constant	0.000E+00
Z-Direction Velocity (W)	Constant	0.000E+00
Pressure	Constant	0.000E+00
Temperature	Constant	3.000E+02

Zone No. : 9
Key No. : 2923
VC Name. : NoName
No. of Cells : 5782

Material Type : Fluid

Variable	Evaluation Method	Value
X-Direction Velocity (U)	Constant	1.045E-01
Y-Direction Velocity (V)	Constant	0.000E+00
Z-Direction Velocity (W)	Constant	0.000E+00
Pressure	Constant	0.000E+00
Temperature	Constant	3.000E+02

Zone No. : 10
Key No. : 2930
VC Name. : NoName
No. of Cells : 18172
Material Type : Fluid

Variable	Evaluation Method	Value
X-Direction Velocity (U)	Constant	1.045E-01
Y-Direction Velocity (V)	Constant	0.000E+00
Z-Direction Velocity (W)	Constant	0.000E+00
Pressure	Constant	0.000E+00
Temperature	Constant	3.000E+02

Zone No. : 11
Key No. : 2991
VC Name. : NoName
No. of Cells : 11662
Material Type : Fluid

Variable	Evaluation Method	Value
X-Direction Velocity (U)	Constant	1.045E-01
Y-Direction Velocity (V)	Constant	0.000E+00
Z-Direction Velocity (W)	Constant	0.000E+00
Pressure	Constant	0.000E+00
Temperature	Constant	3.000E+02

Zone No. : 12
Key No. : 2998
VC Name. : NoName
No. of Cells : 36652
Material Type : Fluid

Variable	Evaluation Method	Value
X-Direction Velocity (U)	Constant	1.045E-01
Y-Direction Velocity (V)	Constant	0.000E+00
Z-Direction Velocity (W)	Constant	0.000E+00
Pressure	Constant	0.000E+00
Temperature	Constant	3.000E+02

Exited patch_intf_st Elapsed Time= 4.313507E+01 Delta-time= 3.126678E+00
Exited patch_intf_st DBM Memory = 5.017220E+01 MAX_DBM Memory= 5.017220E+01
Exited cyclic_bc Elapsed Time= 4.314558E+01 Delta-time= 1.034546E-02
Exited cyclic_bc DBM Memory = 5.017220E+01 MAX_DBM Memory= 5.017220E+01

Summary of Solver Control Parameters

Spatial Differencing for Velocity = 2ndOrder
Blending factor for Velocity = 1.00E-01
Spatial Differencing for Density = 2ndOrder
Blending factor for Density = 1.00E-01
Relaxation for Velocity = 2.00E-02
Relaxation for Pressure Correction = 2.00E-01
Relaxation for Pressure = 1.00E+00
Relaxation for Density = 1.00E+00
Relaxation for Viscosity = 1.00E+00
Solver for Velocity = CGS+Pre
Solver for Pressure Correction = CGS+Pre
Number of sweeps for Velocity = 100
Number of sweeps for Pressure Correction = 3000
Solver Criterion for Velocity = 1.00E-04
Solver Criterion for Pressure Correction = 1.00E-04
Minimum Limit for U = -1.00E+20
Maximum Limit for U = 1.00E+20
Minimum Limit for V = -1.00E+20
Maximum Limit for V = 1.00E+20

Minimum Limit for W = -1.00E+20
Maximum Limit for W = 1.00E+20
Minimum Limit for P = -1.00E+20
Maximum Limit for P = 1.00E+20
Minimum Limit for Density = 1.00E-06
Maximum Limit for Density = 1.00E+20
Minimum Limit for Viscosity = 1.00E-10
Maximum Limit for Viscosity = 1.00E+02

==========
Summary of Face Angles
==========
% of faces with
10.000 < angle < 20.000 = 0.012
20.000 < angle < 30.000 = 0.763
30.000 < angle < 40.000 = 0.959
40.000 < angle < 50.000 = 2.489
50.000 < angle < 60.000 = 7.083
60.000 < angle < 70.000 = 16.931
70.000 < angle < 80.000 = 19.662
80.000 < angle < 90.000 = 52.101
==========
==========
Summary of Geometry Data
==========

Smallest Volume : 1.008505E-12

Largest Volume : 3.764472E-10

Smallest Angle : 1.070057E+01 at face = 152583

Location of face number 152583 is x = 1.9308E-03 y = -1.2574E-03 z = 6.1611E-04

Exited geometry Elapsed Time= 5.522527E+01 Delta-time= 1.207959E+01
Exited geometry DBM Memory = 1.012668E+02 MAX_DBM Memory= 1.012668E+02
Exited sort_bc Elapsed Time= 5.526081E+01 Delta-time= 3.543091E-02
Exited sort_bc DBM Memory = 1.012668E+02 MAX_DBM Memory= 1.012668E+02
Exited cal_bc_profil Elapsed Time= 5.526100E+01 Delta-time= 6.866455E-05
Exited cal_bc_profil DBM Memory = 1.012668E+02 MAX_DBM Memory= 1.012668E+02

```
   Exited init0  Elapsed Time=  5.856235E+01 Delta-time=  3.301277E+00
   Exited init0  DBM Memory  =  1.012668E+02 MAX_DBM Memory=  1.149663E+02
  ==============================
  Start of Iterative Cycle.....
  ==============================
 CGS: W     , SWEEP=    5, SUM0=8.44E-07, SUM=3.10E-09
 CGS: U     , SWEEP=   19, SUM0=1.77E+01, SUM=2.25E-02
 CGS: V     , SWEEP=    3, SUM0=5.73E-01, SUM=2.88E-03
 CGS: P     , SWEEP= 3000, SUM0=1.83E+01, SUM=1.84E+11
 Max. Sweeps reached for var = P
 Data not Updated

ITER =    1, ICMAX  RES(MAX)  RES(SUM)    VALUE
---------------------------------------------------
 VAR =W      78191   1.55E-12  2.99E-10  0.0000E+00
 Cell= 78191 X,Y,Z= -1.09E-01  6.37E-02  8.66E-05
 VAR =U      72367   9.67E-06  1.83E-02  1.0450E-01
 Cell= 72367 X,Y,Z= -1.73E-01  9.76E-02  2.15E-04
 VAR =V      72478   6.65E-07  2.33E-04  0.0000E+00
 Cell= 72478 X,Y,Z= -1.69E-01  1.04E-01  1.84E-04
 VAR =P      73291   2.11E-04  1.62E-01  1.0000E-05
 Cell= 73291 X,Y,Z= -1.62E-01  9.12E-02  2.15E-04

 CGS: W     , SWEEP=    4, SUM0=1.27E-06, SUM=1.40E-09
 CGS: U     , SWEEP=    6, SUM0=2.14E+01, SUM=1.59E-01
 CGS: V     , SWEEP=    4, SUM0=3.06E-01, SUM=2.90E-03
 CGS: P     , SWEEP= 3000, SUM0=5.80E+00, SUM=1.21E+06
 Max. Sweeps reached for var = P
 Data not Updated


ITER =    2, ICMAX  RES(MAX)  RES(SUM)    VALUE
---------------------------------------------------
 VAR =W      78191   3.88E-12  8.36E-10  7.2190E-08
 Cell= 78191 X,Y,Z= -1.09E-01  6.37E-02  8.66E-05
 VAR =U      73291   1.42E-05  2.27E-02 -2.5033E-01
 Cell= 73291 X,Y,Z= -1.62E-01  9.12E-02  2.15E-04
 VAR =V      72394   1.38E-06  9.22E-05 -4.8671E-02
 Cell= 72394 X,Y,Z= -1.69E-01  1.04E-01  2.15E-04
 VAR =P      73599   5.01E-05  3.82E-02  1.0000E-05
 Cell= 73599 X,Y,Z= -1.58E-01  8.91E-02  2.15E-04
```

```
 CGS: W     , SWEEP=    3, SUM0=2.49E-07, SUM=1.25E-09
 CGS: U     , SWEEP=   12, SUM0=3.43E+00, SUM=7.95E-03
 CGS: V     , SWEEP=    5, SUM0=3.19E-01, SUM=3.17E-04
 CGS: P     , SWEEP= 3000, SUM0=1.13E+00, SUM=3.34E+08
 Max. Sweeps reached for var = P
 Data not Updated

ITER =    3, ICMAX  RES(MAX)  RES(SUM)    VALUE
---------------------------------------------------
 VAR =W      77911   8.36E-13  1.46E-10 -4.3444E-08
 Cell= 77911 X,Y,Z= -1.10E-01  6.12E-02  2.15E-04
 VAR =U      73907   2.09E-06  2.41E-03 -5.9474E-02
 Cell= 73907 X,Y,Z= -1.54E-01  8.70E-02  2.15E-04
 VAR =V      72371   5.91E-07  7.92E-05 -3.2692E-02
 Cell= 72371 X,Y,Z= -1.72E-01  9.80E-02  1.85E-03
 VAR =P      73599   1.64E-05  1.52E-02  1.0000E-05
 Cell= 73599 X,Y,Z= -1.58E-01  8.91E-02  2.15E-04

 CGS: W     , SWEEP=    3, SUM0=2.71E-07, SUM=8.91E-10
 CGS: U     , SWEEP=   12, SUM0=9.97E-01, SUM=2.55E-03
 CGS: V     , SWEEP=    5, SUM0=2.90E-01, SUM=1.18E-03
 CGS: P     , SWEEP= 3000, SUM0=5.94E-01, SUM=1.11E+07
 Max. Sweeps reached for var = P
 Data not Updated
                                    .
                                    .
                                    .
(Similar information for iterations 4 - 16 removed because of space considerations)
                                    .
                                    .
                                    .

ITER =   17, ICMAX  RES(MAX)  RES(SUM)    VALUE
---------------------------------------------------
 VAR =W      78807   8.77E-15  2.49E-13 -4.2071E-10
 Cell= 78807 X,Y,Z= -1.03E-01  6.00E-02  8.62E-05
 VAR =U      78471   1.05E-07  6.11E-05  4.5522E-02
 Cell= 78471 X,Y,Z= -1.06E-01  6.15E-02  1.01E-04
 VAR =V      78485   6.09E-08  2.79E-05 -2.8689E-02
 Cell= 78485 X,Y,Z= -1.05E-01  6.32E-02  1.52E-03
 VAR =P      72380   5.43E-06  2.74E-03  1.0000E-05
```

```
 Cell= 72380 X,Y,Z= -1.71E-01  1.01E-01  3.81E-03

 CGS: W     , SWEEP=    6, SUM0=1.41E-09, SUM=2.68E-13
 CGS: U     , SWEEP=    4, SUM0=3.42E-01, SUM=3.06E-03
 CGS: V     , SWEEP=    4, SUM0=1.97E-01, SUM=9.19E-04
 CGS: P     , SWEEP= 1751, SUM0=4.86E-01, SUM=4.38E-03

ITER =   18, ICMAX  RES(MAX)  RES(SUM)    VALUE
---------------------------------------------------
 VAR =W      79115   1.01E-14  2.20E-13 -3.3147E-10
 Cell= 79115 X,Y,Z= -9.94E-02  5.82E-02  8.60E-05
 VAR =U      78779   1.02E-07  5.71E-05  4.7603E-02
 Cell= 78779 X,Y,Z= -1.03E-01  5.97E-02  1.01E-04
 VAR =V      78780   5.90E-08  2.68E-05 -2.6858E-02
 Cell= 78780 X,Y,Z= -1.03E-01  5.97E-02  3.03E-04
 VAR =P      72380   5.43E-06  2.70E-03  1.0000E-05
 Cell= 72380 X,Y,Z= -1.71E-01  1.01E-01  3.81E-03

 CGS: W     , SWEEP=   10, SUM0=1.49E+00, SUM=3.20E-03
 CGS: U     , SWEEP=   10, SUM0=8.48E+00, SUM=5.69E-02
 CGS: V     , SWEEP=   12, SUM0=2.81E+00, SUM=7.39E-03
 CGS: P     , SWEEP=   90, SUM0=8.88E+00, SUM=7.12E-02

ITER =   19, ICMAX  RES(MAX)  RES(SUM)    VALUE
---------------------------------------------------
 VAR =W      44141   5.90E-07  8.95E-04  2.8050E-02
 Cell= 44141 X,Y,Z=  3.98E-03  3.02E-03  5.72E-04
 VAR =U     126235   2.09E-06  1.68E-02  3.7827E-03
 Cell=126235 X,Y,Z=  2.32E-01 -3.46E-03  1.69E-04
 VAR =V      42322   6.43E-07  2.00E-03  4.2295E-02
 Cell= 42322 X,Y,Z=  1.71E-03  3.07E-03  2.16E-04
 VAR =P      85303   2.16E-05  5.76E-02  1.7032E+02
 Cell= 85303 X,Y,Z= -4.26E-02  2.26E-02  2.15E-04

 CGS: W     , SWEEP=    8, SUM0=1.56E+00, SUM=1.04E-02
 CGS: U     , SWEEP=   14, SUM0=3.71E+00, SUM=8.28E-03
 CGS: V     , SWEEP=   14, SUM0=2.20E+00, SUM=9.97E-03
 CGS: P     , SWEEP= 1095, SUM0=5.53E+00, SUM=4.59E-02


ITER =   20, ICMAX  RES(MAX)  RES(SUM)    VALUE
```

```
-------------------------------------------------
 VAR =W      32968   4.79E-07  1.01E-03  2.0543E-02
 Cell= 32968 X,Y,Z= -7.81E-03  1.08E-02  1.82E-03
 VAR =U      32970   1.69E-06  3.66E-03  1.1554E-01
 Cell= 32970 X,Y,Z= -7.81E-03  1.14E-02  3.89E-04
 VAR =V      33026   1.58E-06  1.75E-03 -5.7205E-02
 Cell= 33026 X,Y,Z= -7.81E-03  1.04E-02  3.29E-04
 VAR =P      34482   2.04E-05  3.91E-02  1.6762E+02
 Cell= 34482 X,Y,Z= -5.80E-03  1.13E-02  4.15E-04

 CGS: W     , SWEEP=    9, SUM0=1.34E+00, SUM=3.64E-03
 CGS: U     , SWEEP=   16, SUM0=3.53E+00, SUM=3.03E-02
 CGS: V     , SWEEP=   12, SUM0=2.54E+00, SUM=1.05E-02
 CGS: P     , SWEEP=   41, SUM0=6.86E+00, SUM=3.55E-02
```

(Similar information for iterations 21 - 759 removed because of space considerations)

.
.
.

```
ITER =  760, ICMAX  RES(MAX)  RES(SUM)    VALUE
-------------------------------------------------
 VAR =W      43301   1.17E-11  1.03E-08 -2.5065E-03
 Cell= 43301 X,Y,Z=  3.00E-03  2.18E-03  4.18E-04
 VAR =U      43274   2.57E-11  1.42E-08  2.1402E-01
 Cell= 43274 X,Y,Z=  2.91E-03  2.48E-03  1.75E-04
 VAR =V      43274   3.06E-11  1.77E-08 -8.8192E-02
 Cell= 43274 X,Y,Z=  2.91E-03  2.48E-03  1.75E-04
 VAR =P      43246   3.95E-10  4.16E-07  9.1112E+01
 Cell= 43246 X,Y,Z=  2.84E-03  2.74E-03  2.03E-04

 CGS: W     , SWEEP=    3, SUM0=1.44E-05, SUM=6.21E-08
 CGS: U     , SWEEP=    4, SUM0=1.53E-05, SUM=6.33E-08
 CGS: V     , SWEEP=    6, SUM0=2.44E-05, SUM=2.37E-08
 CGS: P     , SWEEP=    7, SUM0=1.13E-04, SUM=7.90E-07

ITER =  761, ICMAX  RES(MAX)  RES(SUM)    VALUE
-------------------------------------------------
 VAR =W      43301   1.15E-11  1.02E-08 -2.5066E-03
 Cell= 43301 X,Y,Z=  3.00E-03  2.18E-03  4.18E-04
 VAR =U      43610   2.54E-11  1.41E-08  2.1900E-01
```

```
 Cell= 43610 X,Y,Z=  3.38E-03  2.25E-03  1.41E-04
 VAR =V      43274   3.01E-11  1.75E-08 -8.8192E-02
 Cell= 43274 X,Y,Z=  2.91E-03  2.48E-03  1.75E-04
 VAR =P      43246   3.90E-10  4.12E-07  9.1112E+01
 Cell= 43246 X,Y,Z=  2.84E-03  2.74E-03  2.03E-04

 CGS: W     , SWEEP=    3, SUM0=1.42E-05, SUM=6.10E-08
 CGS: U     , SWEEP=    4, SUM0=1.51E-05, SUM=6.17E-08
 CGS: V     , SWEEP=    6, SUM0=2.41E-05, SUM=2.45E-08
 CGS: P     , SWEEP=    7, SUM0=1.12E-04, SUM=7.83E-07

ITER =  762, ICMAX  RES(MAX)  RES(SUM)    VALUE
-------------------------------------------------
 VAR =W      43301   1.14E-11  1.01E-08 -2.5066E-03
 Cell= 43301 X,Y,Z=  3.00E-03  2.18E-03  4.18E-04
 VAR =U      43610   2.52E-11  1.39E-08  2.1900E-01
 Cell= 43610 X,Y,Z=  3.38E-03  2.25E-03  1.41E-04
 VAR =V      43274   2.96E-11  1.73E-08 -8.8192E-02
 Cell= 43274 X,Y,Z=  2.91E-03  2.48E-03  1.75E-04
 VAR =P      43246   3.85E-10  4.08E-07  9.1112E+01
 Cell= 43246 X,Y,Z=  2.84E-03  2.74E-03  2.03E-04

 CGS: W     , SWEEP=    3, SUM0=1.40E-05, SUM=6.00E-08
 CGS: U     , SWEEP=    4, SUM0=1.49E-05, SUM=6.00E-08
 CGS: V     , SWEEP=    6, SUM0=2.38E-05, SUM=2.55E-08
 CGS: P     , SWEEP=    7, SUM0=1.11E-04, SUM=7.76E-07

ITER =  763, ICMAX  RES(MAX)  RES(SUM)    VALUE
-------------------------------------------------
 VAR =W      43301   1.13E-11  1.00E-08 -2.5066E-03
 Cell= 43301 X,Y,Z=  3.00E-03  2.18E-03  4.18E-04
 VAR =U      43610   2.50E-11  1.38E-08  2.1900E-01
 Cell= 43610 X,Y,Z=  3.38E-03  2.25E-03  1.41E-04
 VAR =V      43274   2.91E-11  1.71E-08 -8.8192E-02
 Cell= 43274 X,Y,Z=  2.91E-03  2.48E-03  1.75E-04
 VAR =P      43246   3.80E-10  4.04E-07  9.1112E+01
 Cell= 43246 X,Y,Z=  2.84E-03  2.74E-03  2.03E-04
```

Problem converged with specified criterion = 1.00E-05

==========
End of Iterative Cycle.....
==========

Exited patch_intf_e Elapsed Time= 1.005823E+05 Delta-time= 1.005238E+05
Exited patch_intf_e DBM Memory = 1.012668E+02 MAX_DBM Memory= 1.318134E+02
Final Time Elapsed Time= 1.005823E+05 Delta-time= 0.000000E+00
Final Time DBM Memory = 1.012668E+02 MAX_DBM Memory= 1.318134E+02
lap time (CPU|Wallclock) = 100523.77868652344, 101338.42432099998
cummulative time (CPU|Wallclock) = 100523.77868652344, 101338.42432099998
Normal Termination

APPENDIX C

Post-Processing Protocol for Calculating WSS and WSSG

1) Take file .DTF output from CFD-ACEU and use either the CFD Toolkit on graft.surgery.pitt.edu or dtf2tec executable on fusiform to obtain file.TEC (input for Tecplot)

2) FTP File.TEC to PC and open in Tecplot

3) Tools - CFD Analyzer

- Fluid Properties:
    - incompressible, density=1000, specific heat=default, viscosity=0.001
    - Close
- Calculate Variables: set vector variables as U,V,W
    - set vector variables as U,V,W
    - Vector Variables are velocity
    - choose Pressure and Not Used and select P for pressure
    - under Function choose Grid I Unit Normal (vector)
    - Calculate
    - repeat for Grid J Unit Normal (vector)
    - repeat for Grid K Unit Normal (vector)
    - Close

4) Data - Alter - Specify Equations

- Load Equations - vel_derivs.eqn (dudx, etc):

{Ux}=ddx({U})
{Uy}=ddy({U})
{Uz}=ddz({U})

{Vx}=ddx({V})
{Vy}=ddy({V})
{Vz}=ddz({V})
{Wx}=ddx({W})
{Wy}=ddy({W})
{Wz}=ddz({W})

5) Data - Data Set Info

- determine which direction is the outer shell (J or K) for each anastomosis zone

- for these files, max = 12

6) Data - Create Zone - Subzone

- for each anastomosis zone, pick only the outer shells (1 to 6 or Mx-5 to Mx)

- double check by turning off all other meshes and just looking at outer shells (rotate about y axis)

7) Data - Create Zone - Subzone

- for each subzone, choose I=1,1 so just have 2D cross-section for each zone to check normals

8) 2D - Axis - Assign XYZ

- X = Z and Y = Y

9) Field - Vector - Vector Variable

- X = Z Grid K Unit Normal (or J)

- Y = Y Grid K Unit Normal (or J)

- Make note of what normals are pointing outward (want them all to be INWARD) and the corresponding shell subzone number

10) Data - Delete Zone

- delete all 2D zones that had normal facing outward

11) Data - Alter - Specify Equations

- Load Equations - reverse_normals.eqn:

{X Grid J Unit Normal}=-1.0*{X Grid J Unit Normal} : <Z=[25-26,28-30]>
{Y Grid J Unit Normal}=-1.0*{Y Grid J Unit Normal} : <Z=[25-26,28-30]>
{Z Grid J Unit Normal}=-1.0*{Z Grid J Unit Normal} : <Z=[25-26,28-30]>

- Set zones accordingly (Z = #)

12) Data - Create Zone - Subzone

- recreate the 2D subzones deleted before the normal reversal process

13) Double Check that all normal are facing INWARD.

14) Data - Delete Zone

- delete all 2D zones

15) File - Write Data File

- Choose ONLY the outer shell subzones (6 for asym ellipse, 3 for circle and symm ellipse)

- Choose X,Y,Z, U,V,W, P, STRAIN, XYZ Grid I Unit Normals, XYZ Grid J Unit Normals, XYZ Grid K Unit Normals, dudx, dudy……dwdz

- 26 variables total

- ASCII

- Point

- File.dat

16) FTP File.dat to graft.surgery.pitt.edu

17) Create zone_info_file.dat (need # zones, IJK for each and viscosity)

cp zone_info_file.dat zone_info.dat

cp file.dat input.dat

wss_calc

cp wss_calc.dat file_wss.dat

EXAMPLE ZONE-INFO.DAT:
#This gives the info for the zones for the model input to wss_calc.f
#Number of Zones
3
#Imax, Jmax, Kmax for each Zone
32 6 29
32 6 29
80 29 6

#Dynamic Viscosity (kg/m-s)
0.001

WSS_CALC.F: attached at the end of the protocol

18) FTP File_wss.dat to PC and open in Tecplot

19) Data - Alter - Specify Equations

- Load Equations - wss_derivs.dat (ddx({WSS_ax}), etc)

{WSS_ax_x}=ddx({WSS_ax})
{WSS_ax_y}=ddy({WSS_ax})
{WSS_ax_z}=ddz({WSS_ax})
{WSS_circ_x}=ddx({WSS_circ})
{WSS_circ_y}=ddy({WSS_circ})
{WSS_circ_z}=ddz({WSS_circ})
{WSS_mag_x}=ddx({WSS_mag})
{WSS_mag_y}=ddy({WSS_mag})
{WSS_mag_z}=ddz({WSS_mag})

20) File - Write Data File

- Choose the 5 outer shell subzones (6 for ellipse, 3 for circle)

- Choose X,Y,Z, U,V,W, P, STRAIN, XYZ Normal, XYZ Tangent 1, XYZ Tangent 2, WSS_ax, WSS_circ, WSS_mag, WSS_ax_x, WSS_ax_y ……WSS_mag_z

- 29 variables total

- ASCII

- Point

- File_wss_derivs.dat

21) FTP File_wss_derivs.dat to graft.surgery.pitt.edu

cp zone_info_file.dat zone_info.dat

cp file_wss_derivs.dat input.dat

wssg_calc

cp wssg_calc.dat file_wssg.dat

WSSG_CALC.F: attached at the end of the protocol

22) FTP File_wssg.dat to PC and open in Tecplot

23) Data - Create Zone - Subzone

- for each anastomosis zone, pick only THE outer shell (1-1 or Mx-Mx)

- double check by turning off all other meshes and just looking at outer shells (rotate about y axis)

24) Determine the IJK values and subzone numbers for the 7 regions of interest

- proximal artery, heel, toe, distal artery, graft, floor, hood

25) Data - Create Zone - Subzone

- create subzones for each region of interest (2 for each if ellipse, 1 for each if circle)

26) Tools - CFD Analyzer - Perform Integration

- Type in only the region subzones that have J outer shells (ie 13-15,17,21-22)

- Calculate Average of Variable - WSS_ax

- Integrate Over - J Planes

- Integrate

- Save - in default directory

- avg_wss_ax_perfdate_j.txt

- Repeat for WSS_circ, WSS_mag, WSSG_ax, WSSG_circ, WSSG_mag

- Type in only the region subzones that have K outer shells (ie 16,18-20,23-26)

- Calculate Average of Variable - WSS_ax

- Integrate Over - K Planes

- Integrate

- Save - in default directory

- avg_wss_ax_perfdate_k.txt

- Repeat for WSS_circ, WSS_mag, WSSG_ax, WSSG_circ, WSSG_mag

27) Parcel out wss and wssg data from .txt files into Excel file (perfdate_wss_wssg_ stain.xls) and complete with stain data from data_summary_zeroneg_flow.xls

---

```
      PROGRAM WSS_CALC
      implicit double precision(a-h,o-z)
      character*50 infile, outfile, zonefile
      parameter(nvars=26, numzones=6, numpts=100000)
      parameter(infile='input.dat')
      parameter(zonefile='zone_info.dat')
      parameter(outfile='wss_calc.dat')
      dimension q(numpts,nvars), vnormal(numpts,3)
      dimension tangent1(numpts,3), tangent2(numpts,3)
      dimension wss_ax(numpts),wss_circ(numpts),wss_mag(numpts)
      dimension imax(numzones),jmax(numzones),kmax(numzones)

C     This program calculate the wall shear stress (WSS) from the unit normal
C     vectors output from Tecplot. These are the inward-facing normals so
C     they are inverted to get the outward-facing normals. Tecplot file
C     includes information for only the outer shell of the anastomosis and
C     the direction normal used (JorK) depends on the grid.
C     **********WSS units are dynes/cm2**********

C     The order of the 26 variables from the Tecplot input file are:
C     X,Y,Z,U,V,W,P,STRAIN,X-Inorm,Y-Inorm,Z-Inorm,
C     X-Jnorm,Y-Jnorm,Z-Jnorm,X-Knorm,Y-Knorm,Z-Knorm,
C     dudx,dudy,dudz,dvdx,dvdy,dvdz,dwdx,dwdy,dwdz

C     The first tangential vector follows the I grid direction and is
C     projected onto the cell surface and normalized.

C     The second tangential vector is the vector perpendicular to the
C     normal and 1st tangential vector.

C     These tangential vectors are used to calculate WSS from the
```

```
C     stress tensor.

      open(99,file=zonefile)
      read(99,*)
      read(99,*)
      read(99,*) nzones
      if(nzones.gt.numzones) then
        write(*,*) "Number of Zones is greater than 6.
     *       Change numzones dimension in wss_calc.f and recompile"
        STOP
      endif
      read(99,*)
      npts=0
      do i=1,nzones
        read(99,*) imax(i),jmax(i),kmax(i)
        write(*,*) i,imax(i),jmax(i),kmax(i)
        npts=npts+imax(i)*jmax(i)*kmax(i)
      enddo
      write(*,*) npts
      read(99,*)
      read(99,*) visc
      write(*,*) visc
      if(npts.gt.numpts) then
        write(*,*) "Number of Points ",npts," is greater than 100,000.
     *       Change numpts dimension in wss_calc.f and recompile"
        STOP
      endif
      close(99)


      open(99,file=infile)
      do i=1,nvars+1
       read(99,*)
      enddo
      ntot1=0
      ntot2=0
      do i=1,nzones
       nblk=imax(i)*jmax(i)*kmax(i)
       read(99,*)
       read(99,*)
       read(99,*)
```

```
      ntot1=ntot2+1
      ntot2=ntot2+nblk
      do j=ntot1,ntot2
       read(99,*) (q(j,n),n=1,nvars)
      enddo
     enddo
     close(99)

C     Reorder normals based on grid (J dir used for prox art and graft,
C     K dir used for distal art) and muli by (-1,-1,-1) to get outward
C     normals.
C     Calculate the direction for the 1st tangent (normal(i)-normal(i+1))
C     1st tangent info sorted WRT # I-grid points (prox art and graft=40,
C     dist art = 100)

     ntot1=0
     ntot2=0
     do i=1,nzones
       nblk=imax(i)*jmax(i)*kmax(i)
       ntot1=ntot2+1
       ntot2=ntot2+nblk
       do j=ntot1,ntot2
         if(jmax(i).eq.6) then
           vnormal(j,1)=-1.0d0*q(j,12)
           vnormal(j,2)=-1.0d0*q(j,13)
           vnormal(j,3)=-1.0d0*q(j,14)
C            write(*,*),"Using J normals",i,j
         elseif(kmax(i).eq.6) then
           vnormal(j,1)=-1.0d0*q(j,15)
           vnormal(j,2)=-1.0d0*q(j,16)
           vnormal(j,3)=-1.0d0*q(j,17)
C            write(*,*),"Using K normals",i,j
         else
           write(*,*) "Not know which direction to use (J,K) for normal.
     *           Rewrite data input file so that only have the outer
     *           shell (J or K=1)"
           STOP
         endif
       enddo

       do j=ntot1,ntot2
```

```
          if(mod(j-ntot1+1,imax(i)).ne.0) then
            tangent1(j,1)=q(j+1,1)-q(j,1)
            tangent1(j,2)=q(j+1,2)-q(j,2)
            tangent1(j,3)=q(j+1,3)-q(j,3)
          else
            tangent1(j,1)=tangent1(j-1,1)
            tangent1(j,2)=tangent1(j-1,2)
            tangent1(j,3)=tangent1(j-1,3)
C             write(*,*) "End of I grid",i,j
          endif
        enddo
      enddo

C     Project current tangent1 (along grid direction) onto the cell surface
C     (t1=tgrid-(tgrid*dot*normal)normal)
C     and then normalize it to get final tangent1

      do j=1,npts
        tdotn=tangent1(j,1)*vnormal(j,1)+tangent1(j,2)*
     *       vnormal(j,2)+tangent1(j,3)*vnormal(j,3)
        do k=1,3
          tangent1(j,k)=tangent1(j,k)-tdotn*vnormal(j,k)
        enddo
        tanmag=sqrt(tangent1(j,1)**2.0d0+tangent1(j,2)**2.0d0+
     *       tangent1(j,3)**2.0d0)
        tangent1(j,1)=tangent1(j,1)/tanmag
        tangent1(j,2)=tangent1(j,2)/tanmag
        tangent1(j,3)=tangent1(j,3)/tanmag
      enddo

C     Check to be sure tangent1 is perpendicular to normal
      do j=1,npts
        tdotn=tangent1(j,1)*vnormal(j,1)+tangent1(j,2)*
     *       vnormal(j,2)+tangent1(j,3)*vnormal(j,3)
        if(tdotn.gt.0.0000000001d0) then
          write(*,*) "OOPS - Tangent1 is not perpendicular to",
     *          "the normal at point",j
        write(*,*) j,tangent1(j,1),vnormal(j,1),tangent1(j,2),
     *       vnormal(j,2),tangent1(j,3),vnormal(j,3),tdotn
        endif
      enddo
```

```
C     Calculate 2nd tangent by crossing the normal with tangent1

      do j=1,npts
        tangent2(j,1)=vnormal(j,2)*tangent1(j,3)-
     *       vnormal(j,3)*tangent1(j,2)
        tangent2(j,2)=-1.0d0*vnormal(j,1)*tangent1(j,3)+
     *       vnormal(j,3)*tangent1(j,1)
        tangent2(j,3)=vnormal(j,1)*tangent1(j,2)-
     *       vnormal(j,2)*tangent1(j,1)
        tanmag=sqrt(tangent2(j,1)**2.0d0+tangent2(j,2)**2.0d0+
     *       tangent2(j,3)**2.0d0)
        tangent2(j,1)=tangent2(j,1)/tanmag
        tangent2(j,2)=tangent2(j,2)/tanmag
        tangent2(j,3)=tangent2(j,3)/tanmag
      enddo

C     Check to be sure tangent2 is perpendicular to normal

      do j=1,npts
        tdotn=tangent2(j,1)*vnormal(j,1)+tangent2(j,2)*
     *       vnormal(j,2)+tangent2(j,3)*vnormal(j,3)
        if(tdotn.gt.0.0000000001d0) then
          write(*,*) "OOPS - Tangent2 is not perpendicular to",
     *          "the normal at point",j
        write(*,*) j,tangent2(j,1),vnormal(j,1),tangent2(j,2),
     *       vnormal(j,2),tangent2(j,3),vnormal(j,3),tdotn
        endif
      enddo

C     Check to be sure tangent1 is perpendicular to tangent2

      do j=1,npts
        tdotn=tangent1(j,1)*tangent2(j,1)+tangent1(j,2)*
     *       tangent2(j,2)+tangent1(j,3)*tangent2(j,3)
        if(tdotn.gt.0.0000000001d0) then
          write(*,*) "OOPS - Tangent1 is not perpendicular to",
     *          "the tangent2 at point",j
        write(*,*) j,tangent1(j,1),tangent2(j,1),tangent1(j,2),
     *       tangent2(j,2),tangent1(j,3),tangent2(j,3),tdotn
        endif
      enddo
```

```
C     Calculate the stress tensor (s11-s33) and then dot with the
C     normal to get the stress vector. Then dot this with tangent1
C     to get "axial" wss or dot with the tangent2 to get
C     "circumferential" and calculate magnitude from these squared

      do j=1,npts
        dudx=q(j,18)
        dudy=q(j,19)
        dudz=q(j,20)
        dvdx=q(j,21)
        dvdy=q(j,22)
        dvdz=q(j,23)
        dwdx=q(j,24)
        dwdy=q(j,25)
        dwdz=q(j,26)
        p=q(j,7)
        sxx=-p+2.0d0*visc*dudx
        sxy=visc*(dudy+dvdx)
        sxz=visc*(dudz+dwdx)
        syx=sxy
        syy=-p+2.0d0*visc*dvdy
        syz=visc*(dvdz+dwdy)
        szx=sxz
        szy=syz
        szz=-p+2.0d0*visc*dwdz
        stressx=sxx*vnormal(j,1)+sxy*vnormal(j,2)+sxz*vnormal(j,3)
        stressy=syx*vnormal(j,1)+syy*vnormal(j,2)+syz*vnormal(j,3)
        stressz=szx*vnormal(j,1)+szy*vnormal(j,2)+szz*vnormal(j,3)
C         write(*,*) j, stressx,stressy,stressz
        wss_ax(j)=-10.0d0*(tangent1(j,1)*stressx+tangent1(j,2)*
     *       stressy+tangent1(j,3)*stressz)
        wss_circ(j)=10.0d0*(tangent2(j,1)*stressx+tangent2(j,2)*
     *       stressy+tangent2(j,3)*stressz)
        wss_mag(j)=sqrt(wss_ax(j)**2.0d0+wss_circ(j)**2.0d0)
C         write(*,*),j,wss_ax(j),wss_circ(j), wss_mag(j)
      enddo

      open(99,file=outfile)
      write(99,*)'TITLE = """'
      write(99,*)'VARIABLES = "X"'
      write(99,*)'"Y"'
```

```
      write(99,*)'"Z"'
      write(99,*)'"U"'
      write(99,*)'"V"'
      write(99,*)'"W"'
      write(99,*)'"P"'
      write(99,*)'"STRAIN"'
      write(99,*)'"X Normal"'
      write(99,*)'"Y Normal"'
      write(99,*)'"Z Normal"'
      write(99,*)'"X Tangent 1"'
      write(99,*)'"Y Tangent 1"'
      write(99,*)'"Z Tangent 1"'
      write(99,*)'"X Tangent 2"'
      write(99,*)'"Y Tangent 2"'
      write(99,*)'"Z Tangent 2"'
      write(99,*)'"WSS_ax"'
      write(99,*)'"WSS_circ"'
      write(99,*)'"WSS_mag"'

C     ******************
C     OUTPUT TECPLOT FILE
C     ******************

      itot1=0
      itot2=0
      do i=1,nzones
        write(99,*)'ZONE T="ZONE', i, ""
        write(99,*)'I=', imax(i), ',J=',jmax(i), ',K=',kmax(i),
     *       ',F=POINT'
        itot1=itot2+1
        itot2=itot2+imax(i)*jmax(i)*kmax(i)
        do j=itot1,itot2
          write(99,*)(q(j,n),n=1,8),vnormal(j,1),vnormal(j,2),
     *          vnormal(j,3),tangent1(j,1),tangent1(j,2),tangent1(j,3)
     *          ,tangent2(j,1),tangent2(j,2),tangent2(j,3)
     *          ,wss_ax(j),wss_circ(j),wss_mag(j)
        enddo
      enddo
      close(99)
      end
```

```
      PROGRAM WSSG_CALC
      implicit double precision(a-h,o-z)
      character*50 infile, outfile, zonefile
      parameter(nvars=26, numzones=6, numpts=100000)
      parameter(infile='input.dat')
      parameter(zonefile='zone_info.dat')
      parameter(outfile='wss_calc.dat')
      dimension q(numpts,nvars), vnormal(numpts,3)
      dimension tangent1(numpts,3), tangent2(numpts,3)
      dimension wss_ax(numpts),wss_circ(numpts),wss_mag(numpts)
      dimension imax(numzones),jmax(numzones),kmax(numzones)

C     This program calculate the wall shear stress (WSS) from the unit normal
C     vectors output from Tecplot. These are the inward-facing normals so
C     they are inverted to get the outward-facing normals. Tecplot file
C     includes information for only the outer shell of the anastomosis and
C     the direction normal used (JorK) depends on the grid.
C     **********WSS units are dynes/cm2**********

C     The order of the 26 variables from the Tecplot input file are:
C     X,Y,Z,U,V,W,P,STRAIN,X-Inorm,Y-Inorm,Z-Inorm,
C     X-Jnorm,Y-Jnorm,Z-Jnorm,X-Knorm,Y-Knorm,Z-Knorm,
C     dudx,dudy,dudz,dvdx,dvdy,dvdz,dwdx,dwdy,dwdz

C     The first tangential vector follows the I grid direction and is
C     projected onto the cell surface and normalized.

C     The second tangential vector is the vector perpendicular to the
C     normal and 1st tangential vector.

C     These tangential vectors are used to calculate WSS from the
C     stress tensor.

      open(99,file=zonefile)
      read(99,*)
      read(99,*)
      read(99,*) nzones
      if(nzones.gt.numzones) then
        write(*,*) "Number of Zones is greater than 6.
     *       Change numzones dimension in wss_calc.f and recompile"
```

```
   STOP
 endif
 read(99,*)
 npts=0
 do i=1,nzones
   read(99,*) imax(i),jmax(i),kmax(i)
   write(*,*) i,imax(i),jmax(i),kmax(i)
   npts=npts+imax(i)*jmax(i)*kmax(i)
 enddo
 write(*,*) npts
 read(99,*)
 read(99,*) visc
 write(*,*) visc
 if(npts.gt.numpts) then
   write(*,*) "Number of Points ",npts," is greater than 100,000.
*       Change numpts dimension in wss_calc.f and recompile"
   STOP
 endif
 close(99)


 open(99,file=infile)
 do i=1,nvars+1
  read(99,*)
 enddo
 ntot1=0
 ntot2=0
 do i=1,nzones
  nblk=imax(i)*jmax(i)*kmax(i)
  read(99,*)
  read(99,*)
  read(99,*)
  ntot1=ntot2+1
  ntot2=ntot2+nblk
  do j=ntot1,ntot2
   read(99,*) (q(j,n),n=1,nvars)
  enddo
 enddo
 close(99)
```

```
C     Reorder normals based on grid (J dir used for prox art and graft,
C     K dir used for distal art) and muli by (-1,-1,-1) to get outward
C     normals.
C     Calculate the direction for the 1st tangent (normal(i)-normal(i+1))
C     1st tangent info sorted WRT # I-grid points (prox art and graft=40,
C     dist art = 100)

      ntot1=0
      ntot2=0
      do i=1,nzones
        nblk=imax(i)*jmax(i)*kmax(i)
        ntot1=ntot2+1
        ntot2=ntot2+nblk
        do j=ntot1,ntot2
          if(jmax(i).eq.6) then
            vnormal(j,1)=-1.0d0*q(j,12)
            vnormal(j,2)=-1.0d0*q(j,13)
            vnormal(j,3)=-1.0d0*q(j,14)
C             write(*,*),"Using J normals",i,j
          elseif(kmax(i).eq.6) then
            vnormal(j,1)=-1.0d0*q(j,15)
            vnormal(j,2)=-1.0d0*q(j,16)
            vnormal(j,3)=-1.0d0*q(j,17)
C             write(*,*),"Using K normals",i,j
          else
            write(*,*) "Not know which direction to use (J,K) for normal.
     *           Rewrite data input file so that only have the outer
     *           shell (J or K=1)"
            STOP
          endif
        enddo

        do j=ntot1,ntot2
          if(mod(j-ntot1+1,imax(i)).ne.0) then
            tangent1(j,1)=q(j+1,1)-q(j,1)
            tangent1(j,2)=q(j+1,2)-q(j,2)
            tangent1(j,3)=q(j+1,3)-q(j,3)
          else
            tangent1(j,1)=tangent1(j-1,1)
            tangent1(j,2)=tangent1(j-1,2)
            tangent1(j,3)=tangent1(j-1,3)
```

```
C             write(*,*) "End of I grid",i,j
            endif
          enddo
        enddo

C     Project current tangent1 (along grid direction) onto the cell surface
C     (t1=tgrid-(tgrid*dot*normal)normal)
C     and then normalize it to get final tangent1

        do j=1,npts
          tdotn=tangent1(j,1)*vnormal(j,1)+tangent1(j,2)*
     *       vnormal(j,2)+tangent1(j,3)*vnormal(j,3)
          do k=1,3
            tangent1(j,k)=tangent1(j,k)-tdotn*vnormal(j,k)
          enddo
          tanmag=sqrt(tangent1(j,1)**2.0d0+tangent1(j,2)**2.0d0+
     *       tangent1(j,3)**2.0d0)
          tangent1(j,1)=tangent1(j,1)/tanmag
          tangent1(j,2)=tangent1(j,2)/tanmag
          tangent1(j,3)=tangent1(j,3)/tanmag
        enddo

C     Check to be sure tangent1 is perpendicular to normal

        do j=1,npts
          tdotn=tangent1(j,1)*vnormal(j,1)+tangent1(j,2)*
     *       vnormal(j,2)+tangent1(j,3)*vnormal(j,3)
          if(tdotn.gt.0.0000000001d0) then
            write(*,*) "OOPS - Tangent1 is not perpendicular to",
     *         "the normal at point",j
          write(*,*) j,tangent1(j,1),vnormal(j,1),tangent1(j,2),
     *       vnormal(j,2),tangent1(j,3),vnormal(j,3),tdotn
          endif
        enddo

C     Calculate 2nd tangent by crossing the normal with tangent1

        do j=1,npts
          tangent2(j,1)=vnormal(j,2)*tangent1(j,3)-
     *       vnormal(j,3)*tangent1(j,2)
          tangent2(j,2)=-1.0d0*vnormal(j,1)*tangent1(j,3)+
```

```
*       vnormal(j,3)*tangent1(j,1)
        tangent2(j,3)=vnormal(j,1)*tangent1(j,2)-
*       vnormal(j,2)*tangent1(j,1)
        tanmag=sqrt(tangent2(j,1)**2.0d0+tangent2(j,2)**2.0d0+
*       tangent2(j,3)**2.0d0)
        tangent2(j,1)=tangent2(j,1)/tanmag
        tangent2(j,2)=tangent2(j,2)/tanmag
        tangent2(j,3)=tangent2(j,3)/tanmag
      enddo

C     Check to be sure tangent2 is perpendicular to normal

      do j=1,npts
        tdotn=tangent2(j,1)*vnormal(j,1)+tangent2(j,2)*
*       vnormal(j,2)+tangent2(j,3)*vnormal(j,3)
        if(tdotn.gt.0.0000000001d0) then
          write(*,*) "OOPS - Tangent2 is not perpendicular to",
*           "the normal at point",j
        write(*,*) j,tangent2(j,1),vnormal(j,1),tangent2(j,2),
*       vnormal(j,2),tangent2(j,3),vnormal(j,3),tdotn
        endif
      enddo

C     Check to be sure tangent1 is perpendicular to tangent2

      do j=1,npts
        tdotn=tangent1(j,1)*tangent2(j,1)+tangent1(j,2)*
*       tangent2(j,2)+tangent1(j,3)*tangent2(j,3)
        if(tdotn.gt.0.0000000001d0) then
          write(*,*) "OOPS - Tangent1 is not perpendicular to",
*           "the tangent2 at point",j
        write(*,*) j,tangent1(j,1),tangent2(j,1),tangent1(j,2),
*       tangent2(j,2),tangent1(j,3),tangent2(j,3),tdotn
        endif
      enddo

C     Calculate the stress tensor (s11-s33) and then dot with the
C     normal to get the stress vector. Then dot this with tangent1
C     to get "axial" wss or dot with the tangent2 to get
C     "circumferential" and calculate magnitude from these squared
```

```
      do j=1,npts
        dudx=q(j,18)
        dudy=q(j,19)
        dudz=q(j,20)
        dvdx=q(j,21)
        dvdy=q(j,22)
        dvdz=q(j,23)
        dwdx=q(j,24)
        dwdy=q(j,25)
        dwdz=q(j,26)
        p=q(j,7)
        sxx=-p+2.0d0*visc*dudx
        sxy=visc*(dudy+dvdx)
        sxz=visc*(dudz+dwdx)
        syx=sxy
        syy=-p+2.0d0*visc*dvdy
        syz=visc*(dvdz+dwdy)
        szx=sxz
        szy=syz
        szz=-p+2.0d0*visc*dwdz
        stressx=sxx*vnormal(j,1)+sxy*vnormal(j,2)+sxz*vnormal(j,3)
        stressy=syx*vnormal(j,1)+syy*vnormal(j,2)+syz*vnormal(j,3)
        stressz=szx*vnormal(j,1)+szy*vnormal(j,2)+szz*vnormal(j,3)
C         write(*,*) j, stressx,stressy,stressz
        wss_ax(j)=-10.0d0*(tangent1(j,1)*stressx+tangent1(j,2)*
     *       stressy+tangent1(j,3)*stressz)
        wss_circ(j)=10.0d0*(tangent2(j,1)*stressx+tangent2(j,2)*
     *       stressy+tangent2(j,3)*stressz)
        wss_mag(j)=sqrt(wss_ax(j)**2.0d0+wss_circ(j)**2.0d0)
C         write(*,*),j,wss_ax(j),wss_circ(j), wss_mag(j)
      enddo

      open(99,file=outfile)
      write(99,*)'TITLE = """
      write(99,*)'VARIABLES = "X"'
      write(99,*)'"Y"'
      write(99,*)'"Z"'
      write(99,*)'"U"'
      write(99,*)'"V"'
      write(99,*)'"W"'
      write(99,*)'"P"'
```

```
      write(99,*)'"STRAIN"'
      write(99,*)'"X Normal"'
      write(99,*)'"Y Normal"'
      write(99,*)'"Z Normal"'
      write(99,*)'"X Tangent 1"'
      write(99,*)'"Y Tangent 1"'
      write(99,*)'"Z Tangent 1"'
      write(99,*)'"X Tangent 2"'
      write(99,*)'"Y Tangent 2"'
      write(99,*)'"Z Tangent 2"'
      write(99,*)'"WSS_ax"'
      write(99,*)'"WSS_circ"'
      write(99,*)'"WSS_mag"'

C     ******************
C     OUTPUT TECPLOT FILE
C     ******************

      itot1=0
      itot2=0
      do i=1,nzones
        write(99,*)'ZONE T="ZONE', i, '"'
        write(99,*)'I=', imax(i), ',J=',jmax(i), ',K=',kmax(i),
     *       ',F=POINT'
        itot1=itot2+1
        itot2=itot2+imax(i)*jmax(i)*kmax(i)
        do j=itot1,itot2
          write(99,*)(q(j,n),n=1,8),vnormal(j,1),vnormal(j,2),
     *          vnormal(j,3),tangent1(j,1),tangent1(j,2),tangent1(j,3)
     *          ,tangent2(j,1),tangent2(j,2),tangent2(j,3)
     *          ,wss_ax(j),wss_circ(j),wss_mag(j)
        enddo
      enddo
      close(99)
      end
```

APPENDIX D

To determine the amount of error associated with the quantification of the staining, the Mean Normalized Staining Indices $_{ROI}$ for one experiment quantified by one user were compared to the same data quantified by a second user. The results are shown in the following table, Appendix D.1. The percent difference averaged over all regions of interest ranged from approximately 11 - 52 %, depending on the biologic parameter being quantified. The average value was 29%.

Appendix D.1 The Mean Normalized Staining Indices ROI quantified by two separate users for one experiment and compared to determine the error associated with the staining quantification.

USER #1	ETS prox	ETS heel	ETS toe	ETS distal	ETS graft	ETS floor	ETS hood	ETE prox	ETE anast	nonperf	
C-fos	1.34	1.31	0.67	1.21	0.87	1.20	1.05	0.82	1.55	0.02	
C-jun	1.18	1.17	0.71	1.23	1.14	0.71	0.90	1.12	1.26	0.59	
Egr-1	1.51	1.26	0.91	0.68	1.01	0.77	1.38	0.78	1.44	0.55	
EC Apoptosis	0.20	0.43	1.44	0.69	0.51	1.06	1.04	1.42	1.76	1.48	
SMC Apoptosis	1.70	0.77	0.27	0.92	0.95	0.34	1.48	1.96	0.53	1.08	
USER #2	ETS prox	ETS heel	ETS toe	ETS distal	ETS graft	ETS floor	ETS hood	ETE prox	ETE anast	nonperf	
C-fos	1.65	1.02	0.94	1.83	0.81	1.01	1.41	0.64	0.73	0.04	
C-jun	1.19	0.89	0.83	1.20	1.15	0.86	0.90	1.05	1.17	0.76	
Egr-1	1.16	0.81	0.91	0.70	1.06	1.02	0.77	0.89	1.87	0.59	
EC Apoptosis	0.37	0.65	1.17	0.62	0.55	0.83	0.63	1.23	1.92	2.03	
SMC Apoptosis	1.20	0.62	0.23	0.54	0.86	0.22	2.79	1.92	1.51	0.12	
% Difference	ETS prox	ETS heel	ETS toe	ETS distal	ETS graft	ETS floor	ETS hood	ETE prox	ETE anast	nonperf	Mean % Difference
C-fos	22.63	22.47	39.50	50.45	6.46	16.14	34.68	21.48	52.55	54.56	32.09
C-jun	1.17	23.22	16.96	2.29	0.40	21.28	0.41	6.56	6.96	29.56	10.88
Egr-1	23.38	36.00	0.34	2.76	5.53	32.08	43.98	14.59	29.18	7.98	19.58
EC Apoptosis	85.27	52.55	18.63	9.98	8.64	21.39	39.24	13.21	9.12	37.80	29.58
SMC Apoptosis	29.51	20.32	11.83	41.76	9.22	36.42	88.91	2.00	186.23	89.25	51.55
										Average	28.74

To determine the amount of error associated with the ellipse digitization, the major and minor axes for all ellipses used to develop the CFD model for one ETS anastomosis measured by one user were compared to the same data measured by a second user. The results are shown in the following table, Appendix D.2. The percent difference averaged over all ellipses was 19% for the major axes and 20% for the minor axes.

Appendix D.2 The values for the major and minor axes for all ellipses for one ETS model measured by two separate users to determine the error associated with the lumen digitization.

User 1: Major Diameter (m)	User 1: Minor Diameter (m)	User 2: Major Diameter (m)	User 2: Minor Diameter (m)	% Difference Major Diameter	% Difference Minor Diameter
0.00654	0.00442	0.00849	0.00802	29.75	81.41
0.00824	0.00642	0.00966	0.00748	17.31	16.53
0.00852	0.00633	0.00993	0.00721	16.46	13.91
0.00807	0.00584	0.01061	0.00691	31.40	18.30
0.00753	0.00542	0.01092	0.00664	45.13	22.48
0.00884	0.00473	0.01046	0.00628	18.27	32.61
0.00820	0.00533	0.00609	0.00418	25.75	21.59
0.00924	0.00534	0.00667	0.00418	27.78	21.74
0.00833	0.00472	0.00580	0.00357	30.38	24.37
0.00705	0.00495	0.00517	0.00361	26.70	27.16
0.00798	0.00519	0.00867	0.00583	8.60	12.46
0.00783	0.00516	0.00845	0.00633	8.04	22.77
0.00882	0.00421	0.00894	0.00538	1.42	27.80
0.00736	0.00398	0.01024	0.00450	39.05	13.03
0.00703	0.00422	0.00820	0.00518	16.61	22.66
0.00736	0.00510	0.00756	0.00533	2.67	4.63
0.00822	0.00496	0.00859	0.00506	4.50	2.15
0.00900	0.00457	0.00923	0.00468	2.62	2.44
0.00876	0.00401	0.00874	0.00433	0.14	8.06
0.00799	0.00432	0.00860	0.00479	7.54	10.89
0.00747	0.00468	0.00815	0.00541	9.11	15.52
0.00676	0.00508	0.00771	0.00563	14.05	10.82
0.00721	0.00476	0.00759	0.00505	5.23	6.05
0.00612	0.00357	0.00640	0.00389	4.58	9.11
0.00585	0.00368	0.00831	0.00416	42.13	13.12
0.00504	0.00426	0.00720	0.00531	42.83	24.70
0.00531	0.00381	0.00749	0.00536	41.04	40.80
0.00534	0.00402	0.00659	0.00573	23.47	42.36
0.01120	0.00856	0.00832	0.00681	25.69	20.46
0.01341	0.00693	0.00985	0.00551	26.54	20.58
0.01487	0.00769	0.01083	0.00677	27.15	11.96
0.01330	0.00618	0.01140	0.00503	14.30	18.74
0.01197	0.00614	0.01362	0.00695	13.79	13.18
0.01031	0.00565	0.00974	0.00670	5.45	18.55
0.00734	0.00345	0.00751	0.00459	2.32	33.09
			Mean	**18.79**	**20.17**

BIBLIOGRAPHY

BIBLIOGRAPHY

[1] AHA, "2002 Heart and Stroke Statistical Update," American Heart Association, Dallas 2001.

[2] J. M. Giordano, "Biological and Nonbiological Vascular Grafts," in *The Basic Science of Vascular Surgery*, J. M. Giordano, H. H. Trout, and R. G. DePalma, Eds. Mount Kisco: Futura Publishing Company, 1988, pp. 515-556.

[3] B. L. Zaret, L. S. Cohen, and M. Moser, *Yale University School of Medicine Heart Book*. New York: Hearst Books, 1992.

[4] J. G. Regensteiner and W. R. Hiatt, "Current medical therapies for patients with peripheral arterial disease: a critical review," *Am J Med*, vol. 112, pp. 49-57., 2002.

[5] J. G. Motwani, "Aortocoronary saphenous vein graft disease: pathogenesis, predisposition, and prevention," *Circulation*, vol. 97, pp. 916-31, 1998.

[6] M. G. Davies and P. O. Hagen, "Pathophysiology of vein graft failure: a review," *Eur J Vasc Endovasc Surg*, vol. 9, pp. 7-18, 1995.

[7] J. L. Cox, D. A. Chiasson, and A. I. Gotlieb, "Stranger in a strange land: the pathogenesis of saphenous vein graft stenosis with emphasis on structural and functional differences between veins and arteries," *Prog Cardiovasc Dis*, vol. 34, pp. 45-68, 1991.

[8] P. B. Dobrin, F. N. Littooy, and E. D. Endean, "Mechanical factors predisposing to intimal hyperplasia and medial thickening in autogenous vein grafts," *Surgery*, vol. 105, pp. 393-400, 1989.

[9] S. Moskowitz, B. Lewis, S. Milo, and R. Amar, "Selection of saphenous vein bypass graft diameter to support patency of the stenosed coronary artery.," *Cardiovasc Res*, vol. 13, pp. 370-6, 1979.

[10] R. Rutherford, *Atlas of Vascular Surgery: Basic Techniques and Exposures*. Philadelphia: W.B. Saunders Company, 1993.

[11] W. M. Kirsch, S. Gupta, and Y. Zhu, "Sutureless vascular anastomosis: the VCS clip," *Cardiovasc Surg*, vol. 9, pp. 523-5, 2001.

[12] Y. H. Zhu and W. M. Kirsch, "A New Surgical Technique for Venous Reconstruction: The Nonpenetrating Clip," in *Modern Vascular Surgery*, vol. 5, J. B. Chang, Ed. New York: Springer-Verlag Inc., 1992, pp. 425-463.

[13] E. Pikoulis, D. Burris, P. Rhee, T. Nishibe, A. Leppaniemi, D. Wherry, and N. Rich, "Rapid arterial anastomosis with titanium clips," *Am J Surg*, vol. 175, pp. 494-6, 1998.

[14] V. S. Sottiurai, "Distal Anastomotic Intimal Hyperplasia: Histocytomorphology, Pathophysiology, Etiology, and Prevention," *International Journal of Angiology*, vol. 8, pp. 1-10, 1999.

[15] L. H. Edmunds, *Cardiac Surgery in the Adult.* New York: McGraw-Hill, Health Professions Division, 1997.

[16] W. S. Weintraub, E. L. Jones, J. M. Craver, and R. A. Guyton, "Frequency of repeat coronary bypass or coronary angioplasty after coronary artery bypass surgery using saphenous venous grafts," *Am J Cardiol*, vol. 73, pp. 103-12., 1994.

[17] K. Ouriel, "Peripheral arterial disease," *Lancet*, vol. 358, pp. 1257-64, 2001.

[18] A. W. Clowes, "Pathologic Intimal Hyperplasia as a Response to Vascular Injury and Reconstruction," in *Vascular Surgery*, R. B. Rutherford, Ed., 4th ed. Philadelphia: W. B. Saunders Company, 1995, pp. 285-295.

[19] R. Ross, "The pathogenesis of atherosclerosis--an update," *New England Journal of Medicine*, vol. 314, pp. 488-500, 1986.

[20] A. C. Newby, "An overview of the vascular response to injury: a tribute to the late Russell Ross," *Toxicology Letters*, vol. 112-113, pp. 519-29, 2000.

[21] C. Kleinstreuer, "Hemodynamic parameters and early intimal thickening in branching blood vessels," *Critical Reviews in Biomedical Engineering*, vol. 29, pp. 1-64, 2001.

[22] G. Garcia-Cardena, J. Comander, K. R. Anderson, B. R. Blackman, and J. Michael A. Gimbrone, "Inaugural Article: Biomechanical activation of vascular endothelium as a determinant of its functional phenotype," *Proc. Natl. Acad. Sci. USA*, vol. 98, pp. 4478-4485, 2001.

[23] C. B. Thompson, "Apoptosis in the pathogenesis and treatment of disease," *Science*, vol. 267, pp. 1456-62, 1995.

[24] P. Hamet, "Proliferation and apoptosis of vascular smooth muscle in hypertension," *Curr Opin Nephrol Hypertens*, vol. 4, pp. 1-7, 1995.

[25] B. M. Jehn and B. A. Osborne, "Gene regulation associated with apoptosis," *Crit Rev Eukaryot Gene Expr*, vol. 7, pp. 179-93, 1997.

[26] N. Malik, S. E. Francis, C. M. Holt, J. Gunn, G. L. Thomas, L. Shepherd, J. Chamberlain, C. M. Newman, D. C. Cumberland, and D. C. Crossman, "Apoptosis and cell proliferation after porcine coronary angioplasty," *Circulation*, vol. 98, pp. 1657-65, 1998.

[27] S. Chien, "Effects of mechanical forces on signal transduction and gene expression in endothelial cells," *Hypertension*, vol. 31, pp. 162-9, 1998.

[28] E. S. Silverman, "Pathways of Egr-1-mediated gene transcription in vascular biology. [letter; comment.]," *American Journal of Pathology*, vol. 154, pp. 665-70, 1999.

[29] P. Angel and M. Karin, "The role of Jun, Fos and the AP-1 complex in cell-proliferation and transformation," *Biochim Biophys Acta*, vol. 1072, pp. 129-57, 1991.

[30] S. Q. Liu, "Biomechanical basis of vascular tissue engineering," *Critical Reviews in Biomedical Engineering*, vol. 27, pp. 75-148, 1999.

[31] J. Galea, J. Armstrong, S. E. Francis, G. Cooper, D. C. Crossman, and C. M. Holt, "Alterations in c-fos expression, cell proliferation and apoptosis in pressure distended human saphenous vein," *Cardiovascular Research*, vol. 44, pp. 436-448, 1999.

[32] Y. Hayakawa, G. Takemura, J. Misao, M. Kanoh, M. Ohno, H. Ohashi, H. Takatsu, H. Ito, K. Fukuda, T. Fujiwara, S. Minatoguchi, and H. Fujiwara, "Apoptosis and overexpression of bax protein and bax mRNA in smooth muscle cells within intimal hyperplasia of human radial arteries : analysis with arteriovenous fistulas used for hemodialysis," *Arterioscler Thromb Vasc Biol*, vol. 19, pp. 2066-77, 1999.

[33] M. M. Kockx, B. A. Cambier, H. E. Bortier, G. R. De Meyer, S. C. Declercq, P. A. van Cauwelaert, and J. Bultinck, "Foam cell replication and smooth muscle cell apoptosis in human saphenous vein grafts," *Histopathology*, vol. 25, pp. 365-71, 1994.

[34] A. Wang, Y. Bobryshev, S. Cherian, H. Liang, D. Tran, S. Inder, R. Lord, K. Ashwell, and A. Farnsworth, "Expression of apoptosis-related proteins and structural features of cell death in explanted aortocoronary saphenous vein bypass grafts," *Cardiovascular Surgery*, vol. 9, pp. 319-328, 2001.

[35] A. Saraste and K. Pulkki, "Morphologic and biochemical hallmarks of apoptosis," *Cardiovascular Research*, vol. 45, pp. 528-537, 2000.

[36] A. Haunstetter, "Apoptosis: basic mechanisms and implications for cardiovascular disease," *Circulation Research*, vol. 82, pp. 1111-29, 1998.

[37] Y. L. Hu, S. Li, J. Y. Shyy, and S. Chien, "Sustained JNK activation induces endothelial apoptosis: studies with colchicine and shear stress," *Am J Physiol*, vol. 277, pp. H1593-9, 1999.

[38] T. Stefanec, "Endothelial apoptosis: could it have a role in the pathogenesis and treatment of disease? [see comments.]," *Chest*, vol. 117, pp. 841-54, 2000.

[39] N. J. McCarthy and M. Bennett, "The regulation of vascular smooth muscle cell apoptosis," *Cardiovascular Research*, vol. 45, pp. 747-755, 2000.

[40] P. Cirillo, P. Golino, M. Ragni, C. Battaglia, F. Pacifico, S. Formisano, C. Buono, M. Condorelli, and M. Chiariello, "Activated platelets and leucocytes cooperatively stimulate smooth muscle cell proliferation and proto-oncogene expression via release of soluble growth factors," *Cardiovasc Res*, vol. 43, pp. 210-8, 1999.

[41] S. H. Hall, M. C. Berthelon, O. Avallet, and J. M. Saez, "Regulation of c-fos, c-jun, jun-B, and c-myc messenger ribonucleic acids by gonadotropin and growth factors in cultured pig Leydig cell," *Endocrinology*, vol. 129, pp. 1243-9, 1991.

[42] J. M. Rhoads, R. A. Argenzio, W. Chen, R. A. Rippe, J. K. Westwick, A. D. Cox, H. M. Berschneider, and D. A. Brenner, "L-glutamine stimulates intestinal cell proliferation and activates mitogen-activated protein kinases," *Am J Physiol*, vol. 272, pp. G943-53, 1997.

[43] H. J. Hsieh, N. Q. Li, and J. A. Frangos, "Pulsatile and steady flow induces c-fos expression in human endothelial cells," *J Cell Physiol*, vol. 154, pp. 143-51, 1993.

[44] V. Ranjan and S. L. Diamond, "Fluid shear stress induces synthesis and nuclear localization of c-fos in cultured human endothelial cells," *Biochem Biophys Res Commun*, vol. 196, pp. 79-84, 1993.

[45] T. Nagel, N. Resnick, C. F. Dewey, Jr., and M. A. Gimbrone, Jr., "Vascular endothelial cells respond to spatial gradients in fluid shear stress by enhanced activation of transcription factors," *Arterioscler Thromb Vasc Biol*, vol. 19, pp. 1825-34, 1999.

[46] J. A. Ramirez, L. A. Sanchez, M. L. Marin, R. T. Lyon, R. E. Parsons, W. D. Suggs, and F. J. Veith, "c-MYC oncoprotein production in experimental vein graft intimal hyperplasia," *J Surg Res*, vol. 61, pp. 323-9, 1996.

[47] R. A. Moggio, J. Z. Ding, C. J. Smith, R. R. Tota, M. B. Stemerman, and G. E. Reed, "Immediate-early gene expression in human saphenous veins harvested during coronary artery bypass graft operations," *J Thorac Cardiovasc Surg*, vol. 110, pp. 209-13, 1995.

[48] M. Papadaki and S. Eskin, "Effects of fluid shear stress on gene regulation of vascular cells.," *Biotechnol Prog*, vol. 13, pp. 209-21, 1997.

[49] J. Y. Shyy, "Multiple cis-elements mediate shear stress-induced gene expression," *Journal of Biomechanics*, vol. 28, pp. 1451-7, 1995.

[50] T. Ishida, M. Takahashi, M. A. Corson, and B. C. Berk, "Fluid shear stress-mediated signal transduction: how do endothelial cells transduce mechanical force into biological responses?," *Ann N Y Acad Sci*, vol. 811, pp. 12-23; discussion 23-4, 1997.

[51] G. M. Cooper, *Oncogenes*, First ed. Boston: Jones and Bartlett Publishers, 1990.

[52] A. M. Sylvester, D. Chen, K. Krasinski, and V. Andres, "Role of c-fos and E2F in the induction of cyclin A transcription and vascular smooth muscle cell proliferation," *J Clin Invest*, vol. 101, pp. 940-8, 1998.

[53] D. W. Muller, "The role of proto-oncogenes in coronary restenosis," *Progress in Cardiovascular Diseases*, vol. 40, pp. 117-28, 1997.

[54] M. Ebbecke, C. Unterberg, A. Buchwald, S. Stohr, and V. Wiegand, "Antiproliferative effects of a c-myc antisense oligonucleotide on human arterial smooth muscle cells," *Basic Res Cardiol*, vol. 87, pp. 585-91, 1992.

[55] Y. Shi, H. G. Hutchinson, D. J. Hall, and A. Zalewski, "Downregulation of c-myc expression by antisense oligonucleotides inhibits proliferation of human smooth muscle cells [see comments]," *Circulation*, vol. 88, pp. 1190-5, 1993.

[56] S. Biro, Y. M. Fu, Z. X. Yu, and S. E. Epstein, "Inhibitory effects of antisense oligodeoxynucleotides targeting c-myc mRNA on smooth muscle cell proliferation and migration," *Proc Natl Acad Sci U S A*, vol. 90, pp. 654-8, 1993.

[57] M. R. Bennett, S. Anglin, J. R. McEwan, R. Jagoe, A. C. Newby, and G. I. Evan, "Inhibition of vascular smooth muscle cell proliferation in vitro and in vivo by c-myc antisense oligodeoxynucleotides," *J Clin Invest*, vol. 93, pp. 820-8, 1994.

[58] E. R. Edelman, M. Simons, M. G. Sirois, and R. D. Rosenberg, "c-myc in vasculoproliferative disease," *Circ Res*, vol. 76, pp. 176-82, 1995.

[59] A. Sachinidis, "Oligodeoxynucleotides directed to early growth response gene-1 mRNA inhibit DNA synthesis in the smooth muscle cell," *European Journal of Pharmacology*, vol. 309, pp. 95-105, 1996.

[60] P. F. Li, "Differential effect of hydrogen peroxide and superoxide anion on apoptosis and proliferation of vascular smooth muscle cells," *Circulation*, vol. 96, pp. 3602-9, 1997.

[61] G. A. Preston, T. T. Lyon, Y. Yin, J. E. Lang, G. Solomon, L. Annab, D. G. Srinivasan, D. A. Alcorta, and J. C. Barrett, "Induction of apoptosis by c-Fos protein," *Mol Cell Biol*, vol. 16, pp. 211-8, 1996.

[62] R. J. Smeyne, "Continuous c-fos expression precedes programmed cell death in vivo. [see comments.] [erratum appears in Nature 1993 Sep 16;365(6443):279.]," *Nature*, vol. 363, pp. 166-9, 1993.

[63] E. Bossy-Wetzel, L. Bakiri, and M. Yaniv, "Induction of apoptosis by the transcription factor c-Jun," *Embo J*, vol. 16, pp. 1695-709, 1997.

[64] G. I. Evan, A. H. Wyllie, C. S. Gilbert, T. D. Littlewood, H. Land, M. Brooks, C. M. Waters, I. Z. Penn, and D. C. Hancock, "Induction of apoptosis in fibroblasts by c-myc protein," *Cell*, vol. 69, pp. 119-128, 1992.

[65] M. H. Friedman, C. B. Bargeron, O. J. Deters, G. M. Hutchins, and F. F. Mark, "Correlation between wall shear and intimal thickness at a coronary artery branch," *Atherosclerosis*, vol. 68, pp. 27-33, 1987.

[66] C. K. Zarins, D. P. Giddens, B. K. Bharadvaj, V. S. Sottiurai, R. F. Mabon, and S. Glagov, "Carotid bifurcation atherosclerosis. Quantitative correlation of plaque localization with flow velocity profiles and wall shear stress," *Circ Res*, vol. 53, pp. 502-14, 1983.

[67] P. B. Dobrin, F. N. Littooy, and J. Golan, "Mechanical and histologic changes in canine vein grafts," *J Surg Res*, vol. 44, pp. 259-65, 1988.

[68] F. LoGerfo, W. Quist, M. Nowak, H. Crawshaw, and C. Haudenschild, "Downstream anastomotic hyperplasia. A mechanism of failure in Dacron arterial grafts.," *Ann Surg*, vol. 197, pp. 479-83, 1983.

[69] J. W. Butany, T. David, and M. Ojha, "Histological and morphometric analyses of early and late aortocoronary vein grafts and distal anastomoses. [see comments.]," *Canadian Journal of Cardiology*, vol. 14, pp. 671-7, 1998.

[70] A. M. Imparato, A. Bracco, G. F. E. Kim, and R. Z. Zeff, "Intimal and neointimal fibrous proliferation causing failure of arterial reconstruction," *Surgery*, vol. 72, pp. 1007-17, 1972.

[71] S. T. Nikkari and A. W. Clowes, "Restenosis after vascular reconstruction," *Ann Med*, vol. 26, pp. 95-100, 1994.

[72] K. E. Porter, S. Nydahl, P. Dunlop, K. Varty, A. J. Thrush, and N. J. London, "The development of an in vitro flow model of human saphenous vein graft intimal hyperplasia," *Cardiovasc Res*, vol. 31, pp. 607-14, 1996.

[73] L. Kornet, A. P. Hoeks, J. Lambregts, and R. S. Reneman, "In the femoral artery bifurcation, differences in mean wall shear stress within subjects are associated with different intima-media thicknesses," *Arterioscler Thromb Vasc Biol*, vol. 19, pp. 2933-9, 1999.

[74] L. Hofstra, D. C. Bergmans, K. M. Leunissen, A. P. Hoeks, P. J. Kitslaar, M. J. Daemen, and J. H. Tordoir, "Anastomotic intimal hyperplasia in prosthetic arteriovenous fistulas for hemodialysis is associated with initial high flow velocity and not with mismatch in elastic properties," *Journal Of The American Society Of Nephrology*, vol. 6, pp. 1625-33, 1995.

[75] R. S. Taylor, A. Loh, R. J. McFarland, M. Cox, and J. F. Chester, "Improved technique for polytetrafluoroethylene bypass grafting: long-term results using anastomotic vein patches," *Br J Surg*, vol. 79, pp. 348-54, 1992.

[76] M. R. Tyrrell, M. W. Rampling, J. H. Wolfe, J. F. Chester, and R. S. Taylor, "PTFE, collars, and patches," *J Invest Surg*, vol. 5, pp. 25-34, 1992.

[77] V. S. Sottiurai, J. S. Yao, R. C. Batson, S. L. Sue, R. Jones, and Y. A. Nakamura, "Distal anastomotic intimal hyperplasia: histopathologic character and biogenesis," *Ann Vasc Surg*, vol. 3, pp. 26-33, 1989.

[78] H. S. Bassiouny, S. White, S. Glagov, E. Choi, D. P. Giddens, and C. K. Zarins, "Anastomotic intimal hyperplasia: mechanical injury or flow induced," *J Vasc Surg*, vol. 15, pp. 708-16; discussion 716-7, 1992.

[79] R. S. Keynton, M. M. Evancho, R. L. Sims, N. V. Rodway, A. Gobin, and S. E. Rittgers, "Intimal Hyperplasia and Wall Shear in Arterial Bypass Graft Distal Anastomoses: An In Vivo Model Study," *Journal of Biomechanical Engineering*, vol. 123, pp. 464-473, 2001.

[80] S. Rittgers, P. Karayannacos, J. Guy, R. Nerem, G. Shaw, J. Hostetler, and J. Vasko, "Velocity distribution and intimal proliferation in autologous vein grafts in dogs.," *Circ Res*, vol. 42, pp. 792-801, 1978.

[81] E. J. Mattsson, T. R. Kohler, S. M. Vergel, and A. W. Clowes, "Increased blood flow induces regression of intimal hyperplasia," *Arterioscler Thromb Vasc Biol*, vol. 17, pp. 2245-9, 1997.

[82] F. Loth, S. Jones, D. Giddens, H. Bassiouny, S. Glagov, and C. Zarins, "Measurements of velocity and wall shear stress inside a PTFE vascular graft model under steady flow conditions.," *J Biomech Eng*, vol. 119, pp. 187-94, 1997.

[83] M. Ojha, "Spatial and temporal variations of wall shear stress within an end-to-side arterial anastomosis model.," *J Biomech*, vol. 26, pp. 1377-88, 1993.

[84] D. N. Ku, D. P. Giddens, C. K. Zarins, and S. Glagov, "Pulsatile Flow and Atherosclerosis in the Human Carotid Bifurcation: positive correlation between plaque localization and oscillating shear stress," *Arteriosclerosis*, vol. 5, pp. 293-302, 1985.

[85] D. Steinman, B. Vinh, C. Ethier, M. Ojha, R. Cobbold, and K. Johnston, "A numerical simulation of flow in a two-dimensional end-to-side anastomosis model.," *J Biomech Eng*, vol. 115, pp. 112-8, 1993.

[86] M. Hofer, G. Rappitsch, K. Perktold, W. Trubel, and H. Schima, "Numerical study of wall mechanics and fluid dynamics in end-to-side anastomoses and correlation to intimal hyperplasia.," *J Biomech*, vol. 29, pp. 1297-308, 1996.

[87] F. Henry, M. Collins, P. Hughes, and T. How, "Numerical investigation of steady flow in proximal and distal end-to-side anastomoses.," *J Biomech Eng*, vol. 118, pp. 302-10, 1996.

[88] D. Y. Fei, J. D. Thomas, and S. E. Rittgers, "The effect of angle and flow rate upon hemodynamics in distal vascular graft anastomoses: a numerical model study," *Journal Of Biomechanical Engineering*, vol. 116, pp. 331-6, 1994.

[89] C. R. Ethier, D. A. Steinman, X. Zhang, S. R. Karpik, and M. Ojha, "Flow waveform effects on end-to-side anastomotic flow patterns," *Journal Of Biomechanics*, vol. 31, pp. 609-17, 1998.

[90] C. Kleinstreuer, M. Lei, and J. Archie JP, "Flow input waveform effects on the temporal and spatial wall shear stress gradients in a femoral graft-artery connector.," *J Biomech Eng*, vol. 118, pp. 506-10, 1996.

[91] M. Lei, C. Kleinstreuer, and J. P. Archie, "Hemodynamic Simulations and Computer-Aided Designs of Graft-Artery Junctions," *J Biomech Eng*, vol. 119, pp. 343-348, 1997.

[92] K. B. Chandran, M. J. Vonesh, A. Roy, S. Greenfield, B. Kane, R. Greene, and D. D. McPherson, "Computation of vascular flow dynamics from intravascular ultrasound images," *Med Eng Phys*, vol. 18, pp. 295-304, 1996.

[93] R. Krams, J. J. Wentzel, J. A. Oomen, R. Vinke, J. C. Schuurbiers, P. J. de Feyter, P. W. Serruys, and C. J. Slager, "Evaluation of endothelial shear stress and 3D geometry as factors determining the development of atherosclerosis and remodeling in human coronary arteries in vivo. Combining 3D reconstruction from angiography and IVUS (ANGUS) with computational fluid dynamics," *Arterioscler Thromb Vasc Biol*, vol. 17, pp. 2061-5, 1997.

[94] K. Perktold, M. Hofer, G. Rappitsch, M. Loew, B. D. Kuban, and M. H. Friedman, "Validated computation of physiologic flow in a realistic coronary artery branch," *J Biomech*, vol. 31, pp. 217-28, 1998.

[95] X. Y. Xu, Q. Long, M. W. Collins, M. Bourne, and T. M. Griffith, "Reconstruction of blood flow patterns in human arteries," *Proc Inst Mech Eng [H]*, vol. 213, pp. 411-21, 1999.

[96] D. Steinman, R. Frayne, X. Zhang, B. Rutt, and C. Ethier, "MR measurement and numerical simulation of steady flow in an end-to-side anastomosis model.," *J Biomech*, vol. 29, pp. 537-42, 1996.

[97] J. S. Milner, J. A. Moore, B. K. Rutt, and D. A. Steinman, "Hemodynamics of human carotid artery bifurcations: computational studies with models reconstructed from magnetic resonance imaging of normal subjects," *J Vasc Surg*, vol. 28, pp. 143-56, 1998.

[98] J. A. Moore, D. A. Steinman, D. W. Holdsworth, and C. R. Ethier, "Accuracy of computational hemodynamics in complex arterial geometries reconstructed from magnetic resonance imaging," *Ann Biomed Eng*, vol. 27, pp. 32-41, 1999.

[99] J. A. Moore, D. A. Steinman, S. Prakash, K. W. Johnston, and C. R. Ethier, "A numerical study of blood flow patterns in anatomically realistic and simplified end-to-side anastomoses," *J Biomech Eng*, vol. 121, pp. 265-72, 1999.

[100]H. M. Ladak, J. S. Milner, and D. A. Steinman, "Rapid Three-dimensional Segmentation of the Carotid Bifurcation from Serial MR Images," *Journal of Biomechanical Engineering*, vol. 122, pp. 96-99, 2000.

[101]D. A. Steinman, "Simulated pathline visualization of computed periodic blood flow patterns [In Process Citation]," *J Biomech*, vol. 33, pp. 623-8, 2000.

[102]M. Ojha, C. Ethier, K. Johnston, and R. Cobbold, "Steady and pulsatile flow fields in an end-to-side arterial anastomosis model.," *J Vasc Surg*, vol. 12, pp. 747-53, 1990.

[103]G. B. Nackman, M. F. Fillinger, R. Shafritz, T. Wei, and A. M. Graham, "Flow modulates endothelial regulation of smooth muscle cell proliferation: a new model," *Surgery*, vol. 124, pp. 353-60; discussion 360-1, 1998.

[104]A. V. Sterpetti, A. Cucina, L. Santoro, B. Cardillo, and A. Cavallaro, "Modulation of arterial smooth muscle cell growth by haemodynamic forces," *Eur J Vasc Surg*, vol. 6, pp. 16-20, 1992.

[105]A. V. Sterpetti, A. Cucina, L. S. D'Angelo, B. Cardillo, and A. Cavallaro, "Shear stress modulates the proliferation rate, protein synthesis, and mitogenic activity of arterial smooth muscle cells," *Surgery*, vol. 113, pp. 691-9, 1993.

[106]A. V. Sterpetti, A. Cucina, A. Fragale, S. Lepidi, A. Cavallaro, and L. Santoro-D'Angelo, "Shear stress influences the release of platelet derived growth factor and basic fibroblast growth factor by arterial smooth muscle cells. Winner of the ESVS prize for best experimental paper 1993 [see comments]," *Eur J Vasc Surg*, vol. 8, pp. 138-42, 1994.

[107]H. Ueba, M. Kawakami, and T. Yaginuma, "Shear stress as an inhibitor of vascular smooth muscle cell proliferation. Role of transforming growth factor-beta 1 and tissue-type plasminogen activator," *Arterioscler Thromb Vasc Biol*, vol. 17, pp. 1512-6, 1997.

[108]N. DePaola, M. A. Gimbrone, Jr., P. F. Davies, and C. F. Dewey, Jr., "Vascular endothelium responds to fluid shear stress gradients [published erratum appears in Arterioscler Thromb 1993 Mar;13(3):465]," *Arterioscler Thromb*, vol. 12, pp. 1254-7, 1992.

[109]R. M. Zwolak, M. C. Adams, and A. W. Clowes, "Kinetics of vein graft hyperplasia: association with tangential stress," *J Vasc Surg*, vol. 5, pp. 126-36, 1987.

[110]L. W. Kraiss, T. R. Kirkman, T. R. Kohler, B. Zierler, and A. W. Clowes, "Shear stress regulates smooth muscle proliferation and neointimal thickening in porous polytetrafluoroethylene grafts," *Arterioscler Thromb*, vol. 11, pp. 1844-52, 1991.

[111]R. L. Geary, T. R. Kohler, S. Vergel, T. R. Kirkman, and A. W. Clowes, "Time course of flow-induced smooth muscle cell proliferation and intimal thickening in endothelialized baboon vascular grafts," *Circ Res*, vol. 74, pp. 14-23, 1994.

[112]S. Yamamura, K. Okadome, T. Onohara, K. Komori, and K. Sugimachi, "Blood flow and kinetics of smooth muscle cell proliferation in canine autogenous vein grafts: in vivo BrdU incorporation," *J Surg Res*, vol. 56, pp. 155-61, 1994.

[113]S. Q. Liu, "Focal Expression of Angiotensin II Type 1 Receptor and Smooth Muscle Cell Proliferation in the Neointima of Experimental Vein Grafts: Relation to Eddy Blood Flow," *Arteriosclerosis, Thrombosis and Vascular Biology*, vol. 19, pp. 2630-2639, 1999.

[114]K. Mavromatis, T. Fukai, M. Tate, N. Chesler, D. N. Ku, and Z. S. Galis, "Early effects of arterial hemodynamic conditions on human saphenous veins perfused ex vivo," *Arteriosclerosis, Thrombosis and Vascular Biology* vol. 20, pp. 1889-95, 2000.

[115]K. E. Porter, K. Varty, L. Jones, P. R. Bell, and N. J. London, "Human saphenous vein organ culture: a useful model of intimal hyperplasia?," *Eur J Vasc Endovasc Surg*, vol. 11, pp. 48-58, 1996.

[116]Y. Yoshida, "The effects of augmented hemodynamic forces on the progression and topography of atherosclerotic plaques," *Annals of the New York Academy of Sciences*, vol. 598, pp. 256-73, 1990.

[117]J. J. P. Wentzel, R. M. Krams, PhD, J. C. H. B. Schuurbiers, J. A. M. Oomen, J. M. Kloet, W. J. M. van der Giessen, PhD, P. W. M. Serruys, PhD, and C. J. P. Slager, "Relationship Between Neointimal Thickness and Shear Stress After Wallstent Implantation in Human Coronary Arteries," *Circulation*, vol. 103, pp. 1740-1745, 2001.

[118]D. Kaiser, M. A. Freyberg, and P. Friedl, "Lack of hemodynamic forces triggers apoptosis in vascular endothelial cells," *Biochem Biophys Res Commun*, vol. 231, pp. 586-90, 1997.

[119]S. Dimmeler, J. Haendeler, V. Rippmann, M. Nehls, and A. M. Zeiher, "Shear stress inhibits apoptosis of human endothelial cells," *FEBS Lett*, vol. 399, pp. 71-4, 1996.

[120]C. Hermann, A. M. Zeiher, and S. Dimmeler, "Shear stress inhibits H2O2-induced apoptosis of human endothelial cells by modulation of the glutathione redox cycle and nitric oxide synthase," *Arterioscler Thromb Vasc Biol*, vol. 17, pp. 3588-92, 1997.

[121]S. Dimmeler, C. Hermann, J. Galle, and A. M. Zeiher, "Upregulation of superoxide dismutase and nitric oxide synthase mediates the apoptosis-suppressive effects of shear stress on endothelial cells," *Arterioscler Thromb Vasc Biol*, vol. 19, pp. 656-64, 1999.

[122]A. Karsan and J. M. Harlan, "Modulation of endothelial cell apoptosis: mechanisms and pathophysiological roles," *Journal of Atherosclerosis & Thrombosis*, vol. 3, pp. 75-80, 1996.

[123]Z. Mallat and A. Tedgui, "Apoptosis in the vasculature: mechanisms and functional importance," *British Journal of Pharmacology*, vol. 130, pp. 947-62, 2000.

[124]H. Perlman, L. Maillard, K. Krasinski, and K. Walsh, "Evidence for the rapid onset of apoptosis in medial smooth muscle cells after balloon injury [see comments]," *Circulation*, vol. 95, pp. 981-7, 1997.

[125]M. J. Pollman, J. L. Hall, and G. H. Gibbons, "Determinants of vascular smooth muscle cell apoptosis after balloon angioplasty injury. Influence of redox state and cell phenotype," *Circ Res*, vol. 84, pp. 113-21, 1999.

[126]J. Kamenz, W. Seibold, M. Wohlfrom, S. Hanke, N. Heise, C. Lenz, and H. Hanke, "Incidence of intimal proliferation and apoptosis following balloon angioplasty in an atherosclerotic rabbit model," *Cardiovascular Research*, vol. 45, pp. 766-776, 2000.

[127]A. Wang, Y. Bobryshev, H. Liang, S. Cherian, S. Inder, K. Ashwell, A. Farnsworth, and R. Lord, "Electron-microscopic detection of apoptotic and necrotic cell death in non-atherosclerotic areas of stenotic aortocoronary saphenous vein bypass grafts," *J Submicrosc Cytol Pathol*, vol. 32, pp. 209-19, 2000.

[128]O. Tricot, Z. Mallat, C. Heymes, J. Belmin, L. Leseche, and A. Tedgui, "Relation between endothelial cell apoptosis and blood flow direction in human atherosclerotic plaques," *Circulation*, vol. 101, pp. 2450-3, 2000.

[129]J. M. Isner, M. Kearney, S. Bortman, and J. Passeri, "Apoptosis and Human Atherosclerosis and Restenosis," *Circulation*, vol. 91, pp. 2703-2711, 1995.

[130]M. U. Nollert, N. J. Panaro, and L. V. McIntire, "Regulation of genetic expression in shear stress-stimulated endothelial cells," *Ann N Y Acad Sci*, vol. 665, pp. 94-104, 1992.

[131]N. Resnick, T. Collins, W. Atkinson, D. T. Bonthron, C. F. Dewey, Jr., and M. A. Gimbrone, Jr., "Platelet-derived growth factor B chain promoter contains a cis-acting fluid shear-stress-responsive element [published erratum appears in Proc Natl Acad Sci U S A 1993 Aug 15;90(16):7908]," *Proc Natl Acad Sci U S A*, vol. 90, pp. 4591-5, 1993.

[132]H.-J. Hsieh, N.-Q. Li, and J. A. Frangos, "Shear stress increases platelet-derived growth factor mRNA levels," *Am J Physiol*, vol. 260, pp. H642-646, 1991.

[133]H. J. Hsieh, N. Q. Li, and J. A. Frangos, "Shear-induced platelet-derived growth factor gene expression in human endothelial cells is mediated by protein kinase C," *J Cell Physiol*, vol. 150, pp. 552-8, 1992.

[134]S. L. Diamond, J. B. Sharefkin, C. Dieffenbach, K. Frasier-Scott, L. V. McIntire, and S. G. Eskin, "Tissue plasminogen activator messenger RNA levels increase in cultured human endothelial cells exposed to laminar shear stress," *J Cell Physiol*, vol. 143, pp. 364-71, 1990.

[135]D. C. Chappell, S. E. Varner, R. M. Nerem, R. M. Medford, and R. W. Alexander, "Oscillatory shear stress stimulates adhesion molecule expression in cultured human endothelium," *Circ Res*, vol. 82, pp. 532-9, 1998.

[136]M. Ohno, J. P. Cooke, V. J. Dzau, and G. H. Gibbons, "Fluid shear stress induces transforming growth factor beta-1 transcription and production," *J Clin Invest*, vol. 95, pp. 1363-9, 1995.

[137]Y. J. Shyy, H. J. Hsieh, S. Usami, and S. Chien, "Fluid shear stress induces a biphasic response of human monocyte chemotactic protein 1 gene expression in vascular endothelium," *Proc Natl Acad Sci U S A*, vol. 91, pp. 4678-82, 1994.

[138]A. M. Malek and S. Izumo, "Control of endothelial cell gene expression by flow," *J Biomech*, vol. 28, pp. 1515-28, 1995.

[139]H. J. Hsieh, C. C. Cheng, S. T. Wu, J. J. Chiu, B. S. Wung, and D. L. Wang, "Increase of reactive oxygen species (ROS) in endothelial cells by shear flow and involvement of ROS in shear-induced c-fos expression," *J Cell Physiol*, vol. 175, pp. 156-62, 1998.

[140]W. D. Suggs, S. C. Olson, D. Madnani, S. Patel, F. J. Veith, and D. Mandani, "Antisense oligonucleotides to c-fos and c-jun inhibit intimal thickening in a rat vein graft model [published erratum appears in Surgery 2000 Feb;127(2):135]," *Surgery*, vol. 126, pp. 443-9, 1999.

[141]J. D. Mannion, M. L. Ormont, M. G. Magno, J. E. O'Brien, Y. Shi, and A. Zalewski, "Sustained reduction of neointima with c-myc antisense oligonucleotides in saphenous vein grafts," *Ann Thorac Surg*, vol. 66, pp. 1948-52, 1998.

[142]L. Gan, R. Doroudi, U. Hagg, A. Johansson, L. Selin-Sjogren, and S. Jern, "Differential immediate-early gene responses to shear stress and intraluminal pressure in intact human conduit vessels," *FEBS Lett*, vol. 477, pp. 89-94, 2000.

[143]L. W. Kraiss, R. L. Geary, E. J. Mattsson, S. Vergel, Y. P. Au, and A. W. Clowes, "Acute reductions in blood flow and shear stress induce platelet-derived growth factor-A expression in baboon prosthetic grafts," *Circ Res*, vol. 79, pp. 45-53, 1996.

[144]S. A. Berceli, H. S. Borovetz, R. A. Sheppeck, H. H. Moosa, V. S. Warty, M. A. Armany, and I. M. Herman, "Mechanisms of vein graft atherosclerosis: LDL metabolism and endothelial actin reorganization," *J Vasc Surg*, vol. 13, pp. 336-47, 1991.

[145]N. Bardy, G. J. Karillon, R. Merval, J. L. Samuel, and A. Tedgui, "Differential effects of pressure and flow on DNA and protein synthesis and on fibronectin expression by arteries in a novel organ culture system," *Circ Res*, vol. 77, pp. 684-94., 1995.

[146]R. F. Labadie, J. A. Antaki, J. L. Williams, S. Katyal, J. Ligush, S. C. Watkins, S. M. Pham, and H. S. Borovetz, "Pulsatile Perfusion System for ex vivo Investigation of Biochemical Pathways in Intact Vascular Tissue," *Am J Physiol*, vol. 270, pp. H760-H768, 1996.

[147]D. A. Vorp, D. A. Severyn, D. L. Steed, and M. W. Webster, "A device for the application of cyclic twist and extension on perfused vascular segments," *Am J Physiol*, vol. 270, pp. H787-95, 1996.

[148]L. B. Schwartz, C. M. Purut, M. F. Massey, J. C. Pence, P. K. Smith, and R. L. McCann, "Effects of pulsatile perfusion on human saphenous vein vasoreactivity: a preliminary report," *Cardiovasc Surg*, vol. 4, pp. 143-9., 1996.

[149]J. Golledge, R. J. Turner, S. L. Harley, D. R. Springall, and J. T. Powell, "Circumferential deformation and shear stress induce differential responses in saphenous vein endothelium exposed to arterial flow," *J Clin Invest*, vol. 99, pp. 2719-26, 1997.

[150]S. C. Muluk, D. A. Vorp, D. A. Severyn, S. Gleixner, P. C. Johnson, and M. W. Webster, "Enhancement of tissue factor expression by vein segments exposed to coronary arterial hemodynamics," *J Vasc Surg*, vol. 27, pp. 521-7, 1998.

[151]D. Severyn, S. Muluk, M. Webster, and D. Vorp, "Platelet deposition on human saphenous vein (HSV) segments is increased when subjected to simulated coronary artery vein graft (CAVG) hemodynamics," *FASEB JOURNAL*, vol. 10, pp. 3244, 1996.

[152]D. A. Vorp, D. G. Peters, and M. W. Webster, "Gene expression is altered in perfused arterial segments exposed to cyclic flexure ex vivo," *Ann Biomed Eng*, vol. 27, pp. 366-71, 1999.

[153]S. Kute, S. Muluk, and D. Vorp, "Tissue Factor and Immediate Early Gene Expression in Porcine Vessels Exposed to Disturbed Flow in Vitro," presented at BMES Summer Bioengineering Conference, Snowbird, UT, 2001.

[154]S. Kute and D. Vorp, "The Efffect of Proximal Artery Flow on the Hemodynamics at the Distal Anastomosis of a Vascular Bypass Graft: Computational Study," *Journal of Biomechanical Engineering*, vol. 123, pp. 277-283, 2001.

[155]M. Lei, J. P. Archie, and C. Kleinstreuer, "Computational design of a bypass graft that minimizes wall shear stress gradients in the region of the distal anastomosis," *J Vasc Surg*, vol. 25, pp. 637-46, 1997.

[156]S. Glagov, C. Zarins, D. P. Giddens, and D. N. Ku, "Hemodynamics and atherosclerosis. Insights and perspectives gained from studies of human arteries," *Arch Pathol Lab Med*, vol. 112, pp. 1018-31, 1988.

[157]B. Rosner, *Fundamentals of Biostatistics*, 4 ed. Belmont: Duxbury Press, 1995.

[158]C. Stadelmann and H. Lassmann, "Detection of apoptosis in tissue sections," *Cell & Tissue Research*, vol. 301, pp. 19-31, 2000.

[159]S. V. Patankar, *Numerical Heat Transfer and Fluid Flow*. Washington: Hemisphere Publishing Corporation, 1980.

[160]S. Prakash and C. R. Ethier, "Requirements for mesh resolution in 3D computational hemodynamics," *Journal of Biomechanical Engineering*, vol. 123, pp. 134-44, 2001.

[161]P. F. Davies and S. C. Tripathi, "Mechanical stress mechanisms and the cell. An endothelial paradigm," *Circ Res*, vol. 72, pp. 239-45, 1993.

[162]D. L. Fry, "Acute Vascular Endothelial Changes Associated with Increased Blood Velocity Gradients," *Circulation Research*, vol. 22, pp. 165-197, 1968.

[163]N. Resnick and M. A. Gimbrone, Jr., "Hemodynamic forces are complex regulators of endothelial gene expression," *Faseb J*, vol. 9, pp. 874-82, 1995.

[164]A. Leuprecht, K. Perktold, M. Prosi, T. Berk, W. Trubel, and H. Schima, "Numerical study of hemodynamics and wall mechanics in distal end-to-side anastomoses of bypass grafts," *Journal of Biomechanics*, vol. 35, pp. 225-236, 2002.

[165]S. Hyun, C. Kleinstreuer, and J. P. Archie, Jr., "Hemodynamics analyses of arterial expansions with implications to thrombosis and restenosis," *Med Eng Phys*, vol. 22, pp. 13-27, 2000.

[166]P. Hughes and T. How, "Effects of geometry and flow division on flow structures in models of the distal end-to-side anastomosis.," *J Biomech*, vol. 29, pp. 855-72, 1996.

[167]X.-M. Li and S. E. Rittgers, "Hemodynamic factors at the distal end-to-side anastomosis of a bypass graft with different POS:DOS ratios," *Proceedings of Summer ASME Bioengineering Conference*, vol. 42, pp. 225-226, 1999.

[168]K. Perktold, R. Peter, M. Resch, and G. Langs, "Pulsatile non-Newtonian blood flow in three-dimensional carotid bifurcation models: a numerical study of flow phenomena under different bifurcation angles.," *J Biomed Eng*, vol. 13, pp. 507-15, 1991.

[169]K. Perktold and G. Rappitsch, "Computer simulation of local blood flow and vessel mechanics in a compliant carotid artery bifurcation model.," *J Biomech*, vol. 28, pp. 845-56, 1995.

[170]P. B. Dobrin, "Mechanical Factors Associated with the Development of Intimal Hyperplasia with Respect to Vascular Grafts," in *Intimal Hyperplasia*, P. B. Dobrin, Ed. Austin: R.G. Landes Company, 1994, pp. 85-109.

[171]M. Kissin, N. Kansal, P. J. Pappas, D. O. DeFouw, W. N. Duran, and R. W. Hobson, 2nd, "Vein interposition cuffs decrease the intimal hyperplastic response of polytetrafluoroethylene bypass grafts," *J Vasc Surg*, vol. 31, pp. 69-83, 2000.

[172]A. Gnasso, C. Carallo, C. Irace, V. Spagnuolo, G. De Novara, P. L. Mattioli, and A. Pujia, "Association between intima-media thickness and wall shear stress in common carotid arteries in healthy male subjects," *Circulation*, vol. 94, pp. 3257-62, 1996.

[173]L. Kornet, J. Lambregts, A. P. Hoeks, and R. S. Reneman, "Differences in near-wall shear rate in the carotid artery within subjects are associated with different intima-media thicknesses," *Arteriosclerosis Thrombosis & Vascular Biology*, vol. 18, pp. 1877-84, 1998.

[174]H. Ishibashi, M. Sunamura, and T. Karino, "Flow patterns and preferred sites of intimal thickening in end-to-end anastomosed vessels," *Surgery*, vol. 117, pp. 409-20, 1995.

[175]R. S. Keynton, M. M. Evancho, R. L. Sims, and S. E. Rittgers, "The effect of graft caliber upon wall shear within in vivo distal vascular anastomoses," *J Biomech Eng*, vol. 121, pp. 79-88, 1999.

[176]F. Loth, S. Jones, C. Zarins, D. Giddens, R. Nassar, S. Glagov, and H. Bassiouny, "Relative Contribution of Wall Shear Stress and Injury in Experimental Intimal Thickening at PTFE End-to-Side Arterial Anastomoses," *Journal of Biomechanical Engineering*, vol. 124, pp. 44-51, 2002.

[177]B. S. Conklin, S. M. Suroqiec, P. H. Lin, and C. Chen, "A simple physiologic pulsatile perfusion system for the study of intact vascular tissue," *Medical Engineering & Physics*, vol. 22, pp. 441-9, 2000.

[178]D. F. Del Rizzo, M. Moon, J. Werner, and P. Zahradka, "A novel organ culture method to study intimal hyperplasia at the site of a coronary artery bypass anastomosis," *Annals of Thoracic Surgery*, vol. 71, pp. 1273-9; discussion 1279-80, 2001.

[179]J. L. Devore, *Probability and Statistics for Engineering and the Sciences*, 4th ed. Belmont: Druxbury Press, 1995.

[180]J. A. Madri and S. K. Williams, "Capillary endothelial cell cultures: phenotypic modulation by matrix components," *Journal of Cell Biology*, vol. 97, pp. 153-65, 1983.

[181]A. Merrick, L. Shewring, S. Cunningham, K. Gustafsson, and J. Fabre, "Organ culture of arteries for experimental studies of vascular endothelium in situ.," *Transpl Immunol*, vol. 5, pp. 3-9, 1997.

[182]T. Ziegler, R. W. Alexander, and R. M. Nerem, "An endothelial cell-smooth muscle cell co-culture model for use in the investigation of flow effects on vascular biology," *Annals of Biomedical Engineering*, vol. 23, pp. 216-25, 1995.

[183]R. M. Nerem, R. W. Alexander, D. C. Chappell, R. M. Medford, S. E. Varner, and W. R. Taylor, "The study of the influence of flow on vascular endothelial biology," *Am J Med Sci*, vol. 316, pp. 169-75, 1998.

[184]S. W. Galt, R. M. Zwolak, R. J. Wagner, and J. J. Gilbertson, "Differential response of arteries and vein grafts to blood flow reduction," *J Vasc Surg*, vol. 17, pp. 563-70, 1993.

[185]W. Du, I. Mills, and B. E. Sumpio, "Cyclic strain causes heterogeneous induction of transcription factors, AP-1, CRE binding protein and NF-kB, in endothelial cells: species and vascular bed diversity," *Journal of Biomechanics*, vol. 28, pp. 1485-91, 1995.

[186]M. Ojha, R. Cobbold, and K. Johnston, "Influence of angle on wall shear stress distribution for an end-to-side anastomosis.," *J Vasc Surg*, vol. 19, pp. 1067-73, 1994.

[187]L. Zhang, M. Moskovitz, S. Piscatelli, M. T. Longaker, and J. W. Siebert, "Hemodynamic study of different angled end-to-side anastomoses," *Microsurgery*, vol. 16, pp. 114-7, 1995.

[188]R. S. Keynton, S. E. Rittgers, and M. C. Shu, "The effect of angle and flow rate upon hemodynamics in distal vascular graft anastomoses: an in vitro model study," *Journal Of Biomechanical Engineering*, vol. 113, pp. 458-63, 1991.

[189]Z. S. Jackson, H. Ishibashi, A. I. Gotlieb, and B. L. Langille, "Effects of anastomotic angle on vascular tissue responses at end-to-side arterial grafts," *Journal of Vascular Surgery*, vol. 34, pp. 300-7, 2001.

[190]N. Kipshidze, E. Keane, D. Stein, P. Chawla, V. Skrinska, L. R. Shankar, A. Khanna, R. Komorowski, C. Haudenschild, P. Iversen, M. B. Leon, M. H. Keelan, and J. Moses, "Local delivery of c-myc neutrally charged antisense oligonucleotides with transport catheter inhibits myointimal hyperplasia and positively affects vascular remodeling in the rabbit balloon injury model," *Catheterization & Cardiovascular Interventions*, vol. 54, pp. 247-56, 2001.

[191]N. H. Senden, T. M. Jeunhomme, J. W. Heemskerk, R. Wagenvoord, C. van't Veer, H. C. Hemker, and W. A. Buurman, "Factor Xa induces cytokine production and expression of adhesion molecules by human umbilical vein endothelial cells," *Journal of Immunology*, vol. 161, pp. 4318-24, 1998.

[192]C. Monaco, E. Andreakos, S. Young, M. Feldmann, and E. Paleolog, "T cell-mediated signaling to vascular endothelium: induction of cytokines, chemokines, and tissue factor," *Journal of Leukocyte Biology*, vol. 71, pp. 659-68, 2002.

[193]D. Chen, K. Riesbeck, J. H. McVey, G. Kemball-Cook, E. G. Tuddenham, R. I. Lechler, and A. Dorling, "Human thrombin and FXa mediate porcine endothelial cell activation; modulation by expression of TFPI-CD4 and hirudin-CD4 fusion proteins," *Xenotransplantation*, vol. 8, pp. 258-65, 2001.

[194]M. B. Taubman, P. L. Giesen, A. D. Schecter, and Y. Nemerson, "Regulation of the procoagulant response to arterial injury," *Thrombosis & Haemostasis*, vol. 82, pp. 801-5, 1999.

[195]G. P. Gasic, C. P. Arenas, T. B. Gasic, and G. J. Gasic, "Coagulation factors X, Xa, and protein S as potent mitogens of cultured aortic smooth muscle cells," *Proceedings of the National Academy of Sciences of the United States of America*, vol. 89, pp. 2317-20, 1992.

[196]S. P. Bydlowski, M. M. Pares, R. P. Soares, and A. A. Lopes, "Stimulation of human smooth muscle cell proliferation by thrombin involves increased synthesis of platelet-derived growth factor," *Chest*, vol. 114, pp. 236-40, 1998.

[197]A. A. Weber, T. P. Zucker, and K. Schror, "Platelet surface membranes are highly mitogenic for coronary artery smooth muscle cells--A novel mechanism for sustained proliferation after vessel injury?," *Biochemical & Biophysical Research Communications*, vol. 259, pp. 341-3, 1999.

[198]E. Bretschneider, M. Braun, A. Fischer, M. Wittpoth, E. Glusa, and K. Schror, "Factor Xa acts as a PDGF-independent mitogen in human vascular smooth muscle cells," *Thrombosis & Haemostasis*, vol. 84, pp. 499-505, 2000.

[199]K. Thompson and M. Rabinovitch, "Exogenous leukocyte and endogenous elastases can mediate mitogenic activity in pulmonary artery smooth muscle cells by release of extracellular-matrix bound basic fibroblast growth factor," *Journal of Cellular Physiology*, vol. 166, pp. 495-505, 1996.

[200]N. M. Caplice, C. N. Aroney, J. H. Bett, J. Cameron, J. H. Campbell, N. Hoffmann, P. T. McEniery, and M. J. West, "Growth factors released into the coronary circulation after vascular injury promote proliferation of human vascular smooth muscle cells in culture," *Journal of the American College of Cardiology*, vol. 29, pp. 1536-41, 1997.

[201]D. F. Bowen-Pope, R. Ross, and R. A. Seifert, "Locally acting growth factors for vascular smooth muscle cells: endogenous synthesis and release from platelets," *Circulation*, vol. 72, pp. 735-40, 1985.

[202]A. Koller, D. Sun, and G. Kaley, "Role of shear stress and endothelial prostaglandins in flow- and viscosity-induced dilation of arterioles in vitro," *Circ Res*, vol. 72, pp. 1276-84, 1993.

[203]A. R. Wechezak, D. E. Coan, R. F. Viggers, and L. R. Sauvage, "Dextran increases survival of subconfluent endothelial cells exposed to shear stress," *Am J Physiol*, vol. 264, pp. H520-5, 1993.

[204]K. M. Wieczorek, A. S. Brewer, and L. Myatt, "Shear stress may stimulate release and action of nitric oxide in the human fetal-placental vasculature," *Am J Obstet Gynecol*, vol. 173, pp. 708-13, 1995.

[205]A. Malek and S. Izumo, "Physiological fluid shear stress causes downregulation of endothelin-1 mRNA in bovine aortic endothelium," *American Journal of Physiology*, vol. 263, pp. C389-96, 1992.

[206]Y. Qiu and J. M. Tarbell, "Interaction between wall shear stress and circumferential strain affects endothelial cell biochemical production," *J Vasc Res* , vol. 37, pp. 147-57, 2000.

[207]M. A. Gimbrone, Jr., "Endothelial dysfunction, hemodynamic forces, and atherogenesis," *Annals of the New York Academy of Sciences*, vol. 902, pp. 230-9; discussion 239-40, 2000.

[208]S. Mohan, N. Mohan, and E. A. Sprague, "Differential activation of NF-kappa B in human aortic endothelial cells conditioned to specific flow environments," *American Journal of Physiology*, vol. 273, pp. C572-8, 1997.

[209]A. R. Brooks, P. I. Lelkes, and G. M. Rubanyi, "Gene expression profiling of human aortic endothelial cells exposed to disturbed flow and steady laminar flow," *Physiological Genomics*, vol. 9, pp. 27-41, 2002.

[210]M. Noris, M. Morigi, R. Donadelli, S. Aiello, M. Foppolo, M. Todeschini, S. Orisio, G. Remuzzi, and A. Remuzzi, "Nitric oxide synthesis by cultured endothelial cells is modulated by flow conditions," *Circulation Research*, vol. 76, pp. 536-43, 1995.

[211]R. Lum, L. Wiley, and A. Barakat, "Influence of different forms of fluid shear stress on vascular endothelial TGF-beta1 mRNA expression," *Int J Mol Med*, vol. 5, pp. 635-41, 2000.

[212]S. White, C. Zarins, D. Giddens, H. Bassiouny, F. Loth, S. Jones, and S. Glagov, "Hemodynamic patterns in two models of end-to-side vascular graft anastomoses: effects of pulsatility, flow division, Reynolds number, and hood length.," *J Biomech Eng*, vol. 115, pp. 104-11, 1993.

[213]A. Schretzenmayr, "Uber krelslaufregulatorische vorgange an den grossen arterien bei der muskelarbeit," *Pflugers Arch*, vol. 282, pp. 743-8, 1933.

[214]S. Rodbard, "Negative feedback mechanisms in the architecture and function of the connective and cardiovascular tissues," *Perspectives in Biology & Medicine*, vol. 13, pp. 507-27, 1970.

[215]R. Berguer, R. F. Higgins, and D. J. Reddy, "Intimal hyperplasia. An experimental study," *Archives of Surgery*, vol. 115, pp. 332-5, 1980.

[216]C. S. Shin, J. N. Hatem, and I. F. Abaci, "Effect of diminished distal blood flow on the morphologic changes in autogenous vein grafts," *Surgery, Gynecology & Obstetrics*, vol. 147, pp. 189-92, 1978.

[217]K. Morinaga, K. Okadome, M. Kuroki, T. Miyazaki, Y. Muto, and K. Inokuchi, "Effect of wall shear stress on intimal thickening of arterially transplanted autogenous veins in dogs," *Journal Of Vascular Surgery*, vol. 2, pp. 430-3, 1985.

[218]M. H. Friedman, O. J. Deters, C. B. Bargeron, G. M. Hutchins, and F. F. Mark, "Shear-dependent thickening of the human arterial intima," *Atherosclerosis*, vol. 60, pp. 161-71, 1986.

[219]F. M. White, *Fluid Mechanics,* 3rd ed. New York: McGraw-Hill, 1994.